Les interactions fluide/roche : des vitraux médiévaux à la séquestration géologique du CO2

Département Géosciences, Jérôme Sterpenich

To cite this version:

Département Géosciences, Jérôme Sterpenich. Les interactions fluide/roche : des vitraux médiévaux à la séquestration géologique du CO2. Géochimie. Université de Lorraine, 2011. <tel-01318158>

HAL Id: tel-01318158

https://hal.archives-ouvertes.fr/tel-01318158

Submitted on 19 May 2016

Ecole Doctorale Sciences et Ingénierie des Ressources,
Procédés, Produits et Environnement (RP2E)

Mémoire présenté en vue de l'obtention du diplôme

d'**H**abilitation à **D**iriger des **R**echerches

par

Jérôme STERPENICH

Les interactions fluide/roche : des vitraux médiévaux à la séquestration géologique du CO_2

Soutenu le 13 décembre 2011 devant le jury

Parrain	J. Pironon	Directeur de Recherche CNRS, UMR G2R, Nancy
Rapporteurs	P. Benezeth	Directeur de Recherche CNRS, UMR GET, Toulouse
	M. Dubois	Professeur, EA LGCgE, Lille
	J.-L. Crovisier	Directeur de Recherche CNRS, UMR LHyGeS, Strasbourg
Examinateurs	M. Azaroual	Chef de projets PhD, BRGM, Orléans
	D. Broseta	Professeur, LFCR, Pau
	P. De Donato	Directeur de Recherche CNRS, UMR LEM, Nancy
	F. Farges	Professeur, LMCM, Paris
	V. Lagneau	Maître de Recherche, Mines Paristech, Fontainebleau
	M. Vilasi	Professeur, IJL, Nancy

Département Géosciences

UMR CNRS 7566 G2R

à mes parents

à Lonnie

à sa maman

Remerciements

Pour débuter ce manuscrit, je tenais à remercier un ensemble de personnes que j'ai croisées et qui ont participé d'une façon ou d'une autre à la réalisation de mon métier d'enseignant-chercheur.

Je voudrais tout d'abord commencer les personnes qui ont accepté de juger de ma capacité (ou non) à diriger des recherches. **Pascale Benezeth** que je connais depuis mon implication dans les programmes ANR CO_2. Heureusement qu'elle était là pour nous dire que la Dawsonite n'était peut-être pas le minéral miracle que l'on attendait pour piéger notre CO_2 ! Merci à elle de bien vouloir accepter le travail de rapporteur de ce mémoire.

Jean-Louis Crovisier avait en 1998 accepté d'examiner mon travail de thèse. Je me souviens que Jean-Louis avait qualifié mon mémoire sur les vitraux de « cathédralesque » faisant référence à la taille du document… J'ai compris un peu plus tard sa remarque lorsque je me suis rendu compte qu'il avait lu la thèse dans son intégralité… Comment ça tout le monde le fait ? Je le remercie donc de bien vouloir juger mon travail 13 ans plus en s'attaquant à l'HDR! Mais j'ai fait plus court cette fois !

Michel Dubois est le troisième rapporteur de ce travail. Je suis flatté qu'il ait accepté cette tâche à plusieurs titres. D'une part car j'apprécie ses qualités humaines car c'est une personne avec qui le contact a été facile dès que je l'ai rencontré dans les années 1995 entre le CREGU et le CRPG. Enfin, ses qualités de géochimiste multitâche me laissent entendre qu'il aura un regard critique et constructif sur mon parcours.

J'ai connu **Daniel Broseta** également lors des réunions pour les projets ANR CO_2. Lorsque je lui ai demandé de bien vouloir participer à mon jury de HDR, il a accepté spontanément et j'en suis flatté. Daniel apportera son œil de physicien des fluides à ce travail où les propriétés des fluides doivent être connues d'un point de vue chimique mais également physique.

J'aurais dû travailler avec **François Farges** à l'issue de ma thèse sur les changements de spéciation de certains éléments lors de l'altération des verres, si ma mémoire est bonne. Le post-doc ne s'est pas fait et j'ai perdu l'opportunité de bénéficier de toute son expertise sur les techniques synchrotron, ce que je regrette vivement. François a accepté de juger ce travail qui est aujourd'hui quelque peu éloigné des thématiques qui nous réunissaient mais je serai attentif à son jugement concernant la démarche scientifique que je mène depuis la fin de ma thèse.

Philippe de Donato a vu mes premiers pas en recherche lorsque je venais le voir, lui et Odile, pour essayer de tirer quelque chose de me vitraux à l'aide de leurs outils Infrarouge. Malheureusement ces satanées laminations ont eu raison de nous ! Puis, quelques années plus tard, une thématique émergente à Nancy nous a de nouveaux réunis à travers les projets CO_2. Nous étions les deux coordinateurs nationaux géologues de projets ANR et nous en étions fiers je pense ! Ainsi nous avons partagé nos idées scientifiques, mais pas seulement, et nos points de vue souvent convergeaient. Je compte sur Philippe pour donner son sentiment sur le parcours et la carrière scientifique que j'ai tenté de bâtir depuis un peu plus d'une dizaine d'années. Merci Monsieur le Directeur !

Mohamed Azaroual est pour moi une personnalité que j'apprécie tant humainement que scientifiquement. Nous nous sommes aussi rencontrés à l'occasion des multiples réunions concernant les projets ANR CO_2. Je suis heureux qu'il ait accepté de juger ce travail. Son expertise touchant la géochimie des interactions fluide-roche me sera d'une aide précieuse pour affiner mes projets de recherche.

Vincent Lagneau fait lui aussi partie du récent monde du CO_2 ! Il a présidé le jury de thèse mon premier doctorant et à ce titre je me devais de le faire participer à mon jury d'HDR. Vincent est aussi une personne avec qui le courant passe bien, tant scientifiquement qu'humainement. Je ne désespère pas de venir dans son laboratoire pour parfaire ma connaissance de la modélisation chimie-transport.

Michel Vilasi est Professeur de chimie à Nancy. Je le connais depuis que je suis étudiant en second cycle, période qui m'a fait découvrir la chimie minérale, matière de prédilection pour moi. Michel est non seulement le représentant de l'UHP dans ce jury mais également pour moi le représentant des bons moments de mes années d'étude à la fac des sciences. Merci à lui pour sa bonne humeur constante et sa disponibilité pour juger ce travail.

Je termine ce tour du jury par **Jacques Pironon**. Il a accepté de parrainer cette habilitation et je l'en remercie vivement. En 2003, alors que je pensais que ma carrière de chercheur sur Nancy aurait du mal à s'envoler, Jacques m'a proposé de rejoindre le CREGU pour réaliser des études liées à la séquestration géologique du CO_2. Enthousiasmé par ce sujet, j'ai accepté mais il a fallu que j'attende plus d'un an avant de me plonger dans le sujet. Entre temps, j'ai tenté de modéliser une solution en équilibre avec les argilites du COX, j'ai fait de la TSR avec Laurent Richard et participé à la programmation d'un code thermodynamique avec Jean Dubessy ! Un post-doc enrichissant car me faisant toucher à des disciplines tous azimuts. Lorsque j'ai pu me plonger dans le CO_2 si je puis dire, j'ai rapidement pris goût au développement expérimental et, avec Jacques, nous avons conceptualisé dans le train Paris-Nancy, avant l'ère du TGV, quand les trajets duraient plus de 3 heures, quelques expériences originales dont les acronymes sont issus de notre jus de cerveau commun ! Aujourd'hui IMAGES, MIRAGES et COTAGES ont une renommée quasi internationale ! Merci donc à Jacques pour m'avoir confié ce sujet enrichissant et porteur et merci de m'avoir fait confiance, car sans cela, je ne serais sûrement pas en train de rédiger mon mémoire pour l'HDR.

Je voudrais continuer ces remerciements en citant mes premiers étudiants sans qui les laboratoires, sinon de ne pas exister, du moins seraient beaucoup moins vivants et animés. Merci donc à Foxy, l'aîné, le freeborder fou, Manu le COTAGEUR, Clément le Arcelo-gréseux et Mathieu le premier thésard tomographié ! Je tiens également à donner une mention toute particulière à Anne-Laure, ma seconde thésarde, qui m'a beaucoup fait évoluer dans ma compréhension de la condition humaine. Merci également à tous les étudiants et post-docs du labo, passés ou présents, pour leur bonne humeur : Stéphanie, Lucille, Willfried, Thomas, les Christophe, Aurélien, Vanessa, Apolline, Antonin Richardson, Jérôme, Hicham, et tous ceux que j'aurais pu oublier par mégarde.

La recherche serait pénible sans eux, je pense à tout notre personnel administratif et technique. Merci donc à Marie-Odile et Laurence, Patrick et Zyra de nous faciliter la vie. Une attention également pour M Schumacher pour ses conseils immobilo-financiers. Aurélien, le petit Randaïe, est le pilier indispensable de labo CO_2, épaulé par Gilles qui souvent par magie, nous trouve les solutions adéquates à nos problèmes expérimentaux. Un grand merci également à tout le personnel du SCMEM et en particulier à Sandrine, Jaafar, Olivier et Ludovic.

Merci à tous mes collègues et copains que je côtoie quotidiennement. De façon non exhaustive, je pense à Régine, la Régine, Anne-Sylvie et son Manu, Cécile qui a de très beaux cheveux, Alex mon co-thermo, Jean Coco, Laurent l'ancien et Laurent le nouveau, le VDH sorti de la montagne, Vincent et Laurence nos écolos adorés, Danièle ma chef Viterne, Anne ma sous-chef calcaire, Camille sans la Marie, Bernard le rois des récifs, Kiki la barbichette, Karine la cassoulette, et tous ceux qui par leur bonne humeur apportent à notre métier une ambiance dans laquelle il fait finalement bon de travailler. Comment pourrais-je oublier Cédric la carpette, Head of the Vanderstrum production ?

J’ai une pensée toute particulière et émue pour mes parents qui sont partis beaucoup trop tôt. Il va sans dire que je leur dois beaucoup et que j’avais encore beaucoup à partager avec eux.

Je voudrais terminer ces remerciements en pensant particulièrement aux deux personnes avec qui je partage tous les instants du quotidien. Il s’agit de Judith ma compagne depuis maintenant plus de 23 ans, et Lonnie notre fille adorée.

TABLE DES MATIERES

Synthèse des titres et travaux, des activités d'enseignement, d'administration, de valorisation et de transfert

1. Curriculum vitae

Jérôme STERPENICH
90 rue Pasteur
54220 MALZEVILLE
e-mail: jerome.sterpenich@g2r.uhp-nancy.fr

40 ans
Vie maritale, 1 enfant
Tel bureau 03 83 68 49 40
Tel portable 06 31 69 71 91

Maître de Conférences - Géochimiste Expérimentaliste

Formation

1998	**Docteur** de l'Université Henri Poincaré Nancy1, spécialité **Géosciences**	*(Mention TH et Félicitations du Jury)*
1994	**DEA Géosciences** CRPG-CNRS (Vandœuvre)	*(Mention B)*
1993	**Maîtrise** de **Physico-Chimie des Minéraux et Matériaux Naturels à Finalité Industrielle**	*(Mention AB)*
1992	Licence de Physico-Chimie des Minéraux et Matériaux Naturels à Finalité Industrielle	*(Mention AB)*
1991	**DEUG** A **Physique Chimie Informatique**	
1989	Baccalauréat **C**	

Expérience professionnelle

depuis sept. 05	**Maître de conférences,** Nancy-Université, UHP, Département Géosciences, UMR G2R-CREGU Géologie et Gestion des Ressources Minérales et Energétiques.
janv.-août 05	**Ingénieur de recherche** à l'UMR G2R : **modélisation géochimique de la séquestration du CO_2** en aquifères salins (mi-temps).
juillet 03-déc 04	**Chargé de recherche** au CREGU-UMR G2R : **interactions fluide-roche, thermodynamique des équilibres liquide-gaz, géochimie** (mi-temps).
mai-oct. 2002	**Post-doctorant** au CRPG sur les **mécanismes de formation des gels issus de l'altération des verres** (mi-temps).
2002-2005	**Secrétaire scientifique** du Comité Local d'Information et de Suivi (**CLIS**) du **laboratoire de recherche de Bure** la gestion des **déchets radioactifs** (mi-temps).
mars-déc. 2001:	**Ingénieur de recherche** contractuel du CNRS : Etude des mécanismes **d'altération des verres** de confinement par **traçage isotopique**, en collaboration avec **EDF** et le **CEA**.

août-déc. 2000	Développement d'un projet de **création d'un bureau d'études en Eaux-Déchets-Environnement : Lauréat du Prix pour la Création d'Entreprises de Technologies Innovantes 2001** dans la phase "projet en émergence"
juin-juil 2000	**Ingénieur de Recherche** contractuel du CNRS dans le cadre d'une **expertise pour GDF**
oct-déc.1999	**Formateur** en Bureautique chez LORINFO (Nancy)
1997-1999	**Attaché Temporaire d'Enseignement et de Recherche** (**Thermodynamique, Déchets et Environnement, Géologie**) à l'Université Henri Poincaré Nancy1
1994-1998	Thèse de Doctorat. Etude de **l'altération** des **vitraux médiévaux**. Contribution au comportement à long terme des **verres de confinement** (CRPG-CNRS Vandœuvre)

Formations spécifiques

2006	**Sauveteur Secouriste du Travail**
2006	**Manipulation des gaz**
2006	**Systèmes d'Informations Géographiques.**

2. Notice de Titres et Travaux

Lauréat du Prix Jean Goguel 2001 décerné par l'Association Internationale de Géologie de l'Ingénieur et de l'Environnement pour mon travail sur la cristallochimie des produits d'altération des vitraux médiévaux et son application au vieillissement des déchets vitrifiés.

Articles:

1. Libourel, G., Verney-Carron, A., Morlok, A., Gin, S., Sterpenich, J., Michelin, A., Neff, D., Dillmann, P. (2011). The use of natural and archeological analogues for understanding the long-term behavior of nuclear glasses. *Comptes Rendus Geoscience* **343**, 237-245.
2. Valle, N. Verney-Carron, A., Sterpenich, J. Libourel, G. Deloule, E. Jollivet, P (2010). Elemental and isotopic (29Si and 18O) tracing of glass alteration mechanisms. *Geochimica et Cosmochimica Acta.* , **74** (12) 3412-3431.
3. Sterpenich, J., Sausse, J., Pironon, J., Géhin, A., Hubert, G., Perfetti, E.,Grgic, D., (2009) Experimental ageing of oolitic limestones under CO_2 storage conditions: Petrographical and chemical evidence. *Chemical Geology*, **265**(1-2): 99-112.
4. Sterpenich J, (2008): Crystal-chemistry of alteration products of vitrified wastes: implications on the retention of polluting elements. *Waste Management* , **28**, 120-132
5. Sterpenich J., Libourel G. (2007) Evidence of water diffusion in silicate glasses under natural weathering conditions given by buried medieval stained-glasses. *Journal of Non-Crystalline Solids,* **352**, 5446-5451
6. Dubessy J, Tarantola A., Sterpenich J. (2005). Modelling of liquid-vapour equilibria in the system H_2O-CO_2-NaCl and H_2O-H_2S-NaCl systems to 270°C. *Oil & Gas Science and Technology,* **60**(2): 339-355.
7. Richard L, Neuville N, Sterpenich J, Perfetti E, Lacharpagne JC. (2005) Thermodynamic analysis of organic/inorganic reactions involving sulfur : implications for the sequestration of H_2S in carbonate reservoirs. *Oil & Gas Science and Technology,* **60**(2), 275-285.
8. Sterpenich J (2002) Cristallochimie des produits d'altération des vitraux médiévaux: application au vieillissement des déchets vitrifiés. Crystal chemistry of alteration products of medieval stained-glass windows: application to the ageing of vitrified wastes. *Bull Eng Geol Environ,* **61**, *179-193* **DOI** *10.1007/s10064-001-0150-1*
9. Sterpenich J, Libourel G (2001) Using stained glass windows to understand the durability of toxic waste matrices. *Chemical Geology,* **174**, 181-193.
10. Sterpenich J, Libourel G (1997) Les vitraux médiévaux: caractérisation physico-chimique de l'altération. *Techne (Laboratoire de Recherche des Musées de France),* **6**, 70-78.

Chapitre d'ouvrage

1. Renard, S. Sterpenich, J., Pironon, J., Randi, A. Chiquet, P. Lescanne, M. (2011). Impact of SO_2 and NO on carbonated rocks submitted to a geological storage of CO_2: an experimental study. In: Y.W.a.J.J. Carroll (Editor), Acid Gas Injection and Related Technologies. Advances in Natural Gas Engineering. 377-392. Scrivener publishing, Calgary AB Canada.

Articles en préparation

Les articles suivants sont en cours de rédaction, certains sont soumis ou en cours de soumission. Le nombre important de papiers en phase de finition est lié aux contraintes expérimentales qui ont conduit à l'obtention quasi-simultanée de résultats issus des différentes expériences développées ces cinq dernières années.

1. Jobard, E., Sterpenich, J., Pironon, J., Corvisier, J., Jouanny, M., Randi, A. Experimental modelling of the impact of thermal gradient during geological equestration of CO_2 s: the COTAGES experiment. **Soumis** à *Journal of Greenhouse Gas Control*.
2. Renard, S., Pironon, J., Sterpenich, J., Lescanne, M. Chiquet, P. Geological storage of CO_2 in the Rousse reservoir (France). Part.1 : Reconstruction of geochemical history from mineralogy and fluid analysis in reservoir and caprock. **Soumis** à *Marine and Petroleum Geology*.
3. Caumon, M.-C., Sterpenich, J., Pironon, J., Randi, A, In situ measurement of CO_2 solubility in water using Raman spectroscopy. A soumettre.
4. El Hajj, H., Sterpenich, J., Pironon, J., Jobard, E., Randi, A, Simulated experiment of deep geologic sequestration of carbon dioxide to study the interaction of CO_2 with the reservoir materials. A soumettre à *Chemical Geology*.
5. Renard, S., Sterpenich, J., Pironon, J., Lescanne, M. Chiquet, P. Randi, A. Geochemical study of the rock reactivity in a geological storage of CO_2: implications of co-injected gases. A soumettre à *Geochimica et Cosmochimica Acta*.
6. Sterpenich, J., El Hajj, H., Pironon, J., Jobard, E., Garaffa, L.H., Piquet, G., Rives D., Randi, A. Experimental ageing of cement/rock interface under CO_2 storage conditions. Implications on wells durability. A soumettre à *Chemical Geology*.

Résumés étendus

1. de Donato, P., Pironon, J., Sterpenich, J., Laurent, A., Piedevache, M., Pokryszka, Z., Quisel, N., Barrès, O., Thomas, S., Rampnoux, N., (2011). CO_2 flow baseline: Key factors of the geochemical monitoring program of future CO_2 storage at claye-souilly (Paris basin). *Energy Procedia* **4**, 5438-5446.
2. Renard, S., Sterpenich, J., Pironon, J., Chiquet, P., Lescanne, M., Randi, A. (2011). Geochemical study of the reactivity of a carbonate rock in a geological storage of CO_2 : Implications of co-injected gases. *Energy Procedia* **4**, 5364-5369.
3. Sterpenich J., Renard S, Pironon J. (2006). Reactivity of French Triassic sandstones submitted to CO2 under deep geological storage conditions. *8th International Conference on Greenhouse Gas Control Technologies - GHGT8*, Trondheim, Norway.
4. Sterpenich J, Libourel G. (1998) Crystal-chemistry of alteration products of medieval stained-glasses - In VM Goldschmidt Conference, Toulouse, August 30- September 3, 1998, *Mineralogical Magazine*; **62A**; 1456-1457.
5. Barbey P, Sterpenich J, Libourel G (1996) Altération des vitraux : produits d'altération, états d'oxydation du manganèse, effets des traitements de surface. In : *2ème Colloque du Programme Franco-Allemand de Recherche pour la conservation des Monuments historiques*, Bonn, 12-13 décembre 1996, 61-71.
6. Sterpenich J, Le Forestier L, Libourel G (1995) Ageing of vitrified wastes : an experimental and analogical approach. In : *International Symposium on Environmental Technologies : Plasma Systems and Applications*, Atlanta, USA, October 8-11, 1995, Georgia Institute of Technology, 173-181.
7. Sterpenich J, Le Forestier L, Libourel G (1995) Durability of vitrified wastes as deduced from an experimental and analogical approach. In : *Congrès International sur les Procédés de Solidification et de Stabilisation des Déchets,* Nancy, 28 novembre - 01/12/1995, Cases J, Thomas F (Eds), 444-449.
8. Bottero J-Y, Chatelet L, Le Forestier L, Sterpenich J, Libourel G, Brown W, Yvon J, Bigois M, Remontet S, Olle M, Mosnier F, Bouchelagem A (1995) Les déchets ultimes inertes peuvent-ils devenir des matériaux utiles? In : *Congrès International sur les Procédés de Solidification et de Stabilisation des Déchets*, Nancy, 28 novembre - 01/12/1995, Cases J, Thomas F (Eds), 436-443.
9. Sterpenich J, Le Forestier L, Libourel G (1995) Les vitraux médiévaux : un modèle pour le vieillissement des déchets vitrifiés. In : *Actes du Premier Symposium International "Inertage et Valorisation des déchets ultimes"*, Bordeaux, 12-14 septembre 1995, Université Bordeaux 1, 2-9.
10. Sterpenich J, Le Forestier L, Libourel G, Chaussidon M, Barbey P (1994) - Medieval stained glass: a model for leaching of vitrified wastes - In: VM Goldschmidt Conference, Edinburgh, 29 August-2 September 1994. *Mineralogical Magazine*, **58A**, 877-878.

Autres articles

1. Sterpenich J, Libourel G (2001) Mediaeval Stained Glass Windows: a Physical and Chemical Characterisation of Alteration. In: Sciences and technologies of the materials and the environment for the protection of stained-glass and stone monuments. *Research report n°14, European Commission*, Paris 7 –18 sept. 1998, Roger-Alexandre Lefèvre Ed.
2. Libourel G, Sterpenich J, Barbey P, Chaussidon M (1998) La matériau vitreux: verre et vitraux. In: *Cours Intensif Européen*, Ravello, 28-30 avril 1995, Lefèvre R.A., Pallot-Frossard I. (eds), Edipuglia, Bari, 75-89.
3. Sterpenich J, Libourel G, Le Forestier L, (1994) Les vitraux médiévaux: un modèle pour le vieillissement des déchets vitrifiés, In: *Décision Environnement, Cahier Technique*, Septembre 94 (n°**29**), 5-6.

Mémoires

1. Sterpenich, J., (2010). Alteration Des Vitraux Medievaux, Editions Universitaires Europeennes ed, 456 p.
2. Sterpenich J., (1998) Altération des vitraux médiévaux. Contribution à l'étude du comportement à long terme des verres de confinement. Thèse de l'Université Henri Poincaré, Nancy 1; 461 p.
3. Sterpenich J, (1994) Etude de l'altération des vitraux des cathédrales médiévales : un modèle pour le vieillissement des matrices vitreuses. Mémoire de DEA. Université Henri Poincaré Nancy 1 et CRPG, 29p.
4. Sterpenich J. (1992) Suivi de la corrosion des tôles "sandwich" par mesures d'impédances électrochimiques. Mémoire de Maîtrise au LEDEPP (Laboratoire d'Etude et Développement des Produits Plats) de SOLLAC

Rapports

1. Sterpenich J, Pironon J et Oukili J (mars 2005) Rapport BQR-UHP. Recensement des réservoirs géologiques aptes à séquestrer le CO_2 anthropique en Lorraine et simulation de leur comportement à long terme (32p).
2. Richard L, Sterpenich J. (2004) Rapport à Total. Réduction thermochimique des sulfates. Développement d'un modèle réactionnel quantitatif (32p + annexes).
3. Dubessy J, Tarantola A, Sterpenich J. (2003) Modélisation des équilibres liquide-vapeur dans le système H_2O-CO_2-H_2S-NaCl Contrat TOTAL DGEP/TDO/CA/ACOMS CT n° 13162 A1.
4. Sterpenich J Rapport au CEA (nov. 2002): Etude de la diffusion du silicium dans les gels d'altération du verre ternaire Si, B, Na de référence CJ1 (19p).
5. Sterpenich J Rapport au CEMAGREF (nov. 2001): Analyse et caractérisation des principales phases minérales contenues dans un dépôt colmatant de Caracas par sonde électronique et diffraction des rayons X (26p).
6. Sterpenich J Rapport au CEMAGREF (sept. 2001): Analyse et caractérisation des principales phases minérales contenues dans un dépôt colmatant d'Aboncourt (A2) par sonde électronique (20p).
7. Sterpenich J Rapport à GDF (juillet 2000) Analyse et caractérisation d'espèces soufrées dans des échantillons de la série salifère d'Etrez aux fins d'amélioration de la connaissance de leur genèse. Comparaison avec les produits issus de la corrosion du saumoduc d'Etrez, (48p).
8. Sterpenich J, Libourel G, Barbey P et Chaussidon M (1998) Processus d'altération des verres des vitraux anciens et nature de la zone perturbée. Rapport au Ministère de la Culture et de la Francophonie, septembre 1998, 139 p.
9. Sterpenich J. Rapports d'avancement des travaux de thèse à l'ADEME:

- Rapport juin 1995, 29p.
- Rapport décembre 1995, 27p.
- Rapport décembre 1996, 31p.

10. Sterpenich J. Programme de Recherche "Analyse et inertage des déchets ultimes" CNRS-SITA-Ecotech Rapport d'activité pour la période juin 1994-mars 1995 (19p).

Résumés ayant fait l'objet d'une présentation orale (l'orateur est souligné):

Congrès internationaux:

1. Renard, S. Sterpenich, J., Pironon, J., Randi, A. Chiquet, P. Lescanne, M. (2010). Impact of SO_2 and NO on carbonated rocks submitted to a geological storage of CO2: an experimental study. *International Acid Gas Injection Symposium AGIS 2010*, Sept. 28-29th, 2010, Calgary AB Canada
2. Sterpenich, J., (2010). Rôle des gaz annexes sur l'injection de CO2. In: ANR-BRGM (Editor), Colloque *franco-espagnol et séminaire d'avancement ANR des projets sur le stockage géologique de* CO_2, 22-24 novembre 2010, Pau
3. Sterpenich, J., Pironon, J., Sausse, J. and Randi, A. (2010) Experimental Simulation of Mass Transfer During Limestone Alteration Submitted to a Gradient of Temperature and a High CO_2 Pressure: the COTAGES Experiment. *World Geothermal Congress WGC 2010* Bali, Indonésie.
4. Renard, S., Sterpenich, J.,Pironon, J. (2009). Reactivity of rock and well in a geological storage of CO_2 : role of co-injected gases. *EGU General Assembly 2009*, Vienne, pp. EGU2009-4859.
5. Sterpenich, J., Favre, E., Roizard, D., Jaubert, J.-N., Mutelet, F., Pironon, J., Dubessy, J., Renard, S., Henriot, A.-L., Lagneau, V., Richon, D., El-Ahmar, E., Lachet, V., Creton, B., Azaroual, M., Parmentier, M., Lescanne, M.,Mouronval, G. (2009). Experimental and numerical simulation of thermodynamic properties of water-salt-gas mixtures (CO_2 + co-contaminant) under geological storage conditions, *Les rencontres scientifiques de l'IFP - Deep Saline aquifers for Geological Storage of CO2 and Energy*, Rueil-Malmaison, France.
6. Sterpenich J, Lagneau V., Lachet V., Lescanne M., Azaroual M (2007). Experimental and numerical simulation of thermodynamic properties of water-salt-gas mixture (CO_2 + co-contaminant) under geological storage conditions. *French-German symposium on Geological Storage of* CO_2, 21-22/6/07, Potsdam, DE
7. Sterpenich J, Libourel G (1999) Kinetics of pollutant element release during glass alteration. *EUG 10*, Strasbourg, March 28th-April 1st, 1999, *Terra Nova*, **4** (1), p. 534.
8. Sterpenich J, Libourel G, Le Forestier L (1997) Characterisation of aqueous corrosion of glasses: implications on durability of vitrified wastes. *EUG 9*, Strasbourg, 23-27 March 1997, Terra Nova, suppl.1, p. 638.
9. Le Forestier L, Libourel G, Sterpenich J. (1997) From household refuse to vitrified wastes. In : *IXth Meeting of European Union of Geosciences (EUG 9)*, Strasbourg, 23-27 March 1997, Terra Nova, suppl.1, p. 287.
10. Sterpenich J, Libourel G, Le Forestier L (1997) Ion microprobe applications in trace element mobility during glass alteration. The example of medieval stained glasses. In : *Colloque inaugural de la sonde ionique IMS 1270*, Nancy, 27-28 Novembre 1997.
11. Sterpenich J, Le Forestier L, Libourel G (1995) Ageing of vitrified wastes : an experimental and analogical approach. In : *International Symposium on Environmental Technologies: Plasma Systems and Applications, Atlanta, USA*, October 8-11, 1995, Georgia Institute of Technology, 173-181. Libourel G, Le Forestier L, Sterpenich J. (1995) Leaching experiments on ultimate waste glasses. In : *International Symposium on Environmental Technologies* - Plasma Systems, GEORGIA TECH, USA, October 8-11, 1995.
12. Sterpenich J, Libourel G (1995) Durability of vitrified wastes as deduced from the study of medieval stained glasses. In: *Vth Silicate Melt Workshop*, La Petite Pierre, 4-8 avril 1995.
13. Sterpenich J, Le Forestier L, Libourel G (1995) Durability of vitrified wastes as deduced from an experimental and analogical approach. In: *Congrès International des Procédés de Solidification et de Stabilisation des déchets*, Nancy, 28 novembre-1 décembre 1995.

14. Sterpenich J, Le Forestier L, Libourel G, Chaussidon M, Barbey P (1994) - Medieval stained glass: a model for leaching of vitrified wastes. In: *VM Goldschmidt Conference, Edinburgh*, 29 August-2 September 1994. *Mineralogical Magazine*, **58A**, 877-878.

Congrès nationaux

1. Sterpenich, J. (2007) GAZ-ANNEXES : Rôle des gaz annexes sur l'injection du CO_2 : simulation des propriétés thermodynamiques des mélanges eau-gaz-sels en conditions de stockage géologique. Séminaire ANR Captage et stockage du CO2 Pau, Palais Beaumont 12-13 décembre 2007.

2. Valle, N., Sterpenich, J., Deloule, E., Libourel, G. (2001) Traçage isotopique (^{29}Si et ^{18}O) des mécanismes de l'altération du verre de confinement des déchets nucléaires SON68. GdR Nomade, Méjannes-le-Clap, Octobre 2001.

3. Sterpenich J, Le Forestier L, Libourel G (1996) Altération expérimentale de déchets ménagers vitrifiés et analogues naturels. *16e Réunion des Sciences de la Terre (RST)*, Orléans, 10-12 Avril 1996, Abstracts, p. 172.

4. Sterpenich J, Le Forestier L, Libourel G, Barbey P, Chaussidon M (1994) Altération des vitraux médiévaux: un modèle pour le vieillissement des verres d'inertage., *15e Réunion des Sciences de la Terre (RST)*, Nancy, 26-28 avril 1994, Abs., p. 119.

Résumés ayant fait l'objet d'un poster

1. Sterpenich, J. et al., (2010). Experimental and numerical simulation of thermodynamic properties of water-salt-gas mixtures (CO_2 + co-contaminant) under geological storage conditions, *GHGT10, RAI, Amsterdam, The Netherlands*. 19th-23rd September 2010
2. Corvisier, J., Jobard, E., Randi, A., Lagneau, V., Sterpenich, J., Pironon, J. (2010). Both experimental study and numerical modelling of the effect of temperature gradient on CO2 injection. American Geophysical Union, Fall Meeting 2010.
3. Renard, S., Sterpenich, J., Pironon, J., Chiquet, P., Lescanne, M., Randi, A., (2010). Geochemical study of the reactivity of a carbonate rock in a geological storage of CO_2 : Implications of co-injected gases. *GHGT10, RAI, Amsterdam, The Netherlands*. 19th-23rd September 2010.
4. de Donato, P., Pironon, J., Sterpenich, J., Laurent, A., Piedevache, M., Pokryszka, Z., Quisel, N., Barrès, O., Thomas, S., Rampnoux, N., (2010). CO_2 flow baseline: Key factors of the geochemical monitoring program of future CO2 storage at Claye-Souilly (Paris basin). *GHGT10, RAI, Amsterdam, The Netherlands*. 19th-23rd September 2010
5. Sterpenich, J., Lagneau, V., Lachet, V., Lescanne, M. and Azaroual, M. (2007). Experimental and numerical simulation of thermodynamic properties of water-salt-gas mixture (CO_2 + co-contaminant) under geological storage conditions. In: L. Stroink (Editor), 1. French-German Symposium on Geological Storage of CO2. Science Report. Geotechnologien, Potsdam, pp. 189.
6. Pironon J., Sterpenich J., Gehin A., Perfetti E., Hubert G., Sausse J. (2007) Oolithic calcareous ageing in batch reactor in various CO_2 environments. *French-German symposium on Geological Storage of CO2*, 21-22/6/07, Potsdam, DE
7. Gigleux L., Cleymand F., Mézin A., Testu S.; Sterpenich J., George M. (2007) Controlled crack propagation in soda-lime glass by 4-points bending and Brazilian test. *ICG 2007, XXIst International Congress on Glass*, 1-6 july 1007, Strasbourg.

8. Sterpenich J., Renard S, Pironon J. (2006). Reactivity of French Triassic sandstones submitted to CO_2 under deep geological storage conditions. 8th International Conference on Greenhouse Gas Control Technologies - GHGT8, Trondheim, Norway.

9. Sterpenich J, Pironon J., Oukili J., Perfetti E., Richard L., Dubessy J., Malartre F., Fauvel P.J., Leroux J. (2005) CO_2 sequestration in Lorraine : evaluation of the sequestration potential of regional aquifers. Séminaire "Stockage Géologique des Gaz Acides" Pau, CSTJF du Groupe TOTAL, 31 mai-1er juin 2005.

10. Sterpenich J, Libourel G. (1998) Crystal-chemistry of alteration products of medieval stained-glasses - In *VM Goldschmidt Conference, Toulouse*, August 30- September 3, 1998, *Mineralogical Magazine*; **62A**; 1456-1457.

11. Sterpenich J, Libourel G, Le Forestier L (1996) Durability of vitrified wastes : an experimental approach in the leaching of glasses. In : "*Geochemistry of crustal fluids*", Symposium of the European Union, Seefeld, Austria, 6-11 December 1996.

12. Sterpenich J, Libourel G (1995) Ageing of vitrified wastes as deduced from the study of medieval stained glasses. In : *VM Goldschmidt Conference, University Park, PA,* May 24-26, 1995.

13. Sterpenich J, Le Forestier L, Libourel G, Chaussidon M (1995) The alteration of medieval stained glasses : a model for ageing of vitrified wastes. In : *VIIIth Meeting of European Union of Geosciences (EUG 8)*, Strasbourg, 9-13 April 1995, Abstracts, p. 21.

3. Présentation synthétique des activités d’enseignement

L’enseignement, une volonté depuis que je suis étudiant

Mes activités d’enseignement ont débuté lorsque j’étais étudiant en second cycle et que je dispensais des cours particuliers en mathématiques et en physique à des élèves de 3ème à Terminale. J’ai alors pris conscience que j’éprouvais beaucoup de satisfaction à transmettre et à faire partager mon savoir.

Au cours de ma thèse, j’ai eu la chance d’assurer des vacations à l’Ecole des Mines en Mastère en Maîtrise des déchets. J’ai pu ensuite occuper un poste d’ATER à l’UHP Nancy 1 pendant lequel j’ai été confronté à l’enseignement de matières nouvelles dont je n’étais pas spécialiste. J’ai pu ainsi me rendre compte que j’étais capable de préparer de nouveaux cours et de les enseigner. Le Département des Sciences de la Terre m’a alors renouvelé sa confiance en m’attribuant un poste ATER à temps plein pendant lequel j’ai dirigé les TD de thermodynamique en Licence Sciences de la Terre. A la fin de ce contrat, toujours attiré par la formation, j’ai occupé un poste de formateur en bureautique chez LORINFO. Après avoir tenté l’agrégation en Physico-chimie des procédés, je me suis dirigé à nouveau vers la recherche par l’intermédiaire de différents contrats et post-doctorats en essayant autant que possible de garder le lien avec l’enseignement. C’est ainsi que j’ai pu assurer des vacations dans différents cours spécialisés sur les verres et leur altération mais également participer aux TD de DEUG 1ère année.

Ci-après le détail des enseignements réalisés de 1996 à 2005, avant ma nomination en tant que Maître de Conférences (les volumes horaires sont indiqués en "équivalent TD").

Total : 300H équivalent TD (hors formation dans le privé) de 1996 à 2005

1996/97

Vacation à l'Ecole des Mines de Nancy

Intitulé du cours	Type	Diplôme	Heures
Traitement par vitrification et contrôle de stabilité	CM	Mastère en Maîtrise des Déchets	4H30

1997/98

Demi-poste d'ATER à la Faculté des Sciences, UHP Nancy 1

Intitulé du cours	Type	Diplôme	Heures
Stabilisation des déchets ultimes par vitrification	CM	DEUG 2eme année	3H
Gîtologie, hydrogéologie et hydrocarbures	TD	DEUG 1ere année	42H
Cartographie géologique	TP	DEUG 1ere année	49H

1998/99

Poste d'ATER à la Faculté des Sciences, UHP Nancy 1

Intitulé du cours	Type	Diplôme	Heures
La filière déchet	CM	DEUG 2eme année	4H30
Traitement par vitrification et contrôle de stabilité	CM	Mastère en Maîtrise des Déchets	4H30
Thermodynamique, thermochimie (solutions réelles et diagrammes de phases)	TD	Licence Sciences de la Terre	30H
Gîtologie, hydrogéologie, hydrocarbures	TD	DEUG 1ere année	50H
Cartographie	TP	DEUG 1ere année	69H

Octobre à décembre 1999

Formateur en informatique: Windows NT, Excel et Word

2000

Intervention dans le cadre de l'Ecole Européenne: Sciences and Materials of the Cultural Heritage

Intitulé du cours	Type	Diplôme	Heures
Soiling and weathering of glass and stained-glass windows	CM	Ecole Doctorale	3H

2001

Vacations à l'Ecole des Mines de Nancy

Intitulé du cours	Type	Diplôme	Heures
Traitement par vitrification et contrôle de stabilité	CM	Mastère en Maîtrise des Déchets	4H30

2002

Vacations à l'UHP Nancy 1

Intitulé du cours	Type	Diplôme	Heures
TD Pétrole et Gîtologie	TD	DEUG 1ere année	6H

Animation de formations au sein du Comité Local d'Information et de Suivi (CLIS) du laboratoire de Bure concernant les déchets nucléaires et leurs matériaux de confinement.

2002 à 2005

Vacations à l'Ecole du Génie de l'Eau et de l'Environnement de Strasbourg et à l'UHP Nancy 1

Intitulé du cours	Type	Diplôme	Heures
Vitrification des déchets et problèmes connexes	CM	Mastère en Maîtrise des Déchets	4H30 x4
Les verres	CM	Maîtrise Sciences de la Terre	3H x4

Participation à la formation des Maîtres Verriers sur le problème de la restauration des verres et vitraux en 2004.

Mes activités d'enseignement…

Depuis ma nomination en tant que Maître de Conférences au sein de la Faculté des Sciences et Technologies, dans le Département Géosciences, j'ai été amené à enseigner les disciplines de base de la géologie, en particulier au niveau licence 1ère année, mais j'ai aussi monté en parallèle des enseignements nouveaux afin de compléter l'offre de formation aux niveaux licence et master.

Ainsi, dès ma nomination, je me suis investi dans un cours dispensé en Licence 3ème année et Master 1ère année et basé sur les concepts des **Système d'Information Géographique**. Il s'agissait en particulier de former nos étudiants aux nouveaux outils de cartographie représentés par les logiciels SIG. Pour ceci, un enseignement CM-TD-TP a été développé. La partie cours est basée sur la géodésie et les fondements de l'utilisation des **SIG**. Une partie TD-TP conséquente permet aux étudiants de maîtriser l'outil informatique par l'intermédiaire d'exercices d'application liés à la problématique géologique. Un projet réalisé seul ou en binômes permet enfin à l'étudiant de répondre à une problématique ou à une question complexe en mettant en œuvre ses compétences géologiques, cartographiques et informatiques, tout en manipulant les concepts liés à la gestion de bases de données spatialisées. Les projets livrés aux étudiants concernent par exemple la problématique de l'emplacement d'un centre de stockage de déchets, la mise en place d'une exploitation minière ou d'une carrière ou tout simplement la réalisation numérique de leur carte de terrain.

Une double approche a été choisie pour l'enseignement des SIG : les étudiants de licence abordent l'utilisation d'un logiciel simple, gratuit, qu'ils peuvent s'approprier entièrement, le logiciel ILWIS. Les étudiants de Master, qui s'ouvrent à la fin de leur formation sur le monde du travail, se doivent de maîtriser un logiciel leader sur le marché, ARC GIS. La 1ère année de Master est dédiée à l'utilisation courante de bases de données géoréférencées. Les étudiants de Master 2 se voient en plus offrir une formation au traitement de données géostatistiques particulièrement utile pour les formations Sol-Eau-Environnement.

Concernant mon investissement dans la formation de 1ère année, j'ai également mise en place une série de CM et TD destinés aux étudiants de Licence 1 et destinée à leur montrer que la géologie s'intéressait tout particulièrement aux problèmes majeurs de société et touchant directement notre environnement. C'est ainsi que j'ai créé de nouveaux enseignements dédiés à la **séquestration géologique du CO_2**, à la **gestion des déchets nucléaires**, aux énergies renouvelables, en particulier la **géothermie** et à la problématique de la stabilisation des déchets par **vitrification**.

Suite au départ d'un collègue thermodynamicien et géochimiste, je me suis proposé pour la reprise d'un nombre important d'enseignements touchant aux disciplines de prédilection de mon collègue. Ainsi, je me suis investi dans les cours de **Thermodynamique** dispensés en

Licence 3 de Géosciences, dans les cours de **Géochimie** de Licence 2 et dans les cours sur les **Interactions fluide-roche** de Master 1.

Fort de mon expérience sur les matrices de confinement des déchets et de ma fonction de secrétaire scientifique du CLIS basée sur le suivi des études sur le stockage des déchets nucléaires, j'ai bâti une nouvelle Unité d'Enseignement en Master 2, dédiée totalement aux différentes formes de **stockage géologique**. Cette UE fait appel à un grand nombre de spécialistes des aspects du stockage, des matrices au monitoring de site en passant par la minéralogie des barrières de confinement. Cette UE s'appuie également sur des visites de site de stockage.

En résumé, j'interviens dans une quinzaine Unités d'Enseignement. J'ai animé un nombre important de matières différentes, allant de la géologie générale à des enseignements plus spécifiques tels que les mathématiques, la thermodynamique ou les Systèmes d'Information Géographique (SIG).

Je suis ou ai été responsable des Unités d'Enseignement suivantes dans la licence Terre et Environnement et dans le Master Géosciences

- LG2 15: Géochimie 2: géochimie avancée
- LG1.03: Géoinformatique et outils mathématiques
- LG3 07: Thermodynamique des processus magmatiques et métamorphiques
- M2 S9-71: Statistiques – Géostatistiques – Systèmes d'Informations Géographiques (SIG)
- M2 S9-24: Stockage géologique

Mes enseignements son très majoritairement réalisés au sein de la FST et du secteur PGCM. J'interviens ou suis intervenu cependant aussi dans le secteur STB, à l'antenne de Bar-le-Duc et à l'ENSG.

Je suis également **enseignant référent** depuis 2009-2010 en Licence 1 dans le cadre de la loi Hirsch.

Je participe régulièrement aux **jurys des soutenances** de stage des M1 GGC et M2 CGSE, des stages de recherche des 2A ENSG.

Je suis régulièrement **membre des jurys** de L2, L3, M1 et M2 du Département Géosciences

Bilan des services d'enseignement faits depuis ma nomination jusqu'à aujourd'hui

Année	Niveau Licence	Niveau Master	Total
2005/2006	**123.3**	**46.4**	**169.7**
2006/2007	**137.3**	**46.4**	**183.7**
2007/2008	**154**	**52**	**206**
2008/2009	**51.8**	**33**	**84.8***
2009/2010	**150**	**66.5**	**216.5**
2010/2011	**120**	**86**	**206**

* CRCT de 6 mois pour la période janvier-juillet 2009 accordé par l'UHP expliquant mon déficit d'heure sur la période 2008-2009.

4. Présentation synthétique des activités d'administration, de valorisation et de transfert

Responsabilités administratives

Les fonctions associées au poste d'enseignant-chercheur vont au-delà des missions d'enseignement et de recherche et doivent associer des prises de responsabilité, tant au niveau pédagogique, scientifique qu'administratif. Aussi, depuis le début de ma thèse, je me suis investi dès que cela m'était possible dans diverses tâches d'administration ou de gestion. J'ai débuté avec la présidence d'une association d'étudiant et mon poste de Secrétaire Scientifique m'a permis en particulier de m'essayer dans la gestion des conflits entre partis. Depuis ma nomination en tant que Maître de Conférences, je me suis investi dans la vie pédagogique du Département Géosciences en devant membre du Conseil de Département et en prenant la responsabilité d'un ensemble d'Unités d'Enseignement. Depuis 2008, je suis Conseiller Scientifique de l'Université et seul représentant des Maîtres de Conférences à son bureau. Plus récemment, j'ai été élu au conseil de secteur de la Faculté. J'ai pris en charge la responsabilité du laboratoire CO_2 attaché au laboratoire G2R et la co-responsabilité de la plate-forme de nanotomographie de la Fédération de Recherche Eau-Sol-Terre. A ce titre, je participe activement aux rédactions de projets de recherche nationaux et européens aussi bien qu'à la rédaction des appels d'offres et des cahiers des charges lors de l'acquisition d'équipements de recherche. Je suis également en charge de la coordination sur 4 ans d'un projet ANR regroupant 5 partenaires industriels, EPIC et académiques.

Ci-dessous sont listées mes différentes responsabilités de 1996 à aujourd'hui :

Responsabilités antérieures à ma nomination en tant que Maître de Conférences

- **Secrétaire scientifique** du Comité Local d'Information et de Suivi (CLIS) du laboratoire de Bure de 2002 à 2005: conseil technique, formation des membres (géologie, matériaux), rédaction de synthèses de rapports scientifiques, actions de communication, rôle de médiation
- Rédacteur des **appels d'offres** européens "Analyse critique du programme expérimental de l'ANDRA" et "**Géothermie**" pour le compte du CLIS (2003-2004)
- **Responsable** de 2 enquêtes pour le compte de la délégation régionale du CNRS: Bilan des recherches menées par les laboratoires publics lorrains sur les thèmes "déchets" et "eau" (2001)
- **Organisateur des séminaires** internes du laboratoire (CRPG) en 1995
- **Président** de l'ADEGE (Association des Etudiants en Géosciences de Nancy) en 1995
- **Trésorier** de l'ADEGE en 1996

Responsabilités depuis ma nomination en tant que Maître de Conférences

- **Conseiller Scientifique** de l'Université Henri Poincaré

- **Membre élu du bureau** du CS (2008-…)
- **Membre élu du secteur Physique-Géosciences-Chimie-Mécanique de l'UFR Faculté des Sciences et Technologies (2010-…)**
- **Régisseur secondaire** du Département Sciences de la Terre (2007-…)
- Membre élu du **Conseil du Département** Géosciences (2008-…)
- Membre nommé du **Conseil de Laboratoire** G2R (2009-…)
- Coordinateur national du projet ANR Gaz Annexes (2006-2011)
- Responsable scientifique pour le compte de l'université du projet ANR Interface
- Responsable du laboratoire CO_2
- Membre de la commission Géosciences suite à l'appel à projets Région 2009 et 2010

Les actions d'enseignement et de recherche doivent obligatoirement être complétées par des actions de valorisation et de transfert des métiers de la recherche. De mon point de vue, ces manifestations sont nécessaires pour donner le goût aux jeunes de s'orienter vers les métiers à haute valeur intellectuelle ajoutée. Si je débute toujours mes cours par une présentation de ma fonction, de mon métier et de mes actions en tant qu'enseignant et chercheur, je m'investis dès que possible pour faire connaître notre métier et le fruit de nos recherches, que ce soit lors de conférences invitées dans des lycées, de travaux pratiques en lycée, d'accueil de jeunes de collège dans le cadre de leur stage professionnalisant, ou tout simplement lors des journées portes-ouvertes ou de la Fête de la Science. Je décris ci-dessous quelques-unes des actions que j'ai réalisées ces dernières années.

Actions de valorisation et de transfert

Je participe et j'anime les stands du laboratoire ou du Département à la plupart des manifestations ouvertes au public : Fête de la Science, salon ORIACTION, journées portes ouvertes, Clés de la Réussite. En particulier nous avons organisé une visioconférence sur le thème du CO_2 en 2005. Des expériences pédagogiques sur l'effet de serre et le stockage géologique du CO_2 ont été développées.

Je participe aux actions menées dans les lycées et destinées à attirer les jeunes vers les métiers scientifiques :

- montage du projet AMICO (2007-2008) avec J. Pironon et en collaboration avec l'IUFM (A-S. André) : il s'agit de faire travailler deux classes de seconde de deux lycées nancéiens sur le CO_2 et l'amiante et de concrétiser leurs recherches par une expérience au laboratoire destinée à inerter l'amiante par le dioxyde de carbone.
- conférence au lycée Cormontaigne (2008) de Metz pour sur le CO_2 et les métiers de la recherche aux élèves de première et terminales scientifiques.

- **conférencier invité** dans le cadre de la remise des Olympiades de géologie par le Recteur de l'Académie de Nancy-Metz (2009).
- conférencier invité au Lycée Bichat de Lunéville sur la séquestration géologique du CO_2 (Cordées de la réussite 2011)

5. Encadrements thèses, masters, stages recherche et post-doctorats

Post-doctorants

- Etude du vieillissement du calcaire du Lavoux en condition de stockage géologique du CO_2, projet IMAGES. Erwan Perfetti, post-doctorant, février-avril 2007. Encadrants : Jérôme Sterpenich et Jacques Pironon.
- Mise en place du projet MIRAGES sur l'injection de CO_2 en réservoir géologique. Aurélie Gehin, post-doctorante, avril 2007-mars 2008. Encadrants : Jérôme Sterpenich et Jacques Pironon.
- Etude de l’altération chimique et des propriétés pétrophysiques à l’interface roche/ciment dans le cadre du stockage géologique du CO_2. Jérôme Corvisier, post-doctorant, octobre 2009-mars 2010 (Encadrants: J. Pironon (50%) et J. Sterpenich (50%)). Financement projet ANR Interface
- Etude de l’altération chimique et des propriétés pétrophysiques à l’interface roche/ciment dans le cadre du stockage géologique du CO_2. Hicham El Hajj, post-doctorant, depuis janvier 2011 (Encadrants: J. Pironon (50%) et J. Sterpenich (50%)). Financement projet ANR Interface.

Thèses

- Rôle des gaz annexes sur l'évolution géochimique d'un site de stockage de dioxyde de carbone. Application à la région de Lacq. **Thèse** Stéphane Renard, **octobre 2006- juin 2010**. Encadrants : Jacques Pironon (50%) et Jérôme Sterpenich (50%). Financement: ADEME et TOTAL.
- Développement de la mesure in situ HT-HP des espèces gazeuses par sonde Raman. Applications à la séquestration géologique du CO_2 et des gaz annexes co-injectés. **Thèse** Anne-Laure Henriot, **octobre 2007-décembre 2009** (arrêt de la thèse pour cause de réorientation professionnelle). Encadrants : Jacques Pironon (50%) et Jérôme Sterpenich (50%). Financement : Projet ANR Gaz Annexes
- Modélisation expérimentale de l'altération du puits d'injection dans le cadre du stockage géologique du CO_2 : étude du point triple réservoir/couverture/ciment.

Thèse Emmanuel Jobard, **depuis octobre 2009**. (Encadrants: J. Pironon (50%) et J. Sterpenich (50%)).Financement Ministère et ANR Interface et Proche-Puits.

- Réactivité d'un mélange de gaz réduits sur la géochimie d'un grès rouge. Cas des grès du Trias lorrain soumis à une injection de CO_2. **Thèse** Clément Belogodère, depuis octobre 2010. (Encadrants: J. Pironon (50%) et J. Sterpenich (50%)).Financement ARCELORMITTAL.

Masters et stages écoles

- Séquestration du CO_2 dans des aquifères salins en Lorraine: étude minéralogique du grès à Roseaux et du grès à Voltzia et simulation de leur évolution après injection de CO_2, par Gaëlle Gravier et Stéphane Renard, Projet de laboratoire 3A ENSG Nancy, mai 2005. (Encadrants : J. Pironon (50%) et J. Sterpenich (50%)).
- Cartographie des émetteurs et réservoirs géologiques de CO_2 en Lorraine. Évaluation du potentiel de séquestration, par Julien Oukili Stage recherche 3A Ecoles des Mines de Nancy février 2005 (Encadrants: J. Pironon (50%) et J. Sterpenich (50%)).
- Couplage des modélisations expérimentales et numériques appliqué à la séquestration géologique du CO_2 dans les grès du Trias lorrain, par Stéphane Renard, Master 2, octobre 2005-juin 2006. Encadrants: Jacques Pironon (50%) et Jérôme Sterpenich (50%).
- Mise au point et calibrage de l'analyse Raman in situ des gaz dissous dans les eaux de formations géologiques. Sophie Declerq. Stage recherche 3A Ecoles des Mines de Nancy février 2009 (Encadrants: J. Pironon (50%) et J. Sterpenich (50%)).
- Modélisation expérimentale des interactions fluide-roche en atmosphère de CO_2: application à la zone proximale d'un puits d'injection d'un stockage géologique de CO_2. Stage laboratoire 2A ENSG mars-mai 2009. Laure-Hélène Garaffa, Grégoire Piquet, Diane Rives. Encadrants : Jacques Pironon (50%) et Jérôme Sterpenich (50%).
- Etude des équilibres métastables entre H_2S, les hydrocarbures et les composés organiques soufrés dans les systèmes pétroliers par Sébastien Gazet-Talvande (3A Ecole des Mines de Nancy) et Rakhim Uteyev (Master 2) 2006 - Encadrants : Laurent Richard (80%) et Jérôme Sterpenich (20%).

Participation à des jurys (thèse, master, ingénieur, thèse d’exercice,…)

J’ai participé au jury de thèse de Stéphane Renard en tant que co-directeur de thèse.

Rôle des gaz annexes sur l'évolution géochimique d'un site de stockage de dioxyde de carbone. Application à la région de Lacq. ***Thèse*** *Stéphane Renard ; Soutenance le 04 juin 2010 devant John Ludden (Executive Director BGS), Jacques Schott (DR LMTG), Jacques Pironon (DR G2R), Jérôme Sterpenich (MCF G2R), Vincent Lagneau (Maître de*

Recherche ParisTech), Mohamed Azaroual (BRGM), Nathalie Thybaud (ADEME) et Marc Lescanne (TOTAL).

En tant que responsable d'Unité d'Enseignement en Master 1 et master 2, je participe régulièrement aux jurys des stages de recherche des M1 GGC, M2 CGSE, 3A ENSG.

6. Rayonnement scientifique

Les articles scientifiques présentés dans ma notice de titres et travaux m'ont permis d'être régulièrement sollicité par des éditeurs de journaux scientifiques pour réaliser plusieurs reviews d'articles. J'ai également été contacté pour rendre des expertises sur des appels à projets nationaux ou de collaboration internationale. J'ai également pris la responsabilité scientifique de plusieurs projets ANR de grande ampleur dont un dont j'assure la coordination nationale. Ces travaux sont listés ci-dessous.

- **Coordinateur national** projet ANR Gaz Annexes (2006-2011)
- **Contrat industriel** avec Total pour l'étude des gaz co-injectés sur le site de Lacq
- Invitation en tant que coordinateur ANR à l'inauguration du premier site pilote d'injection de CO_2 à Lacq en présence de la Secrétaire d'Etat en charge des Technologies vertes et des négociations sur le climat, et de Christophe de Margerie, Directeur Général de Total, le 11 janvier 2010.
- **Chairman** au World Geothermal Congress WGC 2010 dans la session "Corrosion and Scaling 2: Calcite Well Scaling"
- **Conférencier invité** à l'Université de la Culture Permanente (UCP) sur les thèmes de la séquestration géologique du CO_2 et sur la gestion des déchets radioactifs.
- **Conférencier invité** lors de la Fête de la Science 2004 sur l'altération des vitraux médiévaux.
- **Membre du Comité de Sélection** (2010) pour le poste MCF Modélisation des interactions fluides-roches à l'UHP Nancy.
- Chercheur prometteur dans le cadre du dossier Labex Ressources21

Responsabilités scientifiques

- co-pilotage du projet BQR-UHP intitulé "*Recensement des réservoirs géologiques aptes à séquestrer le CO_2 anthropique en Lorraine et simulation de leur comportement à long terme*".

- responsable (avec J. Pironon) du volet géochimie du projet ANR Géocarbone Injectivité (2005-2008),
- membre du groupe **IMAGES** (Innovations pour la Maîtrise des Gaz à Effet de Serre) regroupant 7 laboratoires nancéiens autour du thème des gaz à effet de serre (G2R, LTMP, LSGC, LEMTA, LEM, LAEGO, CRPG).
- **coordinateur national du projet ANR "Gaz Annexes"** (2006-2011) (Rôle des gaz annexes sur l'injection du CO_2: simulation des propriétés thermodynamiques des mélanges eau-gaz-sels en conditions de stockage géologique) qui rassemble le groupement IMAGES (INPL), le groupe TOTAL, le BRGM, l'IFPEN et l'Ecole des Mines de Paris. (Budget global : 1M€ dont 340k€ d'aide au groupe IMAGES)
- **responsable des expériences** pour le projet ANR Proche-puits (2007-2011) piloté par le BRGM (partenaires BRGM, IFPEN, IMAGES, LFC, ITASCA, GDF, Schlumberger, Total)
- **responsable scientifique** pour Nancy Université et responsable de tâche du **projet ANR Interface** (2008-2012) (Comportement chimio-mécanique de l'interface ciment-couverture d'un puits en présence de (sc)CO_2 et gaz annexes) sur le stockage et le captage du CO_2 piloté par le BRGM (partenaires : IMAGES, UR Navier, Schlumberger; aide allouée au laboratoire G2R: 200k€).
- **membre du groupe de travail "géochimie appliquée au site de Lacq" de TOTAL** (G2R-CREGU, BRGM, IFPEN, TOTAL)
- partie prenante dans différents projets sur le CO_2 déposés au niveau national (appel à manifestation d'intérêt de l'ADEME avec Véolia, projet européen CO2SAFE, projet ARCELOR-Mittal)
- **responsable du laboratoire d'expérimentation sur le CO_2** du laboratoire G2R

Review articles scientifiques

- 2005 "Viscosity in ammonia acetate buffer solutions of glasses in the Al-Mo-P-O and Fe-Mo-P-O systems " pour *Journal of Non-Crystalline Solids*.
- 2006: sollicité pour la review du papier par Li et Duan "Speciation equilibrium in the H_2O-CO_2-NaCl system from 0 to 250 °C and from 0 to 1000 bar" pour *Geochimica et Cosmochimica Acta*.
- 2010: Shao, Hongbo; Ray, Jessica; Jun, Young-Shin "Effects of Salinity and the Extent of Water on Supercritical CO2-Induced Dissolution and Precipitation of Phlogopite" *Environmental Science & Technology*

Expertises projets de recherche

Mes travaux de recherche sur l'altération des verres m'ont également permis de participer à l'expertise commandée par le gouvernement Suisse à propos de la stabilisation des déchets ultimes par vitrification. "***MSW glasses: the opinion of selected experts***", rapport n°2 par Didier Perret (Université de Lausanne), Octobre 1998.

Je suis régulièrement sollicité pour des missions **d'expertise pour la DGRI**: évaluation de dossiers de coopération internationale avec la Croatie (juin 2008)+ et l'Inde (mars 2010).

Au sein du conseil scientifique, j'évalue régulièrement des dossiers concernant les prix de thèse ou de chercheur, les demandes de reclassement, les demandes de CRCT…

7. Collaborations

Lors de ma thèse est dans mes contrats post-doctoraux axés sur l'altération des verres, j'ai été amené à collaborer avec des partenaires privés, le groupe SITA-ex-Lyonnaise des Eaux qui a financé ma thèse et à qui je rendais régulièrement des comptes, et EDF dans le cadre de la durabilité des verres nucléaires. J'ai également été amené à collaborer très étroitement avec le CEA, l'équipe d'E. Vernaz et S. Gin, le Laboratoire de Recherche des Musées de France et le Laboratoire de Recherche des Monuments Historiques avec qui nous partagions un ensemble d'échantillons de vitraux, mes collègues archéologues de Marseille (D. Foy) et Rennes (Y. Le Maho), et bien sûr l'ADEME qui finançait ma thèse et était également financeur de mon premier thésard, S. Renard.

Ensuite, mes travaux de post-doctorat m'ont amené à diversifier mes collaborations en travaillant sur des problèmes de corrosion pour GDF, ou bien en aidant le CEMAGREF a comprendre l'origine minérale d'encroûtements dans leurs drains, ou en travaillant pour l'ANDRA sur les problématiques de composition des fluides interstitiels de l'argilite de Bure.

Puis la thématique séquestration du CO_2 m'a amené à ouvrir de façon importante mon champ de collaboration. Outre de travailler bien sûr depuis longtemps avec les laboratoires nancéens (CRPG, G2R, LEM, LAEGO, LEMTA), j'ai étendu le travail en commun avec d'autres laboratoires universitaires nancéens comme le LRGP (J-N Jaubert et F. Mutelet, E. Favre et D. Roizard), mais aussi palois (LFC, D. Broseta) et parisiens (ParisTech avec V. Lagneau et C. Coquelet). Une collaboration étroite a aussi été entreprise avec les équipes du BRGM (M. Azaroual) et de l'IFPEN (V. Lachet, T. Parra). Je n'oublie pas les collaborations fortes avec Total dans le cadre du projet pilote de Lacq (M. Lescanne, J. Hy-Billiot, P. Chiquet), et avec ArcelorMittal (J-P Birat) dans le cadre du projet de stockage lorrain lié à la sidérurgie et de la thèse de C. Belgodère. Il existe également un partenariat au travers des projets ANR avec Schlumberger (J. Desroches, B. Huet), l'UR Navier (J-M Perrera) et ITASCA. Je collabore également au projet de monitoring de site engagé par Véolia sur son site de Claye-Souilly.

Si cette liste n'est pas exhaustive, elle montre cependant que j'ai réussi lors de ces dernières années à établir un partenariat avec mes collègues des laboratoires académiques et des EPIC, ainsi qu'à obtenir la confiance des industriels en ayant la charge du pilotage scientifique de grands projets de recherche.

1. Bilan scientifique

Les recherches que j'ai menées lors ces dernières années sont centrées sur l'étude des systèmes "eau-solide minéral-gaz", en particulier sur la compréhension et la quantification des **interactions "solution aqueuse - solide minéral"**. Mes recherches ont débuté lors de mon stage de DEA au cours duquel j'ai pu décrire la minéralogie et la chimie de produits d'altération de verres silicatés anciens. Ce travail important pour la problématique de la restauration et de la conservation des vitraux médiévaux a ensuite été étendu à la thématique plus générale de la compréhension du comportement à long terme des verres dans une optique de confinement de déchets toxiques. Mes travaux de thèse ont ainsi permis de quantifier le comportement d'éléments nocifs pour l'environnement confinés dans une matrice vitreuse soumise à des conditions naturelles d'altération. Une implication fondamentale de cette étude a également été de démontrer que l'altération des verres silicatés résultait de processus complexes impliquant non seulement des mécanismes de dissolution sélective mais également des processus de dissolution-condensation au sein même des pellicules d'altération. Ce résultat majeur a permis d'orienter les travaux du laboratoire vers une nouvelle approche originale basée sur le traçage isotopique de l'altération des verres nucléaires. Outre leur implication environnementale, ces travaux permettent aujourd'hui de définir des lois de dissolution des matrices silicatées. Ces lois peuvent être utilisées tant dans l'industrie que pour résoudre des problèmes géologiques fondamentaux à travers par exemple l'altération des verres basaltiques et son implication dans la quantification des processus d'érosion.

Mes compétences acquises sur l'analyse, la compréhension et la modélisation des interactions eau-verre m'ont amené à développer de nouveaux sujets de recherche en collaboration avec les géochimistes et thermodynamiciens de l'UMR-G2R. Ainsi, l'étude du système "eau-argile" liée à la problématique du stockage géologique de déchets nucléaires m'a donné l'occasion d'aborder le système "eau-solide minéral" par l'intermédiaire de la simulation **thermodynamique** à l'aide de codes géochimiques. La problématique de la réduction thermochimique des sulfates par les hydrocarbures (TSR) m'a donné l'occasion d'introduire une phase supplémentaire, les **hydrocarbures**, dans le système "eau-roche" et de modéliser le comportement de ce système. J'ai pu également traiter la problématique de l'introduction d'une **phase gazeuse** dans le système "eau-sel" par l'intermédiaire du développement d'un code de calcul destiné à prédire le comportement du système H_2O-CO_2-CH_4-H_2S-N_2-NaCl en fonction de la pression et de la température.

Aujourd'hui, mes travaux de recherche sont basés sur l'étude de **la séquestration du CO_2** et des **gaz annexes** en formation géologique. Outre d'exercer et d'améliorer mes compétences sur la compréhension des systèmes "eau-roche-gaz", cette thématique m'a permis de développer des bancs expérimentaux uniques, innovants, permettant de répondre aux questions clés liées à l'injection de CO_2 dans des réservoirs sédimentaires. Il s'agit en particulier d'appréhender la réactivité des roches (réservoirs, couvertures), des minéraux et des matériaux (aciers, ciments) en présence de CO_2 supercritique, en milieu aqueux ou anhydre, sous l'influence de gaz co-injectés agressifs (H_2S, SOx, NOx,…). Les paramètres tels que la température, la pression, la fugacité des gaz, les rapports eau/roche, la salinité ont une influence considérable sur le comportement à court, moyen et long terme des stockages de gaz acides. Pour répondre à ces questions, j'ai développé, en collaboration avec les chercheurs, ingénieurs et étudiants du laboratoire, de nouveaux designs d'expériences destinés à suivre la réactivité des roches réservoirs et couverture en batch (autoclave IMAGES), l'influence des gradients de température sur le transfert de matière (expérience COTAGES) et la réactivité des interfaces (expériences « sandwichs »). Un modèle expérimental de puits d'injection a été développé à travers la maquette MIRAGES. Il permet pour la première fois d'étudier la réactivité d'un puits et de ses interfaces face à l'injection de CO_2 supercritique. Ce modèle expérimental est un outil indispensable pour caler les modèles numériques décrivant l'évolution du proche-puits en condition d'injection. En parallèle, j'ai développé le dispositif expérimental existant qui permettait de conduire des expériences en présence de gaz dangereux (H_2S). Aujourd'hui, le laboratoire est équipé d'une ligne de chargement/déchargement de gaz pour mener des expériences dans les systèmes eau/gaz/roche en présence de gaz d'intérêt dans la problématique du stockage de gaz acides, à savoir SO_2, NO, H_2S, CO et CH_4. Enfin, l'évolution des propriétés pétrophysiques des roches réservoir et de couverture est un des paramètres clés qui doit être pris en compte dans la problématique du stockage du CO_2. Ainsi, les propriétés de porosité et de perméabilité des roches doivent être qualifiées et quantifiées pour, en particulier, appréhender l'évolution de l'injectivité dans le réservoir ou encore les risques de fuite à travers la couverture. Ceci est aujourd'hui réalisé par l'acquisition d'images tridimensionnelles par micro et nanotomographie X. C'est pourquoi je me suis investi dans la procédure d'acquisition du nanotomographe de la FR EST et que j'assure la coresponsabilité scientifique de cette nouvelle plate-forme analytique.

La suite de ce mémoire sera articulée autour des principaux thèmes de recherche que j'ai abordés ces 10 dernières années.

2. Modélisation thermodynamique, géochimique et tridimensionnelle des environnements géologiques

Les recherches menées au sein de l'UMR G2R-CREGU m'ont permis de développer l'aspect modélisation géochimique, mais aussi géo-modélisation 3D, à partir de trois études distinctes :

Séquestration du CO_2 en aquifère profond.

Les accords de Kyoto, signés par 160 pays en décembre 1997, prévoient une réduction des gaz à effet de serre (GES) responsables du réchauffement de la planète. La France émettait en 2002 environ 103 millions de tonnes équivalent carbone, en augmentation de 6,9% par rapport à 1990. La volonté de revenir aux émissions de 1990 à l'horizon 2008-2012 devrait conduire à une émission de 96GtC/an, ce qui reviendrait pour la Lorraine (Figure 1), $2^{ème}$ région en termes d'émission de CO_2 par habitant, à réduire les émissions actuelles d'environ 3,8MtC par an. Ceci est possible d'une part par la réduction des quantités émises en diminuant les consommations d'énergie fossile et/ou en améliorant les rendements de combustion, et d'autre part par la capture du CO_2 émis et sa séquestration. La séquestration de gaz carbonique peut être réalisée à travers différentes méthodes:

- par injection dans des aquifères profonds. Dans ce cas, le CO_2 pourra soit être piégé en tant que fluide supercritique ou gaz selon les conditions de pression et température du réservoir, soit dissous dans la solution aqueuse, soit minéralisé par précipitation sous forme de carbonates.
- par injection dans des réservoirs d'hydrocarbures liquides ou gazeux en fin d'exploitation avec possibilité de récupération assistée des hydrocarbures. La séquestration se fera soit par dissolution dans les hydrocarbures, soit par complexation avec les molécules organiques, soit par adsorption, soit par formation d'un gas-cap.
- par injection dans d'anciennes veines de charbon. Le CO_2 sera soit adsorbé soit piégé sous forme supercritique ou gazeuse.
- par injection dans des séries évaporitiques. Le CO_2 sera sous forme supercritique ou gaz.
- la séquestration par formation de lac de CO_2 liquide sous-marin a aussi été envisagée.

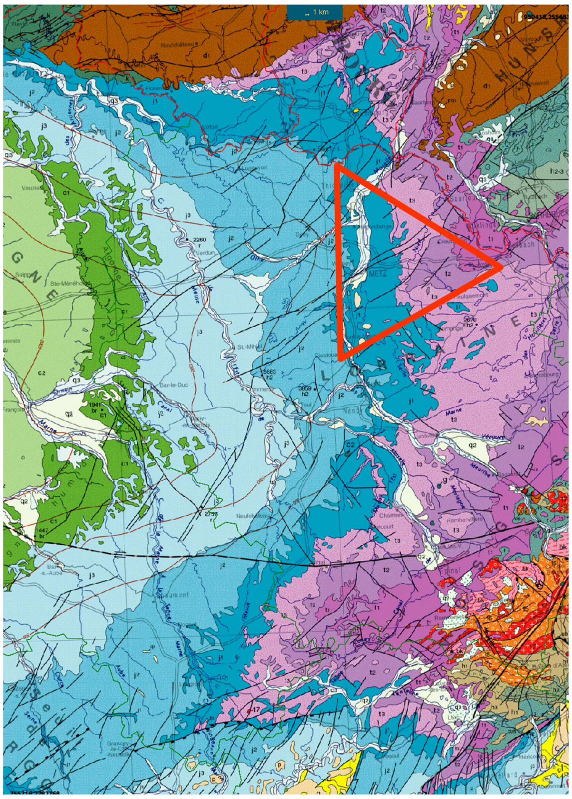

Figure 1 : Carte géologique de la Lorraine, d'après Infoterre (BRGM, carte géologique de la France). Le triangle rouge correspond à la région où sont localisés les principaux émetteurs de CO_2. Les candidats potentiels à la séquestration du CO_2 apparaissent à l'affleurement en bleu et rose (Jurassique et Trias).

En Lorraine, les 4 premiers types de piégeage sont *a priori* possibles. Le but du travail était donc de:

- recenser les roches réservoir candidates en Lorraine.
- calculer leur potentiel de séquestration
- modéliser expérimentalement et numériquement le comportement de roches réservoir et de couvertures soumises à l'action de CO_2.

Parmi les roches potentielles, les aquifères salins ont été choisis dans un premier temps comme candidats potentiels à la séquestration, principalement en raison de la possibilité de minéralisation offrant un piégeage pérenne, et de l'absence de ressource en eau exploitable due aux teneurs élevées en sel. L'injection de CO_2 devant s'effectuer en conditions supercritiques pour des raisons de densité, les aquifères devront se situer à une profondeur minimum de 800m. L'ensemble de ces critères a conduit à choisir le grès à roseaux, le grès à Voltzia et le grès vosgien comme réservoirs potentiels.

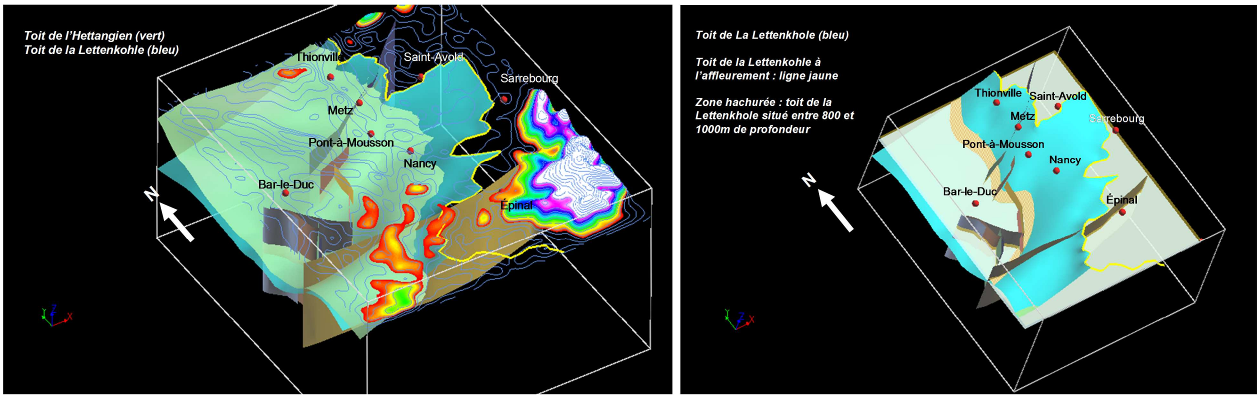

Figure 2 : Représentation 3D Gocad de la région Lorraine. A gauche : la topographie est représentée par les courbes de niveau en bleu. A droite : vue du toit de la Lettenkhole considérée dans l'étude comme le toit des formations réservoir gréseuses d'intérêt. La zone hachurée correspond à la surface du toit de la Lettenkhole située entre 800 et 1000 m de profondeur et marquant la zone potentielle de stockage en conditions de CO_2 supercritique.

Pour déterminer une première localisation des lieux d'injection, j'ai réalisé un modèle 3D gOcad (Figure 2), principalement à partir des données de forages dépouillées et interprétées par Jacques Leroux (UMR G2R), de la topographie de la région Lorraine issue de MNT (collaboration Pierre-Jean Fauvel, UMR G2R), et des données à l'affleurement à partir de cartes géologiques numérisées (Infoterre BRGM) que j'ai compilées. Le modèle intègre également les principales failles régionales. Les données d'émissions de CO_2 classées par secteurs d'activités ont été incluses (source DRIRE Lorraine). Les données géochimiques des formations, les porosités, perméabilités seront intégrées prochainement et font l'objet en des travaux de thèse de Clément Belgodère (*Thèse ArcelorMittal, co-encadrement J. Pironon et J. Sterpenich*). Ce modèle intégré de la géologie régionale en trois dimensions présente d'ailleurs des intérêts multiples puisqu'il pourra être utilisé et complété par la communauté scientifique dans le cadre de thématiques différentes de la séquestration.

Le potentiel de séquestration des différents réservoirs a été estimé à partir du volume molaire du CO_2 en conditions P, T de réservoirs, de la solubilité du CO_2 en solution saline, et bien entendu des dimensions du réservoir et de leur porosité, ainsi que de la capacité d'assèchement du CO_2. Le volume molaire a été estimé à l'aide d'une équation d'état de Peng-Robinson (collaboration Erwan Perfetti, UMR G2R), la solubilité dans la solution saline grâce au logiciel développé en collaboration avec Jean Dubessy et Alexandre Tarantola (UMR G2R). La sensibilité du modèle aux paramètres d'entrée a été étudiée et montre que la saturation en eau est un paramètre crucial.

Les premières simulations géochimiques du système eau salée / grès à l'aide de JCHESS ont été menées en parallèle avec la réalisation d'expériences en autoclaves destinées à suivre l'évolution d'un grès soumis à haute pression et haute température en présence d'eau et de CO_2 *(sujet du Master 2 recherche de S. Renard et projet laboratoire 3A ENSG de G. Gravier et S. Renard*).

Ce travail a fait l'objet d'un rapport pour le BQR-UHP et d'un résumé étendu (*Sterpenich J., Renard S, Pironon J. (2006). Reactivity of French Triassic sandstones submitted to CO2 under deep geological storage conditions. 8th International Conference on Greenhouse Gas Control Technologies - GHGT8, Trondheim, Norway*). Il a nous a permis de devenir le partenaire privilégié du BRGM et d'ArcelorMittal dans la recherche de candidats potentiels capables de stocker le CO_2 issu de la sidérurgie lorraine (*Réactivité d'un mélange de gaz réduits sur la géochimie d'un grès rouge. Cas des grès du Trias lorrain soumis à une injection de CO_2. Thèse Clément Belogodère, depuis octobre 2010. (Encadrants: J. Pironon (50%) et J. Sterpenich (50%)*).

Modélisation de la TSR

La réduction thermochimique des sulfates (TSR) est un processus majeur responsable de la dégradation des hydrocarbures et de la production d'H_2S dans les réservoirs soumis à des températures de 100-140°C. La réaction générale de la TSR peut être schématisée de la façon suivante :

$$\text{hydrocarbures} + SO_4^{2-} \Rightarrow \text{hydrocarbures altérés} + S^\circ + \text{bitumes solides} + H_2S\ (HS^-) + HCO_3^-\ (CO_2) + H_2O + \text{chaleur?}$$

où des hydrocarbures en contact avec une phase aqueuse contenant des ions sulfates réagissent pour donner un ensemble de produits carbonés, du sulfure d'hydrogène et du soufre élémentaire selon les conditions, des ions carbonates et de l'eau. Dans certaines conditions, la réaction peut être exothermique. Cette réaction d'oxydo-réduction est complexe et, à l'heure actuelle, les tentatives de modélisations ne prennent en compte que des hydrocarbures simples comme le méthane. L'objectif du projet réalisé en collaboration avec Laurent Richard (UMR G2R, Amphos 21), est de mieux comprendre les mécanismes gouvernant la TSR, en particulier l'influence des différentes familles d'hydrocarbures, et de développer un code géochimique prédictif. Cette approche est basée sur la quantification des transferts de masse dans le système « eau-roche-matière organique » par la thermodynamique des processus irréversibles.

Les calculs effectués montrent que les réactions globales de réduction thermochimique des sulfates par les hydrocarbures sont irréversibles. De plus, l'affinité chimique des réactions diminue avec le nombre d'atomes de carbone, en accord avec la moindre réactivité du méthane observée par rapport aux hydrocarbures de poids moléculaire plus élevé. Des calculs de transferts de masse reportés dans des diagrammes d'activité (Figure 3) indiquent que l'anhydrite ne peut atteindre d'équilibre chimique dans des réservoirs pétroliers affectés par la réduction thermochimique des sulfates. Enfin, une banque de données thermodynamiques a été constituée pour de futures simulations quantitatives de la TSR.

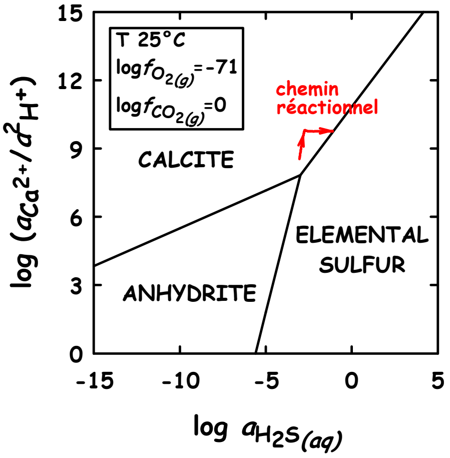

Figure 3 : Domaines de stabilité de la calcite, de l'anhydrite et du soufre élémentaire à 25°C, pour une fugacité de CO2 gaz de 1 bar et des fugacités d'oxygène fixées par l'assemblage pyrite-pyrrhotite-magnétite. Les flèches indiquent le chemin réactionnel.

Ce travail a fait l'objet d'une publication présentée dans ce mémoire (*Richard L, Neuville N, Sterpenich J, Perfetti E, Lacharpagne JC. (2005) Thermodynamic analysis of organic/inorganic reactions involving sulfur : implications for the sequestration of H_2S in carbonate reservoirs. Oil & Gas Science and Technology, 60(2), 275-285*) et d'un rapport à Total accompagné d'un logiciel géochimique incluant la prise en compte d'hydrocarbures.

Prédiction thermodynamique de l'évolution des systèmes eau-gaz-sel.

J'ai également participé au développement d'un code numérique chargé de calculer les isoplèthes du système H_2O-CO_2-CH_4-H_2S-N_2-NaCl (collaboration Jean Dubessy et Alexandre Tarantola UMR G2R, Figure 4). Le but de cette étude était, à partir d'un code décrivant les isoplèthes dans le système H_2O-CO_2-NaCl, de développer un nouveau code capable de prendre en compte les mélanges avec CH_4-H_2S-N_2. Cela a nécessité l'intégration des équations de mélange pour le calcul des coefficients de fugacité et des coefficients d'activité en solution aqueuse. Le code permet aujourd'hui, en fixant la température et la salinité de la phase aqueuse, de déterminer i) la composition de la phase aqueuse à partir de celle de la phase gazeuse, ii) la composition de la phase gazeuse connaissant la phase aqueuse, iii) la pression de vapeur saturante et la pression totale du système. Ce code trouve de nombreuses applications, notamment dans l'utilisation des inclusions fluides pour retracer les conditions de piégeage P, T des fluides. Ce travail a fait l'objet d'une publication présentée dans ce mémoire (*Dubessy J, Tarantola A., Sterpenich J. (2005). Modelling of liquid-vapour equilibria in the system H_2O-CO_2-NaCl and H_2O-H_2S-NaCl systems to 270°C. Oil & Gas Science and Technology, 60(2): 339-355*) et d'un rapport à TOTAL.

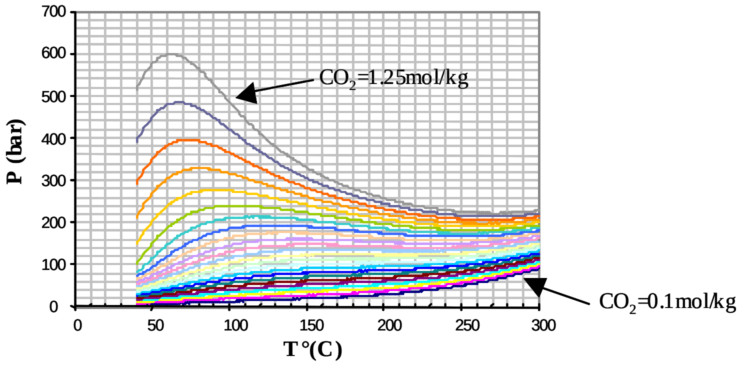

Figure 4 : Graphique P-T dans le système H2O-CO2-NaCl montrant les isoplèthes pour CO2 variant de 0,1 à 1,25 mol/kg.

Modélisation thermodynamique de la chimie d'eaux interstitielles à l'aide du code géochimique DISSOL.

La détermination des propriétés chimiques des eaux interstitielles se révèle extrêmement importante, par exemple dans la problématique du stockage en couche géologique de déchets radioactifs. En effet, les argilites de Bure, choisies pour l'étude de la faisabilité d'un stockage, contiennent de faibles quantités d'eau, peu accessibles (eau interstitielles), rendant le prélèvement délicat. Ainsi, afin de déterminer les propriétés de ces eaux interstitielles qui pourront entrer en contact avec les déchets radioactifs de haute activité et à vie longue, une modélisation à l'aide du code géochimique DISSOL a été réalisée. L'influence de la température sur les interactions eau-argile a également été quantifiée. Cette étude a été réalisée en collaboration avec Laurent Richard, Régine Ruck, Marie-Christine Boiron et Michel Cathelineau (UMR G2R) et a fait l'objet d'un rapport à l'ANDRA.

Publications

Modelling of liquid-vapour equilibria in the system H_2O-CO_2-NaCl and H_2O-H_2S-NaCl systems to 270°C. Dubessy J, Tarantola A., Sterpenich J. (2005). Oil & Gas Science and Technology, 60(2): 339-355.

Thermodynamic analysis of organic/inorganic reactions involving sulfur : implications for the sequestration of H_2S in carbonate reservoirs. Richard L, Neuville N, Sterpenich J, Perfetti E, Lacharpagne JC. (2005). Oil & Gas Science and Technology, 60(2), 275-285

Oil & Gas Science and Technology – Rev. IFP, Vol. 60 (2005), No. 2, pp. 339-355

IFP International Workshop
Rencontres scientifiques de l'IFP

Gas-Water-Rock Interactions ... / Interactions gaz-eau-roche ...

Modelling of Liquid-Vapour Equilibria in the H_2O-CO_2-NaCl and H_2O-H_2S-NaCl Systems to 270°C

J. Dubessy[1], A. Tarantola[1,2] and J. Sterpenich[1]

1 UMR G2R (7566), CREGU, Faculté des Sciences, Université Henri-Poincaré
BP 239, 54506 Vandœuvre-lès-Nancy Cedex - France
2 Mineralogisch-Petrographisches Institut, Bernoullistrasse, 30 CH-4056 Basel - Switzerland
e-mail: jean.dubessy@g2r.uhp-nancy.fr - alexandre.tarantola@unibas.ch - jerome.sterpenich@g2r.uhp-nancy.fr

Résumé — Modélisation des équilibres liquide-vapeur dans les systèmes H_2O-CO_2-NaCl et H_2O-H_2S-NaCl jusqu'à 270 °C — Cet article présente un modèle thermodynamique dissymétrique d'équilibre liquide-vapeur dans les systèmes H_2O-CO_2-NaCl et H_2O-H_2S-NaCl en dessous du point critique de l'eau (250°C pour H_2S, 270°C pour CO_2). La phase vapeur est décrite par une équation d'état cubique. L'eau et les composants gazeux de la phase aqueuse liquide sont respectivement décrits par la loi de Raoult et la loi de Henry combinées avec un modèle de Redlich-Kister de solutions régulières, permettant de calculer les coefficients d'activité. Après une analyse de la base de données expérimentales, plus de 80 % pour CO_2 et 92 % pour H_2S des pressions calculées des isoplèthes concernant les solutions aqueuses diffèrent de moins de 5% des données expérimentales, ce qui est comparable à l'incertitude expérimentale. Bien que le modèle ne soit pas optimisé sur la composition de la phase vapeur, les compositions calculées sont correctes au-dessus de 100 °C. L'effet du sel est modélisé en combinant le modèle de Pitzer pour le calcul du coefficient d'activité de l'eau dans la solution aqueuse et une extension de la loi de Setchenow. Les hypothèses à la base de ce modèle induisent sa validité pour des pressions inférieures à 300 bar.

Abstract* — *Modelling of Liquid-Vapour Equilibria in the H_2O-CO_2-NaCl and H_2O-H_2S-NaCl Systems to 270°C — *An unsymmetric thermodynamic model for the liquid-vapour equilibria in the H_2O-CO_2-NaCl and H_2O-H_2S-NaCl systems for temperatures below the critical point of water (250°C for H_2S, 270°C for CO_2) is presented. The vapour phase is described by a cubic Equation of state. The water and gas components in the liquid aqueous phase are respectively described by Raoult's law and Henry's law combined with a Redlich-Kister's model of regular solutions for the activity coefficients of these two components. After an analysis of the experimental data base, more than 80% for CO_2 and 92% for H_2S of predicted pressures of aqueous isopleths deviate less than 5%, which is comparable to experimental uncertainty. Although the model is not fitted on the composition of the vapour phase, the predicted values are correct above 100°C. The salt effect is modelled by a combination of the model of Pitzer for the water activity and an extension of Setchenow's law. The hypotheses behind this model makes it applicable at pressures below 300 bar.*

INTRODUCTION

The high value of the critical point of water (374.15°C) combined with the salting-out effect result in the existence of a large field in the P-T space of coexistence of two fluid phases. The temperature range up to 250°C corresponds to different geological environments of the upper crust such as sedimentary basins, geothermal and epithermal systems, and incipient metamorphism. Fluid inclusions may also provide invaluable information on the P-T conditions of trapping if immiscibility is identified (Pichavant *et al.*, 1982; Ramboz *et al.*, 1982). A calibration of the Raman techniques in H_2O-gas-salt systems at the homogenisation temperature using synthetic fluid inclusions, made using the aqueous phase coexisting with a vapour phase, and the subsequent use of these data for natural fluid inclusions is possible if the gas solubility in the aqueous phase is well known (Dubessy *et al.*, 2001; Guillaume *et al.*, 2003). The calculation of liquid-vapour equilibria in H_2O-gas-salt systems is also important in various contexts of waste confinement into subsurface reservoirs. The storage of acid gases in deep oil reservoirs will produce fluid phase equilibria in the water-gas-salt system. In addition to the heat budget, several phenomena accompany the immiscibility process from a single fluid phase and were summarised by several authors (Reed and Spycher, 1985; Drummond and Ohmoto, 1985; Shmulovich *et al.*, 1995):

- the increase in pH of the residual liquid phase by CO_2 or H_2S fractionation to the vapour phase with consequences on the hydrolysis and speciation of metals;
- the phase separation and different migration properties of the liquid and vapour phases;
- the frequent increase of the redox state resulting in the removal of H_2, CH_4 and H_2S from the system;
- the change of the mineral solubility due to the variations of all these parameters.

Therefore, the calculation of liquid-vapour equilibria in H_2O-gas-salt systems is important for many geological processes occurring in the upper crust.

There are essentially two ways for modelling liquid-vapour equilibria. The first one consists in using a single Equation of state to represent the thermodynamic properties of both phases. This approach is used for systems with non polar molecules or at least without electrolytes. However, there is no satisfactory Equation of state both for the water-rich salt-bearing aqueous phase and the gas-rich phase free of salts. Therefore, the approach chosen for this work consisted to use an unsymetric model based on Henry's and Raoult's limiting laws for describing the liquid aqueous phase and a cubic Equation of state for the gas-rich phase.

This work has two aims:

- to write the Equations describing the liquid-vapour equilibrium in the H_2O-gas-salt system;
- to develop a software program enabling the calculation of the isopleths (lines at fixed composition in a temperature-pressure diagram) of the aqueous phase, coexisting with the vapour phase, and the composition of this vapour phase in the range 50-270°C and for NaCl concentrations up to 6 molal.

Three phase liquid-liquid-gas equilibria are not considered in this work.

1 THEORY

1.1 Calculation of Isopleths of the Liquid Phase

Two-phase equilibrium between an aqueous liquid phase and a vapour phase in a two component system (no salt) is fully described by the following set of Equations (1):

$$\begin{aligned} &T^{\text{vap}} = T^{\text{aq}} \;;\; P^{\text{vap}} = P^{\text{aq}} \;; \\ &\mu^{\text{vap}}_{\text{H}_2\text{O}} = \mu^{\text{aq}}_{\text{H}_2\text{O}} \;;\; \mu^{\text{vap}}_{\text{gas}} = \mu^{\text{aq}}_{\text{gas}} \end{aligned} \tag{1}$$

Assuming thermal and mechanical equilibrium and using the fugacity instead of the chemical potential, the equilibrium Equations are:

$$f^{\text{vap}}_{\text{H}_2\text{O}} = f^{\text{aq}}_{\text{H}_2\text{O}} \;;\; f^{\text{vap}}_{\text{gas}} = f^{\text{aq}}_{\text{gas}} \tag{2}$$

According to the phase rule ($v = c + 2 - \phi$), the variance of a liquid-vapour equilibrium (two phases: $\phi = 2$) for a two component ($c = 2$) system is two. This means that there are two independent parameters among x_i^{aq}, y_i^{vap}, P and T, where x_i^{aq} is the mole fraction of component i in the aqueous phase, and y_i^{vap} is the mole fraction of component i in the vapour phase. Therefore, two of these intensive properties must be specified for the determination of the two remaining ones (Prausnitz *et al.*, 1986). In the case of the calculation of the projection of an isopleth in the space P-T, the temperature and the composition of the liquid aqueous phase (x_i^{aq}) are specified. The remaining variables are the pressure and the composition of the vapour phase (y_i^{vap}), which are the solutions of Equations (2). At this step, there are three ways to calculate aqueous isopleths depending on the method used for the calculation of the composition of the vapour phase. All the Equations given below are written for a specific temperature, corresponding to a point along the liquid aqueous isopleth.

First case: $y^{\text{vap}}_{\text{H}_2\text{O}} = 0$

With this hypothesis, the vapour phase is made exclusively of the gas component. As the concentration of one component is specified $y^{\text{vap}}_{\text{H}_2\text{O}} = 0$ or $y^{\text{vap}}_{\text{gas}} = 1$, the number of independent intensive variables of the system decreases to one. Thus, the only variable to be determined is the pressure and only one Equation remains to be solved:

$$f^{\text{vap}}_{\text{gas}} = f^{\text{aq}}_{\text{gas}} \tag{3}$$

The fugacity of the gas component in the vapour phase is calculated from the Equation:

$$f_{\mathrm{gas}}^{\mathrm{vap}} = \left(y_{\mathrm{gas}}^{\mathrm{vap}} = 1\right) . \varphi_{\mathrm{gas}}^{\mathrm{vap}}(P) \cdot P \qquad (4)$$

where $\varphi_{\mathrm{gas}}^{\mathrm{vap}}(P)$ is the fugacity coefficient of the gas component inside the pure vapour phase, calculated with an Equation of state, which depends only on P as T is fixed.

The fugacity of the gas component inside the aqueous liquid phase is represented by Henry's law, a limiting law, allowing the calculation of the concentration of a solute in a liquid phase at equilibrium with a vapour phase if the solute concentration is small. Its formulation is the Equation (5):

$$K_{\mathrm{gas,aq}}^{P\mathrm{sat}} = \lim_{x_{\mathrm{gas}}^{\mathrm{aq}} \to 0} \left(\frac{f_{\mathrm{gas}}^{\mathrm{aq}}}{x_{\mathrm{gas}}^{\mathrm{aq}}} \right) \qquad (5)$$

where $f_{\mathrm{gas}}^{\mathrm{aq}}$ is the fugacity of gas component in the aqueous phase, and P_{sat} is the saturation pressure of the pure solvent at the considered temperature (Prausnitz *et al.*, 1986). For the calculation, the limiting condition is no longer written although it stands. If the concentration of the solute deviates significantly from zero, the pressure P is no longer equal to the saturation pressure of the pure solvent. Therefore, an integration of Equation (5) is necessary from P_{sat} to P and results in Equation (6) called the Equation of Krichevsky and Kasarnovsky (Prausnitz *et al.*, 1986):

$$\begin{aligned} \ln\left(\frac{f_{\mathrm{gas}}^{\mathrm{aq}}}{x_{\mathrm{gas}}^{\mathrm{aq}}} \right) &= \ln K_{\mathrm{gas,aq}}^{P\mathrm{sat}} + \frac{\int_{P_{\mathrm{sat}}}^{P} \overline{v_{\mathrm{gas}}^{\infty}} dP}{RT} \\ &= \ln K_{\mathrm{gas,aq}}^{P\mathrm{sat}} + \frac{\overline{v_{\mathrm{gas}}^{\infty}} \cdot \left(P - P_{\mathrm{sat}}\right)}{RT} \end{aligned} \qquad (6)$$

where $\overline{v_{\mathrm{gas}}^{\infty}}$ is the molar volume at infinite dilution of the gas solute in the aqueous solvent at temperature T. The variations of $\overline{v_{\mathrm{gas}}^{\infty}}$ with temperature along the saturation curve are taken into account using the model of Plyasunov *et al.* (2000a). However the change with pressure of $\overline{v_{\mathrm{gas}}^{\infty}}$ above 330°C precludes its integration with pressure considering it is constant as done in Equation (6). Therefore the model is limited in temperature to 300°C. Moreover Equation (6) shows that the only unknown is pressure for the calculation of an isopleth (T and $x_{\mathrm{gas}}^{\mathrm{aq}}$ are specified for the calculation of an isopleth):

$$f_{\mathrm{gas}}^{\mathrm{aq}} = \Psi_H(P) \qquad (7)$$

Therefore using Equation (4), the equilibrium condition is written:

$$\varphi_{\mathrm{gas}}^{\mathrm{vap}}(P) \cdot P = \Psi_H(P) \qquad (8)$$

This Equation with only one unknown, P, is solved by an iterative procedure. This procedure is convenient for pressure-temperature conditions far from the critical line of the H_2O-gas system to satisfy the physical assumption of a quasi water-free vapour phase. This approach was used by Duan *et al.* (1992) in the CH_4-H_2O-NaCl system up to 250°C, with the liquid phase modelled by Pitzer's model. However, the water content inside the vapour phase cannot be neglected.

Second case: $y_{\mathrm{H_2O}}^{\mathrm{vap}} \neq 0$ and addition of partial pressure of gases and water in the vapour phase.

This case, taking into account the presence of water molecules in the vapour phase, was treated previously in two ways. In the first one, the composition of the vapour phase is directly linked to pressure according to Equation (9):

$$y_{\mathrm{gas}}^{\mathrm{vap}} = \frac{P - P_{\mathrm{sat}}}{P} \qquad (9)$$

This approach was used by Drummond (1981) in his PhD Thesis. It is valid only for weak vapour phase density and low pressure. The fugacity coefficient of the gas component in the vapour phase ($\varphi_{\mathrm{gas}}^{\mathrm{vap}}$) depends on the composition of the vapour phase if the vapour phase is not considered as ideal. This dependence is a function of pressure according to Equation (9), and thus equilibrium is described by Equation (10) with P as the only unknown, as in the first case:

$$\begin{gathered} y_{\mathrm{gas}}^{\mathrm{vap}} \cdot \varphi_{\mathrm{gas}}^{\mathrm{vap}}(P) \cdot P = \Psi_H(P) \ or \\ \left(\frac{P - P_{sat}}{P} \right) . \varphi_{gas}^{vap}(P) . P = \Psi_H(P) \end{gathered} \qquad (10)$$

Third case: no hypothesis on the composition of the vapour phase. This is the correct and theoretically well founded approach. A second Equation is required dealing with the water component:

$$f_{\mathrm{H_2O}}^{\mathrm{vap}} = f_{\mathrm{H_2O}}^{\mathrm{aq}} \qquad (11)$$

Both the water and gas fugacities inside the vapour phase are calculated with the same Equation of state that describes the vapour phase. The fugacity of water in the liquid aqueous phase is deduced from Raoult's law Equation and takes into account the effect of pressure via the Poynting correction (Prausnitz *et al.*, 1986):

$$f_{\mathrm{H_2O}}^{\mathrm{aq}} = \left(1 - x_{\mathrm{gas}}^{\mathrm{aq}}\right) \cdot P_{\mathrm{sat}} \cdot \varphi_{\mathrm{H_2O}}^{\mathrm{sat}} \cdot \exp\left[\int_{P_{\mathrm{sat}}}^{P} \frac{\overline{V_{\mathrm{H_2O}}^{\mathrm{liq}}}}{RT} \cdot dP \right] \qquad (12)$$

where $\varphi_{\mathrm{H_2O}}^{\mathrm{sat}}$ is the fugacity coefficient of water at saturation pressure for pure water which is calculated with the Equation of state for the vapour phase; $\overline{V_{\mathrm{H_2O}}^{\mathrm{liq}}}$ is the molar volume of pure water.

The vapour composition and pressure are solutions to the set of two following Equations:

$$\begin{aligned} & f^{aq}_{H_2O} = f^{vap}_{H_2O} \text{ or } \left(1-x^{aq}_{gas}\right)\cdot P_{sat}\cdot \varphi^{sat}_{H_2O} \\ & \cdot\exp\left[\int_{P_{sat}}^{P} \frac{\overline{V^{liq}_{H_2O}}}{RT}\cdot dP\right] = \left(1-y^{vap}_{gas}\right)\cdot P\cdot\varphi^{vap}_{H_2O} \\ & f^{aq}_{gas} = f^{vap}_{gas} \text{ or } K^{P_{sat}}_{gas,aq}\cdot x^{aq}_{gas} \\ & \cdot\exp\left(\frac{\overline{v^{\infty}_{gas}}\cdot\left(P-P_{sat}\right)}{RT}\right) = y^{vap}_{gas}\cdot P\cdot\varphi^{vap}_{gas} \end{aligned} \tag{13}$$

where the fugacity coefficients of components in the vapour phase ($\varphi^{sat}_{H_2O}$ and φ^{vap}_{gas}) are calculated with the Equation of state of the vapour phase and depend on pressure and the composition of the vapour phase.

At this step of the thermodynamic model, the aqueous solution containing water and gas is assumed to be ideal, which results in activity coefficients of the solute and of the solvent in the aqueous phase equal to one. For highly insoluble gases such as methane or nitrogen at low temperature this hypothesis could be valid because the perturbations of the structure of the liquid remain very weak and because the interactions between two gas molecules are unlikely due to their large average distance. However, this assumption does not stand at least for aqueous solutions containing gases with higher solubilities such as carbon dioxide or hydrogen sulfide (Caroll and Mather, 1992, 1993) and the correct system of Equations is the following (14):

$$\begin{aligned} & \gamma^{aq}_{H_2O}\cdot\left(1-x^{aq}_{gas}\right)\cdot P_{sat}\cdot\varphi^{sat}_{H_2O}\cdot\exp\left[\int_{P_{sat}}^{P}\frac{\overline{V^{liq}_{H_2O}}}{RT}\cdot dP\right] \\ & \qquad = \left(1-y^{vap}_{gas}\right)\cdot P\cdot\varphi^{vap}_{H_2O} \\ & \gamma^{aq*}_{gas}\cdot K^{P_{sat}}_{gas,aq}\cdot x^{aq}_{gas}\cdot\exp\left(\frac{\overline{v^{\infty}_{gas}}\cdot\left(P-P_{sat}\right)}{RT}\right) = y^{vap}_{gas}\cdot P\cdot\varphi^{vap}_{gas} \end{aligned} \tag{14}$$

where $\gamma^{aq}_{H_2O}$ and γ^{aq*}_{gas} and are respectively the activity coefficients of water and the gas solute in the aqueous liquid phase which requires to be modelled at least as a function of temperature and composition. The superscript * points out the different normalisation conditions of these two activity coefficients:

$$\gamma^{aq*}_{gas} \to 1 \text{ when } x^{aq}_{gas} \to 0 \text{ and } \gamma^{aq}_{H_2O} \to 1 \text{ when } x^{aq}_{H_2O} \to 1$$

According to Prausnitz *et al.* (1986), the superscript* designates the activity coefficient defined with respect to a reference of an ideal dilute solution in the sense of Henry's law whereas the activity coefficient γ^{aq}_{gas} is defined with respect to a reference state of an ideal solution in the sense of Raoult's law. γ^{aq}_{gas} is related to γ^{aq*}_{gas} by Equation (15):

$$\frac{\gamma^{aq}_{gas}}{\gamma^{aq*}_{gas}} = \lim\gamma^{aq}_{gas} \text{ when } x^{aq}_{gas} \to 0 \quad\text{or}\quad \frac{\gamma^{aq}_{gas}}{\gamma^{aq*}_{gas}} = \gamma^{\infty,aq}_{gas} \tag{15}$$

where $\gamma^{\infty,aq}_{gas}$ is the activity coefficient at infinite dilution of the gas in the aqueous phase.

As the concentration of the gas remains small in the aqueous phase, less than 2 mol%, the aqueous solution of gas and water can be considered as a regular or slightly non ideal solution for which Margules' Equations are relevant (Anderson and Crerar, 1993). The Redlich-Kister's form of the excess energy G^E of a mixture can be written as a function of the mole fraction of components 1 and 2 (x_1 and x_2 with $x_1 + x_2 = 1$) following Equation (16):

$$\frac{G^E}{RT} = x_1x_2\left(B + C\left(x_1 - x_2\right) + D\left(x_1 - x_2\right)^2 + ...\right) \tag{16}$$

In this work, parameter D is considered to be zero. Using the classical Equations relating the activity coefficient γ_i of component i to the excess energy (17),

$$\ln\gamma_i = \frac{\partial\left(nG^E/RT\right)}{\partial n_i} \tag{17}$$

the activity coefficients of the gas component, the solute, and of the solvent (water) are given by Equations (18) and (19):

$$\ln\gamma^{aq}_{H_2O} = \left(B - C + 4Cx^{aq}_{gas}\right)\left(x^{aq}_{gas}\right)^2 \tag{18}$$

$$\ln\gamma^{aq}_{gas} = \left(B + C - 4Cx^{aq}_{gas}\right)\left(x^{aq}_{H_2O}\right)^2 \tag{19}$$

Equation (19) shows that $\gamma^{\infty,aq}_{gas} = \exp(B + C)$. Therefore:

$$\frac{\gamma^{aq}_{gas}}{\gamma^{aq*}_{gas}} = \exp(B + C) \text{ when } x^{aq}_{gas} \to 0$$

Therefore the Equation giving γ^{aq*}_{gas} is the following:

$$\ln\gamma^{aq*}_{gas} = -x^{aq}_{gas}\cdot\left((B + C)\left(x^{aq}_{H_2O} + 1\right) + 4C\left(x^{aq}_{H_2O}\right)^2\right) \tag{20}$$

1.2 Presence of Salts

If NaCl is present, the vapour phase can be considered to be free of salt in this temperature range below the critical point of water. Therefore no additional equilibrium Equations are required since the concentration of NaCl is fixed in the aqueous phase. The modifications of Equations (19) are detailed below:

- The calculations of P_{sat} and of the partial molar volume of water in the aqueous solution $\overline{V_{\mathrm{H_2O}}^{\mathrm{liq}}}$ are carried out in the H_2O-NaCl system at the considered temperature from Haas (1976). $\overline{V_{\mathrm{H_2O}}^{\mathrm{liq}}}$ is considered to be independent of pressure between P_{sat} and P.
- The effect of salt concentration on the molar volumes at infinite dilution of the gas $\overline{v_{\mathrm{gas}}^{\infty}}$ is assumed to be independent of salt concentration, because there are no data or very few data.
- The activity coefficient of solute gases is assumed to be independent of salt concentration as a first assumption:

$$\gamma_{\mathrm{gas}}^{\mathrm{aq,NaCl}} = \gamma_{\mathrm{gas}}^{\mathrm{aq,NaCl=0}} \tag{21}$$

- The activity coefficient of water is considered to be the result of the effect of gas and salt according to Equation (22):

$$\gamma_{\mathrm{H_2O}}^{\mathrm{aq(gas,NaCl)}} = \gamma_{\mathrm{H_2O}}^{\mathrm{aq,NaCl}} \cdot \gamma_{\mathrm{H_2O}}^{\mathrm{aq,gas}} \tag{22}$$

  where $\gamma_{\mathrm{H_2O}}^{\mathrm{aq,NaCl}}$ is calculated from the model of Pitzer (Silvester and Pitzer, 1977) and $\gamma_{\mathrm{H_2O}}^{\mathrm{aq,gas}}$ is calculated using Equation (18) as a function of the pseudo gas mole fraction $z_{\mathrm{H_2O}}^{\mathrm{aq}}$ in the pseudo binary H_2O-gas:

$$z_{\mathrm{H_2O}}^{\mathrm{aq}} = \frac{x_{\mathrm{gas}}^{\mathrm{aq}}}{x_{\mathrm{gas}}^{\mathrm{aq}} + x_{\mathrm{H_2O}}^{\mathrm{aq}}} \tag{23}$$

- The effect of salt concentration on the Henry's constants $K_{\mathrm{gas,aq}}^{P\mathrm{sat}}$, called the salting-out effect, is often modelled using the Setchenow relationships (Lewis *et al.*, 1961):

$$\log_{10}\left(S_{\mathrm{gas,aq}}^{\circ} / S_{\mathrm{gas,aq}}^{\mathrm{NaCl}}\right) = k_s \cdot c_{\mathrm{NaCl}} \tag{24}$$

  where $S_{\mathrm{gas,aq}}^{\circ}$ and $S_{\mathrm{gas,aq}}^{\mathrm{NaCl}}$ are respectively the solubility of the gas in the NaCl-free aqueous solvent and the solubility of the gas in the NaCl-bearing aqueous solvent; k_s is the Setchenow coefficient and c_{NaCl} is the salt concentration. This Equation can be rewritten with the Henry's constants as a function of salt concentration m_{NaCl} in the molality scale:

$$K_{\mathrm{gas,aq},m_{\mathrm{NaCl}}}^{P\mathrm{sat}} = K_{\mathrm{gas,aq}}^{P\mathrm{sat}} \cdot 10^{m_{\mathrm{NaCl}}} \tag{25}$$

This Equation is valid at one temperature. However, the salting-out effect is dependent on temperature and the temperature effect is usually modelled according to Equations (26).

$$K_{\mathrm{gas,aq},m_{\mathrm{NaCl}}}^{P\mathrm{sat}} = K_{\mathrm{gas,aq}}^{P\mathrm{sat}} \cdot 10^{m_{\mathrm{NaCl}} \cdot \beta(T)} \text{ or}$$

$$\log\left(\frac{K_{\mathrm{gas,aq},m_{\mathrm{NaCl}}}^{P\mathrm{sat}}}{K_{\mathrm{gas,aq}}^{P\mathrm{sat}}}\right) = m_{NaCl} \cdot \beta(T) \tag{26}$$

Regression of experimental data on the H_2O-CO_2-NaCl and H_2O-H_2S-NaCl systems was not satisfactory using Equations (26). Therefore, we proposed a new formulation by Equation (27):

$$\log\left(\frac{K_{\mathrm{gas,aq},m_{\mathrm{NaCl}}}^{Psat}}{K_{\mathrm{gas,aq}}^{Psat}}\right) = m_{\mathrm{NaCl}}\beta_1(T) + m_{\mathrm{NaCl}}^2\beta_2(T) + m_{\mathrm{NaCl}}^3\beta_3(T) \tag{27}$$

Finally this results in the following system of two Equations with two unknowns:

$$\begin{aligned}
&\gamma_{\mathrm{H_2O}}^{\mathrm{aq,NaCl}} \cdot \gamma_{\mathrm{H_2O}}^{\mathrm{aq,gas}}\left(1 - x_{\mathrm{gas}}^{\mathrm{aq}} - x_{\mathrm{NaCl}}^{\mathrm{aq}}\right)P_{\mathrm{sat}} \cdot \varphi_{\mathrm{H_2O}}^{\mathrm{sat}} \\
&\cdot \exp\left[\int_{P_{\mathrm{sat}}}^{P} \frac{\overline{V_{\mathrm{H_2O}}^{\mathrm{liq}}}}{RT} \cdot dP\right] = \left(1 - y_{\mathrm{gas}}^{\mathrm{vap}}\right) \cdot P \cdot \varphi_{\mathrm{H_2O}}^{\mathrm{vap}} \\
&\gamma_{\mathrm{gas}}^{\mathrm{aq}*} \cdot K_{\mathrm{gas,aq},m_{\mathrm{NaCl}}}^{P\mathrm{sat}} \cdot x_{\mathrm{gas}}^{\mathrm{aq}} \cdot \exp\left(\frac{\overline{v_{\mathrm{gas}}^{\infty}} \cdot \left(P - P_{\mathrm{sat}}\right)}{RT}\right) \\
&= y_{\mathrm{gas}}^{\mathrm{vap}} \cdot P \cdot \varphi_{\mathrm{gas}}^{\mathrm{vap}}
\end{aligned} \tag{28}$$

2 EQUATIONS AND ALGORITHMS

2.1 The Equation of State of the Nonaqueous Phase

The Stryjek and Vera's Equation of state (Stryjek and Vera, 1986a, 1986b, 1986c) is chosen to model the fugacity coefficients of the different components inside the gas phase and the water fugacity of pure water along the saturation vapour phase. This is a cubic Equation of state derived from the Peng and Robinson's Equation that is recommended by Crovetto (1991) and Prini and Crovetto (1989).

2.2 Henry's Constants

The literature contains several formulations for the Henry's constants describing the solubility of simple gases in pure water. Plyasunov *et al.* (2000b) has developed a new model enabling the calculation of the Henry's constants up to the critical point of water with a high accuracy. For our purpose, we are interested for lower temperatures (< 300°C). Therefore, we used the correlation proposed by Harvey (1996) for many gases (Table 1).

2.3 Properties of the Aqueous Solution

The molar volumes of gases at infinite dilution ($\overline{v_{\mathrm{gas}}^{\infty}}$) were calculated along the saturation curve of water (Plyasunov *et al.*, 2000a). They are assumed to be independent of pressure as the pressure used in these calculations is below 500 bar and fitted as a function of temperature. Values of the Equation parameters for CO_2 and H_2S are given in Table 2. The saturation pressure and molar volume of the liquid phase along the liquid-vapour coexistence curve of the H_2O-NaCl system is calculated from Haas (1976).

TABLE 1

Parameters of the Henry's constant in the formalism of Harvey (1996):

$$\ln K^{Psat}_{gas,aq} = \ln P_{sat} + A_{gas}/T^* + B_{gas} \cdot (1-T^*)^{0.335}/T^* + C_{gas} \cdot (T^*)^{-0.41} \exp(1-T^*)$$

Solute	A_{gas}	B_{gas}	C_{gas}
CO_2	–9.4234	4.0087	10.3199
H_2S	–5.7131	5.3727	5.4227

2.4 Estimation of the *B* and *C* Parameters of the Margules-Redlich-Kister's Equation

The *B* and *C* parameters are fitted *versus* temperature according to Equations (29):

$$B = a + bT + cT^2 + dT^3 \text{ and } C = e + fT + gT^2 + hT^3 \quad (29)$$

For each temperature and gas concentration in the liquid aqueous phase, the activity coefficient γ^{aq}_{gas} and $\gamma^{aq}_{H_2O}$ are calculated iteratively in order to reproduce the experimental pressure and then the fitting parameters are adjusted over the experimental values *(Appendix 1)* .

2.5 The Salt Effect

At each temperature, for a given isopleth (fixed gas and salt concentration in the aqueous phase), the Henry's constant, $K^{Psat}_{gas,aq,m_{NaCl}}$ is calculated iteratively according to the procedure described in Appendix 2. Then the values are fitted with a polynomial as suggested by Battistelli *et al.* (1997).

3 EXPERIMENTAL DATA BASE AND PARAMETERS OF THE MODEL

All the experimental solubility data of the gases in the liquid aqueous phase are given in different units in the literature. They were all converted into the molality and mole fraction scales.

3.1 Experimental Data of the H_2O-CO_2-NaCl System

Experimental data concern mainly the composition of the aqueous phase in terms of gas concentration at given pressure and temperature. Data are very rare for the non aqueous phase. The data source is the following: Bamberger *et al.* (2000), Briones *et al.* (1987), Dhorn *et al.* (1993), Drummond (1981), D'Souza *et al.* (1998), Gillepsie and Wilson (1982), King *et al.* (1992), Malinin and Savelyeva (1972), Malinin and Kurovskova (1975), Matous *et al.* (1969), Müller *et al.* (1988), Nighswander *et al.* (1989), Prutton and Savage (1945), Sako *et al.* (1991), Takenouchi and Kennedy (1964), Tödheide and Franck (1963), Wiebe and Gaddy (1939, 1941), Zawisza and Malesinska (1981), Zel'vinskii (1937). Values are reported in Table 3. Diamond and Akinfiev (2003) have discussed in detail the criteria to discriminate experimental data. First, we did not take into account data below the critical point of pure carbon dioxide because our model does not calculate three phase equilibria (liquid aqueous solution, liquid carbon dioxide, vapour carbon dioxide). All the experimental data were plotted as isotherms in diagrams of total pressure *versus* carbon dioxide solubility in the aqueous phase. These diagrams allow the elimination of discontinuities and conflicting values. After this first selection, the model was fitted over the experimental data. Then the predictions of the model were compared with the experimental data and experimental data deviating by more than 15% were removed. These data correspond usually to high pressures, above 300 bar, and so to high density fluids of the "non"-aqueous phase. The total number of experimental data points used is 257. Ninety percent of calculated pressures differ by less than 8% from the experimental values.

Data of Rumpf *et al.* (1994) above 80°C are not consistent with the data of Drummond (1981), which cover the largest range of *P-T-X* conditions. In the absence of more experimental data, we did not take into account the data of Rumpf *et al.* (1994) without making a judgement on the quality of these data. In addition, Drummond (1981) obtained experimental data in two steps, first at increasing and then decreasing temperatures. For concentrations around 6 molal, the Henry's constants deduced from these two sets of experimental data are not consistent. It is worth noting that the spread of Henry's constants between the two sets of experimental data of Drummond (1981) covers the variations given by Rumpf *et al.*

TABLE 2

Regression of the data of from Plyasunov *et al.* (2000a) using the fitting Equation:

$$\frac{1}{\overline{v}^{\infty}_{gas\ i}} = \sum_{j=0}^{j=4} v_{i,j,} * T^{j}$$

Gas *i*	$v_{i,0}*10^2$	$v_{i,1}*10^4$	$v_{i,2}*10^6$	$v_{i,3}*10^9$	$v_{i,4}*10^{12}$
CO_2	2.439488129	5.790665261	–2.122757825	3.1918934075	–1.862906530
H_2S	–7.987367136	11.17890399	–4.091393094	6.3421129256	–3.701657751

(1994). For the H_2O-CO_2-NaCl system *(Table 4)*, Drummond (1981) does not mention any formation of siderite which could modify the solubility of carbon dioxide. Did some unnoticed phenomenon occur which could modify liquid-vapour equilibrium and explain such conflicting values? The question remains open and underlines the need for more experimental data.

TABLE 3

Experimental data for the H_2O-CO_2 system

Reference	*P* (bar)^a	*T* (°C)	Data
[1]	40.5-141.1	50-80	29, 23*
[2]	68.2-176.8	50	8, 0*
[3]	101.3-152	50-75	4, 0*
[4]	101-301	50	3, 0*
[5]	40.2-211.7	36.3-318.5	53, 42*
[6]	6.9-101.4	31.05-93.3	16, 7*
[7]	48,1-48,3	50-75	2, 2*
[8]	49-52,7	100-150	2, 2*
[9]	50-80	10-40	9, 9*
[10]	3.25-81.1	100-200	49, 46*
[11]	21.1-102.1	79.7-198.1	33, 4*
[12]	23-703	101-120	26, 0*
[13]	101.8-197.2	75.15-148.25	7, 0*
[14]	100-250	110-300	8, 4*
[15]	200	200-300	5, 3*
[16]	50-300	50-100	29, 21*
[17]	25-300	31.04-40	25, 15*
[18]	1.54-53.9	50-200	33, 28
[19]	19-95	50-100	55, 50*

a: range of selected temperatures or pressures; * number of data points selected.
[1]: Bamberger *et al.* (2000); [2]: Briones *et al.* (1987); [3]: D'Souza *et al.* (1998); [4]: Dhorn *et al.* (1993); [5]: Drummond (1981); [6]: Gillepsie and Wilson (1982); [7]: Malinin and Savelyeva (1972); [8]: Malinin and Kurovskova (1975); [9]: Matous *et al.* (1969); [10]: Müller *et al.* (1988); [11]: Nighswander *et al.* (1989); [12]: Prutton and Savage (1945); [13]: Sako *et al.* (1991); [14]: Takenouchi and Kennedy (1964); [15]: Tödheide and Franck (1963); [16]: Wiebe and Gaddy (1939); [17]: Wiebe and Gaddy (1941); [18]: Zawisza and Malesinska (1981); [19]: Zel'vinskii (1937).

3.2 Experimental Data of the H_2O-H_2S-NaCl System

The experimental data base is shown in Table 5 for the NaCl free system. All the data above 270°C were not taken into account because the binary interaction parameters between H_2O and H_2S are determined for temperatures only up to 240°C. Most of the data are consistent. As suggested by Duan *et al.* (1996), data of Kozintseva (1964) underestimate solubility of H_2S compared to other data and thus were discarded. In general, the concentration of H_2S in the aqueous phase determined by Drummond (1981) is a little higher than the values given by Suleimenov and Krupp (1994) whilst the relationship is inverted above 240°C. In addition, the values of the Henry's constant calculated by Drummond (1981) are based on the assumption that the vapour phase behaves like a perfect gas, which explains the important discrepancy in the values of the Henry's constants. Some data from Barret *et al.* (1988) and Wright and Maas (1932) are not self-consistent and conflict with data from other sources: they were discarded. Data of Selleck *et al.* (1952) are considered only along the liquid-gas curve. Their data above 2 molal and data at high concentrations of Lee and Mather (1977) could not be included (above 1.8 molal) because the model could not converge for the determination of the activity coefficients in the aqueous phase for the following reasons:

– the condition of low gas concentration in the aqueous phase required both for the model of the activity coefficients in the aqueous phase and the validity of Henry's law is not fulfilled;
– the existence of a three phase equilibrium (liquid-liquid-vapour) is not included in our model.

After a first fitting of activity coefficients, some data were removed when the deviation in the calculation of pressure exceeded 15%.

For the H_2O-H_2S-NaCl system (Table 6), data of Drummond (1981) obtained at decreasing temperature were removed because the author noticed formation of pyrrhotite and H_2 due to corrosion of the stainless steel vessel. After a first fitting of the extended Setchenow's law, some values, which are not consistent with the model fitted over the set of experimental data, were removed.

TABLE 4

Experimental data for the H_2O-CO_2-NaCl system

Reference	*P* (bar)	*T*(°C)	*m*(NaCl)	Data
[1]	37-290	35-345	0.99-6.28	396, 287*
[2]	48.35-48.51	50-75	0.358-4.458	10,10*
[3]	48.975-52.709	100-150	0.9978-5.9158	9, 8*
[4]	6.02-92.01	40.07-159.93	5.999	28, 25*
[5]	4.67-96.37	39.99-159.83	3.997-4.001	35, 22*

[1]: Drummond (1981); [2]: Malinin and Savelyeva (1972); [3]: Malinin and Kurovskova (1975); [4]: Nighswander *et al.* (1989); [5]: Rumpf *et al.* (1994).
* : number of selected data points.

TABLE 5

Experimental data for the H_2O-H_2S system

Reference	*P* (bar) ᵃ	*T* (°C) ᵃ	Data
[1]	1.01	23.5-94.5	39, 35*
[2]	0.47-0.95	0-49.987	36, 36*
[3]	1.01	2.1-29.82	14, 14*
[4]	8.21-52.28	41-241	75, 73*
[5]	1.01	25	1, 1*
[6]	0.84-2.07 + $P_{\text{sat atm}}$	160-330	14, 0*
[7]	1.548-66.704	10-180	325, 288*
[8]	3.93-138.61	20.8-321	49, 42*
[9]	0.37-2.24	37.78-171.11	66, 27*
[10]	6.90-68.95	5-60	26, 22*

a: range of selected temperatures or pressures; * number of data points selected [1]: Barrett *et al.* (1988); [2]: Clarke and Glew (1971); [3]: Douabul and Riley (1979); [4]: Drummond (1981); [5]: Kendall and Andrews (1921; [6]: Kozintseva (1964); [7]: Lee and Mather 1977); [8]: Suleimenov and Krupp (1994); [9]: Wright and Maas (1932; [10]: Selleck *et al.* (1952).

TABLE 6

Experimental data for the H_2O-H_2S-NaCl system

Reference	*P* (bar)	*T* (°C)	*m* (NaCl)	Data
[1]	1.01	59.5-96-5	1-5	182, 177*
[2]	1.01	2.1-29.82	0.559-2.314	42, 42*
[3]	6.97-55.18	41-242	1-6.04	207, 151*
[4]	1.01	25	0.5-3	9, 9*
[5]	11.96-138.42	155.2-320.4	0.235-2.656	23, 15*

[1]: Barrett *et al.* (1988); [2]: Douabul and Riley (1979); [3]: Drummond (1981); [4]: Gamsjäger and Schindler (1969); [5]: Suleimenov and Krupp (1994).
*: number of selected data points.

TABLE 7

Fitting parameters of the *B* and *C* parameters of the Margules-Redlich-Kister Equation (29)

		CO_2	H_2S
B	*a*	–1127.63016458677	–2407.93265898133
	b	11.8665759834639	16.9917300698207
	c	–0.0363815939147719	–0.0369144016195112
	d	0.0000344533889448619	0.0000244723762962793
C	*e*	359.662899252007	823.685566149131
	f	–3.88804875551428	–5.85727510585188
	g	0.0120996653413114	0.0128724402817956
	h	–0.0000115603635771203	–0.0000086802035546012
	R^2	0.66	0.85

4 RESULTS

4.1 The H_2O-CO_2-NaCl System

Values of the fitting parameters of the Redlich-Kister's model *(Eqs. 18, 20* and *29)* are given in Table 7. The reproducibility of the experimental data for the pressure is significantly improved when the activity coefficients of water and CO_2 in the aqueous phase are taken into account *(Fig.1)*. More than 79 and 93% of the calculated pressure differ respectively by less than 5 and 10% from the experimental

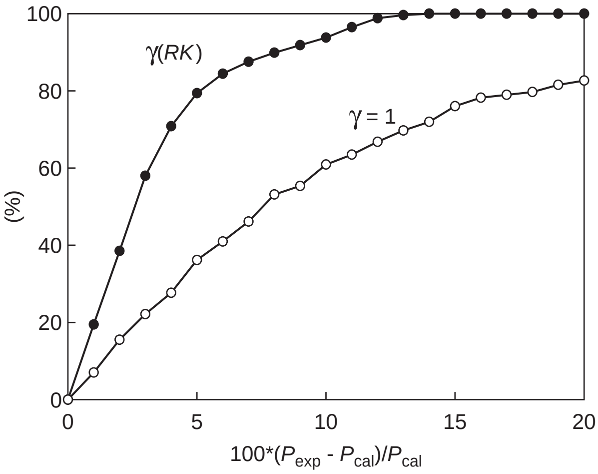

Figure 1

System H_2O-CO_2: percentage of pressure data reproduced with errors expressed by $100^*(P_{\text{exp}}–P_{\text{cal}})/P_{\text{cal}}$ where P_{exp} and P_{cal} are respectively the experimental and calculated pressures. γ *(RK)* curve is calculated using the fitted model (non-ideal behaviour of the aqueous solution and pressure calculated with Equation (14); γ = 1 curve corresponds to the ideal behaviour of aqueous solution (pressure calculated with Equation (13)).

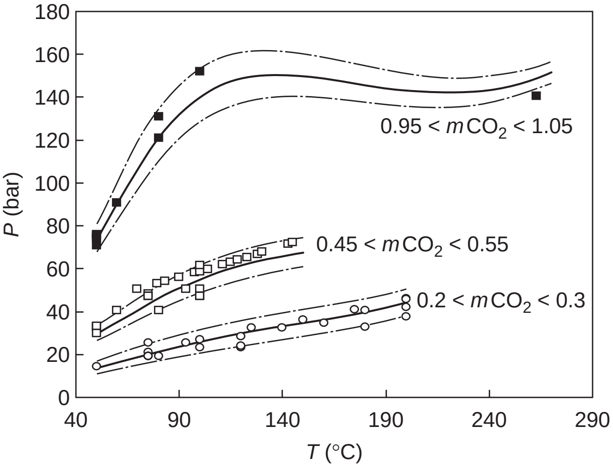

Figure 2

System H_2O-CO_2: comparison of experimental data and the calculated values with the model. As the CO_2 concentrations are not exactly identical within each set of data, three isopleths bracketing the compositions were calculated for each set of values. The lines represent the calculated isopleths with the concentration of CO_2 in molal.

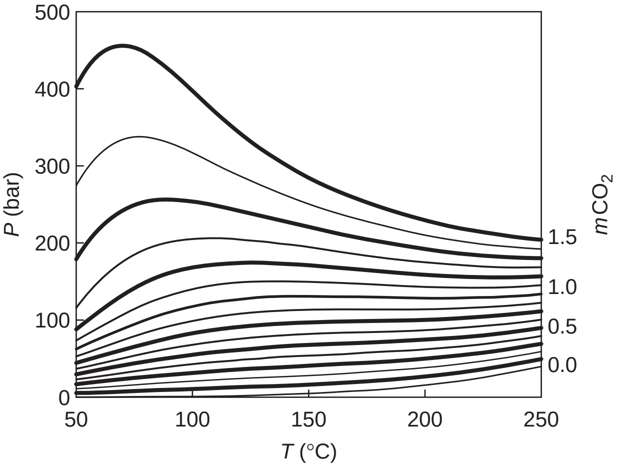

Figure 3

Isopleths in the system H_2O-CO_2 for mCO_2 between 0 and 1.5 molal by steps of 0.1 molal and for mNaCl = 0.

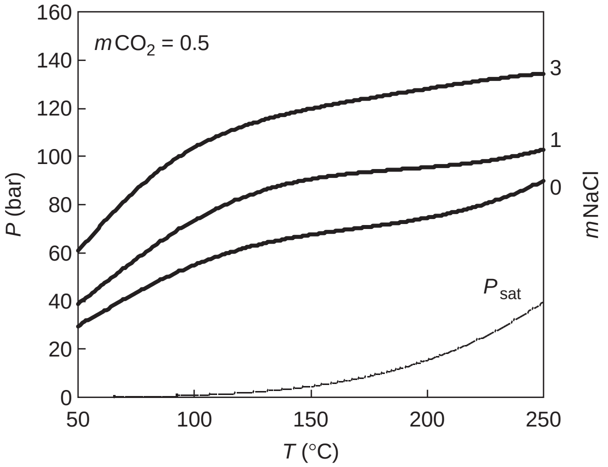

Figure 4

Isopleth of the liquid aqueous phase in the system H_2O-CO_2-NaCl for mCO_2 = 0.5 molal and for different NaCl concentrations between 0 and 3 molal. P_{sat} is the saturation line of pure water.

values with this model whereas the proportion falls at 36% at 5% accuracy with the assumptions $\gamma_{H_2O}^{aq} = \gamma_{CO_2}^{aq} = 1$. A comparison between experimental data and the model is illustrated in the pressure-temperature plane *(Fig. 2)*. The isopleths in the *P-T* plane are given in Figure 3. The model was not constrained using the vapour composition. To verify the model, the estimation of the composition of the vapour phase is compared with respect to the experimental data *(Table 8)*. Up to 100°C and above 100 bar, the model overestimates the concentration of water in the gaseous phase. However the predictions are acceptable above 120°C. More data will be required to optimise the binary interaction parameters between H_2O and CO_2 in the vapour phase, which was not within the scope of this work.

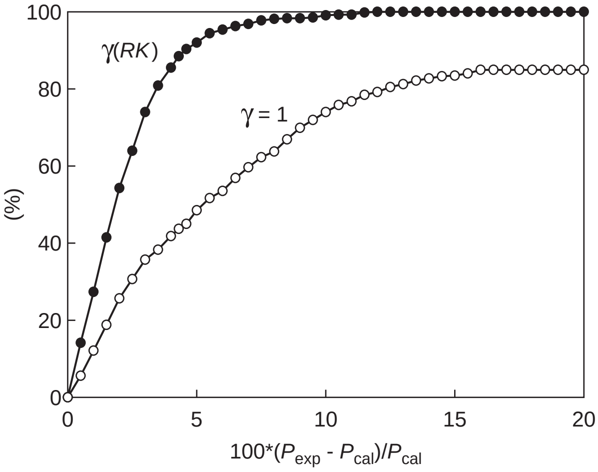

Figure 5

System H_2O-H_2S: percentage of pressure data reproduced with errors expressed by $100(P_{exp}-P_{cal})/P_{cal}$ where P_{exp} and P_{cal} are respectively the experimental and calculated pressures. γ *(RK)* curve is calculated using the fitted model (non ideal behaviour of the aqueous solution and pressure calculated with Equation (14); γ = 1 curve corresponds to the ideal behaviour of aqueous solution (pressure calculated with Equation (13)).

Parameters used to model the salting-out effect of Equation (26) are given in Table 9. Some isopleths with the same gas concentration and different salt concentrations are shown in Figure 4.

4.2 The H_2O-H_2S-NaCl System

The values of the fitting parameters of the Redlich-Kister's model are given in Table 7. The reproducibility of the experimental data for the pressure is significantly improved when the activity coefficients of water and H_2S in the aqueous phase are taken into account *(Fig. 5)*. More than 92% of the calculated pressures differ less than 5% from the experimental with this model whereas it is only 50% with the assumptions $\gamma_{H_2O}^{aq} = \gamma_{H_2S}^{aq} = 1$. A comparison between experimental data and the model is illustrated in the pressure-temperature plane *(Fig. 6)*. Different isopleths of the H_2O-H_2S system are plotted in Figure 7. As for the CO_2-H_2O system, the fitting of the model was not optimised using the composition of the

TABLE 8

Experimental and calculated composition of the vapour phase in the system H_2O-CO_2.
P_{exp}: experimental pressure; P_{calc}: calculated pressure; mCO_2: concentration (molality) of CO_2 in the aqueous phase;
yH_2O_{exp} (‰): experimental concentration of water in mole per mil; yH_2O_{calc} (‰) calculated concentration of water in mole per mil;
$\Delta y/y(\%) = 100^*(yH_2O_{exp}\text{-}yH_2O_{calc})/yH_2O_{exp}$

Ref. [1]

T (°C)	P_{exp} (bar)	mCO_2	yH_2O_{exp} (‰)	P_{calc} (bar)	yH_2O_{calc} (‰)	$\Delta y/y$ (%)
50	25.3	0.433	6.20	25.12	6.81	-9.91
50	50.7	0.769	3.83	50.12	5.06	-32.14
50	76	1.005	3.50	74.13	5.64	-61.12
50	101.3	1.143	4.49	96.61	9.60	-113.71
75	25.3	0.304	18.16	24.90	19.95	-9.83
75	101.3	0.92	8.29	98.14	13.67	-64.85
75	152	1.097	9.56	140.64	21.72	-127.22

Ref. [2]

T (°C)	P_{exp} (bar)	mCO_2	yH_2O_{exp} (‰)	P_{calc} (bar)	yH_2O_{calc} (‰)	$\Delta y/y$ (%)
75	25.3	0.302	18.16	24.73	20.05	-10.40
75	50.7	0.564	10.87	50.09	13.28	-22.17
93.3	25.3	0.242	34.71	23.73	40.90	-17.84
93.3	50.7	0.473	19.7	48.94	25.21	-27.97
93.3	101.4	0.816	13.74	97.27	21.62	-57.35

Ref. [3]

T (°C)	P_{exp} (bar)	mCO_2	yH_2O_{exp} (‰)	P_{calc} (bar)	yH_2O_{calc} (‰)	$\Delta y/y$ (%)
100	3.25	0.025	288	3.37	306.23	-6.33
100	6	0.054	155	6.15	171.92	-10.91
100	9.2	0.088	107	9.45	114.92	-7.40
100	11.91	0.116	77	12.21	90.99	-18.16
100	14.52	0.145	69	15.10	75.31	-9.15
100	18.16	0.183	54	18.97	61.94	-14.71
100	23.07	0.231	45	23.97	51.15	-13.67
120	5.99	0.039	337	6.13	333.93	0.91
120	9.39	0.071	205	9.57	218.90	-6.78
120	12.65	0.101	160	12.84	166.90	-4.31
120	16.31	0.133	122	16.38	134.15	-9.96
120	19.95	0.166	102	20.09	112.32	-10.12
120	24.12	0.202	83	24.19	96.04	-15.71
120	28.48	0.239	74	28.49	84.13	-13.69
140	6.5	0.022	569	6.10	602.58	-5.90
140	9.26	0.047	406	8.94	418.22	-3.01
140	11.93	0.073	317	11.92	319.32	-0.73
140	16.03	0.103	242	15.39	252.49	-4.34
140	20.1	0.139	200	19.62	203.29	-1.65
140	32.47	0.242	128	32.03	134.34	-4.96
160	8.78	0.022	732	8.72	719.14	1.76
160	11.44	0.047	579	11.63	548.06	5.34
160	14.17	0.073	476	14.68	441.49	7.25
160	17.77	0.103	388	18.23	362.38	6.60
160	21.83	0.139	323	22.53	299.99	7.12
160	25.88	0.171	275	26.39	261.38	4.95
160	34.08	0.242	211	35.10	205.80	2.47
180	14.39	0.045	728	15.21	677.24	6.97
180	21.01	0.103	522	21.98	484.38	7.21
180	26.15	0.150	431	27.53	396.92	7.91
180	32.8	0.208	359	34.48	327.38	8.81
180	40.7	0.275	300	42.65	274.95	8.35
180	49.1	0.343	257	51.10	238.70	7.12
200	20.0	0.038	767	19.79	802.00	-4.56
200	24.94	0.087	629	25.31	642.92	-2.21
200	31	0.143	514	31.68	527.83	-2.69
200	37.6	0.208	426	39.18	440.44	-3.39
200	45.7	0.279	365	47.51	376.02	-3.02
200	60.4	0.398	292	61.80	306.60	-5.00
200	20.27	0.051	755	21.25	751.99	0.40
200	26.38	0.109	592	27.80	591.60	0.07
200	34.0	0.178	471	35.71	476.35	-1.13
200	42.0	0.250	392	44.09	399.48	-1.91
200	51.2	0.327	332	53.22	343.67	-3.52
200	65.2	0.441	276	67.08	288.69	-4.60
200	81.1	0.579	238	84.49	246.32	-3.50

[1]: Wiebe and Gaddy (1939); [2]: Gillepsie and Wilson (1982); [3]: Müller *et al.* (1988).

TABLE 9

Fitting parameters for the calculation of the salting out effect on the Henry's constants in the systems H_2O-CO_2-NaCl and H_2O-H_2S-NaCl. The values of $K^{Psat}_{gas,aq,m_{NaCl}}$ are fitted to the Equation:

$$\log K^{Psat}_{gas,aq,m_{NaCl}} = \log K^{Psat}_{gas,a} + m_{NaCl}.\beta_1(T) + \left(m_{NaCl}\right)^2 \cdot \beta_2(T) + \left(m_{NaCl}\right)^3 \cdot \beta_3(T) \quad \text{with } \beta_i^j(T) = \sum_{i=0}^{i=4} B_i^j * (T)^j$$

H_2O-CO_2-NaCl $R^2 = 0.83$	B_i^0	$B_i^1 * 10^2$	$B_i^2 * 10^4$	$B_i^3 * 10^8$	$B_i^4 * 10^{11}$
β_1 (*T*)	3.114712456	-2.7655585	0.9176713976	-12.78795941	6.2704268351
β_2 (*T*)	-2.05637458	2.081980200	-0.765857702	12.011325315	-6.790343083
β_3 (*T*)	0.253424331	-0.26047432	0.0972580216	-1.551654794	0.8948557284
H_2O-H_2S-NaCl $R^2 = 0.74$	B_i^0	$B_i^1 * 10^2$	$B_i^2 * 10^4$	$B_i^3 * 10^7$	$B_i^4 * 10^{10}$
β_1 (*T*)	-12.4617636	12.69373100	-4.791540697	7.9817223650	-4.931093145
β_2 (*T*)	5.327383011	-5.82779828	2.3650333285	-4.207913036	2.7628521914
β_3 (*T*)	-0.75715275	0.831927411	-0.338668040	0.6037602785	-0.397049836

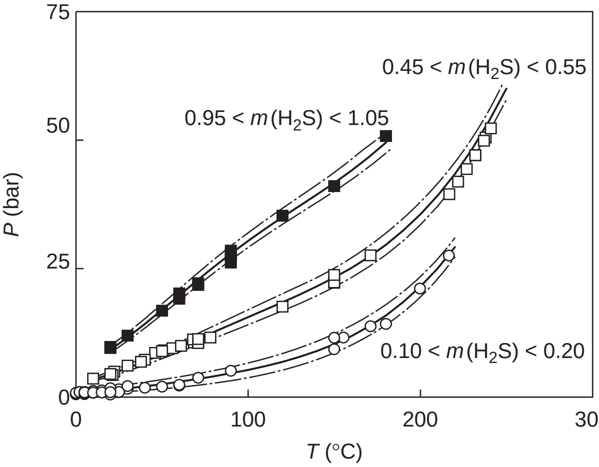

Figure 6

System H_2O-H_2S. Comparison of experimental data and the calculated values with the model. Experimental data are the different symbols. As the H_2S concentrations are not exactly identical within each set of data, three isopleths bracketing the compositions were calculated for each set of values. The lines represent the calculated isopleths with the concentration of H_2S in molal.

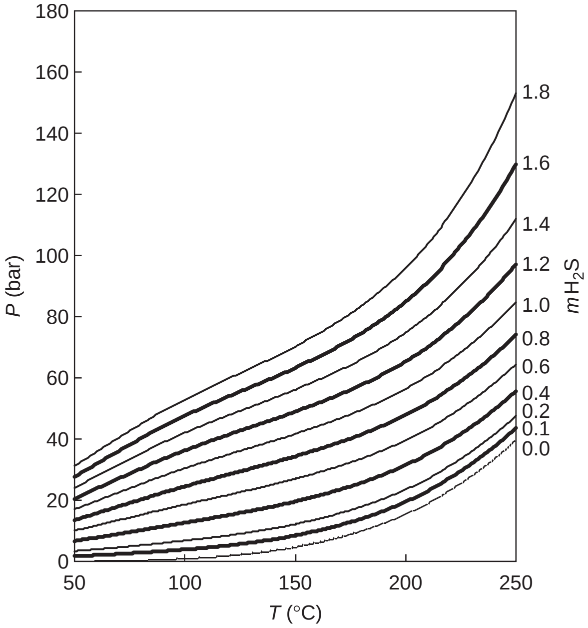

Figure 7

Isopleths in the system H_2O-H_2S for mH_2S between 0 (saturation pressure of pure H_2O) and 1.8 molal and for *m*NaCl = 0.

vapour phase since few data were available. The prediction of the composition of our model was checked with respect to the experimental data of Clarke and Glew (1971). Results *(Table 10)* are satisfactory since the maximum overestimation of the concentration of water is c.a. 5% at the exception of seven experimental data over sixty three.

Parameters used to model the salting-out effect of Equation (26) are given in Table 9. Some isopleths with the same gas concentration and different salt concentrations are shown in Figure 8.

CONCLUSIONS

An unsymmetric thermodynamic model is proposed to calculate the liquid-vapour equilibrium in the system H_2O-CO_2-NaCl system to 270°C and 300 bar and to 250°C and 150 bar

TABLE 10

Composition of the vapour phase in the system H_2O-H_2S. Experimental data from [1]: Clarke and Glew (1971); [2]: Selleck *et al.* (1952). P_{exp}: experimental pressure; P_{calc}: calculated pressure; mH_2S: concentration (molality) of H_2S in the aqueous phase; yH_2O_{exp} (‰) experimental concentration of water in mole per mile; yH_2O_{calc} (‰) calculated concentration of water in mole per mile

$\Delta y/y$ % = 100*(yH_2O_{exp} (‰)-yH_2O_{calc} (‰))/yH_2O_{exp} (‰)

Ref. [1]

T (°C)	P_{exp} (bar)	mH_2S	yH_2O_{exp} (‰)	P_{calc} (bar)	yH_2O_{calc} (‰)	$\Delta y/y$ (%)
0.001	0.55	1123	11.36	0.56	10.95	-3.59
0.001	0.66	0.346	9.52	0.67	9.16	-3.81
0	0.83	0.1697	7.60	0.85	7.28	-4.18
4.956	0.50	0.0862	17.72	0.51	17.29	-2.44
4.958	0.58	0.1009	15.22	0.59	14.82	-2.61
4.955	0.70	0.1223	12.62	0.72	12.27	-2.79
4.955	0.90	0.1568	9.92	0.92	9.61	-3.15
10.019	0.47	0.0687	26.66	0.47	26.24	-1.58
10.018	0.55	0.0807	22.83	0.55	22.43	-1.73
10.019	0.67	0.0984	18.85	0.67	18.49	-1.90
10.019	0.86	0.1272	14.71	0.86	14.38	-2.21
15.008	0.58	0.0735	29.90	0.58	29.63	-0.90
15.008	0.71	0.0903	24.54	0.71	24.27	-1.10
15.006	0.92	0.1182	18.95	0.92	18.68	-1.43
20.01	0.50	0.0547	47.35	0.50	47.22	-0.27
20.011	0.59	0.0649	40.25	0.59	40.09	-0.39
20.011	0.73	0.0803	32.88	0.72	32.69	-0.58
20.009	0.95	0.1061	25.21	0.95	24.97	-0.94
25.018	0.56	0.0534	57.50	0.55	57.59	0.15
25.016	0.68	0.0652	47.73	0.67	47.73	0.00
25.015	0.86	0.0840	37.55	0.85	37.45	-0.26
25.018	0.59	0.0564	54.64	0.58	54.67	0.06
25.017	0.73	0.0704	44.43	0.72	44.38	-0.12
25.017	0.96	0.0940	33.80	0.95	33.65	-0.43
25.03	0.56	0.0536	57.41	0.56	57.45	0.07
25.029	0.69	0.0669	46.62	0.69	46.57	-0.10
25.031	0.92	0.0897	35.35	0.91	35.21	-0.40
29.995	0.58	0.0482	74.79	0.57	75.02	0.31
29.992	0.71	0.0606	60.58	0.70	60.66	0.14
29.995	0.95	0.0818	45.79	0.94	45.72	-0.15
39.991	0.50	0.0312	150.02	0.49	151.26	0.83
39.991	0.62	0.0402	120.57	0.61	121.44	0.73
39.992	0.84	0.0561	89.84	0.82	90.30	0.51
49.987	0.55	0.0267	225.01	0.55	226.42	0.63
49.984	0.70	0.0353	180.00	0.69	180.95	0.53
49.985	0.95	0.0507	133.13	0.93	133.57	0.33

Ref. [2]

T (°C)	P_{exp} (bar)	mH_2S	yH_2O_{exp} (‰)	P_{calc} (bar)	yH_2O_{calc} (‰)	$\Delta y/y$ (%)
37.78	6.90	0.4589	10.6	6.12	11..55	8.94
37.78	10.34	0.6912	7.5	9.32	7.92	5.55
37.78	13.79	0.9313	6.0	12.70	6.09	1.49
37.78	17.24	1.1733	6.0	16.17	5.03	–16.17
37.78	20.69	1.4233	4.6	19.81	4.34	–5.58
71.11	6.90	0.3351	59.2	7.67	45.75	–22.72
71.11	10.34	0.4251	35.2	9.69	36.94	4.94
71.11	13.79	0.5720	27.4	13.03	28.43	3.76
71.11	17.24	0.7767	22.9	17.74	21.95	-4.13
71.11	20.69	0.8682	19.9	19.85	20.07	0.87
71.11	27.58	1.1675	11.3	26.78	16.10	42.47
71.11	34.48	1.4701	14.4	33.72	13.93	-3.27
71.11	41.37	1.7758	13.5	40.53	12.71	-5.84
104.44	13.79	0.4307	95.4	14.11	92.61	-2.92
104.44	27.58	0.8797	523	27.82	52.49	0.36
104.44	41.37	1.3068	40.3	40.65	40.25	-0.12
104.44	55.16	1.7227	35.3	52.45	35.06	-0.67
137.78	13.79	0.3182	212.5	14.72	246.89	16.18
137.78	27.58	0.7140	141.1	28.83	137.47	-2.57
137.78	41.37	1.0809	101.6	41.78	103.29	1.66
137.78	55.16	1.4233	84.5	53.55	87.51	3.57
137.78	68.95	1.7345	75.2	63.82	79.32	5.48
171.11	13.79	0.1614	601.9	14.40	583.59	-3.04
171.11	27.58	0.5267	317.2	28.56	315.71	-0.47
171.11	41.37	0.8739	222.8	42.05	229.63	3.07
171.11	55.16	1.2138	177.6	55.39	187.15	5.38
171.11	68.95	1.5873	153.4	70.36	160.34	4.52

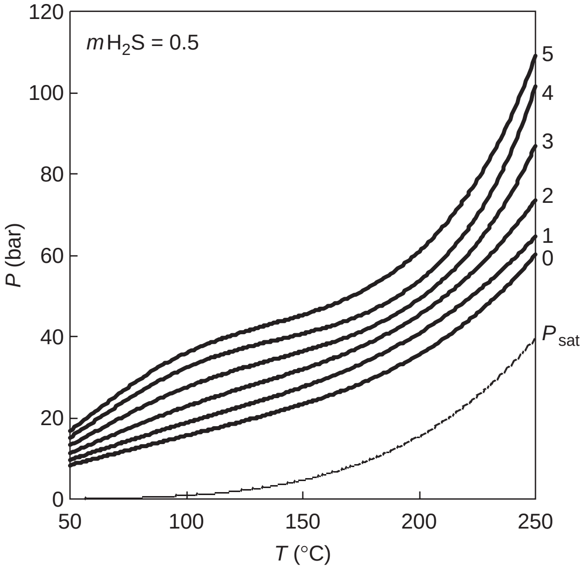

Figure 8

Isopleth of the liquid aqueous phase in the system H_2O-H_2S-NaCl for mH_2S = 0.5 molal and for different NaCl concentrations between 0 and 5 molal labelled along the right y axis. P_{sat} is the saturation line of pure water.

in the system H_2O-H_2S-NaCl. It is based on the description of the gaseous phase by the Stryjek and Vera's Equation of state, derived from the Peng-Robinson's Equation of state, and the combination of Henry's and Raoult's laws to describe the aqueous liquid phase. With respect to the gases, the deviation of the aqueous phase from ideality is taken into account using a Redlich-Kister's Equation. For salt-bearing aqueous solution, the effect of the salt is taken into account both via the Pitzer's formalism for the activity coefficient of water and via an extended Setchenow's law for the salting-out effect of the gases. The available experimental data checked for their consistency (temperature, composition of aqueous liquid phase, pressure) were fitted in order to best reproduce the experimental pressures for each system. The reproduction of experimental data is quite satisfactory. Furthermore, the composition of the vapour phase predicted for the model is correct for both system, but only above 100°C for the H_2O-CO_2 system. The model is restricted by construction to low gas concentrations and total pressures below 500 bar for the following reasons:

- the use of Henry's and Raoult's formalisms which are two limiting laws;
- the hypothesis of non variation with pressure of the molar volume of water and the molar volume at infinite dilution of the gases;
- the use of the Pitzer's Equations which were fitted along the saturation curves of the H_2O-NaCl system;
- the use of the Redlich-Kister's Equation with two parameters to model the activity coefficients of water and gases which requires two assumptions:
  - the nondependence on pressure of activity coefficients;
  - the calculation of the activity coefficient of gases γ_{gas}^{aq} from γ_{gas}^{aq*} and the activity coefficient at infinite dilution $\gamma_{gas}^{\infty,aq}$ (*Eqs. 15*, *19* and *20*), a procedure which is valid only at low gas concentrations and consequently at low pressures.

Taking into account the hypotheses underlying this model, the model can be introduced in more general software for solving water-rock interactions with the assumptions that the NaCl concentration is assumed equal to the ionic strength of the aqueous solution. This hypothesis is valid for dominantly NaCl-bearing aqueous solutions but not for $CaCl_2$ dominant aqueous solutions. In addition, it is worth noting that the calculation takes into account only the dissolved gaseous species $CO_{2,aq}$ and H_2S_{aq}, but not the corresponding ionic species such as HCO_3^-, CO_3^{2-}, HS^-, S^{2-}.

REFERENCES

Anderson, G.M. and Crerar, D.A. (1993) *Thermodynamics in Geochemistry. The Equilibrium Model*, Oxford University Press, New York, Oxford.

Bamberger, A., Sieder, G. and Maurer, G. (2000) High pressure (vapor + liquid) equilibrium in binary mixtures of (carbon dioxide + water or acetic acid) at temperatures from 313 to 353 K. *J. Supercritical Fluids*, **17**, 97-110.

Barrett, T.J., Anderson, G.M. and Lugowski, J. (1988) The solubility of hydrogen sulphide in 0-5 m NaCl solutions at 25-95°C and one atmosphere. *Geochim. Cosmochim. Acta*, **52**, 807-811.

Battistelli, A., Calore, C. and Pruess, K (1997) The simulator TOUGH2/EWASG for modelling geothermal reservoirs with brines and non-condensible gas. *Geothermics*, **26**, 437-464.

Briones, J.A., Mullins, J.C., and Thies, M.C. (1987) Ternary phase equilibria for acetic acid-water mixtures with supercritical carbon dioxide. *Fluid Phase Equilib.*, **36**, 235-246.

Carroll, J. and Mather, A.E. (1992) The system carbon-dioxide-water and the Krichevsky-Kasarnovsky equation. *Journal of Solution Chemistry*, **21**, 7, 607-621.

Carroll, J. and Mather, A.E. (1993) Fluid phase equilibria in the system hydrogen sulphide-water at high pressure. Application of an extended Henry's law. *Chem. Eng. Technol.*, **16**, 200-205.

Clarke, E.C.W. and Glew, D.N. (1971) Aqueous nonelectrolyte solutions. Part VIII. Deuterium and hydrogen sulfides in deuterium oxide and water. *Can. Jour. Chem.*, **49**, 691-698.

Crovetto, R. (1991) Evaluation of solubility data of the system CO_2-H_2O from 273 K to the critical point of water. *J. Phys. Chem. Ref. Data*, **20**, 576-589.

Dhorn, R., Devlieghere, F., and Thelen, D. (1993) Experimental measurements of phase equilibria for ternary and quaternary systems of glucose, water, CO_2 and ethanol with a novel apparatus. *Fluid Phase Equilib.*, **83**, 149-158.

Diamond, L.W. and Akinfiev, N.N. (2003) Solubility of CO_2 in water from –1.5 to 100°C from 0.1 to 100 MPa: evaluation of literature data and thermodynamic modelling. *Fluid Phase Equilib.*, **208**, 265-290.

Douabul, A.A. and Riley, J.P. (1979) The solubility of gases in distilled water and seawater. V. Hydrogen sulphide. *Deep-Sea Res*., **26 A**, 259-268.

Drummond, S.E. (1981) Boiling and mixing of hydrothermal fluids: chemical effects on mineral precipitation. *PhD Thesis*, Pennsylvania State University.

Drummond, S.E. and Ohmoto, H. (1985) Chemical evolution and mineral deposition in boiling hydrothermal systems. *Econ. Geol*., **80**, 126-147.

D'Souza, R., Patrick, J.R., and Teja, A.S. (1998) High pressure phase equilibria in the carbon dioxide-*n*-hexadecane and carbon dioxide-water systems. *Can. J. Chem. Eng*., **66**, 319-323.

Duan, Z., Møller, N., Greenberg, J., and Weare, J.H. (1992) The prediction of methane solubility in natural waters to high ionic strength from 0 to 250°C and from 0 to 1600 bar. *Geochim. Cosmochim. Acta*, **56**, 1451-1460.

Duan, Z., Møller, N. and Weare, J.H. (1996) Prediction of the solubility of H_2S in NaCl aqueous solution: an equation of state approach**.** *Chemical Geology*, **130**, 15-20.

Dubessy, J., Buschaert S., Lamb, W., Pironon, J. and Thiéry, R. (2001) Methane-bearing aqueous fluid inclusions: Raman analysis, thermodynamic modelling and application to petroleum basins. *Chem. Geol*., **173**, 193-205.

Gamsjäger, H. and Schindler, P. (1969) Löslichkeiten und Aktivitätskoeffizienten von H_2S in Elektrolytmischungen. *Helv. Chim. Acta*, **52**, 1395-1402.

Gillepsie, P.C. and Wilson, G.M. (1982) Vapor-liquid and liquid-liquid equilibria: water-methane, water-carbon dioxide, water-hydrogen sulfide, water-*n*pentane, water-methane-*n*pentane. *Research Report RR-48*, *Gas Processors Association*, Tulsa, Oklahoma.

Guillaume, D., Teinturier, S., Dubessy, J. and Pironon, J. (2003) Calibration of methane analysis by Raman spectroscopy in H_2O-NaCl-CH_4 fluid inclusions. *Chem. Geol.* **194**, 41-49.

Haas, J.L. (1976) Physical properties of the coexisting phases and thermochemical properties of the H_2O component in boiling NaCl solutions. *Geological Survey Bulletin 1421-A*.

Harvey, A.H. (1996) Semi-empirical correlation for Henry's constants over large temperature ranges. *AIChE. J*., **42**, 1491-1494.

Kendall, J. and Andrews, J.C. (1921). The solubilities of acids in aqueous solutions of other acids. *J. Am. Chem. Soc.*, **43**,1545-1560.

King, M.B., Mubarak, A., Kim, J.D., and Bott, T.R. (1992) The mutual solubilities of water with supercritical and liquid carbon dioxide. *J. Supercrit. Fluids*, **5**, 296-302.

Kozintseva, T.N. (1964) Solubility of hydrogen sulfides in water at elevated temperatures. *Geochem. Int*., **1**,750-756.

Lee, J.I. and Mather, A.E. (1977) Solubility of hydrogen sulfide in water. *Ber. Bunsenges. Phys. Chem.*, **81**, 1020-1023.

Lewis, G.N., Randall, M., Pitzer, K.S. and Brewer, L. (1961) *Thermodynamics*, McGraw-Hill, New York.

Malinin, S.D. and Savelyeva, N.I. (1972) The solubility of CO_2 in NaCl and $CaCl_2$ solutions at 25, 50 and 75°C under elevated CO_2 pressures. *Geochem. Int.*, **9**, 410-418.

Malinin, S.D. and Kurovskova, N.I. (1975) Solubility of CO_2 in chloride solutions at elevated temperatures and CO_2 pressures. *Geochem. Int*., **12**, 199-201.

Matous, J., Sobr, J., Novak, J.P. and Pick, J. (1969) Solubility of carbon dioxide in water at pressures up to 40 atm. *Collection Czechoslov. Cem. Commun*., **34**, 3982-3985.

Müller, G., Bende, E. and Maurer, G. (1988) Das Dampf-flüssigkeitsgleichgewicht des ternären systems Ammoniak-Kohlendioxide-Wasser bei hohen Wassergehalten im Berich zwischen 373 und 473 Kelvin. *Ber. Bunsenges. Phys. Chem.*, **92,** 148-160.

Nighswander, J.A., Kalogerakis, N. and Mehrotra, A.K. (1989) Solubilities of carbon dioxide in water and 1 wt % NaCl solution at pressures up to 10 MPa and temperatures from 80 to 200°C. *J. Chem. Eng. Data*, **34**, 355-360.

Pichavant, M., Ramboz, C. and Weisbrod, A. (1982) Fluid immiscibility in natural processes: use and misuse of fluid inclusion data. I. Phase equilibria analysis – A theoretical and geometrical approach. *Chem. Geol*., **37**, 1-28.

Plyasunov, A.V., O'Connell, J.P., Wood, R.H. and Shock, E.L. (2000a) Infinite dilution partial molar properties of aqueous solutions of nonelectrolytes. I. Equations for partial molar volumes at infinite dilution and standard thermodynamic functions of hydration of volatile nonelectrolytes over wide ranges of conditions. *Geochim. Cosmochim. Acta*, **64**, 495-512.

Plyasunov, A.V., O'Connell, J.P., Wood, R.H. and Shock, E.L. (2000b) Infinite dilution partial molar properties of aqueous solutions of nonelectrolytes. II. Equations for the standard thermodynamic functions of hydration of volatile nonelectrolytes over wide ranges of conditions including subcritical temperatures. *Geochim. Cosmochim. Acta*, **64**, 2779-2795.

Prausnitz, J.M., Lichtenthaler, R.N. and Gomes de Azevedo, E. (1986) *Molecular Thermodynamics of Fluid-Phase Equilibria*, Second Edition, Prentice-Hall, Englewood Cliffs, New Jersey.

Prini, R.F. and Crovetto, R. (1989) Evaluation of data on solubility of simple apolar gases in light and heavy water at high temperature. *J. Phys. Chem. Ref. Data*, **18**, 1231-1243.

Prutton, C.F. and Savage, R.L. (1945) The solubility of carbon dioxide in water and calcium chloride solutions. *J. Am. Chem. Soc*., **67**, 1150-1154.

Ramboz, C., Pichavant, M. and Weisbrod, A. (1982) Fluid immiscibility in natural processes: use and misuse of fluid inclusion data. II. Interpretation of fluid inclusion data in terms of immiscibility. *Chem. Geol*., **37**, 29-48.

Reed, M.H. and Spycher, N.F. (1985) Boiling, cooling, and oxidation in epithermal systems: a numerical modeling approach. In: *Geology and Geochemistry of Epithermal Systems*, Berger, B.R. and Bethke, P.M. (eds.), *Reviews in Economic Geology*, **2**, 249-272.

Rumpf, B., Nicolaisen, H., Ocal, C. and Maurer, G. (1994) Solubility of carbon dioxide in aqueous solutions of sodium chloride: experimental results and correlation. *J. Solution Chem*., **23**, 431-448.

Sako, T., Sugeta, T., Nkasawa, N., Obuko, T., Sato, M., Taguchi, T. and Hiaki, T. (1991) Phase equilibrium study of extraction and concentration of furfural produced in reactor using supercritical carbon dioxide. *Jour. Chem. Engineering Japan*, **24**, 449-454.

Selleck, F.T., Carmichael, L.T. and Sage, B.H. (1952) Phase behavior in the hydrogen sulfide-water system. *Ind. Eng. Chem*., **44**, 2219-2226.

Shmulovich, K.I., Tkachenko, S.I. and Plyasunova, N.V. (1995) Phase equilibria in fluid systems at high pressures and temperatures. In: *Fluids in the Crust – Equilibrium and Transport Properties*, Shmulovich, K.I., Yardley, B.W.D. and Gonchar, G.G. (eds.), Chapman & Hall, London.

Silvester, F. and Pitzer, K. (1977) Thermodynamics of electrolytes. 8. High-temperature properties, including enthalpy and heat capacity, with application to sodium chloride. *Jour. Phys. Chem.*, **81**, 1822-1828.

Stryjek, R. and Vera, J.H. (1986a) An improved Peng-Robinson equation of state for pure compounds and mixtures. *Can. J. Chem. Eng.*, **64**, 323-333.

Stryjek, R. and Vera, J.H. (1986b) An improved Peng-Robinson equation of state with new mixing rules for strongly non ideal mixtures. *Can. J. Chem. Eng.*, **64**, 334-340.

Stryjek, R. and Vera, J.H. (1986c) A cubic equation of state for accurate vapor-liquid equilibria calculations. *Can. J. Chem. Eng.*, **64**, 820-826.

Suleimenov, O.M. and Krupp, R.E. (1994) Solubility of hydrogen sulfide in pure water and in NaCl solutions, from 20 to 320°C and at saturation pressures. *Geochim. Cosmochim. Acta*, **58**, 2433-2444.

Takenouchi, S. and Kennedy, G.C. (1964) The binary system H_2O-CO_2 at high temperatures and pressures. *Am. J. Sci.*, **262**, 1055-1072.

Tödheide, K., and Franck, E.U. (1963) Das Zweipahsengebiet und die kritische Kurve im system Kohlendioxid-Wasser bis zu Drucken von 3600 bar. *Z. Phys. Chemie. Neue Folge*, **37**, 387-401.

Wiebe, R. and Gaddy, V.L. (1939) The solubility of carbon dioxide at 50 , 75, and 100°, at pressures to 700 atmospheres. *J. Am. Chem. Soc.*, **61**, 315-318.

Wiebe, R. and Gaddy, V.L. (1941) Vapor phase composition of carbon dioxide-water mixtures at various temperatures and at pressures to 700 atmospheres. *J. Am. Chem. Soc.*, **63**, 475-477.

Wright, R.H. and Maas, O. (1932) The solubility of hydrogen sulphide in water from the vapor pressures of the solutions. *Can. J. Res.*, **6**, 94-101.

Zawisza, A. and Malesinska, B. (1981) Solubility of carbon dioxide in liquid water and of water in gaseous carbon dioxide in the range 0.2-5 MPa and at temperatures up to 473 K. *J. Chem. Eng. Data*, **26**, 388-391.

Zel'vinskii, Y. (1937) Carbon dioxide solubility in water under pressure. *Zhurn. Khim. Prom.*, **14**, 1250-1257.

Final manuscript received in November 2004

APPENDIX 1

Equations and Procedure for Calculating the Activity Coefficient of Gas and Water in the Aqueous Solution

The activity coefficients of the gas in the aqueous phase $\gamma^{\mathrm{aq}}_{\mathrm{gas}}$ is calculated from the following Equation:

$$\gamma^{\mathrm{aq}}_{\mathrm{gas}} = \frac{y^{\mathrm{aq,nid},P_{\mathrm{exp}}}_{\mathrm{gas}}}{y^{\mathrm{aq,id},P_{\mathrm{cal}}}_{\mathrm{gas}}} \frac{\varphi^{P_{\mathrm{exp}}}_{\mathrm{gas}}}{\varphi^{P_{\mathrm{cal}}}_{\mathrm{gas}}} \frac{P_{\mathrm{exp}}}{P_{\mathrm{cal}}} \exp\left(\frac{\overline{v^{\infty}_{\mathrm{gas}}}}{RT}\left(P_{\mathrm{cal}} - P_{\mathrm{exp}}\right)\right) \qquad \text{(A1)}$$

$y^{\mathrm{aq,id},P_{\mathrm{cal}}}_{\mathrm{gas}}$ is the mole fraction of the gas in the nonaqueous phase calculated assuming an ideal mixing between gas and water in the aqueous solution by solving the system of Equations (13).

$y^{\mathrm{aq,nid},P_{\mathrm{exp}}}_{\mathrm{gas}}$ is the mole fraction of the gas in the nonaqueous phase calculated considering that the activity coefficient of gas and water in aqueous solution are not equal to 1 by solving the system of Equations (16).

$\varphi^{P_{\mathrm{exp}}}_{\mathrm{gas}}$ is the fugacity of the gas component in the nonaqueous phase calculated at $T, P_{\mathrm{exp}}, y^{\mathrm{aq,nid},P_{\mathrm{exp}}}_{\mathrm{gas}}$.

$\varphi^{P_{\mathrm{cal}}}_{\mathrm{gas}}$ is the fugacity of the gas component in the nonaqueous phase calculated at $T, P_{\mathrm{cal}}, y^{\mathrm{aq,id},P_{\mathrm{cal}}}_{\mathrm{gas}}$

The activity coefficients of water in the aqueous phase $\gamma^{\mathrm{aq}}_{\mathrm{H_2O}}$ is calculated from the following Equation:

$$\gamma^{\mathrm{aq}}_{\mathrm{H_2O}} = \frac{\left(1 - y^{\mathrm{aq,nid},P_{\mathrm{exp}}}_{\mathrm{gas}}\right)}{\left(1 - y^{\mathrm{aq,id},P_{\mathrm{cal}}}_{\mathrm{gas}}\right)} \frac{\varphi^{P_{\mathrm{exp}}}_{\mathrm{H_2O}}}{\varphi^{P_{\mathrm{cal}}}_{\mathrm{H_2O}}} \frac{P_{\mathrm{exp}}}{P_{\mathrm{cal}}} \frac{\exp\left[\int_{P_{\mathrm{sat}}}^{P_{\mathrm{cal}}} \frac{\overline{V^{\mathrm{liq}}_{\mathrm{H_2O}}}}{RT} \cdot dP\right]}{\exp\left[\int_{P_{\mathrm{sat}}}^{P_{\mathrm{exp}}} \frac{\overline{V^{\mathrm{liq}}_{\mathrm{H_2O}}}}{RT} \cdot dP\right]} \qquad \text{(A2)}$$

The flowchart for the calculations of the activity coefficients of the gas component and water in the aqueous phase $\gamma^{\mathrm{aq}}_{\mathrm{gas}}$ and $\gamma^{\mathrm{aq}}_{\mathrm{H_2O}}$ is illustrated below. ε is a number which measures the accuracy in pressure calculation. From the values of $\gamma^{\mathrm{aq}}_{\mathrm{gas}}$ and $\gamma^{\mathrm{aq}}_{\mathrm{H_2O}}$ estimated from this procedure, the parameters *a*, *b*, *c*, *d*, and *e* of Margules-Redlich-Kister's parameters *B* and *C* are estimated to best reproduce the activity coefficients according to Equations (18), (19) and (20) (values in *Table 7*).

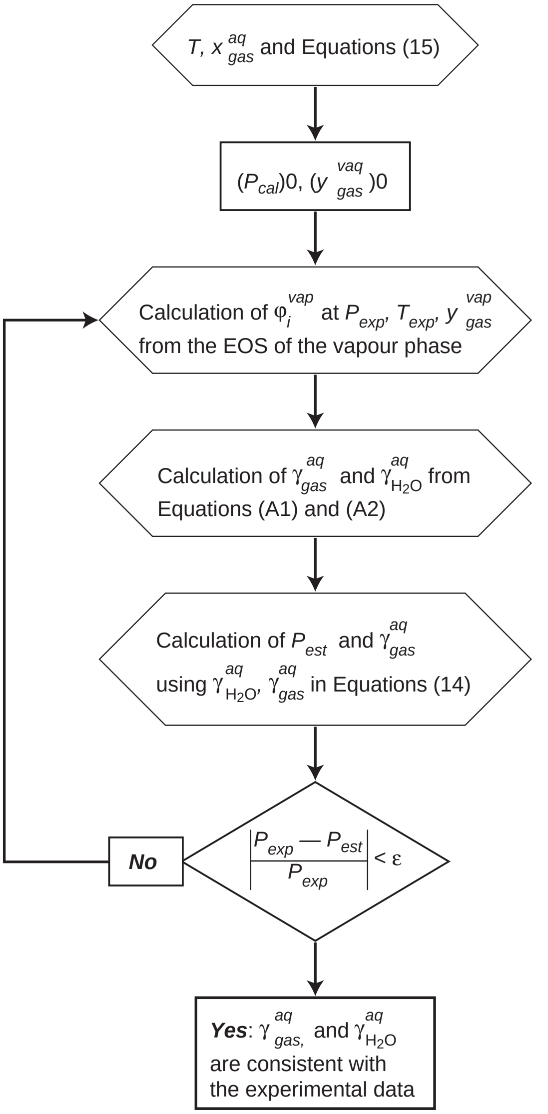

Flowchart illustrating the procedure for estimating $\gamma^{\mathrm{aq}}_{\mathrm{gas}}$ and $y^{\mathrm{aq}}_{\mathrm{H_2O}}$.

APPENDIX 2

Calculation of Henry Constant's for NaCl-Bearing Aqueous Solution

The composition of the aqueous phase and the pressure and temperature conditions are known. The only unknown in the Equation relative to the gas component is the composition of the vapour phase:

$$\gamma^{aq}_{H_2O}\left(1 - x^{aq}_{gas} - x^{aq}_{NaCl}\right) P_{sat} \cdot \varphi^{sat}_{H_2O} \cdot \exp\left[\int_{P_{sat}}^{P} \frac{\overline{V^{liq}_{H_2O}}}{RT}.dP\right] = \left(1 - y^{vap}_{gas}\right) \cdot P \cdot \varphi^{vap}_{H_2O}$$

Using this Equation, the gas concentration in the vapour phase y^{vap}_{gas} is calculated until convergence is obtained. Then the Henry's constant is derived with the following Equation at each temperature:

$$\gamma^{aq*}_{gas} \cdot K^{P_{sat}}_{gas,aq,m_{NaCl}} .x^{aq}_{gas} \cdot \exp\left(\frac{\overline{v^{\infty}_{gas}}.\left(P - P_{sat}\right)}{RT}\right) = y^{vap}_{gas} \cdot P \cdot \varphi^{vap}_{gas}$$

Oil & Gas Science and Technology – Rev. IFP, Vol. 60 (2005), No. 2, pp. 275-285

IFP International Workshop
Rencontres scientifiques de l'IFP

Gas-Water-Rock Interactions ... / Interactions gaz-eau-roche ...

Thermodynamic Analysis of Organic/ Inorganic Reactions Involving Sulfur: Implications for the Sequestration of H_2S in Carbonate Reservoirs

L. Richard[1,2], N. Neuville[1], J. Sterpenich[2], E. Perfetti[1,2] and J.C. Lacharpagne[3]

1 Université Henri-Poincaré, Département des sciences de la Terre, 54506 Vandœuvre-lès-Nancy Cedex - France
2 Géologie et gestion des ressources minérales et énergétiques, UMR 7566 G2R, 54506 Vandœuvre-lès-Nancy Cedex - France
3 Total, CSTJF, avenue Larribau, 64018 Pau Cedex - France
e-mails: laurent.richard@g2r.uhp-nancy.fr - nadineneuville@yahoo.fr - jerome.sterpenich@g2r.uhp-nancy.fr - erwan.perfetti@g2r.uhp-nancy.fr
jean-claude.lacharpagne@total.com

Résumé — Étude thermodynamique des réactions organiques/inorganiques du soufre : implications pour la séquestration de H_2S dans des réservoirs carbonatés — Les interactions eaux-gaz-roches-hydrocarbures impliquant le soufre dans des réservoirs pétroliers carbonatés sont analysées d'un point de vue thermodynamique. Des calculs d'équilibre minéraux-solutions indiquent que les eaux de formation de réservoirs carbonatés du Bassin parisien, du bassin de l'Alberta et de la mer du Nord sont en équilibre avec la calcite et la dolomite, mais qu'elles ne le sont pas avec l'anhydrite. Une augmentation de l'activité du sulfure d'hydrogène dans la phase aqueuse ($a_{H_2S_{(aq)}}$) favorise la formation de soufre élémentaire, laquelle constitue une réaction de séquestration possible pour H_2S.

Il est également suggéré que les fortes pressions partielles de H_2S associées à une réduction thermochimique des sulfates dans des réservoirs carbonatés pourraient être contrôlées par des équilibres métastables entre hydrocarbures, composés organiques soufrés, soufre élémentaire et H_2S gazeux. Ces pressions partielles de H_2S sont de 4 à 6 ordres de grandeur plus élevées que celles observées dans les réservoirs clastiques et pour lesquelles un contrôle par des équilibres entre H_2S, pyrite et carbonates ferrifères a été proposé. Selon les rapports H/C des hydrocarbures et des composés organiques soufrés, H_2S peut être soit produit, soit consommé au cours des réactions de sulfurisation des huiles dans les réservoirs carbonatés.

Abstract* — *Thermodynamic Analysis of Organic/Inorganic Reactions Involving Sulfur: Implications for the Sequestration of H_2S in Carbonate Reservoirs — *A thermodynamic analysis has been made of water-gas-rock-hydrocarbon interactions involving sulfur in carbonate reservoirs. Mineral-solution equilibria calculations indicate that formation waters produced from carbonate reservoirs at temperatures between 40°C and 160°C in the Paris Basin, Alberta Basin, and the North Sea are saturated with respect to calcite and dolomite, but undersaturated with respect to anhydrite. The calculations also suggest that increasing the activity of dissolved H_2S ($a_{H_2S_{(aq)}}$) in the reservoirs favors the formation of elemental sulfur, which constitutes a potential sequestration reaction for H_2S.*

It is also shown that high partial pressures of H_2S generated by thermochemical sulfate reduction in carbonate reservoirs may be controlled by metastable equilibrium states between hydrocarbons, organic *sulfur compounds, elemental sulfur, and H_2S at partial pressures which are 4 to 6 orders of magnitude higher than in clastic reservoirs where the H_2S partial pressures are controlled by pyrite and iron carbonates. Depending on the H/C ratios of the hydrocarbons and organic sulfur compounds, H_2S may be consumed or produced as a result of petroleum sulfurization reactions in carbonate reservoirs.*

INTRODUCTION

Carbon dioxide (CO_2) and hydrogen sulfide (H_2S) are both gases of environmental concern. The constant increase in the concentration of atmospheric CO_2 with increasing industrial activity over the last 150 years is a major cause in today's climate change [1], and the sequestration of CO_2 through dissolution in formation waters and subsequent neutralization of aqueous carbonic acid by rock-forming minerals has been proposed as a short-term means to reduce the level of CO_2 released into the atmosphere [2]. The conversion into elemental sulfur of the hydrogen sulfide which is commonly produced along with CO_2 from sour gas-containing reservoirs is sometimes of doubtful economic interest. A possible alternative is the reinjection of CO_2-H_2S mixtures in depleted hydrocarbon reservoirs [3-5]. Such a reinjection of CO_2-H_2S mixtures in gas-water-rock-hydrocarbon environments will result in thermal and chemical perturbations, which will be manifested by mass transfers among the gas phase, formation waters, liquid hydrocarbons, and rock-forming minerals. The transformations resulting from the injection may include, among others, a drastic decrease in the pH of the aqueous fluids, the dissolution of carbonates and sulfates, the precipitation of sulfides and elemental sulfur, and the formation of organic sulfur compounds through sulfurization of the residual oil. Following the metastable equilibrium approach pioneered by Helgeson *et al.* [6], we present a thermodynamic analysis of the equilibrium relations between minerals, aqueous fluids, hydrocarbons, and hydrogen sulfide in carbonate reservoirs.

1 THERMODYNAMIC RELATIONS

The equilibrium constant $K_{r,T,P}$ of the rth reaction at a given temperature T and pressure P is given by:

$$K_{r,T,P} = \exp \frac{-\Delta G_r^\circ}{RT} \tag{1}$$

where ΔG_r° is the standard molal Gibbs free energy of the rth reaction, R stands for the gas constant (1.9872 cal mol^{-1}K^{-1}), and T and P denote the absolute temperature and total pressure expressed in Kelvin and bar, respectively. The standard molal Gibbs free energy of the rth reaction is defined by:

$$\Delta G_r^\circ = \sum_i n_{i,r} \Delta G_i^\circ \tag{2}$$

where $n_{i,r}$ represents the reaction coefficient of the ith species in the rth reaction, which is negative for reactants and positive for products, and ΔG_i° stands for the apparent standard molal Gibbs free energy of formation of the ith species at the temperature T and pressure P of interest. Omitting the i subscript for simplicity, the latter property can be calculated from [7]:

$$\Delta G_i^\circ \equiv \Delta G^\circ = \Delta G_f^\circ + (G_{T,P}^\circ - G_{T_r,P_r}^\circ) \tag{3}$$

where ΔG_f° stands for the standard molal Gibbs free energy of formation at the reference temperature and pressure of 25°C and 1 bar, and $(G_{T,P}^\circ - G_{T_r,P_r}^\circ)$ represents the difference in the standard molal Gibbs free energy of the ith species at the temperature and pressure of interest, and that at the reference temperature and pressure (T_r and P_r). In accord with [6], the standard state adopted for minerals, liquid H_2O, and liquid hydrocarbons and organic sulfur compounds in petroleum is one of unit activity of the thermodynamic components of stoichiometric minerals and pure liquids at any temperature and pressure. The standard state for aqueous species other than H_2O is one of unit activity of the species in a hypothetical one molal solution referenced to infinite dilution at any pressure and temperature. The standard state for gases is specified as unit fugacity of the pure hypothetical ideal gas at 1 bar and any temperature.

The parenthetical term in Equation (3) is evaluated by integrating in temperature and pressure the expression:

$$\begin{aligned} G_{T,P}^\circ - G_{T_r,P_r}^\circ = & -S_{T_r,P_r}^\circ (T - T_r) + \int_{T_r}^{T} C_{P_r}^\circ \, dT \\ & -T \int_{T_r}^{T} C_{P_r}^\circ \, d\ln T + \int_{P_r}^{P} V^\circ dP \end{aligned} \tag{4}$$

where S_{T_r,P_r}° stands for the standard molal entropy of the species at 25°C and 1 bar, $C_{P_r}^\circ$ denotes the standard molal heat capacity of the species at the reference pressure of 1 bar, and V° represents the standard molal volume of the species at the temperature and pressure of interest. The temperature dependence above 298.15 K of the standard molal heat capacity at 1 bar of minerals, inorganic gases, and organic liquids can be represented by the Maier-Kelley equation [7-9], which is written as [10]:

$$C_{P_r}^\circ = a + bT + cT^{-2} \tag{5}$$

where a, b, and c stand for temperature-independent coefficients. Consideration of compressibility and thermal expansivity data indicates that the standard molal volume of minerals is insensitive to changes in temperature and pressure for the conditions encountered in sedimentary basins [7]. Although the standard molal volumes of organic liquids are much more dependent on temperature and pressure than those of minerals, experimental data indicate that the effects of simultaneously increasing temperature and pressure tend to compensate along typical sedimentary basin geotherms [11]. Consequently, the last integral in Equation (4) reduces to:

$$\int_{P_r}^{P} V^\circ dP = V^\circ_{T_r,P_r}(P - P_r) \tag{6}$$

for minerals and organic liquids, with $V^{o}_{T_r,P_r}$ representing the standard molal volume of the species at the reference temperature and pressure of 25°C and 1 bar. Adopting for gases a standard state of unit fugacity of the pure hypothetical ideal gas at 1 bar and any temperature requires that:

$$V^{o} = 0 \tag{7}$$

for gases at all temperatures and pressures [6]. Finally, the partial molal equivalent of Equation (4) for aqueous species which may be written as:

$$\begin{aligned}\overline{G}^\circ_{T,P} - \overline{G}^\circ_{T_r,P_r} &= -\overline{S}^\circ_{T_r,P_r}(T - T_r)\\ &+ \int_{T_r}^{T} \overline{C}^\circ_{P_r} dT - T\int_{T_r}^{T} \overline{C}^\circ_{P_r} d\ln T + \int_{P_r}^{P} \overline{V}^\circ dP\end{aligned} \tag{8}$$

is evaluated by taking account of the revised Helgeson-Kirkham-Flowers equations of state for the standard partial molal heat capacity and standard partial molal volume at the temperature and pressure of interest, which are given by [12]:

$$\begin{aligned}\overline{C}^\circ_{P_r} &= c_1 + \frac{c_2}{(T-\theta)^2} - \left[\frac{2T}{(T-\theta)^3}\right] \times \left[a_3(P - P_r) + a_4 \ln\left(\frac{\Psi + P}{\Psi + P_r}\right)\right]\\ &+ \omega TX + 2TY\left(\frac{\partial\omega}{\partial T}\right)_P - T\left(\frac{1}{\varepsilon - 1}\right)\left(\frac{\partial^2\omega}{\partial T^2}\right)_P\end{aligned} \tag{9}$$

and:

$$\begin{aligned}\overline{V}^\circ &= a_1 + a_2\left(\frac{1}{\Psi + P}\right)\\ &+ \left[a_3 + a_4\left(\frac{1}{\Psi + P}\right)\right]\left(\frac{1}{T - \theta}\right) - \omega Q + \left(\frac{1}{\varepsilon} - 1\right)\left(\frac{\partial\omega}{\partial P}\right)_T\end{aligned} \tag{10}$$

where a_1, a_2, a_3, a_4, c_1, c_2, and ω represent species-dependent equation of state parameters, ψ and θ designate solvent-dependent parameters equal to 2600 bar and 228 K, ε is the dielectric constant of H_2O, and Q, X, and Y refer to the Born functions. The equations summarized above can be solved with the aid of the SUPCRT92 computer program [13], together with thermodynamic properties and parameters for minerals, gases, aqueous species, and liquid hydrocarbons and organic sulfur compounds [7-9, 14, 15]. The thermodynamic properties at 25°C and 1 bar, heat capacity coefficients, and transition properties at 1 bar for elemental sulfur are the following [16]:

ΔG^{o}_{f} [a]	ΔH^{o}_{f} [a]	S^{o} [b]	V^{o} [c]
0	0	7.6	15.511

a [b]	b [d]	c [e]	T_{t,P_r} [f]	$\Delta H^{o}_{t,P_r}$ [a]	$\Delta V^{o}_{t,P_r}$ [c]
3.58	0.00624	0	368.6	86	0.979
3.56	0.00696	0	392	410	1.137
5.4	0.005	0	718	–	–

[a] cal mol^{-1}; [b] cal $mol^{-1}K^{-1}$; [c] cm^3mol^{-1}; [d] cal $mol^{-1}K^{-2}$; [e] cal K mol^{-1}; [f] K.

2 FORMATION WATER CHEMISTRY IN CARBONATE RESERVOIRS

Thermodynamic calculations indicate that most formation waters produced from carbonate reservoirs are close to equilibrium with respect to calcite and dolomite, but not anhydrite [17-19]. This is illustrated in Figure 1, where values of the saturation index computed in the manner described below with the EQUIL program [20] for these three minerals have been plotted as a function of reservoir temperature. The symbols correspond to formation waters produced from Jurassic reservoirs of the Paris Basin [17] and the North Sea [18], as well as Devonian rocks from the Alberta Basin [19]. Only those waters for which the electric neutrality was respected within:

$$\sum m_i z_i = \pm\, 0.1 \tag{11}$$

where m_i and z_i stand for the molality and charge of the ith ionic species, were considered in the calculations. The saturation index Ω is defined by:

$$\Omega = \log\frac{Q_r}{K_r} \tag{12}$$

where Q_r denotes the ion activity product and K_r represents the equilibrium constant for the rth reaction. The ion activity product is in this case defined by the product of the aqueous activities of the constitutive ions of the mineral for which the saturation test is performed according to:

$$Q_r = \prod_i a_i^{n_i} \tag{13}$$

where a_i and n_i stand for the activity and stoichiometric coefficient of the ith ionic species, respectively. The activity a_i of an aqueous species is defined by:

$$a_i = \gamma_i\, m_i \tag{14}$$

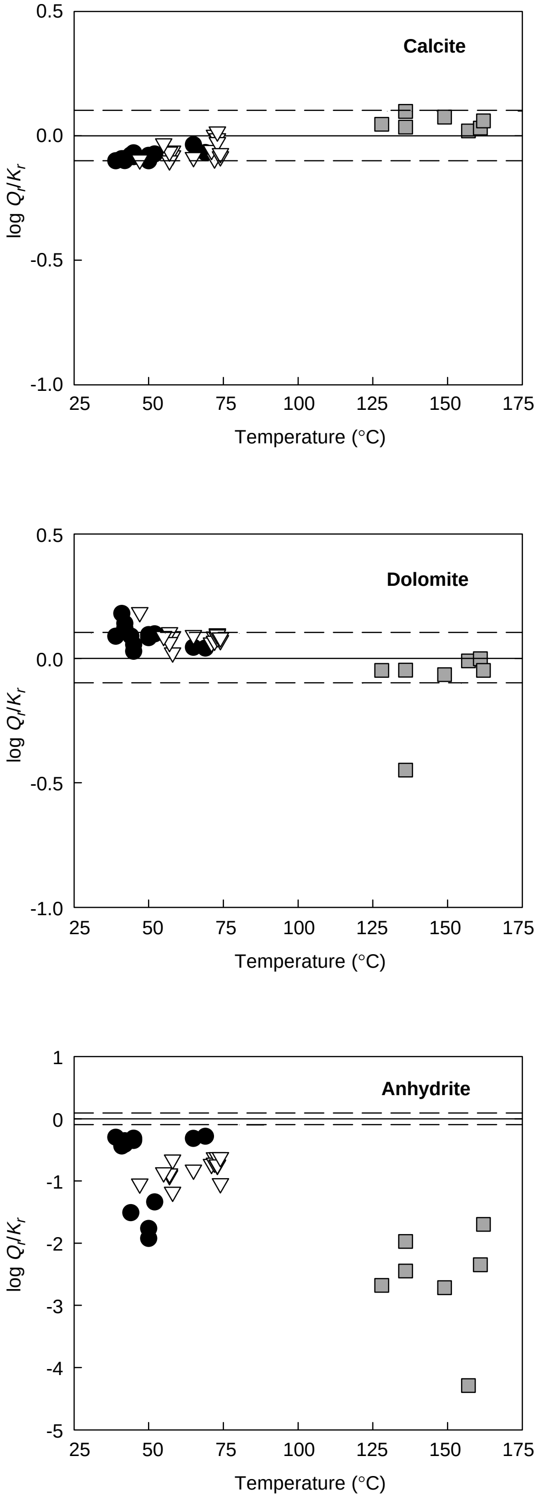

Figure 1

Saturation index for calcite, dolomite, and anhydrite as a function of temperature. The symbols correspond to formation waters of the Alberta Basin (●), the Paris Basin (∇), and the North Sea (■). The solid and dashed lines indicate solution-mineral equilibrium and departures of ± 0.1 log unit from this equilibirum, respectively – see text.

where γ_i and m_i designate the activity coefficient and molality of the ith species in the formation water. Activity coefficients of ionic species are computed by the EQUIL program using the Debye-Hückel equation modified by Helgeson [21].

According to a procedure described elsewhere [19], the pH values of the fluids were first adjusted to bring calcite to within ± 0.1 log unit from equilibrium. This pH adjustment is based on the hypothesis that pH values measured at the surface are somewhat different from the actual values at depth, as well as on the observation that calcite is usually the most abundant mineral in carbonate reservoirs. These recalculated pH values were in all cases less than a unit lower than the corresponding surface values. In addition, the pH adjustment resulted in 29 formation waters of the 34 considered in the calculations to be in equilibrium with respect to dolomite within ± 0.1 log unit (dashed lines in *Fig. 1*).

When sulfate and sulfide concentrations were reported separately for the formation waters [17, 19], the saturation calculations for anhydrite were constrained by specifying oxygen fugacity ($f_{O_{2(g)}}$) values at each temperature which would correctly reproduce the sulfate and sulfide concentrations in the fluid at the adjusted pH value according to the reaction:

$$SO_4^{2-} + 2\ H^+ = H_2S_{(aq)} + 2\ O_{2(g)} \qquad (15)$$

It can be seen in Figure 1 that all formation waters are undersaturated with respect to anhydrite, in particular the higher temperature waters from the North Sea in which the sulfate concentrations are extremely low (0.1-1.1 10^{-3} mol). The oxygen fugacity values constrained by the sulfate-sulfide equilibrium have been plotted as a function of temperature in Figure 2, and compared to those computed for the hematite-magnetite (HM-MT) and pyrrhotite-pyrite-magnetite (PO-PY-MT) buffers, both of which are representative of the oxidation-reduction conditions prevailing in sedimentary basins [6, 22]. These mineral buffers correspond to the reactions:

$$3\ Fe_2O_3 = 2\ Fe_3O_4 + 0.5\ O_{2(g)} \qquad (16)$$

for the hematite-magnetite buffer, and:

$$6\ FeS + 2\ O_{2(g)} = 3\ FeS_2 + Fe_3O_4 \qquad (17)$$

for the pyrrhotite-pyrite-magnetite buffer, respectively. The temperature-log $f_{O_{2(g)}}$ curves corresponding to Reactions (16) and (17) were computed with the SUPCRT92 software [13] along the liquid-vapor saturation curve for the system H_2O. Although the oxygen fugacity values computed assuming equilibrium between sulfate and sulfide species represent a smooth distribution as a function of temperature and pressure, these values plot more than 3 log units above the hematite-magnetite assemblage. It has been demonstrated that the oxygen fugacity values in calcite-bearing reservoirs

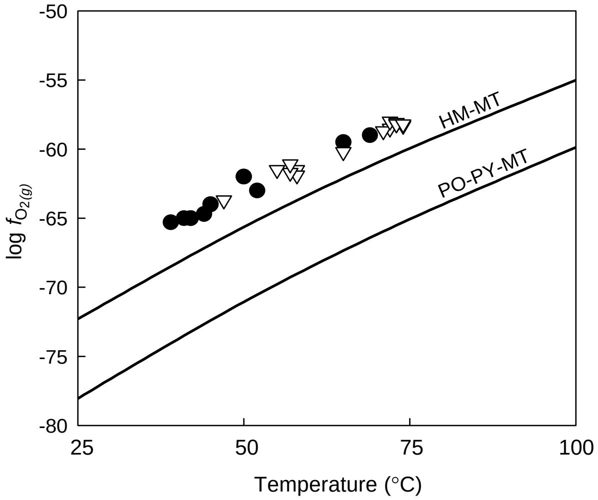

Figure 2

Logarithm of the fugacity of $O_{2(g)}$ as a function of temperature. The symbols represent log $f_{O_{2(g)}}$ values computed assuming equilibrium between sulfate and sulfide aqueous species in the formation waters of the Alberta Basin (●) and the Paris Basin (∇). The curves correspond to log $f_{O_{2(g)}}$ values set by the hematite-magnetite (HM-MT) and pyrrhotite-pyrite-magnetite (PO-PY-MT) buffers.

represent metastable equilibrium states between the heavier hydrocarbons in crude oil (*i.e.* with carbon numbers ≥ 6-15), aqueous organic (*e.g.* carboxylate anions) and inorganic carbon-bearing species, and calcite, and that these values fall within the range defined by the hematite-magnetite and pyrrhotite-pyrite-magnetite assemblages [6, 22]. The reason for these higher oxygen fugacity values is unclear, but may be due to inconsistencies between thermodynamic data in the EQUIL and SUPCRT92 databases.

The fact that anhydrite is not at equilibrium with formation waters in diagenetic environments is well known in carbonate reservoirs associated with appreciable concentrations of hydrogen sulfide (H_2S). As a result, elemental sulfur may form in such reservoirs [23, 24] according to the reaction:

$$CaSO_4 + 3\,H_2S_{(aq)} + 2\,H^+ = 4\,S_{(c\text{ or }l)} + 4\,H_2O + Ca^{2+} \quad (18)$$

A diagram showing the stability domains of elemental sulfur, anhydrite, and calcite at 50°C and 1 bar is depicted in Figure 3. The reactions for the lines corresponding to coexisting calcite and anhydrite, and coexisting calcite and elemental sulfur are:

$$\begin{aligned} &CaSO_4 + 4\,CO_{2(g)} + 3\,Ca^{2+} + 4\,H_2O \\ &\quad = 4\,CaCO_3 + H_2S_{(aq)} + 6\,H^+ + 2\,O_{2(g)} \end{aligned} \quad (19)$$

and:

$$\begin{aligned} &CaCO_3 + 2\,H^+ + H_2S_{(aq)} + 0.5\,O_{2(g)} \\ &\quad = Ca^{2+} + CO_{2(g)} + S_{(c\text{ or }l)} + 2\,H_2O \end{aligned} \quad (20)$$

respectively. The invariant point in Figure 3 corresponds to the reaction:

$$\begin{aligned} &CaSO_4 + 2\,H_2S_{(aq)} + CO_{2(g)} \\ &\quad = 3\,S_{(c\text{ or }l)} + CaCO_3 + 2\,H_2O + 0.5\,O_{2(g)} \end{aligned} \quad (21)$$

The equation of the three lines were obtained from equilibrium constants calculated with the SUPCRT92 software [13] and logarithmic expressions of the law of mass action for Reactions (18)-(20), which can be written as:

$$\log K_{(18)} = \left(a_{Ca^{2+}_{(aq)}} \Big/ a^2_{H^+_{(aq)}} \right) - 3 \log a_{H_2S_{(g)}} \quad (22)$$

$$\log K_{(19)} = \log a_{H_2S_{(aq)}} + 2\,\log f_{O_{2(g)}} - 3\,\log \left(a_{Ca^{2+}_{(aq)}} \Big/ a^2_{H^+_{(aq)}} \right) \quad (23)$$

and:

$$\log K_{(20)} = \log \left(a_{Ca^{2+}_{(aq)}} \Big/ a^2_{H^+_{(aq)}} \right) - \log\ a_{H_2S_{(aq)}} - 0.5\,\log f_{O_{2(g)}} \quad (24)$$

assuming a carbon dioxide fugacity $f_{CO_{2(g)}}$ = 1 bar and an oxygen fugacity $f_{O_{2(g)}}$ value buffered by Reaction (17). It can be seen in Figure 3 that all of the formation waters from the Paris Basin and Alberta Basin plot inside the stability field of calcite. However, it can also be deduced from that figure that the injection of H_2S gas in a carbonate reservoir will tend to move the fluid composition towards the stability field of elemental sulfur. It should be noted that Reactions (18) and (20) both permit the sequestration of H_2S under the form of elemental sulfur. Other possible controls on H_2S partial pressures in carbonate reservoirs are the precipitation

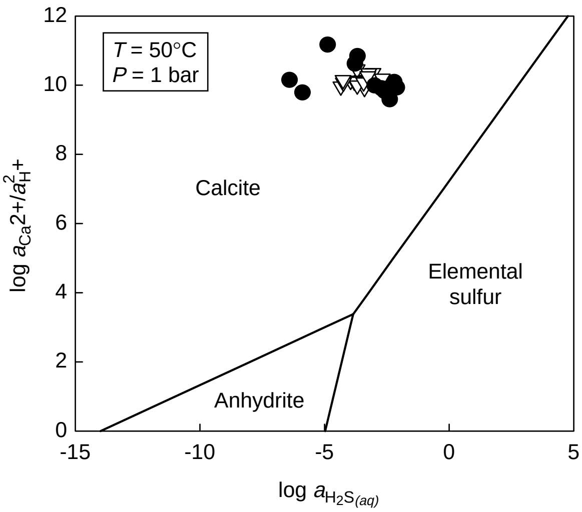

Figure 3

Activity diagram depicting the stability fields of calcite, anhydrite, and elemental sulfur at 50°C and 1 bar. The symbols correspond to formation waters of the Alberta Basin (●) and the Paris Basin (∇).

of metal sulfides and the formation of organic sulfur compounds through sulfurization of residual hydrocarbons in the depleted reservoirs. Precipitation of metal sulfides (*e.g.* pyrite) is a limited process in carbonate reservoirs due to the limited availability of metal ions [24, 25]. Limited amounts of pyrite and marcasite have been formed in the carbonate reservoirs of the Nisku formation [24] as products of bacterial and thermochemical sulfate reduction. The formation of metal sulfides will not be further discussed since metal concentrations have not been reported for the formation waters of the Paris Basin and the North Sea considered in the present study. Petroleum sulfurization reactions leading to the formation of organic sulfur compounds are described in detail below.

3 HIGH H_2S IN PETROLEUM AND NATURAL GAS RESERVOIRS

High concentrations of H_2S gas are encountered in carbonate reservoirs in which thermochemical sulfate reduction has occurred [26-29]. This makes such reservoirs potential natural analogues for geochemical studies related to the sequestration of H_2S in the subsurface. Partial pressures of H_2S ($p_{H_2S_{(g)}}$) as high as ~ 400 bar have been reported in Devonian gas reservoir rocks from the Alberta Basin, Canada [29]. The amount of H_2S gas in these rocks is higher than that of CO_2, and tends to increase with increasing temperature (or depth). To illustrate this dependence of $p_{H_2S_{(g)}}$ with respect to temperature, mole fractions of H_2S ($x_{H_2S_{(g)}}$) reported for the upper Devonian Nisku reservoirs of Alberta [28] have been converted to H_2S partial pressures ($p_{H_2S_{(g)}}$) according to:

$$p_{H_2S_{(g)}} = x_{H_2S_{(g)}} \cdot P \tag{25}$$

where P is the total pressure, and plotted against temperature in Figure 4. It can be seen in this figure that the values of $p_{H_2S_{(g)}}$ start to increase exponentially with increasing present-day temperatures in the Nisku reservoirs above ~ 110ºC. Also plotted in Figure 4 is the highest partial pressure of H_2S (~ 360 bar at ~ 130°C) reported by Hutcheon [29] which is in agreement with the lower temperature data and the exponential trend represented by the dashed curve. A similar exponential relationship between H_2S partial pressures and temperature has been proposed for sandstone reservoirs from the Norwegian Shelf [30]. The partial pressures of H_2S in the Norwegian Shelf and the Alberta Basin are compared in Figure 5 on a log $p_{H_2S_{(g)}}$ *versus* temperature plot. It can be seen in this figure that the values of $p_{H_2S_{(g)}}$ in clastic reservoirs are lower by several orders of magnitude than those observed in carbonate rocks. This difference is classically interpreted as reflecting the lack of available iron in carbonate reservoirs to buffer the $p_{H_2S_{(g)}}$ values by forming iron sulfides [26, 29]. In fact, it has been shown that the values of $p_{H_2S_{(g)}}$ in the clastic reservoirs of the Norwegian Shelf were most probably controlled by an iron sulfide-iron carbonate assemblage [22], for which an equilibrium relation may be written as:

$$FeS_2 + CO_{2(g)} + H_{2(g)} + H_2O_{(l)} = FeCO_3 + 2\ H_2S_{(g)} \tag{26}$$

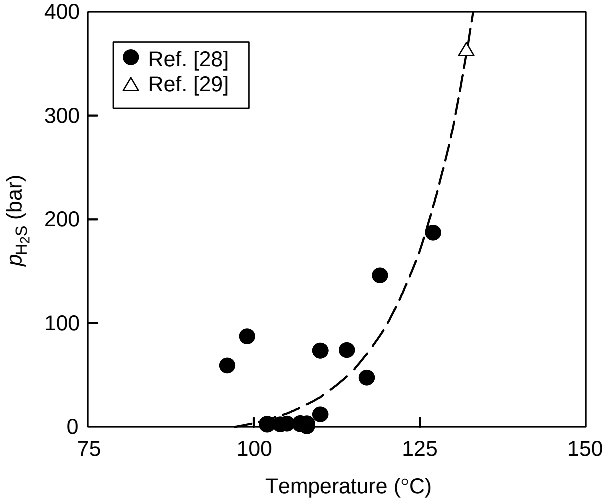

Figure 4

Partial pressure of H_2S as a function of temperature. The symbols correspond to values reported for carbonate reservoirs from the Alberta Basin. The dashed curve has been drawn to illustrate the exponential increase of pH_2S with increasing temperature.

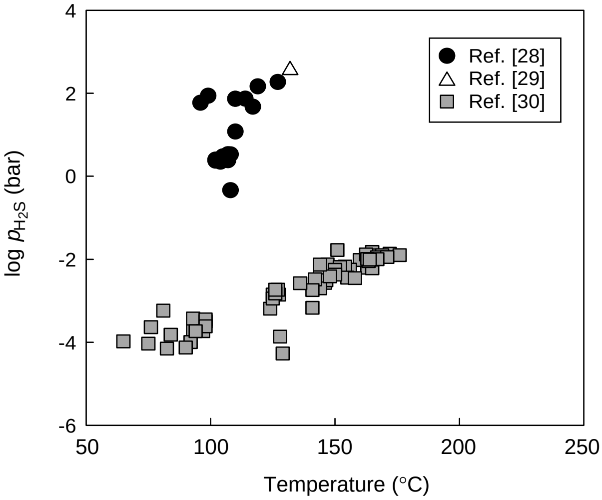

Figure 5

Logarithm of the partial pressure of H_2S as a function of temperature. The symbols correspond to values reported for carbonate reservoirs from the Alberta Basin (● and Δ) and clastic reservoirs from the North Sea (■).

where FeS_2 and $FeCO_3$ represent the minerals pyrite and siderite, $H_2O_{(l)}$ stands for liquid water, and $CO_{2(g)}$, $H_{2(g)}$, and $H_2S_{(g)}$ denote CO_2, H_2, and H_2S in the gas state, respectively. It has also been demonstrated that metastable equilibrium states between hydrocarbons, organic sulfur compounds and H_2S gas could establish in hydrocarbon reservoirs [31]. The possibility that such metastable equilibrium states could control the partial pressures of H_2S in carbonate reservoirs is evaluated below.

4 METASTABLE EQUILIBRIUM STATES AMONG HYDROCARBONS, H_2S, NATIVE SULFUR, AND ORGANIC SULFUR COMPOUNDS

Organic sulfur compounds first form during early diagenetic processes through reactions between bacterially produced hydrogen sulfide and carbon-carbon double bonds or oxygen-bearing functional groups of the biological precursors of sedimentary organic matter [32]. These reactions result in the formation of sulfur-rich kerogens, and the subsequent generation of sulfur-rich crude oils from these kerogens. However, there is ample experimental and field evidence that H_2S, elemental sulfur, and hydrocarbons equally react in petroleum reservoirs to produce organic sulfur compounds. Sulfurization of petroleum in carbonate reservoirs through reactions between hydrocarbons and elemental sulfur has been abundantly discussed in the Russian literature [33, and references therein]. Thiols, sulfides and disulfides have been experimentally produced by reacting low molecular weight hydrocarbons (*e.g.* *n*-heptane and cyclohexane) with elemental sulfur at temperatures as low as 50°C [33]. Hydrogen sulfide was formed as a by-product in some of these experiments. Similarly, a mixture of C_{18} *n*-2,5-dialkylthiophenes has been produced by reacting *n*-octadecane with elemental sulfur at temperatures between 200 and 250°C [34]. It has also been observed that there was an increase in aromatic sulfur compounds (*e.g.* benzothiophenes) in the Nisku reservoirs of Alberta with increasing H_2S in the gas phase of these reservoirs [28]. Although elemental sulfur may accumulate in petroleum reservoirs as a net product of thermochemical sulfate reduction [25], it should perhaps be pointed out that elemental sulfur and hydrogen sulfide may appear as reactants or products depending on the hydrogen to carbon (H/C) ratios of the hydrocarbons and organic sulfur compounds involved in the multitude of sulfurization reactions that may occur in a petroleum reservoir (see below). In any event, experiments and observations of this kind suggest that reactions involving hydrocarbons, elemental sulfur, and organic sulfur compounds may control H_2S partial pressures in carbonate reservoirs.

Recognizing that carbon atoms in organic compounds have different oxidation states depending on the neighboring atom to which they are bonded [35], one can write oxidation-reduction reactions describing metastable equilibrium states between hydrocarbons, elemental sulfur, organic sulfur compounds and hydrogen sulfide. For example, such reactions can be written for liquid 2,4-dimethylbenzo[*b*]thiophene ($C_{10}H_{10}S_{(l)}$) and *trans*-2-methyl-5-*n*-pentylthiacyclopentane ($C_{10}H_{20}S_{(l)}$) coexisting metastably with liquid *n*-decane ($C_{10}H_{22(l)}$) or *n*-butylbenzene ($C_{10}H_{14(l)}$) as:

$$C_{10}H_{22(l)} + 7\ S_{(c\text{ or }l)} = C_{10}H_{10}S_{(l)} + 6\ H_2S_{(g)} \tag{27}$$

$$C_{10}H_{22(l)} + 2\ S_{(c)} = C_{10}H_{20}S_{(l)} + H_2S_{(g)} \tag{28}$$

$$C_{10}H_{14(l)} + 3\ S_{(c\text{ or }l)} = C_{10}H_{10}S_{(l)} + 2\ H_2S_{(g)} \tag{29}$$

and:

$$C_{10}H_{14(l)} + 3\ H_2S_{(g)} = C_{10}H_{20}S_{(l)} + 2\ S_{(c\text{ or }l)} \tag{30}$$

where $S_{(c\text{ or }l)}$ and $H_2S_{(g)}$ stand for crystalline or liquid elemental sulfur and hydrogen sulfide gas, respectively. The two organic sulfur compounds involved in Reactions (27)-(30) have been chosen because alkylthiacyclopentanes and alkylbenzothiophenes are representative of immature and mature crude oils, respectively [32]. Their idealized structures are depicted in Figure 6 along with those of *n*-decane and *n*-butylbenzene.

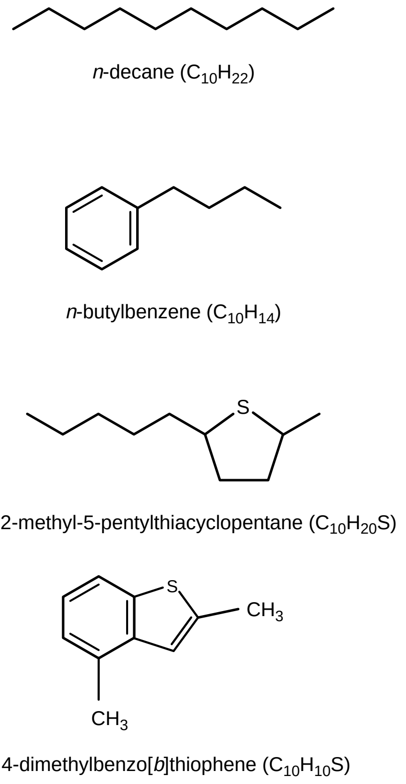

n-decane ($C_{10}H_{22}$)

n-butylbenzene ($C_{10}H_{14}$)

trans-2-methyl-5-pentylthiacyclopentane ($C_{10}H_{20}S$)

2,4-dimethylbenzo[*b*]thiophene ($C_{10}H_{10}S$)

Figure 6

Idealized structures of the hydrocarbons and organic sulfur compounds considered in the metastable equilibrium state calculations – see text.

Adopting a standard state of unit activity for elemental sulfur at all temperatures and pressures, the corresponding logarithmic expressions of the law of mass action for Reactions (27)-(30) are:

$$\log K_{(27)} = \log \frac{a_{C_{10}H_{10}S_{(l)}}}{a_{C_{10}H_{22(l)}}} + 6 \log f_{H_2S_{(g)}} \tag{31}$$

$$\log K_{(28)} = \log \frac{a_{C_{10}H_{20}S_{(l)}}}{a_{C_{10}H_{22(l)}}} + \log f_{H_2S_{(g)}} \tag{32}$$

$$\log K_{(29)} = \log \frac{a_{C_{10}H_{10}S_{(l)}}}{a_{C_{10}H_{14(l)}}} + 2 \log f_{H_2S_{(g)}} \tag{33}$$

and:

$$\log K_{(30)} = \log \frac{a_{C_{10}H_{20}S_{(l)}}}{a_{C_{10}H_{14(l)}}} - 3 \log f_{H_2S_{(g)}} \tag{34}$$

respectively, where $K_{(27)}$, $K_{(28)}$, $K_{(29)}$, and $K_{(30)}$ are the equilibrium constants for the subscripted reactions, $a_{C_{10}H_{10}S_{(l)}}$, $a_{C_{10}H_{20}S_{(l)}}$, $a_{C_{10}H_{22(l)}}$ and $a_{C_{10}H_{14(l)}}$ stand for the activities of the subscripted species, and $f_{H_2S_{(g)}}$ represent the fugacity of hydrogen sulfide gas. Values of the equilibrium constants for Reactions (27)-(30) have been calculated with the SUPCRT92 software [13] at temperatures and pressures representative of those in the Alberta Basin [28], and used together with Equations (31)-(34) to generate the dashed curves shown in Figure 7. These curves have been drawn for

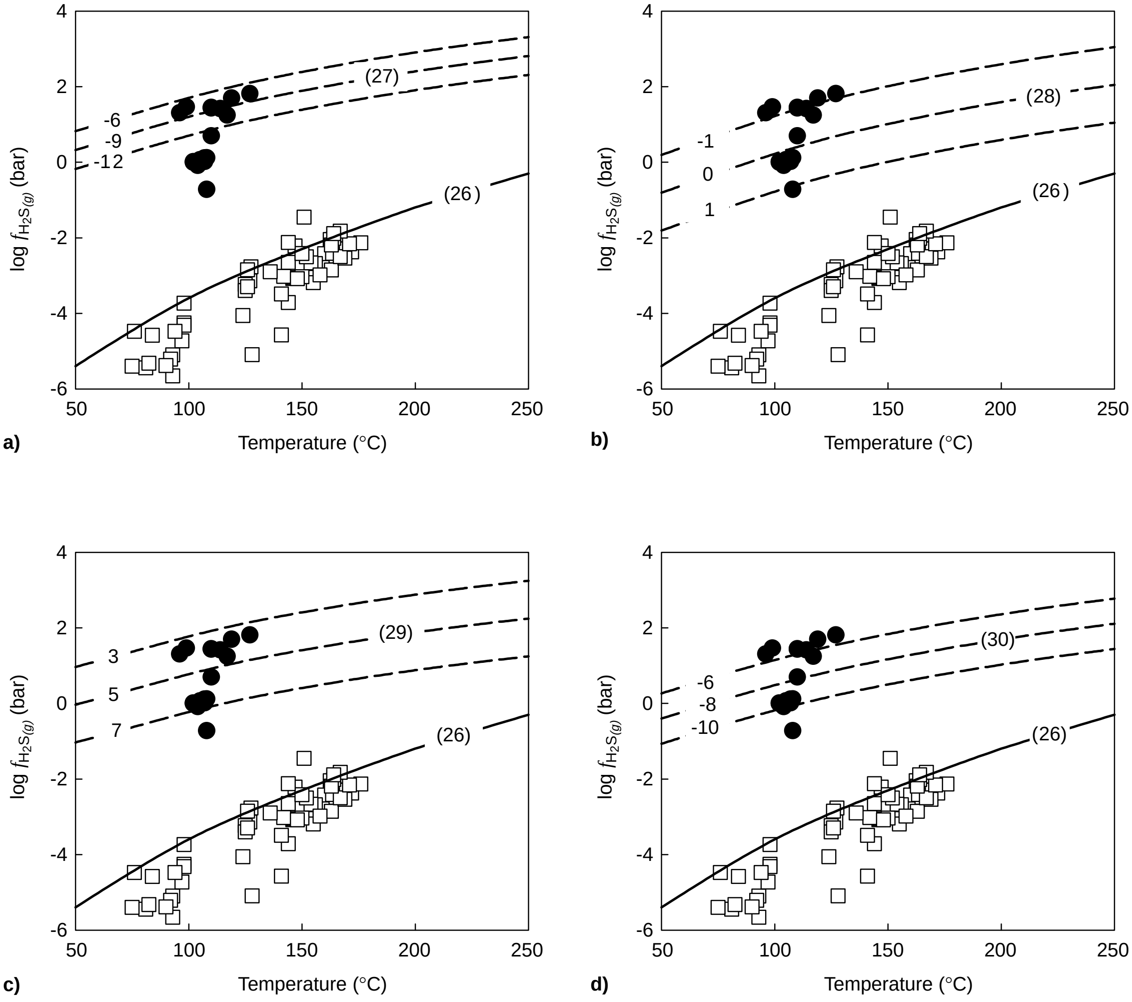

Figure 7

Logarithm of the fugacity of H_2S as a function of temperature. The symbols correspond to values computed from partial pressures of H_2S reported for carbonate reservoirs from the Alberta Basin (●) and clastic reservoirs from the North Sea (□) – see text. The solid curve corresponds to the values fixed by the iron sulfide-iron carbonate assemblage. The dashed curves correspond to values calculated assuming metastable equilibrium states between elemental sulfur, H_2S, and a) *n*-decane and 2,4-dimethylbenzo[*b*]thiophene; b) *n*-decane and *trans*-2-methyl-5-*n*-pentylthiacyclopentane; c) *n*-butylbenzene and 2,4-dimethylbenzo[*b*]thiophene; d) *n*-butylbenzene and *trans*-2-methyl-5-*n*-pentylthiacyclopentane. The numbers between parentheses correspond to Reactions (26)-(30) in the text. The numbers on each curve correspond to different activity ratios of the hydrocarbon and organic sulfur compound in Equations (31)-(34) – see text.

different activity ratios of the hydrocarbon and organic sulfur compound in a given reaction (see caption to *Fig. 7*).

The partial pressures of H_2S ($p_{H_2S_{(g)}}$) shown in Figures 4 and 5 [28, 30] have been converted to their fugacity counterparts ($f_{H_2S_{(g)}}$) according to:

$$f_{H_2S_{(g)}} = \varphi_{H_2S_{(g)}} \cdot p_{H_2S_{(g)}} \tag{35}$$

where $\varphi_{H_2S(g)}$ stands for the fugacity coefficient of H_2S gas, which was evaluated in the present study from the Peng-Robinson equation of state [36]:

$$P = \frac{RT}{V-b} - \frac{a(T)}{V(V+b) + b(V-b)} \tag{36}$$

where *V* stands for the molal volume of the gas mixture, *b* is a constant representing a correction for the repulsion between molecules and is defined by:

$$b = 0.07780 \frac{R\,T_c}{P_c} \tag{37}$$

and *a(T)* is a temperature-dependent constant representing intermolecular attraction forces, which is equal to:

$$a(T) = 0.45724 \frac{R^2\,T_c^2}{P_c} \left[1 + \kappa\left(1 - \left(\frac{T}{T_c}\right)^{1/2}\right)\right]^2 \tag{38}$$

where T_c and P_c designate the critical temperature and pressure, respectively, and κ is a constant characteristic for each gas which is defined by [36]:

$$\kappa = 0.37464 + 1.54226\,\omega - 0.26992\,\omega^2 \tag{39}$$

where ω is the acentric factor. The *a(T)* and *b* parameters in Equation (36) were calculated assuming a CO_2-H_2S binary mixture and the usual mixing rules [37]. The fugacity coefficient for H_2S in the mixture is obtained from [37]:

$$\ln \varphi_{H_2S_{(g)}} = \frac{b_{H_2S}}{b}\left(\frac{PV}{RT} - 1\right) - \ln \frac{P(V-b)}{RT} - \frac{a(T)}{2\sqrt{2}\,bRT} \left[\frac{2\,(z_{CO_{2(g)}}\,a_{CO_2-H_2S} + z_{H_2S_{(g)}}\,a_{H_2S})}{a(T)} - \frac{b_{H_2S}}{b}\right] \ln \frac{V + (1+\sqrt{2})b}{V + (1-\sqrt{2})b} \tag{40}$$

where $z_{CO_2(g)}$ and $z_{H_2S(g)}$ are the mole fractions of CO_2 and H_2S in the gas mixture.

The solid curve shown in Figure 7 represents the H_2S fugacity fixed by the pyrite-iron carbonate assemblage for the clastic reservoirs from the Norwegian shelf [22]. It can be seen in Figure 7 that all but one of the fugacities of H_2S in the Alberta Basin carbonate reservoirs fall within the range defined by Reactions (27)-(30) and the activity ratios indicated on the different curves. Note that the standard molal thermodynamic properties of organic compounds are a nearly linear function of carbon number for homologous series of compounds [8, 9]. Therefore, metastable equilibrium curves calculated for *n*-alkanes, *n*-alkylbenzenes, and *n*-alkylthiacyclopentanes with higher or lower carbon numbers would coincide nearly exactly with the curves shown for *n*-decane, *n*-butylbenzene, and *trans*-2-methyl-5-*n*-pentylthiacyclopentane in Figure 7. Similarly, many other metastable equilibrium states involving hydrocarbons and organic sulfur compounds with different nominal oxidation states are consistent with the range of H_2S partial pressures reported for the Nisku and other carbonate reservoirs in which thermochemical sulfate reduction may have occurred [31]. The important point is that these preliminary calculations suggest that in the absence of detrital iron, metastable equilibrium states between hydrocarbons, hydrogen sulfide, elemental sulfur and organic sulfur compounds may control the partial pressures of H_2S in carbonate reservoirs at values which are 4 to 6 orders of magnitude higher than those encountered in sandstone reservoirs.

CONCLUSION

As part of a research project on the chemical and mineralogical consequences of injecting CO_2-H_2S gas mixtures in geological formations, the water-gas-rock-hydrocarbon reactions involving sulfur in carbonate reservoirs have been analyzed from a thermodynamic point of view. The calculations indicate that increasing the partial pressure of H_2S in a carbonate reservoir, thereby increasing the aqueous activity of H_2S in the formation water, will favor the formation of elemental sulfur. This constitutes a potential sequestration reaction for H_2S.

Considering carbonate reservoirs in which thermochemical sulfate reduction has occurred as natural analogues for the sequestration of H_2S suggests that the partial pressures of H_2S in these reservoirs may be controlled by metastable equilibrium states between hydrocarbons, organic sulfur compounds and elemental sulfur. Changing the fugacity of H_2S in carbonate reservoirs could possibly affect these metastable equilibrium states. Although the kinetics of sulfurization reactions is not known, these reactions may consume or produce H_2S depending on the H/C ratios of the hydrocarbons and organic sulfur compounds involved in the sulfurization reactions. Future research will be aimed at quantifying these reactions by performing mass transfer and Gibbs free energy minimization calculations to confirm the preliminary calculations presented in this communication.

ACKNOWLEDGEMENTS

The authors are grateful to Étienne Brosse for encouraging them to submit this paper. Constructive comments by two anonymous reviewers are sincerely appreciated. This study was carried out with financial support from *Total* (contract TOTAL DGEP/TDO/CA/ACOMS CT No. 13444).

REFERENCES

1 Hansen, J.E., Sato, M., Lacis, A., Ruedy, R., Tegen, I. and Matthews, E. (1998) Climate Forcings in the Industrial Era. *Proceedings of the National Academy of Sciences*, **95**, 22, 12753-12758.

2 Lackner, K.S. (2003) A Guide to CO_2 Sequestration. *Science*, **300**, 5626, 1677-1678.

3 Gunter, W.G., Wiwchar, B., and Perkins, E.H. (1997) Aquifer Disposal of CO_2-Rich Greenhouse Gases: Extension of the Time Scale of Experiment for CO_2-Sequestering Reactions by Geochemical Modelling. *Mineralogy and Petrology*, **59**, 1-2, 121-140.

4 Gunter, W.G., Perkins, E.H., and Hutcheon, I. (2000) Aquifer Disposal of Acid Gases: Modelling of Water-Rock Reactions for Trapping of Acid Wastes. *Applied Geochemistry*, **15**, 8, 1085-1095.

5 Xu, T., Apps, J.A., and Pruess, K. (2004) Numerical Simulation of CO_2 Disposal by Mineral Trapping in Deep Aquifers. *Applied Geochemistry*, **19**, 6, 917-936.

6 Helgeson, H.C., Knox, A.M., Owens, C.E. and Shock, E.L. (1993) Petroleum, Oil Field Waters, and Authigenic Mineral Assemblages: Are they in Metastable Equilibrium in Hydrocarbon Reservoirs? *Geochimica Cosmochimica Acta*, **57**, 14, 3295-3339.

7 Helgeson, H.C., Delany, J.M., Nesbitt, H.W. and Bird, D.K. (1978) Summary and Critique of the Thermodynamic Properties of Rock-Forming Minerals. *American Journal of Science*, **278-A**, 1-229.

8 Helgeson, H.C., Owens, C.E., Knox, A.M. and Richard, L. (1998) Calculation of the Standard Molal Thermodynamic Properties of Crystalline, Liquid, and Gas Organic Molecules at high temperatures and pressures. *Geochimica Cosmochimica Acta*, **62**, 6, 985-1081.

9 Richard, L. (2001) Calculation of the Standard Molal Thermodynamic Properties as a Function of Temperature and Pressure of some Geochemically Important Organic Sulfur Compounds. *Geochimica Cosmochimica Acta*, **65**, 21, 3827-3877.

10 Maier, C.G. and Kelley, K.K. (1932) An Equation for the Representation of High Temperature Heat-Content Data. *Journal of the American Chemical Society*, **54**, 8, 3243-3246.

11 Richard, L. and Helgeson, H.C. (2004) *Calculation of the Standard Molal Volumes of Crystalline and Liquid Organic Compounds as a Function of Temperature and Pressure* (in preparation).

12 Tanger, J.C. and Helgeson, H.C. (1988) Calculation of the Thermodynamic and Transport Properties of Aqueous Species at High Pressures and Temperatures: Revised Equations of State for the Standard Partial Molal Properties of Ions and Electrolytes. *American Journal of Science*, **288**, 1, 19-98.

13 Johnson, J.W., Oelkers, E.H. and Helgeson, H.C. (1992) SUPCRT92: A Software Package for Calculating the Standard Molal Thermodynamic Properties of Minerals, Gases, Aqueous Species, and Reactions from 1 to 5000 bar and 0 to 1000ºC. *Computers and Geosciences*, **18**, 7, 899-947.

14 Shock, E.L. and Helgeson, H.C. (1988) Calculation of the Thermodynamic and Transport Properties of Aqueous Species at High Pressures and Temperatures: Correlation Algorithms for Ionic Species and Equation of State Predictions to 5 kb and 1000°C. *Geochimica Cosmochimica Acta*, **52**, 8, 2009-2036.

15 Shock, E.L., Helgeson, H.C., and Sverjensky, D.A. (1989) Calculation of the Thermodynamic and Transport Properties of Aqueous Species at High Pressures and Temperatures: Standard Partial Molal Properties of Inorganic Neutral Species. *Geochimica Cosmochimica Acta*, **53**, 9, 2157-2183.

16 Gurrieri, S. (1997) Personal Communication.

17 Michard, G. and Bastide, J.P. (1988) Étude géochimique de la nappe du Dogger du Bassin parisien. *Journal of Volcanology and Geothermal Research*, **35**, 1/2, 151-163.

18 Egeberg, P.K. and Aagaard, P. (1989) Origin and Evolution of Formation Waters from Oil Fields on the Norwegian Shelf. *Applied Geochemistry*, **4**, 2, 131-142.

19 Connolly, C.A., Walter, L.M., Baadsgaard, H. and Longstaffe, F.J. (1990) Origin and Evolution of Formation Waters, Alberta Basin, Western Canada Sedimentary Basin. I. Chemistry. *Applied Geochemistry*, **5**, 4, 375-395.

20 Fritz, B. (1981) Étude thermodynamique et modélisation des réactions hydrothermales et diagénétiques. *Mémoire des Sciences Géologiques*, **65**.

21 Helgeson, H.C. (1969) Thermodynamics of Hydrothermal Systems at Elevated Temperatures and Pressures. *American Journal of Science*, **267**, 7, 729-804.

22 Aagaard, P., Jahren, J.S. and Ehrenberg, S.N. (2001) H_2S-Controlling Reactions in Clastic Hydrocarbon Reservoirs from the Norwegian Shelf and US Gulf Coast. In: *Water-Rock Interaction 2001*, Cidu R. (ed.), Swets & Zeitlinger, Lisse, 129-132.

23 Heydari, E. (1997) The Role of Burial Diagenesis in Hydrocarbon Destruction and H_2S Accumulation, Upper Jurassic Smackover Formation, Black Creek Field, Mississippi. *Bulletin of the American Association of Petroleum Geologists*, **81**, 1, 26-45.

24 Riciputi, L.R., Cole, D.R. and Machel, H.G. (1996) Sulfide Formation in Reservoir Carbonates of the Devonian Nisku Formation, Alberta, Canada: An ion microprobe study. *Geochimica et Cosmochimica Acta*, **60**, 2, 325-336.

25 Machel, H.G. (2001) Bacterial and Thermochemical Sulfate Reduction in Diagenetic Settings – Old and New Insights. *Sedimentary Geology*, **140**, 1/2, 143-175.

26 Orr, W.L. (1977) Geologic and Geochemical Controls on the Distribution of Hydrogen Sulfide in Natural Gas. In: *Advances in Organic Geochemistry 1975*, Campos, R., and Goñi, J. (eds.), Empresa Nacional Adaro De Investigaciones Mineras, Madrid, 571-597.

27 Worden, R.H., Smalley, P.C. and Oxtoby, N.H. (1995) Gas Souring by Thermochemical Sulfate Reduction at 140°C. *Bulletin of the American Association of Petroleum Geologists*, **79**, 6, 854-863.

28 Manzano, B.K., Fowler, M.G. and Machel, H.G. (1997) The Influence of Thermochemical Sulfate Reduction on Hydrocarbon Composition in Nisku Reservoirs, Brazeau River Area, Alberta, Canada. *Organic Geochemistry*, **27**, 7/8, 507-521.

29 Hutcheon, I. (1999) Controls on the Distribution of Non-Hydrocarbon Gases in the Alberta Basin. *Bulletin of Canadian Petroleum Geology*, **47**, 4, 573-593.

30 Håland, K., Barrufet, M.A., Rønningsen, H.P. and Meisingset, K.K. (1999) An Empirical Correlation between Reservoir Temperature and the Concentration of Hydrogen Sulfide. *Proceedings SPE International Symposium on Oilfield Chemistry*, 589-596.

31 Richard, L. and Helgeson, H.C. (2001) Thermodynamic Calculation of the Distribution of Organic Sulfur Compounds in Crude Oil as a Function of Temperature, Pressure, and H_2S Fugacity. In: *Water-Rock Interaction 2001*, Cidu R. (ed.), Swets & Zeitlinger, Lisse, 333-335.

32 Orr, W.L., and Sinninghe Damsté, J.S. (1990) Geochemistry of Sulfur in Petroleum Systems. In: *Geochemistry of Sulfur in Fossil Fuels*, Orr W.L. and White C.M. (eds.), American Chemical Society Symposium Series, 429, American Chemical Society, 2-29.

33 Valitov, N.B. and Valitov, R.B. (1975) The Role of Temperature in Formation of Sulfur-Bearing Petroleums and Catagenetic Hydrogen Sulfide in Carbonate Reservoirs (experimental investigations). *Geochemistry International*, **12**, 5, 73-81.

34 Schmid, J.C., Connan, J. and Albrecht, P. (1987) Occurrence and Geochemical Significance of Long-Chain Dialkylthiacyclopentanes. *Nature*, **329**, 6134, 54-56.

35 Helgeson, H.C. (1991) Organic/Inorganic Reactions in Metamorphic Processes. *Canadian Mineralogist*, **29**, 4, 707-739.

36 Peng, D.Y. and Robinson, D.B. (1976) A New Two-Constant Equation of State. *Industrial and Engineering Chemistry Fundamentals*, **15**, 1, 59-64.

37 Prausnitz, J.M., Lichtenthaler R.N. and de Azevedo E.G. (1986) *Molecular Thermodynamics of Fluid-Phase Equilibria*, 2nd Edition, Prentice-Hall.

Final manuscript received in January 2005

3. Altération des verres silicatés en milieu aqueux

Les verres silicatés, soumis à l'action de solutions aqueuses, s'altèrent en se dissolvant de façon congruente ou en développant à leur surface une pellicule constituée d'un gel résiduel et/ou de produits secondaires précipités. L'étude de ces mécanismes d'altération est aujourd'hui d'un intérêt majeur puisque le verre est un matériau utilisé de façon intensive dans de nombreux domaines, de l'optique aux télécommunications, en passant par la stabilisation des déchets et le flaconnage alimentaire. On peut citer le cas du cristal et de la diffusion du plomb dans les boissons, mais également l'altération des vitraux de cathédrales dont certains ont perdu complètement leur translucidité, ou encore les recherches menées dans le cadre de la santé sur les fibres de verre bio-solubles. La corrosion des verres touche aussi les problèmes environnementaux puisque le verre est un matériau de choix permettant de stabiliser de façon efficace les éléments polluants. Le verre nucléaire R7T7 en est d'ailleurs un très bon exemple. Enfin, l'étude de la dissolution des verres trouve une application géochimique en donnant des renseignements fondamentaux concernant les bilans de masse et les transferts de matière dans la géosphère par l'intermédiaire, par exemple, de l'altération des basaltes océaniques.

Les recherches que j'ai réalisées lors de ma thèse s'inscrivaient dans le cadre de l'altération des verres de confinement de déchets et de leur durabilité. Pour répondre à cette problématique, une approche couplée a été réalisée. Parallèlement à l'altération expérimentale de verres modèles, l'étude de vitraux médiévaux, altérés en conditions naturelles pendant près d'un millénaire, a permis d'apporter des informations fondamentales sur les mécanismes d'altération et surtout de fournir des conditions aux limites nécessaires à la modélisation du comportement à long terme des verres de confinement.

Approche expérimentale sur verres modèles:

Cette approche consiste à mener des expériences de lixiviation au laboratoire afin de tester l'influence des paramètres "température, pH de la solution, composition chimique du verre, surface spécifique et durée" sur l'altération de verres modèles (déchets vitrifiés et analogues de vitraux). L'étude du comportement des éléments du point de vue de la solution (ICP-MS et ICP-AES) et du verre (profils en profondeur par SIMS) a permis d'accéder à différents paramètres cinétiques et thermodynamiques (vitesses initiales de dissolution, vitesses à saturation, coefficients de diffusion des éléments dans le verre altéré, énergies d'activation des processus de dissolution). Une caractérisation physico-chimique et minéralogique (MEB, MET, sonde électronique, sonde ionique, Infrarouge, Figure 5) des pellicules d'altération a également permis de déterminer la nature des phases secondaires porteuses des éléments polluants et d'accéder à leurs coefficients de partage.

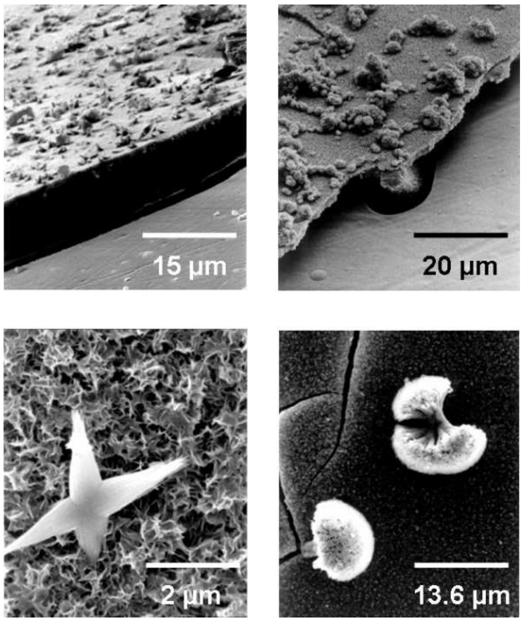

Figure 5 : Vue au microscope électronique à balayage en électrons secondaires de la pellicule d'altération développée sur des verres modèles ou des déchets vitrifiés altérés pendant 6 mois à pH neutre à basique. Noter l'hétérogénéité des produits d'altération constitués d'un gel de silice amorphe et de phosphates de calcium cristallisés présentant différents faciès. D'après Sterpenich J, (2008): Crystal-chemistry of alteration products of vitrified wastes: implications on the retention of polluting elements. Waste Management , 28, 120-132.

➢ Etude de verres de vitraux altérés en conditions naturelles

L'étude des vitraux médiévaux, altérés à même les verrières ou exhumés lors de fouilles archéologiques, a permis d'apporter des informations essentielles à la compréhension des mécanismes d'altération en conditions naturelles.

A ce titre, l'utilisation conjointe de techniques analytiques (MEB, MET analytique et EELS, sonde électronique, SIMS, Infrarouge et Cathodoluminescence) a permis une caractérisation physico-chimique et minéralogique complète et détaillée des pellicules d'altération développées à la surface des vitraux. Les informations recueillies ont servi à quantifier le relâchement dans l'environnement des éléments majeurs mais également des éléments en traces qui sont les éléments polluants confinés dans les déchets vitrifiés (As, Pb, Ni, Co, Cr, etc.). De plus, les phases minérales porteuses ont pu être identifiées permettant de déterminer la cristallochimie des polluants et leurs coefficients de partage.

En outre, les vitraux médiévaux, altérés dans différentes conditions (eaux météoriques ou contexte pédologique) présentent également des différences notables de composition chimique permettant de quantifier l'influence des conditions d'altération et de la composition chimique sur la nature des pellicules d'altération et les taux de rétention des éléments polluants. Par extension, les vitraux constituent un excellent outil pour étudier les relations entre cinétiques d'altération, thermodynamique (énergies d'hydratation, Figure 7) et structure du verre (NBO/T : degré de polymérisation global). Enfin, la modélisation des profils élémentaires en profondeur a permis de quantifier les coefficients de diffusion de l'eau (Figure 6), acteur principal et moteur de la corrosion des verres.

Ces travaux qui ont été récompensés par le prix Jean Goguel 2001, ont fait l'objet de quatre publications internationales et de nombreuses communications dans des congrès internationaux.

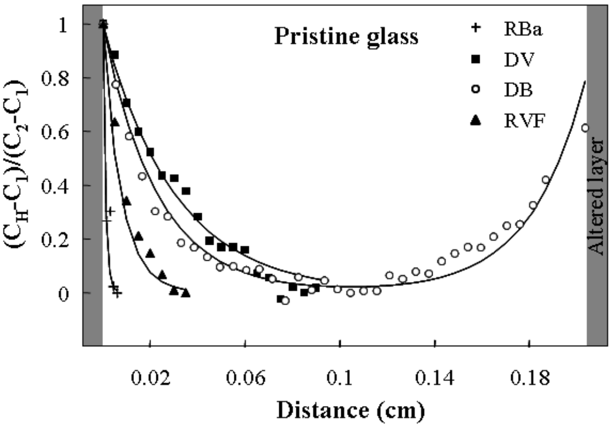

Figure 6 : Concentrations normalisées en hydrogène reportées en fonction de la distance à partir de l'interface verre sain - verre altéré. Les courbes en trait plein correspondent aux analyses effectuées à la sonde ionique dans la zone de diffusion. Les échantillons analysés sont des vitraux archéologiques potassiques provenant des sites de Digne (DB et DV) et Rouen (RVF). Les courbes en trait plein correspondent au calcul des concentrations en hydrogène d'après l'équation de diffusion en régime permanent et pour un milieu semi-infini :

$C_H = \exp\left(\frac{-ax}{D}\right)$ *où C_H est la concentration en hydrogène du verre à une distance x et D le coefficient de diffusion. (D'après Sterpenich J., Libourel G. (2007) Evidence of water diffusion in silicate glasses under natural weathering conditions given by buried medieval stained-glasses. Journal of Non-Crystalline Solids, 352, 5446-5451)*

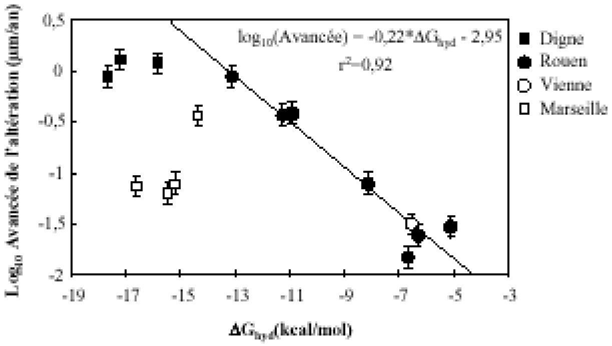

Figure 7 : Avancée moyenne de l'altération exprimée en logarithme décimal de µm/an, en fonction de l'énergie libre d'hydratation calculée à 25°C, pour les verres archéologiques de Digne Rouen, Marseille et Vienne. Si la prédiction semble bonne pour les verres de Rouen et de Vienne, le modèle doit cependant être affiné pour Digne et Marseille.

(Thèse Sterpenich 1998 et Libourel, G., Verney-Carron, A., Morlok, A., Gin, S., Sterpenich, J., Michelin, A., Neff, D., Dillmann, P. (2011). The use of natural and archeological analogues for understanding the long-term behavior of nuclear glasses. Comptes Rendus Geoscience 343, 237-245)

Etude des mécanismes de formation des gels d'altération

Bien qu'actuellement un nombre important d'études soient réalisées sur la dissolution des verres, les mécanismes de dissolution et en particulier les mécanismes de formation des gels demeurent encore mal compris. C'est dans ce contexte qu'une étude sur le traçage isotopique (^{29}Si et ^{18}O) des mécanismes de l'altération du verre de confinement des déchets nucléaires a été entreprise (travaux de thèse de Nathalie Valle, 2000). J'ai été chargé d'approfondir ces travaux en développant des expériences de traçage isotopique sur des verres modèles. Une originalité de ces recherches était d'associer l'étude structurale des gels d'altération par RMN (collaboration T. Charpentier, SCM Paris) à l'étude de la diffusion du silicium dans les gels par SIMS. Cette étude avait pour objectif de permettre pour la première fois d'associer la dynamique d'échange des gels à leur structure locale, pour à terme identifier les mécanismes responsables de leur caractère protecteur.

Ces travaux sont basés sur :

i) le montage d'un protocole expérimental et la réalisation d'expériences de lixiviation,

ii) l'analyse et la caractérisation des solutions et des solides (verre sain et produits d'altération),

iii) la modélisation des profils de diffusion acquis par SIMS (détermination des coefficients de diffusion),

iv) la confrontation avec les résultats structuraux acquis par RMN.

Ils ont fait l'objet d'une publication (*Valle, N. Verney-Carron, A., Sterpenich, J. Libourel, G. Deloule, E. Jollivet, P (2010). Elemental and isotopic (^{29}Si and ^{18}O) tracing of glass alteration mechanisms. Geochimica et Cosmochimica Acta. , 74 (12),* Figure 8) et d'un rapport au CEA.

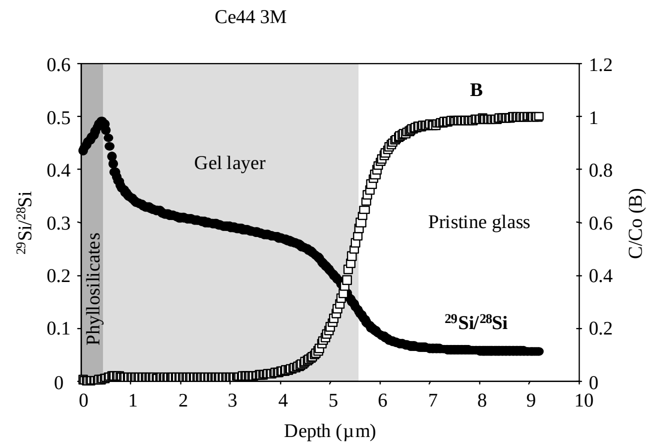

Figure 8 : Profils en profondeur 29Si et B réalisés par SIMS sur un verre nucléaire SON68 (type R7T7). Le verre sain est en blanc, le gel d'altération en gris et les phyllosilicates précipités à la surface en gris foncé. Ce profil montre que i) le bore est lixivié fortement et montre des valeurs proches de 0 dans le gel, ii) le silicium 29 enrichi dans la solution altérante diffuse dans le gel jusqu'à l'interface vers sain / verre altéré et participe à la formation du gel par mécanismes de condensation, iii) les phyllosilicates enregistrent la signature isotopique de la solution. Cette expérience a montré qu'il existe des mécanismes complexes de formation des gels qui ne résultent pas uniquement de la dissolution sélective du verre mais qui mettent en jeu des mécanismes de dissolution / recondensation. (Valle, N. Verney-Carron, A., Sterpenich, J. Libourel, G. Deloule, E. Jollivet, P (2010). Elemental and isotopic (^{29}Si and ^{18}O) tracing of glass alteration mechanisms. Geochimica et Cosmochimica Acta. , 74 (12) 3412-3431)

La connaissance de l'altération des verres me vaut aujourd'hui de développer de nouvelles collaborations avec mes collègues archéologues (René Elter, INRAP) sur de nouveaux analogues potentiels représentés par les tesselles antiques jordaniennes. Une première étude a révélé que ces verres ou pâtes de verres, altérés depuis près de 1700 ans, présentent des pellicules d'altération comparables à celles observées sur les vitraux. Une particularité réside dans les hautes teneurs en plomb et en étain qui peuvent donner des indications importantes quant à la mobilité de tels éléments toxiques en conditions naturelles d'altération. Outre l'aspect environnemental, cette étude doit aussi aider les archéologues à mieux comprendre les techniques d'élaboration des différents types de verres antiques.

Publications

Sterpenich J, Libourel G (2001) Using stained glass windows to understand the durability of toxic waste matrices. Chemical Geology, 174, 181-193.

Sterpenich J (2002) Cristallochimie des produits d'altération des vitraux médiévaux: application au vieillissement des déchets vitrifiés. Crystal chemistry of alteration products of medieval stained-glass windows: application to the ageing of vitrified wastes. Bull Eng Geol Environ, 61, 179-193 DOI 10.1007/s10064-001-0150-1

Sterpenich J., Libourel G. (2007) Evidence of water diffusion in silicate glasses under natural weathering conditions given by buried medieval stained-glasses. Journal of Non-Crystalline Solids, 352, 5446-5451

Sterpenich J, (2008): Crystal-chemistry of alteration products of vitrified wastes: implications on the retention of polluting elements. Waste Management , 28, 120-132

Valle, N. Verney-Carron, A., Sterpenich, J. Libourel, G. Deloule, E. Jollivet, P (2010). Elemental and isotopic (29Si and 18O) tracing of glass alteration mechanisms. Geochimica et Cosmochimica Acta. , 74 (12) 3412-3431.

Libourel, G., Verney-Carron, A., Morlok, A., Gin, S., Sterpenich, J., Michelin, A., Neff, D., Dillmann, P. (2011). The use of natural and archeological analogues for understanding the long-term behavior of nuclear glasses. Comptes Rendus Geoscience 343, 237-245.

ELSEVIER

Chemical Geology 174 (2001) 181–193

CHEMICAL GEOLOGY
INCLUDING
ISOTOPE GEOSCIENCE

www.elsevier.com/locate/chemgeo

Using stained glass windows to understand the durability of toxic waste matrices

Jérôme Sterpenich [a,b], Guy Libourel [a,c,*]

[a] *CRPG-CNRS, BP20, 54501 Vandoeuvre-lès-Nancy, France*
[b] *Université Henri Poincaré Nancy1, BP239, 54506 Vandoeuvre-lès-Nancy, France*
[c] *ENSG-INPL, BP40, 54501 Vandoeuvre-lès-Nancy, France*

Accepted 9 February 2000

Abstract

Using stained glasses sampled from French and German cathedrals, and from different archaeological sites, this work presents an estimation of the effect of weathering conditions and glass composition on glass dissolution. Due to accurate dating, we also show that stained glass windows allow the determination of the average dissolution kinetics of many toxic elements contained in the glass (including transition and heavy metals, actinides, lanthanides). Therefore, a significant advantage of using stained glass windows, over other natural glasses, is that they permit the direct study of non-stoichiometric elemental dissolution rates, under natural conditions of alteration, averaged over more than a thousand years, and hence to constrain the long-term behaviour of vitrified waste matrices. © 2001 Published by Elsevier Science B.V.

Keywords: Glass dissolution; Weathering conditions; Glass composition

---

1. Introduction

An important consideration by several countries for waste management is to confine the toxic products of nuclear, industrial or municipal wastes in silicate glass matrices, and to store them in repositories both underground and on the surface. Despite numerous experimental studies devoted to glass dissolution, determining the behaviour of vitrified wastes for periods of hundreds, to tens of thousands, of years remains problematic. Until now, the lack of reliable information concerning long-term natural weathering of glass prevents validation of laboratory dissolution models. Although volcanic glasses have been used as analogues for vitrified wastes (Ewing, 1979; Grambow, 1985; Heimann, 1986; Jantzen and Plodinec, 1984; Lutze et al., 1985), we suggest here that medieval stained glass windows are better analogues for the study of toxic waste confinement matrices. Manufactured from natural materials (e.g. sand, limestone, plant ashes) and coloured by addition of transition and heavy metals, medieval stained glass windows allow, by analogy, to decipher the long-term behaviour of polluting elements in glasses under natural conditions of alteration (see also Macquet and Thomassin, 1992).

Thanks to a study of the altered layer, we will show that medieval stained glass windows allow to

---

[*] Corresponding author.

0009-2541/01/$ - see front matter © 2001 Published by Elsevier Science B.V.
PII: S0009-2541(00)00315-6

Table 1
Main characteristics of the stained glass windows studied

Sample	Site	Colour	Flux[a]	Date[b]	Type of alteration	Nature of the soil	Thickness of altered layer (μm)[c]	MRC[d] (μm year^{-1})	NBO/T[e]
DV	Digne	Green	Potash	1180–1250	Underground	Embankment	800–1100	1–1.2	1.26
DB		Blue					1000–1300	1–1.6	1.24
DR		Red					650–1000	0.8–1	1.29
DVio		Violet					650–1000	0.8–1	1.39
SVI	Marseille	Colourless					≈ 260	≈ 0.37	1.02
ROa	Rouen	Orange	Potash	841		Clays, latrines	≈ 1000	≈ 0.9	1.09
RV		Green					≈ 1000	≈ 0.9	1.12
RId		Colourless					300–500	0.3–0.45	0.95
RVF		Dark green					350–550	0.3–0.5	1.01
RVJ		Yellow–green					80–90	≈ 0.08	0.81
RBa		Pale blue	Soda	841			≈ 30	≈ 0.03	0.59
RIc		Colourless					20–35	0.02–0.035	0.67
RIa		Colourless					15–20	0.015–0.02	0.68
Op1	Oppenheim	Colourless	Potash	1332–1333	On windows	–	≥ 50	≥ 0.08	1.60
Op2		Red				–	?	?	1.30
Op3		Blue				–	≥ 40	≥ 0.06	1.72
Op4		Brown				–	120–160	0.18–0.21	1.60
To1	Tours	Green		1300–1400		–	≥ 90	≥ 0.14	1.24
To2		Red				–	130–140	0.2–0.21	1.26
To3		Colourless				–	≥ 80	≥ 0.12	1.27
To4		Pale blue				–	110–130	0.17–0.2	1.22
To5		Blue				–	?	?	1.25
To6		Orange				–	130–160	0.2–0.25	1.42
Me	Meissen	Green		1330–1340		–	150–220	0.23–0.34	1.53
Ev	Evreux	Red		1200–1300		–	?	?	1.14

[a] Nature of the most abundant alkali (flux) in the fresh glass: Na or K.

[b] Installation date (samples on windows) or burial date (samples from the soil).

[c] For samples on windows, the thickness given is that measured on the exterior face of the window; the interiors are characterised by dispersed alteration pits on the surface (non measurable).

[d] MRC: Mean rate of corrosion.

[e] The bulk degree of polymerisation of the glass is given by the value of NBO/T (Non-Bridging Oxygen per Tetrahedron, Mysen, 1988).

quantify the influence of (i) the conditions of alteration and (ii) the chemical composition of the pristine glass, on the corrosion rates. A detailed chemical characterisation may be used to estimate the release rate of transition elements, heavy metals and rare earth elements (REE) which are the pollutants of present-day toxic waste matrices.

2. Sample description

To assess the long-term behaviour of glasses under natural weathering conditions, we have studied medieval stained glass windows dating from the 9th to the 14th century, which have been altered under different conditions.

Twelve samples of stained glass taken from windows have been studied, from St. Gatien's cathedral in Tours, Evreux, Ste. Opportune du Bosc and Meissen cathedrals and Ste. Catherine's church in Oppenheim. Dating from the 13th to the 14th centuries, they were provided thanks to the Franco-German Research Programme for the Conservation of Historic Monuments (Table 1).

Thirteen additional samples (Table 1), unearthed in the course of archaeological excavations at sites within St. Victor's Abbey in Marseille, Notre-Dame-du Bourg in Digne and at the bishop's palace in Rouen, were kindly provided by Mrs. Daniele Foy from the Mediterranean Mediaeval Archaeological Laboratory in Marseille and Mr. Jacques Le Maho of the Mediaeval Archaeology Research Centre in Caen. The burying of these stained glasses, accidentally removed from the windows by breakage, fire etc., has been dated in an archaeological context as having occurred between the 9th and the 13th century (Foy, 1989; Le Maho, 1994).

All the studied samples are coloured glass sheets of a few cm^2 with a thickness of 2 to 5 mm, being more or less darkened by alteration products. Despite the occurrence of corrosion products, vitrified paints are often present suggesting preservation of the initial surface. It is of note that the archaeological site of Rouen is the only one containing both Na-rich and K-rich stained-glasses (see below).

3. Analytical techniques

Bulk chemical analyses were performed on both pristine and altered stained-glass samples. Pieces of the altered layer were mechanically removed from the fresh glass and hand picked under a binocular microscope. Each fraction was then crushed and homogenised prior to analysis. Major elements (Si, Al, Fe, Mn, Mg, Ca, Na K, Ti and P) were analysed by inductively coupled plasma atomic emission spectroscopy (ICP-AES), whereas concentrations of trace elements were determined by inductively coupled plasma mass spectrometry (ICP-MS). The analytical methodology for both ICP methods is as follows: a mass of powdered sample is fused in a platinum

Table 2
Representative chemical compositions of pristine stained glass windows

Wt.%	To2	Ev	Op1	Me	SVJ	DB	RVF	RIa	Ch
SiO_2	53.6	54.7	46.9	48.1	48.3	50.0	58.5	67.1	70.5
Al_2O_3	1.5	0.7	3.5	1.0	2.9	2.6	2.2	2.4	1.6
Fe_2O_3	1.0	l.d.	1.3	1.3	1.2	1.1	0.5	1.0	3.3
MnO	1.2	1.5	1.0	0.6	0.6	0.9	0.8	0.8	0.5
MgO	6.9	3.2	4.1	3.2	6.0	5.3	5.0	0.8	0.5
CaO	12.7	17.3	28.5	19.4	16.0	15.6	12.9	8.1	8.1
Na_2O	2.2	0.7	0.3	0.2	0.7	0.9	1.4	15.4	14.3
K_2O	17.8	15.3	11.2	22.4	15.1	17.8	12.9	0.9	1.8
TiO_2	0.2	l.d.	0.2	l.d.	0.2	0.2	0.4	0.1	l.d.
P_2O_5	3.8	5.9	2.2	1.7	4.1	4.2	2.9	0.3	0.8
Total	100.9	99.2	99.2	97.7	95.7	98.6	97.5	96.8	101.4

Major elements in weight percent of oxide were analysed by ICP-AES (DV, RVF, RIa) or by electron microprobe (To2, Ev, Op1, Me). A blue glass from Chartres (Ch) is given for purposes of comparison. l.d.: detection limit.

Table 3
Chemical composition of pristine and altered buried stained glasses

Wt.%	DB Pristine	DB Altered	DV Pristine	DV Altered	DR Pristine	DR Altered	Dvio Pristine	Dvio Altered	RVF Pristine	RVF Altered	RId Pristine	RId Altered	ROa Pristine	ROa Altered	RV Pristine	RV Altered	SVI Pristine	SVI Altered	V_i/V_K	σ	Nbval
SiO_2	50.04	57.71	52.44	56.34	51.86	52.98	49.95	54.27	58.54	43.46	59.28	60.57	57.62	65.72	55.80	69.26	51.47	55.98	0.47	0.02	9
Al_2O_3	2.62	4.07	1.66	2.98	1.08	2.07	2.04	3.43	2.17	5.97	2.25	4.69	1.26	3.16	1.20	2.31	4.16	7.07	0.09	0.09	9
Fe_2O_3	1.14	2.18	0.69	1.3	0.55	1.05	0.8	1.45	0.54	2.95	0.61	2.08	0.57	1.44	0.56	1.53	1.25	2.21	0.00	0.11	9
MnO	0.9	2.36	0.74	1.92	0.91	1.73	1.92	3.35	0.77	1.46	0.67	1.35	0.63	1.66	0.70	0.99	0.95	4.38	0.01	0.18	9
MgO	5.26	0.8	5.08	0.72	4.84	0.94	5.34	0.58	4.96	1.14	4.63	0.32	4.90	0.56	5.10	0.67	4.84	1.69	0.96	0.02	9
CaO	15.55	6.16	15.46	6.4	17.46	12.99	17.54	8.59	12.94	8.54	13.26	4.42	12.82	4.23	13.90	3.89	13.87	6.24	0.83	0.07	9
Na_2O	0.89	l.d.	1.14	0.09	0.43	0.16	0.93	0.05	1.42	0.25	2.17	0.06	1.53	0.11	1.70	0.33	2.10	0.24	0.98	0.03	9
K_2O	17.81	0.82	16.51	0.35	17.48	0.44	17.43	0.36	12.86	1.11	13.44	0.69	11.66	0.43	14.80	1.92	15.03	4.74	1.00	0.00	9
TiO_2	0.18	0.34	0.21	0.43	0.23	0.37	0.2	0.24	0.36	0.79	0.29	0.59	0.18	0.43	0.10	0.33	0.15	0.35	− 0.04	0.13	9
P_2O_5	4.23	2.4	4.05	4.85	4.27	5.82	3.37	3.45	2.86	3.78	2.5	2.1	1.68	1.63	2.00	1.93	4.47	3.86	0.58	0.09	9
L.I.	0.99	19.96	1.69	n.d.	0.63	19.26	0.79	21.64	0.72	13.73	0.75	21.23	5.88	19.8	n.d.	n.d.	n.d.	n.d.			
ppm																					
Rb	222	22	233	10	129	5.3	249	13	224	63	338	45	195	23	n.d.	n.d.	n.d.	n.d.	0.97	0.01	7
Cs	1.5	l.d.	1.4	1.5	0.5	0.1	0.7	0.3	1.3	1.2	3.3	l.d.	0.8	0.4	n.d.	n.d.	n.d.	n.d.	0.80	0.22	7
Be	2.6	5.6	l.d.	1.3	l.d.	l.d.	1.1	1.4	3.5	2.3	l.d.	5.2	l.d.	1.0	n.d.	n.d.	n.d.	n.d.	0.14	0.19	6
Sr	427	1394	285	674	371	1254	616	1496	349	365	291	327	222	183	n.d.	n.d.	n.d.	n.d.	0.49	0.02	3
Ba	1349	817	1081	744	1497	1003	1878	1496	1832	846	1364	1065	660	667	l.d.	l.d.	l.d.	l.d.	0.66	0.05	7
V	17	13	7.9	12	8.6	10	18	16	17	48	20	29	9.4	20	n.d.	n.d.	n.d.	n.d.	0.32	0.24	7
Cr	24	36	14	27	20	31	22	20	44	71	29	50	15	30	n.d.	n.d.	n.d.	n.d.	0.19	0.05	7
Co	342	1013	28	67	14	26	46	82	10	20	11	23	8.8	12	l.d.	l.d.	l.d.	l.d.	0.03	0.09	7
Ni	44	90	23	33	20	59	52	104	44	17	44	77	75	63	l.d.	l.d.	l.d.	l.d.	0.15	0.15	7
Cu	1285	3354	15,470	32,630	3576	3760	482	782	24,287	11,322	141	315	289	476	9,800	11,000	l.d.	l.d.	0.23	0.29	8

Zn	1210	4049	738	1383	651	869	261	407	295	144	220	354	177	281	l.d.	l.d.	l.d.	l.d.	0.23	0.08	7
Y	10	16	8.8	15	9.1	16	7.3	13	13	28	11	24	8.5	17	n.d.	n.d.	n.d.	n.d.	0.10	0.05	7
Zr	97	189	144	224	142	257	81	137	220	517	201	418	121	233	n.d.	n.d.	n.d.	n.d.	0.05	0.09	7
Nb	3.8	7.4	4.1	7.3	3.8	7	3	5.3	6	13.2	6.1	12.5	3.5	7.2	n.d.	n.d.	n.d.	n.d.	0.06	0.04	7
Hf	2.4	4.5	3.7	5.4	3.2	6.1	1.7	3.2	7	16	6.6	12	3	6.5	n.d.	n.d.	n.d.	n.d.	0.05	0.06	7
Ta	0.4	0.8	0.4	0.7	0.4	0.6	0.3	0.5	0.7	1.5	0.6	1.2	0.3	0.7	n.d.	n.d.	n.d.	n.d.	0.06	0.05	7
W	0.7	0.9	l.d.	0.9	0.3	3.3	1.4	9.5	1.1	0.8	1.1	1.8	1.9	3.1	n.d.	n.d.	n.d.	n.d.	0.26	0.11	5
Ga	4.1	8.1	2.1	4.5	2.2	4.7	3.6	5.9	2.4	9.1	4.5	8.4	2.5	5.3	n.d.	n.d.	n.d.	n.d.	0.05	0.12	7
As	5.8	11	22	14	3.8	6.4	11	10	149	61	3.2	11	1.9	6.1	n.d.	n.d.	n.d.	n.d.	0.12	0.55	7
Sn	50	184	1300	1234	215	349	41	74	2646	5700	9.1	84	46	93	l.d.	l.d.	l.d.	l.d.	0.10	0.20	7
Sb	83	26	43	41	9	13	2.8	11	140	162	2	69	1.9	3.6	n.d.	n.d.	n.d.	n.d.	0.24	0.28	7
Pb	533	3289	1940	3706	253	1116	144	674	2305	47,000	142	13,415	56	135	l.d.	l.d.	l.d.	l.d.	− 0.50	− 0.41	7
La	34	70	34	92	51	96	27	46	48	101	33	66	70	160	n.d.	n.d.	n.d.	n.d.	0.00	0.03	7
Ce	45	93	53	122	55	100	34	60	69	145	54	117	91	200	n.d.	n.d.	n.d.	n.d.	− 0.01	0.06	7
Pr	5	11	4.8	10	6.3	12	3.8	6.4	5.9	14	4.9	11	7.6	18	n.d.	n.d.	n.d.	n.d.	− 0.05	0.05	7
Nd	17	32	16	35	18	38	14	23	22	52	17	37	22	52	n.d.	n.d.	n.d.	n.d.	− 0.05	0.07	7
Sm	2.7	6.6	2.1	4.2	1.9	3.8	1.7	3.2	2.7	7.9	2.8	5.9	2.5	5.4	n.d.	n.d.	n.d.	n.d.	− 0.01	0.04	7
Eu	0.5	0.7	0.5	0.6	0.5	0.7	0.6	0.7	0.7	1.2	0.6	0.7	0.5	0.9	n.d.	n.d.	n.d.	n.d.	0.35	0.11	7
Gd	1.9	3.8	1.7	2.5	1.5	2.8	1.3	2.1	2.1	6.1	2.4	4.3	2	4.5	n.d.	n.d.	n.d.	n.d.	0.02	0.14	7
Tb	0.3	0.5	0.3	0.3	0.3	0.5	0.2	0.4	0.3	0.8	0.3	0.7	0.2	0.6	n.d.	n.d.	n.d.	n.d.	− 0.03	0.14	7
Dy	1.6	2	1.6	2.3	1.2	2.5	1	1.9	2	4.3	2.4	3.4	1.3	3.1	n.d.	n.d.	n.d.	n.d.	0.04	0.17	7
Ho	0.3	0.8	0.3	0.5	0.2	0.5	0.2	0.5	0.5	0.9	0.4	0.8	0.2	0.6	n.d.	n.d.	n.d.	n.d.	− 0.01	0.04	6
Er	0.8	1.9	0.8	1.5	0.7	1.3	0.7	1.1	0.9	2.5	1	1.6	0.6	1.5	n.d.	n.d.	n.d.	n.d.	0.03	0.14	7
Tm	0.1	0.2	0.1	0.2	0.1	0.2	0.1	0.2	0.2	0.6	0.2	0.3	0.1	0.2	n.d.	n.d.	n.d.	n.d.	− 0.03	0.23	7
Yb	0.9	2	0.9	1.2	0.7	1.3	0.6	0.9	1	1.6	0.7	1.8	0.6	1.3	n.d.	n.d.	n.d.	n.d.	− 0.06	0.10	6
Lu	0.1	0.3	0.1	0.2	0.1	0.2	0.1	0.2	0.3	0.4	0.1	0.3	0.1	0.2	n.d.	n.d.	n.d.	n.d.	0.08	0.06	7
Th	2.8	6.2	2.9	5.4	2.4	4.5	2.6	4.5	4.2	9.3	4.1	8.8	2.6	6	n.d.	n.d.	n.d.	n.d.	− 0.03	0.06	7
U	0.9	1.1	0.7	1.5	0.7	3.2	0.9	1.4	1.5	0.7	1.2	1	0.5	0.3	n.d.	n.d.	n.d.	n.d.	0.45	0.17	3
Total	99.2	78.32	100.13	79.49	99.84	79.49	99.93	76.33	100.7	76.13	99.4	78.53	93.06	79.65	95.85	83.16	98.41	87.03			
V_K (g m^{-2} day^{-1})	8.9e − 03		8.3e − 03		7.4e − 03		7.5e − 03		2.6e − 03		2.2e − 03		5.4e − 03		5.4e − 03		1.9e − 03				

Major elements in weight percent of oxide were analysed by ICP-AES. Trace elements (in ppm) were analysed by ICP-MS. SVI and RV were analysed using electron microprobe. L.I.: loss on ignition. l.d.: detection limit; n.d.: not determined. V_i/V_K: elemental dissolution rate relative to potassium. V_K: potassium dissolution rate in g m^{-2} day^{-1} (see text for calculation). σ: standard deviation; Nbval: number of values used to calculate V_i/V_K. V_i/V_K for Sr and U was calculated only from three samples because of obvious and unexplained contamination.

crucible with 9 masses of $LiBO_2$ and 6 masses of boric acid in an automated tunnel furnace. The fused melts are dissolved in dilute nitric acid, and the final solutions analysed by ICP-AES (Govindaraju and Mevelle, 1987) and ICP-MS. Depending on the amount of starting material, the quantity of analysed sample ranges between 50 and 100 mg.

In situ analyses and observations of stained-glasses were performed on polished cross-sections after mounting in epoxy. Polished sections were coated with amorphous carbon for electron microprobe analyses and SEM observations. Electron microprobe analyses (EPMA) were performed with a CAMECA SX50 equipped with four spectrometers and a wavelength-dispersive system (WDS). Accelerating voltage was 15 kV and the current intensity 20 nA. The spot size was defocalised to 5 μm. Electron microprobe calibration was conducted using polished geological standards prior to analysis. Quantitative data were obtained by ZAF correction routine. The stained-glass characterisation was completed using and Hitachi S-2500 scanning electron microscope (SEM), equipped with a KEVEX 4850-S energy dispersive spectrometer (EDS).

4. Results

4.1. Pristine glass composition

In the Middle Ages, stained glass was made by melting a mixture of washed siliceous sand and a flux. The flux used was either mineral ("natron") or plant-based (beech or fern-ash). The staining was attained during the fusion process by the addition of variable amounts of different metal oxides (Co, Mn, Cu, Fe etc.) depending on their colouring capacity (Foy, 1989; Perez Y Jorba and Dallas, 1984; Sterpenich, 1998). Accordingly, their compositions (Table 2) are rich in silica ($43 < SiO_2 < 70$ wt.%) and calcium ($8 < CaO < 29$ wt.%) and, depending on the nature of the flux (evolving both regionally and over time), either enriched in potash (up to 16 wt.% K_2O) or in soda (up to 16 wt.% Na_2O), the latter being rarely manufactured during this period. The soda-rich glasses are more silica-rich (up to 70 wt.% SiO_2), and therefore present higher degrees of bulk polymerisation, than those rich in potash. Due to impurities in the starting materials, these medieval stained glasses also contain more than 50 other elements (Table 3), including high concentrations of transition metals (e.g. Cr up to 100 ppm, Ni up to 50 ppm, Co up to 350 ppm), heavy metals (e.g. Cu up to 2.5wt.%, Zn up to 3,000 ppm, Pb up to 2,500 ppm), REE (e.g. La up to 50 ppm, Ce up to 70 ppm), actinides (e.g. Th up to 5 ppm) and other toxic elements (e.g. As up to 150 ppm) which are the polluting elements contained in vitrified wastes.

4.2. Description of the alteration of stained-glass windows

Depending on their exposure, stained glass windows can be used to characterise the effects of various weathering conditions on glass dissolution; stained glass windows are subject to atmospheric weathering (study of their outside surface) and weathering driven by moisture (study of their inside surface); samples excavated from archaeological sites were subject to alteration by groundwater. Whatever the kind of alteration, all the samples studied present traces of corrosion on their surface. However, SEM images (Fig. 1) reveal that the structure and the thickness of the altered zone depend mainly on the type of weathering (Table 1). For fixed glass compositions (K-rich stained glasses in Fig. 1), alteration driven by moisture (as deduced from the study of the inside of the windows) produces only scattered dissolution pits (Fig. 1a), whereas atmospheric weathering (as deduced from the study of the outside of the windows) produces a continuous altered layer up to 200 μm. This altered layer produced by atmospheric weathering, has a thickness made up of three superimposed layers (Fig. 1b). From the surface, they are: (1) a superficial, irregular, neo-formed layer (mainly gypsum, calcite and syngenite); (2) an altered, fractured zone of varying thickness depending on the extent of corrosion; and (3) the pristine glass characterised by its homogeneity and the absence of micro-fracturing (Perez Y Jorba et al., 1984). On the internal stained glass window surface, the pitting corresponds to the development of radial microfractures and micrometric layers centred on these fractures (Fig. 1a). A prominent feature of these weathered zones is the occurrence of a network of microcracks perpendicular and parallel to the surface

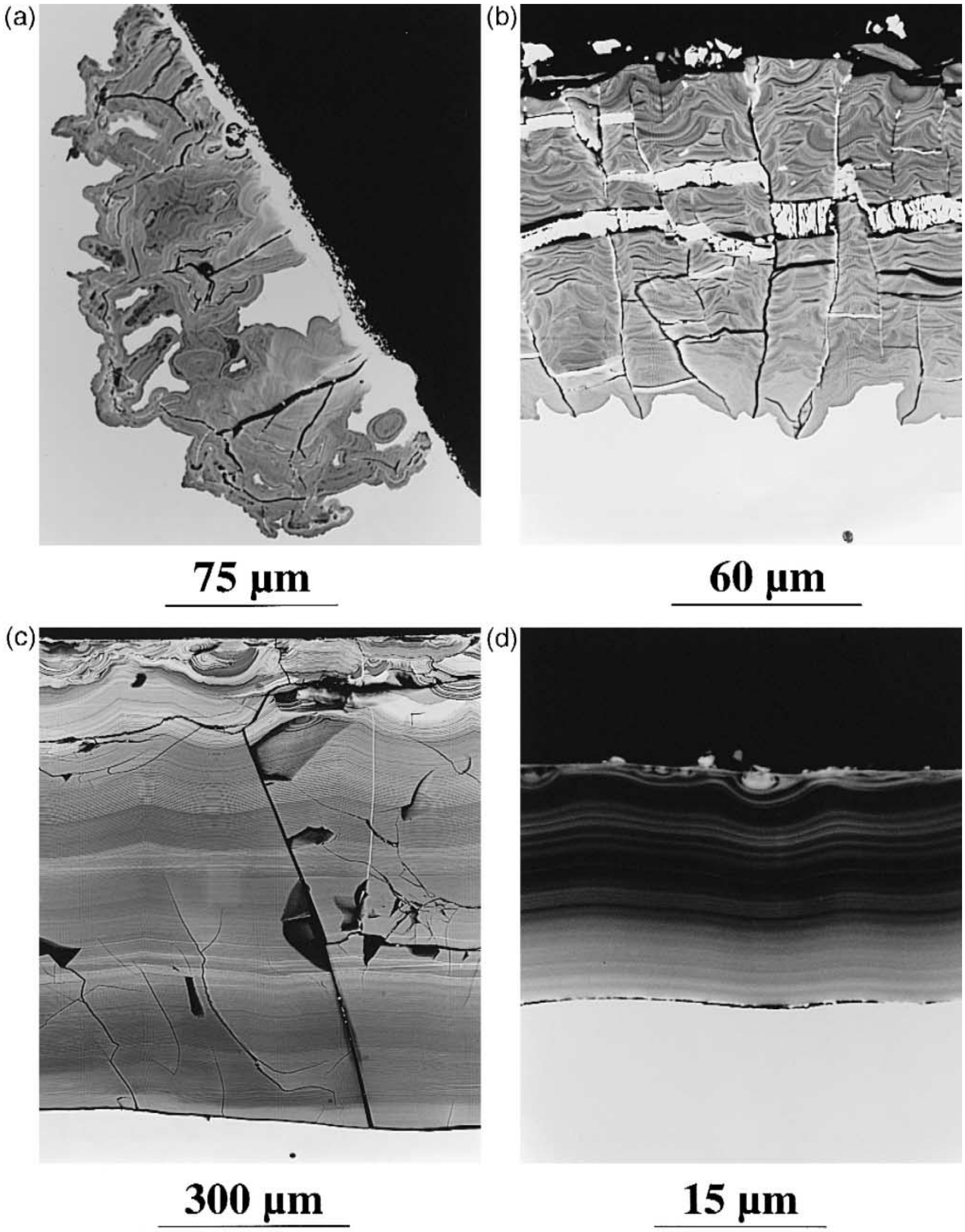

Fig. 1. Scanning Electron Microscope photographs (back scattered electrons) of sections of medieval stained glass windows. The altered layer is grey and the fresh glass is white, in the lower part of the picture. (a) Alteration by moisture condensation: inside window (orange stained glass: To6) from Tours showing corrosion pits. (b) Atmospheric weathering: a thicker layer is observed on the outside of the same glass from Tours. Alteration by groundwater: (c) green K-rich glass DV from Digne (fractures are due to sample preparation); (d) thin alteration zone observed on a pale blue Na-rich glass from Rouen (RBa). Note the recurrence of laminae in c and d which are characteristic of the alteration by groundwater.

of the original glass (Fig. 1b). The cracks parallel to the surface are generally filled by sulphates and carbonates which are responsible for the darkening observed in stained glass windows (Barbey et al., 1996; Libourel et al., 1994; Perez Y Jorba et al., 1984). The unfilled fractures perpendicular to the glass surface interfinger with the corrosion front demonstrating their control on the progression of weathering of the glass.

In contrast, buried K-rich samples show more pervasive weathering (Fig. 1c) with alteration zones of up to 1500 μm. These crusts are devoid of microcracks and typically show a finely laminated structure, in which micron scale lamellae result from hydroxyapatite precipitation in the weathered glass (Cox and Ford, 1993; Sterpenich, 1998). These features, characteristic of underground alteration, have also been observed on windows from different archaeological sites (Gillies and Cox, 1988; Macquet and Thomassin, 1992; Newton, 1971; Sterpenich, 1998). In the near-surface regions of such crusts, pyrolusite- or hausmannite-like Mn-rich phases

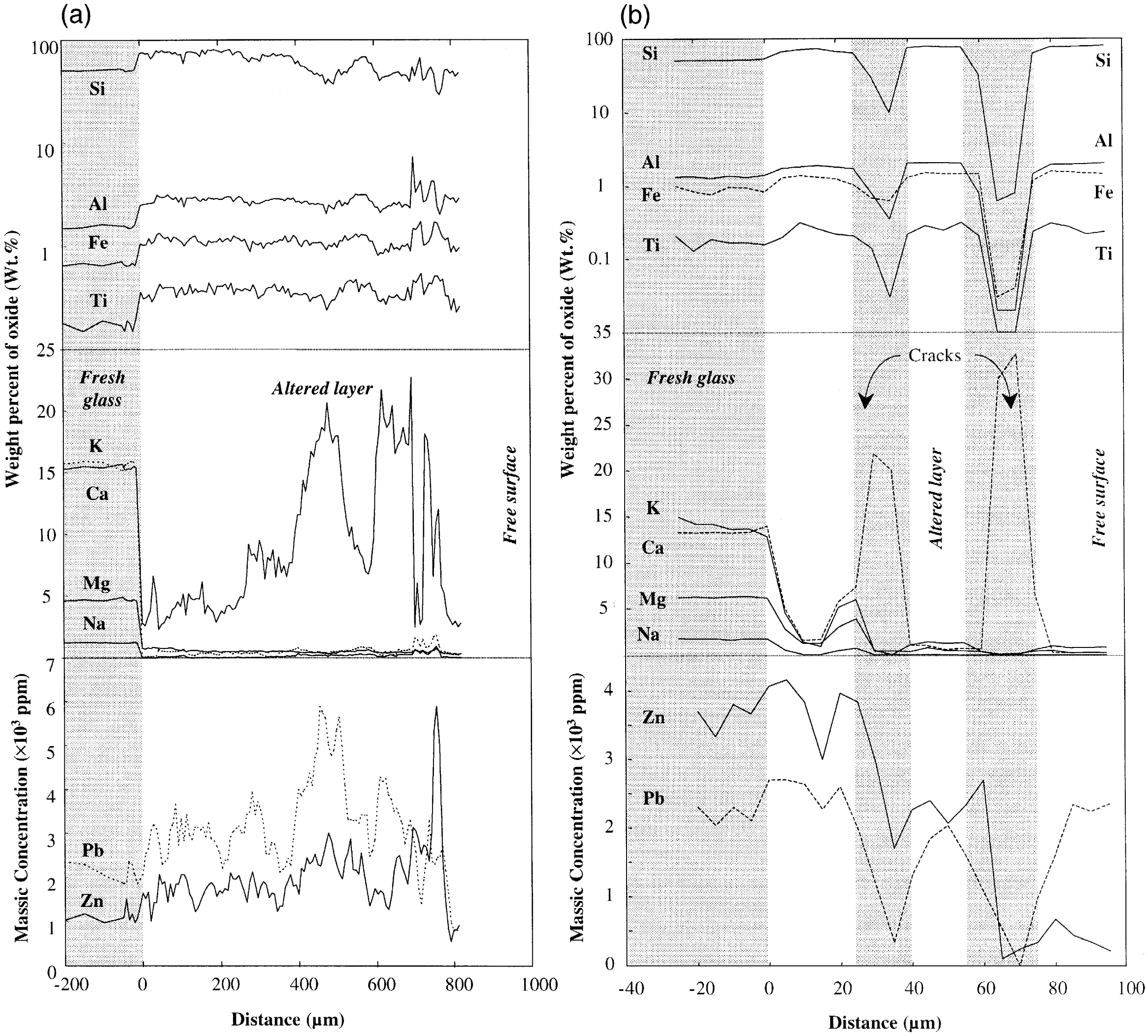

Fig. 2. Chemical profiles (Si, Al, Fe, Ti, Ca, Mg, Na, K, Pb and Zn) perpendicular to the alteration front analysed by electron microprobe. (a) Green K-rich glass from Digne (DV) unearthed during archaeological excavations on the site of Notre-Dame-de Bourg, Digne, dated to the 12th century (see Fig. 1c). Calcium variations in the altered glass are due to hydroxyapatite-like phase precipitation (see text). (b) Blue glass (To3) from St. Gatien's, Tours, dated to the 13th. The two cracks are filled with Ca–sulphate precipitates. The altered/unaltered glass interface, visible by SEM, back-scattered electrons is localised to zero.

cross-cut the laminated structure (Cox and Ford, 1993; Sterpenich, 1998).

Under the same weathering conditions, it is evident that glass dissolution rates depend on the bulk composition of the original glass (Table 1). Under burial conditions at the archaeological site of Rouen for example (9th century), the mean thickness of the altered zone for soda-rich glasses is 35–40 μm (Fig. 1d), while for K-rich samples it may exceed 1000 μm. Similarly, potassic glass windows are always darkened by alteration while Na-rich glasses on the same windows preserve their colour and have alteration zones of < 2 μm; this feature is well demonstrated for Chartres cathedral windows (13th century), where the blue stained glass (Na-rich) is remarkably well preserved.

4.3. Chemical characterisation of the altered layer

Chemical characterisation of the altered layer of glasses weathered underground and on windows was systematically carried out with the electron microprobe along appropriate sections perpendicular to the alteration front (Sterpenich, 1998). As an example, Fig. 2 shows chemical profiles for major elements (Si, Al, Fe, Ti, K, Na, Ca and Mg) and two trace elements (Zn and Pb), measured in the altered layer of two K-rich glasses. Fig. 2b represents profiles obtained from a glass on a window (sample To3 from Tours) whereas Fig. 2a shows behaviour recorded from an underground sample (DV from Digne). Whatever the conditions of alteration and whatever the sample used, major elements show two contrasting behaviours. Compared to the unaltered glass, the altered glass is poor in K, Na, Ca, Mg and relatively enriched in Si, Al, Ti and Fe, suggesting different mobility of network modifying and network forming cations. These results, together with those obtained from hydrogen ion probe measurements (Sterpenich, 1998), show that these altered layers are mainly constituted by an hydrous “silica-gel” highly depleted in alkalis and alkaline earths. However, it is of note that the leaching of trace elements may be dependent on the conditions of alteration as shown by the contrasting chemical profiles of Zn and Pb (Fig. 2). In general, zinc and lead are depleted in the altered layer of glass submitted to atmospheric weathering (Fig. 2b) whereas they are enriched in the corrosion crust of buried samples (Fig 2a).

In order to understand better the behaviour of trace elements during glass weathering, ICP-AES and ICP-MS measurements were performed on both pristine and altered glasses. However, due to the very small thickness of the altered layer of certain samples, analysis of the corrosion crust was only possible for buried K-rich glasses. For each buried stained glass investigated, the altered crust significantly differs in bulk composition from the pristine glass, and consists mainly of an hydrated “silica-gel” with SiO_2 concentration ranging from ~ 43 to ~ 70 wt.% (Table 3). The loss on ignition, as well as direct measurements of water content, indicate a H_2O content from 17 to 24 wt.% (Table 3). Water analysis by Karl Fischer titration and gravimetry (Sterpenich, 1998) reveals that 37–45% of total water is hydroxyl, the majority of H_2O being therefore pore-water. Aluminium (~ 2–7 wt.% Al_2O_3), iron (~ 1–3 wt.% Fe_2O_3), manganese (~ 1–4 wt.% MnO), calcium (~ 4–13 wt.% CaO) and phosphorous (~ 2–6 wt.% P_2O_5) constitute the remaining major elements (Table 3). By comparison with pristine glass, the altered crust is relatively enriched in silicon, aluminium, iron, manganese, and severely depleted in potassium, magnesium and sodium, in agreement with electron microprobe profiles. Calcium and phosphorus are moderately depleted due to the occurrence of hydroxyapatite-like phases in the altered layer. Trace elements are, similarly to major elements, either concentrated or depleted in the altered crust. Amongst these trace elements, Co, Cr, Cu, Ni, Pb, Zn, Zr, and REE are enriched in the corrosion crusts, whereas Cs, Rb, Ba or Sb are depleted compared to the pristine glass.

5. Discussion

Thanks to chemical characterisation of pristine and altered glasses and the accurate dating of medieval stained-glass windows by the historical or archaeological context, it is now possible to assess the main kinetic parameters of natural alteration of stained glasses. Assuming that the alteration of medieval stained glasses was generated at near constant volume, as implied by (i) the frequent presence of vitrified paint at the initial surface of glasses, and (ii) the good mechanical cohesion between weathered and unweathered glass, the mean corrosion rates can be evaluated. In addition, due to their complex composition (more than 50 elements, Table 3), medieval stained glasses allow the estimation of elemental dissolution rates averaged over 600 to 1100 years.

5.1. Mean corrosion rates

An estimation of the corrosion rate of each sample may be made by dividing the mean thickness of weathered crust by the time of weathering. Table 1 summarises the mean corrosion rates obtained from stained glasses altered on windows and buried in the soil. For samples on windows, the thickness given is that measured on the outside of the window; the interiors are characterised by non-measurable dispersed alteration pits on the surface (see Fig. 1a). For the studied medieval stained-glasses, the mean corrosion rates range from 0.01 to 1.6 μm/year and depend on glass composition and on conditions of alteration.

To explore the effect of glass composition on kinetics of alteration, we used samples excavated from the archaeological site of Rouen presenting various bulk composition (Tables 1 and 3) and submitted to the same conditions of weathering (damp soil). Fig. 3 shows the variation of the mean corrosion rate (MRC) against the bulk degree of polymerisation of the pristine glass (NBO/T, Mysen, 1988). For the archaeological site at Rouen (Fig. 3), the mean corrosion rate correlates with degree of polymerisation of the glass, NBO/T, following the equation $\log_{10}$ (MCR) in μm $\text{year}^{-1} = 3.41$ NBO/T − 3.82. These results show that the more the glass is polymerised, the less it is leached and confirm previous findings (Cox and Ford, 1993; Jantzen and Plodinec, 1984; Newton and Paul, 1980). Fig. 3 shows also that buried stained glasses from other sites (Digne, Marseille, Shropshire, Kent and Canterbury) follow the same trend and confirm this compositional dependence. Consistent with the calculation of the free energies of hydration (Paul, 1977), these data suggest maximum corrosion rates of around 1.3 ± 0.4 μm year^{-1} for buried potash-rich stained glasses (Fig. 3). Mean corrosion rates in K-rich glasses are, therefore, 40 to 50 times greater than for Na-rich ones. In contrast, a comparison of the corrosion rates on the outside of stained glass windows with those from buried samples reveals that alteration is, on average, 5–6 times slower (0.17 to 0.34 μm year^{-1} for K-rich glasses, Table 1 and Fig. 3). Thus, we find that differences in glass composition lead to variations in glass dissolution rates an order of magnitude more pronounced than those caused by different weathering conditions.

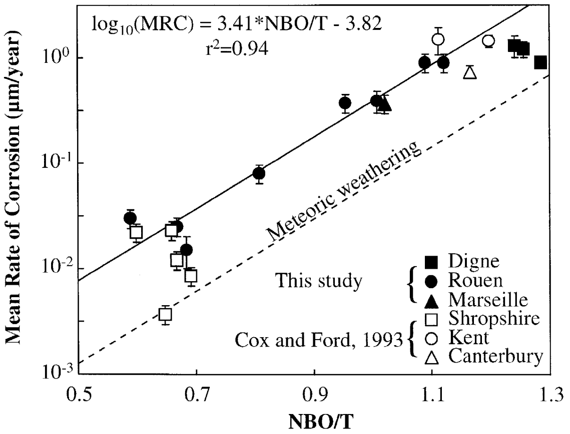

Fig. 3. Mean rate of corrosion versus bulk degree of polymerisation of pristine glass. Samples from Rouen, Digne and Marseille (this study). Samples from Kent, Canterbury and Shropshire (Cox and Ford, 1993) are given for comparison purposes. The more polymerised glasses (low NBO/T values) correspond to soda-rich glasses, whereas the less polymerised correspond to potash-rich glasses. The more the glass is polymerised, the less it is leached. MRC: mean rate of corrosion, in μm year^{-1}. For comparison, the alteration rates for exposed stained glass windows (dashed line) have been calculated assuming kinetics of alteration six times slower than for samples from Rouen altered in the soil.

5.2. Mean elemental dissolution rates for buried samples

One significant feature of medieval stained glasses is that, contrary to other natural glasses or glasses altered in the laboratory, these can be used to determine non-stoichiometric elemental dissolution rates for toxic elements under weathering conditions averaged over more than a thousand years. As the presence of the original surface of the glasses is confirmed by the occurrence of vitrified paint, the release rates for elements can be quantified from buried samples if both bulk composition (mass fraction x_i) and density (ρ) of the pristine (pg) and weathered glass (wg) are known; the normalised elemental dissolution rate (V_i in g m^{-2} day^{-1}) for a given thickness (e) over time (t) is then calculated according to:

$$V_i = \frac{e}{x_i^{\mathrm{pg}} t}\left(x_i^{\mathrm{pg}}\rho_{\mathrm{pg}} - x_i^{\mathrm{wg}}\rho_{\mathrm{wg}}\right)$$

An unweathered glass density of 2.4 ± 0.1 g cm^{-3} was assumed in agreement with density measurements on model glasses; for the weathered glasses, a density close to that of a xerogel (around 1.1 ± 0.1 g cm^{-3}) was assumed (Cooper and Cox, 1994).

Potassium in the K-rich stained glasses shows the highest dissolution rate of ~ 2.2 to 5.4×10^{-3} g m^{-2} day^{-1} for Rouen samples and from 7.4 to 8.9×10^{-3} g m^{-2} day^{-1} for samples from Digne and Marseille (Table 3). In contrast, the leaching of potassium from Na-rich stained glasses from Rouen estimated from electron microprobe results is 1.2 to 1.7×10^{-4} g m^{-2} day^{-1}. Given these rates, bulk kinetics of the dissolution of stained glasses were also determined ($V_t = \Sigma x_i V_i$) and are around 4 to 6×10^{-3} g m^{-2} day^{-1} for K-rich glasses and close to 1 to 2×10^{-4} g m^{-2} day^{-1} for Na-rich samples. The dissolution rates relative to potassium (the most mobile element) V_i/V_K are given in Table 3 and plotted in Fig. 4. Alkalis (K, Na, Rb and Cs) and alkaline-earth elements (Mg, Ca, Sr and Ba) are by far the most leachable elements, consistent with their network-modifying role in the glass structure (Brown et al., 1995) and their depletion in the altered layer depicted in electron microprobe profiles (Fig. 2). With kinetics of dissolution between 50% and 98% of V_K, the mobility of alkali and alkaline-earth elements is, on average, inversely proportional to ionic radius. Despite the siliceous composition of the altered zone, silicon, the major glass network former, is released to the environment with rates close to 45% of V_K. In contrast, the remaining glass-forming cations (Al, Fe, Zr, Ti, etc.) are weakly depleted during weathering, as suggested by their low release rates ($< 10\%$ of V_K). Heavy metal, transition and potentially toxic elements (such as Pb, As, Ni, Cr or Zn) have release rates of $< 30\%$ of V_K and in this group of elements, V, Sb, Zn, Cu, Cr, Ni and As are the most mobile ($V_i/V_K \sim 0.1$ to 0.3). Lanthanides

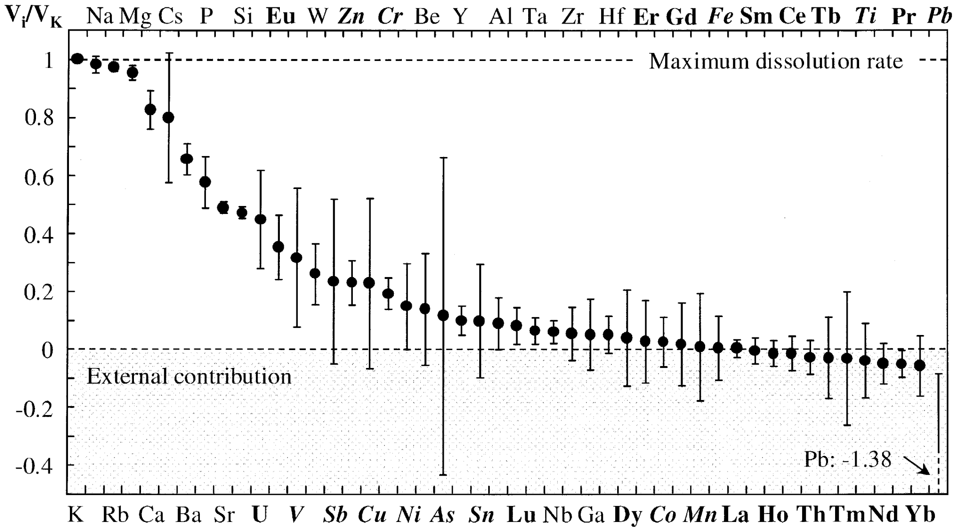

Fig. 4. Elemental dissolution rates (V_i) over dissolution rate of potassium (V_K), where K is one of the most leachable elements. Values correspond to the median calculated from potassic samples from Digne, Marseille and Rouen (see Table 3). After mechanical separation, both fresh and altered glass were analysed by ICP-AES and ICP-MS for major and trace elements respectively. Error bars correspond to the standard deviation. Note, for each element, the weak dispersion of the data despite the three different sites of sampling. The very negative value for Pb is due to the leaching of lead used to hold the glasses. Ratios far from 1 show the highly non-stoichiometric dissolution of stained glass windows. In bold: actinides and lanthanides; in italics: transition and heavy metals.

and actinides, with the notable exception of U and Eu ($V_i/V_K \sim 0.35$ and 0.45), are almost insensitive to weathering and present the lowest dissolution rates (e.g. $V_{Th} \sim 8$–$9\ 10^{-5}$ g m^{-2} day^{-1}). In contrast, electron microprobe analyses performed in the alteration zone of K-rich stained glass weathered on windows show that toxic elements such as Zn, Pb or Cu may be severely leached (see Fig. 2 and Sterpenich, 1998), suggesting that dissolution kinetics and composition of the altered zone strongly depend on the conditions of alteration.

6. Conclusions and implications on the long-term behaviour of vitrified wastes

This study demonstrates that alteration of medieval stained-glass windows is strongly dependent on glass composition and on the weathering conditions with highly variable elemental dissolution rates. Despite the obvious non-stoichiometric dissolution of these glasses, it is not possible to assess the mechanisms responsible of such process because of the lack of information concerning the chemical and physical conditions of alteration including pH, Red–Ox conditions, temperature, degree of saturation of the solution and the characteristics of the leachate (rain, water of porosity, moisture).

The data presented here demonstrate the poor relative durability of K-rich stained glasses. Therefore, the elemental dissolution rates determined may be considered as an upper limit on the durability of present-day vitrified wastes under storage conditions in subsurface repositories for periods of 10^3 years. However, since the physical and chemical conditions of the storage environment may play a major role in the control of elemental dissolution, it is important to take into account the changes in these conditions if storage of waste matrices is proposed at much greater depth than the near-surface conditions of the archaeological stained-glasses.

This study also demonstrates that although alteration zones (weathered glass and precipitates) may play the role of a barrier limiting the release of several pollutants, special care in glass formulation strategy for vitrified nuclear wastes has to be taken since long-lived fission products with activities in excess of 10^3 years (e.g. ^{41}Ca, ^{135}Cs, and ^{59}Ni) may be released to the biosphere.

Acknowledgements

Our thanks go to J. Le Maho, D. Foy and I. Pallot-Frossard for supplying stained glasses samples. We also thank A. Kohler, R. Podor, S. Barda, and J. Carignan for analytical and technical assistance, and F. Mosnier, I. Pallot-Frossard for helpful discussion. Finally, we would also like to acknowledge J. Schott for his critical and thorough review which helped improve the clarity of the manuscript. This work was financially supported by the SITA group (Lyonnaise des Eaux), the French Environment Agency (ADEME) and the French Ministry of the Culture. CRPG-CNRS contribution n° 1509.

References

Barbey, P., Sterpenich, J., Libourel, G., 1996. Altération des vitraux: Produits d'altération, états d'oxydation du manganèse, effets des traitements de surface. In: Filtz, J.F. (Ed.), 2ème Colloque du Programme Franco-Allemand de Recherche pour la Conservation des Monuments Historiques Conservation commune d'un patrimoine commun, Bonn, pp. 61–71.

Brown, J., Farges, G.E., Calas, F., 1995. X-ray scattering and X-ray spectroscopy studies of silicate melts. In: Stebbins, J.F., Mc Millan, P.F., Dingwell, D.B. (Eds.), Structure, dynamics and properties of silicate melt. Reviews in Mineralogy Mineralogical Society of America, pp. 317–410.

Cooper, G.I., Cox, G.A., 1994. A comparative study of the natural and experimental corrosion of poorly durable potash–lime–silica glasses. Mater. Res. Soc. Symp. Proc. 333, 525–531.

Cox, G.A., Ford, B.A., 1993. The long-term corrosion of glass by groundwater. J. Mater. Sci. 28, 5637–5647.

Ewing, R.C., 1979. Natural glasses: analogues for radioactives wastes forms. In: McCarthy, G. (Ed.), Scientific Basis for Nuclear Waste Management. Plenum, New York, pp. 57–68.

Foy, D., 1989. Le verre médiéval et son artisanat en France Méditerranéenne. 467 pp.

Gillies, K.J.S., Cox, G.A., 1988. Decay of medieval stained glass at York, Canterbury and Carlisle: Part 2. Relationship between the composition of the glass, its durability and the weathering products. Glastechnische Berichte 61 (4), 101–107.

Govindaraju, K., Mevelle, G., 1987. Fully automated dissolution and separation methods for inductively coupled plasma atomic emission spectrometry rock analysis. Application to the determination of rare earth elements. J. Anal. At. Spectrom. 2, 615–621.

Grambow, B., 1985. A general rate equation for nuclear waste glass corrosion. Mater. Res. Soc. Symp. Proc. 44, 15–27.

Heimann, R.B., 1986. Nuclear fuel waste management and archaeology: are ancient glasses indicators of long-term durability of man made materials? Glass Technol. 27 (3), 96–101.

Jantzen, C.M., Plodinec, M.J., 1984. Thermodynamic model of natural, medieval and nuclear waste glass durability. J. Non-cryst. Solids 67, 207–223.

Le Maho, J., 1994. Les fouilles de la cathédrale de Rouen de 1985 à 1993: Esquisse d'un premier bilan. Archéologie médiévale, 24: 1–49.

Libourel, G., Barbey, P., Chaussidon, M., 1994. L'altération des vitraux. Recherche(La), vol. 25, pp. 168–188.

Lutze, W., Malow, G., Ewing, R.C., Jercinovic, M.J., Keil, K., 1985. Alteration of basalt glasses: implications for modelling the long-term stability of nuclear waste glasses. Nature 314, 252–255.

Macquet, C., Thomassin, J.H., 1992. Archaeological glasses as modelling of the behaviour of buried nuclear waste glasses. Appl. Clay Sci. 7, 17–31.

Mysen, B.O., 1988. Structure and properties of silicate melts. Developments in Geochemistry, vol. 4 Elsevier Science, Amsterdam, 354 pp.

Newton, R.G., 1971. The enigma of the layered crusts on some weathered glasses, a chronological account of the investigations. Archeometry 13, 1–9.

Newton, R.G., Paul, A., 1980. A new approach to predicting the durability of glasses from their chemical compositions. Glass Technol. 21 (6), 307–309.

Paul, A., 1977. Chemical durability of glasses; a thermodynamic approach. J. Mater. Sci. 12, 2246–2268.

Perez Y Jorba, M. and Dallas, J.P., 1984. Composition et altération des grisailles anciennes. Trois exemples de grisailles du XIIIème siècle étudiés par rayons X et microsonde électronique. News Letters du Comité Technique du Corpus Vitearum, 37–38: 8–13.

Perez Y Jorba, M., Dallas, J.P., Collongues, R., Bahezre, C., Martin, J.C., 1984. La corrosion atmosphérique d'un verre du Moyen-Age. Rôle du phosphore dans le mécanisme d'altération. Rivista della Stazione Sperimentale del Vitro 5, 121–130.

Perez Y Jorba, M., Mazerolles, M., Michel, L., Rommeluere, D., Bahezre, M., 1993. Etude du processus d'altération des vitraux de la cathédrale de Tours. Analyse des verres. Rôle des éléments mineurs. Etude des grisailles. In: Welck, S.F.v. (Ed.), 1er Colloque du Programme Franco-Allemand de Recherche pour la Conservation des Monuments Historiques. Conservation commune d'un patrimoine commun, Karlsruhe, pp. 213–219.

Sterpenich, J., 1998., Altération des vitraux médiévaux. Contribution à l'étude du comportement à long terme des verres de confinement. PhD Thesis, UHP Nancy 1, France, 461 pp.

Cristallochimie des produits d'altération des vitraux médiévaux: application au vieillissement des déchets vitrifiés

Crystal chemistry of alteration products of medieval stained-glass windows: application to the ageing of vitrified wastes

Jérôme Sterpenich

Résumé Les vitraux médiévaux, altérés à même les verrières ou exhumés lors de fouilles archéologiques, fournissent un excellent analogue pour suivre le comportement à long terme de déchets vitrifiés altérés en conditions naturelles. Ils permettent en effet d'étudier l'influence des conditions d'altération et de la composition du verre sur sa dissolution, et de déterminer les cinétiques de dissolution des éléments piégés dans le verre sur des périodes de plus d'un millénaire. Ce travail montre de plus que la dissolution des verres silico-calciques et alcalins est incongruente et que la minéralogie des pellicules d'altération joue un rôle primordial quant au comportement à long terme des déchets vitrifiés, puisque même si le verre s'altère, les produits secondaires peuvent, dans certains cas, piéger la majorité des éléments polluants.

Abstract One of the major problems of modern society is to render inoffensive ultimate wastes produced by municipal, industrial or nuclear activity. These ultimate wastes contain high amounts of toxic elements and have to be stabilised before storage. Among the actual solidification–stabilisation processes, vitrification offers many advantages, such as a reduction of volume, no porosity and good chemical durability. However, before using silicate glasses to stabilise ultimate wastes, it is necessary to ensure the long-term behaviour of these materials and to study their solubility and the possible dispersion of polluting elements into the biosphere. Although many leaching experiments have been carried out, knowledge of the behaviour of vitrified wastes weathered over periods of 100 to 10,000 years remains sparse. Previous work (Sterpenich et Libourel 2001) has shown that medieval stained-glass windows provide a valuable opportunity to study the alteration and long-term behaviour of vitrified wastes under natural conditions of weathering. This study allowed the quantification of the influence of conditions of alteration and of glass composition on dissolution kinetics through the calculation of mean dissolution rates of toxic elements over periods of time of up to one millennium. However, the mineralogy and the chemistry of altered-layer stained glasses are complex. An essential second step is the study of the crystal chemistry of pollutants in order to determine the long-term stability of the phases containing them and thus to ensure the long-term containment of potentially toxic elements.

This work focuses on the identification of mineral phases formed through alteration of medieval stained glasses, either on windows or buried in the soil. Medieval stained-glass windows allow the study of the behaviour of a glass submitted to different alteration conditions over periods of more than one millennium. Due to their chemical complexity, medieval stained glasses permit the quantification of release rates of elements, in particular pollutants belonging to the vitreous silicate matrix. Medieval stained glasses altered on windows by meteoric waters develop an altered layer made of a hydrated silica gel, generally depleted in transition and heavy metals. Secondary products (sulphates and carbonates) precipitated on the surface or in the

Received: 15 Octobre 2000 / Accepted: 24 Septembre 2001

J. Sterpenich
Centre de Recherches Pétrographiques et Géochimiques – CNRS,
15 rue Notre Dame des Pauvres, BP 20,
54501 Vandoeuvre-lès-Nancy, France
e-mail: jerome@crpg.cnrs-nancy.fr
Tel.: +3-83-594244
Fax: +3-83-511798

DOI 10.1007/s10064-001-0150-1

microcracks do not trap significant amounts of toxic elements. In contrast, stained glasses altered in the soil have a thick altered layer (up to more than 1.5 mm) comprised of a hydrated silica-gel and a hydroxyapatite-like phase [$Ca_5OH(PO_4)_3$]. A third phase precipitates in the altered layer close to the free surface of the glass or in the rare microcracks. It is a phase rich in manganese, probably in the form of manganite (γ-MnOOH) or hausmannite (Mn_3O_4).

The dissolution rates of elements are strongly influenced by the mineralogy of the altered layer. The partition coefficients were determined for several polluting elements for potassic buried stained glasses. Transition elements and heavy metals are strongly partitioned into the manganese-bearing phase. Lead, arsenic and zinc are also present in the phosphate phase. Hydrated silica-gel, consisting of around 80 wt% SiO_2 (from an anhydrous composition) principally traps aluminium, iron and sometimes a proportion of copper, zinc and lead.

In summary, the study of medieval stained glasses shows that the dissolution of calcium- and alkali-bearing silicate glasses is incongruent and the altered layer has a protective capacity which depends on the alteration conditions (secondary phases trapping pollutants, cracking phenomena, thickness of altered layer limiting the diffusion of leached species). The mineralogy of altered layers is also of prime interest for the long-term behaviour of vitrified wastes, as even if the glass alters, secondary phases can trap most of the potentially toxic elements.

This study also shows that particular attention must be paid to the choice of glass composition, in particular for vitrified waste formulation. For example, the presence of phosphorus in fresh glass favours the precipitation of secondary minerals which retain polluting elements in the matrix.

Mots clés Altération · Vitraux · Cristallochimie · Déchets · Vitrification · Durabilité

Keywords Alteration · Stained-glass windows · Crystal chemistry · Wastes · Vitrification · Durability

Introduction

Un des problèmes majeurs de la société actuelle réside dans le retraitement des déchets ultimes issus des activités ménagère, industrielle et nucléaire. Ces déchets contiennent en effet des quantités importantes d'éléments toxiques pour notre environnement, et doivent à ce titre subir des opérations de retraitement destinées à les stabiliser. Parmi les différents procédés de stabilisation et de solidification technologiquement réalisables, la vitrification est certainement l'une des techniques les plus efficaces. Néanmoins, l'utilisation des verres silicatés comme matrice de confinement des déchets ultimes pose le problème du comportement à long terme de ces verres de stockage, de la mise en solution et de la dispersion éventuelle des éléments polluants. Bien que de nombreuses expériences de lixiviation aient été menées en laboratoire, connaître le comportement de ces déchets vitrifiés sur des périodes de 100 à 10.000 ans demeure encore problématique. Un précédent travail (Sterpenich et Libourel 2001) a montré que les vitraux médiévaux permettent d'appréhender l'altération de verres en milieu naturel et ainsi de contribuer à la meilleure connaissance du comportement à long terme des verres de stabilisation. Cette étude a en effet permis d'étudier l'influence des conditions d'altération et de la composition des verres sur leur dissolution, et de déterminer les vitesses moyennes de dissolution des éléments toxiques confinés dans le verre, et ce, sur une période de près d'un millénaire. Cependant la pellicule d'altération des vitraux médiévaux est chimiquement et minéralogiquement complexe. Une seconde étape essentielle consiste donc à déterminer la cristallochimie des éléments polluants afin de déterminer la stabilité à long terme des phases porteuses, et de ce fait de s'assurer de la pérennité du piégeage des éléments potentiellement toxiques. Ainsi, ce travail propose d'identifier les phases minérales issues de l'altération des vitraux soumis aux agents atmosphériques ou enfouis dans le sol, et de caractériser les phases porteuses des éléments, et notamment des polluants, pour, à terme, déterminer leurs coefficients de partage.

Description des échantillons

Pour comprendre le comportement à long terme des verres silicatés, des vitraux datant du 9ème au 14ème siècle et soumis à différentes conditions naturelles d'altération ont été étudiés. Une description détaillée a été réalisée par Sterpenich et Libourel (2001). Il s'agit de douze échantillons provenant des verrières de la cathédrale St Gatien de Tours, de la cathédrale d'Evreux (France), de la cathédrale Ste Opportune du Bosc de Meissen et de l'église Ste Catherine d'Oppenheim (Allemagne). Datés du 13ème au 14ème siècle, ces échantillons ont été obtenus dans le cadre du Programme Franco-Allemand de Recherche pour la Conservation des Monuments Historiques.
Treize échantillons supplémentaires exhumés lors de fouilles sur les sites archéologiques de l'Abbaye St Victor de Marseille, Notre Dame du Bourg de Digne et du Palais Episcopal de Rouen, nous ont été aimablement fournis par Mme Danièle Foy du Laboratoire d'Archéologie Médiévale de Marseille, et par M. Jacques Le Maho du Centre de Recherche en Archéologie

Médiévale de Caen. L'enfouissement de ces verres, dû à des destructions accidentelles des verrières (feux, guerres, etc.), a été daté, par l'étude du contexte historique et archéologique, entre le $9^{\text{ème}}$ et le $13^{\text{ème}}$ siècle (Foy 1989; Le Maho 1994).

Tous les échantillons sont des morceaux de verre coloré de quelques cm^2 de surface, de 2 à 5 mm d'épaisseur et plus ou moins opacifiés par la présence de produits d'altération. Malgré la présence de ces produits de corrosion, les peintures vitrifiées ou les grisailles servant à exprimer les reliefs et dessiner les formes, sont encore visibles sur certains échantillons, attestant de la préservation de la surface initiale du verre.

Techniques analytiques

Des analyses en roche totale ont été réalisées, pour les vitraux archéologiques, sur le verre sain et la pellicule d'altération. Cette dernière a été séparée mécaniquement du verre sain et triée sous loupe binoculaire afin de s'affranchir d'une éventuelle pollution par le verre sain et le sol. Les éléments majeurs ont été analysés par ICP-AES (induced coupled plasma-absorption emission spectrometry) tandis que les éléments en traces l'ont été par ICP-MS (induced coupled plasma-mass spectrometry). Les échantillons ont été préparés et analysés en accord avec la méthode décrite par Govindaraju et Mevelle (1987).

Les analyses in situ et l'observation des vitraux ont été réalisées à partir de sections polies indurées dans de la résine de type araldite. Les sections sont métallisées au carbone avant observation au microscope electronique à balayage (MEB) et analyse à la microsonde électronique. Les conditions analytiques de la microsonde électronique CAMECA SX50 (Université Nancy 1) pour cette étude sont les suivantes: tension d'accélération 15 kV, intensité 20 nA, faisceau défocalisé à 5 μm. Pour les éléments en traces, les analyses in situ ont été réalisées par microsonde ionique CAMECA IMS-3f (CRPG Nancy) après métallisation à l'or des sections polies. Les conditions analytiques sont les suivantes: faisceau d'oxygène négatif, primaire de 2 à 5 nA, tension d'accélération: 10 kV, diamètre du faisceau primaire ≈5 μm, filtrage en énergie –60 V, résolution de masse $\Delta M/M$=1.000.

Certaines observations et analyses à l'échelle micrométrique, ainsi que la détermination de la cristallinité des phases, ont été réalisées par microscopie electronique à transmission (MET). Les échantillons ont été préparés soit par ultra-microtomie, soit par amincissement ionique afin de garder l'information spatiale. Les MET utilisés sont du type Philips CM20 (Université Nancy 1) ou CM30 (Université Lille 1) et sont tous deux équipés de spectromètres à dispersion d'énergie (EDS). Le CM20 a permis d'effectuer de la perte d'énergie des électrons (EELS) pour déterminer la valence du manganèse, tandis que le CM30 a été utilisé principalement pour réaliser des profils chimiques à l'échelle micrométrique.

Résultats

Composition du verre sain

Au Moyen-Age, les verres de vitraux étaient confectionnés en portant à fusion un mélange de "terre vitrifiable" (sable siliceux) et de fondant. Les fondants utilisés à cette époque étaient soit d'origine minérale (natron: carbonate de sodium hydraté) ou étaient issus de cendres de plantes (fougère ou hêtre). La coloration était obtenue par ajout lors de la fusion, de faibles quantités d'oxydes d'éléments de transition (Co pour le bleu, Mn pour le violet, Cu pour le rouge ou le vert, Fe pour le brun–orange, etc.; voir Perez Y Jorba et Dallas 1984; Foy 1989; Sterpenich 1998). Ainsi, la composition chimique des verres de vitraux (Tableau 1) était principalement siliceuse ($43 < SiO_2 < 70$ pds%), calcique ($8 < CaO < 29$ pds%), et, selon le fondant utilisé en fonction des régions et des périodes, sodique (jusqu'à 16 pds% Na_2O), ou potassique (jusqu'à 16 pds% K_2O). Les verres sodiques sont aussi plus siliceux (jusqu'à 70 pds% SiO_2), et par conséquent présentent un degré de polymérisation du réseau vitreux beaucoup plus élevé que celui de leurs homologues potassiques. En raison des impuretés présentes dans les matériaux de départ, les vitraux contiennent plus de 50 éléments différents en teneurs significatives, en particulier des concentrations importantes en éléments de transition (e.g. Cr jusqu'à 100 ppm, Ni jusqu'à 50 ppm, Co jusqu'à 350 ppm), métaux lourds (e.g. Cu jusqu'à 2,5 pds%, Zn jusqu'à 3.000 ppm, Pb jusqu'à 2.500 ppm), terres rares (e.g. La jusqu'à 50 ppm, Ce jusqu'à 70 ppm), actinides (e.g. Th jusqu'à 5 ppm) et en autres éléments toxiques (e.g. As jusqu'à 150 ppm). Il est à noter que ces éléments sont les éléments polluants contenus dans les déchets vitrifiés.

Description de l'altération des vitraux médiévaux

Morphologie et chimie des pellicules d'altération

Les vitraux médiévaux peuvent être utilisés pour décrire les effets de différentes conditions d'altération (Sterpenich et Libourel 2001): les vitraux sur verrières sont soumis à une altération météorique (faces externes des vitraux) et à une altération par les eaux de condensation dues à l'humidité de l'édifice (faces internes des vitraux), tandis que les vitraux archéologiques ont subi l'action des eaux de porosité et des acides humiques. Quel que soit le type d'altération, les échantillons étudiés présentent des traces de corrosion à leur surface. Cependant, les observations par MEB montrent que, pour une composition chimique donnée du verre, la structure et l'épaisseur des zones altérées dépend principalement du type d'altération. Pour les verres potassiques, l'altération par les eaux de condensation (faces internes des vitraux sur verrières) produit uniquement des microcratères de dissolution dispersés à la surface du verre, tandis que l'altération par les eaux météoriques (faces externes) entraîne une pellicule d'altération continue, épaisse d'environ 200 μm, et caractérisée par son homogénéité et par la présence d'un réseau de microfractures parallèles et perpendiculaires à la surface du verre (Fig. 1a). D'un point de vue chimique, la

Tableau 1
Composition chimique des verres sains. Exemple d'un échantillon bleu de Digne (*DB*) riche en potassium et pauvre en silice, et un bleu pâle de Rouen (*RBa*) riche en sodium et riche en silice. Ils représentent les deux grandes familles chimiques de vitraux médiévaux. *LD* Limite de détection; *PF* perte au feu

	DB	RBa
Majeurs (pds%)		
SiO_2	50,04	67,62
Al_2O_3	2,62	2,27
Fe_2O_3	1,14	1,12
MnO	0,9	0,53
MgO	5,26	0,87
CaO	15,55	6,41
Na_2O	0,89	18,13
K_2O	17,81	0,62
TiO_2	0,18	0,13
P_2O_5	4,23	0,16
PF	0,99	0,25
Traces (ppm)		
As	5,8	31,8
Ba	1.349	283
Be	2,6	1,5
Bi	LD	0,3
Ce	44,5	13
Co	342	306
Cr	23,6	11,9
Cs	1,5	LD
Cu	1.285	1.726
Dy	1,6	1,0
Er	0,79	0,6
Eu	0,53	0,4
Ga	4,1	4,1
Gd	1,9	1,0
Hf	2,4	1,7
Ho	0,34	0,2
La	34	7,3
Lu	0,1	0,1
Mo	LD	3,7
Nb	3,8	1,8
Nd	17,2	5,3
Ni	44,4	33,7
Pb	533	2.145
Pr	5,0	1,5
Rb	222	10,8
Sb	82,5	7.464
Sm	2,7	1,4
Sn	49,5	189
Sr	427	424
Ta	0,37	0,2
Tb	0,26	0,2
Th	2,8	1,7
Tm	0,09	0,1
U	0,94	1,0
V	16,9	14,9
W	0,7	1,0
Y	9,55	6,4
Yb	0,87	0,6
Zn	1.210	64,3
Zr	96,5	63,2

pellicule d'altération consiste principalement en un gel de silice hydraté, appauvri en éléments modificateurs de réseau (alcalins et alcalino-terreux). Les fractures parallèles à la surface du verre sont généralement remplies de produits précipités responsables pour partie de l'opacification des vitraux (Perez Y Jorba et al. 1984, 1993; Libourel et al. 1994; Barbey et al. 1996). Il est à noter que l'on retrouve ces précipités également sur la surface des vitraux et que leur nature est variable selon les sites d'échantillonnage (Fig. 2). Les fractures perpendiculaires à la surface, quant à elles, sont le plus souvent dépourvues de produits précipités.

Les vitraux enfouis dans le sol présentent un pellicule d'altération beaucoup plus importante pouvant atteindre 1.500 µm. Elle est dépourvue de fracturation et montre une "lamination" caractéristique constituée d'une alternance de fins feuillets micrométriques correspondant à l'alternance de deux phases de composition chimique différente (Fig. 1c, d). Quelle que soit la composition du verre de départ (sodique ou potassique), la pellicule d'altération est constituée principalement d'un gel de silice hydraté appauvri en alcalins et alcalino-terreux mais présentant cependant des fluctuations en calcium et en phosphore. Ces caractéristiques, typiques d'une altération dans le sol, ont été observées sur les verres de nombreux sites archéologiques (Newton 1971; Gillies et Cox 1988; Macquet et Thomassin 1992; Sterpenich 1998). A l'intérieur de la pellicule d'altération et à proximité de la surface libre du verre ou près des rares microfractures précipitent des phases riches en métaux de transition et métaux lourds et notamment en manganèse (Fig. 1b, c).

Influence de la composition du verre

Pour des conditions semblables d'altération, il a été montré que les cinétiques d'altération dépendent fortement de la composition chimique du verre (Sterpenich et Libourel 2001). Pour le site archéologique de Rouen ($9^{ème}$ siècle) par exemple, l'épaisseur moyenne de la zone altérée des verres sodiques (et riches en silice) est de 35 à 40 µm, tandis qu'elle peut excéder 1 mm pour les verres potassiques (et pauvres en silice). De la même façon, les verres potassiques altérés sur verrières développent une pellicule d'altération responsable de leur opacification alors que leurs homologues sodiques ont préservé leur couleur grâce à une pellicule d'altération très peu épaisse (<2 µm). Les vitraux sodiques de la Cathédrale de Chartres ($13^{ème}$ siècle), dont l'état de préservation est remarquable, en sont un bon exemple.

Minéralogie des pellicules d'altération des vitraux sur verrières

Phases présentes à la surface des vitraux

La caractérisation des différentes phases présentes à la surface des vitraux altérés par les eaux météoriques a été effectuée par spectrométrie de dispersion d'énergie (EDS) au MEB, ainsi que par diffraction des rayons X. Les deux principales phases rencontrées sont le gypse ($CaSO_4$–$2H_2O$; Fig. 2a, c) qui présente une structure en feuillets, et la calcite ($CaCO_3$; Fig. 2b). Ces cristaux sont en partie responsables de l'opacification des vitraux. Il est à noter que gypse et calcite ont été observés sur les verres de Tours alors que ceux d'Oppenheim ne présentent que de la calcite. Les observations réalisées sur les verres de Tours sont

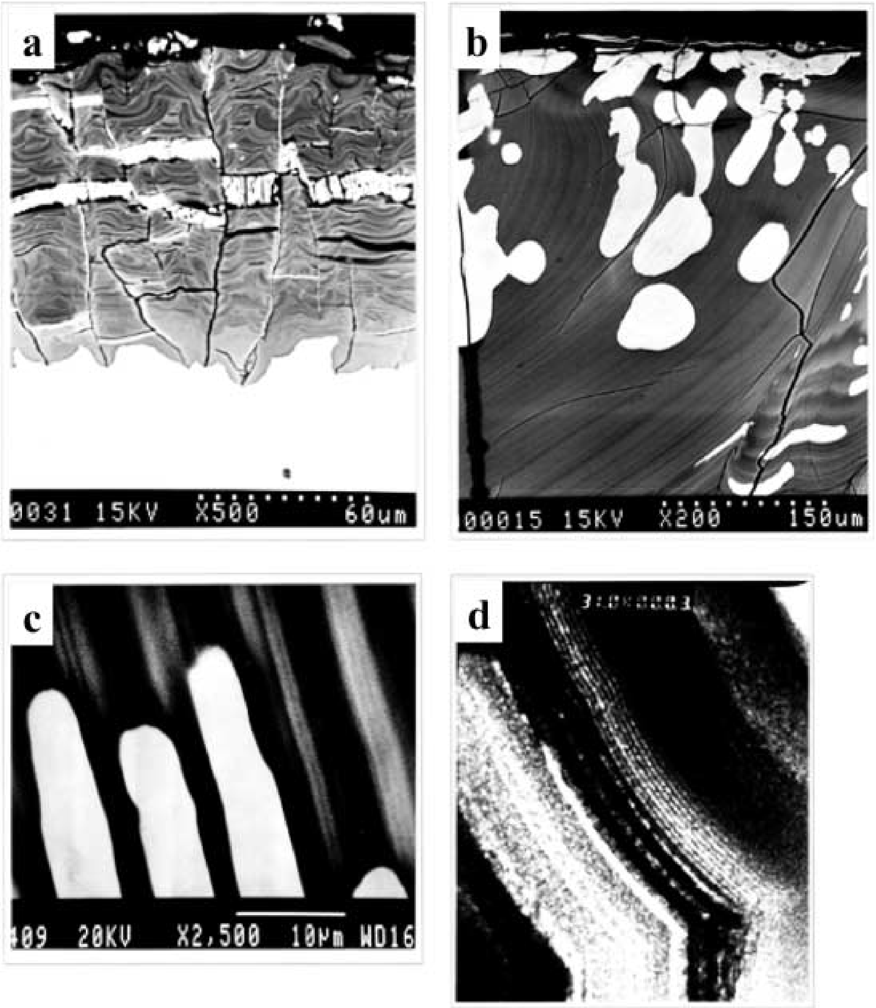

Fig. 1a–d
Vue en section de l'altération de vitraux altérés sur verrières ou dans le sol. **a** Vue en section de l'altération d'un verre orange de Tours (To6). Face externe du vitrail soumise aux agents atmosphériques. Le verre sain apparaît en blanc au bas du cliché, la pellicule d'altération est grise. Noter la présence de deux réseaux de microfractures: le premier, parallèle à la surface, est très ouvert et contient des produits précipités de type gypse ou calcite. Le second, perpendiculaire à la surface, est quasiment dépourvu de matière. Cliché MEB en électrons rétrodiffusés au grossissement 500. **b** Vue en section de l'altération à proximité de la surface. Verre archéologique potassique bleu de Digne (DB). Noter la présence de phases claires enrichies en manganèse et s'organisant de façon concentrique. Cliché MEB en électrons rétrodiffusés au grossissement 200. **c** Vue en section de l'altération d'un verre archéologique potassique bleu de Digne (DB). Les lamines claires sont elles-mêmes constituées d'une succession de lamines de taille inférieure. Noter la configuration des phases lourdes enrichies en manganèse qui croissent à l'intérieur des lamines sombres constituées essentiellement de silice hydratée. Cliché MEB en électrons rétrodiffusés au grossissement 2.500. **d** Vue de la structure de la pellicule d'altération d'un verre archéologique potassique vert de Digne (DV). Echantillon aminci ioniquement. La coupe a été réalisée à proximité de la surface du verre, donc loin du verre sain (≈1 mm), expliquant pourquoi ce dernier n'est pas visible sur le cliché. Noter la présence de lamines de rythmicités différentes. Cliché MET au grossissement 31.000 (1 cm ≈ 0,3 µm)

en accord avec celles de Perez Y Jorba et al. (1993). Les échantillons de Meissen ont révélé la présence de gypse et de syngénite [$K_2Ca(SO_4)_2$–H_2O; Fig. 2d].

La présence d'autres produits précipités, en quantités toutefois moins importantes, peut également être mise en évidence. Ce sont par exemple l'anglésite ($PbSO_4$), la palmiérite [$K_2Pb(SO_4)_2$], des oxalates de calcium, des phosphates de plomb (Perez Y Jorba et al. 1993) ou des sulfates de baryum (Barbey et al. 1996).

Vue en section de la pellicule d'altération

La pellicule d'altération est caractérisée par la présence d'un gel de silice fortement hydraté et recoupé d'un réseau de microfractures parallèles et perpendiculaires à la surface libre du verre. Comme cela a déjà été montré (Sterpenich et Libourel 2001), le gel de silice hydraté est très appauvri en éléments alcalins et alcalino-terreux et très enrichi en eau. Les quantités d'eau mesurées varient de 14 à plus de 20 pds% H_2O; 37 à 45% du total de cette eau est sous forme d'eau de structure (comme le montre une mesure par méthode Karl Fischer; voir Sterpenich 1998), la majorité étant par conséquent de l'eau de porosité. La composition moyenne du gel pour les échantillons de Tours, Oppenheim et Meissen est résumée dans le Tableau 2. Il présente de plus des microstructures visibles en électrons rétrodiffusés et qui correspondent à une zonation chimique. Cette microzonation est à rapprocher de la lamination observée sur les vitraux archéologiques. En

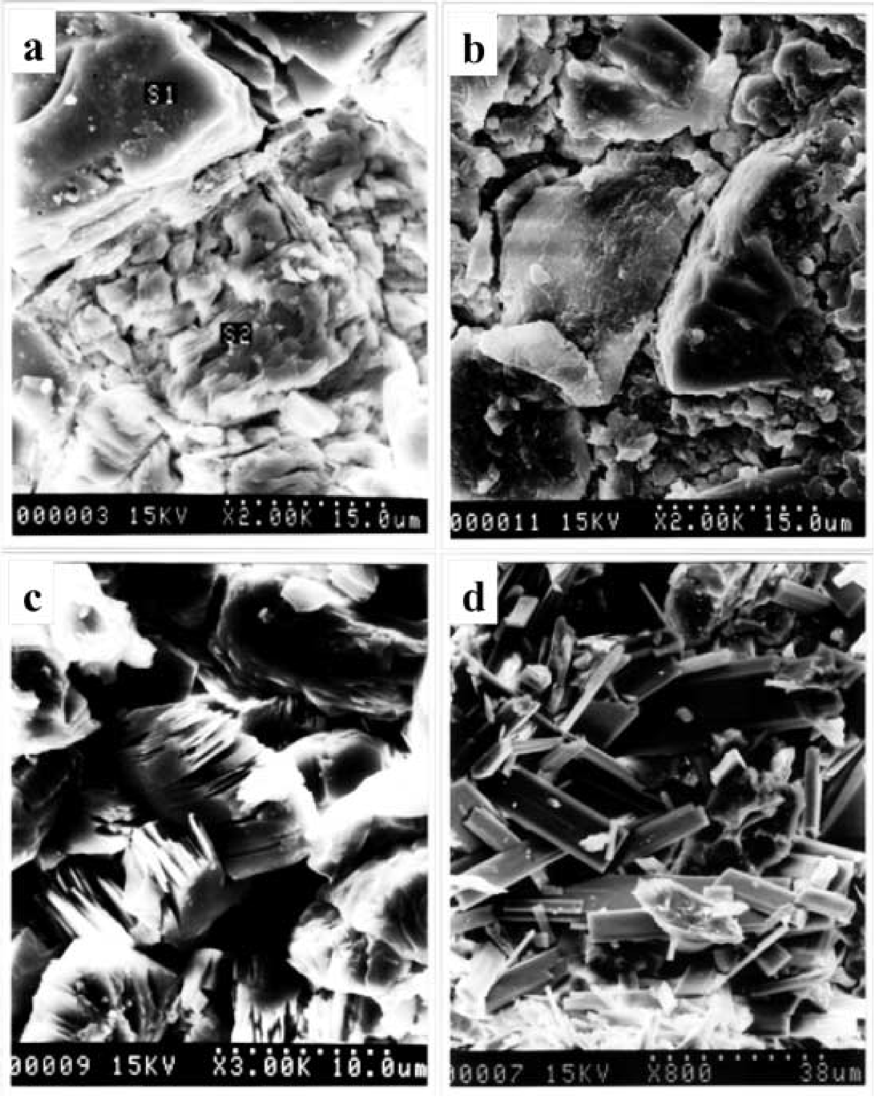

Fig. 2a–d
Vue au MEB en électrons secondaires des produits précipités à la surface des vitraux altérés sur verrières. **a** Verre orange de Tours (To6). *S1* Gel de silice hydratée; *S2* cristaux de gypse. **b** Cristaux de calcite sur le verre bleu d'Oppenheim (Op3). **c** Cristaux de gypse en détail sur le verre orange de Tours (To6). **d** Cristaux de syngénite sur le verre vert de Meissen (Me)

outre, la sonde électronique a permis de déterminer la nature des phases présentes à l'intérieur des fractures. Ces produits, beaucoup plus abondants dans les fractures parallèles que dans les fractures perpendiculaires à la surface, correspondent à des cristaux de gypse, de calcite et parfois de syngénite. Il est également possible de rencontrer de rares cristaux de phosphates de calcium hydratés de type hydroxyapatite (Tours). Il est à noter également que les fractures présentes dans le verre de Meissen contiennent des précipités de sulfates de calcium riches en baryum.

En résumé, la pellicule d'altération des vitraux altérés sur verrières est constituée principalement d'un gel hydraté riche en silice ainsi que de produits néoformés de type sulfates ou carbonates précipités à la surface ou à l'intérieur du réseau de microfractures de la pellicule. Ces sulfates et carbonates sont vraisemblablement issus de la rencontre des espèces dissoutes dans la solution altérante (gaz carbonique et dioxyde de soufre) avec les espèces lixiviées du verre, i.e. principalement calcium et potassium.

Minéralogie des pellicules d'altération des vitraux archéologiques altérés dans le sol

Caractérisation chimique à l'échelle micrométrique

L'observation au MEB et au MET (Fig. 1b–d) a montré que la pellicule d'altération des vitraux archéologiques était constituée d'une alternance de phases de composition chimique différente responsable de la lamination. Une cartographie d'émission X réalisée à la sonde électronique sur l'échantillon vert de Digne (DV) permet d'identifier chimiquement ces phases. La Fig. 3 montre clairement que l'alternance de feuillets sombres et clairs correspond à l'alternance de phases riches en calcium et phosphore et de phases riches en silicium et aluminium. Ces anti-corrélations entre Ca et P d'une part et Si et Al d'autre part ont également été mises en évidence à l'échelle sub-millimétrique grâce à la sonde électronique (Sterpenich 1998). Ces images de photons X révèlent également un troisième type de phase, à proximité de la surface, très riche en manganèse. L'observation au MET de la partie altérée de l'échantillon DV révèle que ces phases riches en man-

Tableau 2
Composition chimique du gel de silice hydraté analysé à la microsonde électronique sur cinq verres de Tours (*To*), deux verres d'Oppenheim (*Op*) et un verre de Meissen

Majeurs (pds%)	To1	To3	To4	To5	To6	Op3	Op4	Meissen
SiO_2	86,1	80,5	84,5	80,8	75,7	73,5	75,8	76,9
Al_2O_3	0,8	2,1	2,2	2,1	1,9	2,1	3,1	1,6
Fe_2O_3	0,5	1,4	0,8	0,8	0,9	1,4	0,7	1,7
MnO	0,1	0,3	0,2	0,3	0,4	1,6	0,3	0,4
MgO	0,5	1,3	0,7	1,4	1,1	1,9	0,6	1,5
CaO	0,6	0,8	0,5	0,6	0,7	3,7	0,5	1,4
Na_2O	0,0	0,0	0,0	0,0	0,1	0,4	0,1	0,1
K_2O	0,3	0,5	0,4	0,3	0,5	0,9	1,1	1,5
TiO_2	0,1	0,3	0,3	0,3	0,2	0,1	0,1	0,0
P_2O_5	1,0	3,2	1,8	2,7	3,4	2,0	0,9	1,7
Total	89,9	90,3	91,4	89,3	84,9	87,4	83,4	86,9

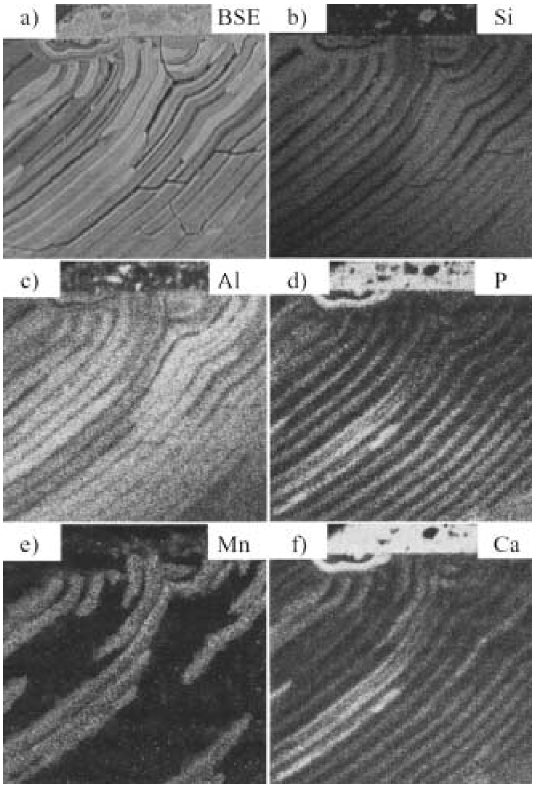

Fig. 3a–f
Cartographie d'émission X réalisée à la sonde électronique par balayage faisceau sur un verre archéologique bleu de Digne (DB). La surface du verre est située sur le haut du cliché. **a** Image en électrons rétrodiffusés; **b** image du silicium; **c** image de l'aluminium (corrélé à Si); **d** image du phosphore (anti-corrélé à Si); **e** image du manganèse concentré dans les zones lourdes; **f** image du calcium (corrélé à P). Noter la présence de grisailles à la surface du verre matérialisant la surface originelle du vitrail

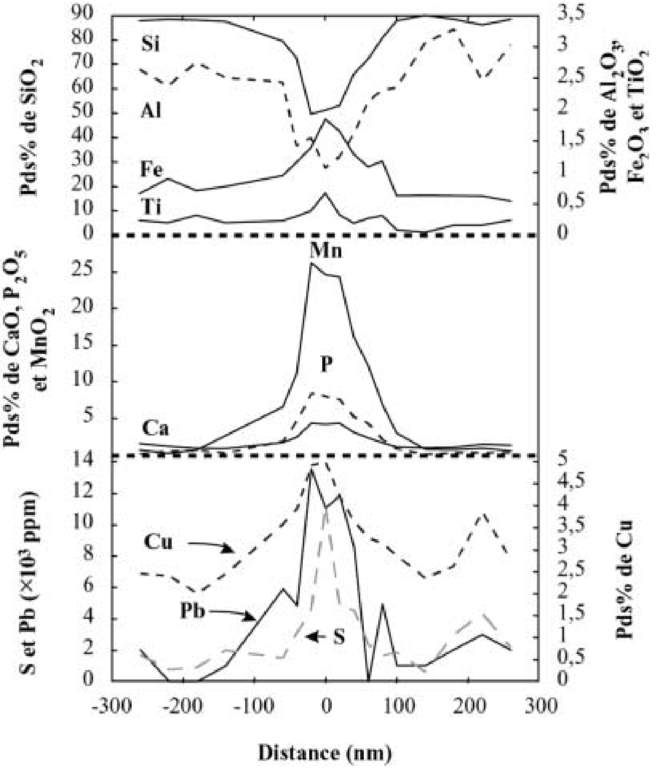

Fig. 4
Profils chimiques réalisés au MET analytique perpendiculairement à la lamination (Fig. 1d). Comportement des éléments majeurs Si, Al, Fe, Ti, Mn, Ca et P, des éléments en traces Cu et Pb et du soufre. Echantillon archéologique DV de Digne

ganèse sont organisées sous forme de lamines ou de petits nodules. Afin de caractériser ces phases, des profils par MET analytique ont été réalisés. La Fig. 4 montre le comportement de plusieurs éléments à proximité et à l'intérieur de l'une de ces lamines sombres. Il est à noter que cette lamine très enrichie en manganèse est centrée sur zéro, et que l'échelle des abscisses est exprimée en nanomètres. Sur ce profil réalisé dans une zone altérée située à proximité de la surface libre de l'échantillon, le comportement des éléments formateurs de réseau tels que Si, Al, Ti et Fe est différent de celui décrit dans le gel. En effet, silicium et aluminium sont corrélés et s'appauvrissent à l'intérieur du feuillet sombre, alors que fer et titane s'y enrichissent, montrant une bonne corrélation avec le manganèse. Les feuillets, ou lamines, observés au MET à proximité de la surface libre du verre, correspondent donc à une succession de phases riches en silice et de phases enrichies en manganèse dans lesquelles on retrouve également des quantités importantes de calcium et de phosphore. Cette phase de manganèse concentre d'autres éléments et en particulier des éléments de transition (Fe et Ti) et des métaux lourds (Cu et Pb). Leurs teneurs peuvent atteindre plusieurs milliers de ppm à quelques pour-cent, avec par exemple des teneurs proches de 5 pds% pour le cuivre. Les teneurs en soufre sont également importantes avec des concentrations pouvant atteindre 1,2 pds%.

Minéralogie des pellicules d'altération des vitraux archéologiques

L'analyse par diffraction des rayons X et des électrons (MET) de la pellicule d'altération des vitraux enfouis a montré que les phases présentes n'étaient que très peu ou pas du tout cristallisées. Par ailleurs, la cartographie d'émission X réalisée à la sonde (Fig. 3) et l'étude par MET (Fig. 4) ont révélé l'existence de trois phases principales: l'une riche en silicium, la deuxième en calcium et phosphore et la troisième en manganèse.

Les analyses effectuées sur les pellicules d'altération des différents échantillons étudiés ont été reportées dans des graphiques Ca/P et Si/P (Fig. 5). La Fig. 5a représente les concentrations atomiques de calcium en fonction du phosphore mesurées dans la pellicule d'altération des échantillons de Digne DV, DR et DB. Il apparaît très nettement que Ca et P sont corrélés positivement, et que le rapport Ca/P est constant quel que soit l'échantillon. Si on reporte les concentrations atomiques du silicium en fonction du phosphore pour les mêmes échantillons (Fig. 5b), on s'aperçoit que ces deux éléments sont parfaitement anti-corrélés. La pellicule d'altération consiste donc en un mélange mécanique de deux phases: une phase riche en silice et une phase riche en calcium et phosphore. Le rapport Ca/P calculé à l'aide de ces données est d'environ 1,8, proche de la stoechiométrie d'une hydroxyapatite [$Ca_5(PO_4)_3OH$].

Afin de confirmer les observations effectuées sur les verres de Digne, un traitement similaire des analyses effectuées sur les échantillons potassiques de Rouen et Marseille a été réalisé. Les rapports Ca/P calculés pour ces sites varient de 1 (Rouen) à 1,3 (Marseille), valeurs inférieures à celle calculée pour Digne. Cette différence de stoechiométrie peut être attribuée à diverses causes. Les variations de Ca et P à travers la pellicule d'altération ne sont pas très importantes (5% pour Ca et 3% pour P). La régression linéaire s'effectue alors sur un nuage de points plus dispersé, induisant une plus grande incertitude quant à la détermination de sa pente ($r^2 \ll 1$). Il est également possible que la nature des phosphates présents dans les échantillons de Digne soit différente de celle de Rouen ou Marseille. Ceci peut être appuyé par le fait que les échantillons de Rouen sont moins riches en phosphore que ceux de Digne. En ce qui concerne les échantillons de Marseille, leurs teneurs en phosphore sont équivalentes à celles mesurées dans les échantillons de Digne. Les dissemblances observées entre ces deux sites pourraient alors s'expliquer par des conditions d'altération différentes, comme en témoignent par ailleurs les compositions très variables des pellicules d'altération (Sterpenich 1998).

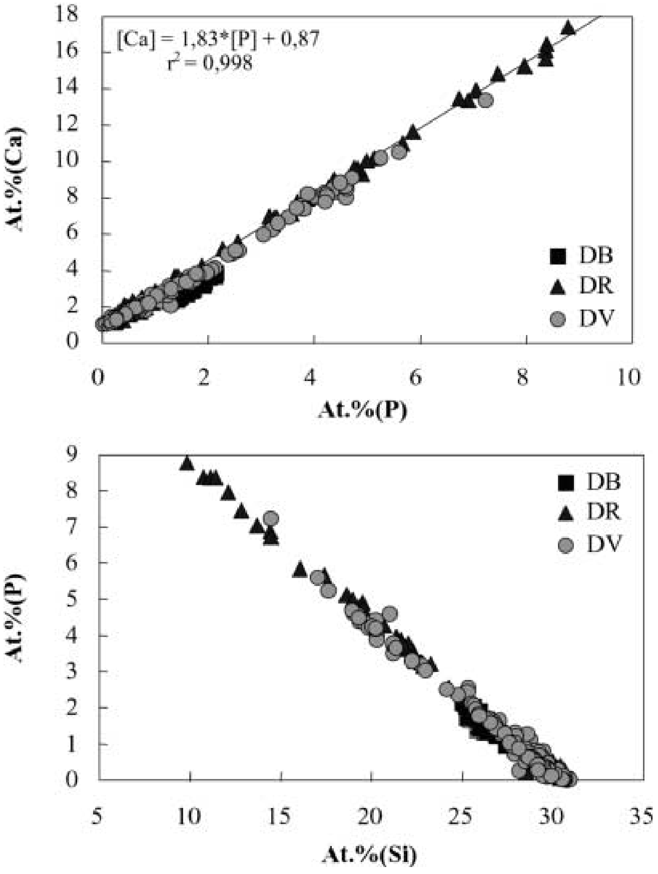

Fig. 5
a Corrélation calcium-phosphore et **b** corrélation phosphore-silicium dans les échantillons de DB, DV et DR de Digne. Concentrations en pourcentages atomiques

Enfin, ces différences peuvent être attribuées à des variations de cristallinité. En effet, les cinétiques de cristallisation peuvent être variables en fonction des conditions d'altération, impliquant des stoechiométries de phosphates de calcium différentes. Ces résultats sont en accord avec ceux de Cox et Ford (1993) qui ont également mis en évidence la présence de phosphates de calcium dont les rapports Ca/P varient de 1 à 1,7 dans les pellicules d'altération de vitraux archéologiques. Les phases annoncées par ces auteurs sont l'hydoxyapatite $Ca_5(PO_4)_3OH$, un phosphate d'octa-calcium $Ca_8H_2(PO_4)_6$–$5H_2O$ et la brushite $CaHPO_4$–$2H_2O$.

Malgré les disparités observées, il apparaît que la pellicule d'altération de tous les échantillons potassiques étudiés est constituée en partie de phosphates de calcium dont la forme la plus fréquente serait l'hydroxyapaptite, et d'un gel de silice hydraté. Les verres sodiques, beaucoup moins riches en phosphore que les verres potassiques, présentent une couche d'altération également constituée d'une alternance de feuillets. Lorsque l'on reporte les concentrations atomiques de calcium et de silicium en fonction du phosphore, on remarque également une corrélation positive entre Ca et P, liée à une anti-corrélation entre Si et P. De façon analogue aux verres potassiques, la pellicule d'altération des verres sodiques semble donc également constituée d'un mélange de gel de silice hydraté et de phosphate de calcium. Le faible rapport Ca/P (0,64) peut être attribué aux mêmes causes que celles invoquées précédemment pour les échantillons potassiques de Rouen et Marseille.

A proximité de la surface ou des quelques rares microfractures, des zones riches en éléments lourds ont été observées. L'analyse de ces zones, présentes sur la plupart des échantillons, met en évidence des concentrations élevées en manganèse. De plus, les observations réalisées au MEB ont montré que le développement de ces zones lourdes était postérieur à la lamination. Ces analyses peuvent donc être traitées en considérant que ces phases correspondent à un mélange ternaire constitué d'un phosphate de calcium et d'un gel de silice formant les lamines et d'une troisième phase dont le constituant majeur est le manganèse. Le Tableau 3 présente la composition chimique déterminée à la sonde électronique de ces zones riches en manganèse dans les échantillons DB, DV et DR de Digne, ainsi que RId, RV et RVF de Rouen. Ces analyses, pourtant effectuées sur des échantillons provenant de deux sites différents, sont relativement constantes. Il est intéressant de noter ici que, en plus de contenir des quantités importantes de manganèse, ces zones sont très enrichies en éléments de transition (Co, Ni), en métaux (Pb, Cu, Zn, Sn), ainsi qu'en baryum. Cox et Ford (1993) décrivent également ces zones de manganèse qu'ils nomment "intruded materials". Ils considèrent que le manganèse constituant ces phases est issu d'un apport extérieur, et ne provient donc qu'en très petite quantité de la lixiviation du verre. Dans notre cas cependant, les éléments initialement présents dans le verre sain apparaissent au sein de ces phases. Ainsi, le cobalt plus abondant dans l'échantillon DB que dans les autres échantillons, est présent en quantités significatives (8.400 ppm) dans les zones riches en manganèse de ce verre, contrairement aux échantillons DV et DR. Ce type de comportement est également observable pour d'autres éléments. Il prouve que, bien qu'il existe une contribution du milieu extérieur, les éléments retenus dans la couche d'altération proviennent également de la lixiviation du verre.

Les analyses présentées dans le Tableau 3 montrent que le manganèse est le plus probablement sous forme d'oxyde. Cependant la caractérisation exacte de cet oxyde de manganèse est rendue difficile du fait de la quantité importante de matériaux amorphes et de particules de très petites tailles. La détermination du degré d'oxydation de Mn est toutefois possible par spectroscopie de perte d'énergie (EELS) au MET. Un essai a été réalisé sur les échantillons DB et DV dans les parties riches en manganèse. La perte d'énergie correspondant à la transition M2,3 du manganèse a été mesurée dans plusieurs régions de la pellicule d'altération. Les données obtenues varient de 53,2 à 53,4 eV (Sterpenich 1998) et correspondraient à une valence moyenne de Mn comprise entre 2,8 et 2,9 (Mansot et al. 1994). Cette valence, proche de 3, pourrait correspondre à différents oxydes tels que la manganite γ-MnOOH ou l'hausmannite Mn_3O_4, qui sont des minéraux fréquemment rencontrés dans les milieux réducteurs et basiques tels que les sols (Wedepohl 1978). Cette hypothèse est appuyée par le fait que les concentrations importantes en Co, Cu, Ni, Ba, Pb et Zn mesurées dans les zones riches en manganèse sont également caractéristiques de ce type de minéraux.

Trois phases principales ont été mises en évidence à l'intérieur de la pellicule d'altération de chaque échantillon étudié. Ces phases, en proportions variables selon les échantillons, sont vraisemblablement:

1. Un phosphate de calcium sous la forme hydoxyapatite $Ca_5(PO_4)_3OH$ et/ou phosphate d'octa-calcium $Ca_8H_2(PO_4)_6$–$5H_2O$ et/ou brushite $CaHPO_4$–$2H_2O$.

Tableau 3
Composition chimique des phases lourdes observées à proximité de la surface ou des fractures dans les échantillons de Digne (*DB*, *DV* et *DR*) et Rouen (*RId*, *RV* et *RVF*). Analyses réalisées à la sonde électronique. *LD* Limite de détection

	DB	DV	DR	RId	RV	RVF
Majeurs (pds%)						
SiO_2	42,4	23,4	38,2	41,8	37,9	18,3
Al_2O_3	3,9	2,2	2,7	3,2	2,3	3,9
Fe_2O_3	1,8	2,1	1,3	1,3	1,3	2,5
MnO_2	22,8	37,8	34,0	29,6	28,2	23,8
MgO	0,4	0,3	0,5	0,1	0,1	0,1
CaO	6,1	5,1	5,4	5,4	4,2	5,7
Na_2O	0,1	0,1	0,1	0,1	0,0	0,1
K_2O	0,3	0,4	0,4	0,5	0,3	0,5
TiO_2	0,3	1,1	0,4	0,4	0,3	0,6
P_2O_5	2,9	1,2	1,7	1,5	1,5	5,3
Traces (ppm)						
Ba	5.700	4.500	12.600	8.200	LD	1.400
Co	8.400	1.300	1.500	LD	LD	LD
Cu	7.500	55.200	19.100	2.300	70.000	114.000
Ni	1.000	LD	LD	900	LD	LD
Pb	2.200	16.500	3.400	LD	1.400	51.100
Sn	LD	1.600	1.500	LD	LD	7.200
Zn	2.300	LD	LD	2.000	LD	LD
S	LD	1.200	LD	LD	LD	LD
Total	83,7	81,8	88,5	85,1	83,2	78,1

2. Un gel de silice hydraté.
3. Un oxyde de manganèse de type manganite γ-MnOOH et/ou hausmannite Mn_3O_4.

Ces phases semblent donc caractéristiques de l'altération dans le sol de ce type de verre. Il devient alors important de déterminer la distribution des éléments considérés comme polluants à l'intérieur de chacune d'elles.

Discussion: détermination de la composition chimique des phases et des coefficients de partage des éléments

La pellicule d'altération des vitraux altérés sur verrières présente deux phases principales: un gel de silice hydraté très appauvri en la plupart des éléments hormis formateurs de réseau, et des produits précipités (sulfates ou carbonates) présents à la surface du verre et dans les fractures du gel. Il a été montré (Sterpenich 1998) que ni le gel ni les produits précipités ne retiennent de façon significative les éléments potentiellement polluants (métaux lourds et de transition pour la plupart). Ainsi, seuls les verres archéologiques, altérés dans le sol et présentant des taux de rétention importants des éléments polluants, seront décrits dans la suite de cette discussion. Il est à noter cependant que les conditions d'altération subies par les vitraux archéologiques semblent les plus proches de celles qu'auront à subir les déchets vitrifiés si on se place dans une logique de stockage en décharge ou de leur valorisation en sous-couche routière par exemple.
Les pellicules d'altération des verres archéologiques étudiés sont composées de trois phases principales (voir ci-dessus), en proportions variables selon les échantillons. Il a de plus été établi que les éléments ne se comportent pas tous de la même manière face à l'altération, en fonction d'une part de leur rôle dans le réseau silicaté, et d'autre part de leur réincorporation dans les phases néoformées. Cependant, les phases secondaires d'altération ne sont que peu ou pas cristallisées et leur petite taille ne permet pas de les individualiser et donc de mener une analyse quantitative précise. La détermination de la répartition des éléments en traces dans ces différentes phases doit, par conséquent, passer par un traitement des analyses réalisées à la sonde électronique, à la sonde ionique et par ICP-AES et ICP-MS. En considérant que chaque point d'analyse réalisé dans le verre altéré moyenne la composition de trois phases en proportions variables, on peut écrire pour chaque élément:

$$C^i_{total} = X_{Ph}.C^i_{Ph} + X_{Si}.C^i_{Si} + X_{Mn}.C^i_{Mn}$$

où:

- C^i_{total} est la concentration totale en l'élément i au point d'analyse;
- X_{Ph} est la proportion de phosphate au point d'analyse;
- C^i_{Ph} est la concentration de l'élément i dans le phosphate;
- X_{Si} est la proportion de gel de silice au point d'analyse;
- C^i_{Si} est la concentration de l'élément *i* dans le gel de silice;
- X_{Mn} est la proportion d'oxyde de manganèse au point d'analyse;
- C^i_{Mn} est la concentration de l'élément *i* dans l'oxyde de manganèse.

Fig. 6
Evolution des proportions modales des phases constituant la pellicule d'altération du verre de Digne DV. Le calcul des proportions a été effectué à partir des analyses à la sonde électronique

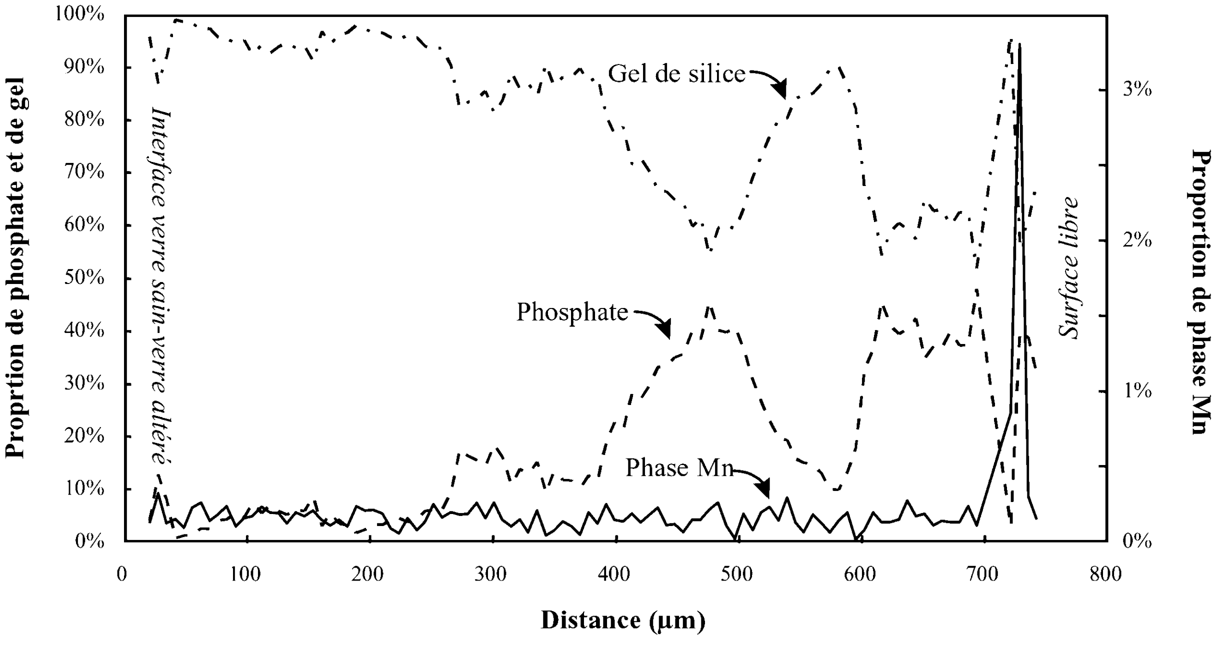

En faisant l'approximation que la proportion de chaque phase en un point d'analyse est donnée par la quantité relative des éléments les plus abondants de cette phase, à savoir Si pour le gel de silice, Ca et P pour le phosphate (rapport atomique Ca/P=1,8) et Mn pour l'oxyde de manganèse, la détermination des proportions modales en chaque point devient possible. A titre d'exemple, les proportions modales de ces phases sont visibles dans la Fig. 6. La résolution du système peut alors être effectuée par un calcul matriciel simple pour l'ensemble des éléments et des points d'analyse. Le bouclage des compositions chimiques de chaque phase renseigne sur la validité des hypothèses avancées. Le calcul a été réalisé sur les échantillons de Digne (DB, DV et DR) et Rouen (RV, RVF et RId). Le Tableau 4 résume les compositions de chaque phase calculées sur une base anhydre.

D'une manière générale et pour l'ensemble des échantillons, le gel de silice se compose principalement de Si (77,3 à 87,5%), Al (3,3 à 6,7% avec une valeur atypique à 11,7%), Fe (0,6 à 2,5%) et Ca (0,7 à 3,4%) et se trouve très appauvri en éléments alcalins et en magnésium. Les éléments en traces sont majoritairement Cu, Pb et Zn.

La phase phosphatée est assez différente d'un site à l'autre. Dans les échantillons de Digne, outre Ca et P, des quantités assez importantes d'aluminium semblent participer au phosphate (de 1,2 à 5,2%). Parmi les éléments en traces, le soufre, le cuivre, le plomb et parfois le baryum atteignent plusieurs milliers de ppm à plusieurs pour-cent. En ce qui concerne les échantillons de Rouen, la phase phosphatée contient des quantités importantes de fer (15 à 20%) et de plomb (20 à 30%). Le soufre est également présent à hauteur de quelques milliers de ppm.

L'oxyde de manganèse est, quels que soient l'échantillon et le site, la phase qui concentre le plus les métaux lourds les éléments de transition. Les teneurs en ces éléments peuvent atteindre plusieurs pour-cent selon les cas.

La Fig. 7 résume, dans un diagramme ternaire, la répartition de quelques éléments à travers ces trois phases. S'il existe des cas particuliers relatifs à chaque échantillon (réels ou liés aux approximations du mode de calcul), il est tout de même possible de dégager quelques comportements généraux. Ainsi, il apparaît que Ni, Ba, Co, Cu et, dans une moindre mesure Sn, sont principalement concentrés dans la phase de manganèse. Le zinc, bien que parfois majoritaire dans cette phase, semble principalement partagé entre le phosphate et le gel de silice. Le plomb est quant à lui partagé entre le phosphate et la phase de manganèse. Le fer, bien que participant au phosphate des échantillons de Rouen, est globalement partagé dans les trois phases. Le soufre appartient essentiellement au phosphate.

Les compositions calculées des trois principales phases formant les pellicules d'altération permettent également de calculer des coefficients de partage des différents éléments. Ces coefficients de partage sont définis par:

$$D^i_{A-B} = \frac{C^i_A}{C^i_B}$$

Tableau 4

Récapitulatif des compositions des phases principales constituant la pellicule d'altération des échantillons DV, DB et DR de Digne et RVF et RId de Rouen. Le calcul a été effectué à partir des analyses à la sonde électronique. À ce titre, les valeurs sont à considérer comme des ordres de grandeur. La mention *Tr.* signifie que l'élément est à l'état de traces. *LD* signifie que les concentrations n'ont pas pu être déterminées par sonde électronique

	DV			DB			DR			RVF			RId		
	Si gel	Phosphate	Phase Mn	Si gel	Phosphate	Phase Mn	Si gel	Phosphate	Phase Mn	Si gel	Phosphate	Phase Mn	Si gel	Phosphate	Phase Mn
Majeurs (pds%)															
SiO_2	86,8	Tr.	Tr.	85,9	Tr.	Tr.	89,1	Tr.	Tr.	77,3	Tr.	Tr.	87,5	Tr.	Tr.
Al_2O_3	3,3	2,2	2,1	6,7	5,0	Tr.	3,8	1,2	2,9	11,7	Tr.	4,6	5,9	3,6	Tr.
Fe_2O_3	1,3	0,9	2,0	2,5	3,2	Tr.	1,5	0,6	1,5	1,1	15,2	Tr.	0,6	21,1	Tr.
MnO_2	Tr.	0,1	71,9	Tr.	0,75	82,8	Tr.	Tr.	81,9	Tr.	0,7	64,5	0,7	Tr.	84,5
MgO	0,8	Tr.	3,6	0,5	1,5	Tr.	0,7	0,5	0,2	0,4	0,1	0,2	0,2	0,2	Tr.
CaO	2,4	52,7	4,7	0,9	46,5	8,8	2,7	57,1	3,2	3,4	14,1	6,0	3,4	17,2	7,4
Na_2O	0,1	0,6	0,1	0,6	0,5	Tr.	0,2	0,2	0,4	1,1	0,2	Tr.	0,2	Tr.	Tr.
K_2O	0,5	0,9	0,5	1,6	0,5	Tr.	0,4	0,1	0,9	1,7	0,3	0,1	0,7	1,0	0,2
TiO_2	0,4	0,3	1,2	0,5	0,6	Tr.	0,5	0,3	0,4	0,4	4,9	Tr.	0,3	6,3	Tr.
P_2O_5	0,2	36,7	Tr.	Tr.	38,6	Tr.	0,2	38,3	Tr.	Tr.	28,7	Tr.	0,2	30,1	Tr.
Traces (ppm)															
S	Tr.	8.100	1.000	Tr.	1.800	Tr.	Tr.	1.400	2.000	Tr.	2.800	Tr.	Tr.	2.400	Tr.
Ba	Tr.	1.000	7.200	Tr.	1.500	18.800	Tr.	Tr.	30.700	Tr.	5.700	1.300	1.100	Tr.	19.100
Co	Tr.	Tr.	2.200	0	1.800	30.700	Tr.	Tr.	2.700	LD	LD	LD	LD	LD	LD
Cu	36.700	44.800	85.800	1100	2.800	25.000	3.000	6.300	42.200	2.0008	Tr.	24.2100	Tr.	Tr.	5.500
Ni	Tr.	Tr.	1.400	Tr.	0	4.800	LD	LD	LD	LD	LD	LD	Tr.	Tr.	2.800
Pb	3.000	7.600	42.000	Tr.	3.700	3.600	1.300	4.700	5.000	Tr.	327.700	Tr.	Tr.	201.200	46.900
Sn	LD	LD	LD	LD	LD	LD	Tr.	Tr.	2.500	8.200	25.300	Tr.	LD	LD	LD
Zn	1.800	3.800	Tr.	2.400	16.100	Tr.	LD	LD	LD	LD	LD	LD	Tr.	Tr.	4.600

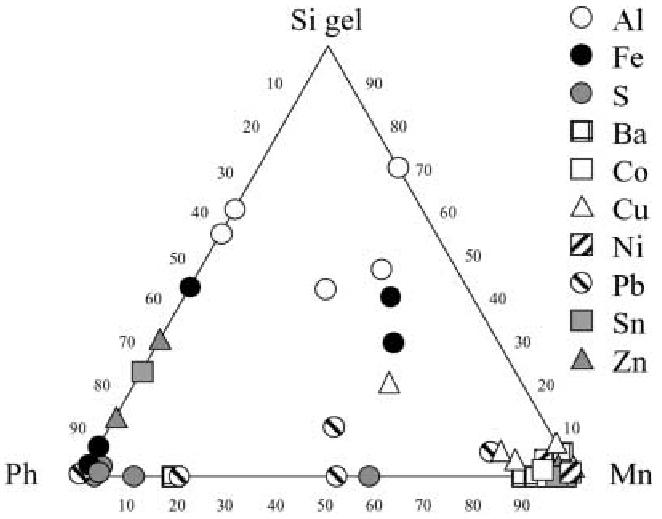

Fig. 7
Diagramme ternaire représentant la répartition de quelques éléments parmi les trois principales phases constituant la pellicule d'altération: le gel de silice (Si gel), le phosphate de calcium (Ph) et l'oxyde de manganèse (Mn). Les échantillons représentés sont DB, DV, DR, RVF et RId

où:

- D^i_{A-B} est le coefficient de partage de l'élément *i* entre la phase *A* et la phase *B*;
- C^i_A est la concentration massique de l'élément *i* dans la phase *A*;
- C^i_B est la concentration massique de l'élément *i* dans la phase *B*.

Ils sont reportés dans le Tableau 5 pour les principaux éléments en traces et pour les verres archéologiques de Digne (DV, DB et DR) et Rouen (RVF et RId). Lorsque les éléments sont entièrement partagés dans une phase, le nom de celle-ci est reporté à la place du coefficient de partage. Les observations effectuées à partir du diagramme ternaire (Fig. 7) sont quantifiées par les coefficients de partage indiqués dans ce tableau. Les valeurs élevées des coefficients de partage des éléments présentés témoignent de leur forte affinité cristallochimique pour la phase de manganèse (Ba, Co, Cu, Ni, Pb et Sn) et/ou le phosphate (S et Pb). Par conséquent, la faible mobilité de ces éléments précédemment décrite correspond en fait à leur réincorporation dans les produits précipités après leur mise en solution plutôt qu'à une réelle passivité face à la dissolution.

L'utilisation de la sonde ionique permet également de documenter le partage d'éléments à l'état de traces difficilement quantifiables à la sonde électronique. Ainsi, le coefficient de partage du carbone et de l'arsenic ont également été calculés sur le verre vert de Digne. Il apparaît sur la Fig. 8 que carbone et arsenic sont corrélés positivement avec la proportion de phosphate de la pellicule altérée. Ainsi, ces deux éléments sont fortement partagés dans la phase phosphate de calcium avec des coefficients de partage très supérieurs à 1 ($D_{As}^{Ph\text{-}Si}$ ~16 et $D_C^{Ph\text{-}Si}$ ~5). Il est à noter que les affinités élémentaires décrites sont en bon accord avec les données cristallochimiques de la littérature pour les oxydes de manganèse (Wedepohl 1978) et les phosphates de type hydroxyapatite, par le biais de substitutions simples ou couplées (Nriagu et Moore 1984; Carpena et Lacout 1997). A titre d'exemple, des substitutions du type Ca/Pb, Ca/Ba, AsO_4^{3-}/PO_4^{3-} ou SO_4^{2-}/PO_4^{3-} peuvent être observées dans les phosphates.

La validité des calculs effectués peut être en partie testée en effectuant l'opération inverse à partir des compositions chimiques des phases et de leurs proportions, et en comparant les valeurs obtenues aux compositions globales des pellicules d'altération déterminées par ICP-AES et ICP-MS. Les proportions calculées pour les verres DV et DB de Digne et RVF et RId de Rouen sont résumées dans le Tableau 6. La composition globale de la pellicule d'altération est ensuite calculée à partir de la composition chimique des trois phases et de leur fraction précédemment déterminée. Le Tableau 7 présente les compositions chimiques calculées et réelles des pellicules d'altération des échantillons DB, DV, RVF et RId. D'une manière générale, la composition calculée de la pellicule d'altération est en bon accord avec la composition réelle, aussi bien pour les éléments majeurs que pour les éléments en traces.

Outre cela, le Tableau 6 permet d'appréhender la composition minéralogique des pellicules d'altération des vitraux archéologiques potassiques. Il apparaît clairement que la phase majoritaire est le gel de silice (80 à 90%), tandis que le phosphate et l'oxyde de manganèse varient de 7,5 à 17% et de 2,5 à 4,5% respectivement. Ceci montre que la

Tableau 5
Récapitulatif des coefficients de partage mesurés entre le gel de silice (*Si*), la phase phosphatée (*Ph*) et l'oxyde de manganèse (*Mn*). Echantillons DV, DB et DR de Digne et RVF et RId de Rouen. Les mentions *Mn* ou *Ph* signifient que l'élément est entièrement partagé dans le phosphate ou l'oxyde de manganèse

Elément	DV			DB			DR			RVF			RId		
	$D_{\text{Ph-Si}}$	$D_{\text{Mn-Si}}$	$D_{\text{Mn-Ph}}$	$D_{\text{Ph-Si}}$	$D_{\text{Mn-Si}}$	$D_{\text{Mn-Ph}}$	$D_{\text{Ph-Si}}$	$D_{\text{Mn-Si}}$	$D_{\text{Mn-Ph}}$	$D_{\text{Ph-Si}}$	$D_{\text{Mn-Si}}$	$D_{\text{Mn-Ph}}$	$D_{\text{Ph-Si}}$	$D_{\text{Mn-Si}}$	$D_{\text{Mn-Ph}}$
S	–	–	0,1	Ph	Ph	Ph	–	–	1,4	Ph	Ph	Ph	Ph	Ph	Ph
Ba	–	–	7,2	–	–	12,6	Mn	Mn	Mn	–	–	0,2	–	17,4	–
Co	Mn	Mn	Mn	–	–	18,3	Mn	Mn	Mn	–	–	–	–	–	–
Cu	1,2	2,3	1,9	2,5	21,8	8,9	2,1	14,1	6,7	–	12,1	–	Mn	17,4	Mn
Ni	Mn	Mn	Mn	Mn	Mn	Mn	–	–	–	–	–	–	Mn	Mn	Mn
Pb	2,5	14,0	5,5	–	–	1	3,6	3,8	1,1	Ph	Ph	Ph	–	–	0,2
Sn	–	–	–	–	–	–	Mn	Mn	Mn	3,1	–	–	–	–	–
Zn	2,1	–	–	6,6	–	–	–	–	–	–	–	–	Mn	Mn	Mn

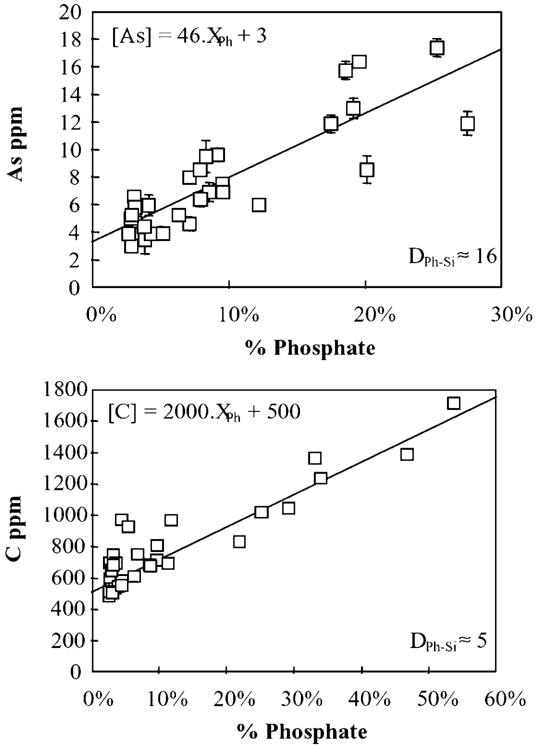

Fig. 8
Teneurs en arsenic et carbone de la pellicule altérée du verre vert de Digne (DV) en fonction de la proportion de phosphate de calcium

rétention d'un certain nombre d'éléments potentiellement polluants (e.g. As, Pb, Ni ou Zn) est assurée par des phases minoritaires.

Conclusions

Cette étude a montré que les vitraux médiévaux permettent de suivre le comportement d'un verre soumis à différentes conditions d'altération sur une période de plus d'un millénaire. En raison de leur complexité chimique, les vitraux permettent en effet de quantifier les taux de relâchement des éléments, et en particulier des polluants, contenus dans une matrice verrière silicatée. Il a été montré que les vitraux soumis à une altération par les eaux météoriques développent à leur surface une pellicule d'altération constituée principalement d'un gel de silice hydraté, appauvri la plupart du temps en éléments de transition et métaux lourds. Les produits (sulfates ou carbonates) qui précipitent à la surface ou dans les fractures du gel ne semblent pas non plus incorporer de quantités significatives d'éléments potentiellement toxiques. Au contraire, les verres altérés dans le sol présentent une pellicule d'altération d'épaisseur importante (plus de 1,5 mm pour certains) constituée d'un gel de silice hydraté et d'une phase de type hydroxyapatite [$Ca_5OH(PO_4)_3$]. Une troisième phase a également été mise en évidence à proximité de la surface libre ou des rares microfractures présentes dans la couche altérée. Il s'agit d'une phase lourde riche en manganèse de type manganite (γ-MnOOH) ou hausmannite (Mn_3O_4).

Tableau 6
Proportion (%) des phases principales constituant la pellicule d'altération des échantillons DV et DB de Digne, RVF et RId de Rouen

Phase	Si gel	Phosphate	Oxyde de Mn
DV	80,2	16,4	3,4
DB	87,0	8,6	4,4
RVF	80,1	16,6	3,3
RId	90,1	7,4	2,5

Le comportement des éléments à l'altération est fortement influencé par la minéralogie de la couche de corrosion. Le partage entre les différentes phases de certains éléments considérés comme polluants a été déterminé dans le cas des vitraux archéologiques potassiques. Il apparaît que les éléments de transition et les métaux lourds sont en concentrations importantes dans la phase de manganèse. Plomb, arsenic et zinc peuvent également être présents dans la phase phosphatée. Le gel de silice, composé d'environ 80 pds% de SiO_2 (calculé sur une base anhydre), incorpore majoritairement l'aluminium, le fer et parfois une partie du cuivre, du zinc et du plomb.

Des expériences de lixiviation sur des verres modèles [vitraux et verres de confinement de REFIOM (Résidus d'Epuration de Fumées d'Incinération d'Ordures Ménagères); Sterpenich (1998)] ont été menées parallèlement à l'études des vitraux médiévaux. Ce travail en mode statique et en milieu non agité a montré qu'une des caractéristiques des verres étudiés est la présence (1) d'un gel hydraté riche en silice et (2) d'une phase phosphatée et calcique constituant la pellicule d'altération, en accord avec les observations réalisées sur les vitraux médiévaux. La présence de ces phosphates a été décrite par de nombreux auteurs à propos de l'altération expérimentale de verres silicatés contenant des quantités plus ou moins importantes de phosphore [vitraux: Cooper et Cox (1996); verres de REFIOM: Colombel (1996); Le Forestier (1996); verres quaternaires Si–Na–Ca–P: Ehret et al. (1986); verres de confinement des déchets nucléaires: Nogues (1984); Advocat (1991); Valle (2000)]. L'ensemble de ces observations indique que les phases phosphatées sont caractéristiques des produits secondaires de l'altération de ces verres, quelle que soit leur composition chimique globale. L'ubiquité de ces phosphates est facilement compréhensible au regard de leur très faible solubilité.

Les gels de silice hydratés décrits dans la littérature sont amorphes ou très faiblement cristallisés et présentent des compositions riches en silice et très appauvries en éléments alcalins. Selon les conditions d'altération et la composition chimique du verre altéré, ils peuvent être caractérisés par des structures (densité, cohésion mécanique, etc.), des textures (cristallinité, porosité, perméabilité, etc.) et des compositions chimiques extrêmement variables (Hench et Clark 1978). De même, la nature des éléments formateurs de réseau joue un rôle important dans la formation du gel selon que le mécanisme pré-

Tableau 7
Comparaison entre la composition de la pellicule d'altération déduite de la composition des différentes phases la constituant et la composition réelle mesurée par ICP-AES et ICP-MS. Deux échantillons de Digne (DV et DB) et de Rouen (RVF et RId) sont présentés

	DV		DB		RVF		RId	
	ICP	Calculé	ICP	Calculé	ICP	Calculé	ICP	Calculé
Oxyde (%)								
SiO_2	70,6	69,6	73,4	75,8	57,0	61,9	77,0	78,8
Al_2O_3	3,7	3,1	5,2	6,3	7,8	9,5	6,0	5,6
Fe_2O_3	1,6	1,3	2,8	2,5	3,9	3,4	2,6	2,1
MnO_2	2,9	2,4	3,7	3,8	2,3	2,2	2,1	2,7
MgO	0,9	0,8	1,0	0,6	1,5	0,3	0,4	0,2
CaO	8,0	10,7	7,8	4,6	11,2	5,3	5,6	4,5
Na_2O	0,1	0,2	0,0	0,6	0,3	0,9	0,1	0,2
K_2O	0,4	0,6	1,0	1,4	1,5	1,4	0,9	0,7
TiO_2	0,5	0,4	0,4	0,5	1,0	1,1	0,7	0,7
P_2O_5	6,1	6,2	3,1	3,0	5,0	4,8	2,7	2,4
Traces (ppm)								
Ba	932	406	1.039	966	1.109	988	1.353	1.461
Co	84	74	1.288	1.498	27	0	29	0
Cu	40.893	39.676	4.264	2.306	14.842	24.015	400	135
Ni	41	47	115	209	23	0	98	69
Pb	4.645	5063	4.182	1.320	61.612	54.348	17.044	16.114
Sn	1.547	0	234	0	7.472	10765	107	0
Zn	1.733	2.068	5.148	3.372	189	0	450	113

pondérant est la précipitation après mise en solution, la recondensation ou la dissolution sélective induisant un gel résiduel. Ceci a été particulièrement bien documenté par différents travaux menés sur les verres nucléaires pour les éléments Si, Al, Fe, Zr et B (e.g. Ricol 1995; Zarembowitch-Deruelle 1997; Valle 2000). La nature de ce gel de silice est primordiale si on considère qu'il peut être protecteur, i.e. qu'il peut limiter la diffusion du silicium et donc ralentir la dissolution du verre.

Les phases manganésifères observées sur les vitraux enfouis n'ont pas été reproduites expérimentalement. Elles semblent très fortement liées aux conditions d'enfouissement (conditions rédox, activité biologique, etc.). Elles sont cependant d'un grand intérêt puisqu'il a été montré qu'elles piègent un nombre important des éléments extraits du verre sain (métaux lourds et de transition).

En conclusion, l'étude des vitraux médiévaux a révélé que la dissolution des verres silico-calciques et alcalins est incongruente, et que la couche qui se développe à la surface des verres altérés développe un caractère protecteur fortement dépendant des conditions d'altération (phases secondaires porteuses d'éléments lourds, présence ou non de fractures, gel suffisamment épais pouvant jouer un rôle de barrière diffusionnelle). La minéralogie de ces pellicules joue également un rôle important quant au comportement à long terme des déchets vitrifiés, puisque même si le verre s'altère, les produits secondaires peuvent piéger la plupart des éléments potentiellement toxiques.

Cette étude démontre de plus qu'une grande attention doit être donnée lors de la formulation des matrices de confinement des déchets puisque, par exemple, la présence de phosphore dans le verre sain favorise la précipitation de phases secondaires qui retiennent un nombre important d'éléments potentiellement toxiques.

Remerciements Mes remerciements vont à J. Le Maho, D. Foy et I. Pallot-Frossard qui nous ont aimablement confiés les échantillons de vitraux. Je tiens également à remercier A. Kohler, R. Podor, S. Barda et J. Carignan pour l'assistance technique et analytique, F. Mosnier et I. Pallot-Frossard pour les discussions très instructives que nous avons eues. Enfin, je voudrais remercier G. Libourel qui m'a confié de travail et m'a aidé dans l'interprétation des données scientifiques. Ce travail a été financé par le groupe SITA (Lyonnaise des Eaux), l'Agence de l'Environnement et de la Maîtrise de l'Energie (ADEME) et le Ministère de la Culture . Cet article est la contribution no. 1556 du CRPG–CNRS et a reçu le prix Jean Goguel, décerné par le Comité Français de Géologie de l'Ingénieur et de l'Environnement.

Références

Advocat T (1991) Les mécanismes de corrosion en phase aqueuse du verre nucléaire R7T7. Approche expérimentale. Essai de modélisation thermodynamique et cinétique. Thèse, Université Louis Pasteur, Strasbourg, 229 pp

Barbey P, Sterpenich J, Libourel G (1996) Altération des vitraux: produits d'altération, états d'oxydation du manganèse, effets des traitements de surface. In: Filtz JF (ed) Proc 2ème Colloque du Programme Franco-Allemand de Recherche pour la Conservation des Monuments Historiques, Conservation Commune d'un Patrimoine Commun, Bonn, pp 61–71

Carpena J, Lacout J-L (1997) Des apatites naturelles aux apatites synthétiques. Actual Chim 2:3–9

Colombel P (1996) Etude du comportement à long terme de vitrifiats de REFIOM. Thèse, Université Poitiers, 310 pp

Cooper GI, Cox GA (1996) The aqueous corrosion of potash-lime-silica glass in the range 10–250 °C. Appl Geochem 11:511–521

Cox GA, Ford BA (1993) The long-term corrosion of glass by groundwater. J Mater Sci 28:5637–5647

Ehret G, Crovisier JL, Eberhart JP (1986) A new method for studying leached glasses: analytical electron microscopy on ultramicrotomic thin sections. J Non-Cryst Solids 86:72–79

Foy D (1989) Le verre médiéval et son artisanat en France méditerranéenne. Editions du Centre National de la Recherche Scientifique, Paris, 467 pp

Gillies KJS, Cox GA (1988) Decay of medieval stained glass at York, Canterbury and Carlisle. Part 2. Relationship between the composition of the glass, its durability and the weathering products. Glastech Ber 61(4):101–107

Govindaraju K, Mevelle G (1987) Fully automated dissolution and separation methods for inductively coupled plasma atomic emission spectrometry rock analysis. Application to the determination of rare earth elements. J Anal At Spectrom 2:615–621

Hench LL, Clark DE (1978) Physical chemistry of glass surfaces. J Non-Cryst Solids 28:83–105

Le Forestier L (1996) Résidus ultimes de l'incinération de déchets ménagers. Caractérisation chimique et minéralogique, essais de stabilisation par vitrification et comportement des verres à la lixiviation. Thèse, Institut National Polytechnique de Lorraine, Nancy, 313 pp

Le Maho J (1994) Les fouilles de la cathédrale de Rouen de 1985 à 1993: esquisse d'un premier bilan. Archéol Médiévale 24:1–49

Libourel G, Barbey P, Chaussidon M (1994) L'altération des vitraux. Recherche 25:168–188

Macquet C, Thomassin JH (1992) Archaeological glasses as modelling of the behaviour of buried nuclear waste glasses. Appl Clay Sci 7:17–31

Mansot JL, Leone P, Palvadeau P (1994) Valence of manganese, in a new oxybromide compound, determined by means of electron enegy loss spectroscopy. Micros Microanal Microstruct 5:79–90

Newton RG (1971) The enigma of the layered crusts on some weathered glasses, a chronological account of the investigations. Archeometry 13:1–9

Nogues J-L (1984) Les mécanismes de corrosion des verres de confinement des produits de fission. Thèse, Université de Montpellier II

Nriagu JO, Moore PB (eds) (1984) Phosphate minerals. Springer, Berlin Heidelberg New York, 442 pp

Perez Y Jorba M, Dallas JP (1984) Composition et altération des grisailles anciennes. Trois exemples de grisailles du 13ème siècle étudiés par rayons X et microsonde électronique. News Lett 37/38, Comité Technique International du Corpus Vitrearum, pp 8–13

Perez Y Jorba M, Dallas JP, Collongues R, Bahezre C, Martin JC (1984) La corrosion atmosphérique d'un verre du Moyen-Age. Rôle du phosphore dans le mécanisme d'altération. Riv Staz Sperim Vitro 5:121–130

Perez Y Jorba M, Mazerolles L, Michel D, Rommeluere M, Bahezre JC (1993) Etude du processus d'altération des vitraux de la cathédrale de Tours. Analyse des verres. Rôle des éléments mineurs. Etude des grisailles. In: Welck SFv (ed) Proc 1er Colloque du Programme Franco-Allemand de Recherche pour la Conservation des Monuments Historiques, Conservation Commune d'un Patrimoine Commun, Karlsruhe, pp 213–219

Ricol S (1995) Etude du gel d'altération des verres nucléaires et synthèse de gels modèles. Thèse, Université Pierre et Marie Curie, Paris, 177 pp

Sterpenich J (1998) Altération des vitraux médiévaux. Contribution à l'étude du comportement à long terme des verres de confinement. Thèse, Université Henri Poincaré, Nancy 1, 461 pp

Sterpenich J, Libourel G (2001) Using stained glass windows to understand the durability of toxic waste matrices. Chem Geol 174:181–193

Valle N (2000) Traçage isotopique (^{29}Si et ^{18}O) des mécanismes de l'altération du verre de confinement des déchets nucléaires: SON 68. Thèse, Institut National Polytechnique de Lorraine, Nancy, 260 pp

Wedepohl KH (ed) (1978) Handbook of geochemistry. Spinger, Berlin Heidelberg New York

Zarembowitch-Deruelle O (1997) Etude in situ de la couche d'altération de verres. Thèse, Université Pierre et Marie Curie, Paris, 186 pp

Available online at www.sciencedirect.com

ScienceDirect

Waste Management 28 (2008) 120–132

waste management

www.elsevier.com/locate/wasman

Crystal-chemistry of alteration products of vitrified wastes: Implications on the retention of polluting elements

Jérôme Sterpenich *

CRPG-CNRS, BP20, 54501 Vandoeuvre-lès-Nancy, France

Accepted 17 November 2006
Available online 18 January 2007

Abstract

Alteration products of vitrified wastes coming from the incineration of household refuse (MSW) are described. Two vitrified wastes containing 50% and 70% of fly ash and a synthetic stained-glass with a composition close to that of an ancient glass (medieval stained-glass) were altered under different pH conditions (1, 5.5 corresponding to demineralized water and 10) during 181 days. Under acidic condition, the alteration layer is made of an amorphous hydrated silica gel impoverished in most of the initial elements. A minor phase $MPO_4 \cdot nH_2O$, where M represents Fe, Ti, Al, Ca and K cations, also constitutes the altered layer of the synthetic stained-glass. Under neutral and basic conditions, the altered layer is made of an amorphous hydrated silica gel and a crystallized calcium phosphate phase. The silica gel is depleted in alkalis and alkali-earth elements but contains significant amounts of aluminium, magnesium and transition elements, whereas the calcium phosphate is a hydroxylapatite-like phase with P–Si substitutions and a Ca/P ratio depending on the pH of the solution. This study shows: (i) the strong influence of pH conditions on the crystal-chemistry of alteration products and thus on the mechanisms of weathering resulting in different trapping of polluting elements, and (ii) that glass alteration does not necessary produce thermodynamically stable phases which has to be taken into account for the prediction of the long-term behavior.

1. Introduction

One of the major problems of the present society is to stabilize ultimate wastes coming from municipal, industrial or nuclear activities. These wastes contain high amounts of toxic elements and have to be stabilized before storage. Among the actual Solidification-Stabilization Processes, vitrification offers many advantages such as a reduction of the volume of wastes, no porosity and a good chemical durability. However, before using silicate glasses to stabilize ultimate wastes, we need to ensure of their long-term behavior and to study the solubility and the possible dispersion of polluting elements into the biosphere. If leaching experiments in the laboratory allowed the quantification of the influence of conditions of alteration and of glass composition on its dissolution, as well as the calculation of mean dissolution rates of toxic elements, the mineralogy and the chemistry of altered layer are complex and give information on the pollutant retention. An essential step is thus the study of the crystal-chemistry of pollutants in order to determine the long-term stability of the phases containing them, and thus to ensure of the trapping of the potentially toxic elements.

This study is devoted to the chemical and mineralogical characterization of the altered layer due to alteration of model glasses under acidic to basic conditions. Two vitrified wastes made from ashes from household refuse (MSW described in Le Forestier and Libourel, 1998) and a glass whose composition is close to that of potassium-rich medieval stained-glasses were weathered at different pH during 6 months. The last composition was chosen to compare the experimental alteration to natural weathering as deduced from the study of medieval stained-glasses (Sterpenich and Libourel, 2001). This work is focused on the

---

[*] Present address: UMR CNRS 7566 G2R-CREGU, Géologie et Gestion des Ressources Minérales et Energétiques, Université Henri Poincaré Nancy 1, Nancy Université, Faculté des Sciences, BP 239, F-54506 Vandoeuvre-lès-Nancy Cedex, France. Tel.: +33 3 83 68 49 40; fax: +33 3 83 68 47 01.

E-mail address: jerome.sterpenich@g2r.uhp-nancy.fr

0956-053X/$ - see front matter © 2006 Elsevier Ltd. All rights reserved.
doi:10.1016/j.wasman.2006.11.004

identification of mineral phases and on the precise determination of their chemistry in order to determine the phases trapping the pollutants.

2. Sample description and experimental protocol

Because this paper is a part of a general study devoted to the long-term durability of glasses as deduced from the study of medieval stained-glasses (Sterpenich and Libourel, 2001; Sterpenich, 2002), one glass whose composition is close to that of medieval glasses (VK, Table 1) and two vitrified fly ashes (FA) from municipal waste incineration (50% FA and 70% FA) were used. The two latter glasses were made with 50% and 70% fly ash, respectively; the remaining products (silica and soda bicarbonate) are added to lower the melting point and to increase glass durability. The mineralogy and the chemistry of fly ash are described in Le Forestier and Libourel (1998). VK glass was doped with polluting elements such as Cd, Cr, Cu, Ni, Pb, Sn and Zn in order to follow their behavior during glass alteration. The chemical composition of the three glasses is reported in Table 1. The samples are polished (<1 μm) discs (monoliths) of about 15.5 mm in diameter and 3.0 mm in height. They weigh around 6 g as a function of glass density. The samples were made by the Corning firm (Fontainebleau, France). They were obtained by fusion at 1400 °C, fast cooling and annealing. They are amorphous and homogeneous in composition.

Table 1
Chemical composition for 50% FA, 70% FA and VK samples

Weight %	50% FA	70% FA	VK
SiO_2	62.6	52.3	52.19
Al_2O_3	9.1	12.5	2.39
Fe_2O_3	0.87	1.26	0.7
MnO	0.04	0.07	0.76
MgO	1.76	2.36	4.9
CaO	13.5	18.9	14.9
Na_2O	6.5	5.9	1.8
K_2O	2.0	2.0	14.9
TiO_2	1.06	1.45	0.24
P_2O_5	0.88	1.22	3.34
Trace elements (ppm)			
As	18	25	2
Ba	907	1010	22
Cd	31	43	341
Co	l.d.	10	0.6
Cr	339	406	326
Cu	160	177	7177
Ni	31	45	343
Pb	532	965	1518
Sb	150	201	7
Sn	636	740	349
Zn	3179	5175	6831
S	l.d.	680	590
Cl	9400	10600	1930
F	1500	2000	80

Leaching experiments were performed in a closed system. Each sample was placed in a Teflon vessel with three solutions: an acidic solution (pH = 1) made with nitric acid (HNO_3 Suprapur®), a solution (pH = 10) basified with ammoniac NH_4OH, and a near neutral solution (pH ≈ 5.5) corresponding to demineralized water. The choice of these solutions was made: (i) because they are poorly complexant and allow quantification of the effect of pH only, and (ii) to minimize the adding of ions still present in the glass composition. A temperature of 80 °C is obtained using a ventilated oven. This temperature is also chosen to enhance the kinetics of reaction because of the limited duration of alteration. The monoliths of glasses were maintained with a concave Teflon basket to minimize the surface of contact. To develop a sufficiently thick alteration layer, the experiments lasted 181 days. However shorter durations of alteration (0.5, 2, 4, 8, 37, 107 days) were also tested to perform leachate analyses and measure diffusion profiles (not presented in this paper); corresponding glasses were submitted to visual observations but not systematically to more indepth analyses. The specific surface area over volume of solution ratio was equal to $0.1\ \mathrm{cm}^{-1}$, corresponding to around 180 ml of solution. The pH, which was not buffered, can freely change during experiments (Table 2).

3. Analytical techniques

In situ analyses and observations of altered glasses were performed on polished cross-sections after mounting in epoxy. Polished sections were coated with amorphous carbon for electron microprobe analyses (EMPA) and scanning electron microscopy (SEM) observations. Electron microprobe analyses were performed with a CAMECA SX50 equipped with four spectrometers and a wavelength-dispersive system (WDS). Accelerating voltage was 15 kV and the current intensity 20 nA. The spot size was defocalized to 5 μm. Electron microprobe calibration was conducted using polished geological standards prior to analysis. Quantitative data were obtained by ZAF correction routine. These ZAF corrections are calculated in refer-

Table 2
Comparison of initial and final pH after 181 days of alteration at 80 °C

Glass sample	Initial pH	Final pH ±0.1
50% FA	1	0.92
70% FA	1	1
VK	1	1.0
50% FA	5.5	7.1
70% FA	5.5	7.3
VK	5.5	9.0
50% FA	10	10.2
70% FA	10	10.1
VK	10	10.2

pH-analyser Tacussel PHN78: pH is measured at room temperature.

ence to the three components of matrix effects affecting X-ray spectrum: atomic number (Z), absorption (A) and fluorescence (F). The glass characterization was completed using and Hitachi S-2500 SEM, equipped with a KEVEX 4850-S energy dispersive spectrometer (EDS).

Micrometric analyses and observations, as well as crystallinity determination of mineral phases, were carried out with transmission electron microscopes (TEM). The samples were collected directly by rubbing the copper grid on the surface of the glass. The TEM used is a Philips CM20 allowing performance of chemical profiles at micrometric scale as well as diffraction patterns.

4. Alteration under acidic conditions

4.1. Observations

Visual observations on 70% FA and VK glasses altered at initial pH = 1 show only a glossy state during the first stage of alteration. When alteration time increases, glasses lose their luster appearance followed by the growth of a translucent and fractured alteration layer. For the 50% FA glass, no visible alteration feature is observable even after 181 days of alteration, implying the absence of a thick altered layer and a near-congruent dissolution as confirmed by leachate analyses (Sterpenich, 1998).

SEM observations of VK and 70% FA samples (Fig. 1) show that the layer has a homogeneous composition (no visible precipitate) and a mean density lower than that of the pristine glass (white part of the picture, Fig. 1a). A polygonal network of microcracks grows with increasing time, which is responsible for the flaking off of the alteration layer (Fig. 1a and b). Of note is the presence of lens shaped features visible on the surface of VK glass (Fig. 1a), likely due to pits of preferential dissolution.

The altered layer observed from polished cross-section of glasses altered at initial pH = 1 has a homogeneous thickness all around the glass samples. Fig. 1c shows a VK glass cross-section observed in backscattering electrons (BSE) mode. The altered layer is visible on the top of the picture and is darker than pristine glass, indicating a lower average atomic number. The altered layer adheres to pristine glass. Its thickness is about 90 μm after 181 days of alteration (around 40 μm for 70% FA). A precise observation of Fig. 1c shows that, although precipitates are present neither on the surface nor in the altered layer, this latter does not have a homogeneous chemical composition. Indeed close to the pristine/altered glass interface thin dark layers, located by horizontal arrows on the left side of the picture (Fig. 1c), are visible in BSE mode. It corresponds to a variation of chemical composition evoking the lamination observed in medieval stained-glasses altered under archaeological conditions (buried in the soil, e.g., Newton, 1971; Gillies and Cox, 1988; Macquet and Thomassin, 1992; Sterpenich and Libourel, 2001; Römich, 2003).

Concerning the 70% FA glass, the SEM observations show that the features are comparable to that of VK glass. No diffraction patterns were found when analyzing the different altered layers with TEM, confirming that they are made of amorphous materials.

4.2. Chemical and mineralogical composition

The chemical composition of the altered layer of VK and 70% FA glasses was analyzed by EMPA (Table 3). For both glasses, the altered layer is made of ≈90 wt.% SiO_2 and 10 wt.% H_2O. Alkali and alkali-earth metals are impoverished in the layer by comparison with their content in the pristine glass (Fig. 2). While they are minor elements in the pristine glass, P, Fe and Ti are enriched in the leached layer and are correlated. Moreover, the P/Si plot shows that these two elements are anti-correlated (Fig. 3a) in the altered layer of VK glass. More than that, P content in one hand and Fe and Ti contents in the other hand are also positively correlated (Fig. 3b). Thus, the edges recorded in the variations of P, Fe and Ti (Fig. 2) can be compared to the lamination observed in the altered layer by SEM (Fig. 1c). These observations imply that the altered layer may be made of 99% of a hydrated silica gel with aluminium (Si/Al = 10) and 1% of a minor phase rich in phosphorus, titanium and iron. The lamination visible only in glasses for which the altered layer is thick could be explained by a phenomenon of local over-concentrations in the silica gel implying the precipitation of a secondary phase rich in phosphorus. The over-concentration phenomenon could be linked to large differences between leaching kinetics of elements and kinetics of transport probably by diffusion processes in the altered layer. Indeed, when the altered layer reaches a certain thickness, the kinetics of diffusion could become the limiting step of the release of elements. If these elements are rapidly leached from the pristine glass, an accumulation can occur in the gel layer, implying the saturation and the precipitation of secondary phases in the porosity of the silica gel. Concerning VK samples, analyses allow the calculation of the stoichiometry of the secondary phase which could be $MPO_4 \cdot nH_2O$ where

$$M \approx 0.45\mathrm{Fe(III)} + 0.2\mathrm{Ti(IV)} + 0.15\mathrm{Al(III)} + 0.15\mathrm{Ca(II)} + 0.1\mathrm{K(I)}$$

Such a phosphate phase is possible if considering the concentrations in the leachate and the solubility diagram of phosphates under the experimental conditions (Sterpenich, 1998).

Concerning trace elements, they are poorly or not incorporated in the altered layer. Leachate analyses (Sterpenich, 1998) show, however, that Sb and Sn were only poorly released under acidic conditions. Comparison of Tables 1 and 3 shows that the altered layer of 70% FA glass is enriched in Sn (2000 ppm) compared to pristine glass (740 ppm). Antimony has low contents in the fresh glass (<200 ppm) and can not be measured by EMPA.

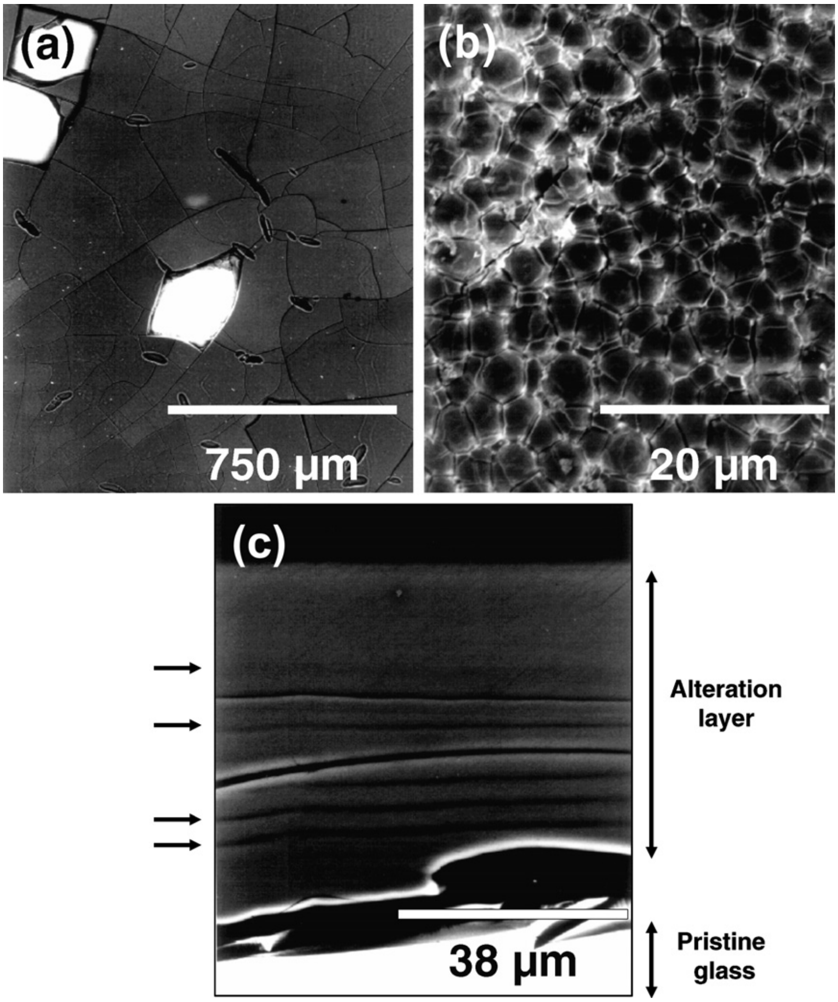

Fig. 1. SEM pictures of VK and 70% FA glasses. (a) Surface of VK glass, backscattered electrons. (b) Surface of 70% FA glass, secondary electrons. (c) Cross-section of VK glass, backscattered electrons. The fresh glass is on the lower part of the picture, in white. Horizontal arrows show four dark layers evoking the lamination observed on archaeological altered glasses.

Table 3
Mean chemical composition of altered layer from Vit.K and 70% ash FA glasses altered at pH = 1

Weight % of oxide	VK	70% FA
Na_2O	l.d.	l.d.
MgO	0.09 ± 0.05	l.d.
Al_2O_3	0.23 ± 0.08	0.35
SiO_2	87.8 ± 2.8	89.8
P_2O_5	1.0 ± 0.6	0.22
K_2O	0.09 ± 0.06	l.d.
CaO	0.16 ± 0.09	0.095
TiO_2	0.26 ± 0.13	0.58
MnO_2	l.d.	l.d.
Fe_2O_3	0.45 ± 0.28	0.19
SnO_2	n.m.	0.27
Total	90.1 ± 4.1	91.5

Sn is the only element whose concentration is above the detection limit (l.d.). The composition for 70% FA glass was determined from one analysis because of the fragility and the poor thickness of the altered layer. The composition of VK glass was determined from a profile performed with EMPA from a cross-section of the glass. The precision corresponds to the standard deviation calculated from 50 analyses. n.m.: non measured.

4.3. Discussion

Phases under thermodynamic equilibrium with the congruent dissolution of pristine glass as predicted by thermodynamic codes such as MINEQL+ (Westall et al., 1976) are quartz, calcic nontronite (zeolite) and titanium oxi-hydroxide, but are not observed from experiments. First of all, such geochemical codes do not take the gel formation into account (e.g., Munier et al., 2004). Moreover, the kinetics of precipitation of some thermodynamically stable phases may not be fast enough at this relatively low temperature and for the durations investigated, quartz and zeolites being rather found at higher temperatures or for longer durations. For example the study of nuclear borosilicate glasses altered during 12 years at 90 °C in pure water (Curti et al., 2006) shows that the presence of thermodynamic stable phases such as quartz as alteration product is possible even under neutral or slightly basic conditions but for longer periods of weathering. Concerning oxide phases, the database used to predict the precipitation

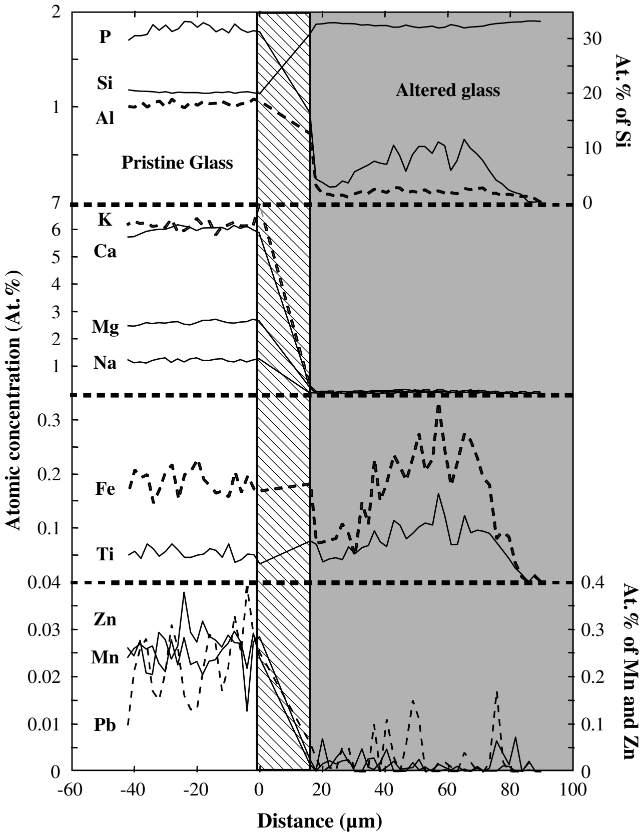

Fig. 2. Chemical profiles perpendicular to the glass surface performed with EMPA in the altered layer of VK glass leached at pH = 1. The concentrations are expressed in atomic percentage. The grey part between 0 and 20 µm corresponds to the empty space between altered and pristine glass due to sample confection.

of mineral phases is limited and does not take into account the possible solid solutions. Moreover equilibrium calculations consider a stoichiometric dissolution of the glass and thus do not take the gel layer formation into account. In situ condensation of silicon likely as silanol was also demonstrated to take place in the formation of gel layers due to the alteration of silicate glasses (see Valle, 2000). This phenomenon is not considered in thermodynamic calculations. In addition, the glass/solution system can be considered as a binary system only during the first time of leaching. From the moment when an altered layer grows on the surface, the system becomes ternary and necessitates taking equilibriums among the fresh glass, the altered layer and the leachate into account. Indeed, the silica gel has to be considered as a new phase reacting with its environment and able to trap elements and to re-equilibrate with solution at each moment.

5. Alteration under basic and near-neutral conditions

5.1. Observation

On the surface of glasses altered under near-neutral or basic pH grows an opaque white layer which does not adhere and thus is easily removed. The separation of the altered layer from the glass, although more pronounced due to desiccation, is visible even when glass is still in contact with water. This phenomenon is more visible when alteration time is increasing together with the thickness of the altered layer.

SEM pictures show that the altered layer under neutral or basic conditions is quite different than that observed under acidic conditions (Fig. 4). Generally it appears as a porous and clay-like film sometimes partially covered with clusters. These characteristics are observed on each glass (50% FA, 70% FA and VK) altered with pure water (thereafter called pH = DW) or under basic conditions (Fig. 4). This type of structure was also described for borosilicate and aluminous glasses altered with demineralized water (e.g., Trotignon et al., 1992; Gin et al., 1994). The surface of the crust also presents crystals organized in various ways according to the conditions of weathering and the composition of starting glass. These crystals have either lengthened shape or form rods dispersed on the surface of altered layer. Cruciform crystals can also be observed (Fig. 4c). Lastly, those can be organized like spherules made up of very fine needles growing starting from a common centre (Fig. 4d). This very particular morphology points out that observed on octa-calcium phosphate crystals (OCP) (LeGeros and LeGeros, 1984) developing inside human tissues.

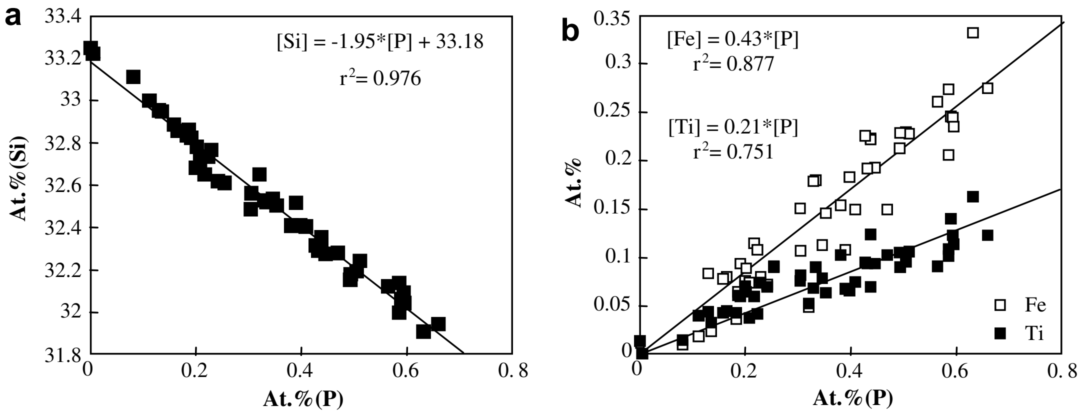

Fig. 3. Concentrations of Si, Fe, and Ti in atomic percent as a function of P in the altered layer of VK glass altered at pH = 1.

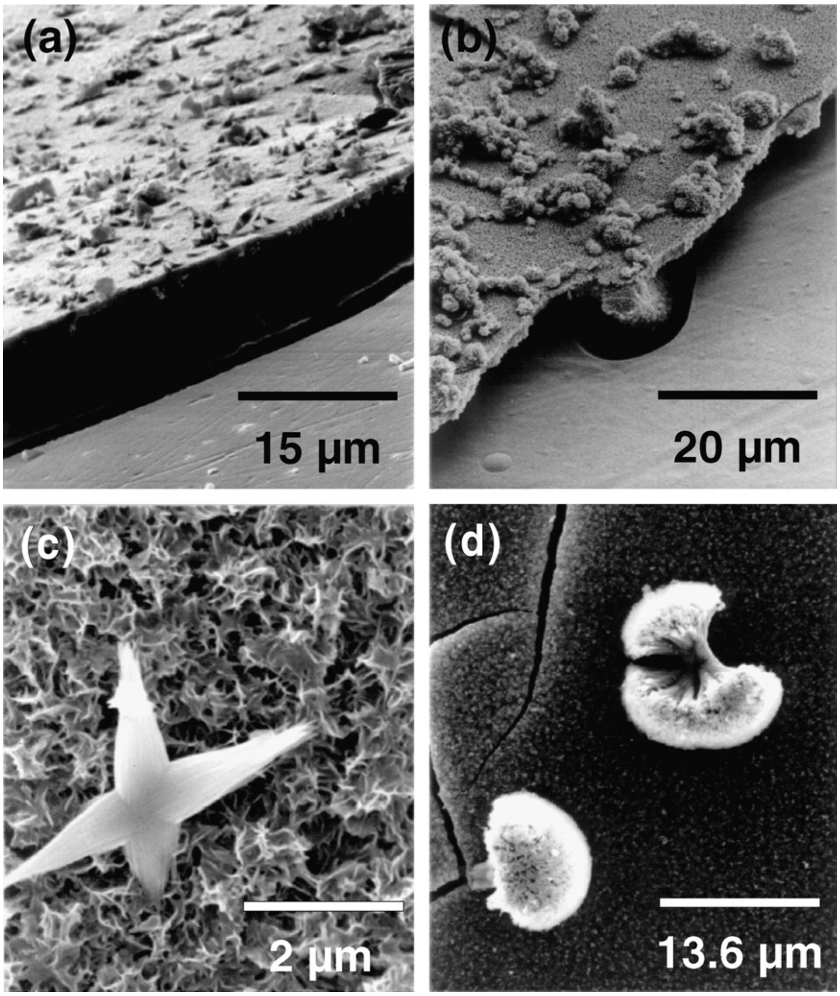

Fig. 4. SEM pictures of VK and 70% FA glasses, secondary electrons. (a) Surface of 50% FA glass, initial pH = 10. (b) Surface of VK glass, initial pH = DW. (c) Surface of 50% FA glass, with a calcium phosphate crystal, initial pH = DW. (d) Surface of 70% FA glass with two calcium phosphate crystals, initial pH = DW.

Cross-section observations could not be carried out on the totality of altered glasses because of their low thickness and their bad cohesion with fresh glass (problems of exfoliation and pulling up when making polished samples). It, however, was possible to observe crusts developed on VK altered at pH = DW and 10. At pH = DW (Fig. 5a), the altered layer located on the top of the picture consists of three distinct phases. On the one hand, a very fine dark layer of a few hundreds of nanometers is located on the surface of glass. Under this first part stands a layer of some micrometers thick and which appears as a lighter phase in BSE. Lastly, a white phase seems to start from this layer to level on the surface of the sample. At pH = 10, the altered layer is much less better preserved than in the preceding cases. It is, however, possible to still distinguish the presence of heavy phases crossing the crust and leveling on the surface.

In complement of SEM observations, a study by TEM was carried out on altered layers from VK, 50% FA and 70% FA glasses weathered at pH = DW and 10. The samples were obtained by simple scraping of crust with the grid used to carry the samples. Generally and whatever the studied glass and the conditions of alteration, the film is composed mainly of two phases. On the one hand, a phase having a form of filaments tangled up one in another composes the major part of the crust (Fig. 5b). It is amorphous or poorly crystallized. Thereafter, this phase will be named silica gel. In addition, a second phase has either a rod or a cruciform shape and is dispersed inside or on the surface of silica gel (Fig. 5c). A more precise observation of this phase reveals a fibrous texture in which whole of fibers follows the same direction. The electron diffraction pattern shows that this phase is relatively well crystallized. The chemical analyses presented in the next section revealed that it is mainly rich in calcium and phosphorus.

5.2. Chemical and mineralogical composition

The two phases described previously were analyzed by energy dispersion spectrometry (EDS) coupled with the TEM, as well as by EMPA when the crust had a sufficient thickness. Generally, the main elements analyzed in these phases are silicon, magnesium, calcium and phosphorus.

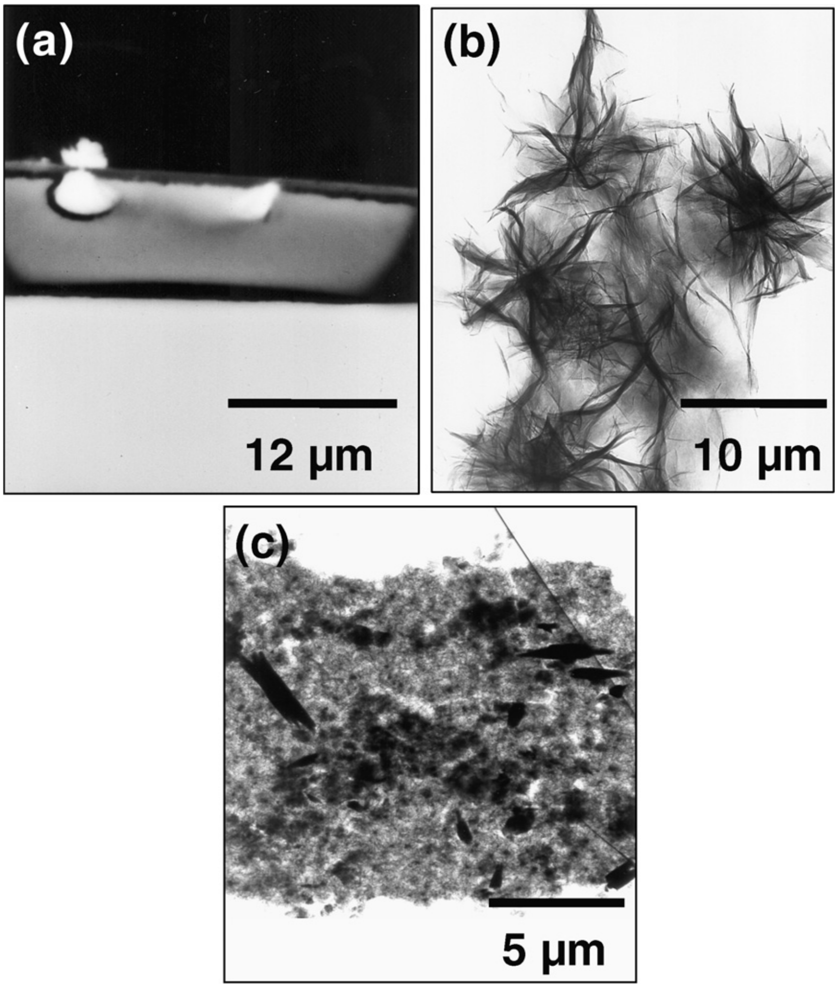

Fig. 5. (a) SEM pictures of VK, initial pH = DW. Backscattered electrons. The fresh glass is the lighter part on the bottom of the picture. A calcium phosphate phase is visible in the gel layer, crossing the surface. (b) TEM observation of the gel layer of VK glass, initial pH = DW. (c) TEM observation of the gel layer and some calcium phosphate phases in darker, 50% FA glass, initial pH = DW.

Two phases being closely dependent within the altered layer, it is difficult to precisely determine the chemical composition of the pure end-members. Thus, it is important to consider that each analysis can be the result of a mixture between the various phases of the altered layer. In order to individualize them, the results of the analyses by electronic microprobe and TEM were plotted in a ternary diagram Si–P–Ca (Fig. 6). The totality of the analyses is aligned on two different linear trends indicating that they are the result of two different mixtures between a Si-Ca rich and Ca–P rich end-member. The composition of the siliceous and calcium-rich end-members varies according to the weathering conditions, as well as the considered glass. Generally, the gel layer of VK glass is less calcium-rich than that of 50% FA and 70% FA vitrified wastes. Moreover, alteration under basic conditions leads in general to the incorporation of calcium in gel layer by comparison with experiments in demineralized water. Concerning the phosphate-rich end-member, it is interesting to note that there is no analysis free of silicon ($Si \neq 0$). This suggests that either silicon is incorporated in the phosphate phase crystalline network or analyzed silicon contents are the result of the contribution of the gel layer under the beam of analysis and thus that all of the performed analyses correspond to a mixture between a phosphate phase and a silica gel.

In order to follow the behavior of magnesium and aluminium among the various phases of the altered layer, their respective contents are plotted in diagrams Mg–P–Ca and Al–P–Ca (Fig. 7). Concerning aluminium (Fig. 7a), the contents once again are aligned between two end-members, an aluminous and calcium-rich in one hand and a phosphorus and calcium-rich in the other hand. The tendencies observed compared with those described previously concerning silicon reveal an important partition of aluminium in silica gel. Behavior of magnesium (Fig. 7b) is similar to that of silicon, also indicating an important Mg partition in silica gel. Moreover, low contents of these elements near the phosphorus-rich end-member is consistent with the fact that: (i) these elements do not easily incorporate the structure of phosphate phase, and (ii) the silicon analyzed under the same conditions would come at least partly from phosphate phase and consequently would not only result from a mixture during analysis between silica gel and phosphate

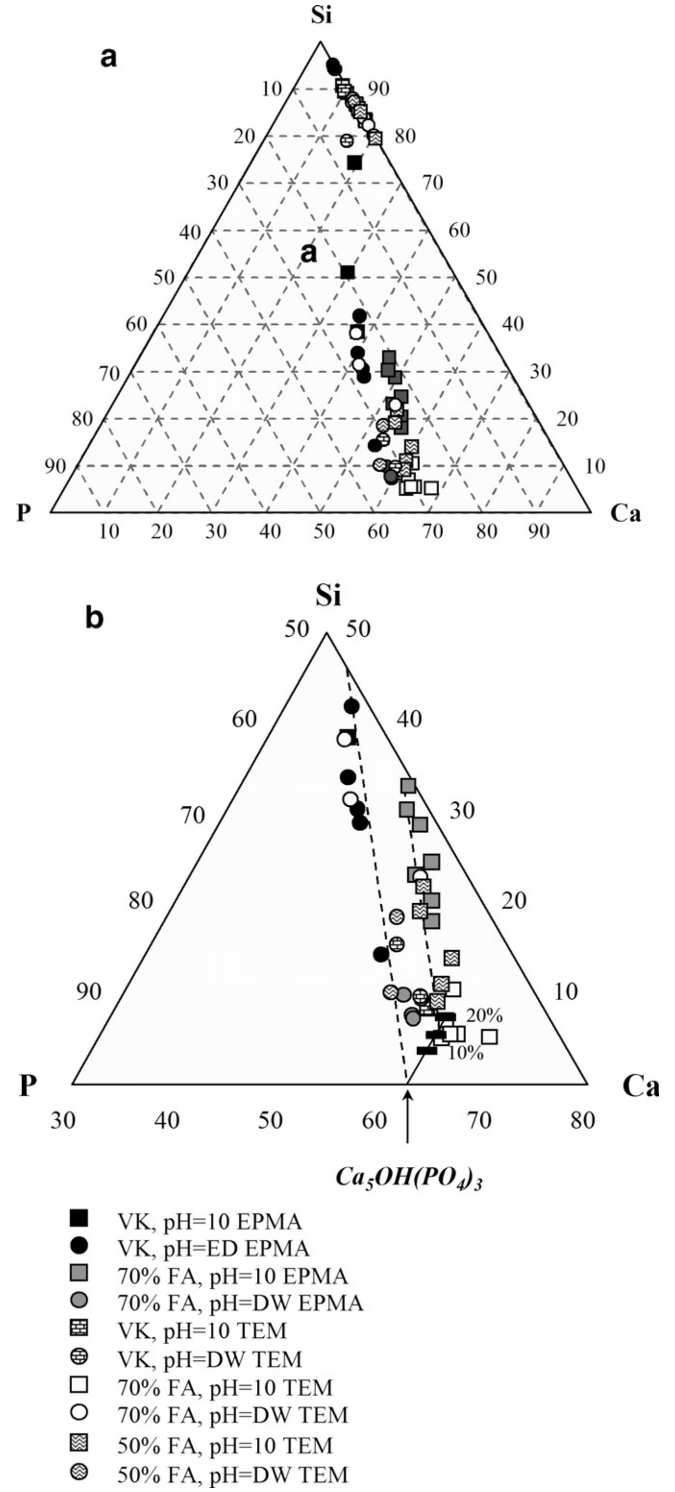

Fig. 6. (a) Ternary diagram in atomic proportion of Si, Ca and P. EMPA and TEM analyses performed on VK, 50% FA and 70% FA glasses altered at pH = DW and 10, 80 °C and during 181 days. (b) Detail of (a) for Si(50%)–P(30–80%). The stoichiometry of hydroxyapatite is plotted with different Si–P substitution ratio (10%, 15%, 20%, black rectangles).

phase. In other words, there would be a substitution of silicon probably with phosphorus inside the calcium phosphate phases. Finally, the analyses of the altered layers show that they are mainly made of two phases: a silica gel

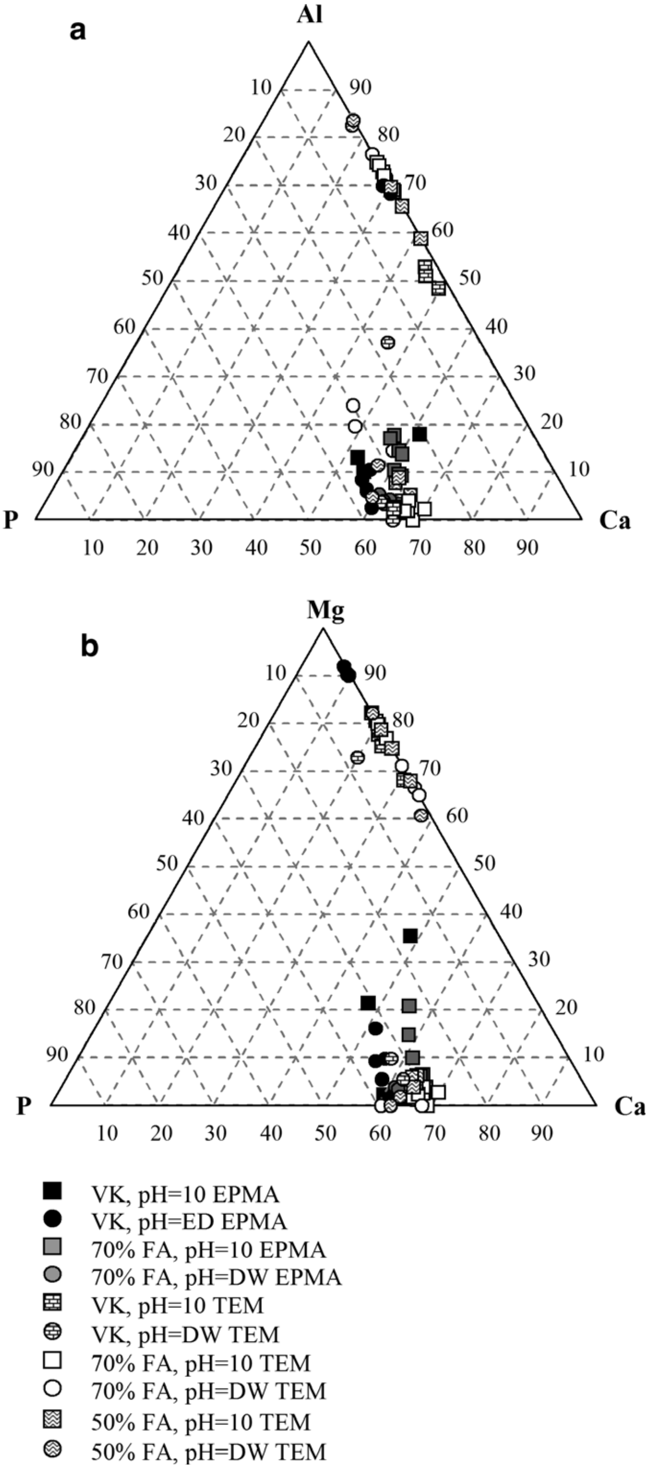

Fig. 7. Ternary diagram in atomic proportion of (a) Al, Ca and P, and (b) Mg, Ca and P. EMPA and TEM analyses performed on VK, 50% and 70% FA altered at pH = DW and 10, 80 °C and during 181 days.

containing aluminium and magnesium, and a calcium phosphate which would be partly substituted by silicon.

5.2.1. Silica-gel description

The mean composition of silica gel from altered layers of VK, 50% FA and 70% FA glasses determined by TEM (and EMPA for VK glass altered at pH = DW) is

Table 4
Mean chemical composition calculated assuming an anhydrous phase of silica gel

Oxide wt.%	pH = 10			pH = DW		
	VK	70% FA	50% FA	VK	70% FA	50% FA
Na_2O	1.83	2.80	2.62	0.14	1.22	5.02
MgO	13.34	15.89	14.59	20.75	10.10	11.04
Al_2O_3	6.15	13.26	11.65	6.37	17.87	20.20
SiO_2	61.60	34.75	35.80	55.75	33.36	33.20
P_2O_5	0.39	l.d.	l.d.	0.14	l.d.	0.28
K_2O	0.39	l.d.	l.d.	0.40	l.d.	l.d.
CaO	6.26	5.66	6.87	3.02	6.78	4.36
TiO_2	1.59	9.07	12.88	0.74	21.14	8.92
MnO	2.37	0.99	0.78	3.21	0.35	0.77
FeO	3.74	11.07	9.31	1.80	7.07	10.55
Cr ppm	1900	l.d.	4200	l.d.	6300	l.d.
Ni ppm	700	l.d.	l.d.	1800	l.d.	l.d.
Zn ppm	20600	57900	44000	33900	14600	56200
Pb ppm	l.d.	7105	6797	3000	l.d.	l.d.
Cu ppm	n.d.	n.d.	n.d.	38,000	n.d.	n.d.

TEM analyses (except for VK, pH = DW: EPMA analysis). VK, 50% FA and 70% FA glasses altered at pH = DW and 10, 80 °C during 181 days. l.d. limit of determination.

summarized in Table 4. Whatever the composition of starting glass and the initial pH of the solution, the silica gel is mainly made of Si (from 33 to 62 wt.% of SiO_2), Mg (10–24 wt.% of MgO), Al (6–20 wt.% of Al_2O_3) and Ca (3–7 wt.% of CaO). In addition to these elements, relatively large quantities of iron (2–11 wt.% of FeO), titanium (up to 21 wt.% of TiO_2), zinc (up to 5.8 wt.% of Zn) and manganese (up to 3.2 wt.% of MnO) are also present in silica gel. The alkaline elements (Na and K) are very impoverished by comparison with fresh glass. However, the comparison of their contents in silica gel shows that sodium is more easily reincorporated than potassium. The analyses also reveal that there is an important influence of pristine glass composition on the stoichiometry of secondary phases. Thus, the silica gel developed on vitrified waste 50% FA and 70% FA is richer in aluminium, titanium and iron than that present on VK glass. On the other hand, the former presents higher quantities of silicon and manganese. It should be noted that the presence of phosphorus can be due to a mixture with a calcium phosphate phase closely related to silica gel. The pH of the solution also seems to play a part as for the stoichiometry of the secondary phases. With regard to vitrified waste 50% FA and 70% FA, the stoichiometry of silica gel is very similar for different glasses altered at the same pH. However when the pH increases, the magnesium content of silica gel decreases from 15 wt.% at pH = DW to 10 wt.% at pH = 10, while the aluminium concentration increases from 12 wt.% at pH = DW to 20 wt.% at pH = 10. For VK glass the tendencies are observable with more difficulty. This can be due to the fact that the differences between the final pH of the experiments for initial pH = DW or 10 are greater than for vitrified waste ($\approx 9_{ED}/\approx 10_{10}$ for VK glass against $\approx 7_{ED}/\approx 10_{10}$ for vitrified wastes).

It is of note that, because of the presence of the Cu-grid, the quantification of copper by TEM is not realizable in our case. However, the analyses by electronic probe reveal large quantities (3.8 wt.%) of copper in the silica gel of VK glass altered at pH = DW. This shows that, although it is not analyzed within the framework of this study, copper must be regarded as an element playing an important part in the composition of silica gel.

The rate of reincorporation of the various elements can be apprehended independently from the pristine glass composition by comparing the “elements over silicon” ratios from silica gel with those from pristine glass. These ratios, which actually represent the variation of the stoichiometry of silica gel compared to fresh glass, are shown in Table 5 for VK, 50% FA and 70% FA glasses. When the ratio is equal to 1, the element considered is in the same proportions to silicon as in pristine glass. When it is higher than 1, the element is in excess in the silica gel compared to silicon and by comparison with pristine glass. It appears in Table 5 that Mg, Al, Ti, Mn, Fe, and Zn are systematically enriched in silica gel compared to their initial contents in pristine glass. On the other hand, K and Ca present a more or less important impoverishment in silica gel. Most of the time, although sodium is impoverished, it remains in higher proportions in silica gel than potassium. Generally, these results show that the transition metals (Ti, Mn, Fe, Ni, Cu) and zinc are elements strongly reincorporated in silica gel, whatever glass and pH (DW or 10) considered. Moreover, rates of reincorporation of certain elements such as magnesium are not equivalent from one glass to another. Thus, vitrified wastes 50% FA and 70% FA present an altered layer incorporating the elements previously quoted better than VK glass. Reincorporation rates of titanium, iron or manganese can for example vary up to a factor of 10 between VK and 50% FA glasses. On the other hand, the reincorporation rate of aluminium seems relatively constant whatever the pH and the glass considered.

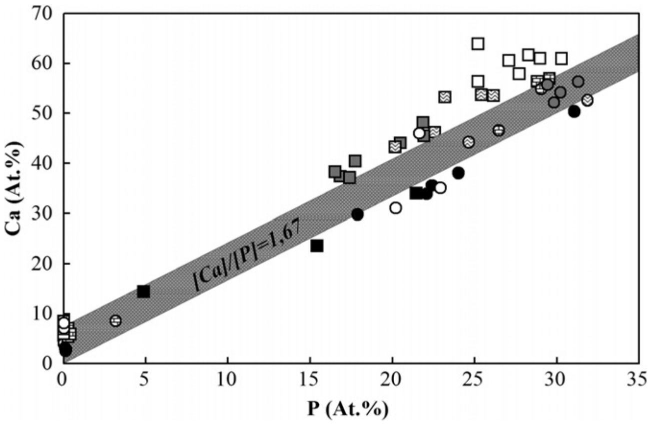

Fig. 8. Calcium against phosphorus concentrations (at.%) of altered layer from VK, 50% FA and 70% FA glasses weathered at pH = DW and 10, 80 °C during 181 days. Hydroxylapatite stoichiometry is represented by the grey zone.

These observations reveal that the major phase of the altered layer, the silica gel, presents a homogeneous composition in terms of the constituting elements but heterogeneous with respect to their contents. The chemical composition of pristine glass thus influences strongly the stoichiometry of the secondary products. This can be attributed initially to the concentrations in solution which differ according to glass considered. It is, however, important to also consider the mechanisms of formation of the altered layer which could be due to several causes, among them precipitation, condensation, and residual silica gel due to a selective weathering (leaching). Thus, the nature of the glass constituting elements should be able to influence such mechanisms by enhancing a reaction rather than another. A convincing example lies in the case of zirconium; it was indeed shown (Zarembowitch-Deruelle, 1997) that the Zr solubilization in a SiO_2–B_2O_3–Cs_2O–ZrO_2–CaO glass is a function of the rate of dissolution of the silicate network. Thus, zirconium dissolves only when silica is not in sufficient concentration in silica gel to ensure the coherence of its network. This observation shows obviously that the strength of T–O–T bonds which is a function of the nature of the network-forming cation, plays an important role for elemental dissolution rates and consequently influences the nature of the altered layer. Elements considered as network-forming cations, namely Si, Al, Ti, Fe^{3+}, as well as the principal transition metals and zinc, are present in large quantities in silica gel of VK, 50% FA and 70% FA glasses. Among alkaline and alkaline-earth elements, only magnesium is highly concentrated in silica gel. The analyses and the observations carried out by TEM did not make it possible to highlight the presence of oxides or hydroxides of transition metals, suggesting that these elements are included in silica gel phase. The amorphous character of this gel does not allow, however, its crystallographic characterization and does not authorize its assignment with a mineralogical class, although its chemical composition can be close to that of clay minerals (smectite type) or zeolites.

5.2.2. *Calcium phosphate phases*

A second phase, rich in calcium and phosphorus was also highlighted in the altered crust of VK, 50% FA and 70% FA glasses weathered under near neutral or basic conditions. The chemical composition of this phosphate phase is summarized in Table 6 for various glasses and initial pH. These analyses, although performed with the TEM and thus at a very fine scale, could result from a mixture between the phosphate phase and silica gel previously described. Generally and whatever glass and pH considered, the phosphate phase (containing from 25 to 35 wt.% of P_2O_5) is rich in calcium (from 35 to 53 wt.% of CaO) and poor, even lacking in alkaline elements. It should be noted that the analyses present relatively important aluminium concentrations (up to 12 wt.% of Al_2O_3), magnesium (up to 4 wt.% of MgO) and silicon (up to 26 wt.% of SiO_2), which are the major elements of silica gel. Thus it is difficult to determine with precision the stoichiometry of the phosphate phase, a contribution of silica gel to the analysis being possible. Moreover, it was shown that: (i) the silica gel contains calcium, and (ii) a Si–P substitution

Table 5
Variation of the stoichiometry of silica gel compared to pristine glass ($(X/Si)_{gel}/(X/Si)_{pg}$)

(X/Si)gel/(X/Si)pg	VK		70% ash		50% ash	
	pH = DW	pH = 10	pH = DW	pH = 10	pH = DW	pH = 10
Na	0.1	0.9	0.3	0.7	1.5	0.7
Mg	4.0	2.3	6.7	10.1	11.8	14.5
Al	2.4	2.2	2.2	1.6	4.2	2.2
K	0.0	0.0	0.0	0.0	0.0	0.0
Ca	0.2	0.4	0.6	0.5	0.6	0.9
Ti	2.5	5.6	23.2	9.6	15.9	21.2
Mn	3.9	2.6	7.9	21.4	36.2	33.9
Fe	2.5	5.1	9.8	14.7	25.4	20.8
Ni	5.0	l.d.	l.d.	l.d.	l.d.	l.d.
Cu	4.4	l.d.	l.d.	l.d.	l.d.	l.d.
Zn	4.2	2.6	5.9	22.3	33.3	24.2

VK, 50% FA and 70% FA glasses altered at pH = DW and 10, 80 °C during 181 days. l.d. limit of determination.

Table 6
Mean chemical composition calculated assuming an anhydrous calcium phosphate phase

Oxide wt.%	pH = 10			pH = DW		
	VK	70% FA	50% FA	VK	70% FA	50% FA
Na_2O	0.66	0.72	0.89	l.d.	0.60	l.d.
MgO	1.86	1.68	2.49	4.33	l.d.	0.83
Al_2O_3	1.82	1.87	3.70	l.d.	11.86	5.44
SiO_2	7.97	6.01	12.66	11.55	26.14	12.34
P_2O_5	34.64	32.04	28.34	33.40	25.47	32.47
K_2O	l.d.	l.d.	l.d.	0.76	l.d.	l.d.
CaO	53.06	55.47	47.60	48.27	34.83	43.96
TiO_2	l.d.	0.64	1.88	l.d.	0.47	1.97
MnO	l.d.	l.d.	l.d.	0.74	0.03	0.15
FeO	l.d.	0.79	1.60	0.11	0.60	1.78
Cr ppm	l.d.	l.d.	l.d.	l.d.	l.d.	l.d.
Ni ppm	l.d.	l.d.	l.d.	l.d.	l.d.	l.d.
Zn ppm	l.d.	7700	8300	8400	l.d.	10,500
Pb ppm	l.d.	l.d.	l.d.	l.d.	l.d.	l.d.

TEM analyses: VK, 50% FA and 70% FA glasses altered at pH = DW and 10, 80 °C during 181 days. l.d. limit of determination.

is plausible within the phosphate phases (e.g., Carpena and Lacout, 1997). No major element allows the discrimination of the main phases, implying a problematic determination of the proportions of phases for each analysis. However, the calcium concentrations of altered layer plotted against the phosphorus contents (Fig. 8) show that these two elements are correlated positively for each glass studied. The slopes calculated from the correlations obtained for various glasses and at pH = DW and 10 are reported in Table 7. It appears that the Ca/P ratio especially depends on the pH of the solution. Indeed, Ca/P ratios for the experiments at pH = DW vary from 1.54 to 1.59, while for pH = 10, they range between 1.65 and 1.93. Once again, the weak differences observed for VK between pH = DW and pH = 10 can be related to the final pH of the solution. Generally, these values are close to that of one of hydroxylapatite $Ca_5(PO_4)_3OH$ (Ca/P = 1.67). It is, however, important to notice that the calcium contents measured in silica gel (for P = 0) are of great importance for the determination of the Ca/P ratio. The slope linear trend is indeed strongly influenced by low Ca and P contents.

Fig. 6b shows a detail of Fig. 6a concerning the Si–P–Ca ternary diagram. First, each analysis has a silicate content of the phosphate phase different to zero. Assuming that a Si–P substitution exists in the phosphate phases of the altered layer, the phosphate end-member should be a hydroxylapatite more or less substituted as a function of the conditions of alteration. For instance, for 50% FA and 70% FA altered at pH = 10 and 80 °C, the phosphate end-member could be a substituted hydroxylapatite with a substitution ratio Si–P ranging between 10% and 15% (Fig. 6b). Indeed, a substitution ratio of 10% corresponds to a hydroxylapatite with a Ca/P = 1.85, whereas 15% corresponds to Ca/P = 1.96. Keeping the same assumption for the pH = DW experiments leads to a phosphate end-member corresponding to a pure hydroxylapatite.

To better characterize the phosphate phase growing in the altered layers, electron diffraction pictures were recorded. The reflection values obtained on phosphate phases of altered at pH = DW and 10 are reported in Table 8. The distances are to be compared with that of a pure synthetic hydroxylapatite and of one coming from an altered layer of a SiO_2–Na_2O–CaO–P_2O_5 glass altered during 1 day at 40 °C and pH = 7.4 (Ehret et al., 1986). Diffraction patterns from VK (pH = DW and 10), 50% FA and 70% FA (pH = DW) were obtained on polycrystalline samples whereas those from 70% FA and 50% FA altered at pH = 10 were made from monocrystals. Under basic conditions, a hexagonal structure for 50% FA glass and a quadratic one for 70% FA glass were revealed. The diffraction patterns do not confirm that phosphate phases are hydroxylapatite. However, the phosphate family contains numerous different phases, more or less chemically and crystallographically stable (Nriagu and Moore, 1984). Moreover, the diversity of the chemical elements released during glass alteration allows numerous substitutions

Table 7
Stoichiometry of calcium phosphate phases

pH sample	DW			10		
	VK	70% FA	50% FA	VK	70% FA	50% FA
Ca/P	1.59	1.54	1.56	1.65	1.93	1.84
[Ca] for P = 0	2.42	6.66	4.29	4.60	6.11	6.80
r^2	0.981	0.963	0.998	0.964	0.987	0.994

From EPMA and TEM analyses performed on the altered layers of VK, 50% FA and 70% FA glasses weathered at pH = DW and 10 and 80 °C during 181days. The “Ca/P” ratio corresponds to the slope of the linear regression calculated from the concentrations of Ca and P of altered layer. “Ca for P = 0” corresponds to the ordinate for P = 0 and informs about the relative calcium contents of silica gel.

Table 8
Principal reflexions measured from the electron diffraction pictures obtained on the crystallized phases rich in calcium and phosphorus

pH sample	DW VK	DW 70% FA	DW 50% FA	10 VK	10 70% FA	10 50%FA	$Ca_5(PO_4)_3OH$[a]	$Ca_5(PO_4)_3OH$[b]
d (Å)	6.95	3.85	4.76	5.27	3.68	5.06	8.17	3.46
	5.27	3.57	3.91	3.8	3.1	3.76	3.44	3.18
	3.34	3.03	3.45	3.13	3.01	3.1	2.81	2.8
	3.19	2.78	3.19	2.78	1.87	3.01	2.78	2.67
	2.7	2.61	2.78	2.7	1.74	2.55	2.72	1.97
	2.57	2.22	2.08	2.19	1.48	2.16	2.63	1.85
	2.27	2.04	1.85	1.91	1.26	2.07	2.26	1.73
	2.04	1.98	1.64	1.75	1.21	1.87	1.94	1.46
	1.81	1.92	1.54	1.62		1.81	1.89	
	1.7	1.71	1.43	1.47		1.74	1.84	
	1.47	1.49	1.26	1.29		1.5	1.81	
	1.43	1.45	1.15	1.09			1.78	
	1.23	1.23	1.12				1.75	
	1.13	1.1	1.03				1.72	
	1.09	1.01	0.86				1.47	

Altered layers of VK, 50% FA and 70% FA glasses leached at pH = DW and 10 and 80 °C during 181 days. The distances obtained are to be compared with those of a synthetic hydroxylapatite and a hydroxylapatite contained in the altered layer of a SiO_2–Na_2O–CaO–P_2O_5 glass.

[a] Synthetic hydroxylapatite (JCPDS file).

[b] Hydroxylapatite from the altered layer of SiO_2–Na_2O–CaO–P_2O_5 glass (Ehret et al., 1986).

implying a deformation of the crystallographic network. Thus the phosphates phases resulting from the alteration of complex silicate glasses can precipitate with different structures as a function of the conditions of alteration (pH, temperature, etc.), the nature of the leached elements, of their concentration, the degree of super-saturation of the solution, and the duration of alteration, but also as a function of the presence of catalytic or inhibitor factors playing a role in the crystallization, such as silanol groups Si-OH. For instance, Mg^{2+}can increase the stability of amorphous calcium phosphates (ACP) hindering their crystallization (Posner et al., 1984).

6. Conclusions on the chemistry and the mineralogy of the altered layers and comparison with altered layers developed under natural weathering

The analyses carried out on VK, 50% FA and 70% FA glasses altered at 80 °C and under acidic, basic or near neutral conditions, reveal the presence of altered layers with complex two-phase structures, and made up of a hydrated silica gel and a phosphate phase. The chemistry of these phases and their proportions are however strongly dependent on the pH of solution.

Under acidic condition, the altered layer is primarily composed of a hydrated silica gel very impoverished of majority of the elements. A minority phase (≈1%) identified as being a $MPO_4 \cdot nH_2O$ mixed phosphate was also highlighted in the altered layer of VK glass.

Under basic and neutral conditions, the silica gel presents a much more complex composition, enriched in Al and Mg and in transition elements (Ti, Mn, and Fe) and Zn. It should be noted that the gel layer of VK glass is systematically richer in silica than that observed on vitrified wastes (50% FA and 70% FA). A second hydroxylapatite-like phase was also described for all of the studied glasses. The Ca/P ratio of this phase seems dependent on the pH of the solution and decreases with the increasing acidity of the solution, in agreement with the possibility of a P–Si substitution.

Excluding calcium phosphates under neutral or basic pH, the whole of the other phases highlighted do not present diffraction patterns, suggesting their amorphous or very slightly crystallized character.

The alteration products of medieval stained-glasses, either altered on windows or buried in the soils over periods of time of up to more than one millennium, were described by Sterpenich (2002) among others. For stained-glasses weathered by meteoric waters, the altered layer is made of a fractured hydrated silica gel with some precipitated phases, mainly calcium sulfates or carbonates, present in cracks and on the surface of the glass. For buried stained glasses, the altered layer consists of a hydrated silica gel alternating with a precipitated amorphous calcium phosphate responsible for a lamination. A third phase rich in manganese oxide and attributed to an external contribution is observable close to the rare fractures or to the free surface of the glass. The comparison of altered layers developed experimentally leads to the following remarks:

(1) Experimental alteration does not allow the precipitation of manganese-rich phases under the investigated conditions. It is understandable if we consider that this kind of phase is due to the specific conditions of the soil.

(2) Experiments allow the formation of a hydrated silica gel. The hydrated silica gel of archaeological glasses is close to that obtained under neutral or basic conditions despite poorer in silica. The silica gel observed on glasses altered on windows has a chemical composition comparable with that obtained under acidic

conditions. However, the detailed chemical composition is quite different of that observed under natural alteration.

(3) Calcium phosphate phases present in archaeological glasses also precipitate during experimental weathering, showing that this kind of phase is characteristic of the alteration of phosphorus bearing glasses. However, their crystallographic features are different, as well as the rate of incorporation of polluting elements.

(4) The sulfates or carbonates precipitates on glasses submitted to meteoric alteration are not present on experimentally leached glasses. This is due to the fact that the precipitation of such phases is due to the particular conditions of meteoric alteration with dissolved SO_2 and CO_2 in the leachate, as well as the alternation of dry and wet sequences due to weather changes.

Acknowledgments

My thanks go to Judith Sausse for comments which helped improve the clarity of the manuscript. Guy Libourel is acknowledged for scientific discussions. I also thank Jaffar Gambadja, Sandrine Barda, Renaud Podor and Alain Kohler for technical and analytical assistance. This work was financially supported by the SITA group (Lyonnaise des Eaux, Suez) and The French Environment Agency (Ademe). CRPG-CNRS contribution no. 1824.

References

Carpena, J., Lacout, J.-L., 1997. Des apatites naturelles aux apatites synthétiques (From natural to synthetic apatites). L'Actualité Chimique 2, 3–9.

Curti, E., Crovisier, J.L., Morvan, G., Karpoff, A.M., 2006. Long-term corrosion of two nuclear waste reference glasses (MW and SON68): A kinetic and mineral alteration study. Applied Geochemistry 21 (7), 1152–1168.

Ehret, G., Crovisier, J.L., Eberhart, J.P., 1986. A new method for studying leached glasses: analytical electron microscopy on ultramicrotomic thin sections. Journal of Non-Crystalline Solids 86, 72–79.

Gillies, K.J.S., Cox, G.A., 1988. Decay of medieval stained glass at York, Canterbury and Carlisle. Part 1. Composition of the glass and its weathering products. Glastechnische Berichte 61 (3), 75–84.

Gin, S., Godon, N., Mestre, J.P., Vernaz, E.Y., 1994. Experimental investigation of aqueous corrosion of R7T7 nuclear glass at 90 °C in the presence of organic species. Applied Geochemistry 9, 255–269.

Le Forestier, L., Libourel, G., 1998. Characterization of flue gas residues from municipal solid waste combustors. Environmental Science and Technology 32, 2250–2256.

LeGeros, R.Z., LeGeros, J.P., 1984. Phosphate minerals in human tissues. In: Nriagu, J.O., Moore, P.B. (Eds.), Phosphate Minerals. Springer-Verlag, pp. 351–385.

Macquet, C., Thomassin, J.H., 1992. "Archaeological glasses as modelling of the behaviour of buried nuclear waste glasses. Applied Clay Science 7, 17–31.

Munier, I., Crovisier, J.-L., Grambow, B., Fritz, B., Clement, A., 2004. Modelling the alteration gel composition of simplified borosilicate glasses by precipitation of an ideal solid solution in equilibrium with the leachant. Journal of Nuclear Materials 324, 97–115.

Newton, R.G., 1971. The enigma of the layered crusts on some weathered glasses, a chronological account of the investigations. Archeometry 13, 1–9.

Nriagu, J.O., Moore, P.B. (Eds.), 1984. Phosphate Minerals. Springer-Verlag, 442 pp.

Posner, A.S., Blumenthal, N.C., Betts, F., 1984. Chemistry and structure of precipitated hydroxyapatites. In: Nriagu, J.O., Moore, P.B. (Eds.), Phosphate Minerals. Springer-Verlag, pp. 330–350.

Römich, H., 2003. Studies of ancient glass and their application to nuclear-waste management. MRS Bulletin 28 (7), 500–504.

Sterpenich, J., 1998. Altération des vitraux médiévaux. Contribution à l'étude du comportement à long terme des verres de confinement. (Alteration of medieval stained-glass windows: contribution to the study of the long term behavior of vitrified wastes). PhD thesis, UHP Nancy 1, Nancy, France, 461 pp. <http://tel.ccsd.cnrs.fr/documents/archives0/00/00/76/65/index_fr.html>.

Sterpenich, J., 2002. Cristallochimie des produits d'altération des vitraux médiévaux: application au vieillissement des déchets vitrifiés – Crystal chemistry of alteration products of medieval stained-glass windows: application to the ageing of vitrified wastes. Bulletin of Engineering Geology and the Environment 61, 179–193.

Sterpenich, J., Libourel, G., 2001. Using stained glass windows to understand the durability of toxic waste matrices. Chemical Geology 174, 181–193.

Trotignon, L., Petit, J.-C., Mea Della, G., Dran, J.-C., 1992. The compared aqueous corrosion of four simple borosilicate glasses: influence of Al, Ca and Fe on the formation and nature of secondary phases. Journal of Nuclear Materials, 228–246.

Valle, N., 2000. Traçage isotopique (^{29}Si et ^{18}O) des mécanismes de l'altération du verre de confinement des déchets nucléaires: SON 68. (Isotopic tracing (^{29}Si and ^{18}O) of alteration mechanisms of the French nuclear glass SON 68). Ph.D. thesis, Institut National Polytechnique de Lorraine, Nancy, 260 pp.

Westall, J., Zachara, J.L., Morel, F., 1976. MINEQL: a computer program for the calculation of chemical equilibrium composition of aqueous systems. Note 18, MIT.

Zarembowitch-Deruelle, O., 1997. Etude in situ de la couche d'altération de verres. (In situ study of alteration layer of glasses.) Ph.D. thesis, Université Pierre et Marie Curie, Paris, 186 pp.

Available online at www.sciencedirect.com
ScienceDirect
Journal of Non-Crystalline Solids 352 (2006) 5446–5451
JOURNAL OF NON-CRYSTALLINE SOLIDS
www.elsevier.com/locate/jnoncrysol

Letter to the Editor

Water diffusion in silicate glasses under natural weathering conditions: evidence from buried medieval stained glasses

Jérôme Sterpenich *, Guy Libourel

CRPG-CNRS, UPR 2300, BP20, 54501 Vandoeuvre-lès-Nancy, France

Received 9 December 2005; received in revised form 24 August 2006

Abstract

In this study, ion-microprobe analyses of four samples of buried medieval stained-glasses are used to demonstrate that water penetrates into the matrix of pristine glasses at low temperatures, thereby showing that glass alteration is not only a surface process. The diffusion coefficients of water determined from concentration profiles of hydrogen are found to be correlated with the bulk polymerization state of the glass. This observation is discussed with respect to glass structure and implies that ionic exchange between hydrogen and network modifying metal cations is the major process responsible for glass hydration.

PACS: 66.30; 61.43.F

Keywords: Chemical durability; Ion exchange; Diffusion and transport; Archaeology; Alkali silicates; Hydration

1. Introduction

Silicate glasses are extensively used as matrices for the confinement of toxic wastes coming from municipal, industrial and especially nuclear industry. To ensure the durability of such waste matrices, many studies were devoted to the understanding of mechanisms responsible for the deterioration of silicate glasses by water (e.g. [1–8]). Three main processes have to be considered during glass alteration : hydration, hydrolysis corresponding to the reaction of metal–oxygen bonds with water to form hydroxyl groups, and an ion exchange mechanism between network modifying cations and the protons or hydronium ions of the aqueous solution. For complex glasses, these three reactions can happen simultaneously [9]. When glass dissolution is not stoichiometric, a corrosion crust grows from the surface. Three extreme hypotheses are usually assumed to explain the formation of the altered layer due to glass weathering: the first one considers incongruent glass dissolution leading to the precipitation of secondary products from a saturated solution [10,11]. The second assumption considers that the formation of an amorphous gel layer at the surface is due to a selective leaching of the glass [12,13], implying diffusion processes. The gel layer is in this case a heritage of the fresh glass and constitutes a residual layer. A third hypothesis considers that in situ silica recondensation plays a key role in the gel layer formation [14]. Glass hydration as well as gel layer formation are thus linked to diffusion processes in fresh or altered glass but mechanisms responsible for water penetration are not well known, especially if simple water permeation [15] or ionic exchange are involved. Based on a study of archaeological medieval stained-glasses, this paper shows that glass alteration is not only a surface reaction because water penetrates beyond the visible interface between fresh and altered glass and that, even at very low temperature, the apparently pristine glass is actually hydrated. Water profiles recorded in the pristine glass are interpreted in terms of diffusion

---

* Corresponding author. Present address: UMR CNRS 7566 G2R – CREGU, Nancy Universities UHP, BP 239, 54506 Vandoeuvre-les-Nancy cedex, France.

E-mail address: jerome.sterpenich@g2r.uhp-nancy.fr (J. Sterpenich).

0022-3093/$ - see front matter © 2006 Elsevier B.V. All rights reserved.
doi:10.1016/j.jnoncrysol.2006.08.041

profiles and the apparent diffusion coefficients are related to the bulk degree of polymerization of the glass.

2. Sample description

Four glasses unearthed in the course of archaeological excavations at two different sites within the Notre-Dame-du-Bourg church in Digne and at the bishop's palace in Rouen (France) were studied. They are dated from the 9th (Rouen) and 13th (Digne) centuries, respectively. They were altered during 800 (glasses from Digne) to 1100 years (glasses from Rouen) by natural humidity of the soil and humic acids. They belong to two different chemical families (Table 1): samples DV and DB from Digne and RVF from Rouen are rich in potassium (13–18 wt% K_2O), calcium (8–16 wt% CaO) and silica (50–59 wt% SiO_2), whereas RBa sample from Rouen is rich in sodium (18 wt% Na_2O), calcium (7 wt% CaO) and silica (68 wt% SiO_2). Each of them presents an adherent corrosion crust bordering the pristine glass (Fig. 1). This crust is highly hydrated (up to 20 wt% H_2O) and mainly consists of an alternation of hydrated silica gel and calcium phosphate phase layers [16]. Its thickness is a function of the bulk chemical composition of the glass (Table 2). It was demonstrated [17] that these archaeological samples were altered at constant volume, the free surface of the glass being conserved during weathering. The bulk degree of polymerization (NBO/T, [18]) is estimated for each glass by calculating the number of non-bridging oxygen per tetrahedron of network forming cation with the following equation:

$$\frac{\mathrm{NBO}}{T} = \frac{1}{T}\sum_i n\mathrm{M}_i^{n+},$$

where T is the number of network forming cations (Si^{4+}, Ti^{4+}, Al^{3+}, Fe^{3+}, P^{5+}), M_i^{n+} is the number of network modifying cations (K^+, Na^+, Ca^{2+}, Mg^{2+}, Mn^{2+}) after deduction of the number of Al^{3+} and Fe^{3+} charge compensators, and n is the electric charge of the ith cation. Because medieval glasses were made under atmospheric conditions, thus in contact with atmospheric oxygen, iron is assumed to be under 3+ oxidation state. Phosphorus is considered to be a network forming cation in agreement with [19]. NBO/T values calculated from our samples are reported in Table 2 and show that the sodic glass (RBa), richer in silica, is more polymerized than the potassic glasses which have a lower silica content. Moreover, comparison of altered layer thickness with NBO/T shows that the more the glass is polymerized, the less it is leached. These samples and the features of alteration are extensively described in [16,20].

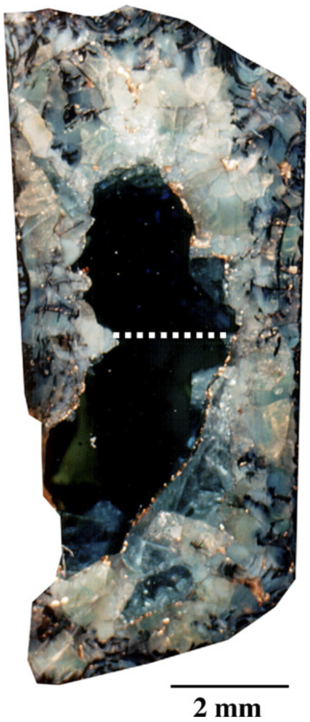

Fig. 1. Cross-section of DB sample (blue potassic stained-glass) buried in the soil during 800 years. The white dashed line shows the ion microprobe profile presented in Fig. 2. The 'fresh' glass (dark) is bordered by a thick altered layer (white).

Table 1
Major elements in weight percent of oxide of the apparent pristine glass analysed by ICP-AES or EPMA for RBa sample

Wt%	DV	DB	RVF	RBa
SiO_2	52.4 ± 1	50.0 ± 1	58.5 ± 1.2	70.0 ± 1.4
Al_2O_3	1.7 ± 0.2	2.6 ± 0.2	2.2 ± 0.2	2.0 ± 0.2
Fe_2O_3	0.7 ± 0.1	1.1 ± 0.1	0.5 ± 0.1	0.4 ± 0.1
MnO	0.7 ± 0.1	0.9 ± 0.1	0.8 ± 0.1	0.3± 0.05
MgO	5.1 ± 0.3	5.3 ± 0.3	5.0 ± 0.3	0.8 ± 0.05
CaO	15.5 ± 0.6	15.6 ± 0.6	12.9 ± 0.5	7.0 ± 0.3
Na_2O	1.1 ± 0.2	0.9 ± 0.1	1.4 ± 0.2	13.6 ± 2.2
K_2O	16.5 ± 0.7	17.8 ± 0.7	12.9 ± 0.5	1.0 ± 0.05
TiO_2	0.2 ± 0.1	0.2 ± 0.1	0.4 ± 0.2	0.1 ± 0.05
P_2O_5	4.1 ± 0.4	4.2 ± 0.4	2.9 ± 0.3	0.1 ± 0.05
Total	98.0 ± 3.7	98.6 ± 3.6	97.5 ± 3.6	95.3 ± 4.45
NBO/T	1.26	1.24	1.01	0.59

Total is not equal to 100% because of the presence of non-measured (coloring elements) or volatile elements (e.g. H_2O, Cl). Values of bulk degree of polymerization NBO/T is also reported for each sample.

3. Analytical techniques

Analyses of hydrogen were performed with ion microprobe CAMECA Ims-3f (modified CRPG). The samples were polished to 1 μm, ultrasonically cleaned in pure alcohol and baked at 40 °C during one night before coating with gold. The intensities on peaks $^{1}H^{+}$ and $^{30}Si^{+}$ were recorded with the following analytical conditions: O^- primary beam without primary filter with an intensity of 2–5 nA and a size of 5–10 μm at a mass resolution of 1000 and with an energy filtering of -80 ± 10 V. A liquid nitrogen cold trap in the source was used to limit H_2O background. These experimental conditions allow a statistical error for H/Si ratio better than 5% [21]. The profiles are carried out on cross-sections, perpendicular to the fresh/

Table 2
Parameters used for the calculation of apparent hydrogen diffusion coefficients

Sample	DV	DB	RVF	RBa
Thickness of altered layer (µm)	1000 ± 200	1100 ± 200	450 ± 100	30 ± 6
Approximate duration of alteration (year)	760 ± 40	760 ± 40	1,145 ± 5	1145 ± 5
Distance of water diffusion (µm)	800	800	600	50
a (m/s)	$4.2 \pm 1 \times 10^{-14}$	$4.4 \pm 1 \times 10^{-14}$	$1.3 \pm 0.3 \times 10^{-14}$	$8.6 \pm 1.8 \times 10^{-16}$
C_1(mol/cm^3)	5.41 10^{-4}	4.40 10^{-4}	7.58 10^{-4}	1.28 10^{-4}
ppm H_2O	*1987*	*1615*	*2786*	*480*
C_2 (mol/cm^3)	6.90 10^{-4}	5.75 10^{-4}	2.04 10^{-3}	2.63 10^{-4}
ppm H_2O	*2534*	*2114*	*7580*	*983*
D (m^2/s)	$1.25 \pm 0.25 \times 10^{-17}$	$1.0 \pm 0.2 \times 10^{-17}$	$1.0 \pm 0.25 \times 10^{-18}$	$1.0 \pm 0.2 \times 10^{-20}$

a is the rate of retreat of the fluid/solid interface corresponding to the rate of progression of the fresh/altered glass interface. C_1 is the hydrogen concentration measured in the centre of the pristine glass considered not to be hydrated, C_2 is the maximum hydrogen concentration measured at the fluid/solid interface, D is the apparent diffusion coefficient of hydrogen into the glass. Accuracy on water content (C_1 and C_2) is better than 20%.

altered glass interface (Fig. 1). Analyses are performed with a constant step of 50–55 µm for potassic samples (DB, DV, RVF) and 15 µm for the sodic one (RBa). Because of the very short distance of water diffusion in the RBa sample (≈60 µm), only 4 analyses were carried out for this glass. All measurements were adjusted with calibration curves from [22] and obtained from the quantification of water in basaltic liquids (MORB). The detection threshold for water with these analytical conditions is better than 300 ppm. Taking into account the main sources of uncertainty [22], the estimated accuracy obtained for H_2O contents is better than ±20%. Considering a profile performed in a same glass with the same matrix properties, the error due to the calibration is uniform for each point. Thus, the statistical error due to ion counting (<5%) has to be taken into account to validate the variations observed for a same profile. The symmetrical shape of the profile obtained for the DB sample (Figs. 2 and 3) shows the reproducibility of the analysis.

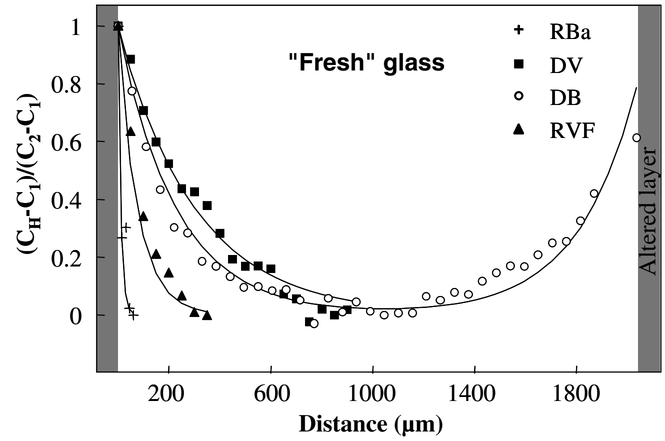

Fig. 3. Normalized hydrogen concentrations as a function of the distance in the pristine glass from the visible interface between fresh and altered glass. The full lines correspond to the calculation from the diffusion equation (see text). The statistical error is better than 5%.

4. Results

Medieval stained-glasses submitted to damp soil for periods of time reaching up to more than one millennium develop an altered layer on their surface [23]. This altered layer mainly consists of a hydrated silica gel in which some minerals such as oxides or phosphates can precipitate. Due to the hydration and very low alkali content of the altered layer, SEM observation allows an easy distinction between this hydrated layer and the pristine glass. This simple criterion was used to define the extent of the apparent pristine glass in order to perform water analysis only into this fresh part and to avoid water contamination from the altered layer. As an example, the diffusion profile recorded in sample DB which was analysed from one side to the other is presented in Fig. 2. The profile has a shape characteristic of a diffusion process. Maximum water concentration in the 'pristine' glass is found at the two visible interfaces between 'fresh' and altered glass. Water content then decreases when going toward the centre of the glass showing that water comes from both sides. The four samples studied show the same behavior (Fig. 3). The water content ranges from ≈2100 to 7600 ppm H_2O close to the interface and from ≈1600 to 2800 ppm H_2O for the centre of the potassic glasses (Table 2) depending on the sample considered. The sodic, the alteration of which is less extensive, has

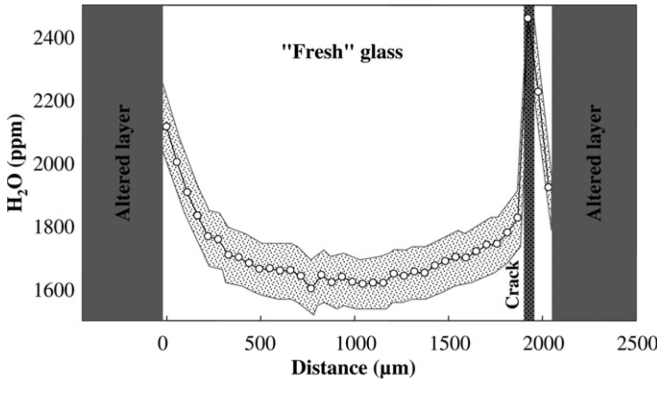

Fig. 2. H_2O concentration analysed by ion microprobe in the pristine glass from a cross-section of DB sample. Error on absolute value of water content is better than 20%. Statistical error for each point is better than 5% and is represented by the grey zone around the profile.

a water content of ≈1000 ppm close to the interface against ≈500 ppm in its centre. H_2O profiles for the four samples are plotted in Fig. 3. The water content is normalized as a function of maximum and minimum H_2O values in order to better compare the different samples and to facilitate the modelling. The normalization parameters (C_1 and C_2) are reported in Table 2. Fig. 3 shows that the depth of water penetration varies with considered samples from 50 μm for the sodic glass to 1100 μm for the less polymerized glass DB.

It is noteworthy that water content recorded in the fresh part of medieval stained glasses submitted to rain, i.e. submitted to a less drastic alteration, have water content of ≈500 ppm H_2O attributed to water trapped during glass confection [17]. Thus, lowest values are measured in the less altered glasses and could indicate that higher values could correspond not to water trapped during glass confection but to deep hydration of the glass. In other words, DB, DV and RVF samples could be fully hydrated due to weathering. For the modelling purpose we assume that minimum water content recorded in the 'pristine' glass corresponds to initial water before alteration. This assumption is supported by the fact that (i) real initial water content cannot be exactly known and can vary from one glass to another due to the conditions of confection, (ii) diffusion model fits better the data with this assumption rather than considering lower initial water content, (iii) RVF sample seems to show that initial water could be high since high water content in the centre of the sample was recorded (2800 ppm) despite the weaker depth of diffusion.

5. Discussion

The mechanisms responsible for hydrogen or water penetration into silicate glasses have been extensively studied (e.g. [1,9,15,24–26]). On a chemical point of view, water in contact with the free surface of the glass enters in the fresh glass by diffusion into the ionic porosity of the glass, and/or by an ionic exchange with leachable cations of the glass according to the following reaction where M is a network modifying cation (mainly alkali or alkali-earth elements):

$$\equiv\text{Si–O–M} + n\text{H}_3\text{O}^+ \leftrightarrow \equiv\text{Si–O–H} + \text{M}^{n+}_{\text{aq}} + n\text{H}_2\text{O}$$

or:

$$\equiv\text{Si–O–M} + n\text{H}_2\text{O} \leftrightarrow \equiv\text{Si–O–H} + \text{M}^{n+}_{\text{aq}} + n\text{OH}^-$$

as a function of the major diffusion species, H_2O or H_3O^+ [27]. However, determination of the mechanism is difficult because of the relatively low amount of water recorded in the fresh glass (7600 ppm max) compared to alkali content (up to 18 wt% of K_2O). In this case, even if alkalis are exchanged with hydronium ions or water molecules, the amount of alkalis removed will not be sufficient to be measurable and still remain in the uncertainties of the analysis. For [9], glass alteration is due to three simultaneous reactions: (1) a glass hydration due to water penetration, (2) a hydrolysis of metal–oxygen bonds and (3) an ionic exchange reaction.

Ion microprobe analyses do not allow to determine the speciation of water incorporated into the fresh glass (molecular H_2O, H_3O^+, H^+, silanols Si–OH, etc.). In this context, the stoichiometry of the reaction cannot be exactly determined, preventing to perform an exact model of water diffusion.

A simple model of water diffusion can be used to first estimate the diffusion coefficient of water into the pristine glass. Assuming that (i) hydrogen is the major species of water diffusing into the glass due to a gradient of concentration, (ii) no chemical reaction occurs between glass and water, (iii) hydration is now in a steady state, (iv) the diffusion coefficient is constant and (v) the diffusion occurs in a semi-infinite medium with a mobile boundary, the general diffusion equation is given by [1]:

$$\frac{\partial C}{\partial t} = \frac{\partial}{\partial x}\left(D\frac{\partial C}{\partial x}\right) + a\left(\frac{\partial C}{\partial x}\right)$$

with

$$a = (x' - x)/t$$

where a is the rate of retreat of the fluid/solid interface corresponding in our case to the mean rate of growth of altered layer, x' is the distance between an arbitrary plane in the altered zone and the initial fluid/solid interface (at $t = 0$), x is the distance of diffusion between this plan and the actual fluid/solid interface, C is the concentration of the diffusing species and t the time of diffusion. Solving this equation by assuming that diffusion profiles are invariant with time ($\partial C/\partial t = 0$) leads to

$$C_{\text{H}} = \exp\left(\frac{-ax}{D}\right)$$

where H is the diffusing hydrogen. If hydrogen exchanges with a modifying network cation M, the concentration of M as a function of the distance in the glass is given by

$$C_{\text{M}} = 1 - \exp\left(\frac{-ax}{D}\right)$$

assuming that H and M have the same diffusion coefficient. Because of the limited amount of water diffusing in the 'pristine' glass, such a profile is unfortunately not measurable. The hydrogen concentrations used in the model are normalized assuming $C_{\text{H}} = 1$ for $x = 0$ and $C_{\text{H}} = 0$ for $x \to \infty$. Table 2 contains the different parameters used to adjust the model to experimental profiles. It should be noted that water concentration C_1 corresponds to the initial water content coming from glass confection. The normalization used allows to subtract this contribution. Simulated curves compared to experimental data are plotted in Fig. 3. The diffusion coefficients were calculated by minimizing the deviation between experimental and calculated points, leading to a calculation error below 10%. Calculated apparent diffusion coefficients range from 9.9×10^{-21} to 1.2×10^{-17} m^2/s, which is in agreement with diffusion coefficients described in the case of glass alteration (e.g. [26]). The lowest value was measured for RBa sample which is the most polymerized glass.

Mean kinetics of alteration [20] as well as mineralogy of the altered layer [16] are comparable whatever the site of alteration, Rouen or Digne, showing that alteration conditions can be considered as equivalent. In this case, the only free parameter explaining the different diffusion coefficients is the chemical composition and thus the structure of glasses.

In order to asses if the diffusion coefficient of water is linked to the glass structure, apparent diffusion coefficients D_H were plotted against the bulk polymerization of the glass (NBO/T). The very good correlation, despite the low number of samples analysed, shows that the more the glass is polymerized, the less the water can penetrate into the glass structure (Fig. 4). A simple linear correlation based on our data gives an equation describing this dependence for alkali–lime–silica glasses altered in burial conditions at low temperature:

$$\mathrm{Log}(D_H) = 4.61 \times \frac{\mathrm{NBO}}{T} - 22.69$$

where D_H is in m^2/s. This relation gives for a total polymerization of the glass (NBO/$T = 0$), a diffusion coefficient D_H equal to 2.04×10^{-23} m^2/s, independent of the nature of the glass network forming cations [28] has calculated hydration rates for obsidian. Assuming a mean temperature of 10 °C for the burial conditions, the hydration rate for obsidian, whose NBO/T is close to zero, is between 3×10^{-23} and 7×10^{-23} m^2/s, which is in good agreement with the values deduced from medieval stained-glasses. This correlation gives direct information on the mechanisms responsible for glass hydration. Because more polymerized glasses have a more open structure due to the adjustment of tetrahedra of network forming cations, glass hydration is not due to a simple permeation in the nanoporosity of the glass, in which case polymerized glasses should be the most hydrated ones. However depolymerization of the glass is due to the presence of ionic metal–oxygens (M–O) bonds which are more easily breakable than covalent Si–O–Si bonds, supporting the idea that glass hydration is mainly due to H–M exchange. The presence of water deep in the 'pristine' glass shows also that glass alteration not only begins with surface reactions. The organization of network modifying cations such as Na, K or Ca in sub-networks or regions (e.g. [29,30]) should play an important role, favouring water penetration and thus explaining the important depth of diffusion measured.

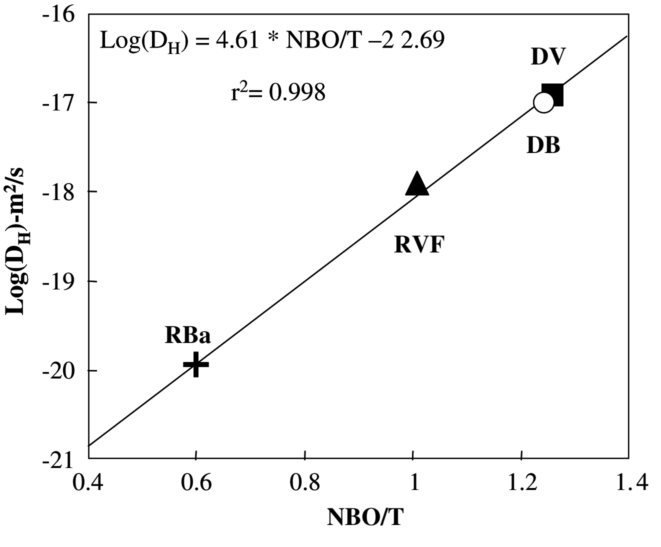

Fig. 4. Logarithm of water diffusion coefficient as a function of bulk degree of polymerization of four archaeological stained-glass samples. Error bars are smaller than symbol size.

6. Conclusion

The study of buried medieval stained glasses allows the quantification of glass alteration under natural conditions over periods of time of up to one millennium. The analysis of hydrogen in pristine glass shows that (i) glass alteration is not only due to surface reactions because water penetrates into the pristine glass beyond the visible interface between pristine and altered glass, (ii) the depth of water diffusion is a function of glass polymerization : the more a glass is polymerized, the less water can enter deeply into its structure, (iii) hydrogen-cation exchange seems to be the major mechanism of glass hydration rather than a simple permeation in the nanoporosity of the glass.

Acknowledgements

Our thanks go to J. Le Maho and D. Foy for supplying stained-glasses samples. We would also like to acknowledge M. Chaussidon and E. Deloule for analytical and technical assistance on ion microprobe. This work was financially supported by the SITA group and The French Environment Agency (Ademe). CRPG-CNRS Contribution No. 1825.

References

[1] R.H. Doremus, J. Non-Cryst. Solids 19 (1975) 137.
[2] A.F. White, H.C. Claassen, Chem. Geol. 28 (1980) 91.
[3] J.O. Isard, A.R. Allnatt, P.J. Melling, Phys. Chem. Glasses 23 (1982) 185.
[4] A.C. Lasaga, J. Geophys. Res. 89 (1984) 4009.
[5] C. Guy, J. Schott, Chem. Geol. 78 (1989) 181.
[6] M.J. Eick, P.R. Grossl, D.C. Golden, D.L. Sparks, D.W. Ming, Geochim. Cosmochim. Acta 60 (1996) 157.
[7] E. Vernaz, S. Gin, C. Jégou, I. Ribet, J. Nucl. Mater. 298 (2001) 27.
[8] T. Advocat, P. Jollivet, J.L. Crovisier, M. Del Nero, J. Nucl. Mater. 298 (2001) 55.
[9] B.C. Bunker, J. Non-Cryst. Solids 179 (1994) 300.
[10] J.C. Touray, La dissolution des minéraux. Aspects cinétiques., 1982, 109p.
[11] J.H. Thomassin, Ph.D Thesis, Université d'Orléans. Etude expérimentale de l'altération des verres silicatés dans l'eau douce et en milieu océanique. Apport des techniques d'analyse de surface des solides, 1984, 215p.

[12] Z. Boksay, G. Bouquet, S. Dobos, Phys. Chem. Glasses 8 (4) (1967) 140.
[13] L.L. Hench, D.E. Clark, J. Non-Cryst. Solids 28 (1978) 83.
[14] B.C. Bunker, T.J. Headley, S.C. Douglas, Mat. Res. Soc. Symp. Proc. 32 (1984) 226.
[15] J.C. Petit, J.C. Dran, A. Paccagnella, G. Della Mea, Earth Planet. Sci. Lett. 93 (1989) 292.
[16] J. Sterpenich, Bull. Eng. Geol. Environ. 61 (2002) 179.
[17] J. Sterpenich, PhD Thesis, UHP Nancy 1. Altération des vitraux médiévaux. Contribution à l'étude du comportement à long terme des verres de confinement. (1998) 461p. Available from: <http://tel.ccsd.cnrs.fr/documents/archives0/00/00/76/65/index_fr.html>.
[18] B.O. Mysen, in: W.S. Fyfe (Ed.), Developments in Geochemistry, Elsevier Science, 1988, p. 354.
[19] M.J. Toplis, T. Schaller, J. Non-Cryst. Solids 224 (1998) 57.
[20] J. Sterpenich, G. Libourel, Chem. Geol. 174 (2001) 181.
[21] E. Deloule, O. Paillat, M. Pichavant, B. Scaillet, Chem. Geol. 125 (1995) 19.
[22] A.V. Sobolev, M. Chaussidon, Earth Planet. Sci. Lett. 137 (1996) 45.
[23] R.G. Newton, Archeometry 13 (1971) 1.
[24] W. Haller, Phys. Chem. Glasses 4 (1963) 217.
[25] B.M.J. Smets, T.P.A. Lommen, Verres et réfractaires 35 (1981) 84.
[26] B. Grambow, R. Müller, J. Nucl. Mater. 298 (2001) 112.
[27] L.R. Pederson, D.R. Baer, G.L. McVay, M.H. Engelhard, J. Non-Cryst. Solids 86 (1986) 369.
[28] I. Friedman, W. Long, Science 191 (1976) 347.
[29] G.N. Greaves, A. Fontaine, P. Lagarde, D. Raoux, S.J. Gurman, Nature 293 (1981) 611.
[30] L. Cormier, D.R. Neuville, Chem. Geol. 213 (2004) 103.

Available online at www.sciencedirect.com

ScienceDirect

Geochimica et Cosmochimica Acta 74 (2010) 3412–3431

Geochimica et Cosmochimica Acta

www.elsevier.com/locate/gca

Elemental and isotopic (^{29}Si and ^{18}O) tracing of glass alteration mechanisms

Nathalie Valle[a], Aurélie Verney-Carron[b,*], Jérôme Sterpenich[c], Guy Libourel[b], Etienne Deloule[b], Patrick Jollivet[d]

[a] *Département Science et Analyse des Matériaux, Centre de Recherche Public-Gabriel Lippmann, 41 rue du Brill, L-4422 Belvaux, Luxembourg*
[b] *Centre de Recherche s Pétrographiques et Géochimiques, CNRS UPR 2300, BP 20, 54501 Vandoeuvre-lès-Nancy Cedex, France*
[c] *G2R, UMR CNRS 7566, Université H. Poincaré, BP 239, 54501 Vandoeuvre-lès-Nancy Cedex, France*
[d] *CEA, DEN, Laboratoire du Comportement à Long Terme, 30207 Bagnols-sur-Cèze, France*

Received 12 November 2009; accepted in revised form 23 March 2010; available online 1 April 2010

Abstract

To better understand glass alteration mechanisms, especially alteration layers formation, leaching experiments of a borosilicate glass (SON68) doped with a different rare earth element (La, Ce, or Nd) with solutions rich in ^{29}Si and ^{18}O were carried out. The coupled analyses of glass, alteration products, and solution led to a complete elemental and isotopic (^{29}Si and ^{18}O) budget. They revealed different behaviours of elements that depend not only on their structural role in the glass, but also on their affinity for alteration products (gel, phyllosilicates, phosphates). However, analyses of both glass and solution are not sufficient to describe the real exchanges occurring between glass and solution. The use of ^{29}Si and ^{18}O tracers gives new insights on the formation of alteration layers. During alteration the phyllosilicates records the isotopic variations of the leaching solution. Their isotopic signatures highlight a mechanism of dissolution/precipitation, which implies equilibrium between the secondary phases and the solution. On the other hand the gel isotopic signature, that is intermediate between the glass and the solution, substantiates the hypothesis that the gel is formed by hydrolysis/condensation reactions. This mechanism can thus explain the influence of the gel formation conditions (alteration conditions, solution saturation) on the structure (reorganisation) and texture (porosity) of this layer and on its protective effect. These hydrolysis/condensation reactions are also certainly involved in the aluminosilicate glass alteration and in the formation of palagonite.

1. INTRODUCTION

The long-term behaviour of nuclear glass (used to confine nuclear wastes) is of prime interest to ensure the safe geological disposal of nuclear wastes. The glass durability prediction models are based on the understanding of alteration mechanisms and on experimental data (e.g. Grambow, 1985; Frugier et al., 2008). However, to ensure the validity of such predictive models, analogues such as basaltic (e.g. Ewing, 1979, 2001; Lutze et al., 1985; Techer et al., 2000, 2001; Crovisier et al., 2003) or historical glasses (Macquet and Thomassin, 1992; Sterpenich and Libourel, 2001, 2006; Verney-Carron et al., 2008) were studied. The ultimate goal is to show that an experimental model can account for the kinetics of long-term alteration (Ewing, 1979, 2001). Likewise because basaltic glass dissolves faster than mineral (Stefánsson and Gíslason, 2001; Wolff-Boenisch et al., 2006) and the alteration of basalt and basaltic glass at the contact of seawater plays a major role on the chemical balance of the oceans and in the evolution of the climate (CO_2 cycle) (e.g. Brady and Gíslason, 1997; Dessert et al., 2003; Gíslason et al., 2009), it is important

---

[*] Corresponding author. Tel.: +33 3 83 59 42 11; fax: +33 3 83 51 17 98.
E-mail address: verney@crpg.cnrs-nancy.fr (A. Verney-Carron).

0016-7037/$ - see front matter © 2010 Elsevier Ltd. All rights reserved.
doi:10.1016/j.gca.2010.03.028

to understand glass alteration mechanisms with the prospect of quantifying elemental release and modelling alteration kinetics.

Concerning the understanding of glass alteration mechanisms, it is crucial to study the formation of the gel layer as it can influence the alteration rate evolution. Silicate glasses in contact with aqueous solution alter and develop an amorphous hydrated silicate material generally called 'gel layer' (for nuclear glass) or 'palagonite' (for basaltic glass) on the surface. The characteristics of this layer are highly dependent not only on the composition but also on the structure of the glass or mineral (e.g. Casey, 2008). In the case of borosilicate glasses used to confine nuclear wastes, this gel layer is depleted in mobile elements (alkalis such as sodium and lithium, but also boron and molybdenum), which causes structural reorganisation (Geneste et al., 2006). But the gel is relatively rich in alkaline-earth elements (Ca, Sr, Ba) and in silicon and aluminium. Elements whose solubility is very low (heavy metals, rare earth elements (REE), and actinides) are largely retained (Ménard et al., 1998). The texture of the gel is porous (Ledieu et al., 2004; Rebiscoul et al., 2004; Cailleteau et al., 2008) and its structure has been investigated by high-resolution solid-state Nuclear Magnetic Resonance (NMR) for probing the glass evolution during alteration (transformation into gel) (e.g. Bunker et al., 1986, 1988; Angeli et al., 2001, 2006, 2008; Tsomaia et al., 2003; Ledieu et al., 2004). The glass composition influences the gel structure and its retention properties. However, the understanding of the gel layer and its role is crucial because it can influence not only the retention of heavy metals, rare earth elements, and actinides, but also the alteration kinetics. The gel is theorized to have a protective effect as it diminishes the dissolution rate (Jégou et al., 2000; Gin, 2001) even if this effect is difficult to distinguish from the saturation effect in solutions. Cailleteau et al. (2008) highlighted the impact of morphological transformations in the alteration layers on the kinetics of simplified borosilicate glasses. They observed densification and pore closure in the gel by coupling experimental techniques (gas adsorption isotherm, X-ray and neutron scattering, mass spectroscopy and electron microscopy) with numerical Monte Carlo simulations. They showed that porosity closure within the gel can drastically decrease the alteration rate. The protective effect of the gel has thus to be taken into account in the glass alteration models (Grambow and Müller, 2001; Frugier et al., 2008, 2009).

In order to explain the formation of the gel layer, three hypotheses are usually suggested. The first one considers that the gel layer at the surface results from a selective leaching of the glass. The gel is formed by interdiffusion between alkalis and hydrogen species (Rana and Douglas, 1961a,b; Doremus, 1975; Lanford et al., 1979) and consists in a residual skeleton of the pristine glass. However, this hydrated layer is not a gel layer and is mainly observed on soda-lime silicate glasses because diffusion kinetics are faster (in relation with polymerisation degree of the glass). Their composition and their structure are also specific. The presence of alkalis leads to the formation of non-bridging oxygens in these glasses, whereas alkalis are mainly charge compensators in the borosilicate and aluminosilicate glasses (e.g. Angeli et al., 2000). The second hypothesis is that the gel layer is formed by precipitation from a saturated solution. The mechanism of dissolution/precipitation is commonly advanced to explain the formation of the palagonite or gel layer on basaltic glass (Crovisier et al., 1987, 2003; Zhou and Fyfe, 1989; Jercinovic et al., 1990; Daux et al., 1994; Stroncik and Schmincke, 2001). The third hypothesis considers that the gel is formed by in situ silica recondensation (Bunker, 1994; Tsomaia et al., 2003) and is often assumed in the nuclear field (Jégou et al., 2000; Gin, 2001; Frugier et al., 2008). The difference between the two last hypotheses concerns the degree of equilibrium. Precipitation assumes a global thermodynamic equilibrium in solution, whereas condensation assumes a local equilibrium (silica condensation increases when silica concentration in solution increases).

To settle this question, isotopic tracers can be a powerful tool as they are able to trace exchanges between the solution and the glass. This technique has already been investigated to better understand the diffusion mechanism with hydrogen isotopes (Smit et al., 1981; Pederson et al., 1986; McGrail et al., 2001; Rébiscoul et al., 2007; Anovitz et al., 2009), to characterise closed porosity of gel either by replacement of the leaching solution (H_2O) by a H_2O/D_2O mixture (and neutron scattering analyses) (Cailleteau et al., 2008), or by a ^{29}Si rich solution (and time-of-flight secondary ion mass spectrometry analyses) (Jollivet et al., 2008), and to distinguish the gel from a residual glass skeleton (^{18}O) (Le Gal et al., 1999). However, silicon and oxygen isotopes tracing has not yet been used to investigate the glass dissolution reactions during the gel formation.

The purpose of this study is to better understand the mechanisms responsible for the formation of altered layers, especially the gel, by using the isotopes of the two main elements of the glass and the gel. For that, alteration experiments of SON68 glass, the inactive simulate of the French R7T7 nuclear glass, were carried out using solutions enriched in ^{29}Si and ^{18}O. First, they lead to a complete mass balance by solution analyses and alteration layers characterisation (classical experimental approach to study glass alteration). This allowed us to establish a distribution of the different elements of the glass in the alteration layers. By coupling Si and O isotopic measurements in the solution and in the altered layers, this study reveals the real exchanges occurring between glass and solution during alteration and allows to determine the respective glass and solution contributions. This gives new insights on the mechanisms responsible for the gel and secondary phases formation.

2. EXPERIMENTAL AND ANALYTICAL TECHNIQUES

2.1. Glass specimen preparation

The nominal composition of SON68 glass is given by Gin and Mestre (2001). It is a borosilicate glass with large amounts (>1 wt.% oxide) of sodium, aluminium, calcium, iron, lithium, molybdenum, zinc, zirconium, caesium, and rare earth elements (REE). Three SON68 glasses (La54, Ce44, and Nd55) have been used for these experiments. They differ from each other by the nature of the incorporated REE (La, Ce or Nd) but the content of each REE is equal (1.63 wt.% oxide). Their composition is given in Table 1. The composition and the chemical homogeneity at the micrometric scale were verified by electron microprobe analyses (Valle, 2000). The three glasses were in the form of glass bars that were cut in monoliths of 10 × 10 × 2 mm^3. Each face was polished with SiC paper to grade 1000 and diamond pastes (7, 3, and 1 μm). The samples were then ultrasonically cleaned in alcohol.

2.2. Leaching solution

The leaching solution was doped in ^{29}Si and ^{18}O from Euriso-Top amorphous silica $^{29}SiO_2$ and water $H_2{}^{18}O$ (Table 2). Amorphous $^{29}SiO_2$ was dissolved in water after an alkaline fusion with potash ($mKOH/mSiO_2 = 10$), and mixed with dissolved silica gel. The leaching solution was adjusted to 20 mg/l of silicon and 250 mg/l of potassium. The isotopic ratios measured by mass spectrometry in the solution are $^{29}Si/^{28}Si = 1.07$ and $^{18}O/^{16}O = 1.088 \times 10^{-2}$ (Table 2). The pH is adjusted to 8 with Suprapur® HNO_3 in order to reproduce pH conditions close to those of storage conditions (Gaucher et al., 2006). The leaching solution was then stored in a polypropylene recipe during the experiment.

Table 1
Chemical composition of glass samples used for leaching experiments.

Wt.% oxide	La54	Ce44	Nd55
Ag_2O	0.03	0.03	0.03
Al_2O_3	5.15	5.22	5.12
B_2O_3	14.53	14.53	14.53
BaO	0.61	0.61	0.63
CaO	4.37	4.05	4.29
CdO	0.03	0.03	0.03
Cr_2O_3	0.34	0.35	0.35
Cs_2O	1.06	1.07	1.08
Fe_2O_3	3.14	3.19	3.13
La_2O_3	1.52	–	–
Ce_2O_3	–	1.63	–
Nd_2O_3	–	–	1.55
Li_2O	2.05	2.08	2.05
MnO_2	0.36	0.37	0.36
MoO_3	1.87	1.88	1.90
Na_2O	10.50	10.58	10.41
NiO	0.37	0.39	0.42
P_2O_5	0.33	0.33	0.33
PdO	0.61	0.61	0.61
Pr_2O_3	0.43	0.40	0.45
RuO_2	1.01	1.01	1.01
SiO_2	46.40	47.03	46.03
SrO	0.34	0.36	0.37
TeO_2	0.23	0.23	0.23
ThO_2	0.27	0.27	0.27
UO_2	0.05	0.05	0.05
Y_2O_3	0.20	0.20	0.22
ZnO	2.45	2.27	2.39
ZrO_2	2.54	2.70	2.65
Total	100.79	101.47	100.49

Table 2
Isotopic composition of water and silica used to prepare the leaching solution and resulting isotopic composition of the leaching solution compared to natural abundances.

	^{28}Si	^{29}Si	^{30}Si
Euriso-top $^{29}SiO_2$	0.20	99.20	0.60
Natural abundance	92.21	4.70	3.09
	^{16}O	^{17}O	^{18}O
Euriso-top $H_2{}^{18}O$	2.32	2.58	95.10
Natural abundance	99.762	0.038	0.200
	$^{29}Si/^{28}Si$	$^{18}O/^{16}O$	
Leaching solution	1.07[a]	0.01088[a]	
Natural ratio	0.051	0.002	

[a] Ratio measured by SIMS for Si and by mass spectrometry for O.

2.3. Leaching experiments

To follow exchanges between glass and solution and to obtain thick alteration layers, leaching experiments were carried out under dynamic conditions. Glass samples were altered under a continuous flow of leaching solution using a peristaltic pump and solutions were recovered at the outlet (Fig. 1). The renewal rate is 12 ± 1 ml d^{-1} corresponding to 6% of solution renewal per day. The temperature of the solution is controlled by an oven at 90 °C. The monoliths are placed in a 240 ml Teflon container (Savillex) on a sample rack. The experiment started with 24 samples (eight of each composition), which corresponds to a glass surface area/solution volume ratio (S/V) of 34 m^{-1}. One sample of each composition (La54, Ce44, Nd55) was taken at various intervals (1 and 2 weeks, 1, 3, and 6 months). Samples were then air dried and broken in two pieces: one for SEM observation, the other for the acquisition of Secondary Ion Mass Spectrometry (SIMS) depth profiles.

The solution was sampled every 3 days at the beginning of the experiment and every 20 days when steady state was reached. The pH was measured at room temperature. The samples were then acidified with Suprapur® HNO_3 and stored in a cool chamber before analyses. Some samples were ultra-filtered (10,000 Da) to verify if colloids were present in solution.

2.4. Analytical methods

Leaching solutions were analysed at the SARM (Service d'Analyse des Roches et des Minéraux, CRPG-CNRS, Nancy) using Inductively Coupled Plasma-Atomic Emission Spectroscopy (ICP-AES) for major elements (Si, Al, Fe, Ca, Na, K, P) and Inductively Coupled Plasma-Mass Spectroscopy (ICP-MS) for trace elements (Ba, Ce, Cr, Cs, La, Mo, Nd, Ni, Pr, Sr, U, Zn, Zr). The relative uncertainty is 5% for Si, 10% for the other major elements, and less than 4% for trace elements. Lithium was analysed by atomic absorption spectroscopy with a relative uncertainty

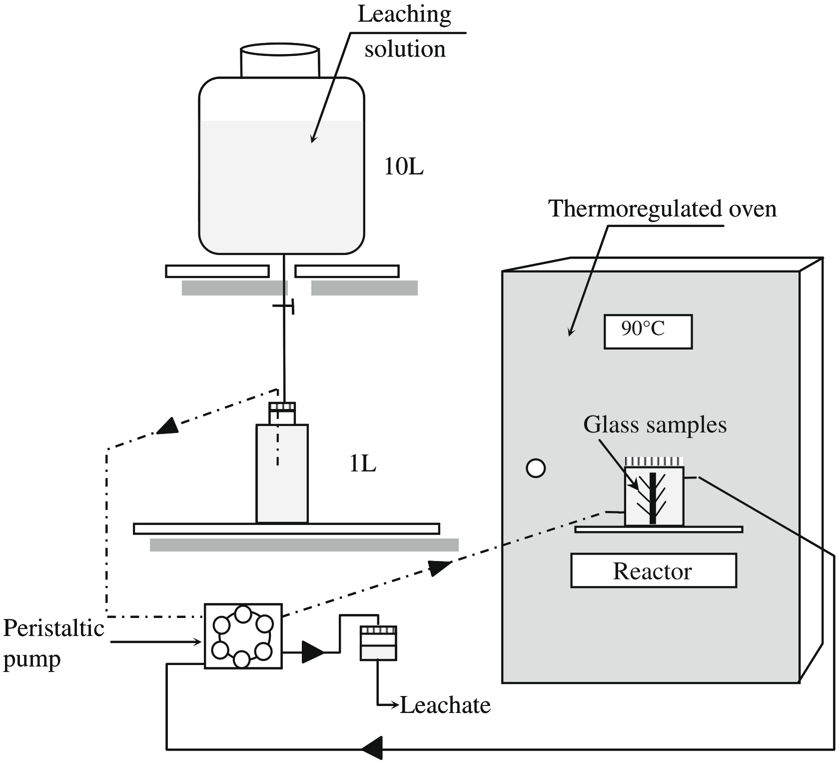

Fig. 1. Scheme of the experimental protocol.

less than 5%. Boron was measured by absorptiometry with a relative uncertainty less than 5%.

Isotopic (Si and O) and elemental depth profiles in the altered glass as well as isotopic composition of the solutions were obtained using the SIMS technique on a CAMECA IMS-3f instrument (CRPG-CNRS, Nancy). The measurements were done with a focused O^- primary beam (10 kV, from 5 nA to few 10 nA depending the thickness of the altered layer) rastered on a 250 × 250 μm^2 area. Secondary positive ions (with an accelerating voltage of 4.5 kV) are collected from a window of 60% centred on the rastered area. The mass spectrometer operated at high mass resolution ($M/\Delta M = 1600$ and $M/\Delta M = 3500$ for O and Si isotopic measurements, respectively) to eliminate isobaric interferences ($H_2{}^{16}O$ at mass 18 and ^{28}SiH at mass 29). The counting times were 3 s and 6 s for ^{28}Si and ^{29}Si, respectively, and 3 s and 6 s for ^{16}O and ^{18}O, respectively. Glass samples were gold coated before analyses. Leachates were deposited and evaporated on a pure platinum sheet. The same above-mentioned analytical conditions were used except that the rastered area was limited to 50 × 50 μm^2. The elemental depth profile was performed with energy filtering (80 ± 20 eV). Three different runs are performed: 'light element' (H, ^{7}Li, ^{11}B, ^{23}Na, ^{27}Al, ^{28}Si, ^{29}Si, ^{30}Si, ^{39}K, and ^{40}Ca), 'heavy elements' (^{52}Cr, ^{56}Fe, ^{58}Ni, ^{64}Zn, ^{90}Zr, ^{133}Cs, and ^{138}Ba) and 'rare earth elements' (La, Ce, Pr, and Nd from mass 137 to 146). After analyses the crater depth caused by sputtering is determined with a profilometer (Dektak, Ecole des Mines de Nancy). The sputtering times were then converted into depths assuming a constant sputtering rate throughout the different analysed layers. This hypothesis was verified by the consistency between the depths calculated by SIMS and the depths observed by SEM on cross-sections. Moreover, the analysed thickness of pristine glass was limited to minimize the error caused by a change of density (between the gel and the pristine glass). Whatever the type of measurements for the glasses, isotopic or elemental, the charge induced by the bombardment was regularly corrected by modifying the sample voltage.

Scanning Electron Microscopy (SEM) observations of the altered samples were carried out with a Hitashi S-2500 at Henri Poincaré University (Nancy, France).

2.5. Mass balances

2.5.1. Solution analyses

In order to compare the dissolution rates of different elements, normalised elemental mass losses were calculated using the following equation:

$$(NL_i)_t = (NL_i)_{t-1} + \left[((C_i)_t - (C_i)_{t-1}) \times Q \times (t - (t-1))\right]/[S \times x_i] \qquad (1)$$

where NL_i is the cumulative normalised mass loss relative to the element i (in g m^{-2}), which corresponds to the quantity of the altered glass per unit area, C_i the concentration of the element i in solution, Q is the flow rate (l d^{-1}), t the alteration time, S the total glass reactive surface area and x_i the mass fraction of the element i in the glass.

Elemental dissolution rates (k_i in g m^{-2} d^{-1}) were calculated using a linear regression:

$$k_i = dNL_i/dt \qquad (2)$$

Equivalent thickness calculated from element i (EE_i in µm) corresponds to the dissolved glass thickness necessary to obtain the concentration of element i in solution:

$$EE_i = NL_i/\rho \qquad (3)$$

where ρ is the glass density (2.75 g cm^{-3}) (Vernaz and Dussossoy, 1992). EE_i can be used for an estimation of the gel layer thickness if calculated from one of the most leachable elements (e.g. boron).The retention rate of element i in the altered layer (f_i in %) is calculated from the normalised mass loss of boron:

$$f_i = (1 - NL_i/NL_B) \times 100 \qquad (4)$$

When f_i is close to 0%, it means that i has the same behaviour than boron, i.e. i is not trapped in the alteration layers. On the contrary, when f_i is close to 100%, i remains completely in the alteration products.

2.5.2. *Isotopic data*

The factor of enrichment ($F(X)$ in %) corresponds to the variation of silicon (Si$_{\text{total}}$, ^{28}Si or ^{29}Si) concentration $[X]_t$ relative to the initial solution $[X]_{t=0}$:

$$F(X) = (([X]_t - [X]_{t=0})/[X]_{t=0}) \times 100 \qquad (5)$$

The concentrations of ^{28}Si and ^{29}Si are deduced from the total silicon concentration and ^{29}Si/^{28}Si and ^{30}Si/^{28}Si ratios. The ^{30}Si/^{28}Si ratio is not known and assumed to be equal to the natural isotopic ratio (^{30}Si/^{28}Si $= 3.35 \times 10^{-2}$) because the enrichment of ^{30}Si in solution is relatively low. The ^{29}Si concentrations in solution are then corrected by deducing the glass contribution. ^{29}Si release is assumed to occur together with ^{28}Si release with a natural isotopic ratio ^{29}Si/^{28}Si, i.e. equal to that of the pristine glass (^{29}Si/^{28}Si $=$ 0.051).

The elemental and isotopic depth profiles performed by ion microprobe are presented as ratios, i.e. normalised to a reference isotope intensity, in order to remove the primary intensity variations. For each element, the ratio between the intensity of the measured isotope and ^{28}Si is normalised to its value measured in the pristine glass:

$$C/C_0(^mX) = (^mX/^{28}\text{Si})/(^mX_0/^{28}\text{Si}_0) \qquad (6)$$

where ^mX is the secondary intensity of element X measured at the mass m, ($^mX_0$/^{28}Si$_0$) is the ratio of secondary intensities measured in the pristine glass.

3. RESULTS

3.1. Solution and solid analyses

3.1.1. *Solution*

The pH of the initial leaching solution, adjusted to 8 at the beginning of the experiment, varies with time (Fig. 2 and Table 3) probably because of atmospheric CO$_2$ dissolution, but rapidly stabilises around 7.5. The solution is always more alkaline than the initial solution. The pH rises up to 8.4 at 30 days, is then constant (~8.2) from 30 to ~80 days and finally decreases until the end of experiment (i.e. around 190 days) to reach a value of 7.8. The decrease of the pH after the steady state is actually related to the variation of S/V ratio consecutive to the sampling of glass monoliths (vertical dashed lines on Fig. 2). This S/V dependence is due to the decrease of the number of reaction sites for a same volume of solution (Feng and Pegg, 1994).

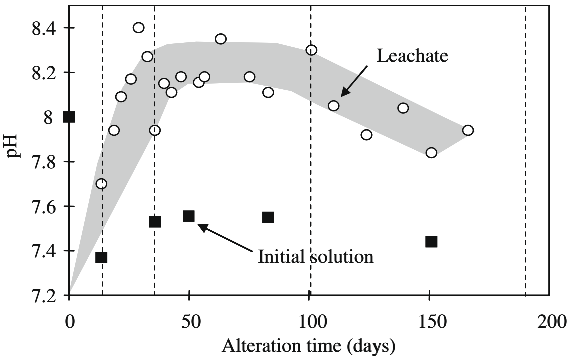

Fig. 2. Evolution of the solution (diamonds) and initial solution (squares) pH during leaching experiment. pH was measured at room temperature with a precision of 0.1 pH unit. Vertical dashed lines correspond to the glass monoliths sampling.

The concentrations of 14 elements (Si, B, Li, Na, K, Ca, Ba, Cr, Cs, Mo, Ni, Sr, U, and Zn) in solution are reported as a function of the alteration time (Table 3 and Fig. 3). Al, Fe, P, La, Ce, Pr, Nd, and Zr were also analysed but their concentrations stay below the detection limit (<1 mg/l by ICP-AES for Al, Fe, P and <1 µg/l by ICP-MS for La, Ce, Pr, Nd, and Zr). In order to test the presence of colloids, some analyses were duplicated with ultra-filtered solutions (empty symbols in Fig. 3). The increase of elemental concentrations at 100 days is due to an experimental bias (stop of the peristaltic pump for a few days).

The measured elements can be divided in three groups:

(i) Al, Fe, P, La, Ce, Pr, Nd, and Zr. The concentrations are close to the detection limits. This result highlights a low solubility and/or retention for these elements in the alteration products.

(ii) Si, B, Mo, Ca, Sr, Ba, Cr, Li, Na, and Cs (Fig. 3a–e). The concentrations increase rapidly during the first 20 or 30 days before reaching a steady state (30 mg/l for Si, 3 mg/l for B, 1 mg/l for Mo, 1.2 mg/l for Ca, 100 µg/l for Sr, 40 µg/l for Ba, 80 µg/l for Cr, 700 µg/l for Li, 7 mg/l for Na, and 650 µg/l for Cs). After 80 days of alteration the concentration in solution progressively decreases until the end of the experiment because of the glass monoliths sampling and the decrease of S/V ratio (similarly to the pH), but also because of the gel diffusive barrier. Analyses of ultra-filtered solutions show that these elements are not linked to colloids.

(iii) Zn, Ni, and U. The concentrations of Zn and Ni (Fig. 3f) reach a maximum after 12 days of leaching ([Zn] ~ 200 µg/l and [Ni] ~ 30 µg/l) and then diminish regularly until the end of experiment. The comparison between ultra-filtered and non-ultra-filtered samples also shows that Ni and Zn form colloids that are removed during ultra-filtration. Uranium has a

Table 3

Solution composition as a function of alteration time. Major elements are given in mg/l, trace elements in µg/l. The pH of the solution is measured at room temperature. NS corresponds to the number of glass samples in the experimental reactor. S/V in cm^{-1} is the surface of glass samples over volume of solution ratio. The silicon isotopic ratio of the solution measured by ion probe is given in the column entitled $^{29}Si/^{28}Si$. nd: not determined.

Time (days)	NS	S/V (cm^{-1})	pH	$^{29}Si/^{28}Si$	Major elements (mg/l)						Trace elements (µg/l)							
					Si	B	Li	Na	K	Ca	Ba	Cr	Cs	Mo	Ni	Sr	U	Zn
0	24	0.349	nd	1.07	20.49	0.00	0.00	1.60	247.0	0.00	0.0	2.5	0.0	0.00	6.4	0.7	0.00	1.0
4	24	0.349	nd	0.89	23.07	0.35	0.09	2.23	268.3	0.60	30.0	0.0	80.0	110.00	nd	21.5	nd	110.0
6	24	0.349	nd	0.74	24.24	0.80	0.20	3.09	261.0	0.60	50.0	0.0	150.0	230.00	nd	40.3	nd	160.0
10[a]	21	0.306	nd	0.68	26.27	1.37	0.31	4.03	242.9	1.24	40.0	0.0	230.0	350.00	nd	52.1	nd	200.0
13	21	0.306	nd	0.59	27.61	1.84	0.44	5.01	251.5	1.16	45.0	0.0	320.0	554.00	nd	71.0	nd	180.0
15[a]	18	0.262	7.7	0.57	29.37	2.33	0.49	6.71	250.0	1.21	47.3	55.7	470.1	728.84	23.8	87.0	7.36	158.7
19	18	0.262	7.9	0.54	30.96	2.70	0.58	7.20	263.0	1.25	48.9	69.7	550.4	875.47	25.8	102.8	8.99	157.9
22	18	0.262	8.1	0.49	31.03	3.18	0.64	6.66	259.0	1.33	43.7	63.4	513.4	828.64	19.4	92.5	8.09	132.9
26	18	0.262	8.2	0.48	30.02	3.25	0.67	7.33	256.0	1.34	43.7	69.5	564.0	907.38	22.4	99.0	7.77	133.2
29	18	0.262	8.4	0.48	30.02	3.17	0.72	7.32	256.0	1.38	40.8	73.3	574.1	961.85	14.9	97.7	7.68	114.4
33	18	0.262	8.3	0.47	29.18	3.34	0.71	6.70	247.0	1.28	39.5	75.4	581.1	975.51	13.3	100.9	7.25	100.0
36[a]	15	0.218	7.9	0.45	29.83	3.29	0.73	7.52	248.0	1.30	45.7	85.5	678.4	1023.78	13.2	102.7	7.96	95.4
40	15	0.218	8.2	0.47	29.07	3.40	0.72	7.13	255.0	1.31	43.7	81.3	654.9	1032.54	11.2	101.2	7.98	88.7
43	15	0.218	8.1	0.48	28.93	3.21	0.74	7.66	245.0	1.28	42.9	89.5	678.2	1041.94	10.5	99.4	7.82	78.6
47	15	0.218	8.2	0.5	30.76	3.34	0.72	8.06	247.0	1.26	38.1	83.4	624.5	1031.91	10.3	107.7	7.00	71.2
50	15	0.218	nd	0.48	30.25	3.48	0.72	7.58	244.0	1.23	40.5	82.3	654.8	1069.32	9.5	99.6	7.85	74.2
54	15	0.218	8.2	0.46	30.17	3.33	0.72	7.60	247.0	1.21	37.8	85.0	654.7	1068.91	8.2	105.5	7.18	58.7
56	15	0.218	8.2	0.46	28.81	3.33	0.70	6.86	242.0	1.20	39.7	80.9	635.5	1034.09	7.9	101.7	6.99	55.7
63	15	0.218	8.4	0.45	28.39	3.47	0.74	7.43	242.0	1.18	35.5	86.0	663.0	1089.1	8.3	102.5	6.33	64.9
75	15	0.218	8.2	0.46	28.56	3.41	0.69	7.45	239.0	1.15	34.0	78.6	599.9	983.8	6.5	87.7	5.98	41.6
83	15	0.218	8.1	0.47	28.12	3.33	0.69	6.55	243.0	1.12	33.3	76.6	738.3	951.8	4.6	89.0	5.45	28.5
101[a]	12	0.175	8.3	nd	35.15	5.76	1.18	10.36	251.0	1.49	47.9	155.5	1147.3	1557.2	3.8	126.3	6.39	66.1
110	12	0.175	8.1	0.42	32.4	4.39	0.92	8.70	254.4	1.28	42.6	115.7	888.3	1139.7	3.4	110.7	5.10	33.9
124	12	0.175	7.9	0.46	28.6	3.17	0.66	6.33	243.2	1.04	35.5	80.7	618.0	821.5	<3	82.9	2.97	16.7
139	12	0.175	8.0	nd	27.68	2.72	0.58	5.59	251.8	0.97	31.0	70.9	520.9	694.1	<3	69.1	2.20	12.9
151	12	0.175	7.8	nd	26.85	2.52	0.54	5.58	245.1	0.91	33.6	68.6	551.1	680.9	<3	75.1	3.40	9.5
166	12	0.175	7.9	0.56	26.72	2.56	0.54	5.98	242.7	0.89	30.3	70.7	542.2	676.8	<3	70.5	1.83	9.3
180	12	0.175	nd	nd	26.02	2.46	0.54	5.26	245.5	0.87	31.4	68.0	539.0	648.4	<3	75.5	1.21	7.8
190[a]	9	0.131	nd	nd	25.97	2.27	0.49	5.38	248.4	0.84	29.7	61.6	508.1	591.5	<3	72.4	1.06	7.3

[a] Time corresponding to the removal of three samples from the reactor.

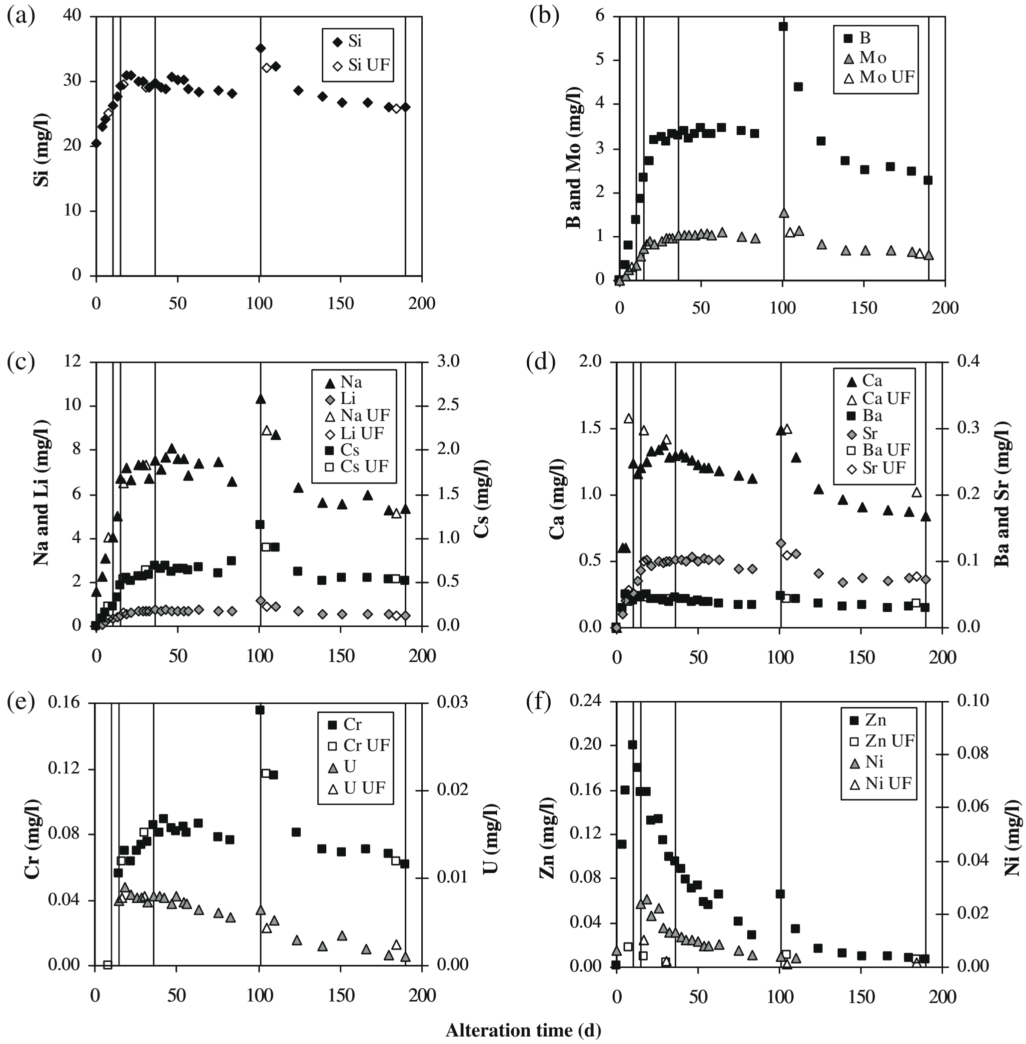

Fig. 3. Evolution of main elements concentrations in the solution during time. Ultra-filtered aliquots are represented by empty symbols. Vertical dashed lines correspond to the glass monoliths sampling.

similar behaviour (Fig. 3e) as its concentration is below the detection limit for 14 days, reaches a maximum (~8 µg/l) for around 50 days, and then decreases until the end of the experiment (1 µg/l). However, U is not linked to the formation of colloids.

3.1.2. Alteration products

Each of the glass monoliths sampled presents an altered layer on the surface. Fig. 4 exhibits the surface of glasses altered during 3 and 6 months. The alteration layers that cover the glass surface are uniform and remain adherent on the glass throughout the experiment. X-ray diffraction performed on this secondary products reveals an important amount of amorphous materials and thus does not permit their exact identification (Valle, 2000). But the mineral appearance suggests the presence of phyllosilicates in agreement with previous studies on SON68 (Abrajano et al., 1990; Frugier et al., 2006). Moreover, Valle (2000) shows that the crystallinity degree of these secondary minerals increases with time.

Cross-sections of the altered glasses from 2 weeks to 6 months were performed (Fig. 5) to observe the alteration products and their evolution with time. Three different alteration layers are identified from the bottom (pristine glass) to the top:

(i) a gel layer that is more abundant and grows faster than phyllosilicates: from around 0.5 µm after 2 weeks up to 1.5 µm, 5.8 µm, and 13.7 µm after 1, 3 and 6 months, respectively. After 6 months the gel layer constitutes 93% of the whole alteration layer. The interface between the gel and the pristine glass is parallel to the surface and neither dissolution pits, nor preferential leaching zone are observed. Some insoluble platinoids are present in the gel after 6 months of alteration (Fig. 5d).
(ii) REE phosphates that are sometimes visible mainly at the gel/phyllosilicates interface (Fig. 5c).

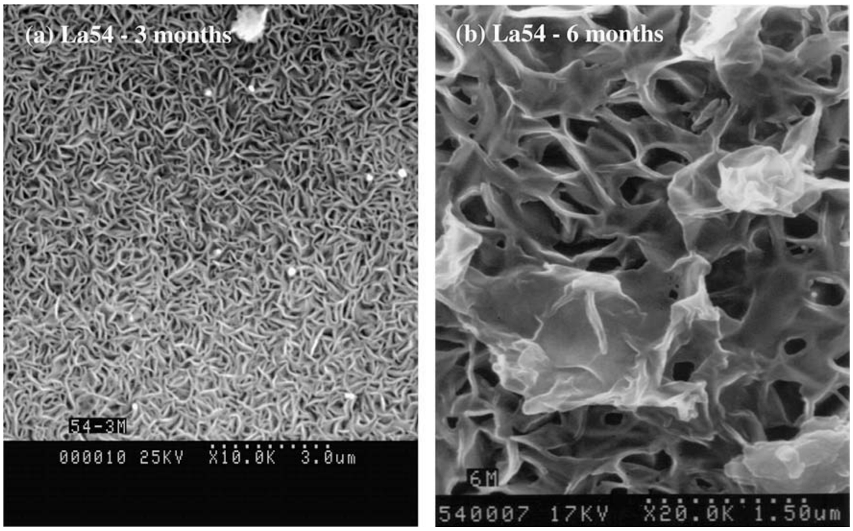

Fig. 4. SEM microphotographs (secondary electrons) of altered glass surface after (a) 3 months and (b) 6 months. Phyllosilicates recovered the surface.

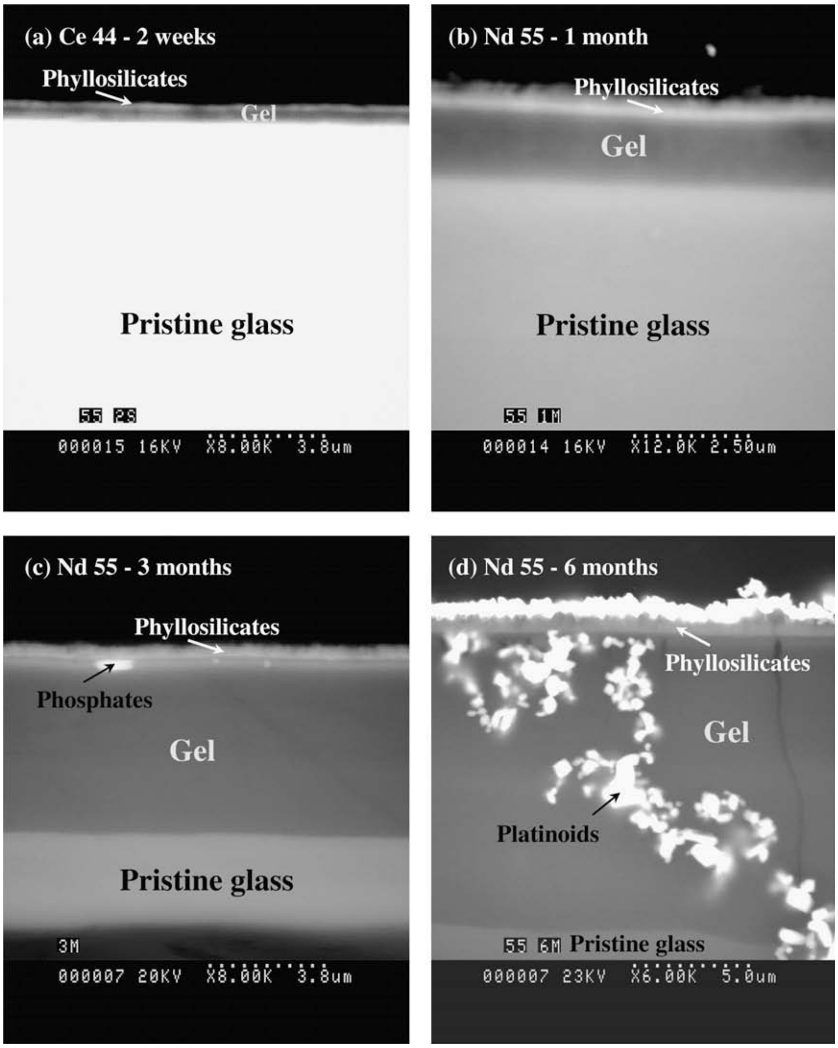

Fig. 5. SEM microphotographs (back-scattered electrons) of altered glass cross-sections after (a) 2 weeks, (b) 1 month, (c) 3 months, and (d) 6 months. From the top to the bottom are visible phyllosilicates, gel layer, and pristine glass. Some phosphates are present on (c). Gold coating at the external surface and platinoids in the gel layer are observed on (d).

(iii) a phyllosilicate-like layer that follows the exact shape of the glass or the gel surface and reaches a thickness of around 1 μm after 6 months of alteration.

Planarity and good parallelism of the different interfaces allowed us to perform ion microprobe depth profiles with a good depth resolution. The observations also led to the location of the different interfaces. In the following, all the secondary products that develop at the surface will be called secondary phases or phyllosilicates without distinction because phosphates are very scarce.

3.1.3. Elemental depth profiles

Elemental ion microprobe in-depth profiles were performed for hydrogen, boron, alkalis (Li, Na, and Cs), alkaline-earths (Ca, Sr, and Ba), aluminium, and transition

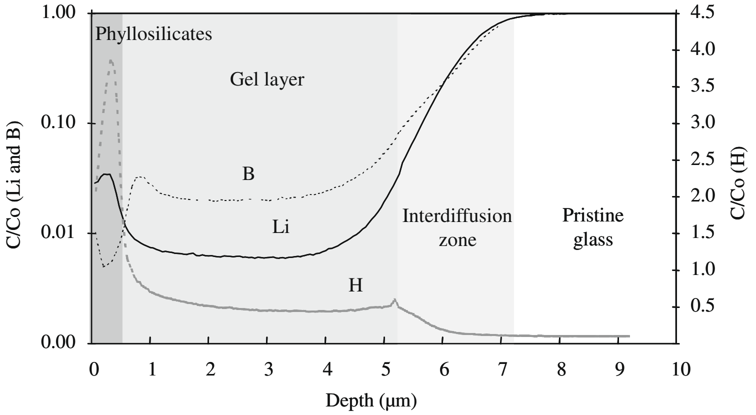

Fig. 6. Boron, lithium, and hydrogen concentrations vs. depth for a glass (Ce44) altered after 3 months. The different grey zones show the phyllosilicates, the gel layer, the interdiffusion zone, and the pristine glass. Concentrations are normalised to the pristine glass composition (C/C_0).

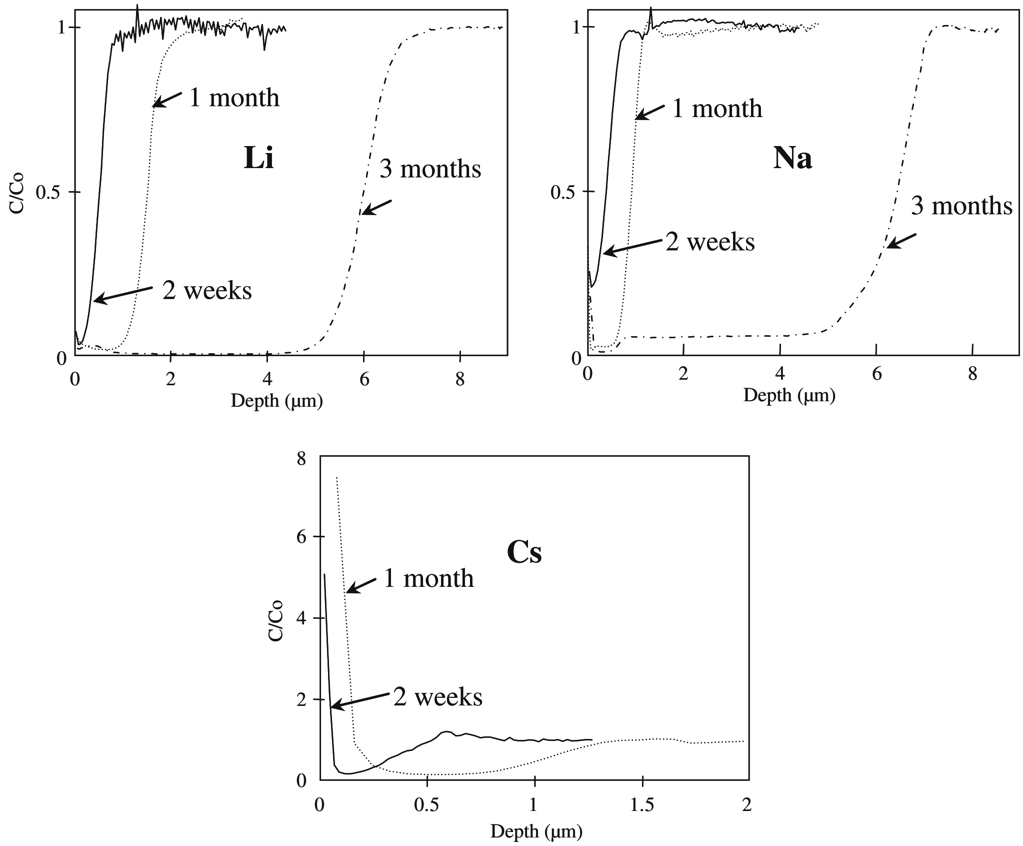

Fig. 7. Depth profiles of alkalis (Li, Na, Cs) performed in the altered layers developed after 2 weeks, 1 month, and 3 months (except for Cs). Concentrations are normalised to the pristine glass composition (C/C_0).

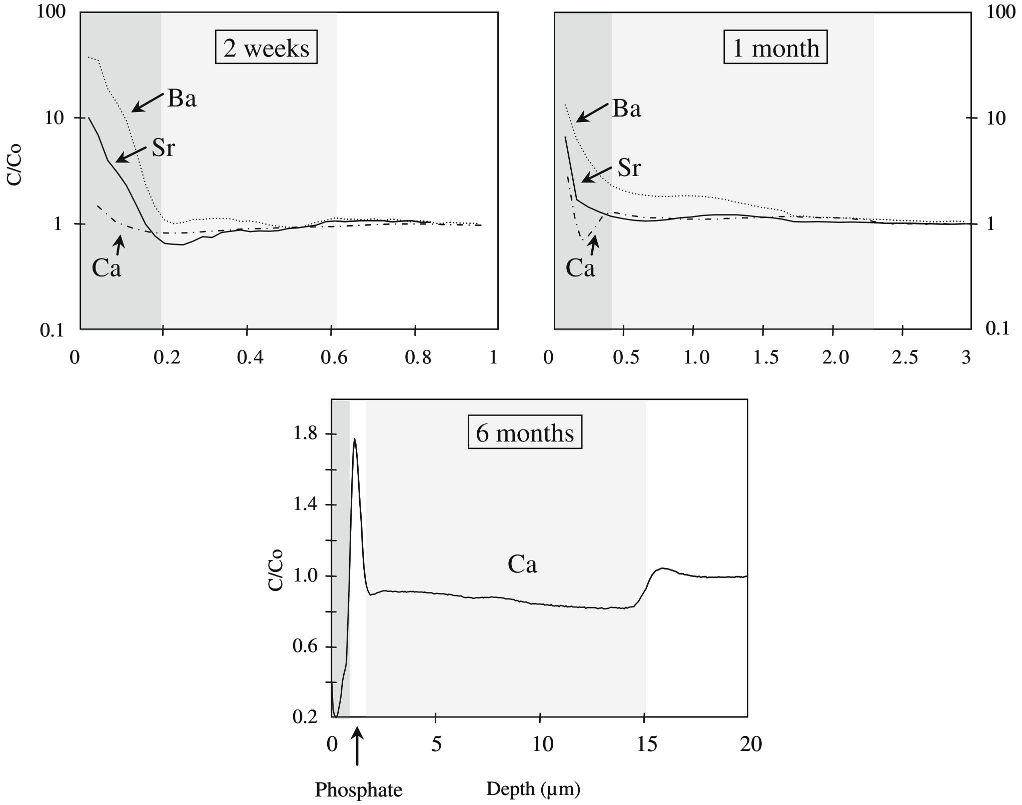

Fig. 8. Depth profiles of alkaline-earth elements (Ca, Sr, and Ba) performed in glasses altered after 2 weeks, 1 month, and 6 months. Concentrations are normalised to the pristine glass composition (C/C_0).

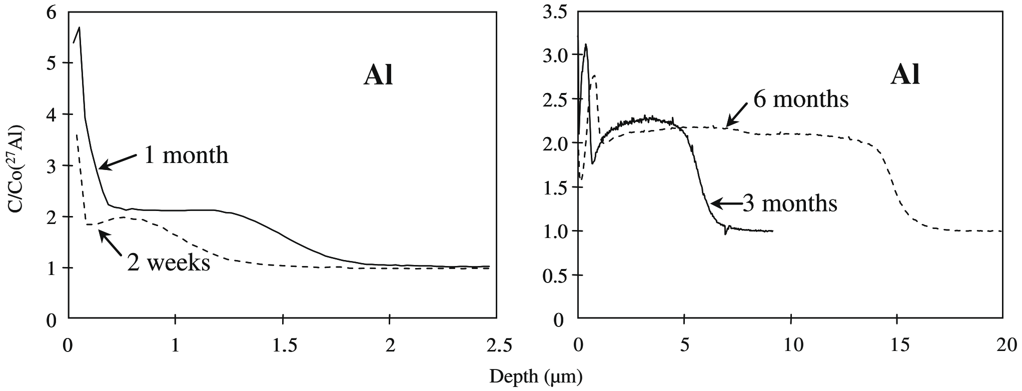

Fig. 9. Depth profiles of aluminium performed in glasses altered after 2 weeks, 1 month, 3 months, and 6 months. Concentrations are normalised to the pristine glass composition (C/C_0).

elements (Cr, Mo, Fe, Ni, Zn, and Zr) for various durations of alteration. They are similar whatever the considered samples (La54, Ce44, and Nd55).

Depth profiles of boron, lithium, and hydrogen are presented in Fig. 6. The borders of the three zones previously identified by SEM (phyllosilicates, gel, glass) are marked by breaks in the profile slope. The pristine glass in the right side displays high B and Li concentrations and a low H content. The decrease of B and Li contents (by one order of magnitude) as well as the anti-correlated increase of H content (by a factor 5) mark the presence of an interdiffusion zone (Houser et al., 1980; Lanford et al., 1979) (between 5.2 and 7 µm). This zone is larger than the mixing zone due to the depth resolution of the ion microprobe, but for this reason its thickness cannot be accurately assessed. The gel layer (0.5–7 µm) shows low constant concentrations for B and Li. Close to the free surface, between 0 and ~0.5 µm, hydrogen and lithium enrichments are observed together with a boron depletion likely corresponding to the secondary products that develop at the surface of the glass (mainly phyllosilicates). The high amount of hydrogen close to the free surface shows a strong hydration of the secondary products in this zone. A peak in the H profile close to the 'gel/pristine glass' interface is also observed.

Li, Na, and Cs depth profiles are presented after 2 weeks, 1, and 3 months of alteration (Fig. 7). Alkalis show profiles similar to that of boron with a strong depletion in the gel layer in agreement with previous studies (e.g. Lanford et al., 1979; Smets and Lommen, 1982). However, Cs, Na, and in less extent Li (Figs. 6 and 7) are present in the external zone of the altered layer suggesting their preferential incorporation in the phyllosilicates.

Alkaline-earths profiles are plotted after 2 weeks, 1, and 6 months of alteration (Fig. 8). The profiles obtained after the two shorter durations allow the comparison of Ca, Sr, and Ba behaviours. As predicted from leachate analyses, Ca, Sr, and Ba are less depleted in the altered layer than alkalis. Ba shows a relative higher concentration in the gel layer than in the pristine glass. Ba and Sr are strongly partitioned in the surface products while Ca shows enrichment at the interface between the gel layer and the phyllosilicates corresponding to the calcium and REE phosphates observed with SEM (Fig. 5c).

Al is relatively enriched in the gel layer compared to the pristine glass (Fig. 9), suggesting that Al remains almost entirely on the gel layer. The higher concentration close to the free surface is likely to reflect the presence of phyllosilicates.

The behaviour of metals (Zn, Ni, Cr, Zr, Fe, and Mo after 2 weeks and 1 month) is given in Fig. 10. Zn and Ni profiles are similar. They are depleted in the gel layer and enriched close to the free surface (in the secondary phases). Fe, Zr, and Cr are relatively enriched throughout the altered layer with high concentrations near the free surface, except for zirconium that is relatively insoluble and mainly

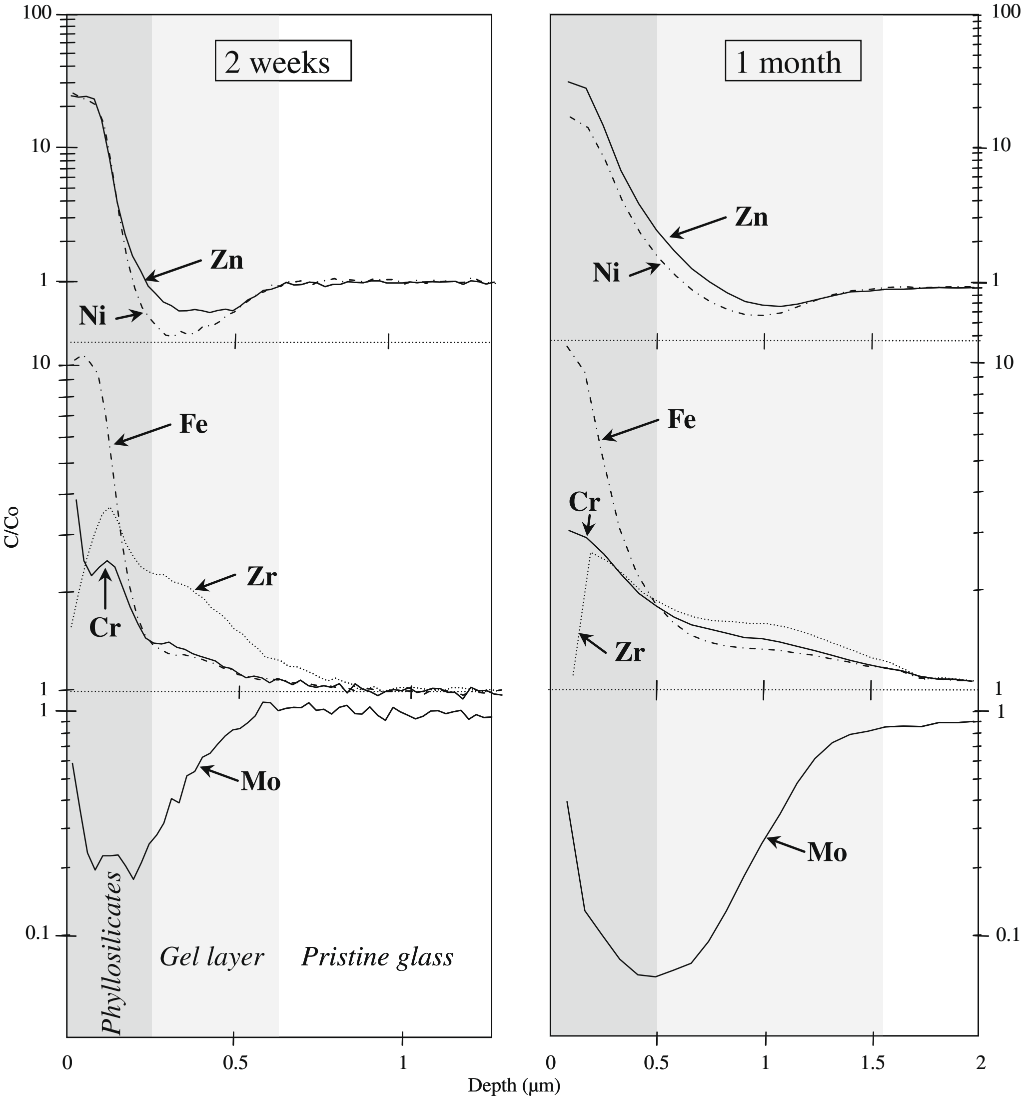

Fig. 10. Depth profiles of metals (Cr, Fe, Ni, Zn, Zr, and Mo) performed in glasses altered during 2 weeks and 1 month. Concentrations are normalised to the pristine glass composition (C/C_0).

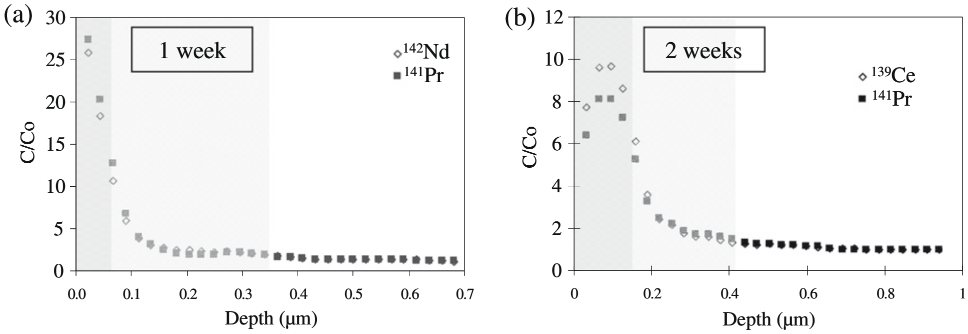

Fig. 11. Depth profiles of REE performed in (a) Nd55 after 1 week of alteration and (b) Ce44 after 2 weeks of alteration. Concentrations are normalised to the pristine glass composition (C/C_0).

present in the gel. Mo has a depth profile similar to that of alkalis in agreement with data from the solution.

REE profiles are given in Fig. 11 for the major REE of Nd55 and Ce44 glasses as well as praseodymium at 1 week and 2 weeks. For both glasses the major REE has the same behaviour than Pr. REE are partly retained within the gel and are also incorporated in phyllosilicates and in phosphates present at the surface of the altered glass. It is of note that the three glasses were altered in the same solution. However, the major REE present in one glass is absent in the gel of other glasses.

3.2. Isotopic analyses

3.2.1. Silicon in solution

The ^{29}Si/^{28}Si ratio measured from the initial solution (^{29}Si/^{28}Si = 1.07) is nominally equivalent to the theoretical value (1.08). The evolution of the silicon isotopic ratios and concentrations with time (Fig. 12 and Table 3) are anti-correlated. During the 20 first days Si concentration increases up to ~30 mg/l, whereas ^{29}Si/^{28}Si ratio decreases from 1.07 to 0.47. Then a steady state is reached for 80 days. A decrease of Si content and an increase of the

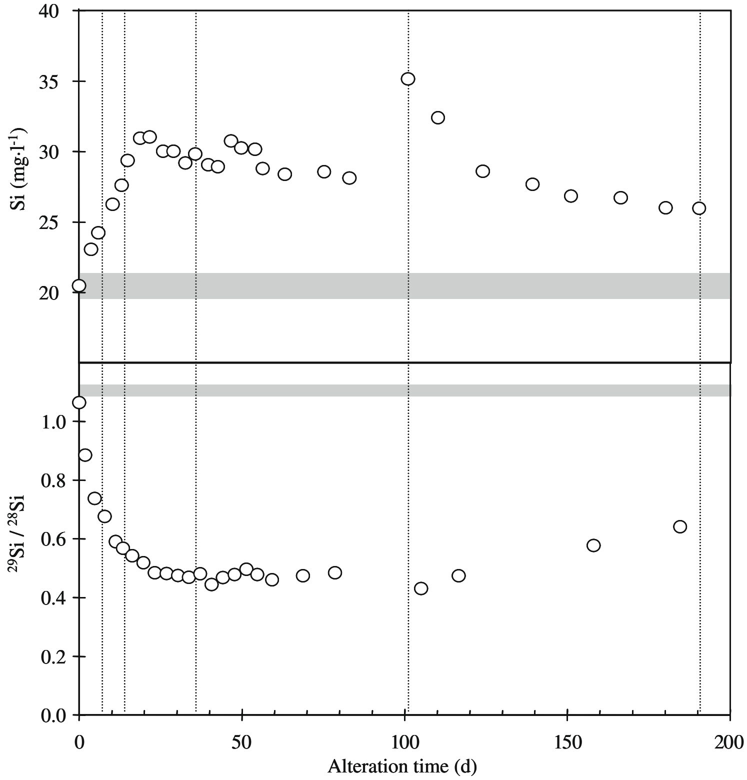

Fig. 12. Evolution of silicon concentration and isotopic ratio ^{29}Si/^{28}Si in the leachate with time of alteration. The isotopic analyses have a precision better than 1% whereas elemental analyses of silicon have a precision of 5%. Grey horizontal lines correspond to the initial silicon concentration and isotopic ratio of the solution, respectively.

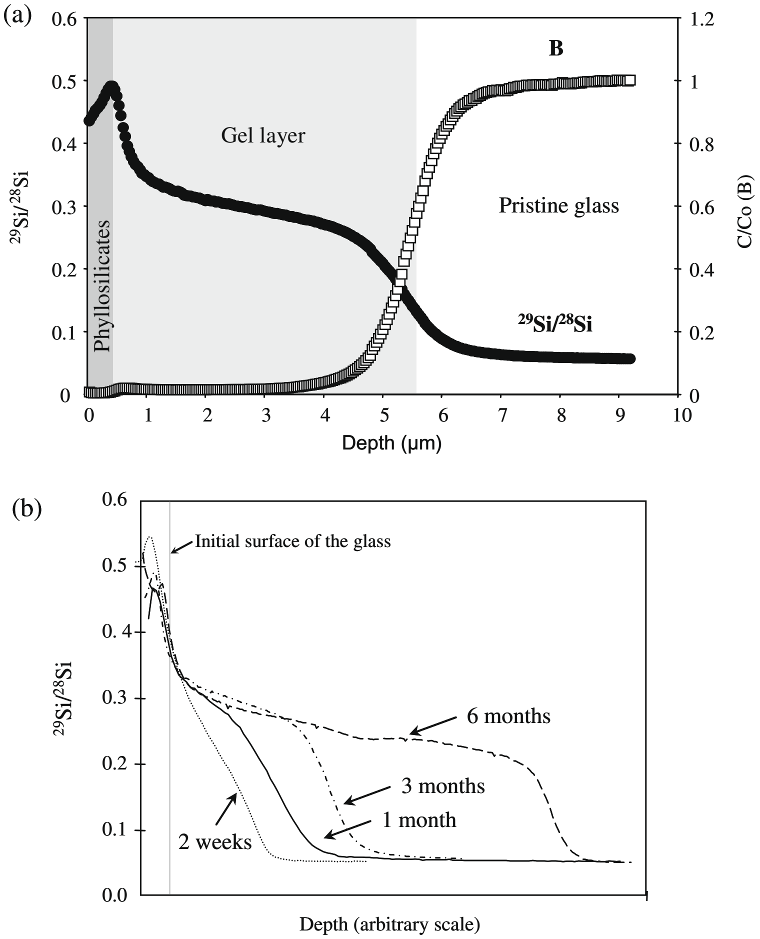

Fig. 13. (a) Isotopic depth profiles ($^{29}Si/^{28}Si$) performed in a glass (Ce44) altered after 3 months compared to that of boron ($C/C_0{}^{11}B$) for the localisation of the different layers. The dark grey zone corresponds to the phyllosilicates and the pale grey zone to the gel layer. (b) Isotopic depth profiles ($^{29}Si/^{28}Si$) at different alteration times (2 weeks, 1, 3, and 6 months). The depth was changed for profiles comparison.

isotopic ratio begin around 100 days and occur until the end of experiment, which can be related to the S/V variations caused by sampling (vertical dashed lines in Fig. 12) and the experimental problem at 100 days (stop of the peristaltic pump).

3.2.2. *Si and O in the altered glass*

Whatever the duration of alteration, the variations of $^{29}Si/^{28}Si$ as a function of depth follow a sigmoidal profile (Fig. 13b). The depth of ^{29}Si penetration in the glass is 0.3 µm after 1 week and increases up to 15 µm after 6 months of alteration. The highest isotopic ratios are measured close to the free surface of the glass and diminish with depth. This depletion occurs in three steps corresponding to three changes of slope delimiting the different phases. Fig. 13a shows the variations of $^{29}Si/^{28}Si$ and boron in a glass (Ce44) altered for 3 months. The boron profile allows the determination of the different interfaces and thus the location of the different layers: the phyllosilicates close to the free surface, the gel layer, and the pristine glass. The changes of slope observed on the $^{29}Si/^{28}Si$ profiles actually correspond to changes of phase. The first positive slope corresponds to the phyllosilicate layer and the inner zone gives the isotopic ratio of the gel layer. The different interfaces are probably affected by mixing effects due to the in-depth resolution. Fig. 13b shows that the outermost part of the gel layer has a $^{29}Si/^{28}Si$ ratio between 0.30 and 0.35 right from two weeks of alteration and this ratio does not evolve with increasing alteration time.

SIMS depth profiles of $^{18}O/^{16}O$ were also performed at different times (Fig. 14). The oxygen profiles present shapes comparable to the silicon profiles although the lower isotopic gradient between glass and leaching solution makes the profiles less pronounced than for silicon. It is also of note that although the oxygen isotopic signatures of the altered glasses are modified by the primary O^- beam (mainly $^{16}O^-$) during the SIMS measurements, these isotopic data allow distinction between the phyllosilicates and the gel. Indeed, the external layer is characterised by the highest $^{18}O/^{16}O$ ratios while the inner layer presents intermediary values between solution and glass. For all the durations of alteration the depth of oxygen penetration is equal to that of the silicon.

4. DISCUSSION

4.1. The distribution of elements between the different alteration layers

In these experiments four different alteration layers were characterised: phyllosilicates, phosphates, and gel, and "interdiffusion zone" at the interface with pristine glass. The evolution of the thickness of these layers over time has been deduced not only from the characterisation of altered glass samples via SIMS depth profiles and SEM observations of cross-sections, but also from solution analyses via the calculation of the equivalent thickness for boron (Fig. 15). The good agreement between the different data validates the analyses. The mean alteration rate deduced from the altered layer thickness is around 0.07 µm/day (0.075 µm/day from SEM observations, 0.066 µm/day from *EE*(*B*) and 0.076 µm/day from SIMS depth profiles).

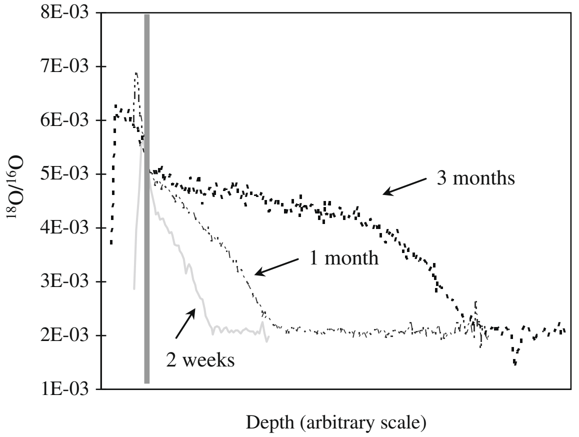

Fig. 14. Isotopic depth profiles (^{18}O/^{16}O) performed in a glass (Ce44) at different alteration times (2 weeks, 1, and 3 months).

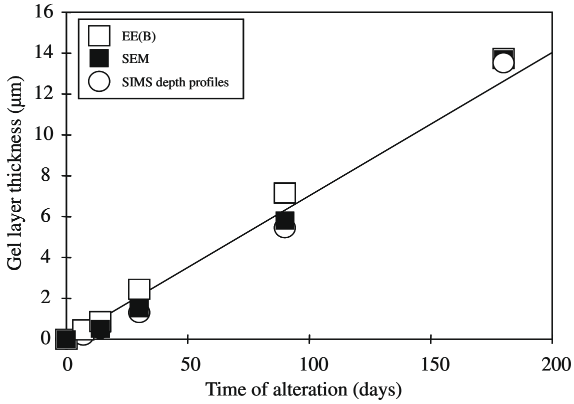

Fig. 15. Gel layer thickness (in µm) as a function of alteration time (in days) determined from solution analysis (*EE*(*B*)), SEM observations, and SIMS depth profiles.

Normalised elemental mass losses *NL*(*i*) were calculated from Li, Na, Cs, Mo, B, Ca, Sr, and Si concentrations. The evolution of *NL*(*i*) as a function of alteration time (Fig. 16) are linear. But the variation of the dissolution rates (Table 4) between different elements shows clearly that the dissolution of SON68 glass is non-stoichiometric in this experiment. The most leachable elements such as Mo, Li, B, Na, and Cs have dissolution rates close to 0.2 g m^{-2} d^{-1}. Ca dissolution rates is below that of alkalis ($\sim$ 0.1 g m^{-2} d^{-1}) and similar to that of silicon.

However, the behaviour of the different glass elements depends not only on the release in solution linked to their structural role in the glass structure (network forming, modifying or charge compensating cations), but also on their affinity for the different alteration phases (solubility, retention, ion size). To classify the elements as a function of their retention in the secondary products, retention factors were calculated from the release of boron, one of the most leachable elements, after 6 months of alteration. The different retention factors are presented in Table 5. For elements with concentrations under the detection limits (i.e. Al, Fe, P, REE, and Zr) they were calculated assuming that concentrations are at least equal to the detection threshold. The factors given for these elements are thus under-estimated. Boron and alkalis (Na, Li, Cs) are mainly present in solution ($f_i < 15\%$). Alkalis are leached by an interdiffusion or ion exchange process with hydrogen species (H^+, H_3O^+, H_2O) in solution (Rana and Douglas, 1961a,b; Doremus, 1975; Lanford et al., 1979; Dran et al., 1989; McGrail et al., 2001; Ferrand et al., 2006), which is supported by the H-alkalis anti-correlated SIMS depth profiles. A part of Cs, and probably Na, is incorporated in the phyllosilicates ($f_i > 0\%$). For Cs, Berger et al. (1988) suggested

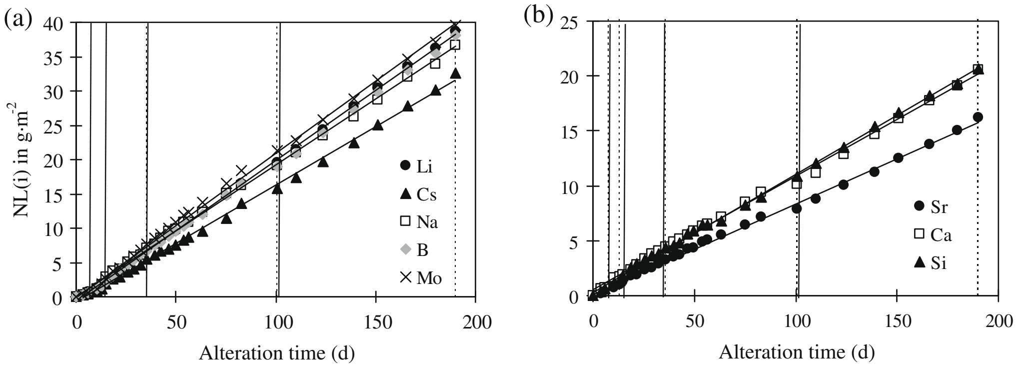

Fig. 16. Normalised elemental mass loss (NL_i) in g m^{-2} d^{-1} as a function of alteration time (in days). (a) Alkalis (Li, Na, and Cs) and mobile elements (Mo and B). (b) Alkaline-earth elements (Ca and Sr) and Si. The dashed lines correspond to glass monoliths sampling.

Table 4
Elemental dissolution rates r determined from the $NL(i) = f(t)$ trends between 0 and 190 days of alteration. The determination coefficients R^2 are given for each fit.

	Mo	Li	B	Na	Cs	Si	Ca
r (g m^{-2} d^{-1})	0.210	0.204	0.201	0.192	0.170	0.107	0.103
R^2	0.998	1.000	0.999	0.999	0.999	0.999	0.997

Table 5
Mean retention factors of elements in the altered layers f_i (in %) after 6 months of alteration. They were calculated from normalised mass loss of boron, one of the most leachable elements. For Al, Fe, P, Zr, and REE the retention factor was calculated assuming that concentrations are at least equal to the detection threshold. REE correspond to La, Ce, Nd and Pr.

Elements	f_i (%)
Li	≈0
Mo	≈0
Na	≈3
Cs	≈15
Ca	≈45
Sr	≈55
Si	≈45–55
Al	⩾55
Ba	≈90
P	⩾98
Cr	≈70
Fe	⩾85
Ni	⩾97
Zn	≈97
Zr	≈100
U	≈95
REE	≈100

an exchange mechanism with the exchangeable cations of clays because of the dependency of the mechanism on the temperature and on the nature of the mineral. The high dissolution rate of boron despite its network former role in the glass is understandable considering that boron in tetrahedral position is charge compensated by alkalis that are sensitive to leaching (Tovena et al., 1994) and that boron is very soluble, contrary to aluminium at alkaline pH (Angeli et al., 2006). The departure of charge compensators by leaching favours the breaking of Si–O–B bonds (Geneste et al., 2006). Molybdenum has the same behaviour as Mo is a modifier cation and is relatively soluble like B. Ca, Sr, Si, and Al are the main constituents of the gel. They are present in solution ($f_i \sim 50\%$) because they are leached by a dissolution process. Their behaviour is congruent (Fig. 16). Zr is mainly present in the gel layer due to its very low solubility (Arab et al., 2008). Galoisy et al. (1999) and Angeli et al. (2008) showed that Zr is 6-fold coordinated and conserves a similar local structural role in the gel. Angeli et al. (2008) also observed that Ca remains in the gel as a Zr charge compensator. Ca, Sr, Si, Al, and Ba are also precipitated in the secondary phases, mainly in phyllosilicates and in phosphates for calcium (Gin et al., 2000). The transition elements Fe, Cr, Zn, and Ni are known to precipitate in the phyllosilicates (Frugier et al., 2008) or as (oxy)hydroxides (Abrajano et al., 1990; Petit et al., 1990; Michaux et al., 1992). In the first days of alteration Zn and Ni are under colloidal form (Fig. 3e). After 105 days, their concentrations in solution are low and non-colloidal due to the development of secondary phases that incorporated them. Uranium and REE are strongly retained in the alteration layers ($f_i \sim 100\%$), especially in the clay minerals, as noted by Daux et al. (1994) for basaltic glass. The mechanisms of retention of actinides and REE are mainly sorption and precipitation (Ames et al., 1982; Berger, 1992; Ménard et al., 1998; Advocat et al., 2001). The distribution of elements in the different alteration layers are summarized in Fig. 17.

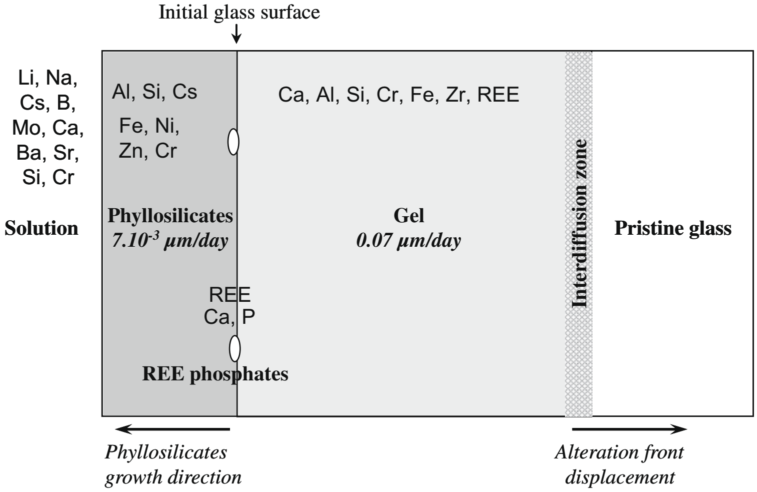

Fig. 17. Distribution of the glass elements in the different alteration layers for a SON68 glass altered at 90 °C for 6 months.

4.2. Isotopic tracing of alteration and implications on the formation of alteration layers

4.2.1. Exchange between glass and solution

Analyses of isotopic and elemental composition of silicon in solution during time (Fig. 12) showed that isotopic exchanges between glass and solution occur from the beginning of glass alteration. In order to quantify such exchanges, factors of enrichment ($F(X)$ in %) (Eq. (5)) were calculated from Si concentrations (Table 3) and isotopic ratios ($^{29}Si/^{28}Si$, Table 3 and $^{30}Si/^{28}Si = 0.0335$). The factor of enrichment for ^{29}Si is calculated from ^{29}Si* concentrations corrected by deducing the contribution of the glass:

$$\begin{aligned} ^{29}Si &= {}^{29}Si* - \frac{^{29}Si}{^{28}Si} \cdot (^{28}Si - {}^{28}Si_i) \\ &= {}^{29}Si* - 0.051 \cdot (^{28}Si - {}^{28}Si_i) \end{aligned} \quad (7)$$

These factors correspond to the variation of silicon (Si_{total}, ^{28}Si, or ^{29}Si) relative to the initial solution. Fig. 18 shows that total silicon and ^{28}Si are enriched in solution, by 50 and 100%, respectively, during the first 20 days of alteration and reach a steady state for 80 days. Then they decrease according to the S/V variations. These results show that the dissolution of the glass rich in ^{28}Si compared to the leaching solution ($^{29}Si/^{28}Si = 1.07$ in the initial solution and 0.05 in the glass) leads to the release of ^{28}Si in solution. Therefore, the ^{28}Si increases in solution during the first 20 days. However, $F(^{29}Si)$ decreases for ~30 days to reach a value of –20% corresponding to a ^{29}Si loss from the solution. It shows that the silicon present in the solution contributes to the formation of the gel. To conclude, Si_{total} analyses in solution reveal only a silicon flow coming from the glass. But isotopic analyses demonstrate that this flow rate is made of ^{28}Si contribution due to the glass dissolution together with a penetration of ^{29}Si from the solution to the altered zone, which explains its impoverishment in the solution.

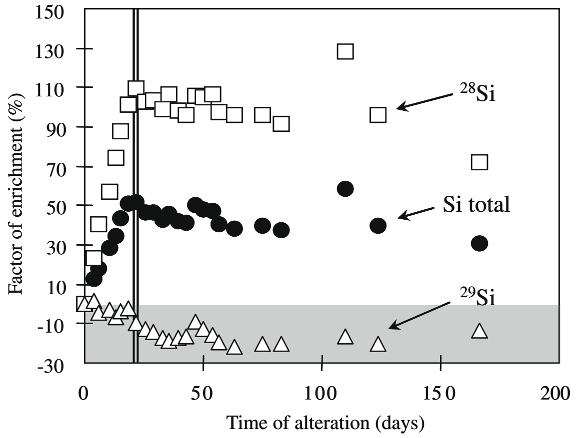

Fig. 18. Enrichment factors (%) in the solution of total silicon, ^{28}Si, and ^{29}Si. The double vertical line corresponds to a steady state reached after 20 days of alteration.

4.2.2. Alteration layers formation mechanisms

Fig. 19a represents silicon isotopic profiles after 1, 3, and 6 months of alteration that are adjusted considering that the initial free surface of the glass (before alteration) is located at a depth corresponding to the $^{29}Si/^{28}Si = 0.5$ (Fig. 13), i.e. the isotopic value of the leaching solution at steady state (Fig. 12). It shows that the phyllosilicate layer becomes thicker during the time: from 0.06 μm (1 month) to 0.9 μm (6 months) in agreement with SEM observations. Fig. 19b displays the evolution of $^{29}Si/^{28}Si$ between 1 and 6 months of alteration. The increase of the $^{29}Si/^{28}Si$ ratio in the phyllosilicates during the alteration is consistent with the increase in the solution. It demonstrates that the precipitated phyllosilicates have recorded the isotopic signatures of the solution as they have the same isotopic signatures and so the same evolution. On the contrary, Fig. 19a and Fig. 13 for Si as well as Fig. 14 for O show that the gel has an intermediate signature between the solution and the pristine glass. The gradient (sigmoid profile) between both signatures suggests diffusion processes.

These observations made from the isotopic systems $^{29}Si/^{28}Si$ and $^{18}O/^{16}O$ indicate that two different mechanisms are responsible for the formation of phyllosilicates and gel layer. The phyllosilicates are formed by dissolution/precipitation mechanisms. Elements are released in solution by hydrolysis and then precipitate as secondary phases when thermodynamic saturation is reached. Therefore they record the same isotopic signature than the solution. The growth of this layer occurs toward the outside.

The gel cannot be considered as a simple residual glass layer resulting from the selective dissolution of the most mobile elements (mainly network modifying cations). Indeed, the gel layer would keep the isotopic signatures of the pristine glass. The results of this study substantiate the hypothesis of the gel formation by hydrolysis/condensation reactions. First, the REE tracing showed that the major REE of one glass is present neither in the gel, nor in the phyllosilicates at the surface of the other glasses. This absence of transfer between glasses suggests that REE are not completely dissolved in solution but either reorganised in situ in the gel and/or trapped in the secondary phases due to their low solubility. These results are consistent with experiments carried out by Berger et al. (1994) on basalt glass at 300 °C. Moreover, the isotopic signatures of the gel ($^{29}Si/^{28}Si$, $^{18}O/^{16}O$) are intermediate between the solution (and thus the precipitated secondary phases) and the pristine glass. The gel is not at thermodynamic equilibrium with the solution. Besides, the contribution of both glass and solution to the Si isotopic signature reveals constant exchange between the solution and the gel layer during its formation. Some authors have examined the incorporation of ^{18}O into dissolving glass or mineral (Westrich et al., 1989 and references herein). Bunker et al. (1988) and Westrich et al. (1989) suggested hydrolysis and condensation reactions in feldspar and glass, respectively (≡ refers to glass or mineral matrix):

$$\equiv Si{-}^{16}O{-}Si \equiv + H_2{}^{18}O \rightarrow \equiv Si{-}^{16}O{-}H + H{-}^{18}O{-}Si \equiv \text{ (hydrolysis reaction)} \quad (8)$$

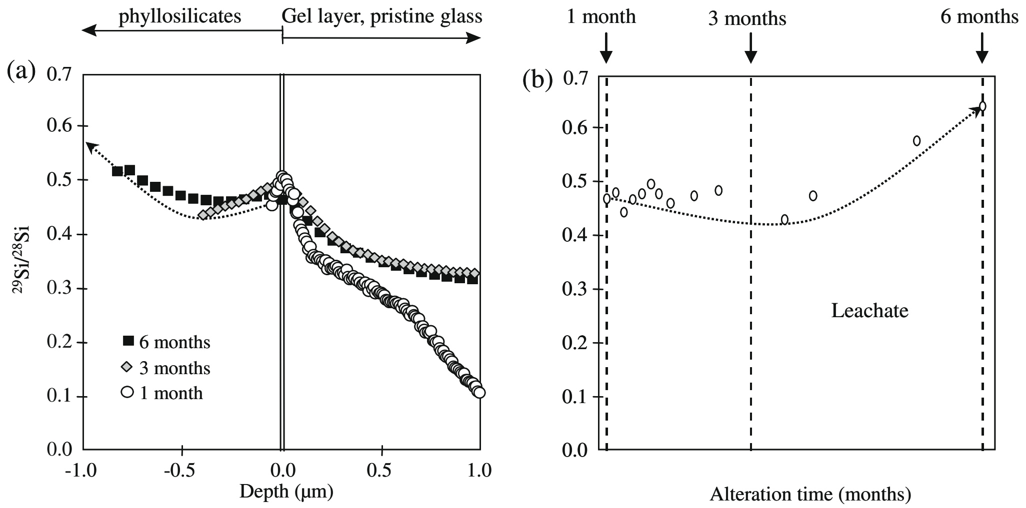

Fig. 19. (a) Isotopic depth profiles ($^{29}Si/^{28}Si$) performed in the phyllosilicates and in the external part of the gel layer on glasses altered during 1 month, 3 months, and 6 months. The depth origin ($x = 0$, double vertical line) is determined from a $^{29}Si/^{28}Si$ ratio equal to 0.5. (b) Evolution of isotopic ratios ($^{29}Si/^{28}Si$) in the solution with alteration time.

$$\equiv \mathrm{Si{-}^{16}O{-}H} + \mathrm{H{-}^{18}O{-}Si} \equiv \rightarrow \equiv \mathrm{Si{-}^{18}O{-}Si} \equiv + \mathrm{H_2{}^{16}O} \text{ (condensation reaction)} \tag{9}$$

The hydrolysis of siloxane bonds in $H_2{}^{18}O$ implies the formation of silanols groups that can condense to form siloxane groups enriched in ^{18}O. On the same way, silicon exchange could be explained by the following reactions (Bunker, 1987):

$$\equiv \mathrm{{}^{28}Si{-}O{-}{}^{28}Si(OH)_3} \equiv + \mathrm{OH^-} \rightarrow \equiv \mathrm{{}^{28}Si{-}O^-} + \equiv \mathrm{{}^{28}Si(OH)_4} \text{ (hydrolysis reaction)} \tag{10}$$

$$\equiv \mathrm{{}^{28}Si{-}O^-} + \mathrm{{}^{29}Si(OH)_4} \rightarrow \equiv \mathrm{{}^{28}Si{-}O{-}{}^{29}Si(OH)_3} \equiv + \mathrm{OH^-} \text{ (condensation reaction)} \tag{11}$$

The hydrolysis of siloxane bonds implies the formation of silanol groups containing mainly ^{28}Si (natural isotopic abundance). These silanol groups polymerise with dissolved silica ($H_4{}^{29}SiO_4$ or $H_3{}^{29}SiO_4{}^-$ depending on the pH) to form siloxane groups enriched in ^{29}Si. These mechanisms imply that the silicon retention in the gel cannot be modelled as a passive process but as an active condensation process that remobilizes elements in solution, especially ^{29}Si et ^{18}O.

4.3. Comparison with aluminosilicate glass alteration and implications for glass alteration modelling

Basaltic glasses have been extensively studied because of their influence on global mass element budget (e.g. Staudigel and Hart, 1983) and in the context of analogy with nuclear glass (e.g. Ewing, 1979, 2001; Lutze et al., 1985; Techer et al., 2000, 2001; Crovisier et al., 2003). The characterised alteration zones consist of ‘palagonite’ and crystallised secondary phases (smectites, zeolites…) (Furnes, 1984; Zhou and Fyfe, 1989; Jercinovic et al., 1990; Stroncik and Schmincke, 2001). The palagonite composition is very similar to the nuclear glass gel because it is an amorphous layer at the interface with the pristine glass. Palagonite composition is also close to that of nuclear glass gel as it is rich in Si, Al, Fe, and Ca. Differences of composition (Mg and Ti in palagonite and Zr and Cr in nuclear glass gel) result from differences in the initial glass composition. Smectites are observed on both nuclear and basaltic glasses. Zeolites are generally present on old altered basaltic glass samples (>1 My) (Crovisier et al., 2003). Therefore, alteration phenomenology is very similar for nuclear and aluminosilicate glasses.

Several arguments are in favour of the analogy of boro- and aluminosilicate glass alteration mechanisms. In the same way, palagonite is not a residual glass skeleton because its isotopic signature (^{18}O) is different from the glass (Le Gal et al., 1999). From a chemical point of view, Le Gal et al. (1999) note a change of oxidation state for iron, which indicates a relative mobility of this element. Moreover, palagonite is a metastable phase whose composition is close to these of smectites. Zhou et al. (2001) observed that palagonite is progressively replaced by crystallised smectites. However, it is frequently assumed that palagonite is formed by dissolution/precipitation reactions (e.g. Crovisier et al., 1987, 2003; Zhou and Fyfe, 1989; Jercinovic et al., 1990; Daux et al., 1994; Stroncik and Schmincke, 2001). To explain this absence of thermodynamic equilibrium, Dibble and Tiller, 1981 and Steefel and Van Cappellen, 1990 advanced the Ostwald step rule (or law of stages) that assumes the precipitation of a more soluble and less stable phase and its replacement by a series of progressively more stable phases. But hydrolysis/condensation reactions can also be advanced to explain the formation of palagonite. The preferential removal of alkalis and alkaline-earths from the glass leads to a leached layer. This layer will be hydrolysed because replacements of charge compensators by protons break bridging bonds and alter the structure as it is observed for borosilicate glass (Geneste et al., 2006). This favours the formation of a 'gel' layer by local condensation reactions and justifies the absence of thermodynamic equilibrium. This hypothesis is not in contradiction with a later evolution to more stable phases.

The gel formation by hydrolysis/condensation explains why the alteration conditions influence the role of the gel and its degree of protection (Gin et al., 2001). Si saturation in solution (in static conditions or at a low solution renewal rate) favours these reactions and improves the protective effect of the gel. On the other hand, dynamic conditions (high flow rate) can limit these reactions and the gel is therefore less passivating. These reactions involve also that the gel can reorganise and its porosity can evolve (e.g. Rebiscoul et al., 2004; Cailleteau et al., 2008). This link between the texture of the gel and its protective role needs to be understood because it has implications on the understanding and the modelling of long-term alteration kinetics of natural and nuclear glasses. Most of glass alteration kinetics laws are based on an affinity term (e.g. Grambow, 1985; Bourcier et al., 1990; Daux et al., 1997) without considering the gel effect. These laws are unable to accurately model the elemental release in all the alteration conditions. Berger et al. (1994) introduced an empiric coefficient to take into account the gel formation, but this coefficient depends also on alteration conditions. The analytical model of Grambow and Müller (2001) considered the potential protective effect of the gel by a mass transfer resistance for silica in the gel layer. The model of Frugier et al. (2008) and its geochemical application (Frugier et al., 2009) introduced also transport through alteration layers by a diffusion law that controls the release of mobile elements from glass into solution.

5. CONCLUSIONS

The combination of solution analyses, alteration products characterisation, and depth profiles in an altered borosilicate glass led to a complete mass balance and to the partition of elements in the different alteration layers (phyllosilicates, phosphates, and gel). Alkalis, boron, and molybdenum are mobile elements and are preferentially released in solution, except for Cs that can be trapped in the phyllosilicates. Alkaline-earth elements are less mobile and are thus present in the gel as well as the phyllosilicates (and the phosphates, in the case of Ca). Al, Si, and Zr are the main constituents of the gel with Si and Al also the main elements in the phyllosilicate layer. The transition and rare earth elements are mainly trapped in the phyllosilicates and phosphates (REE). Therefore, the distribution of elements depends on their mobility (structural role in the glass), but also on their affinity with respect to secondary phases (solubility). Except mobile elements, most of the elements are partly or totally retained in the alteration layers, which limits their migration in the external environment.

Moreover, the use of powerful isotopic tracers (^{29}Si and ^{18}O) also allowed us to follow the real exchanges between glass and solution and their different contributions to the isotopic signatures of alteration layers. This gives new insights on the alteration mechanisms. Phyllosilicates and phosphates are formed by dissolution/precipitation and the gel is formed by hydrolysis/condensation reactions, which can explain the link between its chemistry and its textural properties. Given the similarity of alteration phenomenology these mechanisms can be extended to aluminosilicate glass. The understanding of alteration mechanisms has implications on the glass alteration kinetics modelling as hydrolysis/condensation reactions lead to the formation of the gel. This layer is not at thermodynamic equilibrium with the solution and evolves with time and alteration conditions. The role of this layer needs to be considered in the models.

ACKNOWLEDGMENTS

We sincerely acknowledge A. Rouiller, L. Marin, A. Kohler, F. Diot, S. Barda, and J. Carignan for analytical and technical assistance. This work was financially supported by the CEA and EDF. Our thanks go to E. Vernaz (CEA/DEN/DTCD) and S. Prené (EDF/EMA). Pr. Casey, J.V. Ryan and two anonymous reviewers are thanked for their comments. This is CRPG contribution # 2051.

REFERENCES

Abrajano T. A., Bates J. K., Woodland A. B., Bradley J. P. and Bourcier W. L. (1990) Secondary phase formation during nuclear waste–glass dissolution. *Clays Clay Min.* **38**, 537–548.

Advocat T., Jollivet P., Crovisier J. L. and del Nero M. (2001) Long-term alteration mechanisms in water for SON68 radioactive borosilicate glass. *J. Nucl. Mater.* **298**, 55–62.

Ames L. L., McGarrah J. E., Walker B. A. and Salter P. F. (1982) Sorption of uranium and cesium by Hanford basalts and associated secondary smectites. *Chem. Geol.* **35**, 205–225.

Angeli F., Delaye J. M., Charpentier T., Petit J. C., Ghaleb D. and Faucon P. (2000) Influence of glass chemical composition on the Na–O bond distance: a 23Na 3Q-MAS NMR and molecular dynamics study. *J. Non-Cryst. Solids* **276**, 132–144.

Angeli F., Charpentier T., Gin S. and Petit J. C. (2001) ^{17}O 3Q-MAS NMR characterization of a sodium aluminoborosilicate glass and its alteration gel. *Chem. Phys. Lett.* **341**, 23–28.

Angeli F., Gaillard M., Jollivet P. and Charpentier T. (2006) Influence of glass composition and alteration solution on leached silicate glass structure: a solid-state NMR investigation. *Geochim. Cosmochim. Acta* **70**, 2577–2590.

Angeli F., Charpentier T., Gaillard M. and Jollivet P. (2008) Influence of zirconium on the structure of pristine and leached soda-lime borosilicate glasses: towards a quantitative approach by ^{17}O MQMAS NMR. *J. Non-Cryst. Solids* **354**, 3713–3722.

Anovitz L. M., Cole D. R. and Riciputi L. R. (2009) Low-temperature isotopic exchange in obsidian: implications for diffusive mechanisms. *Geochim. Cosmochim. Acta* **73**, 3795–3806.

Arab M., Cailleteau C., Angeli F., Devreux F., Girard L. and Spalla O. (2008) Aqueous alteration of five-oxide silicate glasses: experimental approach and Monte Carlo modeling. *J. Non-Cryst. Solids* **354**, 155–161.

Berger G., Schott J. and Guy C. (1988) Behavior of Li, Rb and Cs during basalt glass and olivine dissolution and chlorite, smectite and zeolite precipitation from seawater: experimental investigations and modelization between 50° and 300°C. *Chem. Geol.* **71**, 297–312.

Berger G. (1992) Distribution of trace elements between clays and zeolites and aqueous solutions similar to sea water. *Appl. Geochem.* **7**(Suppl. 1), 193–203.

Berger G., Claparols C., Guy C. and Daux V. (1994) Dissolution rate of a basalt glass in silica-rich solutions: implications for long-term alteration. *Geochim. Cosmochim. Acta* **58**, 4875–4886.

Bourcier W. L., Peiffer D. W., Knauss K. G., McKeegan K. D. and Smith D. K. (1990) A kinetic model for borosilicate glass dissolution based on the dissolution affinity of a surface alteration layer. *Mat. Res. Soc. Symp. Proc.* **176**, 209–216.

Brady P. V. and Gíslason S. R. (1997) Seafloor weathering controls on atmospheric CO2 and global climate. *Geochim. Cosmochim. Acta* **61**, 965–973.

Bunker B. C., Arnold G. W., Day D. E. and Bray P. J. (1986) The effect of molecular structure on borosilicate glass leaching. *J. Non-Cryst. Solids* **87**, 226–253.

Bunker B. C. (1987) Waste glass leaching: chemistry and kinetics. *Mat. Res. Soc. Symp. Proc.* **84**, 493–507.

Bunker B. C., Tallant D. R., Headley T. J., Turner G. L. and Kirkpatrick R. J. (1988) The structure of leached sodium borosilicate glass. *Phys. Chem. Glasses* **29**, 106–120.

Bunker B. C. (1994) Molecular mechanisms for corrosion of silica and silicate glasses. *J. Non-Cryst. Solids* **179**, 300–308.

Cailleteau C., Angeli F., Devreux F., Gin S., Jestin J., Jollivet P. and Spalla O. (2008) Insight into silicate-glass corrosion mechanisms. *Nat. Mater.* **7**, 978–983.

Casey W. H. (2008) Dynamics and durability. *Nat. Mater.* **7**, 930–932.

Crovisier J. L., Honnorez J. and Eberhart J. P. (1987) Dissolution of basaltic glass in seawater: mechanisms and rate. *Geochim. Cosmochim. Acta* **51**, 2977–2990.

Crovisier J. L., Advocat T. and Dussossoy J. L. (2003) Nature and role of natural alteration gels formed on the surface of ancient volcanic glasses (natural analogs of waste containment glasses). *J. Nucl. Mater.* **321**, 91–109.

Daux V., Crovisier J. L., Hemond C. and Petit J. C. (1994) Geochemical evolution of basaltic rocks subjected to weathering: fate of the major elements, rare earth elements, and thorium. *Geochim. Cosmochim. Acta* **58**, 4941–4954.

Daux V., Guy C., Advocat T., Crovisier J. L. and Stille P. (1997) Kinetic aspects of basaltic glass dissolution at 90°C: role of aqueous silicon and aluminium. *Chem. Geol.* **142**, 109–126.

Dessert C., Dupré B., Gaillardet J., François L. M. and Allègre C. J. (2003) Basalt weathering laws and the impact of basalt weathering on the global carbon cycle. *Chem. Geol.* **202**, 257–273.

Dibble W. E. Jr. and Tiller W. A. (1981) Kinetic model of zeolite paragenesis in tuffaceous sediments. *Clays Clay Min.* **29**, 323–330.

Doremus R. H. (1975) Interdiffusion of hydrogen and alkali ions in a glass surface. *J. Non-Cryst. Solids* **19**, 137–144.

Dran J. C., Petit J. C., Trotignon L., Paccagnella A. and Della Mea G. (1989) Hydration mechanisms of silicate glasses: discussion of the respective role of ion exchange and water permeation. *Mat. Res. Soc. Symp. Proc.* **127**, 25–32.

Ewing R. C. (1979) Natural glasses: analogues for radioactive waste forms. *Mat. Res. Soc. Symp. Proc.* **1**, 57–68.

Ewing R. C. (2001) Nuclear waste form glasses: the evaluation of very long-term behaviour. *Mat. Tech. Adv. Perf. Mat.* **16**, 30–36.

Feng X. and Pegg I. L. (1994) A glass dissolution model for the effects of S/V on leachate pH. *J. Non-Cryst. Solids* **175**, 281–293.

Ferrand K., Abdelouas A. and Grambow B. (2006) Water diffusion in the simulated French nuclear waste glass SON 68 contacting silica rich solutions: experimental and modelling. *J. Nucl. Mater.* **355**, 54–67.

Frugier P., Gin S., Lartigue J. E. and Deloule E. (2006) SON68 glass dissolution kinetics at high reaction progress: mechanisms accounting for the residual alteration rate. *Mat. Res. Soc. Symp. Proc.* **932**, 305–312.

Frugier P., Gin S., Minet Y., Chave T., Bonin B., Godon N., Lartigue J. E., Jollivet P., Ayral A., De Windt L. and Santarini G. (2008) SON68 nuclear glass dissolution kinetics: current state of knowledge and basis of the new GRAAL model. *J. Nucl. Mater.* **380**, 8–21.

Frugier P., Chave T., Gin S. and Lartigue J. E. (2009) Application of the GRAAL model to leaching experiments with SON68 nuclear glass in initially pure water. *J. Nucl. Mater.* **392**, 552–567.

Furnes H. (1984) Chemical changes during progressive subaerial palagonitization of a subglacial olivine tholeiite hyaloclastite: a microprobe study. *Chem. Geol.* **43**, 271–285.

Galoisy L., Pélegrin E., Arrio M. A., Ildefonse P. and Calas G. (1999) Evidence for 6-coordinated zirconium in inactive nuclear waste glasses. *J. Am. Ceram. Soc.* **82**, 2219–2224.

Gaucher E. C., Blanc P., Bardot F., Braibant G., Buschaert S., Crouzet C., Gautier A., Girard J. P., Jacquot E., Lassin A., Negrel G., Tournassat C., Vinsot A. and Altmann S. (2006) Modelling the porewater chemistry of the Callovian-Oxfordian formation at a regional scale. *C. R. Geosci.* **338**, 917–930.

Geneste G., Bouyer F. and Gin S. (2006) Hydrogen–sodium interdiffusion in borosilicate glasses investigated from first principles. *J. Non-Cryst. Solids* **352**, 3147–3152.

Gin S., Jégou C. and Vernaz E. (2000) Use of orthophosphate complexing agents to investigate mechanisms limiting the alteration kinetics of French SON 68 nuclear glass. *Appl. Geochem.* **15**, 1505–1525.

Gin S. (2001) Protective effect of the alteration gel: a key mechanism in the long-term behavior of nuclear waste glass. *Mat. Res. Soc. Symp. Proc.* **663**, 207–215.

Gin S. and Mestre J. P. (2001) SON 68 nuclear glass alteration kinetics between pH 7 and pH 11.5. *J. Nucl. Mater.* **295**, 83–96.

Gin S., Ribet I. and Couillard M. (2001) Role and properties of the gel formed during nuclear glass alteration: importance of gel formation conditions. *J. Nucl. Mater.* **298**, 1–10.

Gíslason S. R., Oelkers E. H., Eiriksdottir E. S., Kardjilov M. I., Gisladottir G., Sigfusson B., Snorrason A., Elefsen S., Hardardottir J., Torssander P. and Oskarsson N. (2009) Direct evidence of the feedback between climate and weathering. *Earth Planet. Sci. Lett.* **277**, 213–222.

Grambow B. (1985) A general rate equation for nuclear waste glass corrosion. *Mat. Res. Soc. Symp. Proc.* **44**, 15–27.

Grambow B. and Müller R. (2001) First-order dissolution rate law and the role of surface layers in glass performance assessment. *J. Nucl. Mater.* **298**, 112–124.

Houser C. A., Herman J. S., Tsong I. S. T., White W. B. and Lanford W. A. (1980) Sodium–hydrogen interdiffusion in sodium silicate glasses. *J. Non-Cryst. Solids* **41**, 89–98.

Jégou C., Gin S. and Larché F. (2000) Alteration kinetics of a simplified nuclear glass in an aqueous medium: effects of solution chemistry and of protective gel properties on diminishing the alteration rate. *J. Nucl. Mater.* **280**, 216–229.

Jercinovic M. J., Keil K., Smith M. R. and Schmitt R. A. (1990) Alteration of basaltic glasses from north-central British Columbia, Canada. *Geochim. Cosmochim. Acta* **54**, 2679–2696.

Jollivet P., Angeli F., Cailleteau C., Devreux F., Frugier P. and Gin S. (2008) Investigation of gel porosity clogging during glass leaching. *J. Non-Cryst. Solids* **354**, 4952–4958.

Lanford W. A., Davis K., Lamarche P. and Laursen T. (1979) Hydration of soda-lime glass. *J. Non-Cryst. Solids* **33**, 249–266.

Le Gal X., Crovisier J. L., Gauthier-Lafaye Honnorez J. and Grambow B. (1999) Meteoric alteration of Icelandic volcanic glass: long-term changes in the mechanism. *C. R. Acad. Sci. Paris Earth Planet. Sci.* **329**, 175–181.

Ledieu A., Devreux F., Barboux P., Sicard L. and Spalla O. (2004) Leaching of borosilicate glasses. I. Experiments. *J. Non-Cryst. Solids* **343**, 3–12.

Lutze W., Malow G., Ewing R. C., Jercinovic M. J. and Keil K. (1985) Alteration of basalt glasses: implications for modelling the long-term stability of nuclear waste glasses. *Nature* **314**, 252–255.

Macquet C. and Thomassin J. H. (1992) Archaeological glasses as modelling of the behaviour of buried nuclear waste glass. *Appl. Clay Sci.* **7**, 17–31.

McGrail B. P., Icenhower J. P., Shuh D. K., Liu P., Darab J. G., Baer D. R., Thevuthasen S., Shutthanandan V., Engelhard M. H., Booth C. H. and Nachimuthu P. (2001) The structure of Na_2O–Al_2O_3–SiO_2 glass: impact on sodium ion exchange in H_2O and D_2O. *J. Non-Cryst. Solids* **296**, 10–26.

Ménard O., Advocat T., Ambrosi J. P. and Michard A. (1998) Behaviour of actinides (Th, U, Np and Pu) and rare earths (La, Ce and Nd) during aqueous leaching of a nuclear glass under geological disposal conditions. *Appl. Geochem.* **13**, 105–126.

Michaux L., Mouche E. and Petit J.-C. (1992) Geochemical modelling of the long-term dissolution behaviour of the French nuclear glass R7T7. *Appl. Geochem.* **7**(Suppl. 1), 41–54.

Pederson L. R., Baer D. R., McVay G. L. and Engelhard M. H. (1986) Reaction of soda lime silicate glass in isotopically labelled water. *J. Non-Cryst. Solids* **86**, 369–380.

Petit J. C., Della Mea G., Magontier M. C., Mando P. A. and Paccagnella A. (1990) Hydrated-layer formation during dissolution of complex silicate glasses and minerals. *Geochim. Cosmochim. Acta* **54**, 1941–1955.

Rana M. A. and Douglas R. W. (1961a) The reaction between glass and water. Part 1. Experimental methods and observations. *Phys. Chem. Glasses* **2**, 179–195.

Rana M. A. and Douglas R. W. (1961b) The reaction between glass and water. Part 2. Discussion of the results. *Phys. Chem. Glasses* **2**, 196–204.

Rebiscoul D., Van der Lee A., Rieutord F., Né F., Spalla O., El-Mansouri A., Frugier P., Ayral A. and Gin S. (2004) Morphological evolution of alteration layers formed during nuclear glass alteration: new evidence of a gel as a diffusive barrier. *J. Nucl. Mater.* **326**, 9–18.

Rébiscoul D., Rieutord F., Né F., Frugier P., Cubitt R. and Gin S. (2007) Water penetration mechanisms in nuclear glasses by X-ray and neutron reflectometry. *J. Non-Cryst. Solids* **353**, 2221–2230.

Smets B. M. J. and Lommen T. P. A. (1982) The leaching of sodium aluminosilicate glasses studied by secondary ion mass spectrometry. *Phys. Chem. Glasses* **23**, 83–87.

Smit W., Holten C. L. M. and Stein H. N. (1981) Tritium exchange experiments on thin microporous silica layers. *J. Non-Cryst. Solids* **43**, 279–295.

Staudigel H. and Hart S. R. (1983) Alteration of basaltic glass: mechanisms and significance for the oceanic crust-seawater budget. *Geochim. Cosmochim. Acta* **47**, 337–350.

Steefel C. I. and Van Cappellen P. (1990) A new kinetic approach to modeling water–rock interaction: the role of nucleation, precursors, and Ostwald ripening. *Geochim. Cosmochim. Acta* **54**, 2657–2677.

Stefánsson A. and Gíslason S. R. (2001) Chemical weathering of basalts, southwest Iceland: effect of rock crystallinity and secondary minerals on chemical fluxes to the ocean. *Am. J. Sci.* **301**, 513–556.

Sterpenich J. and Libourel G. (2001) Using stained glass windows to understand the durability of toxic waste matrices. *Chem. Geol.* **174**, 181–193.

Sterpenich J. and Libourel G. (2006) Water diffusion in silicate glasses under natural weathering conditions: evidence from buried medieval stained glasses. *J. Non-Cryst. Solids* **352**, 5446–5451.

Stroncik N. A. and Schmincke H. U. (2001) Evolution of palagonite: crystallization, chemical changes, and element budget. *Geochem. Geophys. Geosyst.* **2**.

Techer I., Advocat T., Lancelot J. and Liotard J. M. (2000) Basaltic glass: alteration mechanisms and analogy with nuclear waste glasses. *J. Nucl. Mater.* **282**, 40–46.

Techer I., Lancelot J., Clauer N., Liotard J. M. and Advocat T. (2001) Alteration of a basaltic glass in an argillaceous medium: the Salagou dike of the Lodève Permian Basin (France). Analogy with an underground nuclear waste repository. *Geochim. Cosmochim. Acta* **65**, 1071–1086.

Tovena I., Advocat T., Ghaleb D., Vernaz E. and Larché F. (1994) Thermodynamic and structural models compared with the initial dissolution rates of SON glass samples. *Mat. Res. Soc. Symp. Proc.* **333**, 595–602.

Tsomaia N., Brantley S. L., Hamilton J. P., Pantano C. G. and Mueller K. T. (2003) NMR evidence for formation of octahedral and tetrahedral Al and repolymerisation of Si network during dissolution of aluminosilicate glass and crystal. *Am. Mineral.* **88**, 54–67.

Valle N. (2000) *Traçage isotopique (^{29}Si et ^{18}O) des mécanismes de l'altération du verre de confinement des déchets nucléaires: SON 68*. Ph.D. thesis, INPL Nancy, France.

Vernaz E. Y. and Dussossoy J. L. (1992) Current state of knowledge of nuclear waste glass corrosion mechanisms: the case of R7T7 glass. *Appl. Geochem.* **7**(Suppl. 1), 13–22.

Verney-Carron A., Gin S. and Libourel G. (2008) A fractured roman glass block altered for 1800 years in seawater: analogy with nuclear glass in a deep geological repository. *Geochim. Cosmochim. Acta* **72**, 5372–5385.

Westrich H. R., Casey W. H. and Arnold G. W. (1989) Oxygen isotope exchange in the leached layer of labradorite feldspar. *Geochim. Cosmochim. Acta* **53**, 1681–1685.

Wolff-Boenisch D., Gislason S. R. and Oelkers E. H. (2006) The effect of crystallinity on dissolution rates and CO_2 consumption capacity of silicates. *Geochim. Cosmochim. Acta* **70**, 858–870.

Zhou Z. and Fyfe W. S. (1989) Palagonitization of basaltic glass from DSDP Site 335, Leg 37: textures, chemical composition, and mechanism of formation. *Am. Min.* **74**, 1045–1053.

Zhou Z., Peacor D. R., Alt J. C., Van der Voo R. and Kao L. S. (2001) TEM study of the alteration of interstitial glass in MORB by inorganic processes. *Chem. Geol.* **174**, 365–376.

Associate editor: William H. Casey

C. R. Geoscience 343 (2011) 237–245

Contents lists available at ScienceDirect

Comptes Rendus Geoscience

www.sciencedirect.com

Petrology, geochemistry (Mineralogy)

The use of natural and archeological analogues for understanding the long-term behavior of nuclear glasses

L'utilisation des analogues naturels et archéologiques pour la compréhension de l'évolution à long terme des verres nucléaires

Guy Libourel [a,*,b], Aurelie Verney-Carron [a], Andreas Morlok [a], Stéphane Gin [c], Jérôme Sterpenich [d], Anne Michelin [e,f], Delphine Neff [e], Philippe Dillmann [e,f]

[a] *CNRS UPR2300, centre de recherches pétrographiques et géochimiques (CRPG), Nancy-université, 15, rue Notre-Dame-des-Pauvres, BP 20, 54501 Vandœuvre-lès-Nancy, France*
[b] *INPL, École nationale superieure de géologie (ENSG), Nancy-université, rue du Doyen-Marcel-Roubault, BP 20, 54501 Vandœuvre-lès-Nancy, France*
[c] *Commissariat à l'énergie atomique, Marcoule, DEN/SECM/LCLT, BP 17171, 30207 Bagnols-sur-Cèze cedex, France*
[d] *G2R, CNRS-UMR 7566, Nancy-université, BP 70239, 54506 Vandœuvre-lès-Nancy cedex, France*
[e] *Laboratoire archéomatériaux et prévision de l'altération LAPA/SIS2 M, CEA and CNRS, Bat 637, CEA Saclay, 91191 Gif/Yvette cedex, France*
[f] *LMC IRAMAT UMR5060 CNRS, France*

ARTICLE INFO

Article history:
Received 10 December 2010
Accepted after revision 7 January 2011
Available online 2 March 2011

Written on invitation of the
Editorial Board

Keywords:
Natural and archeological analogues
Nuclear glasses

Mots clés :
Analogues naturels et archéologiques
Verres nucléaires

ABSTRACT

The knowledge of the long-term behavior of nuclear waste in anticipation of ultimate disposal in a deep geological formation is of prime importance in a waste management strategy. If phenomenological models have been developed to predict the long-term behavior of these materials, validating these models remains a challenge, when considering the time scale of radioactive decay of radionuclides of environmental concern, typically 10^4–10^5 yrs. Here we show how natural or archaeological analogues provide critical constraints not only on the phenomenology of glass alteration and the mechanisms involved, but also on the ability of experimental short-term data to predict long-term alteration in complex environments.

RÉSUMÉ

La connaissance du comportement à long terme des déchets nucléaires dans les conditions d'un stockage géologique profond est un point capital de la stratégie de la gestion des déchets. Même si des modèles phénoménologiques permettent de prédire le comportement à long terme de ces matériaux, leur validation reste toujours un challenge devant la durée de la radioactivité, typiquement de l'ordre de 10^4–10^5 ans. Dans cet article, nous montrons comment les analogues naturels et archéologiques peuvent aider à définir, non seulement la phénoménologie et les mécanismes impliqués lors de l'altération des verres, mais également la capacité des expériences de laboratoire pour prédire l'altération sur le long terme dans des environnements complexes.

---

* Corresponding author.
E-mail address: libou@crpg.cnrs-nancy.fr (G. Libourel).

1631-0713/$ – see front matter © 2011 Académie des sciences. Published by Elsevier Masson SAS. All rights reserved.
doi:10.1016/j.crte.2010.12.004

1. Introduction and methodology

Nuclear energy produces long-lived radioactive waste. Their long-term disposal provides a major challenge for materials science. Waste material has to be stored safely for at least 10^5 yrs, in order to decrease significantly the radioactive dose. Many countries that use nuclear energy resort to the vitrification of the long-lived high-level waste in order to stabilize radionuclides. Due to long timescales, 10^5 to 10^6 yrs, for a significant reduction of waste radioactivity, the option for the management of these wastes is the disposal in a deep geological repository (Fig. 1). In France, the geological formation studied is the Callovian-Oxfordian claystone formation located in the northeastern sector of the Paris basin (Trouiller, 2006). The repository is designed as a redundant multi-barrier system, in order to protect the biosphere from radionuclide dispersion: the waste packages are placed in steel containers and confined by engineered barriers and clay layers (Andra, 2005).

The glass being the first barrier, it is necessary to assess its alteration rates in order to quantify the release of radionuclides. This requires the prediction of the long-term behavior of glass packages under geological repository conditions (Fig. 1). Predictive models of glass alteration are based on the understanding of alteration mechanisms and are parameterized with experimental data (see for instance Frugier et al., 2008; Gin et al., 2008; Grambow, 1985; Grambow and Müller, 2001). Their long-term predictive capacity to assess the nuclear glass lifetime may be validated, by using natural or archaeological analogues (Ewing, 1979, 2001; Petit, 1992). The aim is not only to better constrain the phenomenology of glass alteration and to understand its mechanisms, but also to demonstrate that experimental short-term data are able to predict long-term alteration in complex environments (Fig. 2).

The word "analogy" is coming from the ancient Greek and originally meant proportionality in the mathematical sense (A is to B as C is to D). Reasoning by analogy consists in concluding from the relationship that links two terms (A and B) a property of the relationship that links two other terms (C and D), in a similar relation. If a model based on short-term laboratory data accounts for the phenomenology and kinetics of natural or archaeological glasses altered for long timescales, it improves the confidence in the long-term predictions of the models developed for nuclear glasses.

"Analogous" means similar and not identical. In the case of the French nuclear waste glass, archeological or basaltic glasses are good potential analogues because the alteration phenomenology and the mechanisms involved are generally common to all silicate glasses. In contact with water, silicate glasses suffer the same reactions: i) water diffusion in the glass and ion exchange (between glass modifier cations and hydrogen species) (Chave et al., 2007; Hamilton et al., 2000; McGrail et al., 2001; White and Claasen, 1980), ii) hydrolysis of the glassy network (Si-O-Si, Si-O-Al...) and condensation reactions (Bunker, 1994; Oelkers, 2001; Pelegrin et al., 2010; Valle et al., 2010;) with the formation of a "gel" layer, iii) precipitation of secondary phases (Frugier et al., 2006; Stroncik and Schmincke, 2001; Verney-Carron et al., 2010). The evolution of glass alteration kinetics is also similar and depends on the rate limiting reaction. Three rate regimes can be distinguished (Frugier et al., 2008): i) a maximal "initial rate" that corresponds to the hydrolysis of the glassy network, ii) "the rate drop" due to saturation effects in solution and to the formation of a protective gel layer by hydrolysis/condensation reactions (Cailleteau et al., 2008), iii) the "residual rate" that is very low but not nil due to the diffusion of mobile elements through the alteration layers and the secondary phase precipitation. The objective for understanding the long-term behavior of analogous glasses does not rely on an alteration environment similar to that expected in a geological repository, but rather on the interactions between the glass and its environment (steel, clay minerals, groundwater.), glass composition influencing mainly the alteration kinetics (Verney-Carron et al., 2010a and references therein).

In this article, we present several studies of natural or archaeological analogues to show how understanding the nuclear glass alteration phenomenology has led to the choice of specific analogues and has improved the confidence in long-term glass alteration modeling.

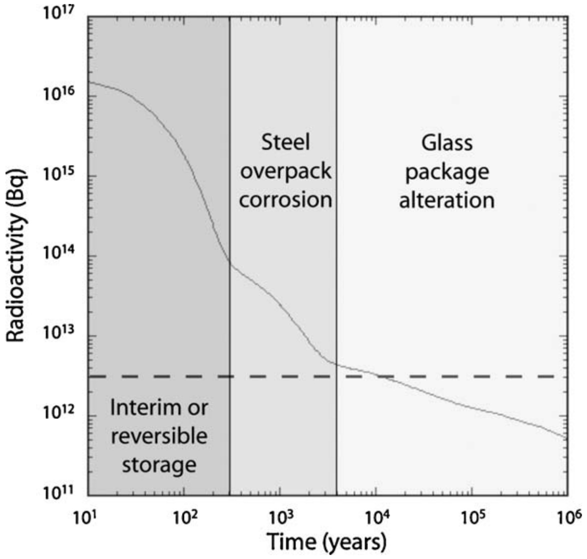

Fig. 1. Temporal evolution of the radioactivity of a nuclear waste after its production. A significant drop occurs after 300 yrs. This explains that nuclear wastes will be stored for this period before their disposal in a deep geological repository. The second drop occurs after 4000 yrs and corresponds to the assessed durability of steel containers. The dashed grey line represents the radioactivity of the quantity of uranium ore necessary to produce the fuel retreated in a glass package. The time after which the radioactivity is under this level is around 10^5 yrs.

Fig. 1. Évolution temporelle de la radioactivité d'un déchet nucléaire après sa production. Une diminution significative apparaît après 300 ans, durée qui correspond à la période de réversibilité du stockage. La durabilité du container en acier est estimée aux alentours de 4000 ans. La ligne grise en pointillé représente la radioactivité du minerai d'uranium nécessaire pour produire le combustible retraité dans le déchet vitrifié. Le temps nécessaire pour abaisser la radioactivité en dessous de ce niveau est de l'ordre de 10^5 ans.

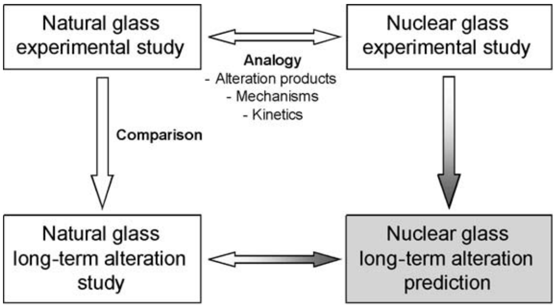

Fig. 2. Principle of the reasoning by analogy applied to the natural or archaeological glass study. If the analogy between natural glass and nuclear glass is demonstrated, then the long-term durability observed for natural glass can be inferred for nuclear glass.

Fig. 2. Principe du raisonnement par analogie. Si l'analogie entre les verres naturels ou archéologiques et les verres nucléaires est établie, alors la durabilité à long terme des verres naturels peut être appliquée aux verres nucléaires.

2. The understanding of alteration mechanisms

2.1. *Alteration of stained glasses: influence of glass composition and weathering conditions*

In the lack of natural borosilicate glasses, well-dated medieval stained glasses provide a good proxy for understanding the processes and kinetics of glass alteration (Macquet and Thomassin, 1992; Sterpenich, 1998; Sterpenich and Libourel, 2001, 2006). Manufactured from natural materials (e.g. washed siliceous sand, limestone, plant ashes, etc.) and colored by transition elements, stained glasses offer a large variety of compositions (i.e., from Na- and Si-rich to K-rich and Si-poor glasses). It is possible to assess how chemical composition controls glass durability and the behavior of minor/trace elements, under natural alteration conditions and over 10^2–10^3 yrs. Depending on their exposure (Fig. 3), stained glasses can also provide a unique way to characterize the effects of weathering conditions on glass alteration (Libourel et al.,

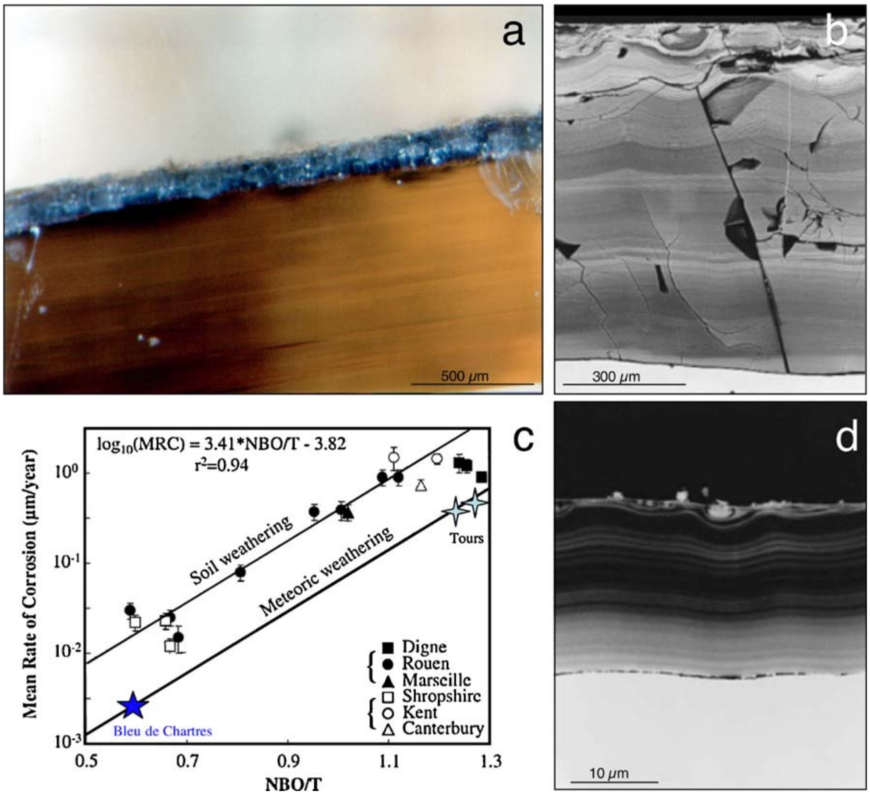

Fig. 3. Alteration of stained glass windows. a) Outside surface of a yellow stained glass from St-Gatien cathedral (Tours, France, 14–15th century), showing a continuous thickness of alteration of 100–150 µm. b) Alteration layer of a green K-rich stained glass excavated from the archeological site of Notre-Dame-du-Bourg church (Digne, France, 13th century). Notice the laminated structure as well as the important thickness of the alteration layer (around 1 mm). c) Mean corrosion rates as a function of the bulk polymerization of the glass. See text for explanations. d) Alteration layer of Na-rich stained glass excavated from the archeological site of the Bishop's palace in Rouen (France, 9th century). The thickness of the alteration layer is an order of magnitude lower than that measured on K-rich glasses (b).

Fig. 3. Altération des verres de vitraux médiévaux. a) Surface extérieure d'un verre jaune potassique de la Cathétdrale St-Gatien (Tours, France, XIV–XV^{e} siècle), montrant une altération continue d'une épaisseur de 100–150 µm. b) Couche d'altération d'un verre vert potassique exhumé du site archéologique de l'église de Notre-Dame du Bourg (Digne, France, XIII^{e} siècle). Noter la lamination et l'épaisseur importante (de l'ordre du 1 mm) de cette couche d'altération. c) Taux moyen d'altération en fonction de la polymérisation globale du verre. (voir explications dans le texte). d) Couche d'altération d'un verre sodique exhumé du site archéologique du Palais episcopal de Rouen (France, IX^{e} siècle). L'épaisseur de la couche d'altération est d'un ordre de grandeur plus faible que celle mesurée sur les verres potassiques (b).

1994): while samples from archaeological sites afford information on alteration by groundwater, stained glass windows are subject to meteoric weathering or to alteration driven by moisture, for outside or inside surfaces, respectively.

Whatever the kind of alteration, stained glasses present traces of corrosion on their surface, including a weathered glass layer (gel) and precipitates. Optical or scanning electron microprobe observations reveal that the structure and thickness of the altered zone depend on the type of weathering (Sterpenich, 1998; Sterpenich and Libourel, 2001). For a fixed glass composition, alteration driven by moisture produces only scattered dissolution pits, whereas atmospheric weathering produces a continuous altered and micro-fractured layer up to 200 μm thick (Fig. 3a). Buried in soils, stained glasses show a more pervasive weathering with alteration of up to 1500–2000 μm (Fig. 3b) and a characteristic laminated structure. Dissolution rates for given weathering conditions depend on glass composition. For instance, under burial conditions in the archaeological site of Rouen (Normandy, France, 9th century), the mean thickness of the altered zone for soda-rich glasses is around 30 μm, while for K-rich samples it may exceed 1000 μm (Fig. 3b and d). Similarly, potassic glass windows are always darkened by alteration layers while Na-rich glasses on the same windows preserve their color and have alteration zones less than 2 μm thick, as in the blue stained glass of the Chartres cathedral (France, 13th century).

Due to the good mechanical cohesion between weathered and unweathered glass, mean corrosion rates can be estimated by dividing the mean thickness of the alteration crust by the duration of weathering. Mean corrosion rates for stained glasses in natural conditions over the last 1100 yrs, are ranged approximately 0.005–1.5 μm.yr^{-1} and are dependent on glass composition and on alteration conditions. Mean corrosion rates being correlated with the bulk degree of polymerization of the glass, the NBO/T parameter (NBO/T denotes bulk melt non-bridging oxygen per tetrahedral cation, Mysen, 1988) allows to evaluate the specific role of glass composition and alteration conditions (Fig. 3c). For K-rich depolymerized (silica-poor) glasses, mean corrosion rates are almost two orders of magnitude greater than for polymerized Na-rich glasses. However, for the same composition, glass dissolution rates on the outside of windows are only 6–7 times slower than for glasses buried in soils. This suggests that variations in glass composition lead to variations in glass dissolution rates an order of magnitude more pronounced than those caused by different weathering conditions. Mean elemental dissolution rates can be also estimated for weathering durations over more than 10^3 yrs (Sterpenich and Libourel, 2001). Alkalis (K, Na, Rb and Cs) and alkaline-earth elements (Mg, Ca, Sr and Ba) are the most leachable elements, with leaching rates ranging from 10^{-2} to 10^{-3} g.m^{-2}.day^{-1}, while network forming elements (Al, Fe, Zr, Ti) are less depleted $\approx 10^{-4}$ g.m^{-2}.day^{-1}, Si being intermediate. Lanthanides and actinides, with the noticeable exception of U and Eu, are almost insensitive to alteration with the lowest dissolution rates at around 10^{-5} g.m^{-2}.day^{-1}.

The alteration of medieval stained glasses is thus strongly dependent on glass composition and on the weathering conditions with highly variable elemental dissolution rates. While alteration zones may play the role of a barrier limiting the release of several elements, stained glass studies reveal that a special care has to be taken in nuclear waste management strategy for the glass formulation and the weathering condition and their modifications in the repository during very long timescales ($> 10^5$ years).

2.2. Archaeological glass blocks and the impact of the fracturing

Nuclear glass packages are fractured due to a rapid cooling of the melt in the stainless steel canister (Fig. 4; Laude et al., 1982; Minet and Godon, 2003). Due to the release of strain upon glass cooling, fractures increase the reactive surface area and influence the alteration kinetics. Because of differences in the glass surface/water volume ratio or in the transport processes between the external border and the inside part of the cracks (Fig. 4c and d), surfaces can evolve with different alteration kinetics. In the following, it is shown how fractured archeological glasses can be used to assess the long-term alteration kinetics in the cracks and address the impact of fractures on the glass alteration.

Archaeological glass blocks (0.5–10 kg) were recovered from a shipwreck in the Mediterranean Sea near the island of Embiez (Var, France; Fig. 4a). They have been altered for 1800 yrs in seawater at a depth of 56 m and a fixed temperature of 15 °C (Fontaine and Foy, 2007; Foy et al., 2005). The glass was produced in the eastern Mediterranean region. The materials were melted in a large furnace and cooled in air, which caused the fracturing. Glass slabs were cut into blocks to be shipped to Europe, where they would have been manufactured (Fontaine and Foy, 2007; Foy et al., 2005). The composition is typically that of a Roman soda-lime glass ($\sim$ 70 wt% SiO_2, 20 wt% Na_2O, 5 wt% CaO, and 2 wt% Al_2O_3).

The altered glass (Verney-Carron et al., 2008) reveals, in addition to a small pristine core, an external zone, in contact with seawater, where the cracks have a large alteration thickness of $400 - 500$ μm (Fig. 4c), and an internal zone, where the cracks become denser but are less altered, 5–30 μm thick (Fig. 4d). All cracks are filled with alteration products that were characterized by electron microprobe and μ-X-ray diffraction. The cracks in the external zone contain Mg- and Fe-rich smectites, whereas internal cracks have a large (relative to the total thickness) hydrated glass layer at the interface with the pristine glass and only a few μm thick of Mg-rich smectites in the center of the crack (Fig. 4). This shows that the kinetics of the alteration mechanisms (ion exchange and dissolution) differs according to crack location. These differences are well explained by a coupling between alteration kinetics and element transport in solution (Verney-Carron et al., 2010a). The continuous renewal of the seawater in contact with external cracks maintained an “initial rate” for 1800 yrs and leads to thick neoformed smectite layers. In the internal cracks, the transport is assumed to be

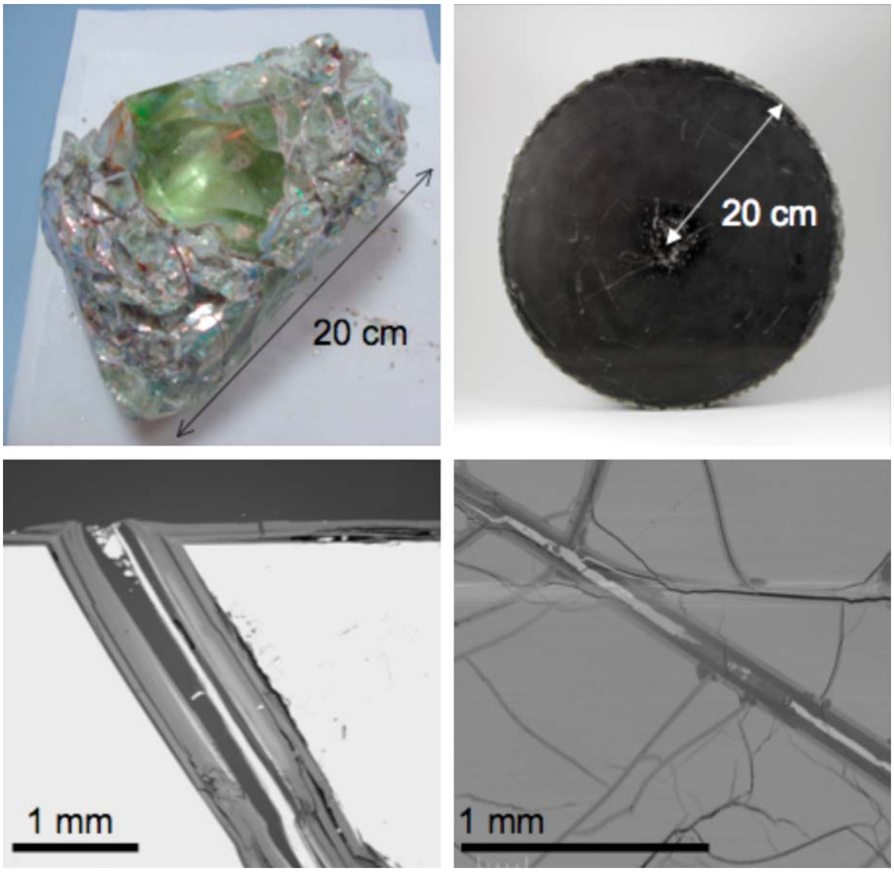

Fig. 4. Impact of fracturing on glass alteration. Photography of an Embiez glass block (a) and a cross-section of the R7T7 nuclear waste glass block (b). Notice the importance of the fracturing in both cases. SEM microphotograph (Back-scattered electrons) of the crack network in the Embiez glass block in contact with seawater (c) and in the internal zone (d).

Fig. 4. Effet de la fracturation sur l'altération des verres. Photographie d'un bloc de verre des Embiez (a) et coupe d'un bloc du verre R7T7 de déchet nucléaire (b). Noter l'importance de la fracturation dans les deux cas. Microphotographie au microscope électronique à balayage (électrons rétrodiffusés) du réseau de fractures du bloc de verre des Embiez dans la partie externe en contact avec l'eau de mer (c) et dans la zone interne (d).

diffusive and the slow renewal of the solution favored saturation effects and low alteration rates. Moreover, crack sealing by alteration products slowed down the diffusive transport (Verney-Carron et al., 2008, 2010a).

In the present French models of R7T7 alteration rates, used in safety calculations, the increase of the reactive surface area is taken into account via two fracturing ratios (τ): τ_0 for the external cracks and τ_r for the internal cracks that are assumed to be altered at the "residual rate" (Gin et al., 2005). The study on Embiez archaeological validates that this hypothesis remains conservative (Verney-Carron et al., 2010b).

2.3. *Archeological iron making sites and primitive meteorites: insights on the alteration at the glass–metal–clay interfaces*

To gain insight in the long-term behavior of nuclear waste packages at the glass–metal–clay interfaces in their geological repository conditions, we show in the following how slags from ancient iron making sites or primitive meteorites can be used as valuable proxies (Fig. 5). The stainless steel canister of nuclear waste is expected to corrode in anoxic conditions. Both analogues provide unique information about long-term corrosion under anoxic conditions of metal iron, which is rare on Earth.

Ancient slags: The question of the interaction between glass and iron is particularly important because nuclear glasses are poured in a stainless steel canister and the resulting package is expected to be surrounded by a thick carbon steel overpack (Andra, 2005). Some laboratory experiments under anoxic conditions have shown that the presence of iron and, more generally, iron corrosion products sustain glass alteration at a rate higher than the glass would undergo in the presence of site water only. This enhancement of glass alteration is due to the strong affinity of iron rich phases with respect to silicon, the main component of the glass (De Combarieu et al., 2011; Jollivet et al., 2000). It has been asserted that the formation of Fe-Si containing phase delay the formation of the protective gel layer responsible for the drop of alteration rate observed in glasses altered by water under static or low flow rate conditions (De Combarieu et al., 2011). That is why understanding and modeling interactions between glass, iron and clay is a key preliminary step in order to predict

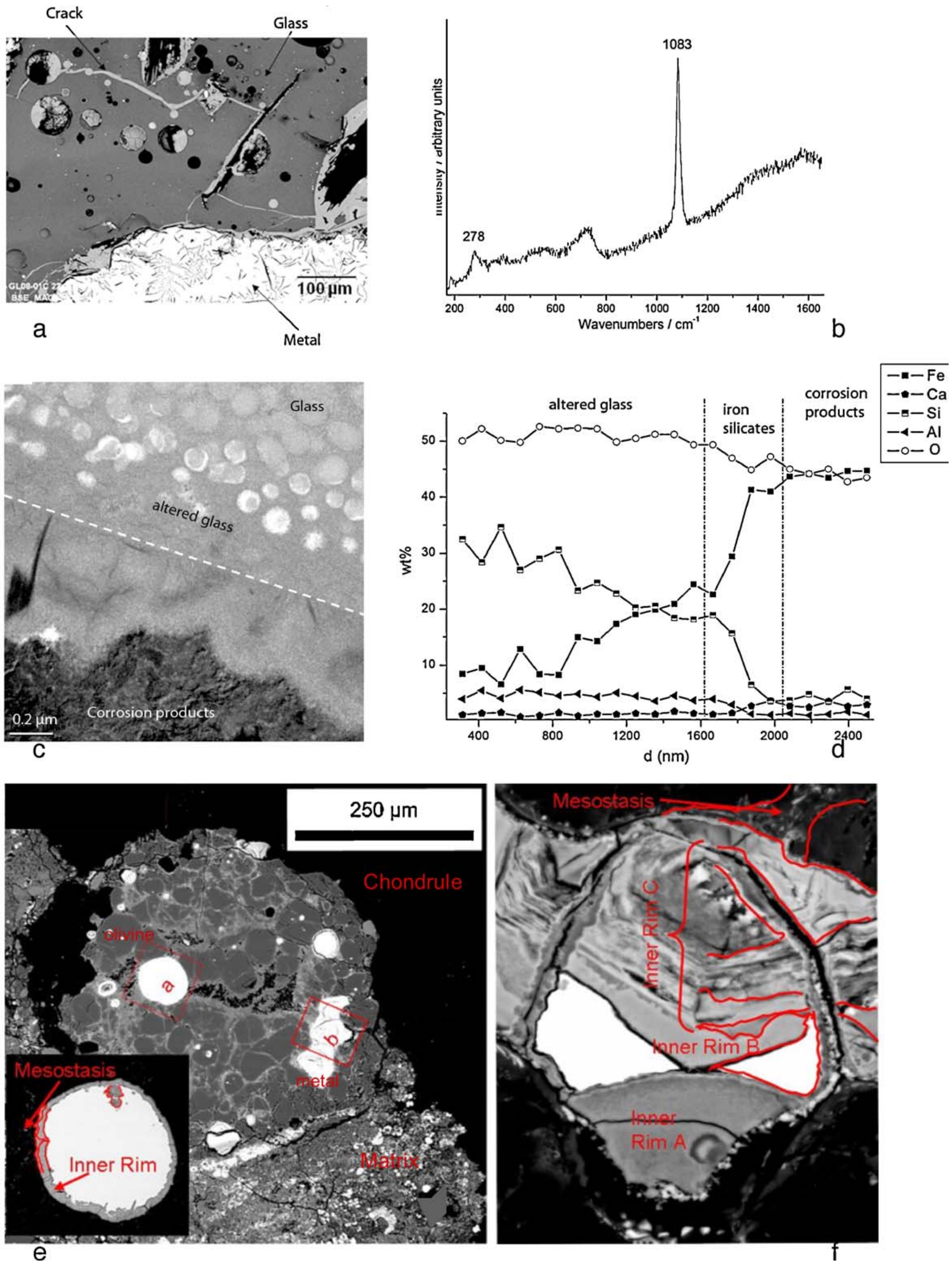

Fig. 5. Slags from ancient iron making sites (a to d) and primitive meteorites (e and f) as analogues of the alteration of glass-metal interfaces in anoxic repository conditions. (a) SEM. Ironmaking slag sample containing metal, glass and the crack network filled with corrosion products, (b) µRaman spectra of siderite ($FeCO_3$) from the corrosion products, (c) TEM photograph of the glass/corrosion product interface, (d) EDS-STEM chemical distribution (K_α lines) perpendicularly to the interface. e) Back scattered SEM image of magnesian porphyritic chondrule of the Al Rais CR2 chondrite. Olivines and metals grains are associated with a glassy mesostasis. The insert shows details of the metal grains labeled (a). Notice the continuous rim of corrosion products surrounding the Fe-Ni metal grain. f) Enlargement of the altered metal grain labeled (b). There are three blebs of metal left, surrounded by layers of alteration phases (inner rim).

long-term behavior of nuclear glass packages. Consequently, studies of natural or archaeological analogues give precious observational insight for this issue. For example, the site of Glinet dated from the 16th century (Neff et al., 2010), has been taken as a reference site for studying glass/iron interactions. Indeed, the by-product slags produced by the blast furnace present partly glassy matrix and contain metallic particles of micrometric to millimetric sizes. The blocks present numerous cracks that were immediately saturated with water as they were buried at depths continuously under the water level. It has been verified by on-field measurements and laboratory tests that at the sample location, water was carbonated and anoxic. Moreover, the crack network connects the metallic zones of the slags to the external solution of the soil and is entirely filled by corrosion products of iron such as those found in desaerated media (Fig. 5a). Microstructural characterization of the network embedded with the corrosion products by μRaman spectroscopy, reveal the presence of siderite ($FeCO_3$ – Fig. 5b). This siderite contains several % of calcium partially substituting the Fe atoms. This substitution was also observed on iron artefacts corroded in the same medium and could come from the groundwater but also, in the present case, from the glass matrix, that contain this element. Glasses identified in Glinet are calcium silicate glass enriched in iron and aluminum (MgO: 0.7–2.2 wt%, Al_2O_3: 5.1–8.8 wt%, SiO_2: 61.9–76.5 wt%, K_2O: 1.8–2.3 wt%, CaO: 15.6–25.1 wt%, MnO: 0.2–2.9 wt%, FeO: 1.2–9.1 wt%). This range of compositions for the ternary CaO-A_2O_3-SiO_2 defines an area known for its immiscibility. SEM-FEG observations confirm a non-homogeneous nanostructure characterized by the presence of spheroids of several hundreds of nanometers distributed in a glass matrix. This specific structure of the glass implies different alteration kinetics for each of the phases observed by TEM (Fig. 5c). The spheroids, mainly constituted of SiO_2, are less altered than the embedding matrix containing higher concentration the other elements.

At the interface between glass and iron corrosion products, different layers have been observed, linked to the variation of composition (Fig. 5c and d). EDS analyses coupled to STEM indicate that the altered glass is depleted in Ca but not in Al. Interestingly, an external festooned layer between altered glass and siderite, made of amorphous iron silicates is observed (Fig. 5c). The study of this layer can give insight into the influence of iron on the glass corrosion. Moreover, iron coming from the metal corrosion products has penetrated into the altered layers of the glass. Laboratory experiments simulating a crack have been conducted for 120 days at 50 °C on synthetised glass samples with the structure and the chemical composition of the slag glass matrix. The chemical profiles of the glass alteration layers are very comparable to the archaeological ones and are currently under study. The results are expected to help discriminating between the controlling parameters of glass alteration: transport *vs* chemical equilibria.

Meteorites: CR chondrites collected immediately after their fall, are primitive meteorites that have experienced aqueous alteration of metal and glass in their parent bodies. Constituted of mixtures of ferro-magnesian minerals and alumino-silicate glasses in chondrules (Fig. 5e), iron-nickel metal and sulfides blebs seated in phyllosilicate-rich matrices, CR chondrites show a range of low-temperature aqueous alteration stages, from pristine, unaltered (type 3) to completely hydrated (type 1) material (Weisberg et al., 1993). They provide an analogue for alteration and corrosion processes at the glass–metal–clay interfaces over a longer time frame than is possible in laboratory. In addition, they allow the investigation of all steps in the expected corrosion of nuclear waste, given that the physico-chemical environment of the parent body during the alteration (e.g., Zolensky et al., 1993), i.e. temperature (50–150 °C), water/rock ratio (0.4 to 1.1), low oxygen fugacity and mineralogy, is similar to that expected in a disposal facility (Andra, 2005).

Fig. 5e depicts the corrosion products after partial alteration at the metal/glass interface in a chondrule from the Al Rais CR2 chondrite. This chondrule contains several metal grains at different alteration stages. SEM images show that Fe-Ni metal grains are surrounded by several alteration layers, with intrusions of neoformed phases into metal grains (Fig. 5e and 5f). These corrosion products have a complex mineralogy, with magnetite-rich layers alternating with layers enriched in sulfides (Fig. 5f). A genetic sequence for metal/glassy mesostasis, confirmed by elemental mapping, would be metal/magnetite ± sulfide/phosphate? ± carbonate? ± sulphate?/(altered) mesostasis. The alteration layers shown in Fig. 5e and f are enriched relative to the metal in S, Si, Mg, Ca and Mn. They also have significant contents in Ni, Cr, Co, P, which are enriched in some parts compared to the metal. In the case of metal/matrix interfaces, the sequence of corrosion products is: metal/magnetite ± sulfide/magnetite/phosphate + matrix.
The alteration rims become more complex with increasing alteration, with steel components moving into the surrounding environment.

In addition to document corrosion processes at metal/glass/clay interfaces, such extraterrestrial analogues provide information on the elemental mobility during alteration in anoxic environments, even if the time-frame of parent body alteration is not well constrained (10^4–10^6 yrs or more). Chemical distribution maps show that most of the "dissolved" elements, including iron, does not go very far. Even for the most altered metal grains, the phases precipitate at distances of several 100 μm. This happens in the form of sulfides, phosphates, sometimes

Fig. 5. Scories d'anciens sites de fabrication du fer (a à d) et météorites primitives (e et f) utilisées comme analogues de l'interface verre-métal dans des conditions anoxiques de stockage. a) Scories contenant du métal et du verre, fracturées par un réseau de microfractures envahies de produits de corrosion, b) Spectre μRaman de sidérite provenant des produits de corrosion, c) Image en microscopie électronique en transmission de l'interface verre/produits de corrosion, d) Profil de composition chimique (STEM-EDS) à l'interface. e) Image en électrons rétrodiffusés au microscope électronique à balayage d'un chondre porphyrique de la chondrite Al Rais CR2. Les grains d'olivine et de métal sont dispersés dans la mésostase vitreuse. L'encadré montre le détail du grain de métal (a). Noter la couche continue de produits de corrosion entourant la bille de Fe-Ni. f) Agrandissement du grain de métal (b). Noter l'existence de 3 grains de métal reliques, entourés par des couches d'altération.

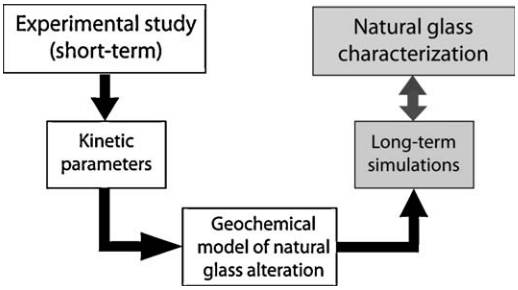

Fig. 6. Principles of the long-term predictive capacity of the natural (or archaeological) glass alteration modeling.

Fig. 6. Principes de la capacité predictive de la modèlisation de l'altération des verres naturels (ou archéologiques).

carbonates, and Fe-oxides, which tend to form characteristic rings in the near vicinity of the corroded grains. At the metal/glass interface, element migration is even smaller even less, in the order of tens of μm.

3. The prediction of glass alteration long-term kinetics

An important objective of the studies on natural and archaeological analogues is to validate the long-term capacity of predictive alteration models (Fig. 6). These models are based on experimental data to determine the kinetics parameters. The extrapolation to longer timescales of the models helps predict the long-term behavior of nuclear glasses. Long-term simulations can be compared with the characterization (phenomenology, apparent kinetics) of natural samples altered for a long time. If the results are in agreement, this validates the predictive capacity of the natural analogue and improves the confidence in the models predicting the evolution of nuclear glasses (Ewing, 1979, 2001).

3.1. The Embiez archaeological glass blocks

This methodology was applied to the Embiez glass blocks, altered for 1800 yrs in seawater at a constant temperature of 15 °C (Verney-Carron et al., 2008, 2010a). The stability of these alteration conditions allows long-term modeling. Verney-Carron et al. (2010a, b) demonstrated that a model parameterized in the laboratory is able to simulate the alteration of fractured historical glass blocks. Moreover, the coupling of alteration chemistry and transport in solution explains that external cracks in direct contact with renewed seawater were altered at a high dissolution rate (400 – 500 μm), whereas internal cracks are less altered (by 1 or 2 orders of magnitude) because the low renewal of interstitial water and the sealing of the cracks by alteration products favored low alteration kinetics.

3.2. The basaltic glass

A key issue to make a reliable and robust prediction of the long-term behavior of nuclear glasses is to determine realistic values of residual rate. Basaltic glasses, with a silica content close to nuclear glasses, altered in different environments (seawater, groundwater, meteoric water) can help in this direction, with the advantage of long timescales but large uncertainties on the alteration history. This 'residual rate' kinetic regime is expected to be the longest one in geological disposal conditions and explains most of glass alteration (Techer et al., 2001). The mechanisms involved at this stage of reaction progress are water diffusion through the passivating gel layer and precipitation of secondary crystalline phases that consume elements from the gel (Frugier et al., 2008). It has been shown that the residual rate depends on glass and water composition, the latter being influenced by chemical reactions in the near-field. Even if residual rates are accurately measured in laboratory, natural analogues may help to determine how this rate evolves as a function of water composition, renewal rate and time. Studying basalt alteration therefore provides a new challenge for geochemists.

4. Conclusion

This paper presents an overview of the major advances offered by natural and archeological analogues in the validation of predictive models of the nuclear glass alteration in a deep geological repository. Based on terrestrial or extraterrestrial analogues, it summarizes a rational methodology to tackle the difficulty of predicting the long-term behavior of waste materials, with the expectation of reconstructing their alteration history in the past and/or forecasting their evolution in the future. This approach represents a significant advance toward assessing the uncertainties on nuclear glass alteration rates in a geological repository, giving sound arguments to reach a decision for the disposal of these materials.

Acknowledgments

G.L and the authors are much indebted to Georges Calas, Gordon Brown, and the scientific committee of the Académie des Sciences and Institut de France for their invitation at the Colloque de l'Académie des Sciences (14-15 september, 2009) and to participate to this C.R. Geoscience issue on the Environmental Mineralogy. We are grateful to Christelle Martin, Nicolas Michau, Didier Crusset and Stephan Schumacher from Andra (French National radioactive waste management Agency) for many useful discussions and suggestions during the course of this research. Part of this work was financially supported by the GL-VFA of Andra contract n° 30010180. This is CRPG contribution n° 2097.

References

Andra, 2005. Dossier 2005 Argile. Tome Évolution phénoménologique du stockage géologique. Collection Les Rapports, Andra. 520 p.

Bunker, B.C., 1994. Molecular mechanisms for corrosion of silica and silicate glasses. J. Non-Cryst. Solids 179, 300–308.

Cailleteau, C., Angeli, F., Devreux, F., Gin, S., Jestin, J., Jollivet, P., Spalla, O., 2008. Insight into silicate-glass corrosion mechanisms. Nat. Mater. 7, 978–983.

Chave, T., Frugier, P., Ayral, A., Gin, S., 2007. Solid state diffusion during nuclear glass residual alteration in solution. J. Nucl. Mater. 362, 466–473.

De Combarieu, G.D., Schlegel, M., Neff, D., Foy, E., Vantelon, D., Barboux, P., Gin, S., 2011. Glass-iron-clay interactions in a radioactive waste geological disposal: An integrated laboratory-scale experiment, Applied Geochemistry, 26, 65–79.

Ewing, R.C., 1979. Natural glasses: analogues for radioactive waste forms. Mat. Res. Soc. Symp. Proc. 1, 57–68.

Ewing, R.C., 2001. Nuclear waste form glasses: The evaluation of very long-term behaviour. Mat. Tech. Adv. Perf. Mat. 16, 30–36.

Fontaine, S.D., Foy, D., 2007. L'épave Ouest-Embiez 1, Var–Le commerce maritime du verre brut et manufacturé en Méditerranée occidentale dans l'Antiquité. Rev. Archeol. Narb. 40, 235–268.

Foy, D., Jezegou, M.P., Fontaine, S.D., 2005. La circulation du verre en Méditerranée au début du III^{e} siècle : le témoignage de l'épave Ouest Embiez 1 dans le Sud de la France (fouilles 2001–2003). Annales du 16^{e} congrès de l'Association Internationale pour l'Histoire du Verre, pp. 122–126.

Frugier, P., Gin, S., Lartigue, J.E., Deloule, E., 2006. SON68 glass dissolution kinetics at high reaction progress: mechanisms accounting for the residual alteration rate. Mat. Res. Soc. Symp. Proc. 932, 305–312.

Frugier, P., Gin, S., Minet, Y., Chave, T., Bonin, B., Godon, N., Lartigue, J.E., Jollivet, P., Ayral, A., De Windt, L., Santarini, G., 2008. SON68 nuclear glass dissolution kinetics: Current state of knowledge and basis of the new GRAAL model. J. Nucl. Mater. 380, 8–21.

Gin, S., Ribet, I., Frugier, P., Chave, T., Angeli, F., Lartigue, J.E., de Combarieu, G., Godon, N., 2005. Assessment of nuclear glass behavior in geological disposal conditions: current state of knowledge and recent advances. Eur. Nucl. Conf., Versailles, France.

Gin, S., Jégou, C., Frugier, P., Minet, Y., 2008. Theoretical consideration on the application of the Aagaard-Helgeson rate law to the dissolution of silicate minerals and glasses. Chem. Geol. 255, 14–24.

Grambow, B., 1985. A general rate equation for nuclear waste glass corrosion. Mat. Res. Soc. Symp. Proc. 44, 15–27.

Grambow, B., Müller, R., 2001. First-order dissolution rate law and the role of surface layers in glass performance assessment. J. Nucl. Mater. 298, 112–124.

Hamilton, J.P., Pantano, C.G., Brantley, S.L., 2000. Dissolution of albite glass and crystal. Geochim. Cosmochim. Acta 64, 2603–2615.

Jollivet, P., Minet, Y., Nicolas, M., Vernaz, E., 2000. Simulated alteration tests on non-radioactive SON 68 nuclear glass in the presence of corrosion products and environmental materials. J. Nucl. Mater. 281, 231–243.

Laude, F., Vernaz, E., Saint-Gaudens, M., 1982. Fracture appraisal of large scale glass blocks under realistic thermal conditions. Mat. Res. Soc. Symp. Proc. 11, 239–247.

Libourel, G., Barbey, P., Chaussidon, M., 1994. L'altération des vitraux. La Recherche 25, 168–188.

Macquet, C., Thomassin, J.H., 1992. Archaeological glasses as modelling of the behaviour of buried nuclear waste glasses. Appl. Clay Sci. 7, 17–31.

McGrail, B.P., Icenhower, J.P., Shuh, D.K., Liu, P., Darab, J.G., Baer, D.R., Thevuthasen, S., Shutthanandan, V., Engelhard, M.H., Booth, C.H., Nachimuthu, P., 2001. The structure of Na_2O-Al_2O_3-SiO_2 glass: impact on sodium ion exchange in H_2O and D_2O. J. Non-Cryst. Solids 296, 10–26.

Minet, Y., Godon, N., 2003. Leaching full-scale fractured glass blocks. Proc. Am. Ceram. Soc., St-Louis, U S A 275–282.

Mysen, B.O., 1988. Structure and properties of silicate melts. Developments in Geochemistry, 4. Elsevier Science, Amsterdam, 354 p.

Neff, D., Saheb, M., Monnier, J., Perrin, S., Descostes, M., L'Hostis, V., Crusset, D., Millard, M., Dillmann, P., 2010. A review of the archaeological analogue approaches to predict the long-term corrosion behaviour of carbon steel overpack and reinforced concrete structures in the French disposal systems. J. Nucl. Mater. 402, 196–205.

Oelkers, E.H., 2001. General kinetic description of multioxide silicate mineral and glass dissolution. Geochim. Cosmochim. Acta 65, 3703–3719.

Pelegrin, E., Calas, G., Ildefonse, P., Jollivet, P., Galoisy, L., 2010. Structural evolution of glass surface during alteration: Application to nuclear waste glasses. J. Non-Cryst. Solids 356, 2497–2508.

Petit, J.C., 1992. Reasoning by analogy: rational foundation of natural analogue studies. Appl. Geochem. Suppl. Issue 1, 9–11.

Sterpenich, J., 1998. Altération des vitraux médiévaux. Contribution à l'étude du comportement à long terme des verres de confinement. PhD Thesis, UHP Nancy 1, France, 461 p.

Sterpenich, J., Libourel, G., 2001. Using stained glass windows to understand the durability of toxic waste matrices. Chem. Geol. 174, 181–193.

Sterpenich, J., Libourel, G., 2006. Water diffusion in silicate glasses under natural weathering conditions: evidence from buried medieval stained glasses. J. Non-Cryst. Solids 352, 5446–5451.

Stroncik, N.A., Schmincke, H.U., 2001. Evolution of palagonite: Crystallization, chemical changes, and element budget. Geochem., Geophys., Geosyst. 2.

Techer, I., Advocat, T., Lancelot, J., Liotard, J.M., 2001. Dissolution kinetics of basaltic glasses: control by solution chemistry and protective effect of the alteration film. Chem. Geol 176, 235–263.

Trouiller, A., 2006. Le Callovo-Oxfordien du bassin de Paris : du contexte géologique à la modélisation de ses propriétés. C. R. Geoscience 338, 815–823.

Valle, N., Verney-Carron, A., Sterpenich, J., Libourel, G., Deloule, E., Jollivet, P., 2010. Elemental and isotopic (^{29}Si and ^{18}O) tracing of glass alteration mechanisms. Geochim. Cosmochim. Acta 74, 3412–3431.

Verney-Carron, A., Gin, S., Libourel, G., 2008. A fractured roman glass block altered for 1800 years in seawater: analogy with nuclear glass in a deep geological repository. Geochim. Cosmochim. Acta 72, 5372–5385.

Verney-Carron, A., Gin, S., Frugier, P., Libourel, G., 2010a. Long-term modeling of alteration-transport coupling: application to a fractured Roman glass. Geochim. Cosmochim. Acta 74, 2291–2315.

Verney-Carron, A., Gin, S., Libourel, G., 2010b. Archeological analogs and the future of nuclear waste glass. J. Nucl. Mater. 406, 365–370.

Weisberg, M.K., Prinz, M., Clayton, R.N., Mayeda, T.K., 1993. The CR (Renazzo-type) carbonaceous chondrite group and its implications. Geochim. Cosmochim. Acta 57, 1567–1586.

White, A.F., Claasen, H.C., 1980. Kinetic model for the short-term dissolution of a rhyolitic glass. Chem. Geol. 28, 91–109.

Zolensky, M., Barrett, R., Browning, L., 1993. Mineralogy and composition of matrix and chondrule rims in carbonaceous chondrites. Geochim. Cosmochim. Acta 57, 3123–3148.

4. *Séquestration géologique du CO_2 et des gaz annexes : une nouvelle approche expérimentale*

Contexte et projets en développement

Cette thématique, qui est aujourd'hui ma thématique principale, s'attache à la simulation expérimentale de l'injection de CO_2 et des gaz co-injectés en stockage géologique. Elle est basée sur le développement d'expériences au laboratoire ainsi que sur la modélisation thermodynamique des systèmes mis en jeu. Le laboratoire G2R, par l'intermédiaire du groupe IMAGES (Innovation pour la MAîtrise des Gaz à Effet de Serre) de l'INPL, est impliqué dans un nombre important de projets dédiés à l'étude de la séquestration géologique du CO_2. J'ai été impliqué dès mon recrutement dans les projets ANR Géocarbone Intégrité et Injectivité pilotés par le BRGM et l'IFPEN. Puis j'ai rapidement pris la responsabilité scientifique de volets expérimentaux, comme dans le projet ANR Proche-Puits piloté par le BRGM, ou la responsabilité scientifique pour le compte de Nancy dans le projet ANR Interface. J'assure également actuellement la coordination nationale du projet ANR Gaz Annexes. L'ensemble de ces projets a permis d'acquérir un nombre important d'équipements analytiques et expérimentaux. Ainsi, un réacteur de 2 litres (IMAGES) permettant de travailler en CO_2 supercritique a été acquis en 2005. En 2006, deux nouveaux appareils ont été conçus et livrés. Il s'agit de MIRAGES (Modèle d'Injection RAdial pour l'injection de Gaz à Effet de Serre) qui permet de réaliser une injection de CO_2 à l'intérieur d'une carotte de roche afin de suivre le vieillissement du trio réservoir/ciment/acier du puits face à l'injection de CO_2. COTAGES (COlonne Thermorégulée à grains pour l'injection de Gaz à Effet de Serre) est un réacteur original permettant de réaliser des expériences en système supercritique avec gradient de température. En 2007, un spectromètre Raman avec sondes à immersion a été acquis avec un financement exclusif sur le projet Gaz Annexes, afin de réaliser des mesures *in situ* dans les autoclaves IMAGES et MIRAGES. Ce spectromètre permet pour la première fois de suivre les espèces moléculaires gazeuses et aqueuses en conditions d'expérimentation à haute pression et haute température sans prélèvement et donc sans perturbation du système. 2007 et 2008 voient la réalisation d'une ligne de chargement, déchargement et analyse de gaz dangereux. En effet, selon les conditions de captage et selon les industries considérées, le CO_2 pourra contenir des impuretés en quantités plus ou moins importantes. Il s'agit de gaz tels que N_2, O_2 ou Ar mais également de gaz dangereux tels que H_2S, CO, NOx ou SOx. L'impact de ces phases co-injectées sur le stockage géologique doit être étudié. Cependant, travailler avec ces gaz dangereux nécessite de manipuler de faibles quantités et d'équiper le laboratoire de façon adéquate (capteurs, extracteurs, électro-vannes asservies). Le laboratoire du G2R a été récemment équipé pour manipuler ces gaz et la ligne de chargement/déchargement/analyse est aujourd'hui opérationnelle et fait l'objet d'une utilisation intense des différentes équipes du laboratoire.

Au cours de ces cinq dernières années de recherche je me suis principalement consacré au développement de la plate-forme expérimentale dédiée au CO_2 et aux gaz co-injectés à travers 5 projets

1. Développement de la mesure in situ HT-HP des espèces gazeuses par sonde Raman. Applications à la séquestration géologique du CO_2 et des gaz annexes co-injectés. Ce projet s'est appuyé sur les travaux d'Anne-Laure Henriot (financement ANR Gaz Annexes) que j'ai co-encadrée d'octobre 2007 à décembre 2009, et sur le projet ANR Gaz Annexes que je coordonne (projet de 4,5 ans débuté en décembre 2006 et regroupant les partenaires INPL-IMAGES, BRGM, IFPEN, Ecole des Mines de Paris et TOTAL). Il est basé sur l'acquisition de nouvelles données à haute pression et haute température sur les mélanges de gaz et sur les solubilités (CO_2 et gaz annexes) par le développement de l'analyse par spectrométrie Raman *in situ*. Le calibrage de l'expérience Raman fait l'objet d'une publication en cours de rédaction: *The mutual solubilities of H_2O and CO_2 in the liquid and vapor phases measured by in situ Raman spectroscopy at 100 and 150°C and from 1 to 200 bar*. Les premiers résultats acquis dans un système H_2O/CO_2 pur à 100 et 150°C et pour des pressions de 10 à 200 bar sont donnés dans les figures ci-dessous (Figure 9 et Figure 10). Il apparaît une très bonne corrélation entre les données acquises par Raman *in situ* et les données prévues par le modèle de Duan et al (2003). Les résultats sont spécialement encourageants concernant la phase vapeur pour laquelle peu de données sont disponibles dans la littérature. Cette méthode semi-quantitative révélera tout son intérêt lorsque la phase de calibrage sera terminée et que de nouvelles conditions de pression et températures pourront être investiguées. En particulier, l'acquisition de nouvelles données proches du

point critique seront un atout important pour valider les modèles thermodynamiques prédisant les équilibres dans le système H_2O/CO_2/sel dans ces conditions P-T encore mal documentées.

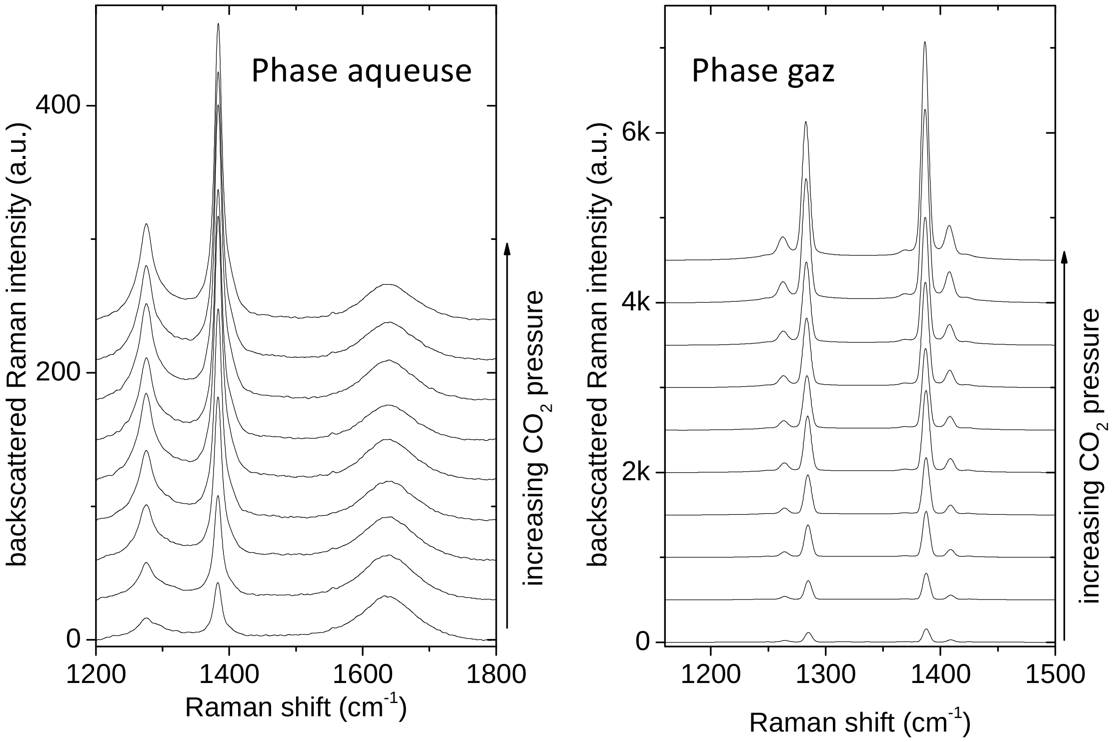

Figure 9 : Spectres de diffusion Raman enregistrés dans la phase aqueuse et la phase gaz à l'aide des sondes à immersion à 100°C et à des pressions variant régulièrement de 10 à 200 bar. Les spectres sont centrés sur les bandes du CO_2.

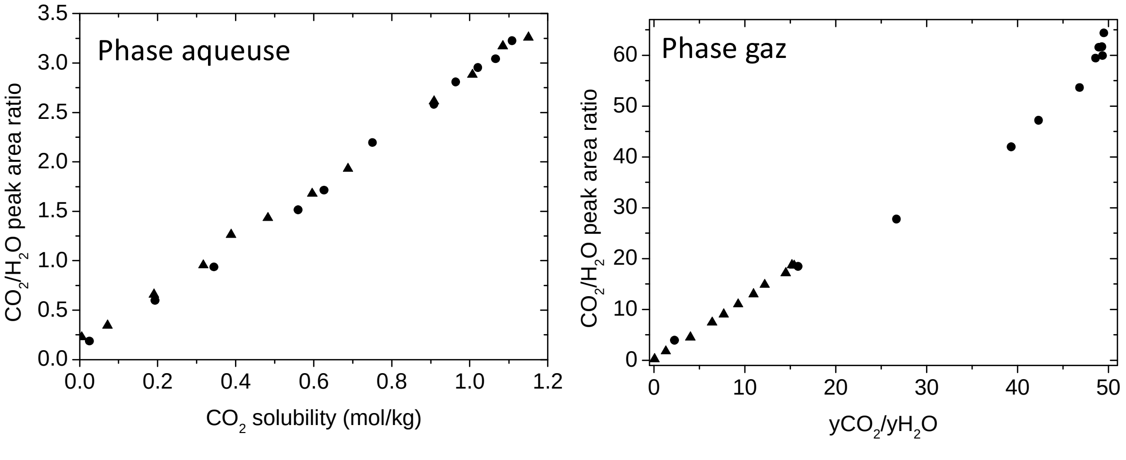

Figure 10 : Rapport des pics d'intensité Raman de CO2 et H2O reportés en fonction de la solubilité du CO_2 dans la phase aqueuse et du rapport molaire des phases CO_2 et H_2O dans la phase gaz. Les données théoriques sont issues du modèle de Duan et al. 2003. Expériences à 150°C (triangles) et 100°C (cercles).

2. Simulation expérimentale de l’injection CO_2 à l’aide de l’autoclave MIRAGES. Suivi du vieillissement du réservoir et des matériaux de puits face à l’injection de CO_2 supercritique. Ce projet est partie intégrante du projet ANR Proche-Puits débuté en décembre 2007 et terminé en mai 2011 et regroupant les partenaires BRGM, INPL-IMAGES, IFPEN, LFC, Itasca, GdF, Schlumberger et TOTAL. Afin de suivre l’évolution pétrophysique de la roche au cours du vieillissement, nous avons développé une maquette reproduisant un puits d’injection à l’échelle 1/10ème. Le schéma ci-dessous (Figure 11) décrit le dispositif qui permet de reproduire les conditions de pression et de température qui sont celles d’une injection en situation réelle, et d’imposer un débit d’injection pendant une durée choisie. Ce dispositif permet en outre d’étudier les interfaces ciment/roche de couverture/roche réservoir/casing de puits. Pour cette raison, il fait partie des expériences de référence du projet ANR Interface piloté par le BRGM. L’ensemble des paramètres physico-chimiques sont maîtrisés pendant l’expérience, facilitant la simulation numérique ultérieure et donc le changement d’échelle. Les premiers résultats font partie de la publication en cours de finalisation : *El Hajj, H., Sterpenich, J., Pironon, J., Jobard, E., Randi, A, Simulated experiment of deep geologic sequestration of carbon dioxide to study the interaction of* CO_2 *with the reservoir materials. A soumettre à Chemical Geology.*

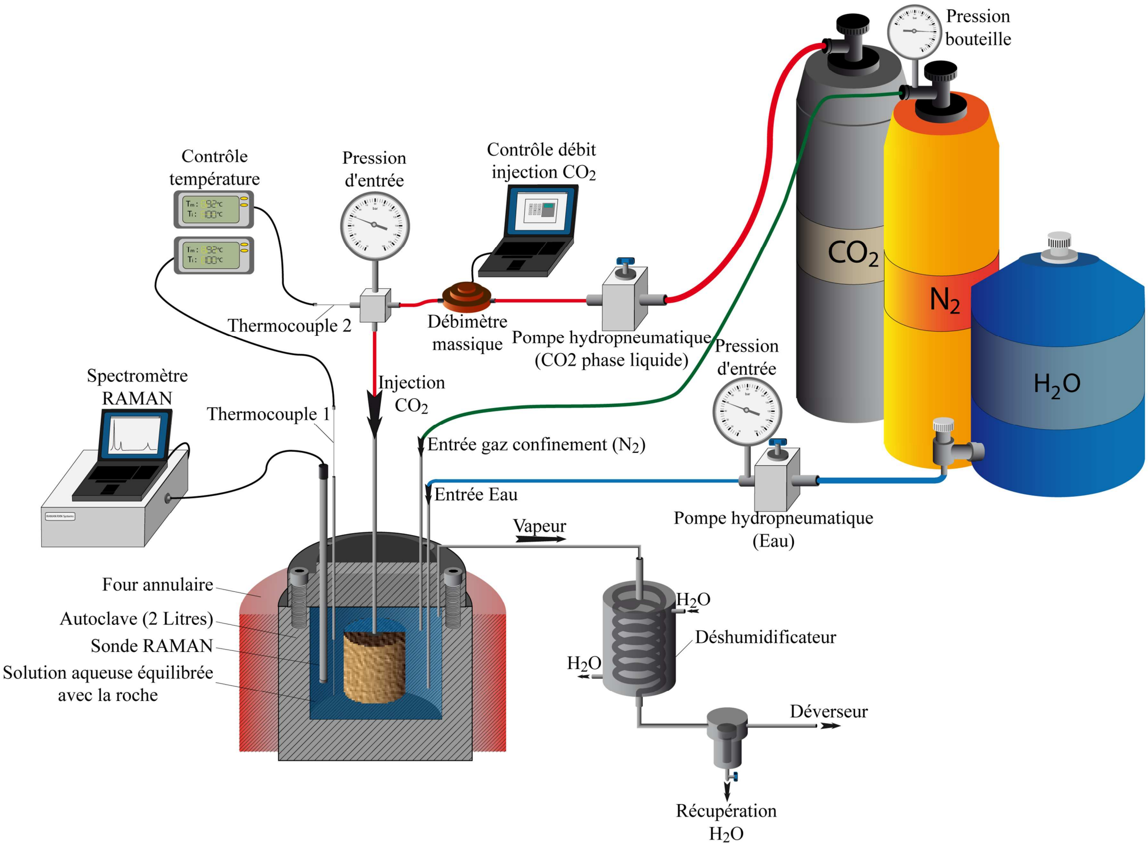

Figure 11 : Schéma du dispositif MIRAGES dédié à la simulation expérimentale de la réactivité des roches réservoir, couverture et des matériaux de puits face à l'injection en continu de CO_2 supercritique.

3. Simulation expérimentale de l'influence d'un gradient de température sur l'évolution des propriétés pétro-physiques des roches réservoir et de couverture. Ce travail, initié dans le cadre des projets ANR Géocarbone, a été repris dans le projet ANR Interface. Ce projet est d'une grande importance si on considère que l'injection de CO_2 sera réalisée dans un réservoir chaud et qu'un ensemble de phénomènes thermiques conduiront à des changements de propriétés pétrophysiques de la roche pouvant influencer l'injectivité à plus ou moins long terme. La Figure 12 illustre les derniers résultats acquis dans le cadre de la thèse d'E. Jobard que je co-encadre. On montre très clairement que le gradient de température induit des transferts de masse à très court terme et que les recristallisations observées ne se font pas aléatoirement. En particulier, la précipitation en périphérie de grain inhibe de façon considérable l'accès à la porosité intra-oolithes affectant la connectivité de la porosité et donc l'injectivité dans le réservoir. Ces travaux ont été présentés lors du *World Geothermal Congress*

2010 de Bali et font l'objet d'une publication soumise à Chemical Geology et présentée dans ce mémoire : *Experimental modelling of the impact of thermal gradient during geological sequestration of* CO_2*: the COTAGES experiment*

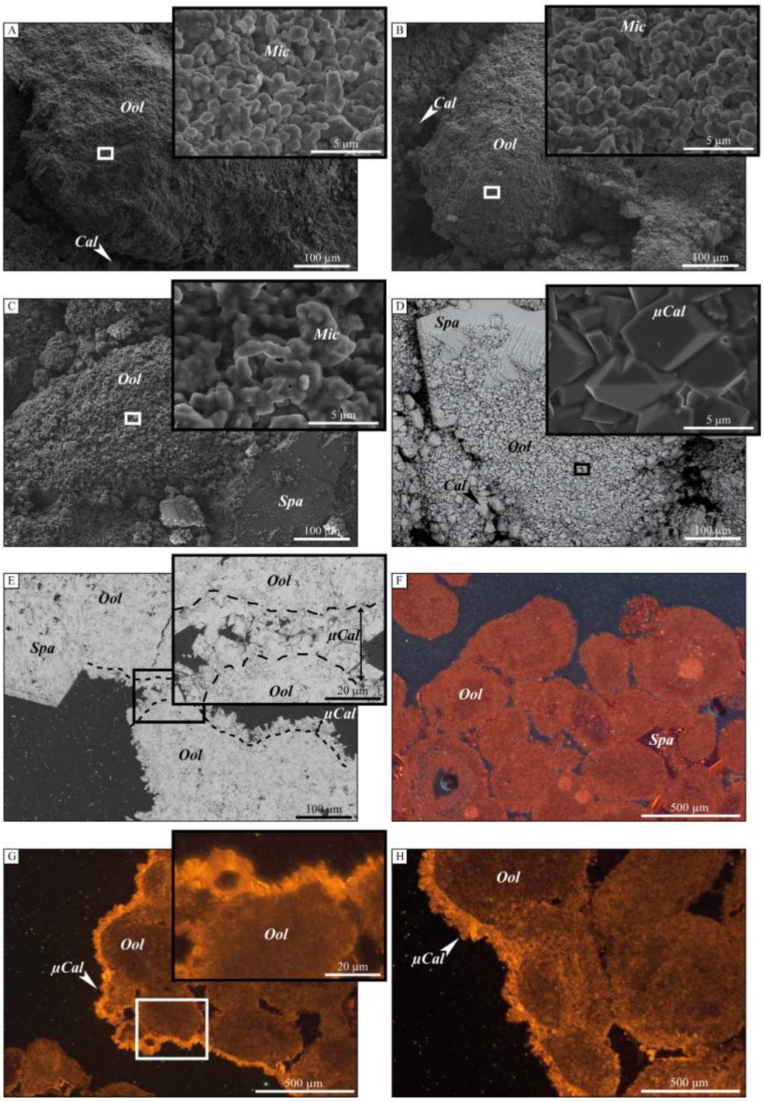

Figure 12 : Photographie MEB et cathodoluminescence d'un calcaire oolithique, analogue des réservoirs potentiels du Bassin de Paris. Cette expérience menée en gradient de température (35 à 100°C) montre qu'il y a un transfert important de matière de la zone froide vers la zone chaude et que les cristallisations affectent particulièrement la périphérie des grains par précipitation de micro-calcite. A et F: échantillon sain, B : zone froide (35°C), C : zone intermédiaire (55°C), D, E, G et H: zone chaude (100°C).

4. Etude du vieillissement des matériaux de puits et des roches couverture et réservoir en présence de CO_2 et de gaz annexes. Ce projet s'articule autour de deux types d'expériences : d'une part des expériences mettant en jeu des gaz annexes et leur influence sur la tenue d'un stockage de CO_2. Cette partie s'appuie sur la thèse de Stéphane Renard que j'ai co-encadrée du 1^{er}

octobre 2006 au 4 juin 2010. Il s'agissait d'une thèse financée par TOTAL et l'ADEME qui portait sur le seul pilote français d'injection de CO_2 détenu par Total sur le site de Lacq. Elle a permis de quantifier l'impact des gaz co-injectés (SO_2 et NO) sur le comportement du puits, du réservoir et de la couverture en condition de stockage, et par conséquent sur le comportement à long terme du stockage. Ces travaux ont fait l'objet de plusieurs communications à congrès, d'un chapitre d'ouvrage, d'un résumé étendu et deux publications dont une est soumise à Marine and Petroleum Geology. Ces quatre papiers sont présentés dans le mémoire.

Le second type d'expériences, appelées expériences SANDWICH, a été mis en place en parallèle du projet MIRAGES. Il s'agissait en effet de créer un nouveau design expérimental qui devait permettre de suivre l'influence de CO_2 dissous ou supercritique sur les différents interfaces. Les premières expériences ont testé les interfaces ciment/grès et ciment/calcaire. Une publication servant de livrable au projet ANR Proche-Puits est en cours de rédactions (Sterpenich, J., El Hajj, H., Pironon, J., Jobard, E., Garaffa, L.H., Piquet, G., Rives D., Randi, A. Experimental ageing of cement/rock interface under CO_2 storage conditions. Implications on wells durability. A soumettre à Chemical Geology). Ces expériences avaient fait l'objet d'un stage 2A de l'ENSG dont les étudiants apparaissent comme auteurs de l'article. De nouvelles expériences et un nouveau design ont été développés dans le cadre de la thèse d'Emmanuel Jobard (Figure 13). Ces expériences mettent en jeu les interfaces au niveau du puits d'injection de CO_2, entre la roche de couverture (argilite du Callovo-Oxfordien), le ciment et l'acier du casing.

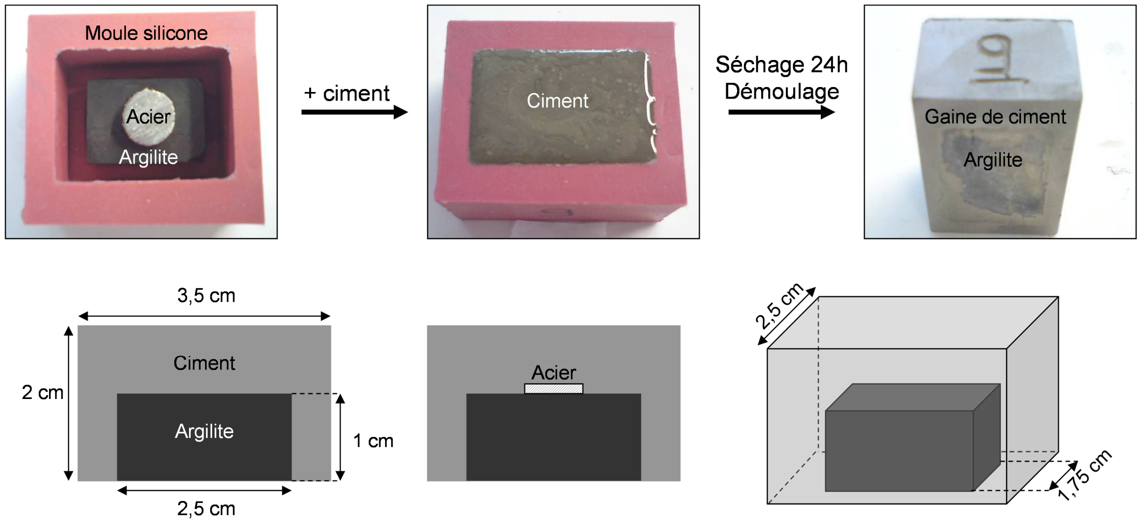

Figure 13 : Expériences « sandwich » destinées à suivre l'évolution des interfaces argilite/ciment/acier soumis à de fortes pressions de CO_2 en phase aqueuse ou en phase supercritique. Thèse Emmanuel Jobard et projet ANR Interface.

Ces expériences sandwich ont montré que la cristallisation de carbonates aux interfaces était responsable de l'ouverture de fractures qui permet la circulation de fluides accélérant les transformations minérales de l'argilite (oxydation de pyrites) et la carbonatation de la phase cimentaire de façon concomitante avec l'altération des phases C2S et C3S (Figure 14).

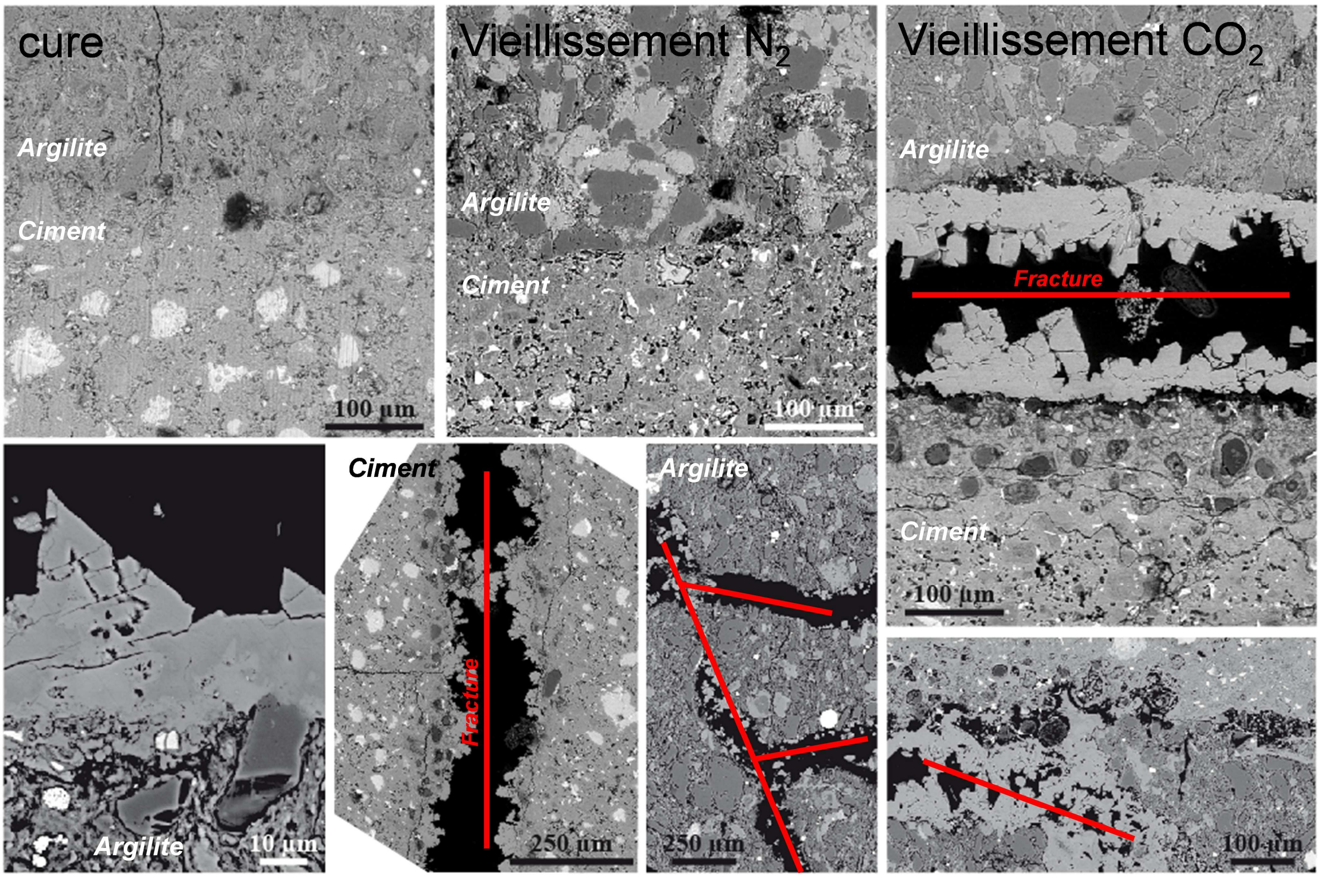

Figure 14 : Résultats de l'expérience « sandwich » décrivant le comportement de l'interface argilite/ciment après cure (7 jours à 100 bar de N_2 et 80°C), après vieillissement à l'azote ou après vieillissement au CO_2 en phase aqueuse (30 jours à 110 bar et 80°C). L'expérience montre très clairement l'influence du CO_2 et de la carbonatation sur l'ouverture de l'interface et sur la fracturation de l'argilite. Ces résultats doivent être interprétés en terme d'intégrité des puits d'injection au voisinage de la couverture. Thèse Emmanuel Jobard et projet ANR Interface.

5. Etude par microtomographie X des propriétés pétrophysiques des roches soumises à l'injection de CO_2 et de gaz annexes. Cette étude fait suite à l'acquisition d'un tomographe X par la fédération Eau-Sol-Terre sur crédit PCER et Institut Carnot (ICEEL). Il s'agit de développer les méthodes de micro-caractérisation tridimensionnelle des échantillons de roche (couverture et réservoir) afin de suivre l'évolution de leurs porosités et perméabilités en conditions de stockage géologique. Cette méthode est également appliquée au suivi des interfaces (roche/ciment/acier ou couverture/réservoir) afin d'appréhender ces zones identifiées comme critiques dans la problématique des risques de fuite. Les objets sur lesquels les caractérisations se sont portées sont issus de la problématique du stockage de CO_2 (calcaire oolithique du Dogger, grès du Trias, ciments de puits) mais également du stockage de déchets nucléaires (argilites du COX,

argiles de Tournemire). Ainsi, l'évolution des propriétés pétrophysiques des argiles peut être suivie dans le cadre d'expériences de saturation/désaturation ou d'influence du panache alcalin ou pour suivre la répartition tridimensionnelle de bioturbations.

Le papier traitant de l'expérience en gradient de température COTAGES montre certains résultats acquis en tomographie X (Figure 15).

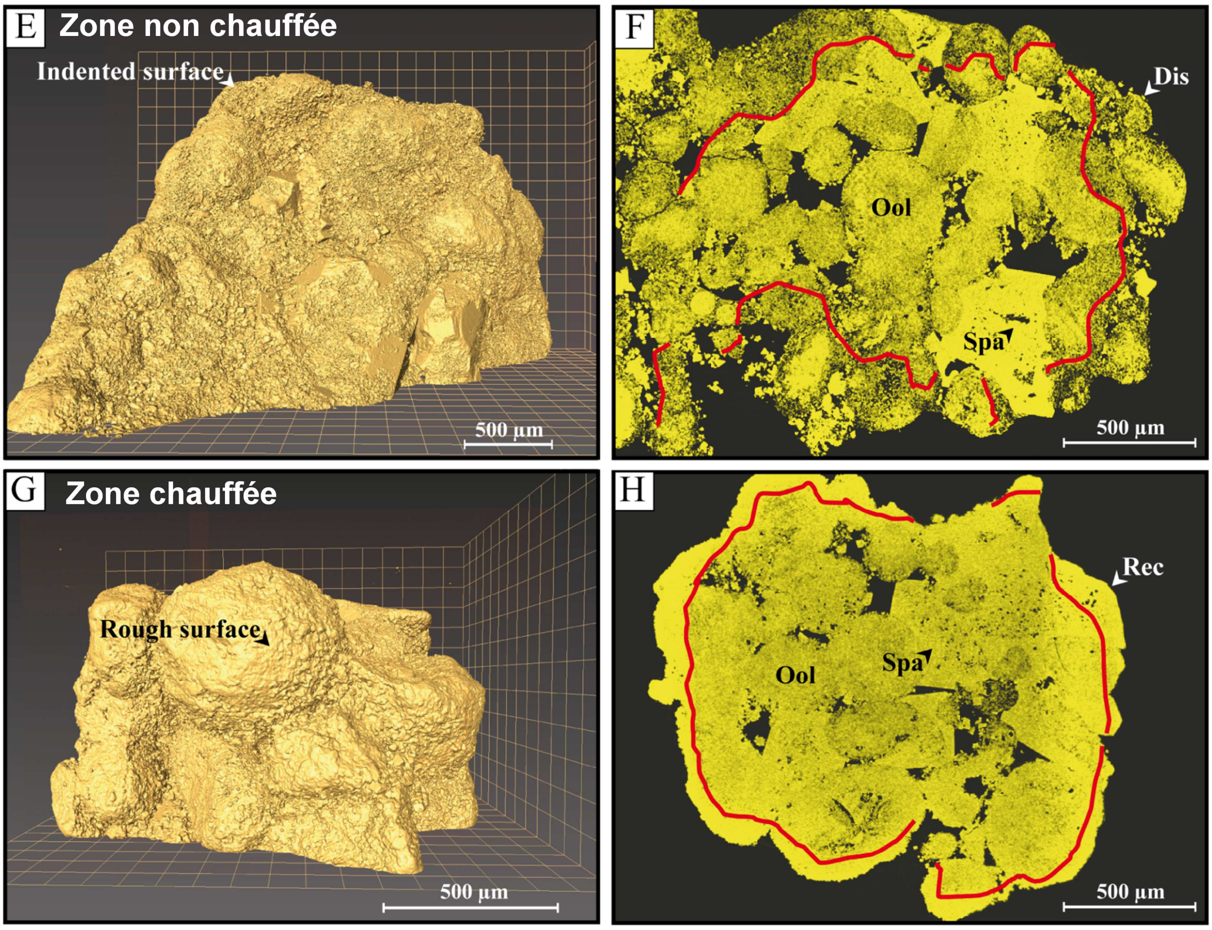

Figure 15 : Utilisation de la microtomographie X pour quantifier les propriétés pétrophysiques d'un réservoir (calcaire oolithique du Lavoux) soumis à un gradient de température et à l'action de CO_2 supercritique en milieu saturé (expérience COTAGES). D'importants transferts de masse par diffusion en solution se manifestent par une dissolution marquée des oolithes périphériques en zone froide (35 à 55°C) et une précipitation en périphérie de grain dans la zone chauffée (100°C). Le traitement d'images a permis de quantifier les variations de porosité lors de l'expérience (article Jobard et al soumis).

Publications et résumés étendus

Geochemical study of the reactivity of a carbonate rock in a geological storage of CO_2 : Implications of co-injected gases. Renard, S., Sterpenich, J., Pironon, J., Chiquet, P., Lescanne, M., Randi, A. (2011). Energy Procedia 4, 5364-5369.

Impact of SO_2 and NO on carbonated rocks submitted to a geological storage of CO_2: an experimental study. In: Y.W.a.J.J. Carroll (Editor), Acid Gas Injection and Related Technologies. Renard, S. Sterpenich, J., Pironon, J., Randi, A. Chiquet, P. Lescanne, M. (2011). Advances in Natural Gas Engineering. Scrivener publishing, Calgary AB Canada.

Experimental modelling of the impact of thermal gradient during geological equestration of CO2 s: the COTAGES experiment. Jobard, E., Sterpenich, J., Pironon, J., Corvisier, J., Jouanny, M., Randi, A. Soumis à Journal of Greenhouse Gas Control.

Geological storage of CO_2 in the Rousse reservoir (France). Part.1 : Reconstruction of geochemical history from mineralogy and fluid analysis in reservoir and caprock. Renard, S., Pironon, J., Sterpenich, J., Lescanne, M. Chiquet, P. Soumis à Marine and Petroleum Geology.

Geochemical study of the rock reactivity in a geological storage of CO_2: implications of co-injected gases. Renard, S., Sterpenich, J., Pironon, J., Lescanne, M. Chiquet, P. Randi, A. A soumettre à Geochimica et Cosmochimica Acta.

Available online at www.sciencedirect.com

ScienceDirect

Energy Procedia 4 (2011) 5364–5369

Energy
Procedia

www.elsevier.com/locate/procedia

Geochemical study of the reactivity of a carbonate rock in a geological storage of CO_2 : implications of co-injected gases.

Stéphane Renard[1], Jérôme Sterpenich[1], Jacques Pironon[1], Pierre Chiquet[2], Marc Lescanne[2], Aurelien Randi[1]

[1] Nancy-Université, CNRS, CREGU, G2R laboratory, B.P. 70239, F-54506 Vandœuvre-lès-Nancy, France
[2] TOTAL, CSTJF, 64018 Pau Cedex, France

Abstract
In the context of the limitation of global warming, geological storage of acid gases is one of the main options retained to reduce anthropogenic gas emissions to the atmosphere The work presented here documents the reactivity of a carbonate rock in the presence of a gas containing CO_2 and co-injected gases: 4% SO_2, 4% O_2, 4% N_2 and 6% Ar representative of oxycombustion flue gas before any purification (eg. desulfurisation) process. The study is based on experiments conducted in batch reactors simulating the interactions occurring between the rock and acid gases that would be injected in a geological storage context. It shows that the main mineral transformations of the rocks are due to the co-injected gases SO_2 and O_2 despite their low concentration (less than 4%). These transformations should have different impacts on the petrophysical properties of the rocks such as porosity and permeability.

Keywords : geological storage, SO_2, O_2, carbonate rock, experiments

Date of submission
08/31/2010

doi:10.1016/j.egypro.2011.02.519

1. Introduction

In order to limit the global warming, several options to reduce greenhouse gas emissions were established, including the CO_2 capture and geological storage. This latter solution consists in a whole chain from gas capture from boilers to injection into geological reservoirs such as unmineable coal beds, structural traps in deep saline aquifers or depleted oil and gas fields [1]. The capture is performed through different processes which can however not provide a complete separation of CO_2 from the other fumes components for energetic and economical reasons. Other gas components such as N_2, Ar, O_2, SO_x and NO_x are obviously present up to a fraction of 5 to 10 %mol [2]. The chemical effects on the host rocks of these co-injected gases must be evaluated in order to assess the impact of their presence on the long term stability of the storage.

The work presented here documents the experimental reactivity of a carbonate rock in the presence of a gas containing CO_2 and 4% SO_2, 4% O_2, 4% N_2 and 6% Ar. This mixture is representative of an oxycombustion flue gas before desulfurisation unit. The rock sample is representative of a deeply buried, low porosity carbonate reservoir composed of a dolomitic matrix, with minor clay, pyrite and quartz, cross-cut by dolomite and calcite cemented fractures.

Experiments were conducted in batch reactors of 2 cm^3 in the presence of a rock sample, saline water (25 g/l NaCl) and gas. The reactors were placed at 100 bar and 150°C during one month.

After experiments, rocks and fluids were analysed with different techniques (SEM, TEM, Raman and XRD). Gases were also collected and analysed by Raman spectrometry whereas the aqueous solution is analysed with ICP-MS, ICP-AES and ionic chromatography.

This study shows the first results of a study developed in [7] concerning the mineralogical transformations of carbonate rocks that have undergone CO_2 mixtures containing co-injected gases.

2.Apparatus and methods

Experiments are performed in batch conditions during one month at 150°C and 100 bar, which represent conditions in agreement with the context of geological storage of CO_2. The batch reactors are constituted by gold capsules of 2 cm^3 chosen for their chemical inertia, and their high ability to conduct pressure and temperature [8]. Thermodynamic conditions of the experiments are controlled by a pressure vessel of 100 cm^3 heated by a coating device. The device is presented in details in [3]. It has been routinely employed for several experimental studies under similar pressure and temperature couples [3, 5, 9] mimicking geological environments. Mass balances are established after experiment using analytical characterization of each phase.

2.1.Solids and aqueous solution

The rock samples come from cores drilled in a fractured Portlandian dolomite from the south of France, namely the Mano Dolostone. They were previously analyzed using SEM, EPMA and TEM [7]. They are constituted by a low porosity (< 3%) matricial dolostone crossed by fractures filled with dolomite and calcite. The matrix is always separated from fractures by a thin layer of calcite (20 μm thick).

The global mineralogy of the rock has been established from global (ICP-MS and OES) and punctual analyses (EPMA, SEM, TEM). The fracture of the Mano Dolostone is made of 93% Fe-Dolomite, 5% Calcite and 2% Dolomite. The matrix of the Mano Dolostone contains 92% Dolomite, 4% Illite and Interstratified Illite/Smectite, 3% Quartz, 1% pyrite and traces of Calcite.

The rock samples are cut to form stick fragments of 10 mm x 2 mm x 2 mm (figure 1). Each sample contains both matrix and fracture facies of the rock. Each fragment is polished on one face in order to detect the slights changes (dissolution or precipitation) on its surface.

The composition of the aqueous solution used for the experiments is representative of saline formation waters with a salinity of 25g/l of NaCl. The respective rock/water/gas proportions introduced into the reactor are given in table 1: the water/rock and water/gas mass ratios are respectively set near 3 and 5.

Experiment	**Rock (mg)**	**Solution (mg)**	**Gas (mg)**
CO_2	120	402	75
Gas mixture	133	450	100

Table 1: Mass (mg) of rock, aqueous solution and gas used for the experiments on the reservoir rock and caprock.

At the end of experiment, each phase is collected and analysed. A mass balance is performed using the final composition of the water and the structural formula of each mineral phase present at the start and the end of experiment, using the method developed by [7].

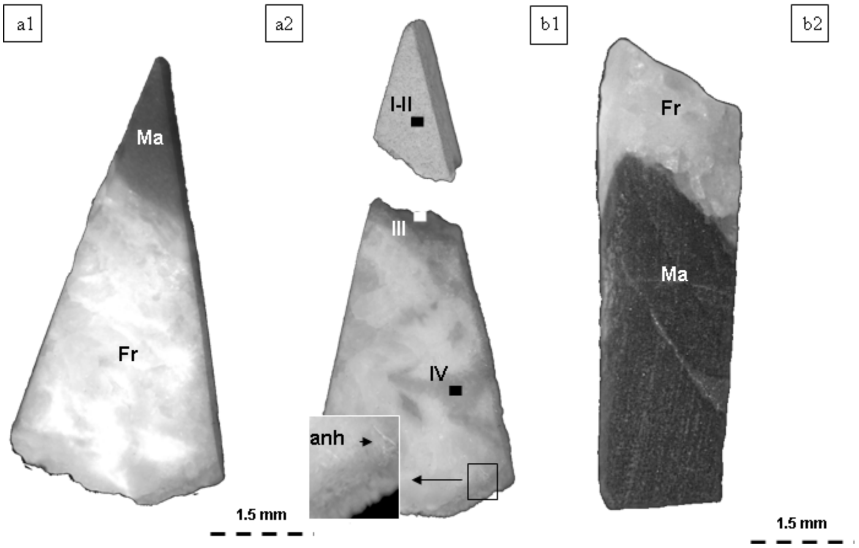

Figure 1: Observation with binocular lens of the rock samples before and after experiment. (a1) and (b1) samples before experiment, (a2) sample after experiment with the gas mixture, (b2) sample after experiment with pure CO_2. (anh) glitter of anhydrite, (Ma) Matrix of the rock, (Fr) fracture of the rock. Points I to IV refer to pictures on Figure 3.

2.2.Gases

Two sets of gases were selected: pure CO_2 and a gas mixture composed of 82 ± 0.18 %mol CO_2, 4 ± 0.2 %mol SO_2, 4 ± 0.2 %mol O_2, 4 ± 0.2 %mol N_2 and 6 ± 0.12 %mol Ar. The gas mixture corresponds to the composition of the exhaust fumes from an oxyboiler with no desulfurization process. The injected quantities are displayed in table 1.

The gases are loaded in the capsules using the gas loading device adapted from [3] (see [7]) associated to a cold trap by liquid nitrogen. When the capsule is filled with the gas, it is cut and immediately welded in liquid nitrogen. After experiment, the capsules are pierced in the line and the gases are collected by the same cold trap and are condensed in a raman cell for analysis.

3. Results and discussion

3.1. Reactivity of the rock with pure CO_2

	CO_2			**Gas mixture**		
	Start (mol)	**End (mol)**	**% variation**	**Start (mol)**	**End (mol)**	**% variation**
Pyrite	$1.5\ 10^{-5}$	$1.4\ 10^{-5}$	- 6 %	$7.1\ 10^{-7}$	0.0	- 100 %
Dolomite	$6.5\ 10^{-4}$	$6.5\ 10^{-4}$	+ 0.3 %	$6.8\ 10^{-4}$	$6.5\ 10^{-4}$	- 4.2 %
Calcite	$1.1\ 10^{-5}$	$1.0\ 10^{-3}$	- 8.5 %	$2.9\ 10^{-5}$	$5.4\ 10^{-7}$	- 98.1 %
Clays	$1.5\ 10^{-5}$	$1.5\ 10^{-5}$	- 0.5 %	$6.0\ 10^{-6}$	$6.0\ 10^{-6}$	- 5 %
Quartz	$1.1\ 10^{-3}$	$1.0\ 10^{-3}$	- 0.4 %	$1.1\ 10^{-3}$	$1.1\ 10^{-3}$	- 0.3 %
Hematite	-	-	-	0.0	$3.1\ 10^{-7}$	-
Barite	0.0	$2.8\ 10^{-10}$	-	0.0	$1.8\ 10^{-8}$	-
Anhydrite	0.0	$1.2\ 10^{-6}$	-	0.0	$4.4\ 10^{-5}$	-

Table 2: Mineralogical transformations in the rock samples after experimental reactivity with pure CO_2 and the gas mixture. Values are expressed in mol and were calculated from the composition of water and the mineral formulae [7].

After experiment, the gas is still composed by pure CO_2. The rock sample shows a frosted aspect, due to a slight dissolution of carbonates on its surface whatever the facies (figure 2). Calcite of fractures seems to be much affected than dolomite (the sample shows a dissolution of 8.6 % for calcite against 0.3 % for dolomite. See table 2), presenting negative relief by comparison with the other minerals. Quartz and pyrite are still present. Pyrites show a slight oxidation on their surface when analysed by EDS (Electron Dispersive Spectrometry). A calculation give a disappearance of less than 6% of their initial quantity. Clays have undergone a slight dissolution (less than 1 %).

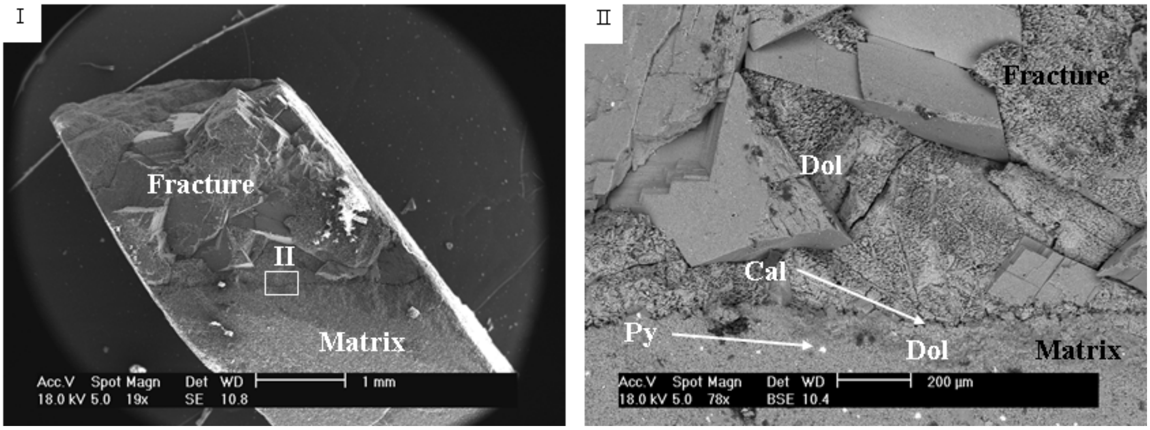

Figure 2: SEM images of the reservoir rock sample after experiment with CO_2 and saline water (25 g/l). (Cal) calcite, (Dol) dolomite, (Py) pyrite.

The observed reactivity corresponds to the equilibration of the rock with the acidity brought by CO_2 dissolution into the water. It can be resumed as follows:

$$CO_{2,g} = CO_{2,aq} \tag{1}$$

$$CO_{2,aq} + H_2O = HCO_3^- + H^+ \tag{2}$$

$$\text{Dolomite} + 2H_+ = Ca^{2+} + Mg^{2+} + 2\ HCO_3^- \tag{3}$$

$$\text{Calcite} + H^+ = Ca^{2+} + HCO_3^- \tag{4}$$

Clays are also concerned by this acidification but in a lower order of magnitude, explaining their really slight dissolution. Silicon detected in the water is due to partial dissolution of clay but also to equilibration of quartz with the water:

$$\text{Quartz} = SiO_{2,aq} \tag{5}$$

$$\text{Amorphous silica} = SiO_{2,aq} + n\ H_2O \tag{6}$$

A reduced fraction of gaseous oxygen is inherent to the system due to the loading procedure [7], explaining the partial oxidation of pyrites and leading to the formation of in situ hematite and sulfates detected in the water:

$$2\ \text{Pyrite} + 4\ H_2O + 7{,}5\ O_2 = \text{Hematite} + 4\ SO_4^{2-} + 8\ H^+ \tag{7}$$

The mass balance calculated from the water analyses shows that less than 1% of the total dolomite and quartz, 10% of the calcite and 6% of the pyrites were dissolved during experiment. Calcite and pyrites are the most altered minerals in our conditions.

3.2. Reactivity of the rock with the gas mixture

After experiment, the gas is composed by a mixture of 88 mol% CO_2, 1,5 mol% O_2, 4,5 mol% N_2 and 6 mol% Ar. It corresponds to an increase of 4 mol% of the initial CO_2 and a loss of more than 60 mol% of the initial O_2. SO_2 is absent from the final composition of the gas.

The rock sample was cleaved in two part on the wall rock of the fracture. High figures of dissolution are visible on the sample surface whatever the facies. In the matrix, the dolomite crystals are rounded, creating porosity between the grains (Figure 3-I and II). In the fracture zone, dolomite shows a specific pattern due to preferential dissolution along the cleavages of the crystals (Figure 3-IV). It lost almost 5% of it initial quantity (table 2). Pyrites are oxidized in hematite (Figure 3-II). Calcite is completely dissolved, explaining the separation of the sample into two pieces observed after experiment. Quartz is still present and does not seem to have undergone any specific alteration (table 2). Clays have slightly dissolved (less than 5%). A closer observation shows sparse sulphate crystals mainly represented by anhydrite onto the whole sample, especially the wall rock area where it replaced calcite (Figure 3-III). Barite has also precipitated in micrometric crystals (< 3 µm) spread over the rock surface, independently from the initial mineralogy.

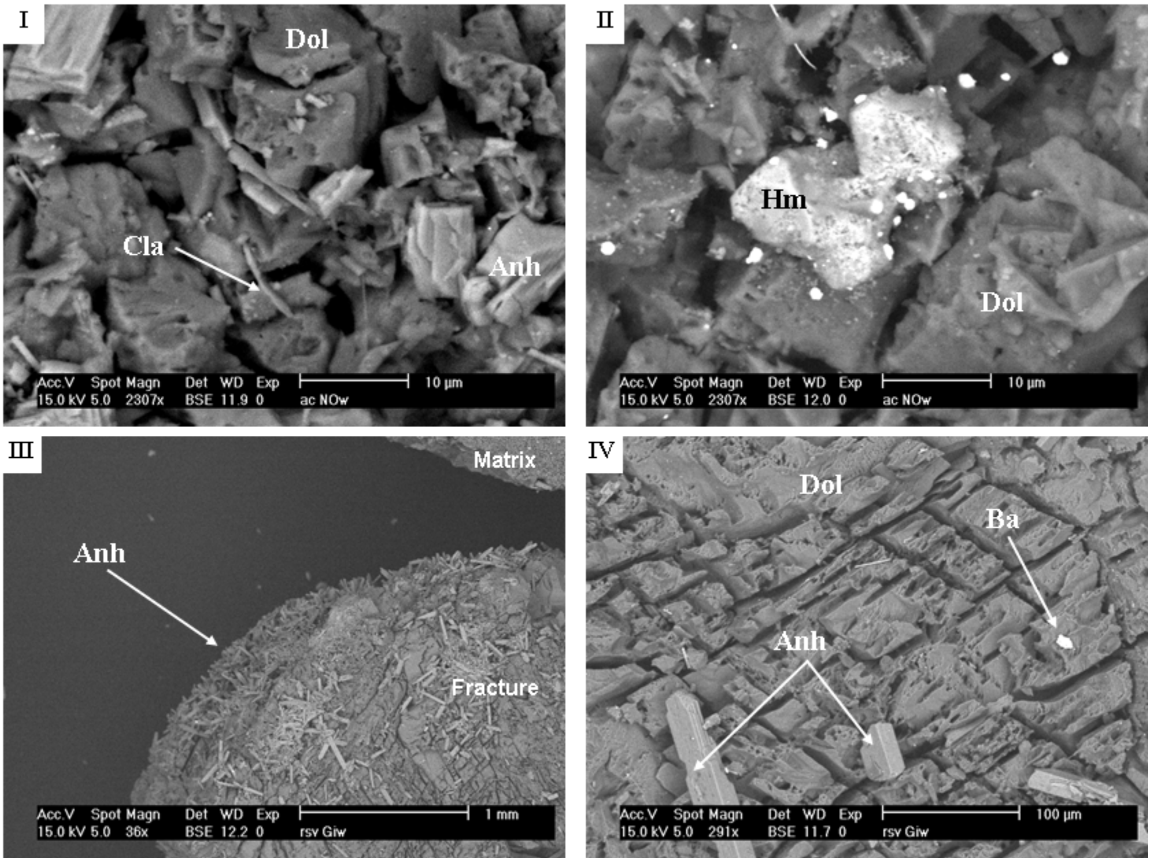

Figure 3: Backscattered scanning electron micrographs showing the rock sample after experiment. (I-II) matrix of the rock; (III) wall rock of the fracture; (IV) fracture of the rock. (Anh) anhydrite, (Ba) Barite, (Cla) clay minerals, (Dol) dolomite, (Hm) hematite .

The observed reactivity is much higher than for pure CO_2. N_2 and Ar are known to be inert at the thermodynamic conditions used for experimentation. Thus, the reactivity can be attributed to the co-injected fraction of O_2 and SO_2.
SO_2 can easily be oxidised by O_2. As it is highly soluble in water at 150°C and 100 bar [10], the oxidation must have occurred in the water phase, producing sulfates at pH higher than 3:

$$SO_2 + H_2O + \frac{1}{2} O_{2,g} = SO_3^{2-} + 2\,H^+ + \frac{1}{2} O_2 = SO_4^{2-} + 2\,H+ \qquad (8)$$

This reaction must have been total in the aqueous phase. It is classically used as a method for SO_2 removing from coals. It is proven to occur at very low SO_2 and O_2 concentrations for temperatures set between 80 and 150°C [6].
Dissolution and oxidation of SO_2 led to acidification of the solution which was counterbalanced by the buffer effect of carbonates (reactions 3 and 4). The calcium and sulfate concentration bluid up in the solution led to the saturation of anhydrite:

$$\text{Calcite} + 2\,H^+ + SO_4^{2-} = \text{Anhydrite} + CO_{2,aq} + H_2O \qquad (10)$$

$$\text{Dolomite} + 4\,H^+ + SO_4^{2-} = \text{Anhydrite} + 2\,CO_{2,aq} + 2\,H_2O + Mg^{2+} \qquad (11)$$

The carbonate dissolution also released trace elements such as strontium and barium. Because of its very low solubility, barite also precipitated:

$$Ba^{2+} + SO_4^{2-} = \text{Barite} \qquad (12)$$

The remaining O_2 fraction reacted with the pyrites to give hematite according to the equation 7. The fugacity of O_2 given by SUPCRT92 [4] for this equilibrium in experimental conditions is near 10^{-41} bar. As a fraction of gaseous O_2 remains at the end of experiment, it is possible to consider that 1) O_2 was in excess comparing to the quantity of pyrites accessible to the fluids, 2) pyrites contacted by the were completely oxidized. Thus, the final conditions remain highly oxidative in the reactor.

Conclusion

This work presented the reactivity of a carbonate rock in case of an injection of a CO_2 gas containing fractions of SO_2, O_2, N_2 and Ar. Two comparative experiments were performed, using pure CO_2 and a mixture of CO_2 with fractions of inert gases and O_2 and SO_2. They showed that SO_2 dissolves in the water and reacts with O_2, resulting in production of aqueous sulfates and a high acidification of the water. This has for primary consequence to enhance drastically the reactivity of the rock, implying the dissolution of calcite, shortly followed by dolomite. When saturation is reached for anhydrite and barite, they start to precipitate in place of the dissolved carbonates. Pyrite is oxidized in hematite by the remaining O_2 fraction. Finally, 5 to 10% of the initial rock were dissolved or altered by the co-injected gases against less than 1% for pure CO_2. Carbonate dissolution and anhydrite precipitation are the main reactions. They could induce high changes in the petrophysic properties of the rock.

This study is a preliminary but necessary work to understand and model the evolution of CO_2 geological storage.

Acknowledgments

This work is supported by TOTAL and ADEME (France). It is included in the project "Gaz Annexes" of the French National Agency for Research (ANR).

References

[1] Holloway, S. An overview of the underground disposal of carbon dioxide. Ener Conv Man 38:S193-S198.

[2] IEA Greenhouse Gas R&D Programme. Retrofit of CO_2 Capture to Natural Gas Combined Cycle Power Plants. report 2005/1

[3] Jacquemet N., Pironon J., Caroli E. A new experimental procedure for simulation of $H_2S + CO_2$ geological storage. Application to well cement aging. OGST 60;1:193-206.

[4] Johnson J.W., Oelkers E.H., Helgeson, H.C. SUPCRT92: a software package for calculating the standard molal thermodynamic properties of minerals, gases, aqueous species, and reactions from 1 to 5000 bars and 0 to 1000 degrees C Comput Geosci 18:899–947.

[5] Landais P., Michels R., and Poty B. Pyrolysis of organic matter in cold-seal pressure autoclaves. Experimental approach and applications. J anal App Pyr 16:103-115

[6] Lizzio A.A., DeBarr J.A. Mechanism of SO_2 removal by carbon. Ener Fu 11;2:284-291.

[7] Renard S., 2010. Rôle des gaz annexes sur l'évolution géochimique d'un site de stockage de dioxyde de carbone. Application à des réservoirs carbonatés. INPL, Nancy. Thèse de doctorat. 1 vol., 422 p.

[8] Seyfried W. E. J., Janecky D. R., Berndt M. E. The flexible reaction-cell system. Hydrothermal experimental techniques. In: Ulmer GC and Barnes HL, editors. Rocking autoclaves for hydrothermal experiments, New York: John Wiley & Sons; 1987, p. 216-239.

[9] Teinturier S., Pironon J. Synthetic fluid inclusions as recorders of microfracture healing and overgrowth formation rates. Am Min 88;8-9:1204-1208.

[10] Van Berkum J.G., Diepen G.A.M. Phase equilibria in $SO_2 + H_2O$: the sulfur dioxide gas hydrate, two liquid phases, and the gas phase in the temperature range 273 to 400 K and at pressures up to 400 MPa. J Chem Therm 11;4:317-334.

Impact of SO_2 and NO on carbonated rocks submitted to a geological storage of CO_2: an experimental study.

Stéphane Renard[a], Jérôme Sterpenich[a], Jacques Pironon[a], Aurélien Randi[a], Pierre Chiquet[b] and Marc Lescanne[b]
a Nancy-University, CNRS, CREGU, UMR G2R, B.P. 239, F-54506 Vandoeuvre-lès-Nancy, France
b TOTAL, CSTJF, Avenue Larribau, F-64018 Pau, France

Abstract

Geological storage of acid gases in carbonated rocks (deep saline aquifers or oil depleted reservoirs) is one of the solutions studied to limit the emissions of greenhouse gases in the atmosphere This paper is devoted to the study of the reactivity of rocks that could be submitted to CO_2 and annex gases (SO_2 and NO) during the injection of a CO_2 rich gas in a geological storage. This experimental study focuses on the interactions that take place between carbonate rocks (dolomite and calcite rich) and CO_2 co-injected annex gases. The results, interpreted in terms of petrophysical and chemical impacts of the injected gases can be used to improve thermodynamical and geochemical modelling.

Keywords: geological storage, SO_2, NO, CO_2, carbonate rocks, experiments

Table of Contents

Date of submission
08/31/2010

1. Introduction

The CO_2 capture and geological storage from high emitting sources (coal and gas power plants) is one of a panel of solutions proposed to reduce the global greenhouse gas emissions. Different pre- , post- or oxy-combustion capture processes are now available to separate associated gases (SOx, NOx, etc.) and the CO_2. However, complete purification of CO_2 is unachievable for cost reasons as well as for CO_2 surplus of emissions due to the separation processes. By consequence, a non-negligible part of these gases could be co-injected with the CO_2. Their impact on the chemical stability of reservoir rocks, caprocks and well has to be evaluated before any large scale injection procedure. Physico-chemical transformations could modify mechanical and injectivity properties of the site and possibly alter storage safety.

The study presented here is focused on experiments of geochemical interactions between rocks and gases (SO_2 and NO) which could be co-injected with CO_2.

The rocks we studied are carbonate rocks (dolomite and calcite rich) which are some possible analogues of reservoir rocks and cap-rocks.

Samples are placed in $1cm^3$ gold capsules together with saline water (25 NaCl g/l). Gases are hermetically transferred by cold trap into the gold reactors that are sealed by electrical welding and placed in an autoclave during one month at 150℃ and 100 bar, which represent geological conditions of a depleted deep reservoir.

After experiments, solid samples are observed and analysed with different techniques (SEM, TEM, Raman and XRD). Gases are also collected and analysed by Raman spectrometry whereas the aqueous solution is analysed with ICP-MS, ICP-AES and ionic chromatography. As sampling during experiments wasn't possible, we developed the synthetic fluid inclusions technique to trap and analyse the fluids under experimental conditions. This allows to characterise the different phases and the nature of dissolved species. Mass budgets are established in order to quantify the ratio of mineral transformation.

This study shows the first results concerning the mineralogical transformation of rocks and well materials submitted to the chemical action of possible annex gases, NO and SO_2.

The results, interpreted in terms of petrophysical and chemical impacts of the injected gases can be used to improve thermodynamical and geochemical modelling

2. Apparatus and methods

Experiments are performed on natural rock samples in batch conditions during one month at 150℃ and 100 bar, which represent realistic conditions in the context of geological storage of CO_2 into depleted reservoir. The batch reactors are made of gold capsules hermetically welded. Gold is used because of its chemical inertia, and its ability to conduct pressure and temperature (Seyfried et al., 1987). The volume of the reactors is around 2 cm^3 (inner diameter of 0.5 cm for a length of 10 cm). After welding capsules are placed in a pressure vessel of 100 cm^3 heated by a coating device (figure 1). The pressure is controlled by a hydraulic pump. The device is presented in more details in Jacquemet et al. (2005). It has been routinely employed for several experimental studies under similar pressure and temperature conditions (Landais et al., 1989; Teinturier and Pironon, 2003; – Jacquemet et al., 2005) mimicking geological environments. Mass balances are established after experiment using analytical characterization of each phase.

2.1. Solids and aqueous solution

The rock samples come from cores drilled in the Aquitania basin (France) in a fractured Portlandian dolomite, namely the Mano Dolostone, and in Early Cretaceous limestones, namely the Campanian Flysch. They were sampled respectively at 4580 m and 4500 m deep and were previously analyzed by Renard (2010.) using Scanning Electron Microscopy (SEM), Electron Probe Micro Analysis (EPMA) and Transmission Electron Microscopy (TEM).

The sample of Mano Dolostone is made of a dolomitic matrix crossed by a fracture filled with Fe-dolomite and with a thin layer of calcite. For the experiments, we selected samples containing both facieses separated according to a ~ 20 um-thick layer of calcite. The Campanian Flysch is mainly calcitic. The fracture of the Mano Dolostone is made of 93% Fe-dolomite $(CaMg)_xFe_{2-x}(CO_3)_2$, 5% calcite $CaCO_3$ and 2% dolomite $CaMg(CO_3)_2$. The matrix of the Mano Dolostone contains 92.2% dolomite, 4.2% illite $Si_{3.4}3Al_{2.26}Fe_{0.06}Mg_{0.24}K_{0.71}Na_{0.07}Ca_{0.02}$ and interstratified illite/smectite, 3% quartz SiO_2, 0.5% pyrite FeS_2 and 0.1% calcite.

The Campanian Flysch is made of 63.2% calcite, 10.5% quartz SiO_2, 8.3% illite $Si_{3.42}Al_{2.18}Fe_{0.2}Mg_{0.2}K_{0.7}Ca_{0.05}$, 6.5% interstratified chlorite/smectite, 4.5% chlorite $Si_{2.56}$ $Al_{2.7}Fe_{3.56}$ $Mg_{1.27}$, 4.6% ankerite $Fe_x(Ca,M,Mn)_{1-x}CO_3$, 2.1% dolomite, 0.3% pyrite.

The rock samples were cut into stick fragments of around 10 mm x 2 mm x 2 mm. They were then polished on one face in order to better detect the mineralogical changes (dissolution or precipitation) on the surface.

We partially filled the gold capsules with a 25g/l NaCl brine. The water/rock and water/gas mass ratios were respectively about 3 and 5 as specified in Table 2-1.

Experiment	**Mass**	**Rock (mg)**	**Solution (mg)**	**Gas (mg)**
N_2	Reservoir rock	127	434	38
N_2	Caprock	145	550	40
SO_2	Reservoir rock	103	510	423
SO_2	Caprock	130	630	220
NO	Reservoir rock	130	520	160
NO	Caprock	135	510	155

Table 2-1 : Quantities expressed in mg of rock, aqueous solution and gas used for the experiments on the reservoir rock and caprock.

For each experiment, a decrepited quartz was added to the system in order to trap the fluids during the experiment in synthetic fluid inclusions.

At the end of experiment, gold capsules were opened to collect the gas phase, the aqueous solution and the minerals for analyses.

2.2. Gases

The two different types of gases selected for experiments are SO_2 and NO. A blank capsule containing the same phases (aqueous solution and solid) was filled with N_2 as an inert gas phase. The injected quantities for each experiment are displayed in Table 2-1.

The gases are loaded in the capsules using the gas loading device adapted from Jacquemet et al., 2005 (Figure 2-1). During the loading procedure, the gold capsules are hermetically fixed on the capsule connector which is plugged to the loading device through the valve E. Knowing the volume of the loading line and controlling the pressure in the system, it is possible to fill the reactor with a known mass of gas thanks to a nitrogen cold trap. After experiment, cold capsules are pierced in an appropriate device plugged to valve C. After trapping, the gas can be driven to a Raman cell for analysis.

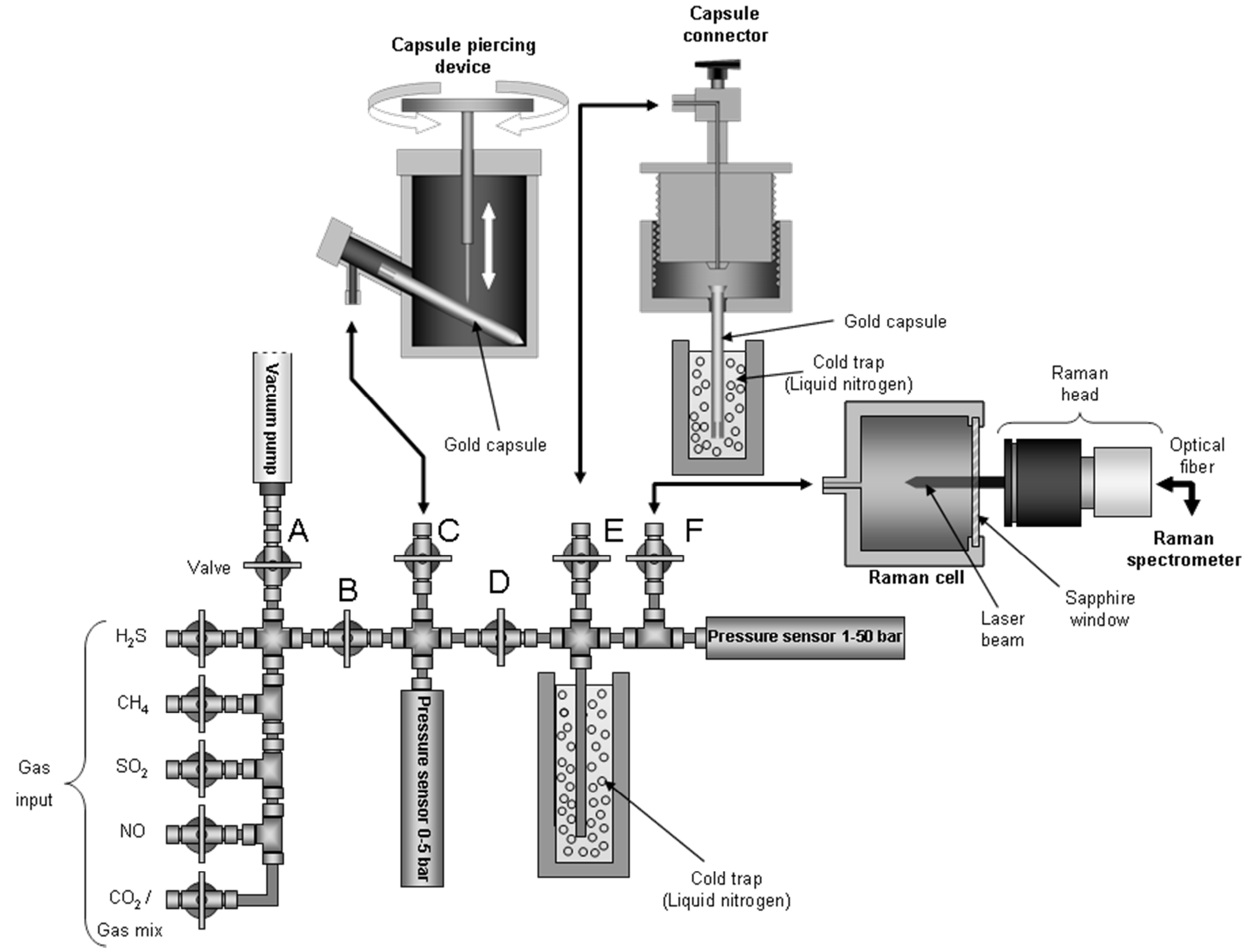

Figure 2-1: Gas loading and sampling line used during the experimental phase, adapted from Jacquemet et al. (2005). (A-E) valves. Different devices can be connected to the line: a capsule piercing device used to collect gases after experiment, a capsule loading device used to trap gases in the capsule and a cell for the Raman analysis of the gases.

3. Results and discussion

This section is devoted to the description of the mineral changes observed from the solid samples of reservoir and caprock aged with N2 (blank experiments) SO2 and NO during one month at 150℃ and 100 bar.

3.1. Reactivity of the blank experiments

After experiment, the samples of the reservoir rock do not present any visible transformation except a slight frosted aspect of the initially polished face. SEM observations (Figure 3-16) show that the frosted aspect is due to a slight dissolution of the carbonate phases, the dolomite of the matrix and the calcite of the fracture. However the dolomite of the fracture does not seem to have undergone any significant dissolution. Pyrite and quartz keep unaltered whereas the analyses of the clay fraction (Renard 2010) show a partial leaching of Na and Ca cations.

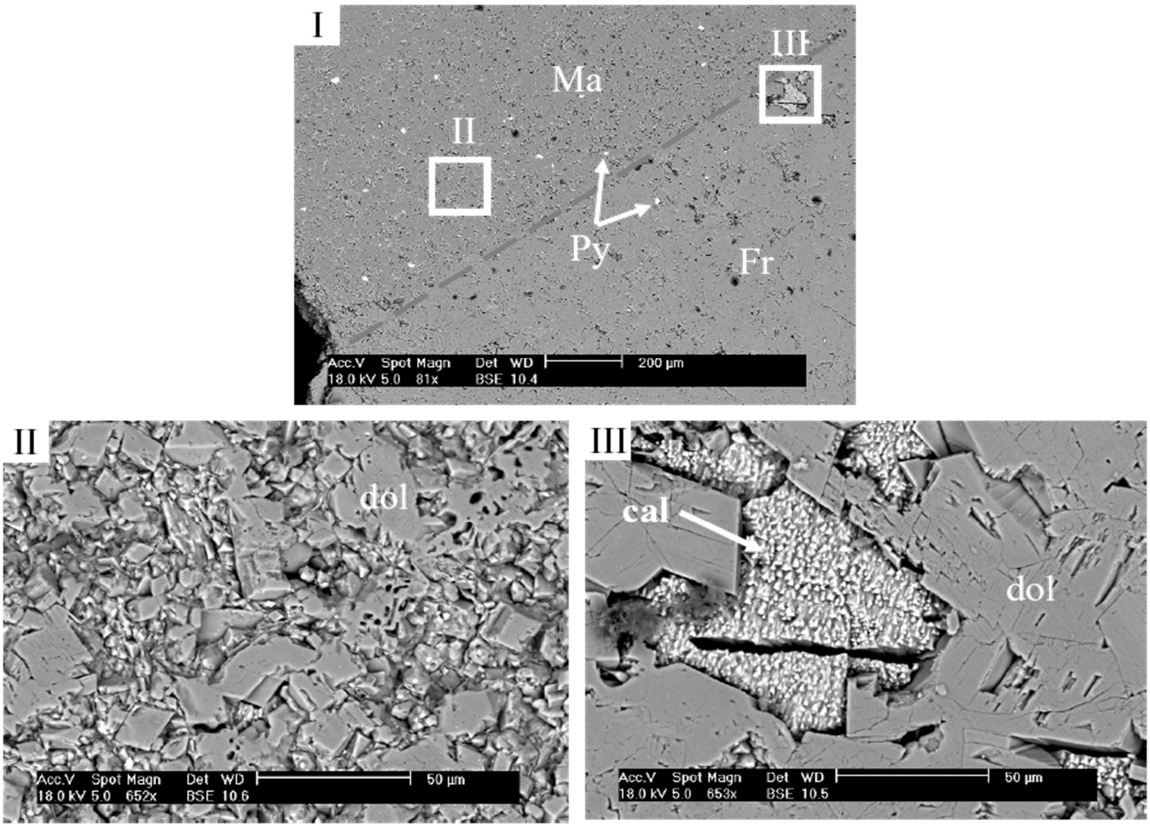

Figure 3-16 : SEM backscattered images of the reservoir rock sample after experiment with N_2 and saline water (25 g/l). (I) Global view of the matrix (Ma) and the fracture (Fr), (II) zoom on the matrix, (III) zoom on close to the wall of the fracture. (cal) calcite, (dol) dolomite, (Py) pyrite.

Concerning the caprock, the optical observations show a slight frosted aspect as well as the presence of a brown-orange colour on the surface. The limited reactivity is observable with SEM (*Figure 3-17*Figure 3-2). The surface of the calcite is slightly dissolved. The grains of quartz and the framboidal pyrites seem to be unaltered. However EDS (Energy Dispersive Spectrometry) analyses show that the surface of the pyrites is oxidised explaining the brownish aspect of the sample. Clay minerals analysed by TEM before and after experiment do not react significantly during experiment.

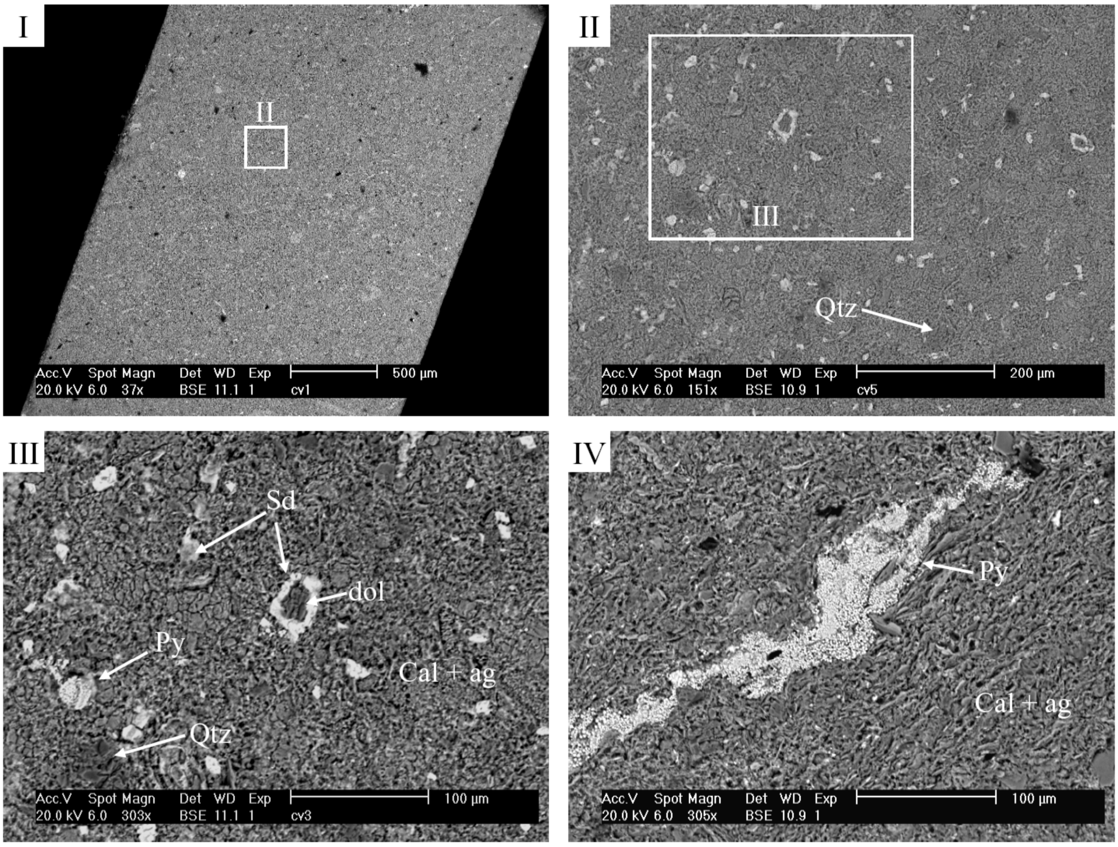

Figure 3-17 : SEM backscattered images of the caprock sample after experiment with N2 and saline water (25 g/l). (I) Global view of the sample, (II-III) zoom on a zoned siderite, (IV) zoom on a pyrite rich zone. (ag) clay minerals, (cal) calcite, (dol) dolomite, (qtz) quartz, (sd) siderite, (py) pyrite.

The blank experiments both with the caprock and the reservoir show a very limited reactivity of the minerals corresponding to the equilibration between the initial aqueous solution and the different minerals. The pH of the solution is rapidly buffered by carbonate minerals (dolomite and calcite).

The main chemical reactions considered during the experiment that can affect the pH as well as the elemental concentrations of the solution are:

(1) $$CaMg(CO_3)_2 + 2H^+ = Ca^{2+} + Mg^{2+} + 2\ HCO_3^-$$

(2) $$CaCO_3 + H^+ = Ca^{2+} + HCO_3^-$$

(3) $$(CaMg)_{0,13}Fe_{0,74}CO_3 + H^+ = 0,13\ Ca^{2+} + 0,13\ Mg^{2+} + 0,74\ Fe^{2+} + HCO_3^-$$

(4) $$\text{Quartz} = SiO_{2,aq}$$

(5) Amorphous silica = $SiO_{2,aq} + n\ H_2O$

(6) $HCO_3^- = CO_{2g} + H^+$

(7) $H_2O = H^+ + OH^-$

During the loading of the reactors, gaseous oxygen can be trapped leading to a partial oxidation of the reduced mineral such as pyrite. This phenomenon, enhanced by the framboidal shape of the mineral increasing its reactive surface area, can be resumed by the following chemical reaction leading to the formation of hematite (Fe_2O_3) and sulfates (mainly anhydrite $CaSO_4$).

(8) $2\ FeS_2 + 4\ H_2O + 7.5\ O_2 = Fe_2O_3 + 4\ SO_4^{2-} + 8\ H^+$

The mass balance calculated from these blank experiments confirm that the mineral dissolution is very limited with less than 5% of the initial quantity of the minerals affected by the mineral transformations. Calcite and pyrite seem to be the most sensitive minerals in our experimental conditions.

3.2. Reactivity with pure SO_2

The initial reservoir and caprock samples were completely crumbled after the experiment with SO_2. After drying, a powder made of fibrous crystals of anhydrite and amorphous native sulphur was observed in association with an amorphous silica rich phase (Figure 3-18, Figure 3-19) containing iron sulphur, aluminium and potassium. Quartz and pyrite couldn't be detected. Large amounts of CO_2 were released in the gas phase as a proof of the high reactivity of the carbonates towards SO_2.

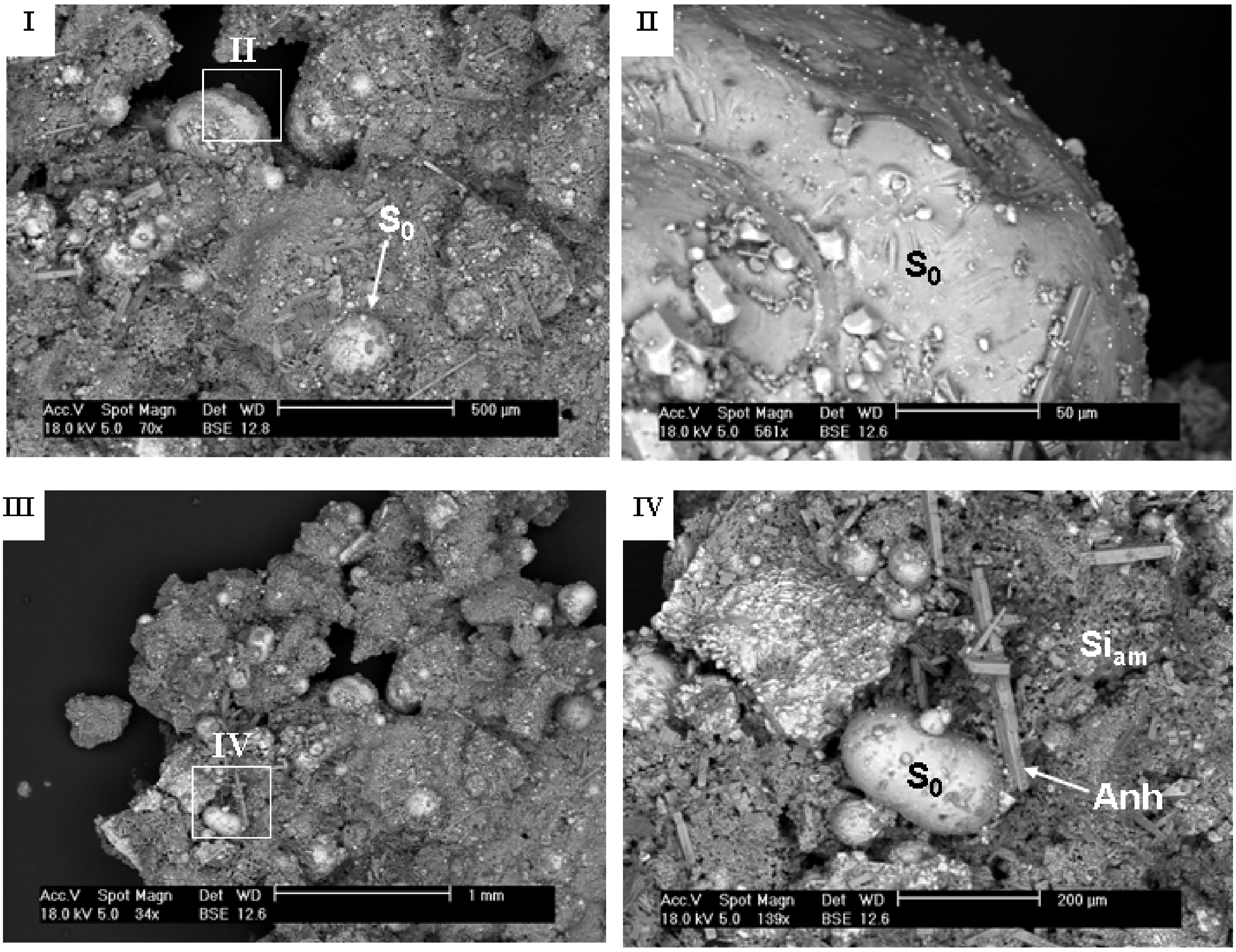

Figure 3-18 : SEM backscattered images of the reservoir rock sample after experiment with SO2 and saline water (25 g/l). (I, III) global view; (II) zoom on native sulfur; (IV) zoom on a zone containing native sulfur, anhydrite and amorphous silica. (S0) native sulfur, (Anh) anhydrite, (Siam) amorphous silica rich phase.

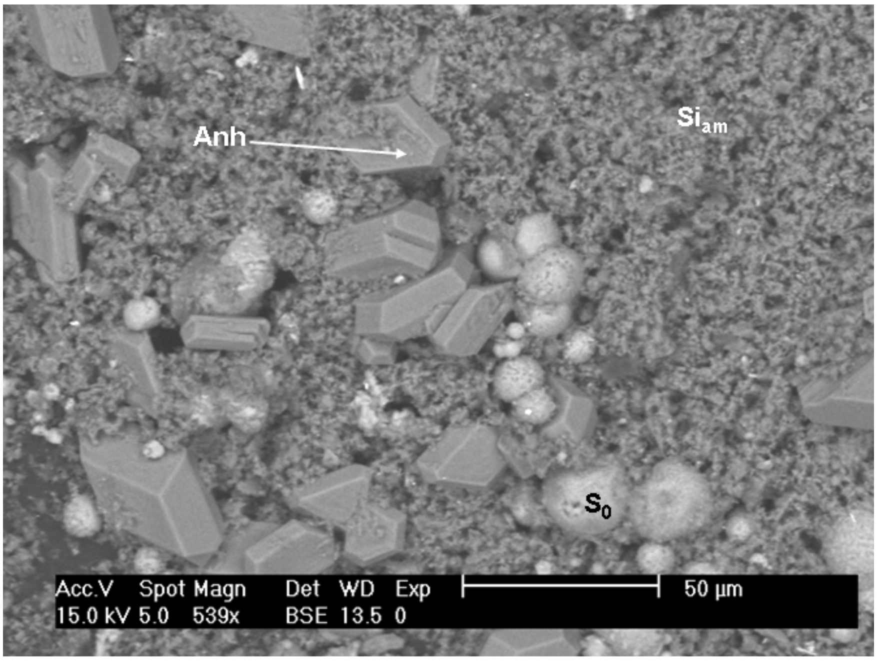

Figure 3-19 : SEM backscattered images of the caprock sample after experiment with SO2 and saline water (25 g/l). (S0) native sulfur, (Anh) anhydrite, (Siam) amorphous silica rich phase.

Under experimental pressure, temperature and water molar ratio, respectively 100 bar, 150℃ and 0.6 to 0.9, the SO_2-H_2O system is monophasic with a complete dissolution of the SO_2 in the liquid water (Van Berkum et al., 1979). The effect of NaCl is not documented under the experimental conditions but the synthetic fluid inclusions analyses show that no gaseous SO_2 was trapped during the experiments implying its quasi- total dissolution in the saline water.

When SO_2 is in solution, a reaction of disproportionation occurs leading to sulphuric acid and native sulphur according to the reaction:

(9) $$2\ H_2O + 3\ SO_{2,aq} = 2\ H^+ + SO_4^{2-} + 1/8 S_8$$

This reaction accounts for the presence of native sulphur after experiment as well as the strong alteration of minerals due to high acidic conditions. The main mineral transformations can be sum up by the following reactions involving carbonate minerals:

(10) $$\text{Dolomite} + SO_4^{2-} + Ca^{2+} + 4\ H^+ = 2\ \text{Anhydrite} + 2\ CO_{2,aq} + Mg^{2+}$$

The clay minerals are also strongly affected by the high acidity of the solution. They dissolved to give mainly Si and Al in solution that can combine to form an amorphous phase called amorphous silica rich phase. This gel can incorporate sulfur and a part of the alkalis and alkaline-earth elements coming from the dissolution of carbonates and silicates.

If we consider muscovite as a proxy for clay minerals, the reaction could be expressed as follows:

(11) $$Si_3Al_3KO_{10}(OH)_2 + 10\ H^+ = 3\ SiO_{2,am} + 3\ Al^{3+} + K^+ + 6\ H_2O$$

Pyrite is also concerned both by the acidic attack and the oxidizing power of SO_2. Pyrite is thus transformed by the following reaction enhanced in acidic conditions:

(12) $$4H^+ + SO_{2,aq} + 2\ FeS_2 = 2\ Fe^{2+} + 5/8\ S_8 + 2\ H_2O$$

The dissolution of clay minerals, especially illites, can release Fe^{3+} but the presence of SO_2, as a reducing compound in this case, leads to its reduction in Fe^{2+} in agreement with Palandri et al. (2005) according to:

(13) $$2\ Fe^{3+} + SO_{2,aq} + 2\ H_2O = 2\ Fe^{2+} + HSO_4^- + 3\ H^+$$

Thus, the presence of high amounts of SO_2 leads to a total dissolution of carbonates, silicates and pyrite and to the precipitation of anhydrite, native sulfur and an amorphous silica rich phase. The mass budget of the experiment was calculated thanks to the chemistry of the solution, the stoichiometry of the mineral phases and the composition of the gaseous phase (consumed SO_2 and produced CO_2). For both the reservoir and the caprock, the total amount of carbonates disappeared whereas it was the case only for 15 to 20% of the clayey fraction. After reaction, about 15% of the initial SO_2 gave anhydrite, 25% gave native sulfur and less than 1% gave barite ($BaSO_4$).

3.3. Reactivity with pure NO

After experiment with NO the caprock and reservoir samples kept their initial shape but showed strong visible transformations on their surface.

The matrix dolomite of the reservoir rock sample (Figure 3-20), disappeared from the surface and was only detectable deeper below the surface. Clay minerals and quartz are still present. The fracture wall calcite is altered, and the dolomite is partially dissolved according to its cleavages. The pyrites of the rock was completely oxidized into hematite. A part of the sulfur coming from the oxidation of the sulfides re-precipitated in anhydrite and in a lesser extent in barite ($BaSO_4$) from the calcium of carbonates and the barium as a trace element in the calcites.

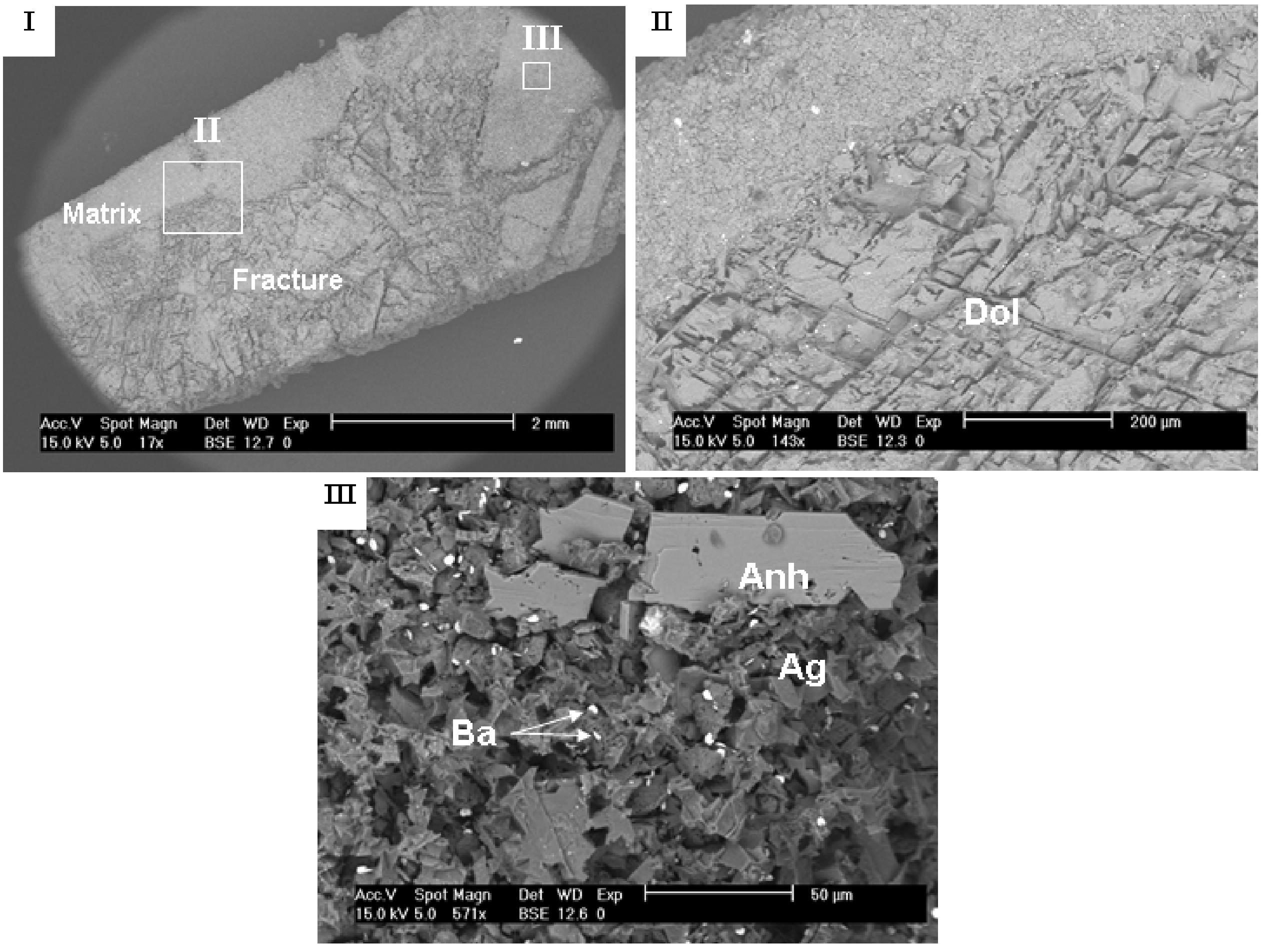

Figure 3-20 : SEM backscattered images of the reservoir rock sample after experiment with NO and saline water (25 g/l). (I) global view; (II) zoom on the limit between matrix and fracture; (III) zoom on the matrix. (Dol) dolomite, (Anh) anhydrite, (Ba) barite, (Ag) clay minerals.

Concerning the caprock (Figure 3-21), the calcite was strongly dissolved. Fe-containing minerals (siderite and pyrite) were oxidized leading to the precipitation of hematite. The sulfur from pyrites partially precipitated into anhydrite and barite. The ferriferous chlorites were also oxidized.

The observations of both the reservoir and the caprock show two main chemical mechanisms responsible for the mineral transformations: reactions under acidic conditions and oxydo-reduction reactions.

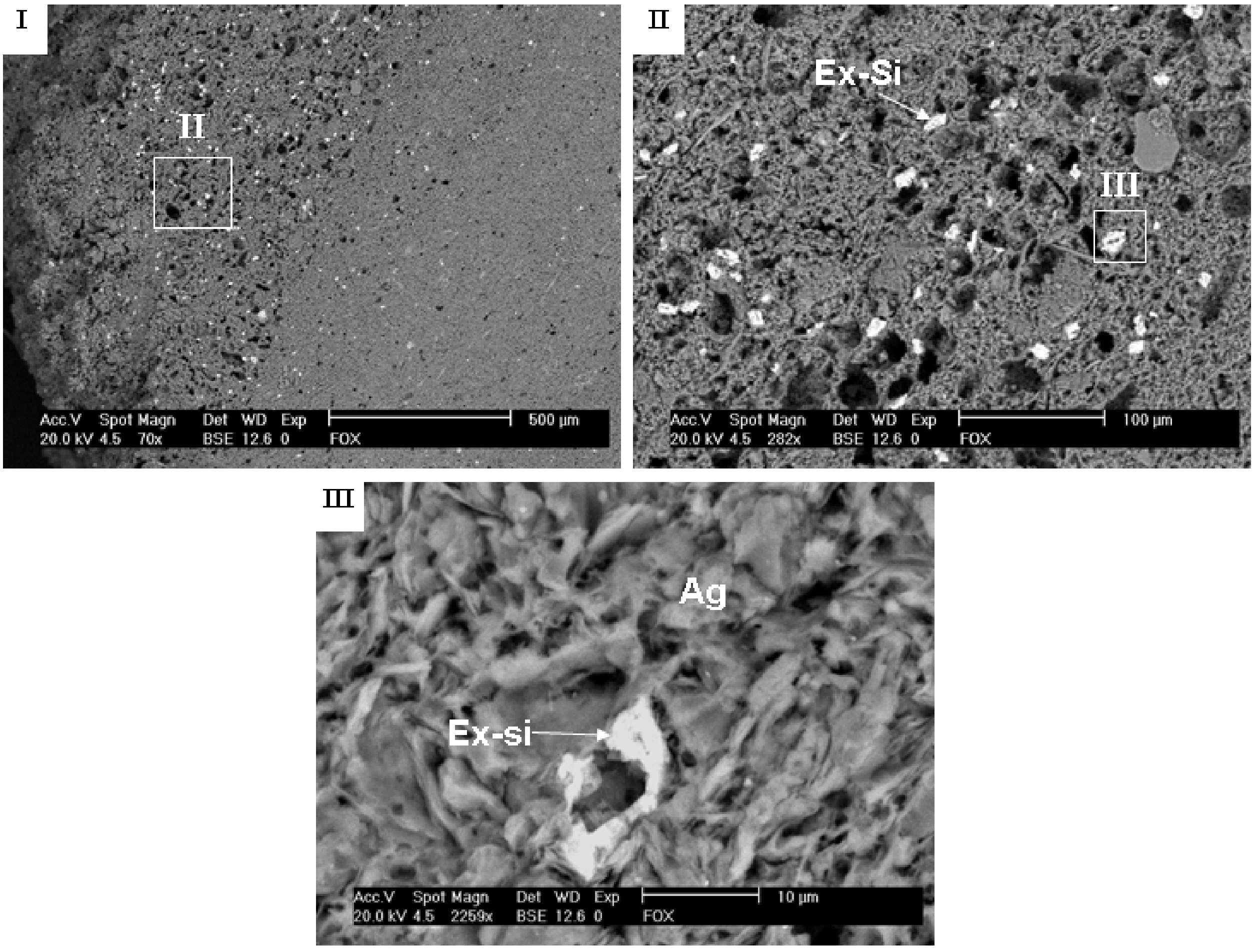

Figure 3-21 : SEM backscattered images of the caprock sample after experiment with NO and saline water (25 g/l). (I) global view; (II and III) successive zooms on the matrix. (Ex-Si) ex-siderite transformed in hematite, (Ag) clay minerals.

There are very few thermodynamical data for NO under the experimental pressure and temperature range. The analyses performed onto the gaseous and aqueous phase indicate that NO is not stable under these conditions. The chemistry of nitrogen oxides is complex and numerous phases appear during the experiment such as N_2O, NO_2, N_2, O_2, NH_4^+, NO_3^-. In the gaseous phase some reactions of oxydo-reduction can run such as:

(14) $3\ NO = NO_2 + N_2O$

(15) $2\ NO = N_2 + O_2$

(16) $2\ NO = \frac{1}{2} N_2 + NO_2$

(17) $2\ NO = \frac{1}{2} O_2 + N_2O$

In the queous phase, the following reaction can explain the presence of N_2O and the nitrates and leading to a very acidic solution:

(18) $4\ NO + ½\ H_2O = 3/2\ N_2O + H^+ + NO_3^-$

The dissociation of N_2O in N_2 and O_2 was also descibed in the littretaure but under different conditions (Li et al., 1992, Rivallan et al., 2009).

Whatever the occuring reactions, the presence of NO in an aqueous system leads to a dual reactivity due to the presence of protons H^+ and oxidising agents such as O_2. In this case, several chemical mechanisms can be written to explain the complete oxidation of iron bearing phases (pyrite and siderite) as well as the presence of ammonium or nitrates in the aqueous solution. The following reactions can be proposed athough they are not exhaustive.

The presence of CO_2 in the fluid phase after experiment proves that the carbonates phases are altered by the acidic solution due to the initial presence of NO. The same reactions as for the dissolution of carbonates in an acidic solution (reactions 1 to 3) can be also envisaged here:

(19) $CaCO_3 + 2H^+ = Ca^{2+} + H_2O + CO_2$

(20) $CaMg(CO_3)_2 + 4\ H^+ = Ca^{2+} + Mg^{2+} + 2\ H_2O + 2\ CO_2$

The reactions lead to emission of gaseous CO2 and the release of Ca2+ and Ba2+.

The oxidation of pyrites cans be described differently if considering either the presence of ammonium or di-nitrogen, or considering the oxidising agent to be nitrate or di-oxygen:

(21) $8\ FeS_2 + 31\ H_2O + 15\ NO_3^- = 4\ Fe_2O_3 + 15\ NH_4^+ + 16\ SO_4^{2-} + 2\ H^+$

(22) $2\ FeS_2 + H_2O + 6\ NO_3^- = Fe_2O_3 + 3\ N_2 + 4\ SO_4^{2-} + 2\ H^+$

(23) $2\ FeS_2 + 4\ H_2O + 7{,}5\ O_2 = Fe_2O_3 + 4\ SO_4^{2-} + 8\ H^+$

For each reaction used, sulphates are formed that combine with Ca and Ba to form anhydrite and barite:

(24) $Ca^{2+} + SO_4^{2-} = CaSO_4$

(25) $Ba^{2+} + SO_4^{2-} = BaSO_4$

Contrary to the experiments with SO_2, silicate minerals, mainly quartz and clay minerals, are slightly affected by NO with only a few percents dissolved.

To sum up, experiments with NO are complex and lead to a complete oxidation of iron bearing phases (mainly pyrite and siderite), to a partial dissolution of carbonates with an enhanced reactivity of calcite by comparison with dolomite, and keep the silicates phases almost free of dissolution. For the chosen conditions of experiment, the mass budget shows that between 20 and 50% percent of the calcite is dissolved as against 15 to 20% of the dolomite. 100% of the siderite and the pyrite are oxidised in hematite. Less than a few percent of the silicates is affected by NO.

4. Conclusion

The experiments performed in the context of the injection of CO_2 and co-injected gases in a geological storage have demonstrated that SO_2 and NO should play a role on the mineralogy of both the reservoir and the caprock. First, this study has shown that SO_2 and NO have a complex behaviour with a dual action, oxidising and acidic, on the minerals. Second, many disproportionation reactions can occur when SO_2 and NO are placed under geological conditions of pressure and temperature. These oxydo-reduction reactions complicate the system by multiplying the possible oxidising agents and thus the possible reactions and products of reactions. Third, the reactivity of both the reservoir rock and the caprock is strongly dependent on the nature of the mineral phases (silicates, carbonates, sulphides, etc.) but also on the nature of the reacting gas. For example it is noticeable that the presence of SO_2 should lead to the formation of sulphate mineral and native sulphur, when the presence of NO should be responsible for the strong oxidation of iron bearing phases.

In any case, since the molar volumes of initial minerals are different of those of secondary products (as an example the molar volume of calcite is 36.93 $cm^3.mol^{-1}$ against 45.16 $cm^3.mol^{-1}$ for anhydrite), the minerals transformations occurring with the injection of reacting gases should be interpreted in terms of petrophysical properties (porosity and permeability) of the hosting rock.

This study shows also that experiments with the gases of interest under geological conditions of storage are necessary to predict the evolution of the storage submitted to the injection of CO_2 and co-injected gases.

References

Seyfried, W. E. J., Janecky, D. R., and Berndt, M. E. (1987). Rocking autoclaves for hydrothermal experiments. The flexible reaction-cell system. Hydrothermal experimental techniques (ed. Ulmer, G. C. and Barnes, H. L.), pp. 216-239. John Wiley & Sons.

Jacquemet, N., J. Pironon and E. Caroli (2005). A new experimental procedure for simulation of H_2S + CO_2 geological storage. Application to well cement aging. Oil and Gas Science and Technology 60(1), pp. 193-206.

Landais, P., Michels, R., and Poty, B. (1989) Pyrolysis of organic matter in cold-seal pressure autoclaves. Experimental approach and applications. Journal of analytical and applied pyrolysis 16, 103-115.

Teinturier, S., Pironon, J. (2003). Synthetic fluid inclusions as recorders of microfracture healing and overgrowth formation rates. American Mineralogist, 88 (8-9), pp. 1204-1208.

Renard, S (2010) Rôle des gaz annexes sur l'évolution géochimique d'un site de stockage de dioxyde de carbone. Application à des réservoirs carbonatés., PhD thesis Nancy Université INPL, p. 422.

Van Berkum, J.G., Diepen, G.A.M. (1979). Phase equilibria in SO_2 + H_2O: the sulfur dioxide gas hydrate, two liquid phases, and the gas phase in the temperature range 273 to 400 K and at pressures up to 400 MPa. The Journal of Chemical Thermodynamics, 11 (4), pp. 317-334.

Palandri, J. L., R. J. Rosenbauer and Y. K. Kharaka (2005). Ferric iron in sediments as a novel CO_2 mineral trap: CO_2-SO_2 reaction with hematite. Applied Geochemistry 20(11), pp. 2038-2048.

Li, Y., Armor, J.N. (1992). Catalytic decomposition of nitrous oxide on metal exchanged Zeolites. Applied Catalysis B, Environmental, 1 (3), pp. L21-L29.

Rivallan, M., Ricchiardi, G., Bordiga, S., Zecchina, A. (2009). Adsorption and reactivity of nitrogen oxides (NO_2, NO, N_2O) on Fe-zeolites. Journal of Catalysis, 264 (2), pp. 104-116.

Acknowledgments

This work is supported by TOTAL and ADEME (France). It is included in the project "Gaz Annexes" of the French National Agency for Research (ANR).

Experimental modelling of the impact of thermal gradient during geological sequestration of CO_2: the COTAGES experiment

Emmanuel JOBARD [a]

Jérôme STERPENICH [a]

Jacques PIRONON [a]

Jérôme CORVISIER [b]

Mathieu JOUANNY [a]

Aurélien RANDI [a]

[a] G2R, Nancy Université, CNRS, Boulevard des aiguillettes, BP 239, 54506 Vandoeuvre lès Nancy, France

[b] Mines Paristech, 60-62 Boulevard Saint Michel, 75272 Paris cedex 06, France

Corresponding author Tel.: +33 3 83 68 47 69. E-mail address: emmanuel.jobard@g2r.uhp-nancy.fr (E.Jobard)

Abstract:

The reactivity of an oolithic crushed limestone exposed to a high CO_2 pressure and a thermal gradient (100 to 35°C in a tubular reactor of 78 cm) was experimentally investigated during 30 days. The original COTAGES experiment described in this paper was carried out in the presence of saline aqueous solution (NaCl 4g/L) equilibrated with $CaCO_3$ at 100°C. A mass transfer was observed from the cold area (35-55°C) to the warmest area (100°C). This mass transfer, of about 10% of the initial mass for the most reactive sample, suggests calcite dissolution/precipitation. Petrographical analyses using electronic and cathodoluminescence microscopes and X ray microtomography showed that the dissolution has mainly affected the cortex of ooliths located in the periphery of the grains and creating more than 700 pore/mm² in the most reactive sample. However, because of their small sizes (mostly inferior to 100 µm²) the pore created does not lead to a significant raise of the porosity value (2% in average). The crystallisation of a microcalcite fringe in the warmed area covers the entire surface of the grains and could isolate the porous network of several grains in a sample. This study demonstrates a strong reactivity of the oolithic limestone in presence of a thermal gradient and pressure mimicking realistic CO_2 geological sequestration conditions with a mass transport from the injection well towards the reservoir rock.

Keywords: CO_2 storage, oolithic limestone, thermal gradient, experiments, mass transfer

INTRODUCTION

Even if the anthropogenic implication in the global warming is still debated, greenhouse gases from fossil fuel combustion should be reduced as a precaution. The emissions of CO_2 from fossil fuel represent almost 60% of the total anthropogenic emissions of greenhouse gases (Metz *et al.*, IPCC, 2005). Emissions of CO_2 reached 29.4 Gt in 2008 (IEA, 2010), and should raise up to 40.2 Gt in 2030, according to a reference scenario estimating an increase of the world demand in primary energy of 1.5% between 2007 and 2030 (IEA, 2009). The CO_2 geological storage is very seriously considered as a mean for reducing emissions of greenhouses gases since about one third of CO_2 emissions are linked to the industrial activities involving a geographical concentration of high amounts of CO_2. In many cases, industrial areas are located nearby potential geological storage sites (Bradshaw and Dance, 2004) hence reducing the transportation cost and leading to a better profitability. At present, the three main geological modes of sequestration envisaged involve depleted oil and gas fields, deep saline aquifers, and unminable coal seams. Deep saline aquifers and depleted oilfields represent huge volumes at the international scale, with estimated volumes of 920 Gt CO_2 and 400-10 000 Gt CO_2 respectively (Gale, 2004; Michael *et al.*, 2009). Regardless of the type of reservoir, it must fulfil a number of conditions, such as a high injection rate, a high storage capacity, and a good retention of the injected gases (Bachu, 2008). The CO_2 is directly trapped from the source and injected into the chosen geological formation, which could be carbonated or silicoclastic. The first step in a geological storage of CO_2 consists in the carbon capture from the flue gases, it is then transported through a pipeline and injected in the geological reservoir.

Concerning carbonated rock reservoir behavior under the influence of a CO_2 injection, scientists elaborated some conceptual models, covering a broad range of geological storage conditions. Sterpenich *et al.*, 2009, performed batch experiments to study the reactivity of an oolitic limestone in presence of supercritical CO_2 conditions (80°C temperature and 150 bar pressure). Results showed a limited dissolution of calcite, and the conservation of initial petrophysical properties of the studied limestone. Luquot and Gouze, 2009, made a percolation of CO_2 enriched fluid through limestone rock cylinder, under *in-situ* storage conditions (100°C and 120 bar). Results showed dissolution of the carbonated rock, and a modification in the Φ-k properties. Similar results were obtained by Rosenbauer *et al.*, 2005.

The purpose of this work is to study the thermal effect on matter transfers occuring in the reservoir after the injection. Indeed, as it is mentioned in André *et al.*, 2010, several parameters could lead to the setting up of a thermal gradient and heat transfer between the warm part of the rock formation and the cold part near the injection point. The CO_2 flow through the pipeline runs for a relatively short time and therefore CO_2 is not thermally equilibrated with the host formation (House *et al.*, 2006). So the mains parameters are the temperature of CO_2 injected and the temperature of the host rock formation, but the thermal gradient could also be influenced by petrophysical properties of the reservoir and also the Joule-Thomson effect. For example, the Joule-Thomson effect is stronger in lower permeability formations (Oldenbourg 2007).

This thermal disequilibrium has an impact on the solubilisation of solicited phases (CO_2 and minerals from the host rock), and could favour some transfer of matter.

COTAGES batch experiment should help estimating the mass transfer occurring during a CO_2 injection under supercritical conditions (pressure above 74 bar and temperature above 31°C). Indeed, even if calcite solubility decreases when temperature decreases, the chemical competition between dissolution and precipitation processes are difficult to estimate. From this perspective, a mass balance study has been made in order to quantify the mass transfer during the experiment. Another part of this study is focused on the petrographical and petrophysical properties modifications during the experiment. Secondary Electron Microscopy (SEM) allows the visualization of the modifications of the initial mineral composition, and of the crystals neoformation. An X-ray micro-tomography (XMT) study has also been performed in order to monitor the eventual modifications of the petrophysical properties. This work should allow to understand whether a CO_2 injection could yield various responses regarding the concerned temperatures, the generated gradient and the induced thermal perturbation, and to determine the main processes which could affect the reservoir rock after the injection in colder area.

1. MATERIALS AND METHODS

1.1. Materials

Lavoux Limestone was chosen as a natural analogue of Dogger Limestone of the Paris Basin (Bathonian “Oolithe Blanche” Formation) and identified as a potential host formation for CO_2 storage. The Oolithe Blanche Formation was thoroughly studied within the framework of CO_2 geological storage. The ANR-géocarbone PICOREF project, supported by the French National Agency for Research (ANR) identified this limestone formation as the best potential storage site in the Paris Basin (eg. Grataloup *et al.*, 2009; Vidal-Gilbert *et al.*, 2009). The Oolithe Blanche Formation presents porosity values ranging from 16 to 23%, and permeability values of 0.1 to 10 mD. Lavoux Limestone presents a stack of stratum with a variable blocky calcite cementation, explaining the scattered porosity and permeability values, between 12-24% and 19-100 mD respectively, that can be collected in the literature (Andre *et al.*, 2007; Fleury and soualem 2009; Lagneau *et al.*, 2005; Noiriel *et al.*, 2010; Sterpenich *et al.*, 2009). Strong correlations between petrophysics and facies properties of Oolithe Blanche Formation and Lavoux Limestone emphasized the choice of Lavoux Limestone as an analogue made in several national research projects, ANR-Geocarbone Injectivité and ANR Interfaces for example.

1.2. Experimental apparatus

In order to gain a better understanding of the behaviour of a geological reservoir submitted to a gradient of temperature in presence of supercritical CO_2, the COTAGES (COlonne Thermorégulée A Grains pour Gaz à Effet de Serre) apparatus was developed.

The COTAGES batch reactor (Figure 1) is a horizontal cylinder made of stainless steal (type 316) with an inner diameter of 22 mm and a length of 780 mm representing a total volume of 1.2 L. The conception of the tubular reactor allows reaching pressures of up to 350 bar. Three separate ovens allow to heat independently three areas of the reactor and temperature can reach up to 600°C. Both CO_2 and aqueous solution injections are performed with two independent pneumatic pumps.

Both temperature and pressure are measured and recorded with analogic pressure sensors. A 3-point thermocouple allows to measure and then to control the temperature of the three ovens. The thermocouple used in this experiment is a T type (Cu/Cu-Ni) allowing measurement with a precision of 0.5°C.

In this experiment, only one area located on the extremity of the autoclave is warmed. Therefore two areas will be considered: the cold one (not warmed), and the hot area, warmed at 100°C.

Concerning the sample preparation, grains of the Lavoux limestone were crushed and separated with sieves based on their sizes. The samples were prepared with five classes of grain size (4-3.15 mm / 3.15- 2.5 mm / 2.5-2 mm / 2-1.41 mm / 1.41-1 mm). A mixing of 2.5 g from of each granulometry set, leading to a total mass of rock of 12.5 g per sample, was then wrapped in a fibreglass braided tissue covered with Teflon (Figure 2). This microporous tissue, inert to CO_2, and thus allows the mass transfer between the different samples. The 12 samples (i.e packet of oolitic grains), representing a bulk mass of 150 g of rock, were numbered in order to keep track of their position in the autoclave.

The saline aqueous solution was then prepared with demineralised water warmed at 100°C for one hour with a powder of calcium carbonate (Lavoux Limestone). The pre-equilibrated solution was immediately filtered using a 0.22 filter µm and cooled down to room temperature before NaCl (4 g.L^{-1}) was added.

After placing the rock samples in the autoclave, a first CO_2 sweeping was performed in the reactor under a 20 bar of pressure, in order to sweep away the air trapped in the rock pores. Then the reactor was pressurised with a pressure of 55 bar of CO_2 during 15 minutes. After this step, the reactor was depressurized down to 3.6 bar, and pressurized again with CO_2 up to 30 bar for 5 minutes and depressurized to 3.6 bar, in the order to reach the smallest pore.

276 g of saline solution was then injected with the pneumatic pump and the reactor was isolated (the entry and exit valves are closed). The massic water to rock ratio W/R was 1.84. Because the solution is undersaturated with respect to calcite in these conditions, no precipitation occured during the first stage of the injection.

In this experiment, only the one oven warming second zone of the reactor was used to reach a temperature of 100°C in the middle of this zone. The gradient of temperature was then linked to the thermal conductivity of the reactor and the filling materials (rock, aqueous solution, CO_2). At thermal equilibrium, the temperature was approximately 35°C at 13 cm of the cold extremity of the reactor, and around 55°C at 40 cm from the left extremity of the reactor.

When the desired temperature was reached, CO_2 was injected to get a total pressure close to 110 bar. During the first five minutes, the pressure was adjusted by CO_2 injection to compensate its dissolution in the water and the associated fall of pressure. The experiment ran for 796 hours. At the end of experiment, samples were removed one by one from the reactor, the fibreglass tissues were opened and the grains are dried at room temperature for 48 hours.

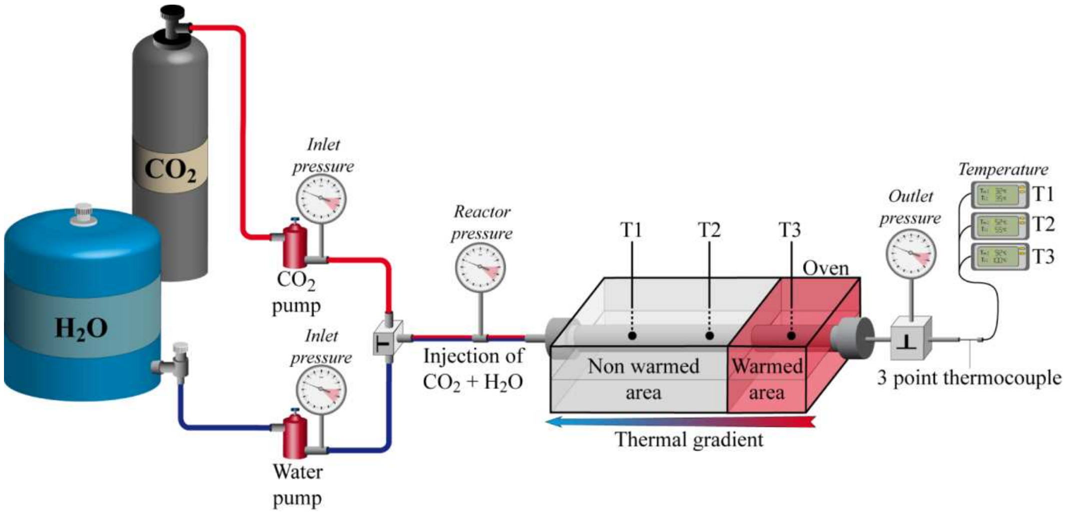

Figure 22: COTAGES experimental setup

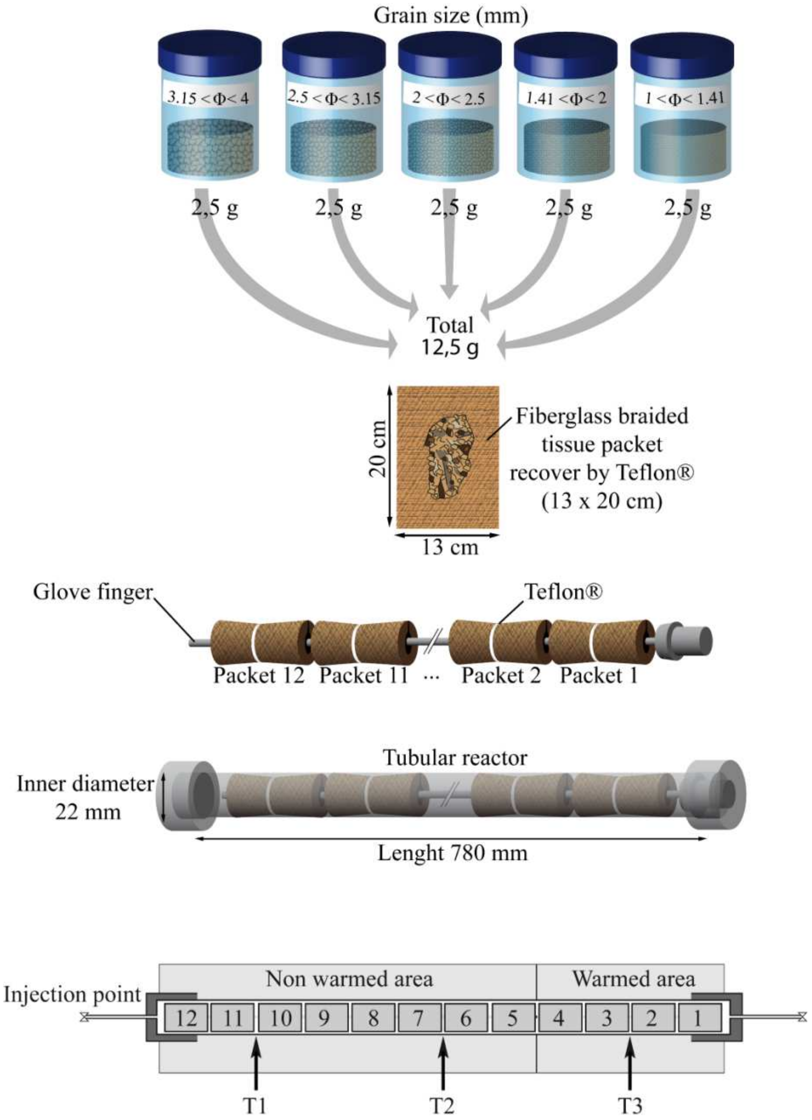

Figure 23 : The different steps of sample preparation used for the COTAGES experiment

1.3. Mass balance and granulometry

A mass balance was performed by weighing the samples before and after the experiment. Variations of the mass samples as well as variations of the grain size for each sample allow quantifying mass transfers between the different thermal zones. Samples were weighed of drying, with a Denver Instruments® scale, allowing measurement up to 400 g with a precision of 0.01 g. After mass determination, the granulometry of each sample was determined using a column of eight sieves with different mesh sizes (4, 3.15, 2.5, 2, 1.41, 1, 0.71 and 0.5 mm). Recrystallization or aggregate formation was monitored in the >4 mm class. Conversely, the formation of fine particles (by dissolution or grain fracturation) was classified in the 1-0.710 mm, 0.710-0.5 mm and <0.5 mm classes.

1.4. Petrography

1.4.1. MEB

Petrographical analysis were performed on fresh and aged samples in order to evaluate the potential variation of the initial mineral phases (dissolution and precipitation). A study by scanning electron microscopy (SEM) was carried out on fresh samples and on polished surfaces (after epoxy resin impregnation). The secondary electron (SE) mode and the back scattered electron (BSE) was used on a HITACHI S-4800 SEM with field effect (SCMEM laboratory of Université de Lorraine). Images were acquired with a current of 10 to 15 kV.

1.4.2. Cathodoluminescence

To improve sample characterization, a cathodoluminescence microscopy study was also made on fresh and aged samples. The microscope used is an Olympus BX50 with a Zeiss® Axio CAM MRC image acquisition system. Images were acquired with a 500 µA gun current and a 15 kV voltage.

1.4.3. X-ray computed tomographic microscopy

A study with X-ray microtomography (Nanotom 180 kV Phoenix-GE, SCMEM Université de Lorraine) was carried out on grains from fresh and aged samples. X-ray computed tomographic microscopy (microCT) allows acquiring a 3D image of solid samples without destruction. Numerous cross sections were acquired and later assembled to form a three dimensional reconstruction corresponding to X-rays attenuation of the analyzed material. X-ray attenuation depends on the material thickness and density (i.e. average atomic number per volumetric unit of rocks). The microCT size limitation of the object is 12.70 cm in height and 15.24 cm in diameter. Samples analyzed within the framework of this study were grains of about 3 mm radius, corresponding to the best compromise between the number of pore studied, the size of the object and the resolution. Analysed samples were glued with nail polish on a glass stick used as a support for the acquisition. The chosen distance between the X-ray source and the sample was 6.5 mm and 220 mm separated the X-ray source and the detector. This device allowed image acquisition with a resolution of 5 megapixels, with an associated voxel size of 1.48 μm^3.

This resolution allows a good representation of samples, mainly composed of about 500 µm ooliths, with an associated porosity throat diameter of about 10 µm (Sterpenich *et al.*, 2009).

The reconstruction in three dimensions of the object was carried out with the DatosRec software (1.2.0.22 v).

1.5. Image analysis

Images from microCT acquisition were analysed in order to obtain information on the evolution of the porosity of the grains during the experiment. The 2D images were extracted in a 8 bit format (256 grey levels) from the reconstructed volume according to the three perpendicular planes XY, YZ, XZ (Figure 3). Five images per axis were selected to perform image analysis. Because the grains do not have a cubic shape and thus because of a lack of information in the four corners, only the pictures corresponding to the centre of the grain were selected (Figure 3-A). The first selected image shows the middle of the grain. The other selected images were selected on both sides of the middle image by keeping a constant distance corresponding to 1/10 of the total length of the plane (Figure 3-A). In total, 15 images per grain (5 per plane), 2 grains per sample and 4 samples (fresh sample, cold, intermediate and hot areas) were studied, corresponding to a total number 120 images.

The following operations of image analysis were performed with ImageJ software (1.43 v, http://rsb.info.nih.gov/ij/; Abramoff *et al.*, 2004). After the image was selectede, a thresholding was performed to separate material (limestone) and porosity. The thresholding process consisted in the selection of pixels whose intensity was above a chosen threshold value (see for example Pironon *et al.*, 1998). In this study, the threshold value was determined using the second derivative of the grey level distribution (as in Sterpenich *et al.*, 2009). For our samples, this method allowed to extract the studied material from the background (Figure 3-B). A binarization of the previously thresholded images was then carried out in order to represent limestone in white and porosity in black. An erosion/dilatation process was then performed in order to filter the remaining noise caused by the nail polish used to fix the grain (Figure 3-C). The last step of this treatment consisted, on one hand, in extracting the pore and measuring its area, and on the other hand, in measuring the rock surface (Figure 3-D). The surface area corresponding to the external part of the grain was removed from the analysis considering that after binarization, it corresponded to the unique biggest pore with a non-realistic size. From all the samples, 152,829 pores were measured corresponding to a mean value of 2547 pores per image. For each image, the porosity value was calculated using the equation 1.

(1) $\Phi_T = S_p/(S_p+S_r)$

where Φ_T is the total porosity, S_p is the pore surface (surface area of black pixels), and S_r is the limestone surface (surface area of white pixels). The number of pore for each sample (NS_T) was also calculated and normalized to its surface area to allow comparison between the thermal zones (equation 2).

(2) $NS_T = N_T/(S_p+S_r)$

where NS_T is the total pore number normalized to the surface area of the grain, N_T is the total pore number in the grain, S_p is the surface area of the pores (black pixels) and S_r is the surface area of the limestone (white pixels).

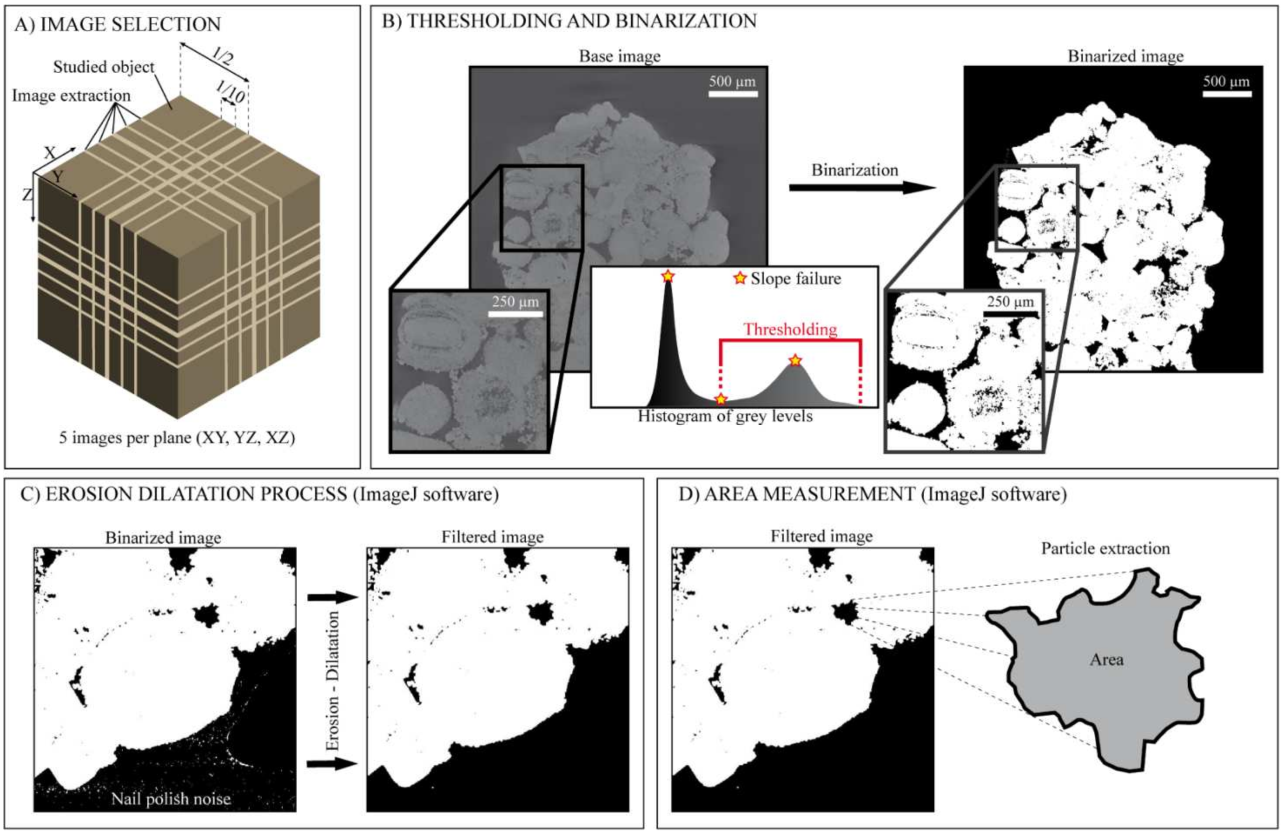

Figure 24: Image analysis protocol. A: image selection. B: thresholding method and binarization. C: erosion-dilatation process. D: particle extraction.

2. RESULTS

2.1. Evolution of pressure and temperature

Pressure and temperature were recorded during the experiment. The variations of temperature are linked to the thermal conductivity of the materials (steel, rock and aqueous solution) and to the thermal regime imposed by both the oven and the room temperature. As a consequence of the possible chemical reactions occurring in the reactor, endothermic or exothermic effects could also be recorded. The variations of pressure could be due i) to the variations of temperature of the system linked to oven regulation or to the influence of the room temperature ii) to exothermic or endothermic reactions, iii) to the solubilisation of the gas phase in the aqueous solution or iv) to chemical reactions with variations of phases molar volume or gaseous compounds production or consumption (mainly CO_2).

The pressure and temperature variations during the experiment are reported in Figure 4. In order to better visualize the phenomena occurring during the first part of the experiment, a logarithmic scale was chosen to represent the elapsed time.

During the first hour of the experiment, the oven warmed up to reach the chosen temperature of 100°C. The oven regulation was responsible for the oscillations recorded in the hot part of the autoclave and visible for about one hour on the T3 profile (Figure 4). Temperatures in the non-warmed zone (T1 and T2) followed the increase of the temperature of the hot zone due to the thermal conductivity of the involved materials: reactor, rock and aqueous solution. The temperatures began to be stabilised after approximately 5 hours. T3 was stabilised at a temperature of 100°C when T2 was stabilised at 55°C and T1 at 30-35°C.

The variations in pressure within the autoclave can be divided in three phases based on the profile shape. The first phase with a rapid increase up to 100 bar corresponds to the CO_2 injection, followed by a slight increase and oscillations due to thermal regulation for the first hour. Together with the stabilisation of the temperature, the pressure began to decrease to reach 55 bar. This second phase lasted at approximately 60 hours and highlighted the solubilisation of gaseous CO_2 in the aqueous solution. However the presence of two sills and the rapid decrease of pressure after 15 and 38 hours of experiment which could be noticed and could be linked to chemical reactions between limestone and the reactant fluids. The last phase corresponds to the stabilisation of the pressure during the remaining time of experiment. Some slight oscillations were linked to variations of the room temperature and especially to night/day cycles.

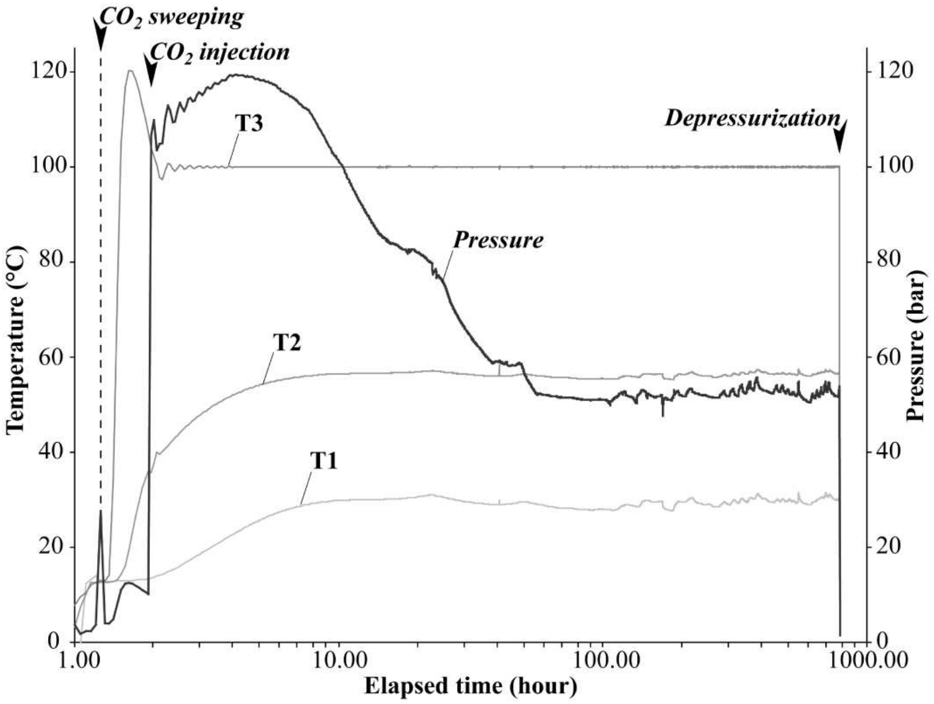

Figure 25: Variations of pressure and temperatures in the autoclave during experiment. Notice the use of a logarithmic scale to represent the elapsed time. T1 and T2 were recorded in the non-warmed zone, T3 was recorded in the warmed zone.

2.2. Mass Balance study

In order to quantify the mass transfers between the different thermal zones and that occur during the experiment, a global mass balance study was made from the weighing of the twelve samples. The mass of each sample before and after experiment, the deduced variations as well as the temperatures recorded in the autoclave are reported on Figure 5. Before experiment, each sample had the same weight of 12.5 ± 0.05 g. After the experiment, the samples n°2, 3 and 4, located in the hot area, were found to have a weight of 13.55 ± 0.09, 14.07 ± 0.09 and 13.65 ± 0.09 g respectively. This corresponds to a 12% (1.48 g) of mass increase for the heaviest sample (n° 3). At the opposite, all the other samples show a mass loss that can reach up to 10% (1.29 g) for the sample n° 6 located in the non-warmed area with intermediate temperature. In the colder area, the mass loss is lower than 2% (between 0.13 and 0.27 g) for the samples n°10, 11 and 12. The global mass balance calculated from the 12 samples shows a difference corresponding to a mass loss of limestone of 0.81 g after the experiment. It is to compare to the initial mass used for the experiment (150 g) was taken as a control to validate the measures.

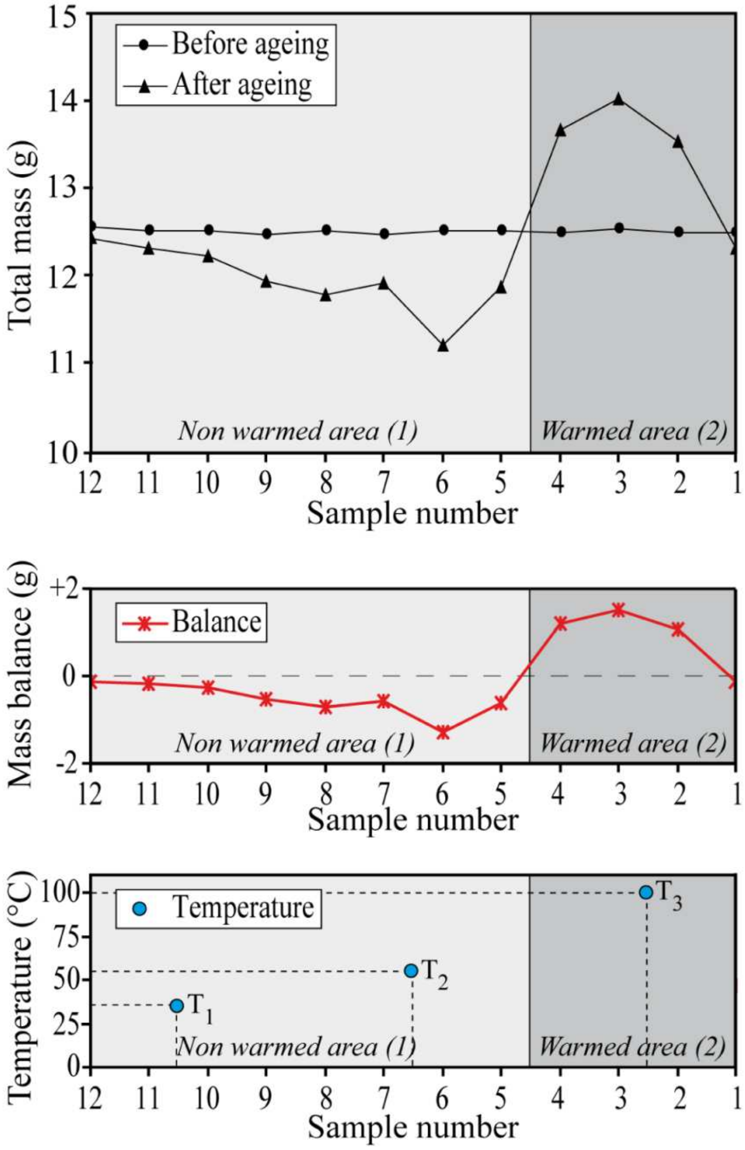

Figure 26 : Mass of the twelve samples before and after experiment, deduced mass balance and temperatures recorded in the autoclave.

Every sample was sieved to monitor the change in mass according to the size grading. The Figure 6 shows mass balance for each sample as a function of the initial granulometric classes (A) and for newly formed grains, mainly fine particles and aggregates (B).

The global shape of the curve for the initial granulometric classes follows that tendency for the entire sample, that is to say a gain of mass in the warmed zone and a mass loss in the colder area. Two important observations were made. First, concerning sample n°6, the most affected in terms of dissolution, its mass loss concerns mainly the class 3.15 – 2.5 mm class. Second, in the warmed zone, the samples n°3 and 4 are heavier by the formation of aggregates of grain (> 4 mm) due to calcite cementation. There is no aggregate for the sample n°2 and the total mass gain is distributed between each fraction but with a predominance for the classes < 3.15 mm. Finally, whatever the sample observed, the experiment leads to the formation of fine particles < 1 mm.

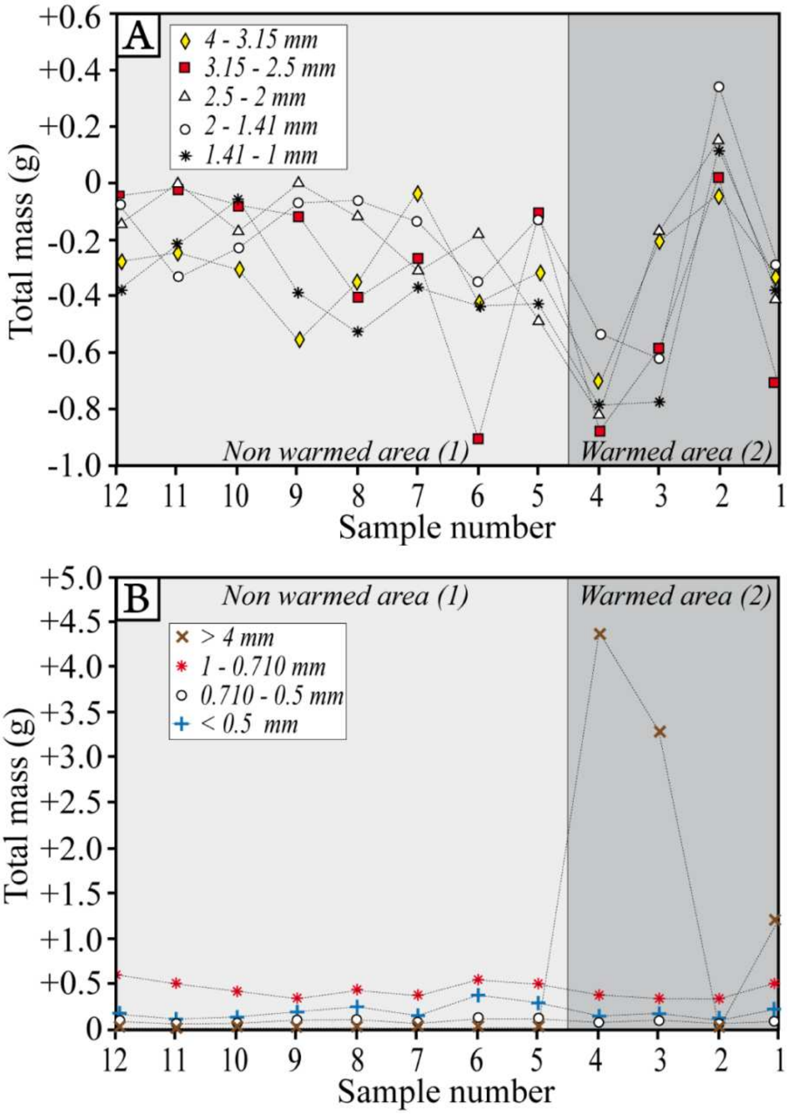

Figure 27 : Differences between the masses measured before and after experiment for the five initial granulometric classes (A) and corresponding to new classes created during experiment (B, fine particles and aggregates).

2.3. Petrographical analysis

Observations of the pressure, temperature and mass balance profiles show that processes of dissolution and precipitation obviously occur during experiment. In order to locate the preferential sites for these chemical reactions, we proceeded to observations and also performed analyses and observation owing to electronic microscopes, cathodoluminescence and X-ray microtomography. Image analysis is then presented to quantify the variations in terms of porosity between the different thermal zones.

2.3.1. X-ray computed microtomograpic microscopy (microCT)

In order to precise morphological changes of grains in each temperature zone, several grains of the most representatives samples (according to mass balance) were examined with the X ray tomography device. The acquisition was performed on fresh samples, and on samples from the warmed and non-warmed areas (n°12, 6 and 3, Figure 7). Avizo software was used to perform a 3D treatment of the acquired data. The voxel resolution is 1.48 µm² due to tomography adjustment. Avizo software also allowed providing sections in the sample according to a chosen cutting plane. These sections offer a better visualization of the inner part of the grain.

As observed with SEM, ooliths of the fresh sample present a smooth surface with no recrystallization or traces of dissolution (Figure 7-A). The observation of the section from the fresh sample confirms that ooliths are homogeneous in terms of density (Figure 7-B).

The ooliths of the colder sample (n°12, Figure 7-C) are strongly similar to the ooliths of the fresh sample. The section in this sample reveals, as observed from the fresh sample, that the ooliths have homogeneous porosity and density and present no traces of dissolution or secondary precipitation (Figure 7-D).

Ooliths of the sample n°6 have an indented surface (Figure 7-E) with truncated ooliths. A section view reveals some evidence of dissolution mainly located in the periphery of the grain (Figure 7-F).

Conversly, the ooliths from the warmed area sample (n°3) show a rougher surface (Figure 7-G) due to secondary precipitation. A section from this sample confirms that ooliths located in the periphery of the grain are denser than ooliths from the fresh sample. The observation of ooliths indicates that the porosity of their cortex seems to undergo secondary precipitation (Figure 7-H). By opposition to the fresh sample, this precipitation leads to a cortex denser than the core of the ooliths.

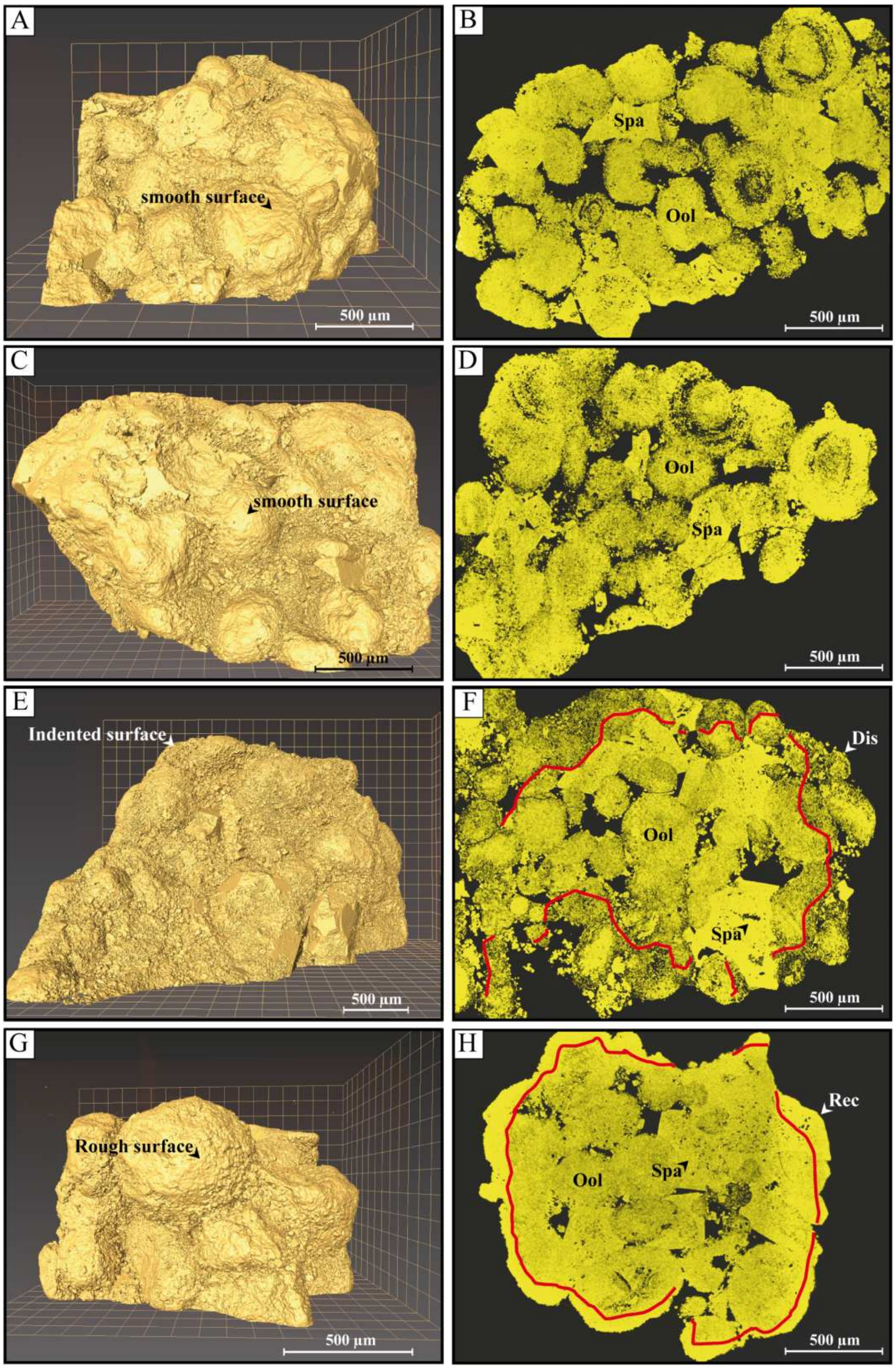

Figure 28 : 3D and 2D images on fresh and aged samples of Lavoux limestone acquired with XMT and treated with Avizo software (V 6.3.1, fire edition). A : Ooliths (Ool) from the fresh sample show a regular and smooth surface. B : Section in the fresh sample shows ooliths with an homogeneous density , and dense sparite crystals (Spa) without any trace of alteration. C : Ooliths from the colder sample (n°12) present a surface comparable to that of the fresh sample. D : section in the colder sample shows, as in the fresh sample, ooliths with an homogeneous density . E: Ooliths from the sample n°6 present an indented surface due to the dissolution of ooliths. F : Section in the sample n°6 brings to light evidence of dissolution processes (Dis). By opposition to the fresh sample, the periphery of the oolith is less dense than its heart. G : Ooliths surface from the sample n°3 (warmed area) is rougher than that of the fresh sample. H : section in the sample n°3 underlines evidence of recrystallization at the periphery of the grain where ooliths are denser than their heart.

2.3.2. SEM and cathodoluminescence

The mineralogical and morphological transformations of the different samples from the different thermal areas were studied with SEM and cathodoluminescence (Figure 8).

Lavoux Limestone is an oolithic limestone made of micritic ooliths, with a limited cementation of euhedral rhomboedral calcite. The organisation and the small size of the micrites give to the surface a smooth shape (Figure 8-A). The crystals composing the ooliths are rounded micrite with sub-punctic contact (*sensu* Lambert *et al.*, 2006) between them. The size of micrite crystals is about 2 to 4 µm (Figure 8-A).

The grains of the cold area samples (T1 = 35°C) are strongly similar to the grains of the fresh samples. Rhomboedral calcite presents a surface without defects or dissolution pits, and seems not to be affected by the experiment. The surface of ooliths is similar to that of the fresh sample (Figure 8-B), composed by rounded micrites with a size of 2 to 4 µm and forming sub-punctic contacts between them.

The grains from the samples in the intermediate area (T2 = 55°C) show strong differences by comparison with the grains from the fresh samples. Indeed, even if the crystals of calcite kept a smooth surface and marked edges after the experiment, the ooliths present an indented and strongly altered shape (Figure 8-C). Micrite crystals of the Ooliths are rounded and forming gulfs between them, leading to the observation of concretions that could reach 10 µm in size.

Concerning the hot area (T3 = 100°C), the grains surface is fully recrystallised (Figure 8-D). Newly formed euhedral micro-calcites of about 5 µm cover the ooliths (Figure 8-D). The recrystallisation leads sometimes to the aggregation of grains by micro-calcite bridge precipitation (Figure 8- E).

A study with cathodoluminescence microscopy allows distinguishing the newly crystallised calcites. The oolithic cortex of the fresh sample presents a homogeneous luminescence (Figure 8-F). By comparison, the microcalcite fringe previously observed with SEM on the samples from the warmed area shows a high luminescence. This sample is characterised by a strong contrast between the newly crystallized calcites and the underlying oolithic cortex (Figure 8-G). Furthermore, most of the time the ooliths located on the periphery of the grain present a stronger luminescence than the ooliths located in the middle part of the grain showing that recristallisation of calcite preferentially occurs at the surface of grains. Some differences also exist between different grains of the same sample showing that the crystallised fringe could vary in thickness from 5 to 50 µm (Figure 8-H).

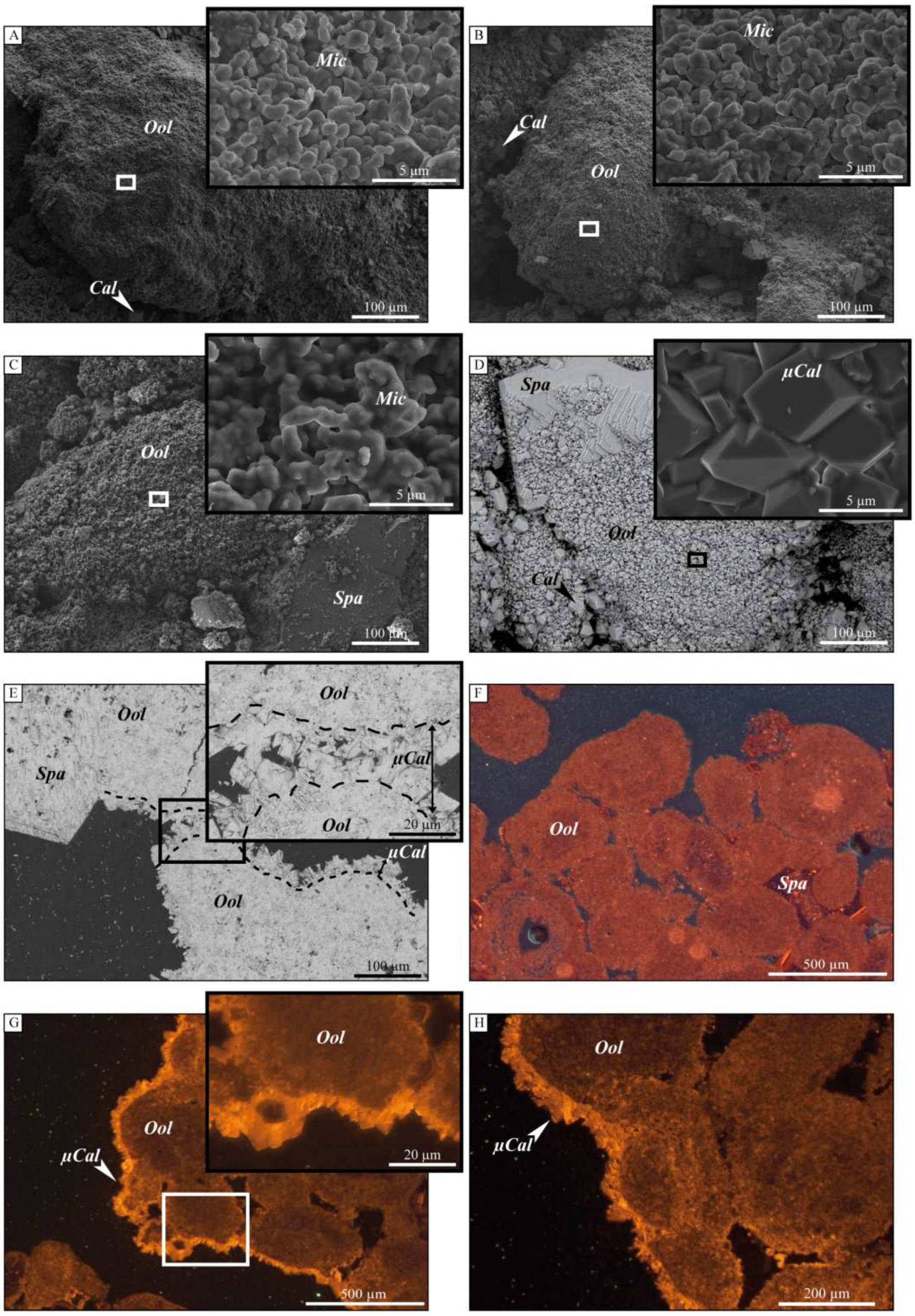

Figure 29: A : SEM (SE) picture of an oolith (Ool) of the fresh sample, showing rhomboedral euhedral crystals of calcite (Cal) in the interoolith porosity. At a better enlargement, well individualized crystals of rounded subhedral micrite (Mic) are visible. B : SEM (SE) picture of an oolith from a sample (n° 12) in the cold area. At higher enlargement, crystals micrite are strongly similar to that of the fresh sample. C: SEM (SE) picture of an altered oolith from a sample (n° 6) in intermediate area. At higher enlargement crystals of subrounded micrite linked with gulf are observable. D: SEM (SE) picture of a recrystallized oolith from sample n° 3 in the warmed area. A crystal of sparite (Spa) is visible. At higher enlargement, crystals of euhedral microcalcite (µCal) are visible on the surface of oolith. E: SEM (BSE) picture from a polished section showing an aggregate of grains due to recrystallization in the hot area (sample n°3). F: cathodolumiescence picture of the fresh sample. G and H: Cathodoluminescence picture of a grain from the hot area (sample n°3) showing the crystallisation of microcalcites.

2.4. Image analysis

An image analysis was made on the 3D data acquired previously. Fresh samples were analyzed as references in order to better visualise morphological changes of aged samples. Image analysis was performed from X ray tomography acquisitions (30 images per sample in the 3 thermal areas and the fresh rock) in order to quantify the variations of both porosity and pore size in the different areas of the reactor (Figure 9). Considering the more important gain or loss of weight during the experiment, one sample for each area was chosen: the sample n°3 for the warmed area (100°C) and the n°6 for the non warmed area (55°C). The sample n°12 was also chosen in the same way for the non warmed area to represent the coldest conditions (35°).

The variations in porosity and pore size are expressed using the fresh sample as a reference (Figure 9). The dashed line corresponds to the values measured from the fresh sample and the hatched zone corresponds to the standard deviation calculated from the 30 images. Therefore, positive values on the left axis represent an increase in porosity (Figure 9.A) or in the number of pores (Figure 9.B). Raw values for each sample are represented on the right axis.

The variations in the total porosity and of the pore number of the samples are given in Figure 9. The fresh sample has a mean porosity of 6.4 ± 2.2%, while sample 6 shows a higher porosity of 8.7 ± 2.1% representing a relative porosity gain of 36%, relatively to the fresh sample. Concerning the colder sample (samples n°12) and the warmed area sample (sample n°3), the variations in porosity by comparison with the fresh samples are weak, with total porosities of 5.8 ± 3.9% and 6.2 ± 1.4% respectively.

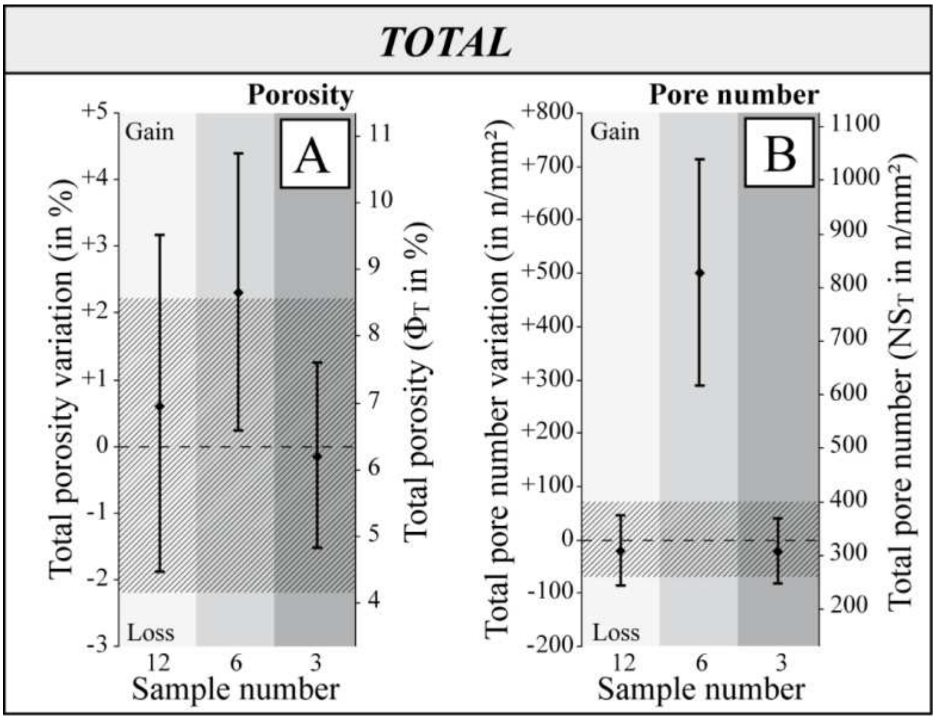

Figure 30 : Variations of the total porosity and the total pore number for the three studied samples (12, 6 and 3) in comparison with the fresh sample

Concerning the total number of pores, the sample 6 shows a significant raise in pore number in comparison to the fresh sample. Indeed, it presents a number of 829 ± 213 pores/mm² in average in comparison to the fresh samples which contains 329 ± 69 pores/mm² on average. It represents a relative gain of 150%. Similarly to the observations performed on the total porosity, the total pore number of the samples from the colder and warmed areas (sample 12 and 3) does not vary significantly from the fresh samples, with 247 ± 69 and 307 ± 62 pores/mm² respectively.

In order to determine the types of porosity which are affected by the dissolution/precipitation processes, we studied the variations of porosity and number of pores according to their size distribution. The distribution of pore size in the fresh sample (Figure 10) shows a high number (more than 20.000) of small pores (<100 µm²) and a small number (about 3.000) of large pores (>100 µm²).

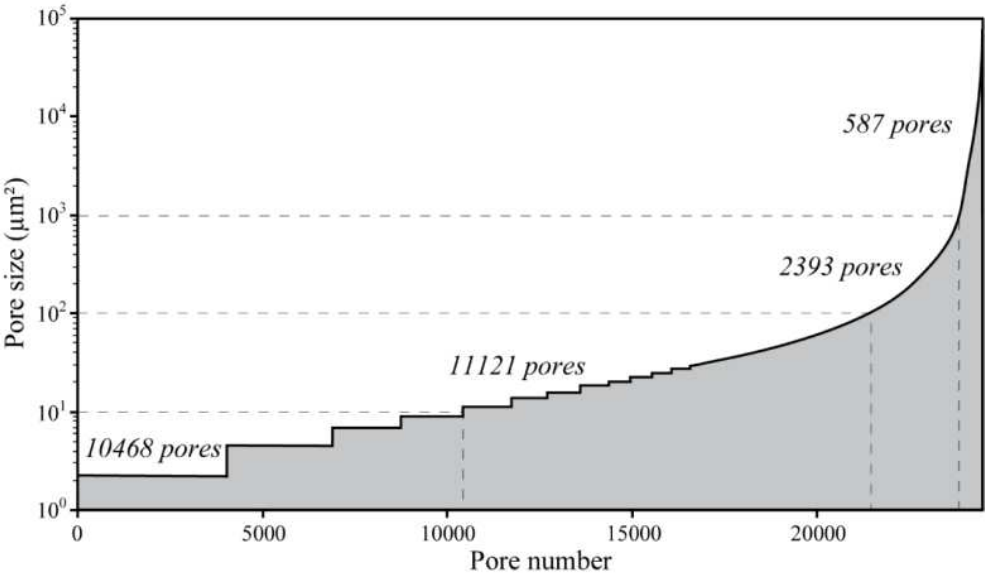

Figure 31 : Pore size distribution in the fresh sample

In order to characterise the number of the pores and their size variations during the experiment, the totality of pores was classified according to four logarithmic classes of surface area allowing the description of the distribution: 2.2-10 µm², 10-100 µm², 100-1000 µm² and >1000 µm². Values of porosity as well as number of pores were also calculated for these four groups to determine which pores were concerned by the dissolution/precipitation processes (Figure 11-A to 11-D). For the four classes, the sample n°6 (55°C) is the most affected, with a significant gain (263±82 pores/mm²) for the small pores (<10 µm²). It is associated to a porosity gain of 0.12±0.04%. The number of pores from 10 to 100 µm² also increases in the 55°C zone with about 214±113 pores/mm² more than for the fresh sample, representing a porosity gain of about 0.62±0.37%. For the pores of the class 100-1000 µm², a gain of 22±20 pores/mm² in the 55°C (samples n°6) zone is calculated in comparison with the fresh sample, and it corresponds to a porosity gain of 0.50±0.47%. Finally the variation of the number of the largest pores (>1000 mm²) is weak, ranging from 0 to 5 pores/mm², but could imply an important increase of the porosity due to their big size. The gain of porosity for this class is of 1% on average, but is associated with a high standard deviation value deviation (2.7%).

The values of porosity and of pore numbers for the colder and warmed zones are close to that of the fresh sample (Figure 11).

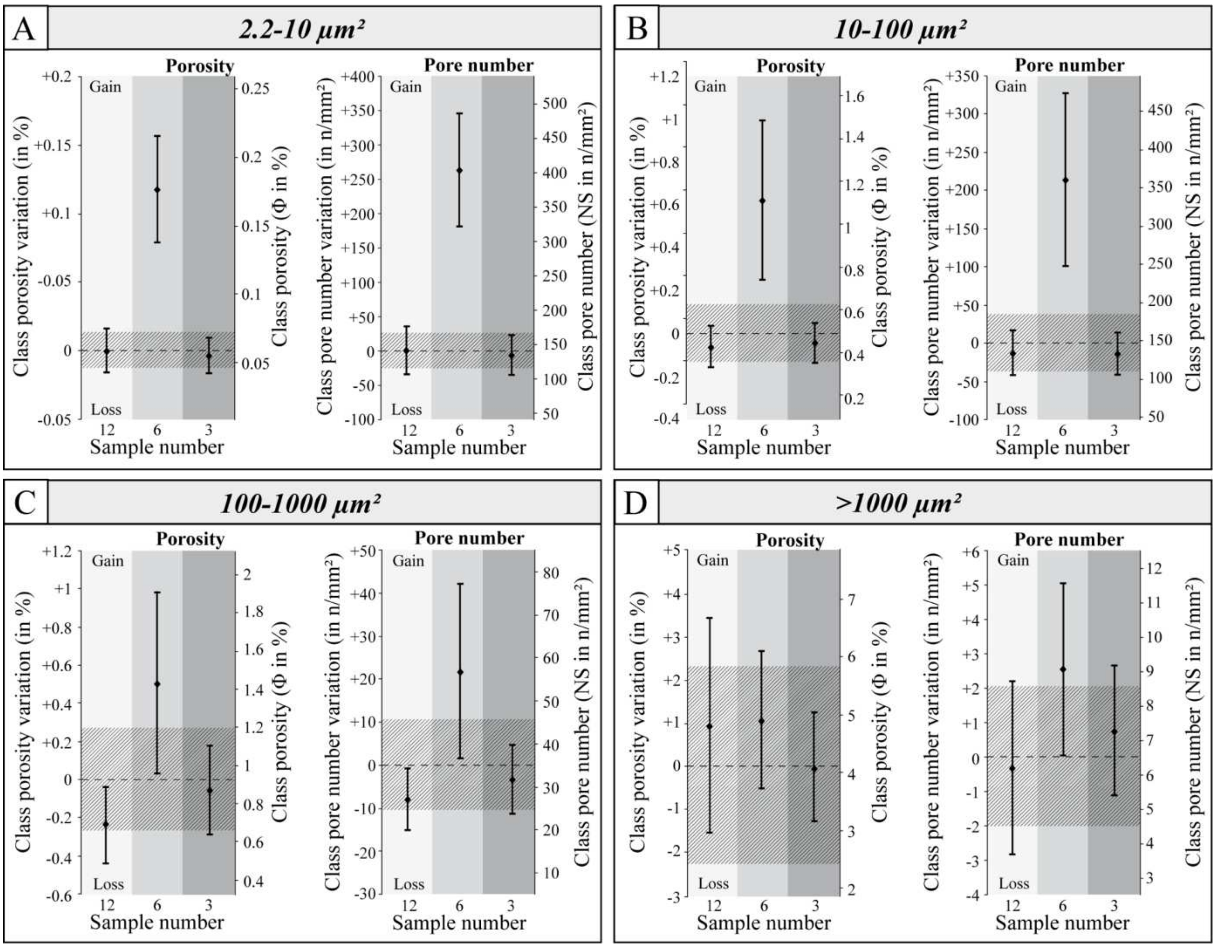

Figure 32 Variations of the porosity and the pore number for each determined class in the three studied samples (3, 6 and 12) compared with the fresh sample

3. DISCUSSION

Submitted to CO_2 injection, the reservoir will undergo several thermo-physical processes linked to the PVTX conditions (Pressure, Volume, Temperature, Composition) of the injected fluid, and to the thermal and petrophysical properties of the reservoir. These phenomena could occur during the injection (André *et al.*, 2011), as the Joule Thomson effect, leading to the cooling of the storage (well, reservoir, fluid and caprock). This cooling could induce a decrease of the injectivity, due for instance to a possible local freeze of water in the vicinity of the injection well (Oldenburg, 2007). The Joule Thomson effect can also reduce mechanical stress and consequently the initiation and propagation of fractures (Goodarzi *et al.*, 2011, Luo and Bryant, 2011). The temperature gradient between the injected fluid and the reservoir rock also implies the setting up of a heat transfer leading to physico-chemical transformations. In particular, the solubility of CO_2 and the thermodynamic constants of dissolution and precipitation of minerals are strongly dependant of the system temperature. These reactions could induce an important mass transfer between zones of different temperatures, and thus impact petrophysical properties of the host rock. Indeed, if the dissolution reactions will increase the porosity of the reservoir, the reactions of precipitation could lead to a located decrease of the permeability, inferring important variations of CO_2 injectivity.

The original COTAGES experiment was used to reproduce the effect of a thermal gradient on the behaviour of a limestone reservoir for CO_2 storage. The experimental design and protocol allows the control of important parameters that are the pressure, the temperature and the mass transfers. Despite the relative simplicity of the system, some complex phenomena occurred during the experiment resulting in important mass transfers implying changes in the petrophysical properties of the material as well as in the global regime of pressure.

By imposing a thermal gradient on the reservoir rock, this experiment rather reproduces the thermal conditions during the injection process.

From a chemical point of view, the system is composed by three main components: salted water (4 $g.L^{-1}$), calcite and CO_2. The monitoring of pressure and temperature in the reactor gives information on the chemical reactions occurring between the three components. The initial aqueous solution is saturated with respect to calcite at 100°C implying its dissolution in the non warmed area according to equation 3.

(3) $CaCO_{3(s)} + H_2O = + Ca^{2+} + HCO_3^- + OH^-$

As soon as the solution is injected into the reactor this reaction competes with the dissolution of CO_2 into the water (equation 4).

(4) $CO_{2(g)} = CO_{2(aq)}$

The dissociation of carbonic acid leads to the acidification of the solution and increases the dissolution of calcite (equation 5).

(5) $H_2O + CO_{2(aq)} = HCO_3^- + H^+$

On one hand, during the first 60 hours of the experiment, the main process is the dissolution of CO_2 in the water (eq2), leading to a decrease of the pressure in the reactor (Figure 4). On the other hand, this reaction competes with the dissolution of calcite, according to equation 6.

(6) $CaCO_{3(s)} + 2H^+ = CO_{2(g)} + Ca^{2+} + H_2O$

If the rate of CO_2 production given by reaction 4 is equal to the rate of CO_2 consumption given by the reaction 2, then the pressure of the system remains constant.

By migrating from the injection point (about 35°C) to the warmed area (100°C), CO_2 will undergo a thermal dilatation and could lead to a raise of pressure due to its PVT properties.

The tight position of samples due to the loading process of the reactor could locally creates a narrowing of the solution pathway. This could affect the apparent permeability of the system and consequently the migration of fluids in the reactor, hindering equilibrium processes. Reactions of dissolution can help to open the porous network locally, and counterbalance this latter effect. The step observed on the pressure curve after 15 and 38 hours of experiment could result from the combination of these phenomena. After 60 hours, pressure is constant and the temperatures are stables suggesting that the system reached an equilibrium state. However, it has to be considered as a dynamical equilibrium since thermal and chemical gradients take place in the reactor.

The chemical gradient is caused by the difference between the species solubility (CO_2 and $CaCO_3$). Indeed, the solubility of CO_2 in a NaCl aqueous solution (0.069 mol/L) decreases jointly with the temperature. At 100 bar and 35, 55 and 100°C, the solubility is of 1.28, 1.06 and 0.77 mol/L respectively (Duan and Sun 2003, Duan *et al.*, 2006). Some PHREEQC (Parkhurst and Appelo, 1999) simulations helped to determine the calcite solubility in a NaCl aqueous solution (0.069 mol/L) of about 6.10^{-2}, 4.10^{-2} and 2.10^{-2} mol/L at 100 bar and 35, 55 and 100°C respectively. Therefore, the solubility of CO_2 and calcite is respectively two and three times less in the warmest area than in the coldest. Differences of calcite solubility generate a gradient of calcium in solution leading to a mass transfer from the coldest to the warmed area.

Looking at the Figure 5, the most reactive zone corresponds to the samples located at the interface between the warmed and the not warmed area, where the thermal gradient is the most important (more than 1.5°C/cm versus 0.7°C/cm in the cold area). These gradients allow the setting up of a calcium pump between cold and warmed area. The calcium migrates from the cold zone to feed the precipitation of calcite in the hot zone. According to a diffusion coefficient of $1,6.10^{-5}$ cm²/s at 37°C (Ribeiro *et al.*, 2008), the involved times to transport the calcium by diffusion from the non-warmed area to the warmed area is in the order of few hours. It is consistent with the duration observed experimentally and allows a simplification of the system considering a mainly diffusive transport. These dynamic mass transfers occur until a complete dissolution of calcite or a complete filling of the available porosity in the hot zone is reached. According to a dissolution rate of about 0.1g/day, a complete dissolution could arise after 1000 day of experiment. The mass transfer will be most probably stopped by the formation of a plug in the hot area due to a massive calcite precipitation.

Mass transfers occurring in the reactor modify the petrophysical properties of the system (porosity and permeability). In this experiment, two levels of porous network could be considered. The first corresponds to the macroporosity (pore of few millimetres) between several grains of crushed limestone in a same sample and is called the intergrain porosity (Figure 12). This porosity is due to the chosen experimental set-up for which the limestone is initially crushed. The second corresponds to the porous network of the rock itself, called intragrain porosity. This porosity is constituted by the interoolith macroporosity (pore size in the order of few hundred micrometers) and by intraoolith microporosity (pore size in the order of few micrometers).

The crystallisation of calcite observed in the warmed area occurs mainly in the intergrain porous network. Microcalcite crystals, in the order of few microns, cover the grain surface, suggesting that in these experimental conditions, nucleation is favoured by comparison with crystal growth. Factors which can explain the important nucleation are either the high specific surface area of grains artificially increased by the crushing of limestone, or the presence of magnesium in the solution inhibiting the crystal growth or a combination of the two factors (Davis *et al*., 2011). It is noted that a SEM analysis reveals Mg traces in the neo-precipitated calcite crystals. This porosity could be considered as an analogue of a fracture or a channel porosity type (*sensu* Choquette and Pray, 1970) in a reservoir. The formation of aggregates as observed in Figure 8 shows that the precipitation of microcalcite could lead to a complete closure of fractures especially in bottleneck area. The crystallisation reaches rarely the heart of the grains, and hence do not affect significantly the porosity value of the grains (Figure 9). However, the crystallisation leads to the formation of a fringe surrounding the grain thus has a major impact by isolating the intragrain porous network from the rest of the system.

Mainly the ooliths of the non warmed area located at the periphery of the grain are submitted to the dissolution of their cortex. This dissolution of the edges of micrite crystals by acid water leads to the formation of a gulf between them, as explained in Lambert *et al*., 2006. This could lead to an enlargement of the channel/fracture porosity. The dissolution results in the creation of about 800 pore/mm² for the most affected sample, the pore class with an area inferior to 100 µm² being the most impacted. It corresponds to an increase of about 2% of the total porosity of the studied grains, and has to be compared with the number of pores of the fresh sample (about 300 pore/mm²). However the porosity is calculated on the totality of the grain surface, but the heterogeneous dissolution observed on the grain in the non warmed area (Figure 7) suggests a more important pore creation in the periphery of the grains. More than the porosity value itself, the variation of the pore number needs to be considered, as it can play a role in the connectivity of the porous network and consequently on the CO_2 injectivity. Both crystallisation and dissolution phenomena affect without distinction all the studied granulometric classes, suggesting that the described phenomenon does not impact the samples in a millimetric scale. Figure 12 sums up the evocated processes occurring during the COTAGES experiment.

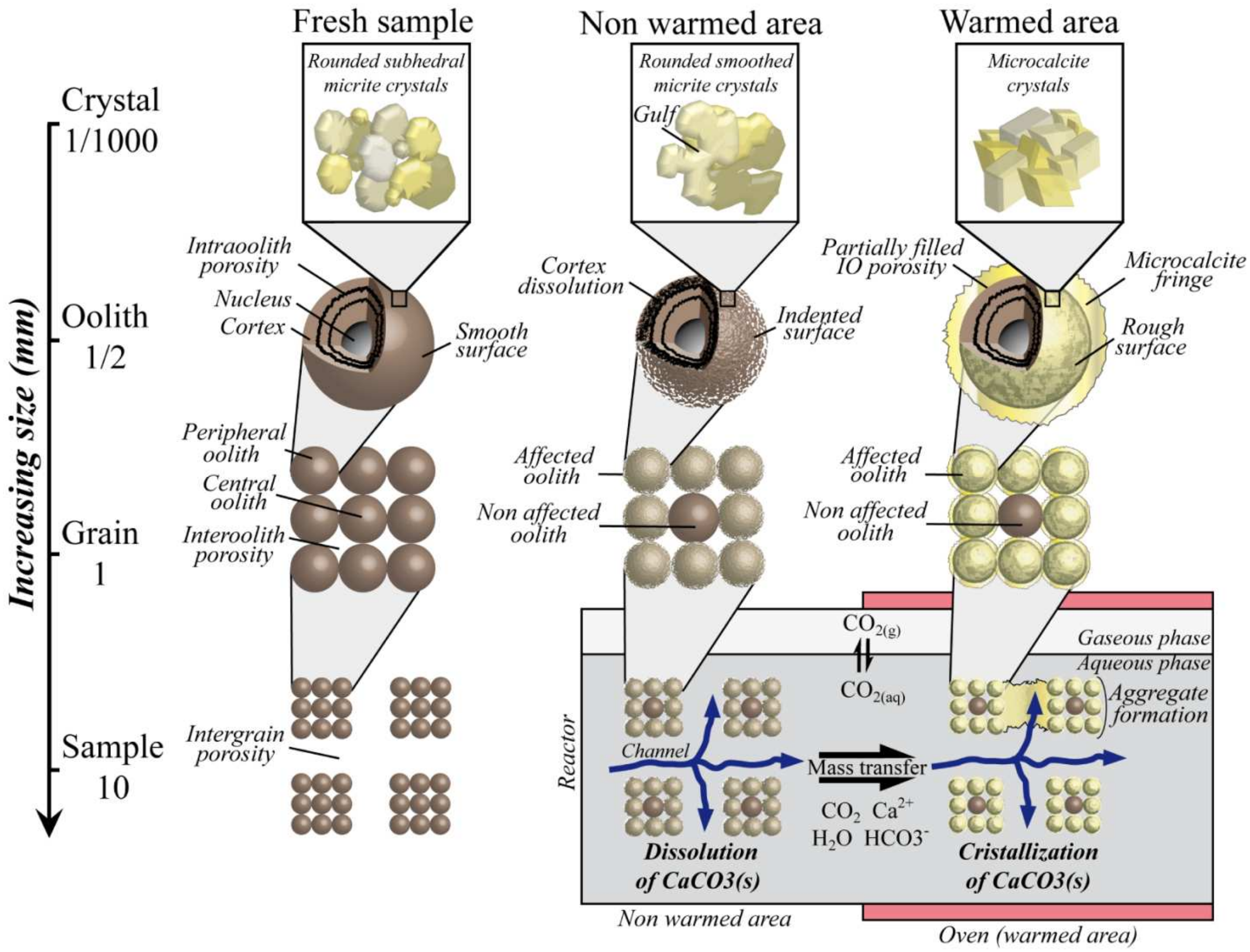

Figure 33 : Simplification of the various phenomenons occurring in the reactor in consideration of the different scale from the micrometer to the millimeter.

4. CONCLUSION

This paper is focused on the development of a new experimental protocol used to study the effect of a thermal gradient on petrophysical properties of a reservoir submitted to a CO_2 injection under storage conditions. An oolithic limestone (Lavoux limestone), analogous to the carbonated reservoir of the Dogger of the Paris Basin, was used to perform the experiment. Twelve samples composed of crushed limestone with grain a size from 1 to 4 mm were submitted to a thermal gradient (from 35 to 100°C) during 1 month, in presence of a saline aqueous solution under an initial CO_2 pressure of about 100 bar. At the end of the experiment, a mass balance was been carried out, as well as a complete petrographical study with an electron microscopy, cathodoluminescence, X-ray microtomography techniques and image analysis.

Our results have shown an important mass transfer, in the order of 10% of initial mass, from the cold to the hot area. According to the mass balance, the most impacted samples are located in the area which presents the strongest thermal gradient. Mass transfers result in the dissolution of the cortex of ooliths located at the periphery of grains in the non warmed area, whereas the crystallisation in the warmed area occurs mainly as a microcalcite fringe which surrounds the grains. Dissolution processes lead to a significant increase of the number of pores, suggesting a possible increase of the connectivity in the porous network. Conversely, the precipitation processes do not affect significantly the total porosity of the grain, but could be responsible for on one hand the filling of the intergrain porous network, and on the other hand of the isolation of intragrain porous network.

In a CO_2 storage site, these results suggest a possible dissolution of the limestone close to the injection point where the thermal gradient is the most important. Matter transfers in solution toward the warmest part of the reservoir could lead to a crystallisation of calcite in the poral space and could degrade the injectivity properties.

These processes could occur at a limited scale of time and space since our experiment shows massive modifications of petrophysical properties of the limestone after only 30 days of experiment with transport phenomenon mainly governed by diffusion processes.

In perspective, experiments of different durations could bring new insights on the kinetics of dissolution/precipitation processes which affect the reservoir rock. Because the thermal gradient plays an important role on the geometry of the areas affected by the dissolution/precipitation processes, it is of prime interest to carry out other experiments testing different realistic thermal gradients.

ACKNOWLEDGMENTS

This work was supported by the ANR Injectivité (ANR-05-CO2-007) and Interface (ANR-08-PCO2-006). The authors would like to acknowledge Ludovic Mouton and Sandrine Mathieu (SCMEM, Université de Nancy) for the technical assistance, Judith Sausse, Christophe Durlet and Cédric Carpentier for scientific discussions.

REFERENCES

Abramoff, M.D., Magelhaes, P.J., Ram, S.J., 2004. Image processing with ImageJ. Biophotonics Int. 11 (7), 36–42.

André, L., Audigane, P., Azaroual, M., Menjoz, A., 2007. Numerical modeling of fluid-rock chemical interactions at the supercritical CO_2-liquid interface during CO_2 injection into a carbonate reservoir, the Dogger aquifer (Paris Basin, France). Energy Conversion and Management. 48 (6), 1782–1797.

André, L., Azaroual, M., Menjoz, A., 2010. Numerical simulations of the thermal impact of supercritical CO_2 injection on chemical reactivity in a carbonate saline reservoir. Transport in porous media (82), 247-274.

Bachu, S., 2008. CO_2 storage in geological media: Role, means, status and barriers to deployment. Progress in Energy and Combustion Science (34), 254-273.

Bradshaw, J., and Dance, T., 2004. Mapping geological storage prospectivity of CO_2 for the world’s sedimentary basins and regional source to sink matching. Seventh International Conference on Greenhouse Gas Control Technologies (1): Vancouver, Canada, 583-591.

Choquette, P.W., Pray, L.C., 1970. Geologic nomenclature and classification of porosity in sedimentary carbonates. AAPG bulletin (54), 207-244.

Davis, K.J., Dove, P.M., De-Yoreo, J.J., 2001. The Role of Mg^{2+} as an Impurity in Calcite Growth. Science (290), 1134-1137.

Duan, Z., Sun, R., 2003. An improved model calculating CO_2 solubility in pure water and aqueous NaCl solutions from 273 to 533 K and from 0 to 2000 bar. Chemical geology (193), 257-271.

Duan, Z., Sun, R., Zhu, C., Chou, M., 2006. An improved model for the calculation of CO_2 solubility in aqueous solutions containing Na^+, $K^{+,}$ Ca^{2+}, Mg^{2+}, Cl^-, and SO_4^{2-}. Marin chemistry (98), 131-139.

Fleury, M., Soualem, J., 2009. Quantitative analysis of diffusional pore coupling from T2-store-T2 NMR experiments. Journal of Colloid and Interface Science (336), 250–259.

Gale, J., 2004. Geological storage of CO_2: What do we know, where are the gaps and what more needs to be done?. Energy, (29), 1329-1338.

Goodarzi, S., Settari, A., Keith, D., 2011. Geomechanical modeling for CO_2 Storage in Wabamun Lake Area of Alberta, Canada. Energy procedia (4), 3399-3406.

Grataloup, S., Bonijoly, D., Brosse, E., Dreux, R., Garcia, D., Hasanov, V., Lescanne, M., Renoux, P., Thoraval, A., 2009. A site selection methodology for CO_2 underground storage in deep saline aquifers: case of the Paris Basin. Energy Procedia, (1), 2929–2936.

Key world energy statistics, 2010. © ***OECD/IEA.***

Kurt Zenz House, K. Z., Schrag, D. P., Harvey, C. F., Lackner, K. S., 2006. Permanent carbon dioxide storage in deep-sea sediments. PNAS (103), 12291–12295.

Lambert, L., Durlet, C., Loreau, J.-P., and Marnier, G., 2006. Burial dissolution of micrite in Middle East carbonate reservoirs (Jurassic-Cretaceous): keys for recognition and timing. Marine and Petroleum Geology, (23), 79-92.

Lagneau, V., Pipart, A., Catalette, H., 2005. Reactive transport modelling of CO_2 sequestration in deep saline aquifers. Oil Gas Sci. Technol. 60 (2), 231–247.

Lambert, L., Durlet, C., Loreau, J.-P., Marnier, G., 2006. Burial dissolution of micrite in Middle East carbonate reservoirs (Jurassic-Cretaceous): keys for recognition and timing. Marine and Petroleum Geology (23), 79-92.

Luo, Z., Bryant, S., 2011. Influence of thermo-elastic stress on fracture initiation during CO_2 injection and storage.

Luquot, L., Gouze, P., 2009. Experimental determination of porosity and permeability changes induced by injection of CO_2 into carbonate rocks. Chemical Geology (265), 148-159.

Metz, B., Davidson, O., Coninck, H.d., Loos, M., and Meyer, L., 2005. IPCC Special Report on Carbon Dioxide Capture and Storage. Intergovernemental Panel on Climate Change. Special report on carbon dioxide capture and storage. Cambridge university press.

Michael, K., Arnot, M., Cook, P., Ennis-King, J., Funnell, R., Kaldi, J., Kirste, D., Paterson, L., 2009. CO_2 storage in saline aquifers I. Current state of scientific knowledge. Energy Procedia (1), 3197-3204.

Noiriel, C., Renard, F., Doan, M. L., Gratier, J. P., 2010. Intense fracturing and fracture sealing induced by mineral growth in porous rocks. Chemical geology (269), 197–209.

Oldenburg, C.M., 2007. Joule-Thomson cooling due to CO_2 injection into natural gas reservoirs. Energy conversion and management (48), 1808-1815.

Parkhurst, D., Appelo, C., 1999. User's guide to PHREEQC (version 2) – A computer program for speciation, batch-reaction, one-dimensional transport, and inverse geochemical calculations. U.S. Geological Survey Water-Resources Investigations Report (99), 4259-4571.

Pironon, J., Canals, M., Dubessy, J., Walgenwitz, F., Laplace-Builhe, C., 1998. Volumetric reconstruction of individual oil inclusions by confocal scanning laser microscopy. European journal of mineralogy (10), 1143-1150.

Ribeiro, A.C.F., Barros, M.C.F., Teles, A.S.N., Velente, A.J.M., Lobo, V.M.M., Sobral, A.J.F.N., Esteso, M.A., 2008. Diffusion coefficients and electrical conductivities for calcium chloride aqueous solutions at 298.15K and 310.15K. Electrochimica acta (54), 192-196.

Rosenbauer, R.J., Koksalan, T., Palandri, J.L., 2005. Experimental investigation of CO_2-brine-rock interactions at elevated temperature and pressure: implications for CO_2 sequestration in deep-saline aquifers. Fuel Process. Technol. 86 (14–15),1581–1597.

Sterpenich, J., Sausse, J., Pironon, J., Géhin, A., Hubert, G., Perfetti, E., Grgic, D., 2009. Experimental ageing of oolitic limestones under CO_2 storage conditions: Petrographical and chemical evidence. Chemical Geology (265), 99-112.

Vidal-Gilbert, S., Nauroy, J. F., Brosse, E., 2009. 3D geomechanical modelling for CO_2 geologic storage in the Dogger carbonates of the Paris Basin. International Journal of Greenhouse Gas Control (3), 288-299.

World energy outlook, 2009. © ***OECD/IEA***.

Publications

Reconstruction of geochemical history of the Rousse field (France) from mineralogy and fluid analysis in reservoir and caprock.

Stéphane Renard[1], Jacques Pironon[1], Jérôme Sterpenich[1], Marc Lescanne[2]

[1] Nancy-Université, CNRS, CREGU, G2R laboratory, B.P. 70239, F-54506 Vandœuvre-lès-Nancy, France

[2] TOTAL SA, 64018 Pau Cedex, France

Abstract

The first French pilot of CO_2 storage will be held in the Rousse field Near Pau in the south-west of France. This paper is devoted to describe the mineralogy and petrography of the Rousse reservoir as well as the reconstruction of its thermal and pressure history. The rocks composing the field were sampled on cores from the wells Rousse 1 and 2 and were analyzed through ICP-MS, XRD, SEM, EPMA, TEM, cathodoluminescence and microthermometry coupled to a Raman microprobe. The resulting mineralogy showed a predominance of carbonates associated to quartz, clays and pyrite. The PT conditions were derived from the fluid inclusions trapped in the fracture minerals of the Upper Jurassic “Dolomie de Mano” and the Upper Cretaceous breccia corresponding respectively to the reservoir rock and the base of the caprock of the field. The results show a double-time fluid circulation with a first stage during the Late Jurassic to Early Cretaceous for the reservoir rock corresponding to the rifting period of the Aquitaine basin and a second stage during Paleocene in breccias corresponding to the Pyrenean compression period. The field has already known CO_2-rich fluids, at the origin of the carbonates in the fractures in the “Dolomie de Mano”. Two main episodes of gas demixion are detected with gas compositions different from the present day composition. Limited reactions have been detected between fluids and diagenetic minerals and are essentially marked by late oxidation of Fe-dolomite in contact with pore space or late calcite in reservoir fracture network. Re-injection of CO_2 in the depleted gas field will equilibrate rapidly with the carbonates and should have a limited reactivity with the clays.

1.Introduction

The injection of the CO_2 into deep geological formation could be a good way to limit the greenhouse gas emissions from anthropogenic sources. However, carbon dioxide and some of the co-injected gases are chemically active (oxidizing, reducing or acidic) and could react with the reservoir rocks and the caprock (Kaszuba et al., 2003, Oelkers et Schott, 2005, Xu & al., 2007). This could lead to the petrophysical modifications of the rocks and finally to the leakage of the stored gases. Thus, before any operation of storage, the long-term stability of the field submitted to CO_2 and co-injected gases has to be demonstrated.

In this context TOTAL wants to demonstrate the feasibility of an integrated CO_2 capture, transportation, injection and storage scheme from a boiler at a 1/10th reduced scale. This industrial project conducted at Lacq in the south-west of France is the first French CCS (Carbon Capture and Storage) pilot project. The CO_2 is injected into the Rousse depleted gas field at 4500 m into the Upper Jurassic reservoir of the “Dolomie de Mano” Formation. Initial reservoir pressure was 485 bar at 4500 m depth. Discovered in 1967, producing since 1972, the field was largely depleted with, for the “Dolomie de Mano” reservoir, an average downhole pressure of 35 bars in 2008. Pressure should reach 80 bars at the end of the two years injection of CO_2 which has just started at the beginning of 2010. This pressure far from the initial pressure of the field should prevent from any CO_2 flow out of the reservoir rock.

The first step to predict the reactivity of the host rock is to study the geology and the mineralogy of the target. Moreover, the understanding of the history of the gas field in terms of pressure and temperature, as deduced from the study of fluid inclusions (Roedder, 1984) coupled to geology, can give information about the pressure regimes undergone by the reservoir and about ancient fluid-rock interactions. This paper is devoted to the description of the mineralogy and petrography of the Rousse reservoir as well as to the reconstruction of its thermal and pressure history. Implications on the long-term stability of the storage will finally be discussed.

1.1. Geological setting.

The geological history of the Aquitaine Basin was described by De Chevilly et al., 1969, Biteau et al., 2006 and Serrano et al., 2006. The Aquitaine basin of 35 000 km² is located in the southwest of France between the Poitou threshold to the north and the Pyrenean Mountain chain to the south. It is divided in three units from north to south: the Parentis basin, the North Aquitaine Platform and the North Pyrenean Foreland (figure 1).

The structure developed on the Palaeozoic basement, starting with a carbonate reef created in a shallow sea during late Malm. In Early Cretaceous an extensional context led to the creation of a rifting phase fracturing and structuring the carbonate platform. But the beginning of the subduction of the Iberian plate under the European plate stopped the extension at the end of Albian, prior to the development of an oceanic crust. During Late Cretaceous, the continued subduction led to the formation and migration of northward flexural basins. The paroxysmal phase of the compression operated during the Eocene leading to the Uplift of the Pyrenean Mountain chain and the deformation of the foreland basins.

The gas reservoirs developed mainly in fractured and diagenetically modified carbonates in the Parentis Basin, the middle of the North Pyrenean and the eastern part of the North Aquitain Platform (Figure 1).

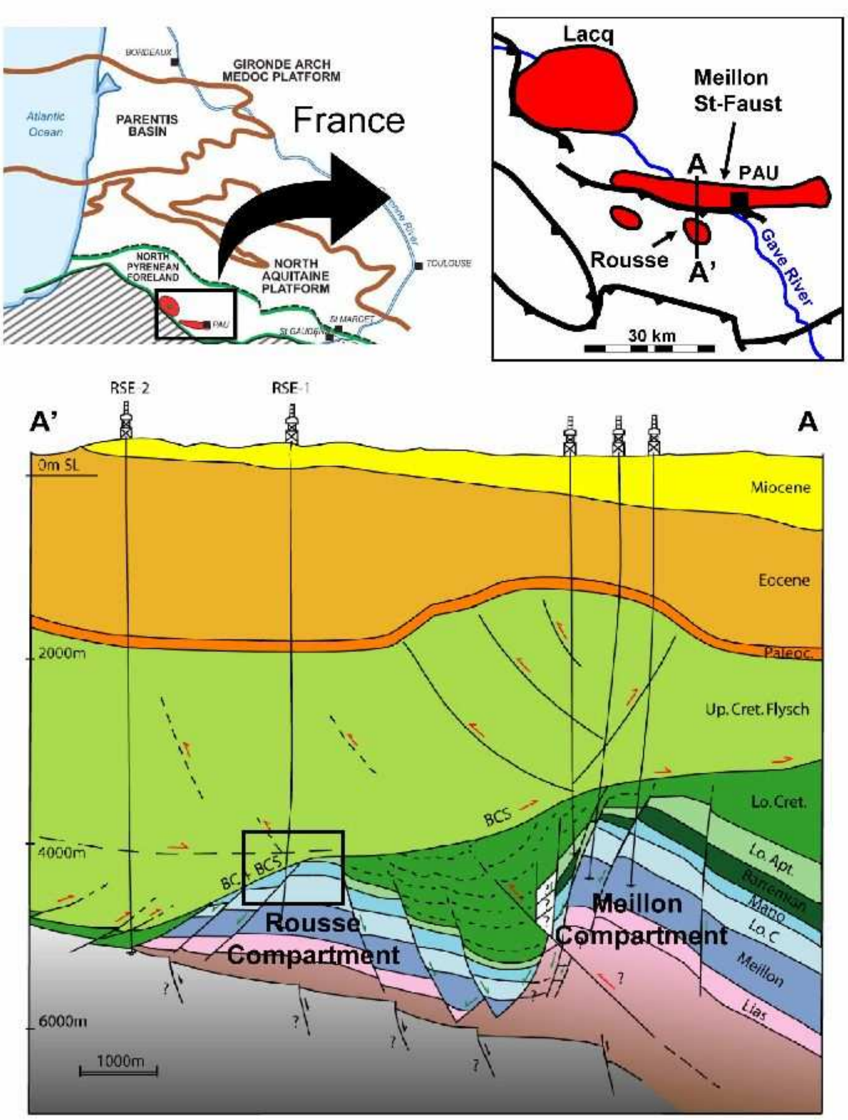

Figure 1: Regional location and cross section of the Rousse Field. Red zones represent the main gas fields of the area. The cross section corresponds to the AA' line on the location scheme and presents the Meillon and Rousse carbonates compartments. The Rousse field is located at the top of the Rousse compartment. From Biteau et al., 2006 ; Gapillou et al., 2008

1.2. The Rousse reservoir.

The Rousse gas field is situated to the south-east of the acid gas field of Lacq and 5 km to the South of Meillon (De Chevilly & al., 1969 – figure 1). The reservoir is constituted by the Jurassic platform faulted by the Early Cretaceous extensional episode. As shown on the cross section in figure 1, the Meillon block was uplifted during the first compressive phase from Late Albian to Senonian, isolating itself from the Rousse compartment (De Chevilly & al., 1969 and Biteau & al., 2006). An unconformity defines the transition between the Upper

Jurassic reservoir rocks and the thick Upper Cretaceous flysch underlying the syn-compressive Tertiary sediments. The opposite evolution of the sediment thickness from the south to the north between the flysch and the tertiary sediments is due to the high migration of the foreland basins during the Tertiary. The flower shape structure overlying the traps, known as the Pau anticline, is interpreted as a transpressive structure induced by a slight thrust movement initiated by the North Pyrenean Frontal overthrust, some ten to fifteen kilometers to the south (Biteau et al., 2006). The deformation was propagated toward the north due to thin evaporitic bedding-planes (BC and BCS on figure 1) within the base of the Upper Cretaceous playing the role of a decollement level.

	Lacq	**Meillon**	**Rousse**
N_2	-	0.44	0.75
H_2S	15.23	5.84	0.77
CO_2	10.00	8.52	4.58
CH_4	69.23	77.81	76.52
C_2H_6	3.30	3.57	4.57
C_3H_8	1.11	1.19	2.04
C_4H_{10}	0.51	0.89	1.62
C_5H_{12}	0.31	0.50	0.80
C_6^+	0.31	1.24	8.26

Table 1 : Composition of the downhole gas for the Meillon, Rousse and Lacq reservoirs in mol%. From De Chevilly et al., 1969.

The Jurassic palaeoplatform is constituted by a succession of partially dolomitized limestones and dolomites overlapped by Lower Cretaceous shales as shown on the stratigraphic sequence in figure 2 (De Chevilly et al., 1969 and Bourrouilh et al., 1995) deposited in a peritidal context during Portlandian. It has been formed by a succession of three stages of dolomitization. The first stage occurred during the deposition of the sediments, followed by the second stage at the start of the burial. They conducted to the high cementation of the rock by recrystallization of crypto to microcrystalline dolomite. The third stage led to deposition of the fractures carbonates (figure 2c) in association with the tectonic fracturing during late Jurassic to Early Cretaceous. Considered as a late dolomitization it conferred to the rock its reservoir quality (Grimaldi M.H., 1988). Over the Mano dolostone, the Barremian to Lower

Cretaceous sediments at 4545 m have been eroded during Early Upper Cretaceous. A sedimentary Upper cretaceous breccia makes the transition between the “Dolomie de Mano” formation and the overlying Campanian flysch (figure 2b). It probably acted as a bedding plane in the Upper Cretaceous flysch displacement during the compression phase of the Pyrenees Mountains (figure 1). With a thickness of around 2 000 m, the flysch acts as the caprock of the field (figure 2a), mainly made of silico-calcareous shales. The 2 500 m of sediments above are composed by successions of shales and limestones, interlayered by sandstone formations. The end-member of Miocene molassic deposit is made of clays and sandstones corresponding to the filling of foreland basin by the beginning of the erosion of the Pyrenean Mountains (De Chevilly et al., 1969).

The Rousse reservoir, such as the Meillon compartment has a very low porosity and permability. The matrix porosity is estimated to be between 3 and 4 % and the permeability near 0.1 mD. The reservoir quality lays in the intense fracture network, upgrading the average permeability of the whole rock to 20 mD (De Chevilly & al., 1969). No active aquifer is present (no water was produced during the exploitation), and the water saturation (Sw) is supposed to be between 20% and 40%. The Rousse gas field was charged by an in situ system involving the Upper Kimmeridgian source rock. The charge is considered to occur during the Miocene. The gas initially present at a quantity of 150.10^9 SCF (Standard Cubic Feet) (Biteau et al., 2006) presents some differences on the CO_2 and H_2S content towards other gas fields in the area (Table 1).

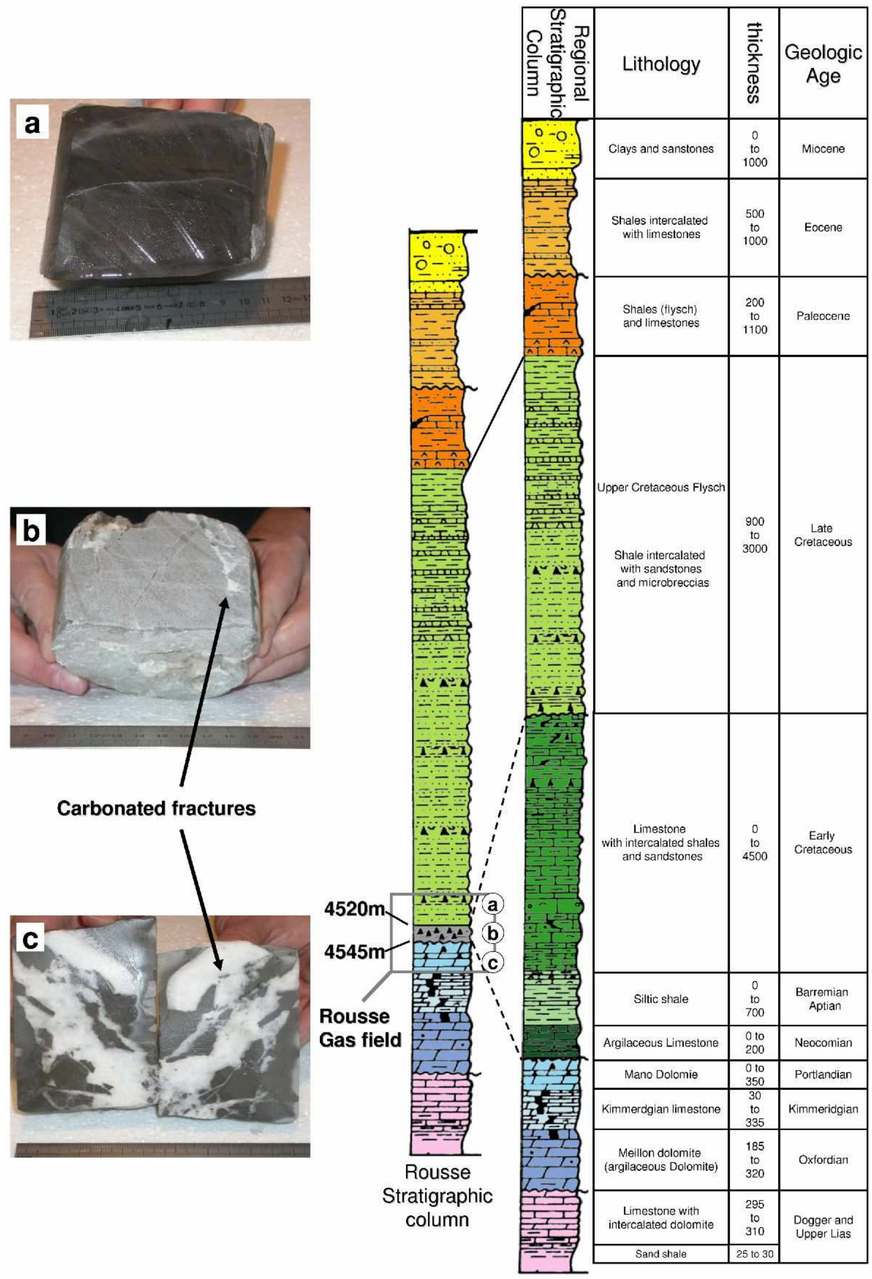

Figure 2 : Stratigraphic log and lithology of the Aquitaine basin and the Rousse gas field with pictures of the main rock facies of the field. (a) Campanian Flysch, (b) Campanian Breccia, (c) “Dolomie de Mano”. Adapted from De Chevilly et al., 1969 and Bourrouilh et al., 1995.

The low content of non hydrocarbon gases could be explained by local absence of the Barremian source rock, eroded during Late Cretaceous. Two wells were drilled in Rousse (figure 1). The well RSE 1 opened the field and was directly drilled in the structure. The well RSE 2 was drilled several years after and never produced gas.

The hydrostatic and lithostatic gradients for the Mano Dolomite and the Campanian Breccia were modeled on Petromod 1D with geological data from the bibliography presented herein. In regard with the rock sampling for these formations, the evolution of the “Dolomie de Mano” and the Upper Cretaceous breccia were respectively calculated on the profile of the

RSE 1 and RSE 2 wells. For each well, the evolution of the temperature was calculated from surface heat flows. As the data are missing, we have chosen to take mean values from observed present values in similar geological contexts (Lucazeau and Vasseur, 1989 revised by the BRGM, 2006). The heat flow was respectively fixed at 130 mW/m², 80 mW/m² and 60 mW/m² for the rifting phase, the start of the Pyrenean compression and the present time. The resulting gradients are displayed in the figure 10 with the corresponding geological times. Whatever the formation is, the gradients are not linear. This is due to the variation of heat flow with time but also to the sedimentation and compaction rates, which vary from a layer to an other. The loops are due to erosion stages, especially the erosion of the Lower Cretaceous around -100 Ma. This preliminary basin modeling should be improved in the future, taking into account 2D and 3D approaches.

2. Materials and methods

Studied samples are representative of the three main facies of the sedimentary pile (fractured “Dolomie de Mano”, breccia and flysch). The Campanian flysch and the “Dolomie de Mano” were sampled on the core issued from RSE 1 at respectively 4500 m and 4580 m deep. The Upper Cretaceous breccia is not present on the RSE 1 core. It has been sampled on core from RSE 2 at 5293 m, assuming a lateral continuity of the facies.

The samples were first analyzed by ICP-MS (bulk analysis) and XRD as powders. The rocks were porphyrized before any study. The fracture and matrix facies of the Mano Dolomite were previously separated under microscope after a rough grinding stage (size of the clasts around 1 mm). The bulk analyses were carried out at the SARM-CRPG (Nancy, France). The powders were fused at 1080°C with $LiBO_2$, and then dissolved in a solution of HNO_3. The resulting solution was analyzed by ICP-AES on a type II Jobin-Yvon JY 70 for major and minor elements and ICP-MS on a Perkin-Elmer Elan 5000 for minor elements. Carbon dioxide and sulphur were analyzed by impulsion coulometry after calcination. All analytical details (detection limits and procedures) are described in Carignan et al., 2001. The XRD were performed at the Institut Jean Lamour (Nancy, France) with a diffractometer X'Pert Pro MPD from Panalytical with a vertical axis. It contains a copper anticathode and a X'Celerator detector. The diffractograms were registered on a range of 2θ from 5° to 75° with a measure step of 0.017° and a timestep of 34.92 s for 12.12°.

Cathodoluminescence (CL) petrography was performed on a CITL type cold cathode equipment on thin-sections polished on one side at G2R laboratory, Nancy Université. Thin sections of the rocks were also analyzed by SEM and EPMA at the SCMEM (Nancy-Université, France) for the mineralogical determination. The SEM micrographs and EDS analyses were performed on a Philips XL30 coupled with an EDS probe using a Si(Li) semi-conductor detector. The accelerating tension was fixed at 20 kV and the counting time was fixed at 60 s for EDS analysis. The electron microprobe analyses (EPMA) were carried out for elements (Al, Mg, Si, K, Ca, Mn, Ni, Fe Sr, S and Pb) on a CAMECA SX100 equipped with a wavelength dispersive spectrometer and calibrated using natural and synthetic oxides (albite, olivine, orthose, wollastonite, $MnTiO_3$, NiO, hematite, $SrSO_4$). The analyses were performed under the following conditions: current of 10 nA, accelerating voltage of 15 kV, defocalized electron ray on a surface with a diameter of 5 µm and counting time of 15 s per element except for Sr and Ni for which it was of 30 s. The total Fe was analyzed as FeO. Thus, the EPMA was used to perform elemental mapping of selected areas on thin sections. The analytical conditions for each point were: current of 100 nA, accelerating voltage of 15 kV, focalized electron ray corresponding to an analyzed volume of 0.42 μm^3, and counting time of 3 µs per element. The resulting maps were treated on Photoshop©. All the micrographs were superimposed. The corresponding zones of the elements were colored in accordance with the elements composing the minerals, set by previous XRD, SEM and EPMA (see figure 3-E for example).

A special treatment was used for the clay analysis, including a decarbonation of the rock by acid attack and then a study by XRD and TEM. The rocks were partly ground in millimetric fragments and added to a solution of pure water. The decarbonation was performed by adding droplets one by one of chlorhydric acid to the solution controlling the pH so that it did not fall under 3. After decarbonation, the solution was washed with pure water 5 times. During this operation, the temperature was set to ambient temperature for calcitic rocks and 80°C for dolomitic rocks. TEM microphotographies, electron dispersive spectra and electron diffraction patterns were obtained on the resulting powder samples dispersed in ethanol and deposited on a micro grid (Formvar/Carbon 300 Mesh Ni, Agar Scientific). They were carried out at the SCMEM (Nancy-Université, France) on an electron microscope Philips CM20 equipped with a Si-Li detector and Li super ultra-thin windows at 200 kV.

During the geological history of the Rousse gas field, fluids have been trapped in minerals. They are witnesses of the past events which occured in the rocks (Roedder, 1984). The fluid inclusions contained in the diagenic minerals or minerals in fractures of the “Dolomie de

Mano" and the Upper Cretaceous Breccia were analyzed in thin sections of 200 µm. The samples were studied at the G2R laboratory (Nancy-Université, France) by microthermometry using a Linkam MDS600 heating-cooling stage adapted to an Olympus optical microscope. According to the calibration curves, temperatures of phase changes (homogenization temperature, Th) are given with an accuracy of ± 1°C. Horiba Dilor-Labram Raman microspectrometer was used for the measurement of the composition of the gas phase in the fluid inclusions (Dubessy et al., 1989), and for the dissolved gas in the liquid aqueous phase according to the procedure described by Guillaume et al. 2003. The chlorinity (expressed in mole NaCl per kg of H_2O) of the aqueous phase was also determined by Raman by a method based on the modification of the Raman band of stretching vibrations of water produced by the chloride ion (Dubessy et al., 2002). The isopleths (bubble point curve) of the two-phase liquid-vapor inclusions are calculated using the Duan equation of state (Duan, 2000) in case of H_2O-NaCl-CH_4 system. Then, the isochores (isodensity curves) are calculated from the Zhang and Franz equation (Zhang and Frantz, 1987) considering dissolved methane has no effect on the isochore. Isochores of the vapor inclusions are calculated using two softwares developed by Bakker (Bakker, 1999, 2001 and 2003). First, the soft Loner 8.exe calculates the density of the fluid and its pressure at Th from the gas composition and the Th using the Bakker equation of state (Bakker, 1999). Second, the soft ISOC.exe establishes the P-T relation of the isochores.

3. Results

The study has been split according to the three geological formations composing the field. The selected samples are representative of the main units even if they cannot be considered as an exhaustive sampling. By consequence, some secondary minerals can be over or under estimated.

3.1. Dolomie de Mano (RSE 1, 4580 m)

The "Dolomie de Mano" is composed of a matrix of dolomicrosparite (mineral diameter around 5 µm) crosscut by fractures, partly filled by carbonates (figure 3A and 3B), with apertures from 200 µm to several millimeters. They randomly cut the matrix stratigraphy underlined by thin beds of quartz. The fractures are dispatched in two types depending on their size: the microfractures and the macrofractures, which have an aperture respectively lower and higher than to 1 mm. The microfractures often crosscut the macrofractures.

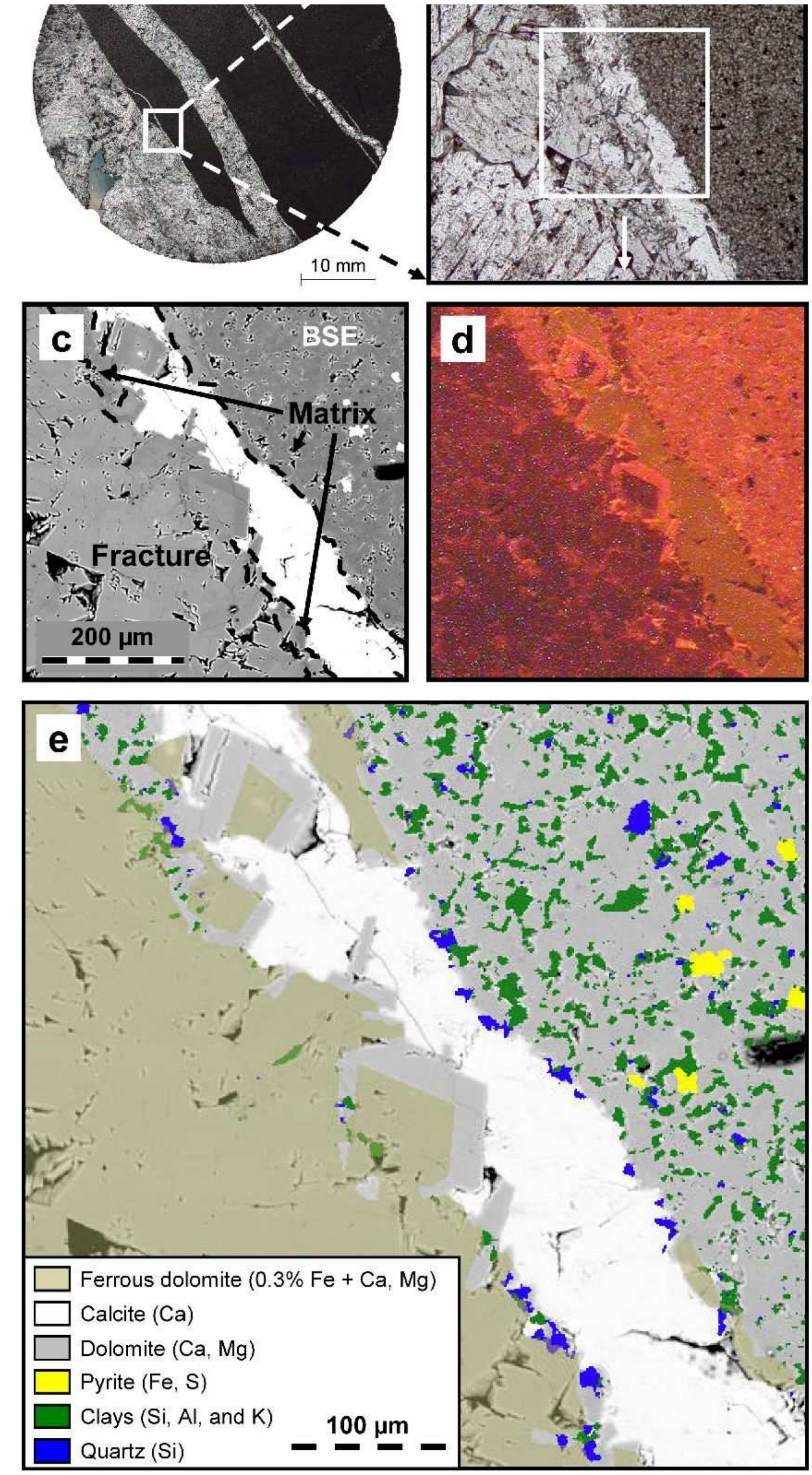

Figure 3 : Mineralogical assemblage of the “Dolomie de Mano” facies. (a) and (b) : pictures from optical microscopy showing the matrix and fractures of the rock. (c) backscattered scanning electron picture of the zone defined on (b). (d) Cathodoluminescent picture of the zone (c). (e) false color picture edited from X-ray mapping on zone (c).

3.1.1. Matrix mineralogy:

The chemical analysis of the matrix of the “Dolomie de Mano” is mainly composed of Mg, Ca and CO_2 (table 2), showing that the carbonates are the major minerals.

Oxide	"Dolomie de Mano"		Campanian Flysch
	Matrix	Fracture	
SiO_2	5.84	< L.D.	23.14
Al_2O_3	1.67	0.07	5.72
Fe_2O_3	0.49	0.51	3.90
MnO	0.01	0.01	0.08
MgO	18.77	18.64	1.07
CaO	28.42	33.14	33.90
Na_2O	< L.D.	< L.D.	0.22
K_2O	0.42	< L.D.	1.04
TiO_2	0.07	< L.D.	0.24
P_2O_5	0.55	< L.D.	0.10
CO_2 total	42.44	46.26	29.12
S total	0.22	< L.D.	0.13
LI[1]	42.74	47.09	29.12
Total	99.20	99.47	98.65
Ba (ppm)	45	4	132
Sr (ppm)	98	202	799
V (ppm)	15	3	49
Cu (ppm)	6	< L.D.	10
Cr (ppm)	14	< L.D.	36

Table 2: Bulk composition of matrix and fractures of the “Dolomie de Mano” and the Campanian Flysch expressed in wt%. [1] Includes the CO_2.

The secondary elements are silicon representing almost 6 wt% followed by aluminium, phosphorus, iron, potassium, sulfur, titanium and manganese. The high presence of carbonates is confirmed by XRD analyses showing mainly dolomite. However, we can recognize also quartz, pyrite and clays mainly represented by illite. The dolomite shows on EPMA analyses a constant Ca/Mg ratio of 1.06 (Table 3).

	Mineral	Nb of Analyses		Mg	Al	Si	K	Ca	O	Fe	Minor elts[1]	Total
Dolomie de Mano	**Matricial Dolomite**	**5**	Mean	24.0	0.2	0.2	0.1	25.3	50.0	0.0	0.1	100.0
			Std Dev.	0.3	0.1	0.1	0.0	0.2	0.1	0.0	0.1	
	Fracture Calcite	**5**	Mean	0.7	0.0	0.0	0.0	49.3	49.9	0.0	0.1	100.0
			Std Dev.	0.2	0.0	0.0	0.0	0.2	0.0	0.0	0.0	
	Fracture Non-ferrous	**5**	Mean	23.6	0.0	0.0	0.0	26.3	50.0	0.0	0.2	100.0
			Std Dev.	0.1	0.0	0.0	0.0	0.1	0.0	0.0	0.1	
	Fracture Ferrous	**11**	Mean	23.5	0.0	0.0	0.0	26.2	50.0	0.2	0.1	100.0
			Std Dev.	0.3	0.0	0.1	0.0	0.3	0.0	0.1	0.1	
Camp. Flysch	**Calcite**	**3**	Mean	0.3	0.0	0.0	0.0	48.1	50.6	1.0	0.1	100.0
			Std Dev.	0.1	0.0	0.1	0.0	0.1	0.9	0.8	0.1	
	Siderite	**2**	Mean	6.1	0.2	0.3	0.0	6.6	50.1	35.8	1.0	100.0
			Std Dev.	0.3	0.2	0.2	0.0	0.1	0.2	0.8	0.3	
	Dolomite	**2**	Mean	24.3	0.0	0.0	0.0	25.2	50.0	0.4	0.1	100.0
			Std Dev.	0.1	0.0	0.0	0.0	0.1	0.0	0.3	0.0	
Camp. Breccia	**Calcite**	**3**	Mean	0.2	0.0	0.0	0.0	49.7	49.9	0.1	0.1	100.0
			Std Dev.	0.1	0.0	0.0	0.0	0.1	0.0	0.1	0.1	

		Nb of Analyses		S	Fe	Cu	Pb	Total
Dolomie de Mano	**Pyrite**	**3**	Mean	66.5	33.5	0.0	0.0	100.0
			Std Dev.	0.0	0.0	0.0	0.0	
Camp. Flysch	**Pyrite**	**3**	Mean	65.9	34.1	0.0	0.0	100.0
			Std Dev.	1.1	1.1	0.0	0.0	
Camp. Breccia	**Pyrite**	**3**	Mean	66.4	33.6	0.0	0.0	100.0
			Std Dev.	0.1	0.1	0.0	0.0	
	Galena		4	49.5	0.7	0.0	49.8	100.0

Table 3 : Composition of the carbonates and pyrites present in the “Dolomie de Mano”, Upper Cretaceous Breccia and the Campanian Flysch in atom%. Results obtained from WDS analysis in EPMA. [1] Concerns the sum of K, Cl, Mn, Ni and Sr

It presents a regular ratio Fe / S of 0.5. Most of them present constant composition measured by TEM on individual particles (table 4). Its Al content is due to neighboring clays. They are mainly made of silicon and aluminum, but contain non negligible fractions of potassium, iron and magnesium. Their composition is very variable as showed by the table 4. Their formulae were calculated by the Harvey’s method (Harvey, 1943) based on 11 oxygens and Fe^{3+} from TEM analyses and were placed in the diagram showing tetrahedral silicon versus interlayer charge (figure 4) in order to understand their organisation.

Sample	Nb of analyses		Si	Al	Fe	Mg	K	Na	Ca	O
Camp. Flysch: Illites and Smectites	**17**	Mean	18.39	13.23	1.58	0.73	2.93	0.20	0.12	62.82
		Median	17.93	12.81	1.16	0.71	2.72	0.00	0.11	63.61
		std dev.	1.58	1.57	1.15	0.49	1.70	0.46	0.10	2.53
Camp. Flysch : Chlorites	**8**	Mean	14.04	11.31	9.02	3.68	0.68	0.00	0.16	61.12
		Median	14.30	11.29	8.34	3.96	0.67	0.00	0.18	61.91
		std dev.	2.13	0.80	3.10	0.78	0.53	0.00	0.07	3.96
Dolomie de Mano	**27**	Mean	19.53	12.90	0.34	1.84	3.60	0.29	0.16	61.35
		Median	19.80	12.84	0.29	1.61	3.85	0.07	0.16	61.29
		std dev.	1.88	1.14	0.24	1.08	1.21	0.79	0.09	2.56

Table 4 : Composition of the clay minerals from the Campanian flysch and the “Dolomie de Mano” in atom% obtained from TEM analyses.

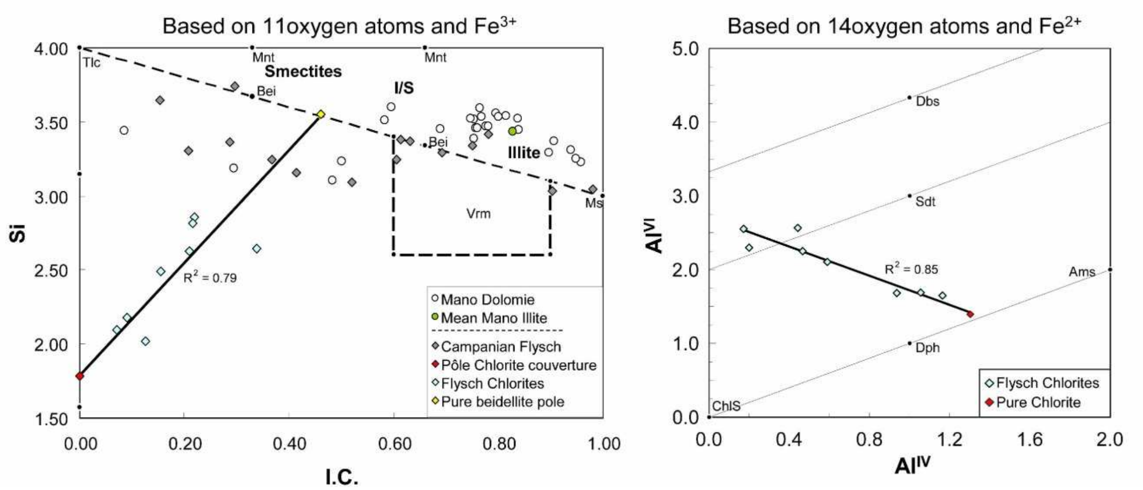

Figure 4 : Diagram Si vs interlayer charge for the Campanian Flysch and the “Dolomie de Mano”, and AlVI vs 4-Si for the Campanian Flysch. Data were calculated from TEM analysis by the Harvey’s method (Harvey, 1943). Whereas the clays of Mano Dolmite are mainly illites, the clays of the Campanian Flysch are more spread and present a constant evolution from chlorites to smectites. Diagrams are adapted from Guillaume, 2002. Ams: amesite, Bei: Beidellite, Dbs: Donbassite, Dph: daphnite, I.C.: interfolial charge, I/S: interstratified Illite/Smectite, Mnt: montmorillonite, Ms: muscovite, Sdt: sudoïte, Tlc: Talc, Vrm: Vermiculite.

The position of the points confirmed the XRD analysis showing a concentration of most of the points in the illite area. A mean illite formula was calculated. It corresponds to a high-charged illite: $(Si_{3,53}Al_{0,47})^{IV}(Al_{1,67}Fe_{0,04}Mg_{0,27})^{VI}K_{0,69}(Na_{0,02}Ca_{0,04})O_{10}(OH)_2$. However, some dispersed points reveal the presence of rare interstratified illite/smectite and smectite/chlorite and the probable presence of muscovite. No individual chlorite particles are detected, but acid attack could cause some chlorite dissolution and by consequence chlorite underestimate. Pyrite is the single type of sulfides detected in the matrix.

The spatial organization of the minerals has been studied by elemental X-ray mapping and is shown on figure 3E. It confirms that Dolomite is the main mineral phase of the matrix. Clays are scattered around the dolomite grains of matrix where quartz is present in grains of around 20 µm. Quartz proportion can vary from 3 volume % to 15 volume % in zones where it is organized in thin stratified beds. The pyrite is spread in massive anhedral crystals of 10 µm in very low concentrations (from 0.1 to 1 volume %). Its distribution is not controlled by stratigraphy.

3.1.2. Fracture mineralogy:

The bulk chemical composition (table 2) shows that the fractures are mainly composed of calcium, magnesium and carbon under CO_2-form. They contain neither silica nor sulfur or phosphorus. The aluminum fraction can be attributed to the clay contamination due to the separation process between the fractures and the matrix. We can notice the presence of iron. In the trace elements, strontium is highly represented with 200 ppm whereas barium concentration is low (4 ppm). The XRD shows two main sorts of carbonates in fractures: calcite and dolomite. The composition of the dolomite, determined by SEM analysis, shows a higher Ca / Mg ratio (1.13 ± 0.02) in comparison with the matrix dolomite (table 3). Fe-content permits to discriminate two types: a “pure” dolomite and a ferrous saddle dolomite with a maximal content of 0.3 at% of Fe (table 3). These two types are clearly evidenced in backscattered electron micrography (figure 3C) and X ray mappings (figure 3E). Mineralogy in fractures is also correlated to cathodoluminescence (figure 3D): calcite, ferrous dolomite and dolomite respectively correspond to yellow, brown, and light red luminescence. The main part of the fractures is filled by the ferrous dolomite. The non-ferrous dolomite is always located between the ferrous dolomite and the calcite or next to the porosity. CL observation on ferrous saddle dolomites in contact with pores shows a continuous gradient of colors from light red to brown, from rim to core (figure 5). Analyses in SEM-WDS confirmed that it is correlated to a sigmoidic evolution of the Fe-content from 0 in the vicinity of the pore to 0.3 at% in the mineral core (figure 5), whereas Ca/Mg ratio is quite constant.

The calcite developed in the microfractures or on wallrocks of the macrofractures, crosscutting the dolomites as can be seen on figure 3. Some massive pyrite is observed in several microfractures. However, this mineral remains anecdotic.

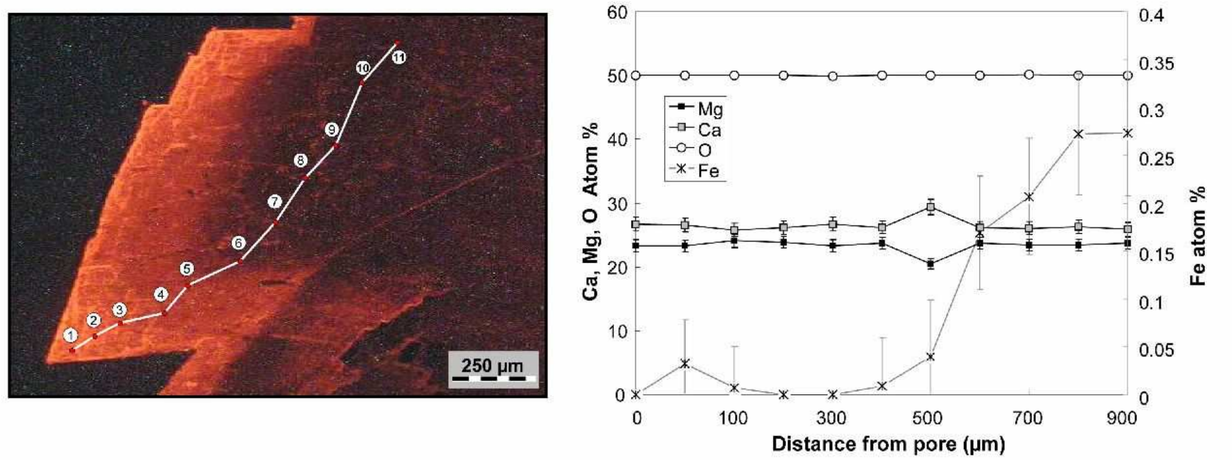

Figure 5 : left: CL image of saddle dolomite in contact with pore in fracture from “Dolomie de Mano”, with locations of WDS analyses on EPMA. Right: Ca, Mg and Fe concentration evolution with distance from pore. The evolution of the Fe-content follows a sigmoïdal increase when we move far from porosity.

The fluid inclusions are organized in several types, depending on the host mineral (figure 6), which is here calcite (inclusions c) or dolomite (inclusions d), the number and types of phases, and their spatial organization (isolated: inclusions *i* or in planes: inclusions *p*). They are vapor single-phase (inclusions V) or liquid-vapor two-phase (inclusions LV). The vapor inclusions are only present in the calcite and do not exceed 10 µm in size, whereas the LV inclusions are displayed in the two types of minerals and are sized from 3 µm to 20 µm. Most of inclusions V and LV have a negative crystal shape. None of them contain any oil droplet because they show no fluorescence under UV light.

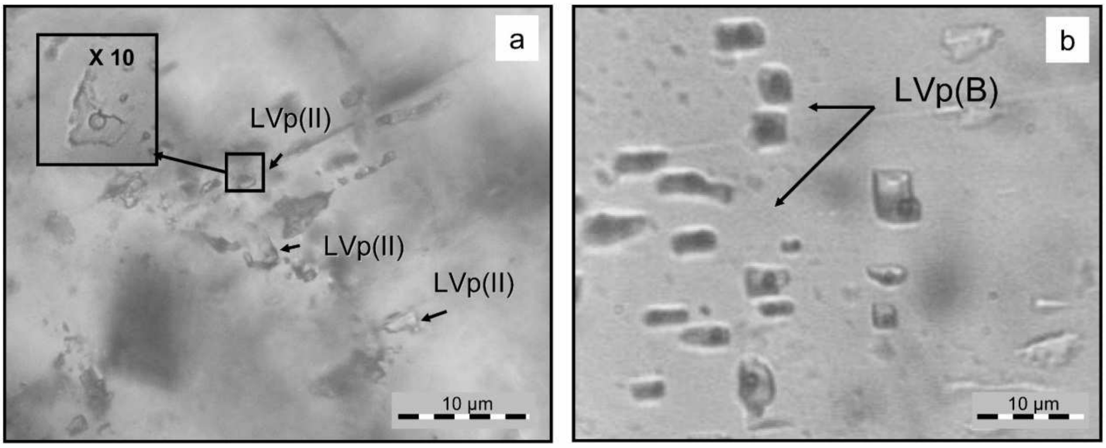

Figure 6 : Photomicrographs of fluid inclusions contained in the fractures of the “Dolomie de Mano” (a) and the Upper Cretaceous breccia (b). (LV) Two-phase liquid-vapor inclusions, in planes (p), in dolomite (II) and in the second type of calcite (2).

The homogenization temperatures of the LV inclusions are spread in two populations: 145 - 152°C and 160 - 166°C (figure 7). The first population includes the whole calcite inclusions and a part of the dolomite inclusions. The second population corresponds to the main part of the dolomite inclusions. The homogenization temperatures in the V inclusions of the calcite were difficult to obtain because of the size of the inclusions and the darkness of the crystals. They were measured by optical microthermometry on rare inclusions and confirmed by Raman microscopy. The inclusions showed a transition with a growing non-wetting phase when the increasing temperature approached the homogenization temperature. The Raman analyses confirmed that the growing phase corresponds to vapor by presenting a peak with a higher Raman shift than the wetting phase (respectively 2912.5 cm^{-1} for the growing non-wetting phase against 2911.3 cm^{-1} for the wetting phase). Only one optical measurement of Th at -56.4°C has been acquired. However, the other V fluid inclusions presented a similar behavior in similar temperature range (between -60°C and -40°C) under the Raman microprobe.

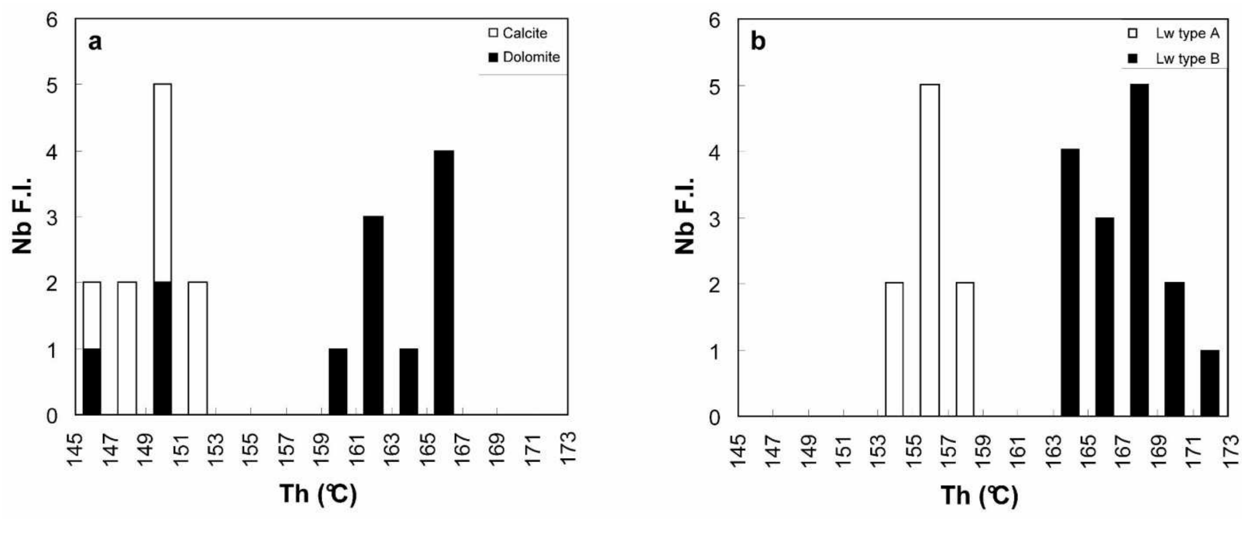

Figure 7 : Histograms of homogenization temperatures of the two-phase fluid inclusions (Lw) from the "Dolomie de Mano" (a) and the Upper Cretaceous Breccia (b). The two formations show dual ranges of temperatures.

Due to bad transparency and double refringence, melting temperature measurement of two-phase inclusions was not possible to acquire by microthermometry. By consequence, salinity expressed in the form of NaCl content was measured using Raman technique. Salinities are all included between 0.2 and 1 molal (table 5). The inclusions in calcite are included in the interval 0.2-0.8 molal whereas the dolomite inclusions have higher salinities between 0.5 and 1 molal.

Raman analyses of the gas phase of LV inclusions at room temperature show the presence of methane, carbon dioxide and ethane (table 6). While the methane represents the majority of the gas composition in each inclusion, the ethane concentration does not exceed 1.5 mol% whatever the inclusion type is. However, the proportions can vary in function of the type of inclusion. Calcite Lw inclusions are methane-rich and CO_2-poor with respective proportions over 96% and under 3.5%, and most of dolomite inclusions have a CO_2 proportion over 10% reaching 25% for one inclusion. Raman analysis at room conditions of V inclusion in calcite gives 97.3 mole % of CH_4, 2.2 mole % of C_2H_6 and 0.5 mole % of C_3H_8.

		inclusion type	**Th (°C)**	**Salinity[1] (eq NaCl)**	**mCH_4[2] (molal)**	**Gas composition (mol%)**			
						CO_2	**CH_4**	**C_2H_6**	**C_3H_8**
Mano dolomie	1	LV Calcite	146	0.7	n.m.	n.m.	n.m.	n.m.	0
	2	LV Calcite	148	0.2	0.116	0	100	0	0
	3	LV Calcite	149	n.m.	n.m.	2	96.5	1.5	0
	4	LV Calcite	150	0.5	0.125	3.5	96.5	0	0
	5	LV Calcite	150	0.8	0.132	0	100	0	0
	6	**V Calcite**	**-56.4**	**n.m.**	**n.m.**	**0**	**97.3**	**2.2**	**0.5**
	7	LV Dolomite	166	0.6	0.077	24	75	1	0
	8	LV Dolomite	150	0.5	0.073	0	100	0	0
	9	LV Dolomite	150	0.5	n.m.	n.m.	n.m.	n.m.	0
	10	LV Dolomite	160	1	n.m.	n.m.	n.m.	n.m.	0
	11	LV Dolomite	161	0.5	0.086	15 ± 5	85 ± 5	0	0
	12	LV Dolomite	162	1	n.m.	n.m.	n.m.	n.m.	0
	13	LV Dolomite	165	0.6	0.081	14.5	84	1.5	0
Camp. Flysch	1	LVC2	155	n.m.	0.27	0	100	0	0
	2	LVC2	155	2.9	0.27	0	100	0	0
	3	LVC2	156	2.8	0.32	0	100	0	0
	4	LVC2	156	2.6	0.31	n.m.	n.m.	n.m.	0
	5	LVC2	157	2.9	0.3	0	100	0	0
	6	LVC1	163	1.5	0.25	3	97	0	0
	7	LVC1	163	n.m.	0.33	n.m.	n.m.	n.m.	0
	8	LVC1	164	2.2	0.31	n.m.	n.m.	n.m.	0
	9	LVC1	164	2	0.34	0	100	0	0
	10	LVC1	167	2	0.3	0	100	0	0
	11	LVC1	167	2.1	0.36	0	100	0	0
	12	LVC1	167	2.5	0.21	0	100	0	0
	13	LVC1	168	1.7	0.24	2.3	97.7	0	0
	14	LVC1	168	2	0.34	2	98	0	0
	15	LVC1	169	1.9	0.16	3	97	0	0
	16	LVC1	205	2.5	0.27	0	100	0	0
	17	**VC1**	**-82**	**n.m.**	**n.m.**	**2.4**	**97.6**	**0**	**0**
	18	**VC1**	**-82**	**n.m.**	**n.m.**	**2.1**	**97.9**	**0**	**0**

Table 5 : Main parameters measured in the fluid inclusions of the “Dolomie de Mano” and the Upper Cretaceous breccia. (1) measured by Raman microprobe at room temperature, (2) molality of aqueous methane measured by Raman microprobe at homogenization temperature, n.m.: not measured.

Mineral	Mano Dolomie Fracture	Mano Dolomie Matrix	Campanian Flysch
Pyrite	0.0	0.5	0.3
Ankerite	0.0	0.0	4.6
Fe Dolomite	93.1	0.0	0.0
Non-Fe Dolomite	2.0	92.2	2.1
Calcite	4.9	0.1	63.2
Quartz	0.0	3.0	10.5
Illite	0.0	3.4	8.3
Interstratified	0.0	0.8	6.5
Chlorites	0.0	0.0	4.5

Table 6 : Mean composition of the “Dolomie de Mano” and the Campanian Flysch. Results calculated from the bulk chemical analysis and the composition of each mineral. Fractions are expressed in %mol.

The analysis of dissolved gases in LV inclusions were performed with the Raman microprobe at homogenisation temperature. For each inclusion, the only detectable gas is methane. The CH_4 concentration varies with inclusion types: type LVI inclusions in calcite have methane molalities from 0.11 to 0.13, whereas type LVII inclusions in dolomite shows weaker molalities around 0.08 (table 5). No relation between molality, salinity and homogenization temperature have been evidenced for LV inclusions in the fractures of “Dolomie de Mano”.

3.3. Upper Cretaceous breccia (RSE 2, 5293 m)

In RSE 2, the Upper Cretaceous Breccia is buried between 5192 m and 5302 m in depth. It is constituted by polygenic elements from Lower Cretaceous to Triassic formations. Fracturing affects the base of the Breccia and is mainly filled by carbonate minerals (figure 8).

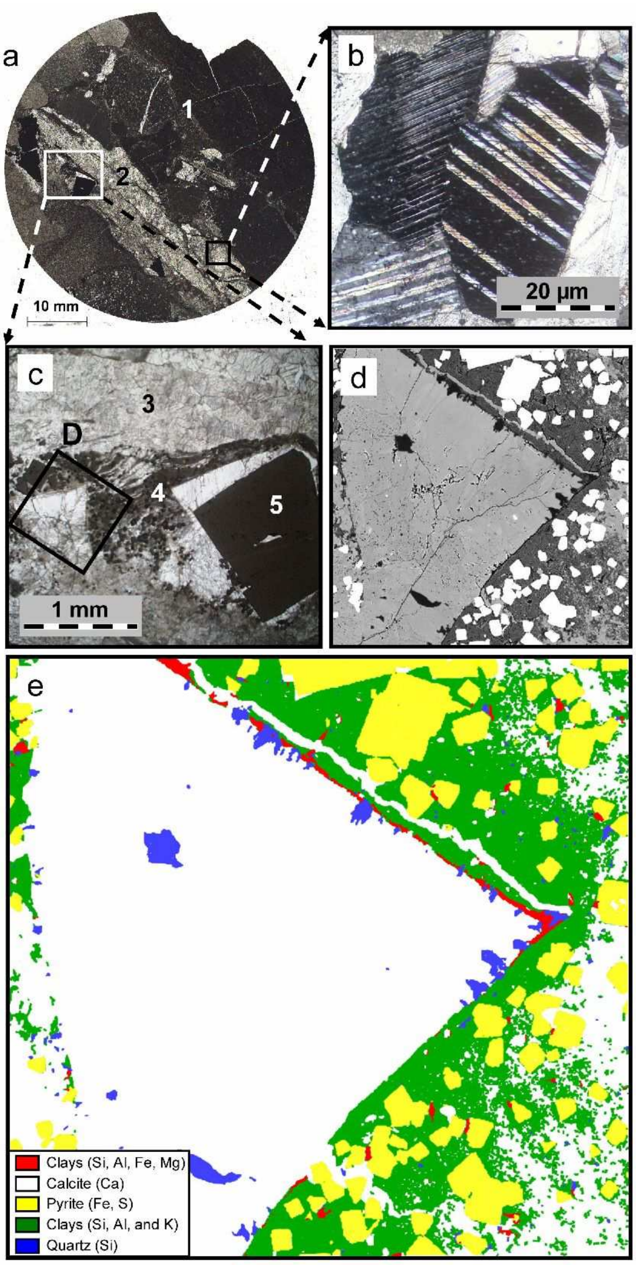

Figure 8 : Mineralogical assemblages of the Upper Cretaceous breccia. (a) optical picture of the thin section showing a lens and the different clasts, (b) fracture calcite seen in plane-polarized light showing pseudomacles, (c) zoom in lens showing calcite, clays and sulfides, (d) backscattered scanning electron micrograph in the fracture, (e) colored micrograph edited from a X-ray mapping on zone D. (1) clast of the breccia, (2) lens, (3) calcite, (4) clays, (5) pyrite.

3.3.1. Petrography of the Matrix of the breccia

The size of the clasts are highly variable (from millimeter to centimeter as can be seen on figure 8). A trend in vertical succession of clasts starts by Lons limestone on the bottom to “Dolomie de Meillon” around 5260 m and “Dolomie de Mano” around 5280 m (Grimaldi, 1988). The mineral composition of these clasts is marked by a carbonate matrix (calcite or dolomite) including minor fractions of clays, quartz and pyrite in variable proportions. Clasts are affected by fracturing prior to deposition. A calcareous shale fills the spaces between the clasts. It is dolomitized in the base of the formation (between 5280 m and 5302 m). It shows lenses filled by euhedral diagenetic minerals.

3.3.2. Petrography of the lenses

The lenses have been filled after the rock deposition. Calcite is the dominant filling material in the form of two different facies: wall rock tiny calcites and large calcites in the center part of the lens presenting pseudomacles characteristic of a late diagenetic precipitation (figure 8B). The wall rock calcites form a 30 µm fringe at the contact of the breccia clasts. We can notice the presence of other types of minerals such as sulfides and clays. Sulfides are represented by euhedral crystals of pyrite sometimes in close association with galena. Clays occur around euhedral calcite crystals as it can be seen on figure 8C. The black frame in this photomicrography was analyzed by X-ray mapping. The results are exposed on figure 8E.

A succession of three mineral assemblages is observed from the edge of the calcite crystals. First, an extensive layer of silicon corresponding to quartz precipitated perpendicular to the edges of the calcite. Second, a Mg-clay layer (Mg-smectite or chlorite) is marked by the presence of silicon, aluminum, iron and magnesium. Third, a clay-pyrite association marked by the presence of two element associations: silicon-aluminum-potassium-magnesium and iron-sulfur. The presence of high concentration of potassium is typical of illites or smectites. Pyrites are embedded in K-clays in the form of numerous euhedral cubic crystals. Pyrite can also be found inside the euhedral calcites (figure 8C).

Calcite minerals found in the lenses contain some fluid inclusions which were studied by microthermometry and Raman miscrospectrometry. They present specific organization dependant on the type of calcite. The inclusions in the wall rock calcite are all isolated whereas some inclusions in the large calcites are isolated and others are organized in planes. The majority of inclusions are two-phase liquid-vapor inclusions (inclusions LV). However, some one-phase inclusions (inclusions V) are observed in wall rock calcite at room conditions.

The homogenization temperatures of the LV inclusions are distributed in two populations: 153-157°C (inclusions LVC2) and 163-172°C (inclusions LVC1) with two modes respectively centered at 156°C and 166°C (figure 7). Most of inclusions in planes show T_h located in the high temperature interval. The L+V=>V phase transition in the V inclusion was observed at -82°C and is confirmed by Raman microthermometry using the same method as for the vapor inclusions of "Dolomie de Mano".

The aqueous inclusions have salinities deduced from Raman varying from 1 to 3 molal. Inclusions with the lowest T_h have the highest salinities around 3 molal of equivalent NaCl. There is no clear evidence of correlation between T_h and salinity for inclusions with the highest T_h.

The composition of gases measured at room conditions by Raman into the gas phase is similar for inclusions V and LV with the highest T_h (table 5). These two types of fluid inclusions were considered as cogenetic and then called "inclusions C1". The methane content exceeds 97 mole%, the rest corresponding to CO_2. The LV inclusions with the lowest T_h do not contain CO_2.

Methane is the only measured dissolved gas at homogenization temperature for LV inclusions. The molalities are spread from 0.15 to 0.35 molal (Table 5). There are no clear relations between CH_4 content, T_h and salinities.

3.2. Campanian Flysch (RSE 1, -4580 m)

The Campanian flysch is a clayey carbonate with thin layers of quartz and pitches of organic matter (figure 9). No fractures or mineralized lenses have been observed on the drillcores from RSE-1 and RSE-2 wells.

According to the bulk chemical analysis (table 2), the rock is mainly composed of calcium, carbon as CO_2 and Silica. These three elements represent 85% of the weight of the rock. Aluminum, iron, magnesium and potassium take part for 11 wt% of the rock. Titanium, sodium, phosphorus and manganese are detected as trace elements. XRD patterns confirm that the rock mainly contains carbonates, quartz and clays. Electron Microprobe analysis reveals different carbonate compositions (table 3): a Ca-Mg siderite of constant formula $Fe_{0.73}Ca_{0.13}Mg_{0.13}Mn_{0.01}CO_3$ often surrounding a dolomite core of formula $Ca_{1.04}Mg_{0.94}Fe_{0.01}(CO_3)_2$ (figure 9C) with a constant Ca/Mg ratio but an Fe-content varying from 0 to 0.6 mol%. Sulfides are always present in the form of framboïdal pyrites (figure 9), indicators of an early bacterial activity in the formation. Two main populations of clays have been recognized: an illite to smectite population covering a wide interlayer charge range, and a smectite-IS to chlorite trend with various Si content (figure 4). These results calculated from TEM analysis by the Harvey’s method (Harvey, 1943) based on 11 oxygens and Fe^{3+} were confirmed by the XRD analyses. We can notice that chlorites and interstratified chlorites/smectite or chlorites/IS are linked by a constant Al-content fixed at 2.7 (for a calculation based on 14 oxygens and Fe^{2+} for the chlorites and on 11 oxygens and Fe^{3+} for the other clays). The trend can be explained by a mix between a chlorite and a smectite or an IS with various proportions of each pole, with a chlorite proportion varying from 85 to 40%.

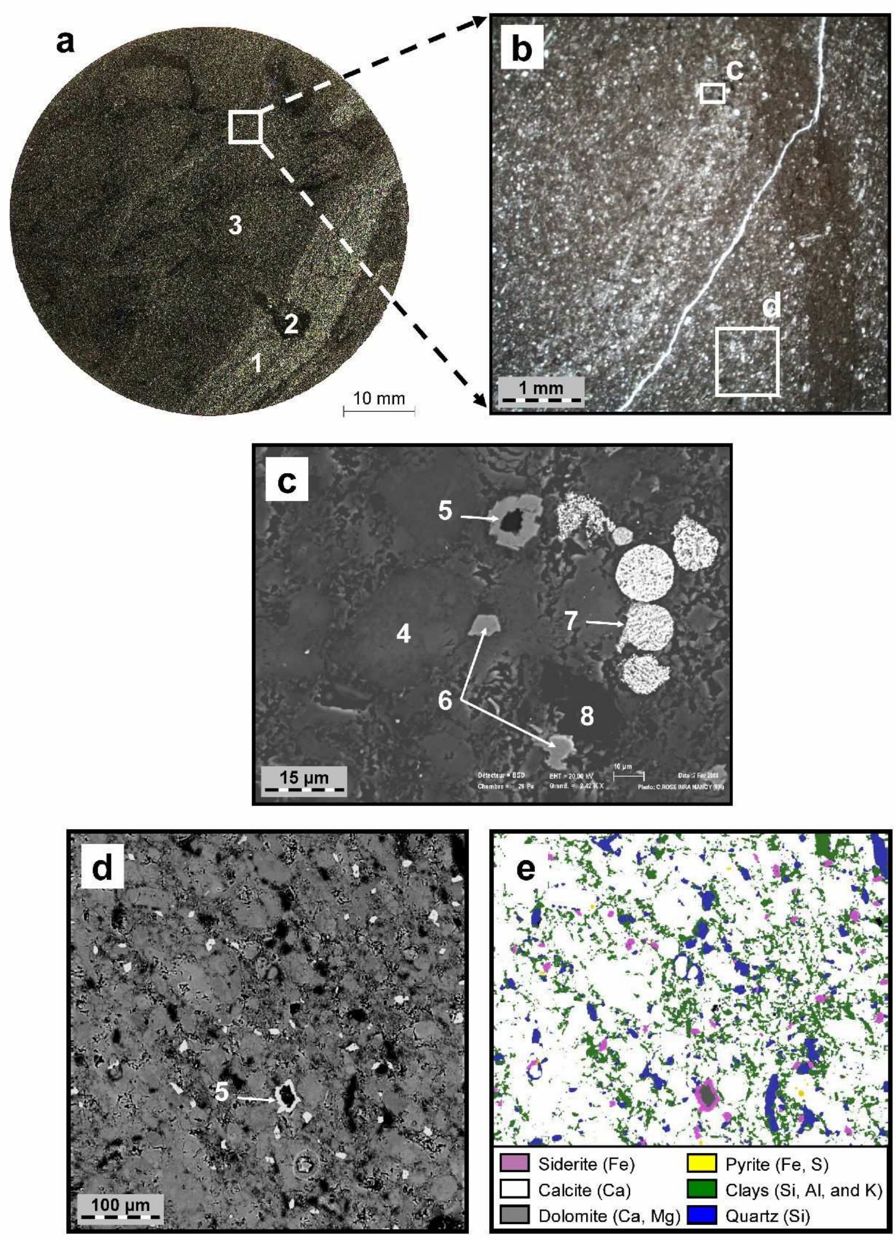

Figure 9 : Mineralogical assemblage of the Campanian Flysch. (a) and (b) pictures from optical microscopy showing the global organization of the rock, (c) and (d) backscattered scanning electron image of the rock, (e) colored image edited from a X-ray mapping on zone (d). (1) quartz zone, (2) clay zone, (3) calcite zone, (4) clayey calcite, (5) carbonate with dolomite in the center coated by a Ca-Mg-siderite rim, (6) Ca-Mg-siderite, (7) framboidal pyrite, (8) organic matter. Crack of figure b is due to thin section making.

The mineralogical formulae of the clay poles were calculated by extrapolating the best-fitting correlation line of the chlorite-smectite/IS points (see figure 4). We obtained the following formulae: $(Si_{2.56}\ Al_{1.3})^{IV}(Al_{1.4}\ Fe_{3.56}\ Mg_{1.27})^{VI}\ O_{12}(OH)_4$ for the chlorite and $(Si_{3.55}\ Al_{0.45})^{IV}(Al_{1.12}\ Fe_{0.69}\ Mg_{0.28})^{VI}(K_{0.4}Ca_{0.03})O_{10}(OH)_2$ for the smectite or the IS. The smectite pole should correspond to a low-charged beidellite. The mean formula for illite pole is $(Si_{3.42} Al_{0.58})^{IV}(Al_{1.6}Fe_{0.2}Mg_{0.2})^{VI}(K_{0.7}Ca_{0.05})O_{10}(OH)_2$.

Quartz, siderite and zoned dolomite-siderite carbonates are embedded in clays. Proportions of quartz and clays can vary in the rock as a function of the stratigraphy, which shows quartz-rich layers and more clayey levels (figure 9-A). However calcite remains the main mineral in these zones.

4. Discussion

The objective of this work is to characterize the nature of minerals and included fluids in Rousse reservoir and caprock. The discussion will be focused on the reconstruction of ancient fluid-rock interactions taking into account the geodynamical context of the Aquitaine basin.

The mean mineralogical composition of the rock is established from the bulk chemical analysis of the rock (table 2). The calculation is based on a matrix regression between the mean composition of each mineral type and the bulk chemical composition.

Concerning the “Dolomie de Mano”, two different facies (fractures and matrix) were considered. The matrix minerals taken into account are the following: dolomite $Ca_{1.02}Mg_{0.98}(CO_3)_2$, calcite ($CaCO_3$), quartz SiO_2, pyrite FeS_2, illite $Si_{3.43}Al_{2.26}Fe_{0.06}Mg_{0.24}K_{0.71}Na_{0.07}Ca_{0.02}$, and interstratified illite/smectite clays. The fracture minerals are the following: calcite $CaCO_3$, ferrous dolomite $Ca_{1.056}Mg_{0.934}Fe_{0.013}(CO_3)_2$ and non-Fe dolomite $Ca_{1.06}Mg_{0.94}(CO_3)_2$. The smectite pole was estimated to be near a high-charged beidellite. The results are displayed in the table 6. The dolomite represents more than 90 mol % of the rock (matrix and fractures). It corresponds to a late dolomitization of the formation during its burial (Grimaldi, 1988). Dolomite is mainly ferrous in the fracture (the non-Fe dolomite represents only 5 mol%) and non ferrous in the matrix. Clays (4 mol%) and quartz (3 mol%) are the secondary minerals of the matrix. Pyrite is absent in the fractures and very low concentrated in the matrix.

Concerning the Campanian Flysch, the theoretical minerals used for the calculation are the following: pyrite FeS_2, siderite $Fe_{0.73}Ca_{0.13}Mg_{0.13}Mn_{0.01}CO_3$, dolomite $Ca_{1.04}Mg_{0.94}Fe_{0.01}(CO_3)_2$, calcite $CaCO_3$, Quartz SiO_2, illite $Si_{3.42}Al_{2.18}Fe_{0.2}Mg_{0.2}K_{0.7}Ca_{0.05}$, chlorite $Si_{2.56}$ $Al2_{.7}Fe_{3.56}$ $Mg_{1.27}$ and smectite $Si_{3.55}$ $Al_{1.57}Fe_{0.69}Mg_{0.28}K_{0.4}Ca_{0.03}$. The chlorite/smectite mixed-layer formula is based on an equal mix between the chlorite and the smectite formulae. The results confirm the observations made previously (table 6) and allow to quantify a calcite proportion around 60 mol% of the rock. Siderite and dolomite represents 4 mol% and 1.5 mol% respectively. The clay minerals represent almost 20 mol% of the mineralogical phases. The majority corresponds to illite (8 mol%), but we also find chlorites (4 mol%) and some interstratified clays (6 mol%). The quartz content is around 10 mol%. The pyrite is rare as for the "Dolomie de Mano" and do not exceed 1 mol%. The organic matter is not included in the composition.

In the two formations, some uncertainties remain on the respective proportion of each type of clay, especially concerning the interstratified fraction and the presence of a possible chlorite fraction in the matrix of the reservoir. The frontier between illite and interstratified clays is however not a sharp limit because of the high variations of the clay compositions in the Campanian Flysch and the unknown smectite pole in the reservoir.

Diagenesis of the "Dolomie de Mano" is dominated by fluids with high Mg/Ca ratio responsible for late dolomitization and fracture filling. Then, chemical and/or PT changes led to calcite precipitation during late fracturing event. Cathodoluminescence observations confirm the calcite was the last mineral to precipitate because it crosscuts the dolomite in fractures. This fluid circulation was probably responsible for iron weathering of ferrous dolomite, by high redox conditions. These high redox conditions have not affected the caprock (Campanian flysch), where Fe^{2+} is shared by siderite and pyrite. Siderite precipitated from dolomite cores, implying probably an iron enrichment during early diagenesis.

Only two available mineral associations have conducted to fluid inclusion analysis: dolomite and calcite in fractures of the "Dolomie de Mano" and the calcite in lenses of the Upper Cretaceous breccia. They represent two main events of fluid migration in the geological system of the Rousse gas field:

1) The fractures of "Dolomie de Mano" show two types of fluids with respect to the trapping mineral: i) the fluid inclusions LVC (figure 10a) are trapped in the wall rock calcite. It shows quite constant parameters with a Th between 145°C and 152°C, salinity varying between 0.2 and 0.8 molal of eq. NaCl, are CH_4-rich and CO_2-poor. Inclusions of type VC have a similar composition than the gas phase of LVC inclusions at room condition. The presence of butane in VC inclusions and its absence in LVC inclusions can be explained by a higher Raman detection limit in VC inclusions than in LVC where the gas phase is too small. The presence

of VC inclusions demonstrate that a gas phase migrated in fracture at the time of calcite precipitation. This gas phase is probably equivalent in composition to the dissolved gases in LVC inclusions and the two inclusions types could be trapped together in same conditions. The calculated isochores for LVC and VC inclusions show an intersection on the isopleth at a pressure between 170 and 190 bar and a temperature of 145°C. Such conditions imply that the LVC inclusions are saturated with respect to CH_4 and probably are co-genetic to VC inclusions. ii) The fluid inclusions LVD (figure 10b) are trapped in dolomite. Their homogenization temperatures vary from 145 to 167°C, their salinities lie between 0.5 and 1 molal eq NaCl. At ambient temperature, the gas phase is CO_2-rich (10 to 25 mol%). At Th, the methane was the only gas detected into the water, at 0.08 M. All these data confirms that fluid inclusions in dolomite are different in nature than fluid inclusions in calcite. The reconstructed domain for the isopleths is located at lower pressure than the isopleth domain for LVC inclusions. The isochores start at higher temperature. As only one population of inclusions has been studied, no accurate PT conditions can be proposed. Trapping conditions of LVD inclusions are somewhere on the isochores.

Several hypotheses can be proposed from the PVTX reconstruction concerning fluid migration in fracture in the “Dolomie de Mano” at Rousse. Fluids are ancient fluids with composition far from the composition of the present day gas field (no gas condensate, no H_2S). It can be proposed that at 105 Ma CH_4- and CO_2-rich fluids accompanied the fracturing episode of the Mano Dolostone, leading to the precipitation of dolomite and consuming CO_2 in the same time, at around 160°C in hydrostatic regime (200 bar). The pressure and temperature dropped down (145°C-180 bar), and the residual fluid led to the precipitation of the wall rock calcite in hydrostatic conditions, corresponding to a sedimentary stack of around 1,800 m. If the fluid is considered to be in thermal equilibrium with the host rocks, the temperature of 145°C at this depth gives a geothermal gradient around 75°C per km. Such a gradient is in agreement with gradients measured during extensional phase like a passive rifting with high geothermal activity. The corresponding stack of sediments agrees with the mean thickness of the Lower Cretaceous sediments in the Aquitaine basin before the Pyrenean uplift (Bourrouilh et al., 1995). Thus, previous observations (M.H. Grimaldi, 1988) on the regional rocks show that fragments of the Mano dolostone containing fractures are present in the Upper Cretaceous Breccia. The fracturing episode must have therefore been prior to the Upper Cretaceous. In respect with M.H. Grimaldi, 1988, fracturing should be the consequence of the beginning of the uplift due to the Pyrenean compression at the transition between Lower and Upper Cretaceous near -100 Ma. No other modifications were observed in the Mano Dolostone. It seems therefore that the rock underwent no other major transformation during the earlier geological ages.

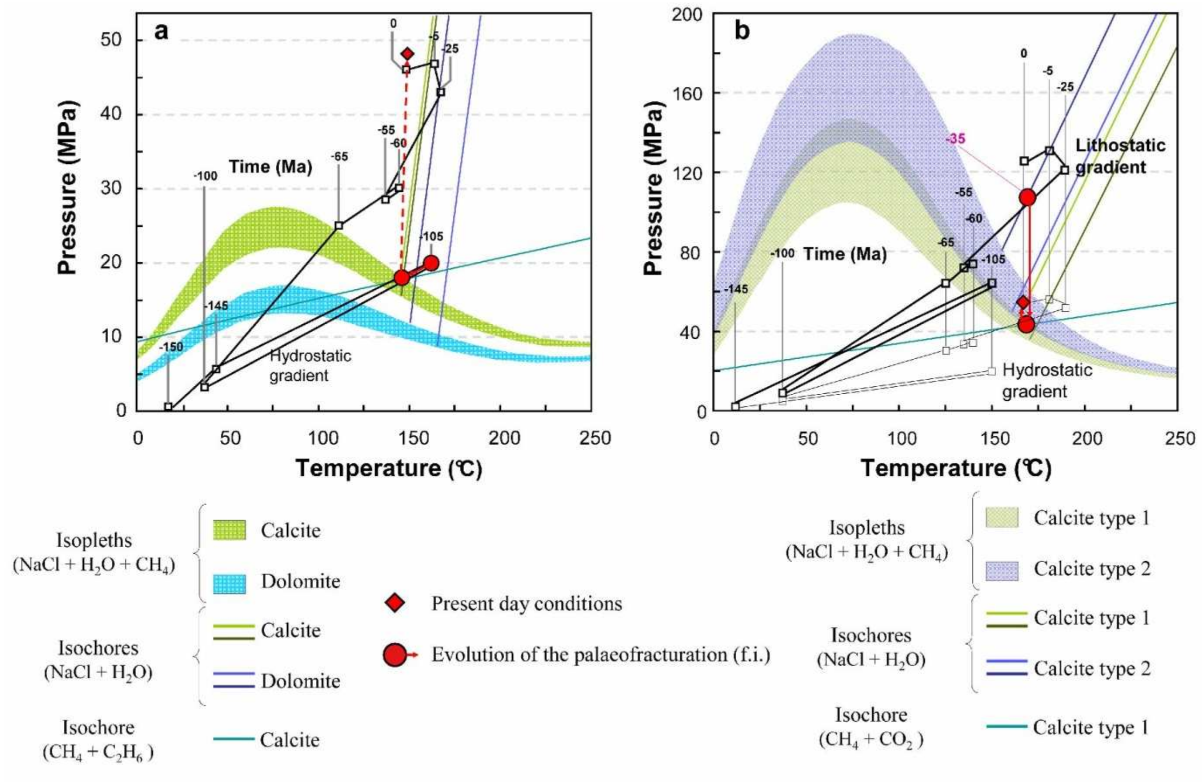

Figure 10 : P-T diagram for the “Dolomie de Mano” (a) and the Upper Cretaceous breccia (b) showing the evolution of the geothermic gradients with time and the isopleths and isochors for the studied fluid inclusions.

2) The Upper Cretaceous breccia also contains two types of fluid inclusions in the calcite of lenses. They are discriminated by their homogenization temperatures: i) The LVC1 fluid inclusions have T_h in the range 163-173°C, and a salinity between 1.5 and 2.5 molal eq. NaCl. At room temperature gas phase is mainly composed by methane and it contains rarely CO_2 (less than 3%). At T_h, the molalities of methane are spread from 0.24 to 0.36 molal. Vapor inclusions contain CO_2 in same proportion than inclusions LVC1. It is a good argument to consider vapor inclusions (VC1) and LVC1 are co-genetic. ii) the second fluid inclusion population (LVC2) corresponds to the T_h range 153-159°C, with higher salinity between 2.5 and 3 molal eq. NaCl. At room temperature no other gases than methane are detected. At T_h the gas composition is similar than for type LVC1.

The PT reconstruction is proposed figure 10b. The two fluid populations show high-pressure isopleths. The LVC1 inclusions have isochores/isopleths intersections in the range 164°C/43

MPa and 172°C/38 MPa. The isochore of the vapor inclusions VC1 have an isochore crossing this domain of intersection. These data confirm that the LVC1 and VC1 fluid inclusions were trapped together in the P-T range of isochores/isopleths intersection. LVC1 inclusions are saturated with respect to CH_4. These conditions of trapping are near a hydrostatic gradient of 30°C/km and correspond to a burial of around 4100 m. The LVC2 inclusions have isochores/isopleths intersections in the range 154°C-80 MPa and 158°C-47 MPa. In absence of associated gas inclusions the trapping conditions cannot be accurately determined. They are located somewhere onto the isochores from the isochores/isopleths intersections to the isochores/lithostatic gradient intersections at 105 Mpa for a temperature range of 170-190°C. The trapping pressure of the LVC2 inclusions is higher than the trapping pressure of LVC1 inclusions. It corresponds to an overpressure regime. Trapping temperatures for LVC1 and LVC2 inclusions could be similar around 170/175°C.

4.2.4. Elements of reconstruction for the ancient fluid-rock interactions in Rousse gas field.

The combined petrographic and inclusions studies can lead to the establishment of the following scenario:

The dolomitization of the carbonate rocks was previously described M.H. Grimaldi, 1988. The episodes are resumed on the figure 11 for the “Dolomie de Mano” and the Upper Cretaceous Breccia. Pyrite of the “Dolomie de Mano” is found in massive anhedral crystals dispersed in the matrix, between the microcrystals of dolomite. Its formation is therefore synchronous to the dolomitization of the rock and could have been induced by thermal sulfato-reduction by oxidation of the methane during the late stage of dolomitization or by extraction of the sulphur compounds in the local organic matter (Worden et al., 2003). Pyritization continued during the fracturing stage because some pyrite was observed in several microfractures in association with ferrous dolomite. After the consolidation of the “Dolomie de Mano” an important fracturing event has been detected. Its anteriority to Upper Cretaceous breccia and the fluid inclusion analysis led us to conclude to one episode of fracturing with fracture filling around -105 Ma at a depth of 2,000 m, with a thermal gradient of 75°C/km. Such high geothermal gradient is in good accordance with the rifting episode in the Aquitaine basin (Biteau et al., 2006, BRGM, 2006) lying from -150 to -100 Ma. Such fluid episode is of the same age than the HT/LP metamorphism paroxysm detected in Pyrenees near 100 Ma. Dolomite precipitates into the fracture from a gas-rich fluid with high content of CH_4 and CO_2 and no evidence of H_2S. An intense erosion episode starts and the pressure and temperature decrease, following the evolution of the hydrostatic gradient. The PT conditions become favorable for fluid demixion. Re-opening of the ancient fractures is observed. The wall rock calcite precipitates, trapping both two-phase fluid and vapor inclusions. Ferrous dolomite loses iron probably by ingress of oxidizing fluids. Fluid is always gas-rich, hydrocarbons are dominant with more than 97 mole% of CH_4. Gas generation should come from local source rocks at shallow depth, the organic matter having reached oil window thanks to the high thermal gradient. Fluids from this fracturing period show salinities similar to sea-water in good agreement with shallow depth deposits in rifting context. In the following geological ages, the "Dolomie de Mano" will never register other fracturing event.

The fluid inclusions trapped in euhedral minerals in lenses. of the Upper Cretaceous breccia gives an age deduced from fluid inclusion study around -35 Ma, much more later than for the "Dolomie de Mano". This period corresponds to the paroxysmal phase of the Pyrenean compression and the play of the BC and BCS faults at the origin of the Pau anticline (figure 1). Breccia could act as a decollement developed under more than 4,000 m of sediments. The creation of the lenses network induces the precipitation of a complex paragenesis with calcite, pyrite, quartz and clays. Fluid inclusions recorded a pressure drop that cannot be quantified, leading to the fluid demixion at 40 MPa. The salinity reaches 150 g/l of NaCl that is in good accordance with the presence of brines from deep origin. Gas composition is CH4-dominated very different from the present day gas accumulation. This episode is the last visible diagenetic episode involving fluid migration in fractures.

The Campanian Flysch was only partially dolomitized during the same period as the Upper Cretaceous Breccia but remains mainly calcitic. It contains framboïdal pyrites witnessing a sulfato-reduction phenomenon by a bacterial activity (Machel et al., 1995). This type of pyrite is formed during the first or second stages of dolomitization, when the temperature do not excess 90°C, then during the early ages of the burial story of the rock. No trace of a deeper sulphates activity was observed. The pyrite remained stable in the rocks until present, which means that the mineral is in thermodynamical equilibrium in the formations. Reduced conditions were preserved. Some evidences of diagenesis are observed in the flysch sediments (siderite precipitation) but cannot be dated. The fracturing and diagenetic history of the sedimentary pile is summarized in the figure 11.

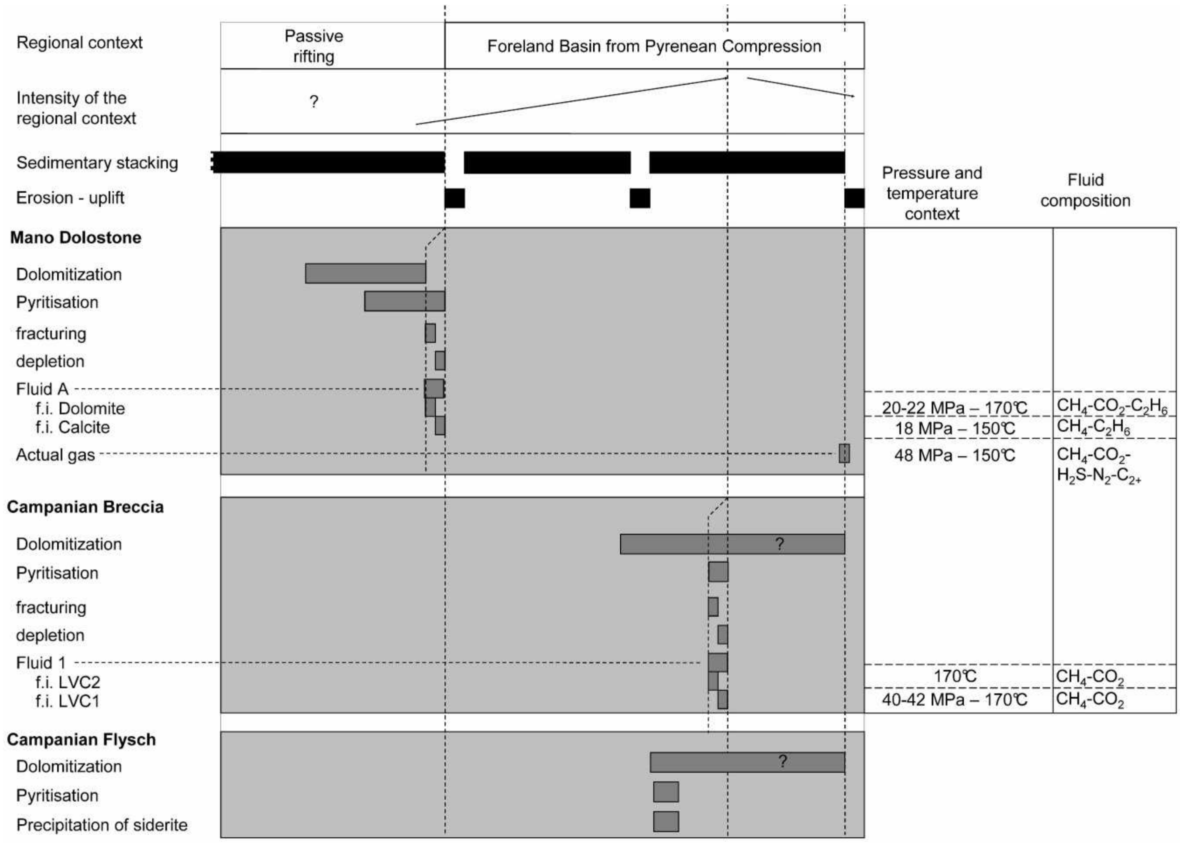

Figure 11 : Geological story of the formations composing the Rousse gas reservoir.

5.Conclusion

This work gives new arguments for the reconstruction of the geological history of the Rousse gas field. It permitted in a first step to precise the complete mineralogy of each formation composing the field and in a second step to characterize and date the fracturing and associated fluids that percolated through the rocks. The “Dolomie de Mano” corresponding to the reservoir rock is mainly composed of dolomite but also quartz, illite, interstratified clays illite/smectite and pyrite. It is crosscut by fractures created during the Jurassic rifting stage by at least two successive fluids responsible for dolomite then wall rock calcite precipitation. The Upper Cretaceous Breccia makes the transition between the reservoir rock and the caprock. It is constituted by rock fragments coming from several regional formations, especially the fractured “Dolomie de Mano”. Fluid circulations are dated of the Pyrenean compression stage and are responsible for calcite, quartz, clay minerals and sulfides precipitation. The Campanian Flysch representing the caprock consists mainly of calcite and quartz but also Ca-Mg-siderite and clays represented by illites, interstratified illite/smectite and

Chlorite/smectite. Except for the caprock, the formations composing the field have ever known fluids with CO_2, leading to the formation of fracture carbonates. Three main episodes of gas invasion are detected, at around -105 Ma, -35 Ma and last episode responsible for the present day gas field composition. These results confirm that the gas field was invaded by gas during a long period of time limiting water presence to residual saturation. Water salinity in the fluid inclusions from fractures of “Dolomie de Mano” shows salinity near sea-water, whereas salinity of the fluid inclusions from Upper Cretaceous breccia is high.
These results help us to build a geological model of the Rousse gas field and gives arguments in favor to the limited geochemical risk of the injection of CO_2 in the “Dolomie de Mano” reservoir. On another hand this work contributes to the better understanding of the complex geodynamic history of the foreland basin in the Aquitaine basin.

Acknowledgments

This work has been supported by the ADEME and TOTAL.

Bibliography

Bakker, R. J., 1999. Adaptation of the Bowers and Helgeson, 1983 equation of state to the H2O-CO2-CH4-N2-NaCl system. Chem. Geol. 154, 225-236.

Bakker RJ, 2001. FLUIDS: new software package to handle microthermometric data and to calculate isochores. XVI ECROFI European Current Research on Fluid Inclusions, Porto 2001, Abstracts (eds. F. Noronha, A. Doria, A. Guedes) Faculdade de Ciencias do Porto, Departamiento de Geologia, Memoria 7, 23-25.

Bakker R.J., 2003. Package FLUIDS 1. Computer programs for analysis of fluid inclusion data and for modelling bulk fluid properties. Chem. Geol. 194, 3-23.

BRGM, ELF-RAP, ESSO-REP, SNPA, 1974. Géologie du bassin d’Aquitaine. Bureau de recherches géologiques et minières. Atlas.

Biteau, J. J., A. Le Marrec, M. Le Vot and J. M. Masset, 2006. The Aquitaine Basin. Petrol. Geosc. 12[3], 247-273.

Bourrouilh, R., J. P. Richert and G. Zolnai, 1995. The north Pyrenean Aquitaine Basin, France: evolution and hydrocarbons. Am. Ass. Petrol. Geol. Bull. 79[6], 831-853.

Carignan, J., 2001. Routine analyses of trace elements in geological samples using flow injection and low pressure on-line liquid chromatography coupled to ICP-MS: A study of geochemical reference materials BR, DR-N, UB-N, AN-G and GH. Geos. News. 25[2-3], 187-198.

De Chevilly, F., G. Colo, G. Henry, A. Nicolai, J. Quoix and E. Winnock, 1969. Meillon-Rousse natural gas field and stratigraphic deep structure of Pau anticline, (le champ de gaz de Meillon-Rousse et la structure profonde de l'anticlinal de Pau) france sud-ouest. I. F. P. et Ann. Comb. Liqu. Rev. 24[5], 564-578.

Duan, Z., N. Møller and J. H. Weare, 2000. Accurate prediction of the thermodynamic properties of fluids in the system H2O-CO2-CH4-N2 up to 2000 K and 100 kbar from a corresponding states/one fluid equation of state. Geochim. Cosmochim. Acta 64[6], 1069-1075.

Dubessy, J., B. Poty and C. Ramboz, 1989. Advances in C-O-H-N-S fluid geochemistry based on micro-Raman spectrometric analysis of fluid inclusions. Euro. J. Mineral. 1[4], 517-534.

Dubessy, J., T. Lhomme, M. C. Boiron and F. Rull, 2002. Determination of chlorinity in aqueous fluids using Raman spectroscopy of the stretching band of water at room temperature: Application to fluid inclusions. Appl. Spectrosc. 56[1], 99-106.

Grimaldi, M. H., 1988. La dolomie tidale du Jurassique terminale des Pyrénées occidentales: sédimentogenèse, diagenèse polyphasée et contexte dynamique. Pau University. Ph.D, 2 vol., 471 p.

Gapillou, C., S. Thibeau, G. Mouronval and M. Lescanne, 2009. Building a geocellular model of the sedimentary column at Rousse CO2 geological storage site (Aquitaine, France) as a tool to evaluate a theorical maximum injection pressure. Ener. Proced. 1[1], 2937-2944.

Guillaume, D., S. Teinturier, J. Dubessy and J. Pironon, 2003. Calibration of methane analysis by Raman spectroscopy in H2O-NaCl-CH4 fluid inclusions. Chem. Geol. 194[1-3], 41-49.

Harvey, C. O., 1943. Some notes on the calculation of molecular formulae for glauconite. Am. Mineral. 28, 541–543.

Kaszuba, J. P., D. R. Janecky and M. G. Snow, 2003. Carbon dioxide reaction processes in a model brine aquifer at 200°C and 200 bars: Implications for geologic sequestration of carbon. Appl. Geochem. 18[7], 1065-1080.

Machel, H. G., H. R. Krouse and R. Sassen, 1995. Products and distinguishing criteria of bacterial and thermochemical sulfate reduction. Appl.Geochem.10[4], 373-389.

Oelkers, E. H. and J. Schott, 2005. Geochemical aspects of CO2 sequestration. Chem. Geol. 217[3-4], 183-186.

Pironon, J., J. O. W. Grimmer, S. Teinturier, D. Guillaume and J. Dubessy, 2003. Dissolved methane in water: Temperature effect on Raman quantification in fluid inclusions. J. Geochem. Explor. 78-79, 111-115.

Roedder, E., 1984. Reviews in Mineralogy, Volume 12: Fluid Inclusions, (Mineralogical Society of America), 11-45.

Worden, R. H., P. C. Smalley and S. A. Barclay, 2003. H2S and diagenetic pyrite in North Sea sandstones: due to TSR or organic sulphur compound cracking? J. Geochem. Explor. 78-79, 487-491.

Xu, T., J. A. Apps, K. Pruess and H. Yamamoto, 2007. Numerical modeling of injection and mineral trapping of CO2 with H2S and SO2 in a sandstone formation. Chem. Geol. 242[3-4], 319-346.

Zhang, Y. G. and J. D. Frantz, 1987. Determination of the homogenization temperatures and densities of supercritical fluids in the system NaC-lKCl-CaCl2-H2O using synthetic fluid inclusions. Chem. Geol. 64[3-4], 335-350.

Geochemical study of the rock reactivity in a geological storage of CO_2: implications of co-injected gases.

Stéphane Renard[1], Jérôme Sterpenich[1], Jacques Pironon[1], Marc Lescanne[2], Aurelien Randi[1]

[1] Nancy-Université, CNRS, CREGU, G2R laboratory, B.P. 70239, F-54506 Vandœuvre-lès-Nancy, France
[2] TOTAL - Cstjf, 64018 Pau Cedex, France

Abstract

This paper is devoted to the experimental reactivity of a reservoir rock submitted to the injection of CO_2 dominant gas mixture in the context of the limitation of the emission of greenhouse gases. The injected gas mixture corresponds to the exhaust fumes of an oxyboiler without desulfurization. It is made of 82 % mol CO_2, 4 % mol SO_2, 4 % mol O_2, 4 % mol N_2 and 6 % mol Ar. In parallel pure CO_2 experiments provide a benchmark. The reservoir is a low porosity dolostone with micrometric to centimetric fractures. The sample, drilled at 4600 m in depth, comes from a reservoir in the south of France. The fracture network represents the main volume available for storage. It is partly filled with dolomite and is separated from the rock matrix by a thin layer of calcite on wall rocks, where the porosity is located. Experimental reactivity of the rock was tested in batch reactors on samples about 2 cm^3 encapsulated with saline water (25 g/l NaCl) and pure CO_2 or the gas mixture to compare the results with the injection of pure CO_2. Chemical analyses of the reacting solution after experiment showed that the mineralogical assemblage after experiment was in equilibrium with the aqueous solution for pure CO_2 experiment. Raman analyses on the gas phase and optical and electronic microscopy showed only partial dissolution of carbonates and oxidation of pyrites only on surface. When injecting the gas mixture, a total dissolution of the calcite and a partial dissolution of the dolomite were observed. This is accompanied by anhydrite and barite precipitation, especially in the zones where calcite was initially present. Similarly, pyrite was completely oxidized in hematite. Powder analyzes of the crushed rock sample showed a partial transformation of the clay minerals of matrix in potassic beidellite for pure CO_2 and solely in vermiculites for gas mixture experiment. As a conclusion, SO_2 results in a drastic acidification of the water, inducing an important reactivity of the carbonates (total dissolution of the calcite and 6% of the dolomite) and a partial transformation of clay minerals

(87% of illite and 100% of smectites) in beidellite-K. Pyrites and aqueous Fe were completely oxidized by O_2 resulting in hematite and Fe^{3+} production. The mineralogical transformations and the consequent volume change in the experimental conditions result in an average loss of 11% of porosity in the fractures and even more in zones where porosity is controlled by calcite in the wall rock.

1.Introduction

Anthropogenic emissions of carbon dioxide have been accumulated in the atmosphere for decades, modifying the atmosphere gas composition. Several options to reduce the CO_2 content in the atmosphere envision CO_2 geological storage. It consists in injecting CO_2 from stationary generators (industries, coal, gas and hydrocarbon power plants) into deep geological reservoirs such as unmineable coal beds, structural traps in deep saline aquifers or depleted oil and gas fields (Holloway, 1997). The latter present several advantages such as the existing infrastructures (wells) and geological knowledge of the site. However, before any industrial size injection, the site should be demonstrated as safe for several centuries. previous studies on the subject, deal with natural analogues (Baines et Worden, 2004; Moore et al., 2005), large-scale pilot sites (e.g. Sleipner – Korbol et Kaddour, 1995; or Lacq in France), experimental studies (e.g. Kazsuba et al., 2003; Pokrovsky et al., 2005; Rosenbauer et al., 2005; Bertier et al., 2006; Sterpenich et al., 2009) or numerical simulations (Gunter et al., 2000; Xu et al, 2004; Gaus et al., 2005, Knauss et al., 2005; Lagneau et al., 2005; Xu et al., 2005; Xu et al., 2006; Zeraï et al., 2006). All those studies considered pure CO_2 injection. However, a complete separation of CO_2 from the other fumes components is not energetically and economically viable. Other gas components are obviously present such as N_2, Ar and O_2 up to a fraction of 5 to 10 %mol or SO_x and NO_x if the desulphurization and denitrogenation is avoided to limit the energy consumption (IEA GHG report, 2005). The implications those components have on the host rocks should be analyzed since studies devoted to their effect are still limited. Experimental simulations only deal with pure SO_2 in the context of sulphur capture by limestones at high temperatures in bed boilers (Lyngfelt et Leckner, 1989; Hansen, 1991; Mattisson et Lyngfelt, 1998) and the reduction of hematite by a CO_2-SO_2 gas in aqueous conditions at 150°C and 300 bar (Palandri et al., 2005). Numerical simulation only examined a geochemical analysis coupling of CO_2, SO_2 and H_2S on a sandstone formation (Xu et al., 2007). Other studies were also conducted on the behaviour of the well materials submitted to co-injected gases such as H_2S in conditions of borehole (Jacquemet et al., 2005).

The present study examines the specific reactivity of potentially co-injected gases such as N_2, Ar, O_2, SOx and NOx. It compares the reactivity of carbonate rocks during injection of pure CO_2 with the reactivity using a gas mixture. The rocks were sampled on cores from a 4600 m deep site in a carbonate reservoir, located in the south of France near Pau. Raman analyses on the gas phase and optical and electronic microscopy on the matrix minerals examine the mineral changes.

2.Apparatus and methods

The experiment is conducted under realistic pressure-temperature conditions. The starting and final mineral products are optically observed and geochemically determined, the whole being completed by geochemical interpretation. The different fluid-rock reactions result in noticeable mineral dissolutions and precipitations correlating with the gas composition.

2.1. Experimental equipment

Experiments are performed on a natural sample in batch conditions during one month at 150°C and 100 bar. The experimental temperature corresponds to the measured bottom-hole temperature, whereas the experimental pressure corresponds to the one expected after two years of CO_2 injection. The batch reactors are constituted by gold capsules hermetically welded. Gold is used because of its chemical inertia, and its ability to conduct pressure and temperature (Seyfried et al., 1987). The volume of capsules is limited to 2 cm^3 (inner diameter of 0.5 cm for a length of 10 cm) regarding the risks inherent to the handling of gases such as SO_2 in case of leakage. The welded capsules are placed into a pressure vessel of 100 cm^3 heated by a coating device (figure 1). The pressure is set by a fluid (water-oil) compressed by a hydraulic pump and controlled by a pressure gauge. The device is presented in details in Jacquemet et al., 2005. It has been routinely employed for several experimental studies under similar pressure and temperature conditions (Landais et al., 1989; Teinturier and Pironon, 2003; – Jacquemet et al., 2005) mimicking geological environments. Mass balances are established after experiment using analytical characterization of each phase.

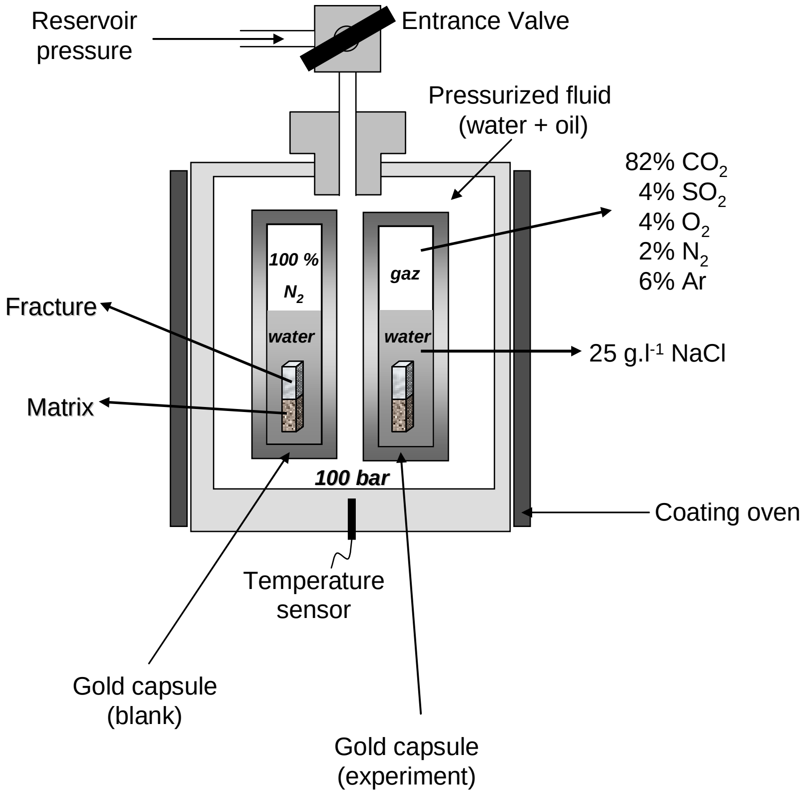

Figure 1: scheme of the pressurized autoclave. Gold capsules are filled with rock samples, saline water and gas phase and are placed in the autoclave. Pressure is controlled by a fluid linked to a pump and a manometer. The heating device surrounds the autoclave, to have the homogeneous heating. Percentages of gases are expressed in % mol. A capsule where the reacting gas is replaced by N_2 is used as a blank.

2.2. Reactants

2.2.1. Solids and water

The rock samples come from cores drilled in a fractured Portlandian dolomite, namely the Mano Dolostone. They were previously analyzed using SEM, EPMA and TEM (Renard et al., in prep.). The low porosity (< 3%) dolostone shows carbonaceous fractures. An initial Photoshop treatment of elemental X-Ray mapping (Figure 2), allow determining the mineral composition . The matrix is composed at 90 % by a dolomicrosparite (grain diameter of 5 µm) with a Ca/Mg ratio of 1.06.

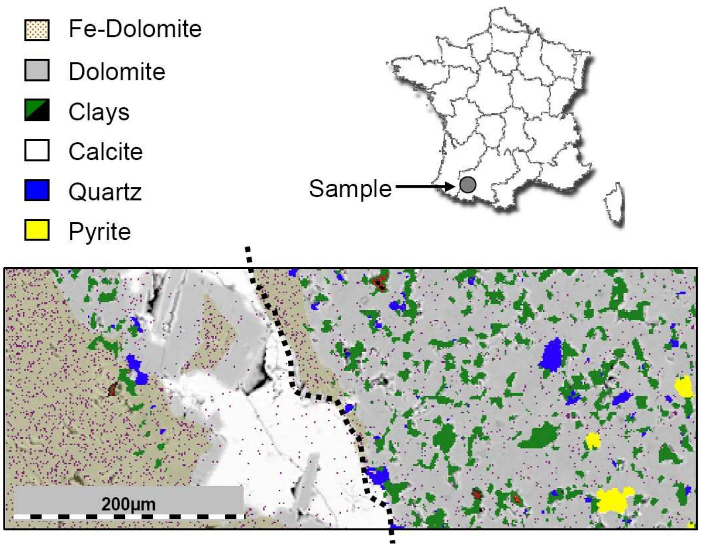

Figure 2: Overview of the rock used in the experiments. The coloured picture was built from the treatment on Photoshop of elemental X-Ray mapping, knowing the composition of each mineral. The dotted corresponds to the separation between matrix and filled fracture (wall rock of the fracture).

The remaining fraction of the rock shows quartz, clays and pyrite scattered between the dolomite grains (Figure 2). Clays were analyzed by TEM on a decarbonated sample of the rock. They are mainly represented by a high-charged illite with formula $(Si_{3.43}Al_{0.57})^{IV}(Al_{1.69}Fe_{0.06}Mg_{0.24})^{VI}\ K_{0.71}(Na_{0.09}Ca_{0.,02})O_{10}(OH)_2$, but some interstratified illite/smectite is associated to the illite. Quartz is present as blunt grains of 20 µm scattered within the matrix. It represents 3 to 4% of the volume but can reach 10 to 15% of the volume in zones where it is organized in thin stratified beds. Pyrite is spread as massive anhedral crystals of 10 µm and represents 0.1 to 1% of the volume. Its repartition is independent from the stratigraphy. Cross-cutting fractures are micrometer to centimeter in scale. They are mainly filled by ferrous dolomite (with an average Fe content of 0.3 %mol). Dolomites are Fe-depleted when located close to the calcites or to region of higher porosity. Calcites developed in thin layers (10 to 20 µm thick) in most fractures, always separating the dolomite from the wall rock. EPMA-WDS analyses showed that traces elements such as barium and strontium are present in carbonates. The global mineralogy of the rock has been established from global (ICP-MS and OES) and punctual analyses (EPMA, SEM, TEM). They are summarized in table 1.

Mineral	composition	Fracture facies	Matrix facies	Mean rock composition		
				N_2	CO_2	Gas mixture
Pyrite	FeS_2	0.0	0.5	0.3	2.1	0.1
Dolomite	$Ca_{1.1}Mg_{0.9}(CO_3)_2$	95.1	92.2	93.1	92.4	94.6
Calcite	$CaSr_{2.6\ E\text{-}4}Ba_{6.4\ E\text{-}4}CO_3$	4.9	0.1	1.6	1.5	4.0
Quartz	SiO_2	0.0	3.0	2.1	1.7	0.6
Illite	$Si_{3.43}Al_{2.26}K_{0.71}Mg_{0.24}Fe_{0.06}Na_{0.09}Ca_{0.02}O_{10}(OH)_2$	0.0	3.4	2.4	1.9	0.7
Interstratified		0.0	0.8	0.5	0.4	0.2

Table 1: Global composition of each facies composing the Mano dolostone (expressed in %mol) calculated from a regression between the bulk analysis of the rock and the composition of each mineral phase present in the rock. Tne uncertainty on minor phases is considered to be less than 10% The composition is given for each experiment, sorted by the type of the gas included.

The rock samples are cut to form stick fragments of 10 mm x 2 mm x 2 mm to be inserted into the gold-encapsulated reactors. Each sample contains the two facies constitutive of the Mano Dolostone (fracture and matrix, Figure 3) separated by a thin layer of calcite (20 µm thick) on the wall rock side of the fracture. Each fragment is polished on one face in order to detect the slights changes (dissolution or precipitation) on its surface. The sample used for pure CO_2 experiments presents a microfracture filled with pyrite and separated from matrix by the thin layer of wall rock calcite (Figure 3). The phases proportion between fracture and matrix varies from one sample to another. The mineralogical proportions for each sample have been estimated from surface proportions using image analysis with ImageJ© (http://rsbweb.nih.gov/ij/) and results are presented in table 1. The composition of the aqueous solution used for the experiments has been chosen to be representative of saline formation waters with a salinity of 25g/l of NaCl. The respective proportions in each phase introduced into the reactor are given in table 2: the water/rock ratio is about 3 and the water/gas ratio is about 5. For each experiment, a decrepited quartz is added to the system in order to trap the fluids during the experiment in synthetic fluid inclusions.

	rock (mg)	water (mg)	gaz (mg)	quartz (mg)
N_2	127	434	38	53
CO_2	120	402	75	60
Giw	133	448	100	68

Table2: Quantities of rock, water and gas used for each experiment. (N_2) blank sample with dinitrogen, (CO_2) experiment with pure CO_2, (Giw) gas mixture experiment.

At the end of experiment, gold capsules are opened to collect the gas phase, the aqueous solution and the minerals for analyses. The liquids are collected with micropipettes and solids are dried.

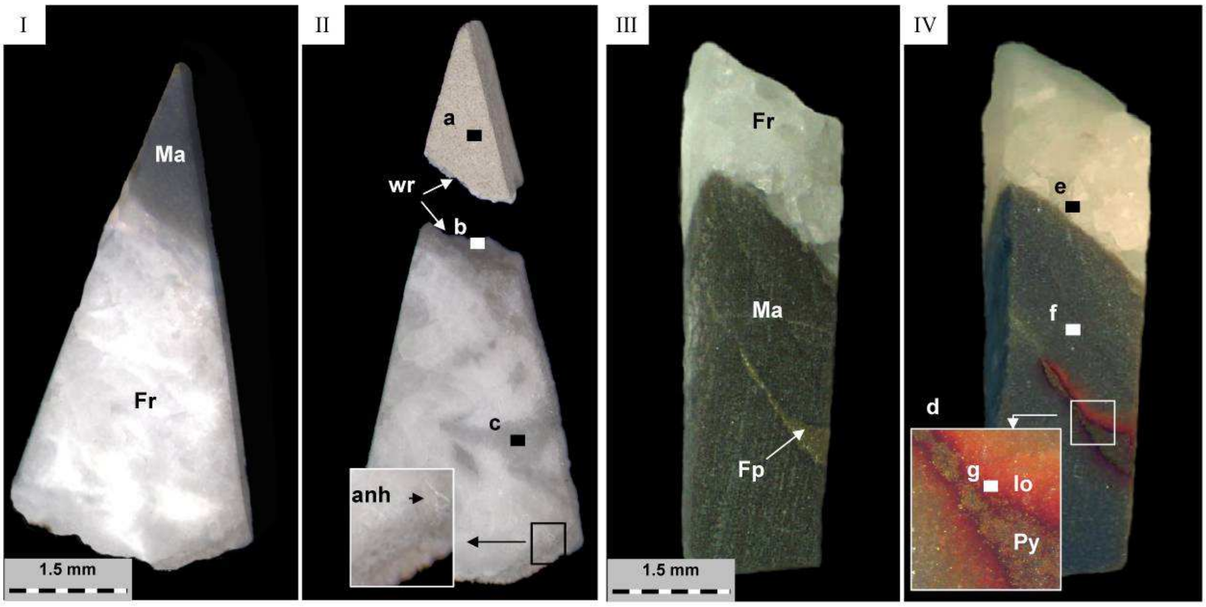

Figure 3: Observation with binocular lens of the rock samples before and after experiment. (I) and (III) samples before experiment, (II) sample after experiment with gas mixture, (IV) sample after experiment with pure CO_2. (anh) glitter of anhydrite, (Io) iron oxide, (Ma) Matrix of the rock, (Fp) pyrite in fracture, (Fr) fracture of the rock, (wr) wall rock of the fracture. Points a, b, c, e, f and g refer to pictures on Figure 7. Picture d is treated in Figure 8.

2.2.2. Gases

The two different types of gases selected for experiments consist in pure CO_2 on one hand and a gas mixture made of 82 ± 0.18 %mol CO_2, 4 ± 0.2 %mol SO_2, 4 ± 0.2 %mol O_2, 4 ± 0.2 %mol N_2 and 6 ± 0.12 %mol Ar on the other hand. It has been established according to the composition of the exhaust fumes from the Lacq's oxyboiler in case of a theoretical absence of the highly energetic desulfurization process. A blank capsule containing the same phases (solution and solid) was filled by nitrogen N_2 as an inert gas phase. The injected quantities for each experiment are displayed in table 2.

The gases are loaded in the capsules using the gas loading device adapted from Jacquemet et al., 2005 (Figure 4). All the tubes and seals of the device are made of stainless steel to avoid reactivity with the dry gases. During the loading procedure, the gold capsules are hermetically fixed on the capsule connector which is plugged to the loading device through the valve E. The capsule is plunged into liquid nitrogen in order to freeze the water fraction avoiding its vaporization when the device is under vacuum. At start of the gas loading all valves are shut. The loading of the gas is processed as follows : 1) vacuum is set in the whole line by opening valves A, B, D and E. 2) Valve A is shut and gas is injected from gaz input valves. 3) Gas is condensed in the liquid nitrogen cold trap. 4) Valve D is closed and the liquid nitrogen is removed from the cold trap. The quantity of gas is controlled by the measure of the pressure at room temperature using the perfect gas law and the pressure sensor 1-50 bar. 5) The valve E is opened. The gas is transferred to the gold capsule still plunged in liquid nitrogen. 5) When the residual pressure is stabilised, the gold capsule is cut and hermetically welded. The final stabilization pressure reaches 50 mbar. It corresponds to the equilibrium pressure between the gas phase at room temperature in the line and the solid phase in the capsule at temperature of vaporization of liquid nitrogen at 1 atm (-195,8°C).

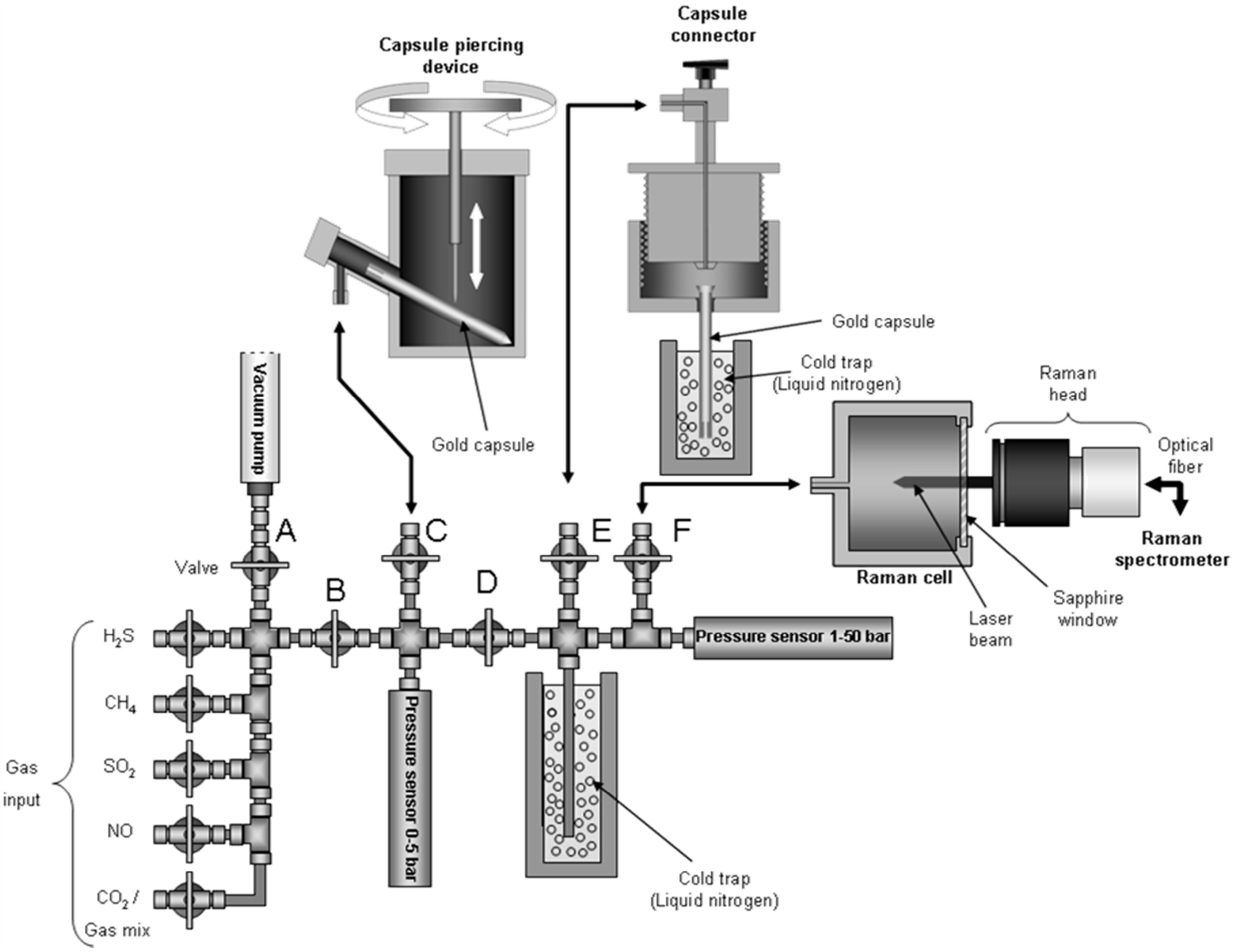

Figure 4: Gas loading and sampling line used during the experimental phase, adapted from Jacquemet et al., 2005. (A-E) valves. Different devices can be connected to the line: a capsule piercing device used to collect gases after experiment, a capsule loading device used to trap gases in the capsule and a cell for the Raman analysis of the gases.

At the end of experiment, the following procedure is used to collect gases: 1) the gas piercing device containing the capsule is connected to the line. 2) Vacuum is set in the whole gas loading device by opening valves A, B, C, D and F. 3) Valve B is shut and the capsule is pierced. 4) The residual gas coming from the capsule is condensed in the liquid nitrogen cold trap. 5) Valve D is shut and the liquid nitrogen is removed, allowing the gas to concentrate in the Raman cell. 5) Steps 4 and 5 are repeated several times until the final pressure measured by the sensor 2 overpasses 2 bars. 6) Valve F is shut and the Raman analysis of the gases can be performed.

2.3. Analyses

The analyses of the gases before and after experiments were carried out in the G2R laboratory (Nancy, France) on a Raman spectrometer Kaiser RXN1 equipped with a CCD detector and a Nd/YAG laser with a wavelength of 532 nm and a power of 100 mW. Incident laser radiation and Raman scattering are transferred via optical fibers. A ×20 objective is fixed on the Raman head in order to focus the laser beam and to collect the Raman scattering from the gas cell equipped with a sapphire window. The analyses result in spectra corresponding to an accumulation of five acquisitions of 60 seconds. Each spectrum presented in the document was previously treated to remove the contribution of the thin air layer located between the Raman head and the sapphire window of the Raman cell: Raman spectrum of air was previously registered and subtracted to the spectrum of the gas analyses.

Aqueous solutions were analyzed at the SARM-CRPG (Nancy, France). They were diluted in 15 ml of 2 %mol HNO_3 solution and analyzed with Inductively Coupled Plasma – Optical Emission Spectroscopy (ICP-OES) for major elements and Inductively Coupled Plasma – Mass Spectroscopy (ICP-MS) for traces. All analytical details (detection limits and procedures) are described in Carignan et al., 2001. After experiment, the rock samples were firstly analyzed by Scanning Electron Microscope (SEM) and Electron Probe Microanalyzer (EPMA) at the SCMEM (Nancy-Université, France). The SEM micrographs and Energy Dispersive Spectroscopy (EDS) analyses were performed on a Philips XL30 coupled with an EDS probe using a Si(Li) semi-conductor detector. The accelerating tension was fixed at 20 kV and the counting time was fixed at 60 s for EDS analysis. The electron microprobe analyses (EPMA) were carried out for elements (Al, Mg, Si, K, Ca, Na, Fe Sr, S, Ba) on a CAMECA SX100 equipped with a wavelength dispersive spectrometer and calibrated using natural and synthetic oxides (albite, olivine, orthose, wollastonite, hematite, $SrSO_4$, Barite). The analyses were performed under the following conditions: current of 10 nA, accelerating voltage of 15 kV, defocalized electron ray on a surface with a diameter of 5 µm and counting time of 15 s per element, 30s for Sr. Crushed samples were and analyzed by XRD at the Institut Jean Lamour (Nancy, France) with a diffractometer X'Pert Pro MPD from Panalytical with a vertical axis. It contains a copper anticathode and a X'Celerator detector. The diffractograms were registered on a range of 2θ from 5° to 75° with a measure step of 0.017° and a timestep of 34.92 s for 12.12°.

3.Results

3.1.1. Gases

For the CO_2 pure experiment, carbon dioxide remains the only detected gas by Raman spectroscopy after experiment. Concerning the gas mixture, the Raman spectra (Figure 5) shows the gas composition before and after experiments. Contribution of gases from the atmosphere was systematically subtracted for each spectrum. For readability, the spectra were normalized to the intensity of the CO_2 peaks (1285 and 1388 cm^{-1} including their doublet peaks - van den Kerkhof et Olsen, 1990). After experiment, the SO_2 (1151 cm^{-1} – Clochiatti et al., 1981) and O_2 (1555 cm^{-1} – Dubessy et al., 1988) peaks have disappeared or have an intensity slightly decreased. On the contrary, the N_2 (2331 cm^{-1} – Darimont, 1986) peak has rather the same intensity after experiment. (Figure 5)

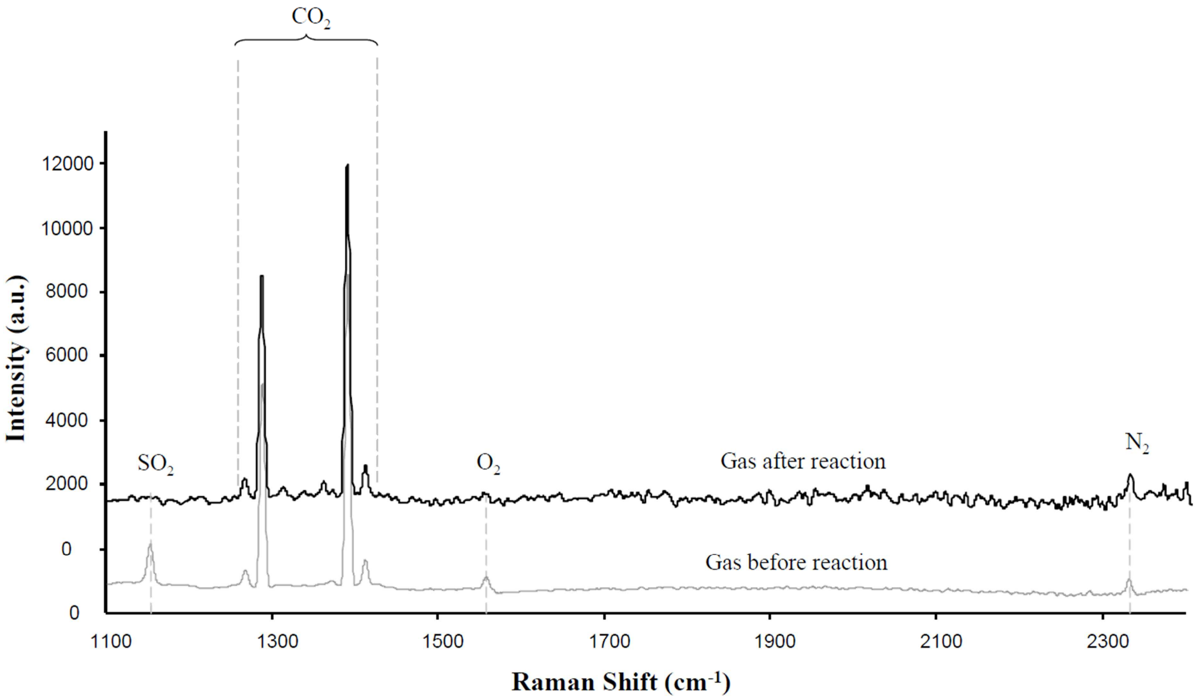

Figure 5: Raman spectrums of the gas mixture before and after experiment. SO_2 peak has completely disappeared and O_2 peak has diminished, implying the reactivity of the gases. The quantification is displayed in table 3.

The spectrum of the initial gas mixture recorded before experiment is used to calibrate the Raman spectra by calculating area peak ratios between the different components of the gas mixture. These ratios are then put in relation with the initial molar composition of the gas which is known. After experiment, the composition of the gas phase can be estimated considering that the total amount of CO_2 is equal to the initial mass injected plus the mass produced by carbonate dissolution. The quantity of CO_2 due to carbonate dissolution is calculated from the analysis of the aqueous calcium and magnesium in solution. (see next section).

Argon, a non reactive gas, was considered to be constant during experiments because of its low solubility in these conditions. The results are given in table 3. As observed, SO_2 was totally consumed and 62 % of O_2 reacted. CO_2 increased by 4%, due to the partial dissolution of carbonates. An increase of 6% of N_2 content after experiment is observed but should not be considered as significant because of the few amount of moles analyzed by comparison with CO_2 (around 9.10^{-5} mol for N_2 against 2.10^{-3} for CO_2).

		CO_2	**SO_2**	**O_2**	**N_2**	**Ar**	**Total**
before exp.	mol%	82%±0.35%	4%±0.07%	4%±0.08%	4%±0.08%	6%±0.12%	100%
	n (mol)	$1.8\ 10^{-3}$	$9.0\ 10^{-5}$	$9.0\ 10^{-5}$	$9.0\ 10^{-5}$	$1.3\ 10^{-4}$	$2.2\ 10^{-3}$
after exp.	mol%	88%±0.6%	0%±0.1%	1.5%±0.2%	4.5%±0.2%	6%±0.12%	100%
	n (mol)	$1.9\ 10^{-3}$	0.0	$3.4\ 10^{-5}$	$9.5\ 10^{-5}$	$1.3\ 10^{-4}$	$2.2\ 10^{-3}$
rel. var.	(% mol)	4%	-100%	-62%	6%	0%	-2.5%

Table 3: Quantities of gas components before and after experiment for the gold capsule Giw (table 2) and their molar variation. Percentages were obtained by Raman analysis of the gas after reaction (Figure 5). As Ar is not detected, it is considered to be constant. Quantities were calculated from the initial amount of gas and the final quantity of CO_2, including initial CO_2 and produced CO_2 from carbonate dissolution. Errors were deduced from the uncertainties on the composition of initial the gas mixture supplied by Air Liquide and the errors due to spectrum manipulations.

Usually, the gas phase can be analysed from fluid inclusions which should trapp the fluids during experiment. In these experimental conditions, no fluid inclusions were formed, forbidenning additional Raman analyses.

Concerning the blank capsule, N_2 was the only detected gas phase. No analyses were possible on the decrepited quartz because no fluid inclusions were formed.

3.2. Aqueous solution

The composition of the aqueous phase sampled after each experiment at room temperature is compared to that of the blank capsule (table 4). Sodium remains constant for the three experiments and corresponds to the initial concentration of 25g/l NaCl. Conversely, calcium is equivalent in the pure CO_2 experiment and three times higher in the gas mixture experiment when compared to the blank experiment. Magnesium concentration is below the detection limit in the blank experiment, but its content is nine times higher in the gas mixture than in pure CO_2 experiments. This can be explained by increasing carbonate dissolution from blank to gas mixture. Sulfates show molarities twelve times higher in the pure CO_2 experiment and thirty times higher in the gas mixture compared to the blank. This could be attributed to SO_2 and pyrite reactivity. The high value for pure CO_2 experiment can be put in relation with the amount of pyrite located in a microfracture in the rock sample (2.1%mol of the rock for the pure CO_2 experiment against less than 0.3 %mol for the blank and the gas mixture experiment). Inversely, iron content is slightly higher in the blank than in the other experiments and is twice lower in the gas mixture experiment compared to the pure CO_2 experiment.

	Na	**Ca**	**Mg**	**SO_4**	**Fe**	**Si**	**Al**	**K**	**Ba**	**Sr**
N_2	$4.3\ 10^{-1}$	$6.1\ 10^{-3}$	n.d.	$1.2\ 10^{-3}$	$4.2\ 10^{-4}$	$2.8\ 10^{-2}$	$1.5\ 10^{-3}$	$1.6\ 10^{-3}$	$1.3\ 10^{-5}$	$1.1\ 10^{-10}$
CO_2	$4.1\ 10^{-1}$	$6.8\ 10^{-3}$	$7.2\ 10^{-3}$	$1.5\ 10^{-2}$	$3.0\ 10^{-4}$	$2.3\ 10^{-2}$	$1.1\ 10^{-3}$	$1.2\ 10^{-3}$	$1.9\ 10^{-6}$	$8.5\ 10^{-7}$
Giw	$4.0\ 10^{-1}$	$1.7\ 10^{-2}$	$6.1\ 10^{-2}$	$3.6\ 10^{-2}$	$1.4\ 10^{-4}$	$1.3\ 10^{-2}$	$5.8\ 10^{-4}$	n.d.	$1.1\ 10^{-6}$	$1.6\ 10^{-5}$

Table 4: Concentrations of aqueous elements in the water phase at the end of experiment. Experimental analyses were performed by ICP-MS and ICP-OES at the SARM in Nancy (France). They correspond to the capsules presented in table 2. They are expressed in mol/l. (CO_2) pure CO_2 experiment, (Giw) gas mixture experiment, (N_2) blank experiment.

Silicon, aluminium and potassium concentrations show a gradual evolution from the blank to the gas mixture experiments. The content in those elements for pure CO_2 experiment are almost similar to that of the blank experiment whereas they are two times lower in the gas mixture, except for potassium which was not detected. These elements, exclusively found in the silicate minerals, can be considered as tracers of the reactivity of the clay minerals. Several trace elements also provide interesting information. Barium and strontium mainly included in calcite show a reverse correlation. Sr concentration increases from the blank to the gas mixture whereas Ba decreases compared to the blank experiment. Thus values of barium for pure CO_2 experiment and the gas mixture are almost similar. Barium and strontium are released through calcite dissolution but barium associates with sulfates to give insoluble barytine.

3.3. Rocks

Observations on samples from blank experiment did not reveal a strong reactivity of the solid phase after experiments since the polished faces keep their aspect. The rock sample in the blank experiment showed no specific transformation: the XRD spectrum is similar to that of the rock before experiment. Thus, the polish of the sample is preserved and calcite shows only slight corrosion pits on the surface of the rock sample. The TEM analyses of the clay minerals, leading to their structural formula are examined before and after experiments. They are plotted in a diagram Si vs interlayer charge (Figure 9) after calculation of their corresponding structural formulae from the Harvey's method based on 11 oxygens and Fe^{3+} (Harvey, 1943). The clays of the rock before experiment show a dominance of illite in the clay fraction, with several interlayered clays smectite-illite in comparison, the clays of the blank experiment show a horizontal shift on the graph, corresponding to a decrease in the interlayering by a slight loss of interlayered ions (K, Ca, and Na). This could be due to the partial leaching of this space by the water added to the experiment and doesn't transform the mineralogical structure of the clay.

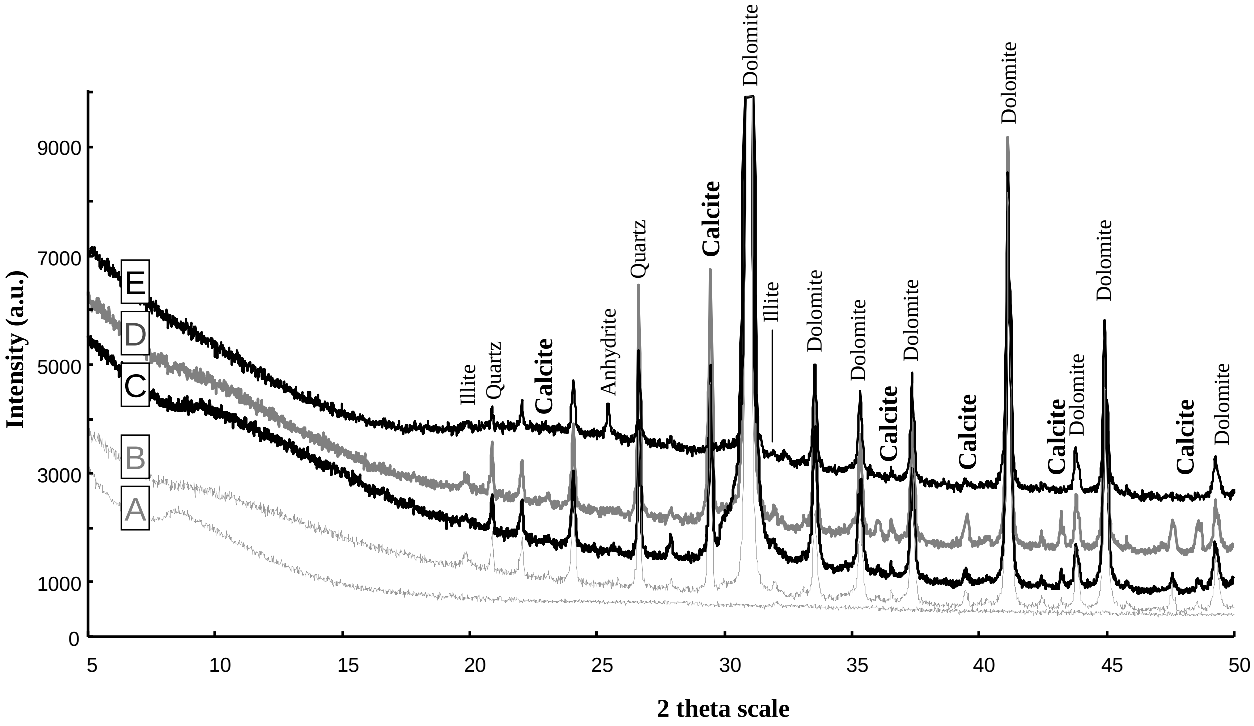

Figure 6: XRD spectra of the reservoir rock (Mano dolostone) before and after experiments. (A) stand, (B) rock before experiment, (C) blank experiment, (D) rock with pure CO_2, (E) rock with the gas mixture. The analyses were performed on crushed samples.

The rock sample submitted to pure CO_2 shows no transformation of their general aspect except on an area close to the microfracture filled with pyrite, which is coloured in red (Figure 3). The XRD data are almost similar to that of the blank experiment, indicating that the observed transformations were limited (Figure 6). SEM observations put in evidence the slight reactivity of the carbonates, especially for the calcite of the wall rock of the fracture containing pyrite (Figure 7-e). Dolomite shows only a loss of the polish of the sample surface. The main reactivity located on the microfracture filled with pyrite is responsible of a layer of anhydrite and Fe-minerals with a shape of iron oxides or siderite on the area: they present a facies of tangled micro lamellas (Figure7-g and h). They are associated to amorphous silica. It was impossible to precisely analyse those new species because they disappeared when the sample was polished after experiment for EPMA analysis. The pyrites of the matrix do not show such reactivity and are still visible at sample surface (Figure 7-f). The pyrite area which reacted was studied by x-ray mapping on EPMA. The element maps were stacked and computed with Photoshop to determine the organisation of minerals considering their composition. The result (Figure 8) shows that pyrite is still present under the anhydrite/fe-mineral/amorphous silica layer. Porosity was created in the calcite separating matrix from pyrite and in the neighbouring dolomite of the matrix facies. Clays of the altered matrix zone may also have reacted. TEM analyses (table 5) show an enrichement in Al, and depletion in Si, Mg, K, and Na. Si, Al and K remain the dominant cations. Each measure plots on the diagram Si vs interlayer charge after calculation of its corresponding structural formulae (Figure 9). Illites have lost a part of their silica and the most altered of them were transformed into beidellites and vermiculites. The interstratified illite-smectite are still present in the sample.

The sample submitted to the gas mixture shows an obvious reactivity with an initial grey colour turning to a light beige colour (Figure 3). The XRD data comparing the initial sample and that after experiment point out to obvious mineralogical transformations (Figure 6): the calcite signal disappears when the anhydrite signal appears. Thus, the signal of illite is weaker. The dolomite shows pervasive dissolution on surface of the rock sample (Figure 7-f). It probably represents the source of the high Mg concentration detected in water (table 4). Its dissolution patterns depend on the rock facies. In the matrix, the dolomite crystals are rounded, creating porosity between the grains. In the fracture zone, dolomite shows an elephant skin pattern by preferential dissolution along the cleavages of the crystals (Figure 7-c). Therefore aqueous solution could reach minerals sparse in the matrix such as clays and pyrite located deeper in the rock sample (Figure7-b). Calcite is completely dissolved, implying the separation of the sample in two pieces, each corresponding respectively to the fracture and matrix facies. A closer observation shows sparse glitters of anhydrite onto the whole sample (Figure7-a and b), especially the wall rock area where it replaced the dissolved calcite (Figure7-c).

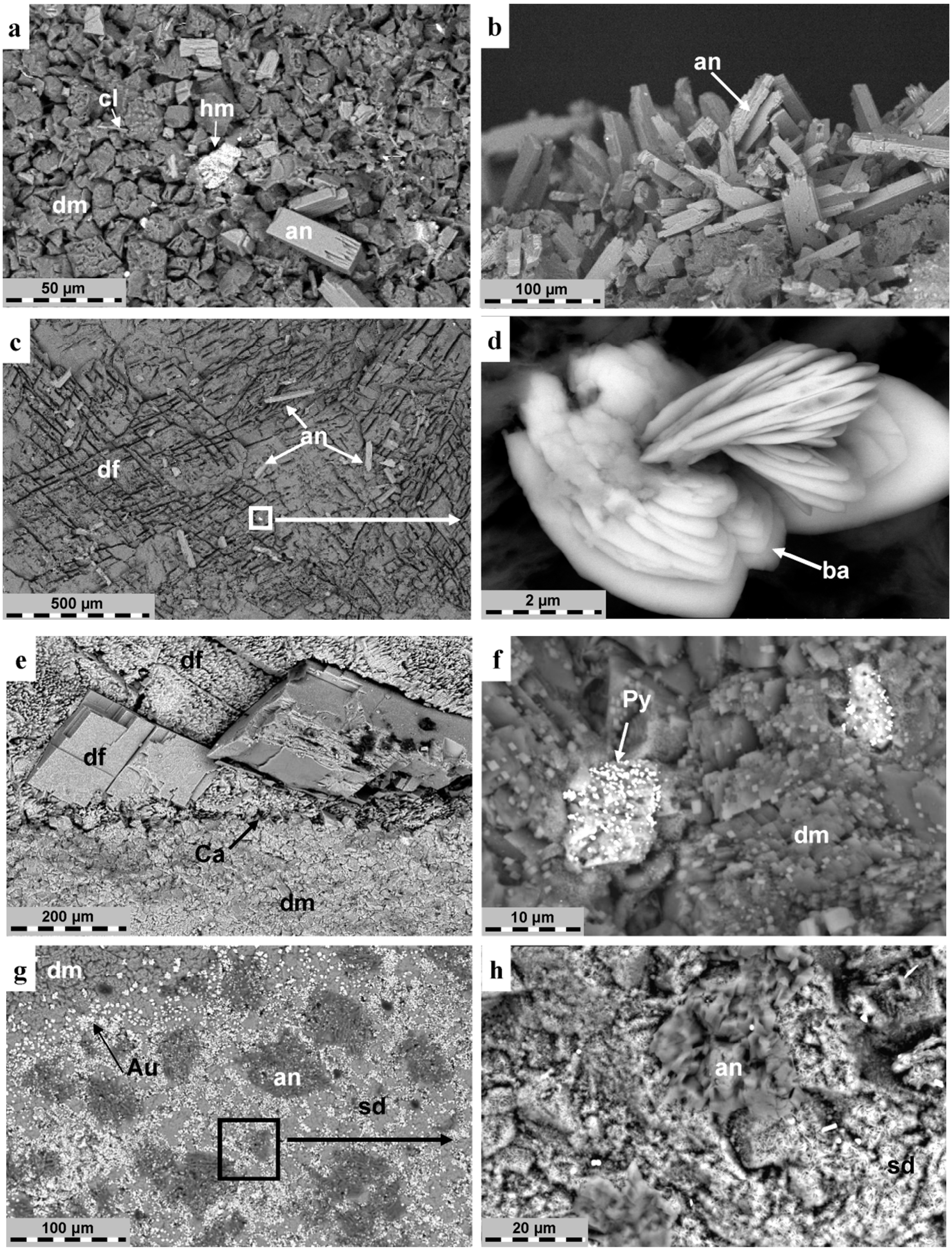

Figure 7: Backscattered scanning electron micrographs showing the rock samples after experiment. (a-d) Rock after experiment with gas mixture. (e-f) rock after experiment with pure CO_2. (a) matrix of the rock; (b) wall rock of the fracture; (c) fracture of the rock, (d) zoom on barite. (e) limit beween matrix and fracture, (f) zoom on matrix, (g) zone of initial pyrite of fracture, (h) zoom on the picture g. (an) anhydrite, (Au) gold, (ba) Barite, (ca) calcite, (cl) clay minerals, (df) fracture dolomite, (dm) Matricial dolomite, (hm) hematite, (Py) pyrite, (sd) siderite or iron oxide associated to amorphous silica.

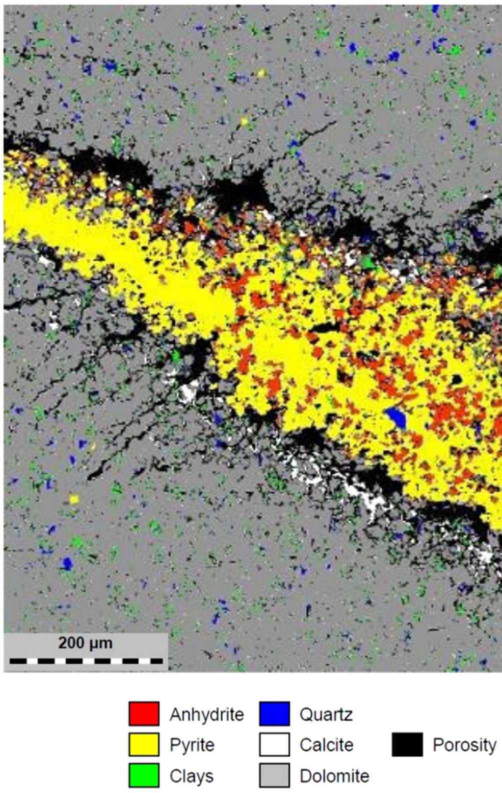

Figure 8: Cartography of the mineral repartition on the area of the pyrite of fracture on the sample with pure CO_2 (Figure 3-d). The sample has been polished under water, suppressing the iron-rich layer. The cartography has been set on Photoshop using element X-Ray mapping and analyses of the mineral composition previously established with EPMA.

Pyrites show in situ transformation into hematite (Figure7-b). Some barite microcrystals (less than 5 µm) are associated to the presence of anhydrite (Figure7-d). Despite no clear optical modification, TEM analyses (table 5) reveal chemical modifications of the clay minerals.

Sample	Nb analysis	Analyse	Si	Al	Fe	Mg	K	Na	Ca	O
CO_2	**28**	**Mean**	**18.49**	**13.67**	**0.35**	**1.44**	**3.35**	**0.06**	**0.11**	**62.54**
		Median	**18.56**	**13.60**	**0.32**	**1.32**	**3.77**	**0.00**	**0.09**	**62.66**
		std dev.	**1.52**	**1.42**	**0.24**	**1.27**	**1.32**	**0.10**	**0.10**	**2.02**
Gaz mixture	**20**	**Mean**	**19.61**	**13.20**	**0.39**	**1.49**	**3.02**	**0.01**	**0.13**	**62.16**
		Median	**19.15**	**12.82**	**0.37**	**1.48**	**2.98**	**0.00**	**0.12**	**62.74**
		std dev.	**2.39**	**1.15**	**0.12**	**0.63**	**0.70**	**0.02**	**0.12**	**3.20**
Blank Sample	**27**	**Mean**	**19.53**	**12.90**	**0.34**	**1.84**	**3.60**	**0.29**	**0.16**	**61.35**
		Median	**19.80**	**12.84**	**0.29**	**1.61**	**3.85**	**0.07**	**0.16**	**61.29**
		std dev.	**1.88**	**1.14**	**0.24**	**1.08**	**1.21**	**0.79**	**0.09**	**2.56**

Table 5: TEM-EDX analyses on clay minerals of the Mano dolostone after experiment with pure CO_2 and gas mixture. The analyses were performed at the SCMEM in Nancy (France). Concentrations are expressed in %mol.

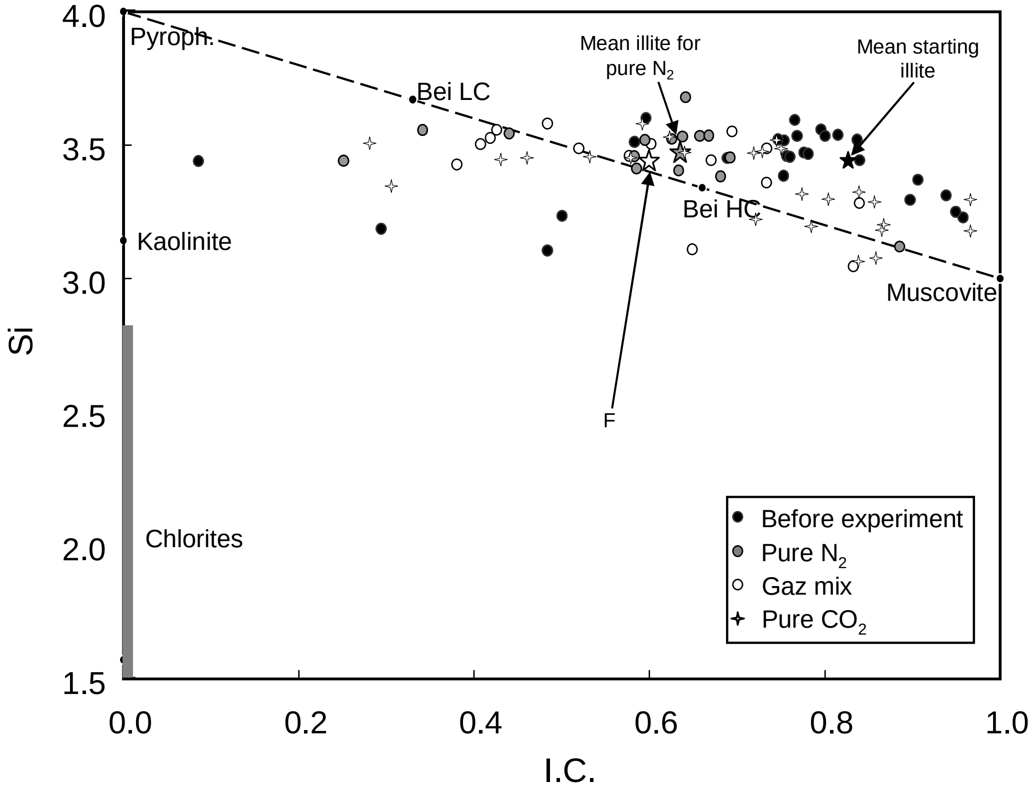

Figure 9: Diagram Si vs interfolial charge for the clay fraction of Mano dolostone, before (black points) and after experiment with gas mixture (white points), pure N_2 (blank experiment - grey points) and pure CO_2 (crosses). Data were calculated from TEM analysis by the Harvey's method (Harvey, 1943). Data from experiments are given in table 5. (Bei LC) low-charged beidellite, (Bei HC) high charged beidellite, (F) Position of the structural formulae corresponding to mean product of clay reactivity for the Gas mixture experiment. The diagram shows a partial beidellitization of the illite and a disappearance of the interstratified illite-smectite of the Mano dolostone, in contact with the gas mixture or pure CO_2. The transformation is more pronounced for the gas mixture case. The experiment with N_2 shows only a shift of the initial points, corresponding to the leaching of the interlayering space.

Clay minerals are richer in Al, Si and Fe and depleted in K, Na and Mg after reaction. Si, Al and K remain the dominant cations (table 5). In the diagram Si versus interlayering charge (Figure 9), the sample corresponding to the gas mixture shows an organization of its clays from illite to beidellite, with the majority lined up on a trend from a low-charged beidellite to a high charged beidellite. According to their high potassium content, the average composition of newly formed clay corresponds to a beidellite-K with the following composition: $(Si_{3.43}Al_{0.57})^{IV}\ (Al_{1.80}Fe_{0.07}Mg_{0.25})^{VI}\ Ca_{0.03}K_{0.40}O_{10}(OH)_2$

4. Discussion

4.1. Mechanisms of experimental reactivity

4.1.1. Reactivity of rocks in presence of pure CO_2

Concerning reactivity with pure CO_2, carbonates, whether they consist in calcite or dolomite behave as pH-buffers and show a really slight dissolution:

$2\ H^+ + CaCO_3 = Ca^{2+} + CO_{2,aq} + H_2O$ (1)

Calcite

$4\ H^+ + CaMg(CO_3)_2 = Ca^{2+} + 2\ CO_{2,aq} + Mg^{2+} + 2\ H_2O$ (2)

Dolomite

The pyrite also reacted, implying precipitation of iron-rich minerals and anhydrite. Before any interpretation we tried to check if it was not an artefact due to the experimental manipulations. Before the injection of the gas, the capsule is hermetically linked to the gas loading device. Water is frozen by plunging the capsule in liquid nitrogen, to avoid condensation of the remaining air contained in the capsule. Then, vacuum is made in the capsule. The O_2 fraction which remains in the capsule is the initially aqueous O_2 in the water. At room conditions (20°C, 1 atm), the solubility of O_2 is calculated on SUPCRT92 (Johnson et al., 1992) at 2.69 10^{-4} molal. Considering the amount of water contained in the capsule (table 2), the total quantity of O_2 is near 1.3 10^{-7} mol. This quantity of O_2 leads to a dissolution of 0.25 %mol of the pyrite when calculated on CHESS© in the same conditions as the experiment. Thus, this fraction of O_2 cannot explain the experimental reactivity of the rock, and the observation of the rock revealed local reactivity between pyrite, carbonates and clays, showing highest dissolution rates than in the rest of the sample. Two mechanisms are possible to explain this reactivity:

1) pyrite was dissolved in response with the acidification of the water due to the presence of CO_2, giving both sulfates and sulfures:

Pyrite + $H_2O + 1.5\ H^+ = 0.25\ SO_4^{2-} + Fe^{2+} + 1.75\ H_2S$ (3) $\log K = -8.65$

H_2S was not quantified in the water. We can estimate its maximal activity from this equation, the pH obtained on CHESS© in the same conditions as the experiment (the activities of aqueous species were calculated with the B-dot model), considering all the aqueous iron as Fe^{2+}:

$$\text{Log}\ (a_{H_2S}) = \frac{4}{7}\log K - \frac{1}{7}\log(a_{SO_4^{2-}}) - \frac{4}{7}\log(a_{Fe^{2+}}) - \frac{6}{7}pH = -6.52$$

This activity corresponds to a molality less than 10^{-6} molal. However, the solubility of H_2S in water at 150°C, 100 bar and 25 g/l NaCl is near 2.5 molal, according to Duan et al., 2006 model. H_2S should remain completely dissolved in the water, explaining why it was not detected in the gas at the end of experimentation. This reactivity however involves a consumption of protons which is in contradiction with the local activation of the dissolution of carbonates and clay minerals in comparison with the rest of the rock sample.

2) Sulphur of the pyrite was oxidized. The oxidizing agent can only be the iron contained in the clays:

$$\underset{\text{Pyrite}}{FeS_2} + 8\ H_2O + 14\ Fe^{3+} = 15\ Fe^{2+} + 2\ SO_4^{2-} + 16\ H^+ \quad (4) \qquad \log K = 96.44$$

The mechanism has been checked on CHESS© with varying concentrations of Fe^{3+}. Pyrite showed an oxidation of its sulphur² when the aqueous Fe^{3+} reached 10^{-5} molal. So we can imagine a local disequilibrium which started with the dissolution of carbonates and clay minerals. The proximity of the microfracture filled with pyrite could have then created a self-maintained processus of dissolution-oxidation accompanied by a local pH drop, until the local concentration of Fe^{3+} equilibrated with the concentration of Fe^{2+}. This reaction needs a high amount of Fe^{3+}. However clay minerals contain only a low proportion of iron and its valence is unknown. We can imagine that equilibriums 3 and 4 worked together to explain this high reactivity of the rock.

Iron released in the solution as Fe^{2+} could then combine with the aqueous CO_2 to give siderite or react with H_2O or the fraction of dissolved O_2 to give iron oxides.

Concerning quartz and amorphous silica, the activity of aqueous SiO_2 can determine the phase at equilibrium with the fluid:

Quartz = $SiO_{2,aq}$ (5) $\log K_9 = \log (a_{SiO_{2aq}}) = -2.71$

Amorphous silica = $SiO_{2,aq} + n\ H_2O$ (6) $\log K_{10} = \log (a_{SiO_{2aq}}) = -1.96$

The activity of $SiO_{2,aq}$ calculated from water data (table 4) with the B-dot equation on CHESS© is equal to 2.1 10^{-2}, corresponding to a $\log (a_{SiO_{2aq}})$ equal to -1.67. Quartz is then thermodynamically oversaturated and amorphous silica is near equilibrium. The fact that fluid inclusions were not sealed during the experiment indicates that the kinetic of quartz precipitation is really slow in the experimental conditions, as confirmed by Rimstidt et Barnes, 1980. It explains why quartz is oversaturated and confirms that aqueous silica released by clay minerals dissolution precipitated in amorphous silica instead of quartz.

4.1.2. Reactivity with gas mixture

Concerning reactivity with the gas mixture, the transformations observed on the three types of minerals present in the experiment can be explained by the rock reactivity with some of the gas components. But before looking at the mineralogy we must discuss the presence of sulfates in the water. SO_2 is oxidised by O_2 which is the strongest oxidant in the reaction capsule. The reactivity could take place in the gas phase. However, we saw previously that SO_2 could be completely dissolved in water (Van Berkum et al., 1978). The oxidation must have occurred in the water phase, producing sulfates when pH remains higher than 3:

$SO_2 + H_2O + ½\ O_{2,g} = SO_3^{2-} + 2\ H^+ + ½\ O_2 = SO_4^{2-} + 2\ H+$ (7) $\log K_{total} = 19.27$

If we consider that SO_2 was completely consumed, according to experimental results, the activity of SO_2 is negligible:

Then $\log f O_2 = 2 \times (\log (a_{SO_4^{2-}}) - \log K_{total} - 2\times \mathrm{pH})$

The activity of sulfates calculated with the software CHESS© from experimental data (table 4) is 5.2 10^{-2}. If we consider that the final pH of the solution of the rock with the gas mixture is down to 8, the equivalent $f O_2$ of this equilibrium at 150°C calulated from data of SUPCRT92

(Johnson et al., 1992) is then less than 10^{-59} bar. Regarding the initial quantity of oxygen and its solubility extrapolated from Tromans (1998), this reaction must have been total in the aqueous phase. This reaction is classically used as a method for SO_2 removing from coals (Lizzio et DeBarr, 1997). It is proven to occur at very low SO_2 and O_2 concentrations (2500 ppm of SO_2 under constant flux of N_2, 5% O_2 and 7% H_2O at 120°C during one hour. The SO_2 fixed on carbon reacted with O_2 and H_2O to form H_2SO_4) and at temperatures from 80 to 150°C.

This must have led to a high acidification of the water, buffered by a mineral dissolution. Dissolution and oxidation of SO_2 led to acidification of the solution which was counterbalanced by the buffer effect linked to the dissolution of carbonates (reactions 1 and 2). The carbonate dissolution also released trace elements such as strontium and barium. Because of its very low solubility, barite was the first sulfates to precipitate according to the equilibrium:

$BaSO_4 = Ba^{2+} + SO_4^{2-}$ (8) log Ks = -9.62

Barite

The pKs of this equilibrium, given by the log Ks of the reaction is 9.62 (calculated on SUPCRT92). The final experimental activities of Ba^{2+} and sulfates were calculated with the B-dot equation on CHESS© from water data (table 4) estimated from their final molalities (respectively $4.7\ 10^{-7}$ and $3.2\ 10^{-2}$). These values show that barite is slightly oversaturated.
The concentration of calcium and sulfates in the solution led to the saturation of anhydrite:

$CaCO_3 + 2\ H^+ + SO_4^{2-} = CaSO_4 + CO_{2,aq} + H_2O$ (9)

Calcite Anhydrite

$CaMg(CO_3)_2 + 4\ H^+ + SO_4^{2-} = CaSO_4 + 2\ CO_{2,aq} + 2\ H_2O + Mg^{2+}$ (10)

Dolomite Anhydrite

Clay minerals also reacted under the acidic conditions. Smectite dissolved partially and illite transformed partially in beidellite-K according to the results:

$$\begin{aligned}&1\ \text{Illite} + 0.11\ Al^{3+} + 0.01\ Mg^{2+} + 0.01\ Fe^{3+} + 0.01\ Ca^{2+}\\&\qquad = 0.31\ K^{+} + 0.09\ Na^{+} + \text{Beidellite-K} \qquad (11)\end{aligned}$$

Beidellitisation of illite incorporates the ions released by the partial dissolution of smectites, explaining the low water-content of Al.

The remaining O_2 fraction reacted with the pyrites to give hematite:

$$2\ FeS_2 + 4\ H_2O + 7.5\ O_2 = Fe_2O_3 + 4\ SO_4^{2-} + 8\ H^{+} \quad (12) \qquad \log K = 271.78$$

Pyrite Hematite

Then $\log fO_2 = -2/15 \times (\log K - 4 \times \log (a_{SO_4^{2-}}) + 8\times \text{pH})$

The f_{O_2} calculated from experimental data for sulfates (table 4) is near 10^{-41} bar, explaining why reaction is total. However, the f_{O_2} of the oxidation of SO_2 is much lower. This confirms that pyrites are oxidised only if there is O_2 left after the oxidation of this aqueous component. This is the case in the experiments because this reaction consumed only the half of the initial quantity of O_2.

Aqueous O_2 was consumed during the reactivity with SO_2 and Fe-minerals. The water phase equilibrated each time with O_2 present in the vapour phase, depending on the kinetic of the O_2 equilibrium between gaseous and aqueous phases. O_2 is still present at the end of experimentation in the gas phase, showing that it is in excess towards the reactions where it acts or that the mineralogical reactions have not yet reached the thermodynamic equilibrium after one month of reactivity. The final conditions in the experimentation are then highly oxidative.

Concerning equilibria of quartz and amorphous silica, the activity of $SiO_{2,aq}$ calculated from water data (table 4) with the B-dot equation on CHESS© is equal to 1.2 10^{-2}, corresponding to a log ($a_{SiO_{2aq}}$) equal to -1.92. As for the pure CO_2 experiment, quartz is thermodynamically oversaturated and amorphous silica is at equilibrium. Silica released by clay minerals dissolution precipitated in amorphous silica instead of quartz.

4.2. Quantitative analysis of the rock reactivity

Elements mole-balance during experiments are established from mineralogy (table 1), initial fluid/rock mass ratios (table 2) and concentrations of elements in water after experiments (table 4). Considering that the Mg content of the octahedral site of beidellite is similar to that of illite, the total aqueous magnesium was attributed to the dissolution of dolomite. Its increase by a factor of 1.1, is attributed to the proportion of magnesium contained in one mole of dolomite. It allows determining the number of moles of the dissolved dolomite. Sr was only detected in calcite (table 1) and its aqueous concentration is, by consequence, assigned to the dissolution of calcite (the calcite molar ratio Ca / Sr is equal to 3760). The estimation of the quantity of barite that precipitated is based on the barium released by the dissolution of carbonates considering the Ba-content of calcite (table 1), and subtracting the remaining quantity of barium in water. In pure CO_2 and blank experiments, the aqueous content of SO_4^{2-} is due to the partial dissolution of pyrites. Newly formed anhydrite is considered as negligible because it developed only on a very small area on the surface of the rock sample. The total dissolved sulfates are considered to represent twice the amount of oxidized pyrite. Concerning the gas mixture the number of moles of hematite is estimated by the subtraction of the iron released in the solution from the iron released by the total oxidation of pyrite. Concerning pure CO_2 experiment, hematite is considered as the direct product of the partial pyrite oxidation. Because one mole of pyrite gives 2 moles of sulphur and one mole of iron, the quantity of precipitated hematite is estimated from the difference between the aqueous iron and the half of the aqueous sulfate content according the reaction 12:

$$n_{hematite} = (n_{sulfate} / 2 - n_{Fe,aq}) / 2$$

The CO_2 produced by the dissolution of carbonates is added to the initial CO_2 to calculate the final CO_2 content after experiment. Clays are more difficult to evaluate because of their variable compositions and intern transformations. It is only estimated for the blank, considering that most of the clay minerals have a composition similar to the mean illite of the initial rock. As no transformation of the clay was observed, except a loss in interlayering charge, aqueous aluminium was attributed to their dissolution. Quartz is set to its solubility according to equilibrium 5. Results of mole balances are presented in table 6.

	N_2 (blank)			CO_2			Gas mixture		
	Start (mol)	End (mol)	% dissolution	Start (mol)	End (mol)	% dissolution	Start (mol)	End (mol)	% dissolution / consumption (gas)
Pyrite	2.5 10-6	2.4 10^{-6}	3.2%	1.5 10-5	1.4 10^{-5}	8.6%	7.1 10-7	0.0	100.0%
Dolomite	6.7 10-4	6.7 10^{-4}	0.0%	6.5 10-4	6.5 10^{-4}	0.3%	6.8 10-4	6.5 10^{-4}	4.2%
Calcite	1.1 10-5	1.1 10^{-5}	3.2%	1.1 10-5	1.0 10^{-5}	8.5%	2.9 10-5	5.4 10^{-7}	98.1%
Quartz	9.0 10-4	8.9 10^{-4}	0.4%	1.0 10-3	1.0 10^{-3}	0.4%	1.1 10-3	1.1 10^{-3}	0.3%
SO_2[1]	-	-	-	-	-	-	9.0 10-5	2.4 10^{-5}	73.1%
O_2[1]	-	-	-	-	-	-	9.0 10-5	4.0 10^{-5}	53.0%
Goethite /siderite	-	-	-	-	2.5 10^{-6}	-	-	-	-
Hematite	0.0	1.1 10^{-8}	-	0.0	-	-	0.0	3.1 10^{-7}	-
Barite	0.0	0.0	-	0.0	2.8 10^{-10}	-	0.0	1.8 10^{-8}	-
Anhydrite	0.0	0.0	-	0.0	1.2 10^{-6}	-	0.0	4.4 10^{-5}	-

Table 6: Mineralogical transformations in the rock samples after experimental reactivity with pure CO_2 and the gas mixture. The blank is given for comparison. Values are expressed in mol.

The blank experiment shows a slight dissolution of calcite and pyrite (around 3 %mol) whereas dolomite remains stable and quartz is barely altered (less than 1 %mol).

Concerning the experiment with pure CO_2, calcite and pyrite are more altered. They loose almost 10 %mol of their initial content whereas quartz and dolomite are barely altered. The carbonate and pyrite dissolution are linked to with the alteration of clay minerals precipitates 1 10^{-6} mol of anhydrite and 2.5 10^{-6} mol of Fe-minerals. The activities of barium and sulfates calculated from experimental data (table 4) on CHESS© with the B-dot activity model (respectively 4 10^{-7} and 1.1 10^{-2}) show a slight saturation considering the equilibrium 8. The quantitative calculation give then some traces of barite (around 3 10^{-10} mol) despite it was not detected on the rock. The quantity corresponds to traces. It can have precipitated in association with anhydrite which can explain why it was not visible.

In the experiment with the gas mixture, the reactivity is really higher than for pure CO_2 and N_2 experiments. Calcite is almost completely dissolved (98 %) whereas only 4 % of dolomite are dissolved. Barite precipitation is rapidly limited by the availability of barium and reaches 1.8 10^{-8} moles after experiment with gas mixture. 3.1 10^{-7} mole of hematite are formed. The final quantity of anhydrite is 1.5 time higher than the initial quantity of calcite. Concerning the gas fractions, calculations give a consumption of 100 %mol of SO_2 and 53 %mol of O_2. Thus 73% of sulfates were mineralized into anhydrite. The 27% left remainedin water. These results show an error of 15% for O_2 comparing with the values issued from Raman analyses

(61% for O_2). This can be due to uncertainties on the treatment of the Raman spectrums and the uncertainty concerning the theoretical mineralogy of the rock given in table 1, N_2 and Ar are non reactive gases, and they are considered to remain constant during experiment.

4.3. Effect of co-injected gases on the properties of the reservoir

CO_2 reactivity is based on the variations of pH and the evolution of the f_{CO2} in the system. The decrease pH induced by the solubilisation of CO_2 will enhance partial dissolution of carbonates rapidly compensated by the presence of aqueous CO_2 (Sterpenich et al., 2009) and of clay minerals. The dissolution of clays releases aqueous iron that could precipitate to form siderite. Some local effects such as a microfracture filled with pyrite next to a zone rich in clays could increase the reactivity of the rock. Thus, porosity of the reservoir rock of the study is mainly located in the carbonate fractures partly filled with dolomite and calcite. These local effects won't change much the chemistry of the fluids present in the reservoir, except by potentially activating the mineralisation of CO_2 into new carbonate phases.

when some fractions of SO_2 and O_2 are added to CO_2 the later is no more the main reactive molecule. The co-reactivity of SO_2 and O_2 results in the pronounced acidification of the water, dissolving calcite and dolomite and precipitating anhydrite. The incorporation of aqueous calcium to anhydrite enhances the carbonate reactivity according to the Le Chatelier's principe. But clay minerals also react showing a higher alteration than in the case of injection of pure CO_2. The remaining O_2 fraction oxidizes pyrites in hematite, as well as the Fe^{2+} released by the dissolution of clays. The transformation of carbonates in anhydrite increases the porosity in zones where dolomite is dominant, regarding their molar volumes (table 7).

Dolomite	Calcite	Siderite	Anhydrite
64.93	36.93	29.93	45.16

Table 7: molar volumes of anhydrite, dolomite, calcite and siderite expressed in cm^3/mol.

However, the fractures seem to open on wall rocks, where calcite has precipitated as the last mineral during the geological story of the reservoir. If we consider that anhydrite coat the rock when it precipitates, it could rapidly fill the porosity in zone where calcite is accessible: the average volume ratio of calcite in fractures is 2.5 % (table 1). If we imagine a homogeneous repartition of the porosity, the total reactivity of this mineral with aqueous SO_2 could lead to a loss of 11% of the total porosity of the rock. It could reach 100% in zone where porosity follows the wall rock calcite. This could limit the propagation of the gas in the reservoir and redistribute porosity on zones where dolomite is predominant. Concerning the reactivity of iron, pyrites and aqueous Fe^{2+} from clay alteration will be oxidized and will precipitate as hematite, creating a competition with the expected reaction of stabilization of CO_2 into siderite.

5. Conclusion

The reactivity of a carbonate rock is examined in case of an injection of a CO_2 gas containing fractions of SO_2, O_2, N_2 and Ar. This should exemplify the behaviour of reservoir rocks to store CO_2. Three tests are performed, using inert N_2 as a blank, pure CO_2 and a mixture of CO_2 with O_2 and SO_2. The SO_2 fraction dissolved in the water present in the reservoir reacts with the O_2 fraction to give sulfates and a high acidification of the water. This has for primary consequence to break the stability barrier of the carbonate set by pure CO_2, implying the dissolution of calcite, shortly followed by dolomite. When saturation is reached for anhydrite and barite, they start to precipitate in place of the dissolved carbonates. Pyrite is oxidized in hematite by the remaining O_2 fraction. Concerning the silicates, the experiments show a partial transformation of illites in beidellite-K. Finally, calcite and pyrite are completely altered whereas it remained respectively 90% and 99% of these minerals after reactivity of the rock with pure CO_2. 6% of dolomite is dissolved whereas it remained stable towards pure CO_2. 95% of clays are transformed in beidellite-K against 75% for pure CO_2. The main reactions concerning carbonate dissolution and anhydrite precipitation could lead to the filling of the fracture porosity, located along the wall rock calcite. Thus, the oxidation of iron located in clays and pyrite will enter in competition with the precipitation of siderite and should prevent the CO_2 from mineral stabilization.

Acknowledgements

This work was supported by TOTAL and the French national agency ADEME.

References

Baines, S.J., Worden, R.H. (2004). The long-term fate of CO_2 in the subsurface: Natural analogues for CO_2 storage. Geological Society Special Publication, (233), pp. 59-85.

Bertier, P., Swennen, R., Laenen, B., Lagrou, D., Dreesen, R. (2006). Experimental identification of CO_2-water-rock interactions caused by sequestration of CO2 in Westphalian and Buntsandstein sandstones of the Campine Basin (NE-Belgium). Journal of Geochemical Exploration, 89, pp. 10-14.

Carignan, J. (2001). "Routine analyses of trace elements in geological samples using flow injection and low pressure on-line liquid chromatography coupled to ICP-MS: A study of geochemical reference materials BR, DR-N, UB-N, AN-G and GH." Geostandards Newsletter 25(2-3): 187-198.

Chou, L., Garrels, R.M., Wollast, R. (1989). Comparative study of the kinetics and mechanisms of dissolution of carbonate minerals. Chemical Geology, 78 (3-4), pp. 269-282.

Clochiatti, R., Massare, D., Jehanno, C. (1981). Origine hydrothermale des olivines gemmes de l'ile de Zabargad (St Johns) Mer Rouge, par l'étude de leurs inclusions. Bulletin de Mineralogie, 104 (4), p. 360.

Darimont, A., Coipel, J. (1982). Dispersion des températures d'homogénéisation des inclusions aqueuses - Ébullition ou division par étranglement. Chemical Geology, 37 (1-2), pp. 151-163.

Duan ZH., Sun R., Zhu C. and Liu R. (2006) An accurate model for the calculation of H2S solubility in pure water and brine. To be published by Chemical Geology.

Dubessy, J., Pagel, M., Beny, J.-M., Christensen, H., Hickel, B., Kosztolanyi, C., Poty, B. (1988). Radiolysis evidenced by H_2-O_2 and H_2-bearing fluid inclusions in three uranium deposits. Geochimica et Cosmochimica Acta, 52 (5), pp. 1155-1167.

Dubessy, J., Tarantola, A., Sterpenich, J. (2005) Modelling of liquid-vapour equilibria in the H_2O-CO_2-NaCl and H_2O-H_2S-NaCl systems to 270°C. Oil and Gas Science and Technology, 60 (2), pp. 339-355.

Gaus, I., Azaroual, M., Czernichowski-Lauriol, I. (2005) Reactive transport modelling of the impact of CO2 injection on the clayey cap rock at Sleipner (North Sea). Chemical Geology, 217, pp. 319-337.

Gunter, W.D., Perkins, E.H., Hutcheon, I. (200). Aquifer disposal of acid gases: Modelling of water-rock reactions for trapping of acid wastes. Applied Geochemistry, 15 (8), pp. 1085-1095.

Hansen, P.F.B.(1991) Sulphur Capture in Fluidized Bed Combusters. Ph.D Thesis.

Harvey, C. O. (1943). "Some notes on the calculation of molecular formulae for glauconite." American Mineralogist 28: pp. 541–543.

Holloway, S. (1997) An overview of the underground disposal of carbon dioxide. Energy Conversion and Management, 38, pp. S193-S198.

Jacquemet, N., Pironon, J., Caroli, E. (2005). A new experimental procedure for simulation of H_2S + CO_2 geological storage. Application to well cement aging. Oil and Gas Science and Technology, 60 (1), pp. 193-206.

Johnson, J.W., Oelkers, E.H., Helgeson, H.C., (1992). SUPCRT92: a software package for calculating the standard molal thermodynamic properties of minerals, gases, aqueous species, and reactions from 1 to 5000 bars and 0 to 1000 degrees C. Comput. Geosci. 18, pp899–947.

Kaszuba, J.P., Janecky, D.R., Snow, M.G. (2003). Carbon dioxide reaction processes in a model brine aquifer at 200°C and 200 bars: Implications for geologic sequestration of carbon. Applied Geochemistry, 18 (7), pp. 1065-1080.

Knauss, K.G., Johnson, J.W., Steefel, C.I. (2005). Evaluation of the impact of CO_2, co-contaminant gas, aqueous fluid and reservoir rock interactions on the geologic sequestration of CO_2. Chemical Geology, 217, pp. 339-350.

Korbøl, R., Kaddour, A. (1995).Sleipner vest CO_2 disposal - injection of removed CO_2 into the utsira formation. Energy Conversion and Management, 36 (6-9), pp. 509-512.

Lagneau, V., Pipart, A., Catalette, H. (2005) Reactive transport modelling of CO_2 sequestration in deep saline aquifers. Oil and Gas Science and Technology, 60 (2), pp. 231-247.

Landais, P., Michels, R., and Poty, B. (1989) Pyrolysis of organic matter in cold-seal pressure autoclaves. Experimental approach and applications. Journal of analytical and applied pyrolysis 16, 103-115

Lizzio, A.A., DeBarr, J.A. (1997). Mechanism of SO_2 removal by carbon. Energy and Fuels, 11 (2), pp. 284-291. Cited 43 times.

Lyngfelt, A., Leckner, B. SO_2 capture fluidised-bed boilers: re-emission of SO_2 due to reduction of $CaSO_4$. Chemical Engineering Science, 44 (2), pp. 207-213.

Marini, L. (2007). geological sequestration of carbon dioxide -Thermodynamics, kinetics, and reaction path modelling, Elsevier B.V.

Mattisson, T., Lyngfelt, A. (1998) Reaction between sulfur dioxide and limestone under periodically changing oxidizing and reducing conditions - Effect of cycle time. Energy and Fuels, 12 (5), pp. 905-912.

Moore, J., Adams, M., Allis, R., Lutz, S., Rauzi, S. (2005). Mineralogical and geochemical consequences of the long-term presence of CO_2 in natural reservoirs: An example from the Springerville-St. Johns Field, Arizona, and New Mexico, U.S.A. Chemical Geology, 217, pp. 365-385.

Palandri, J.L., Rosenbauer, R.J., Kharaka, Y.K. (2005). Ferric iron in sediments as a novel CO_2 mineral trap: CO_2-SO_2 reaction with hematite. Applied Geochemistry, 20 (11), pp. 2038-2048.

Plummer, L.N., Wigley, T.M.L., Parkhurst, D.L. (1978). kinetics of calcite dissolution in CO_2-water systems at 5° to 60°C AND 0 to 1.0 atm CO_2. Am J Sci, 278 (2), pp. 179-216.

Pokrovsky, O.S., Golubev, S.V., Schott, J., Castillo, A. (2009). Calcite, dolomite and magnesite dissolution kinetics in aqueous solutions at acid to circumneutral pH, 25 to 150 C and 1 to 55 atm pCO2: New constraints on CO_2 sequestration in sedimentary basins. Chemical Geology, 265 (1-2), pp. 20-32.

Pokrovsky, O.S., Golubev, S.V., Schott, J. (2005). Dissolution kinetics of calcite, dolomite and magnesite at 25 °C and 0 to 50 atm pCO_2. Chemical Geology, 217, pp. 239-255.

Rimstidt, J.D., Barnes, H.L. (1980). The kinetics of silica- water reactions. Geochimica et Cosmochimica Acta, 44 (11), pp. 1683-1699.

Rosenbauer, R.J., Koksalan, T., Palandri, J.L. (2005). Experimental investigation of CO_2-brine-rock interactions at elevated temperature and pressure: Implications for CO_2 sequestration in deep-saline aquifers. Fuel Processing Technology, 86 (14-15), pp. 1581-1597.

Seyfried, W. E. J., Janecky, D. R., and Berndt, M. E. (1987). Rocking autoclaves for hydrothermal experiments. The flexible reaction-cell system. Hydrothermal experimental techniques (ed. Ulmer, G. C. and Barnes, H. L.), pp. 216-239. John Wiley & Sons.

Sterpenich, J., Sausse, J., Pironon, J., Géhin, A., Hubert, G., Perfetti, E., Grgic, D. (2009) Experimental ageing of oolitic limestones under CO_2 storage conditions. Petrographical and chemical evidence. Chemical Geology, 265 (1-2), pp. 99-112.

Teinturier, S., Pironon, J. (2003). Synthetic fluid inclusions as recorders of microfracture healing and overgrowth formation rates. American Mineralogist, 88 (8-9), pp. 1204-1208.

Van Berkum, J.G., Diepen, G.A.M. (1979). Phase equilibria in $SO_2 + H_2O$: the sulfur dioxide gas hydrate, two liquid phases, and the gas phase in the temperature range 273 to 400 K and at pressures up to 400 MPa. The Journal of Chemical Thermodynamics, 11 (4), pp. 317-334.

Van der Lee, J. (1998). Thermodynamic and mathematical concepts of CHESS. Technical Report No. LHM/RD/98/39, École des mines de Paris, Paris.
http://chess.ensmp.fr/download/concepts.pdf

van den Kerkhof, A.M., Olsen, S.N. (1990). A natural example of superdense CO_2 inclusions: Microthermometry and Raman analysis Geochimica et Cosmochimica Acta, 54 (3), pp. 895-901.

Wolery, T. J., and Daveler, S. A., (1992). EQ6, A Computer Program for Reaction-Path Modeling of Aqueous Geochemical Systems: Theoretical Manual, User's Guide, and Related documentation (Version 7.0): UCRL-MA-110662-PT-IV, Lawrence Livermore National Laboratory, Livermore, California.

Xu, T., Apps, J.A., Pruess, K. (2004). Numerical simulation of CO_2 disposal by mineral trapping in deep aquifers. Applied Geochemistry, 19 (6), pp. 917-936.

Xu, T., Apps, J.A., Pruess, K. (2005). Mineral sequestration of carbon dioxide in a sandstone-shale system Chemical Geology, 217, pp. 295-318.

Xu, T., Apps, J.A., Pruess, K., Yamamoto, H. (2007) Numerical modeling of injection and mineral trapping of CO_2 with H_2S and SO_2 in a sandstone formation. Chemical Geology, 242 (3-4), pp. 319-346.

Zerai, B., Saylor, B.Z., Matisoff, G. (2006) Computer simulation of CO_2 trapped through mineral precipitation in the Rose Run Sandstone, Ohio. Applied Geochemistry, 21 (2), pp. 223-240.

5. Perspectives de recherche

Mes recherches tant sur l'altération des verres que sur la modélisation géochimique des interactions eau/gaz/roche m'ont permis d'acquérir une expérience axée sur l'étude :

- des matériaux inorganiques et des méthodes de caractérisation (MEB, MET, sonde électronique, sonde ionique, tomographie X, etc.)
- des solutions aqueuses, diluées ou salines, et de leur chimie
- des systèmes eau-gaz-sel et de leurs interactions
- de la thermodynamique des phases minérales et de leur interaction avec les solutions aqueuses,
- de la thermodynamique des hydrocarbures
- des phénomènes cinétiques de réaction et de transport.
- de l'évolution des roches et matériaux soumis à l'action de CO_2 et de gaz annexes.
- des mécanismes d'altération des verres silicatés.

Aujourd'hui, le laboratoire CO_2 que j'ai contribué à développer est opérationnel et un nombre important de résultats sortent simultanément, expliquant les 6 publications en cours de rédaction actuellement.

Je suis actuellement en co-encadrement de deux thèses, E. Jobard et C. Belgodère, et d'un post-doctorant, H. El Hajj, qui travaillent tous sur les thématiques touchant à la séquestration géologique du CO_2 par une approche expérimentale.

Je me suis aussi investi dans l'acquisition du nanotomographe X qui est un outil indispensable pour appréhender les changements pétrophysiques inhérents à la réactivité des matériaux avec les gaz agressifs injectés. Aussi, j'aimerais continuer à développer l'approche tridimensionnelle couplée aux expériences de vieillissement des roches pour apporter des réponses sur l'évolution de l'injectivité des roches réservoir et sur la tenue des interfaces ciment/couverture et ciment/réservoir afin d'appréhender les possibles risques de fuite.

L'acquisition du spectromètre Raman et les mesures in-situ à haute pression et haute température, ont permis d'obtenir de nouvelles données sur le système carbonate en conditions de stockage. Il s'agit i) de nouvelles données de solubilité du CO_2 à haute pression et en condition supercritique, ii) de la détermination de pH *in-situ*, paramètre indispensable au calage de la modélisation géochimique, et iii) de la détermination des vitesses de diffusion du CO_2 dans les solutions aqueuses. Ces données cruciales, tant du point de vue fondamental qu'appliqué, doivent être complétées et consolidées et j'en fais une de mes priorités dans l'avenir.

La manipulation de gaz dangereux tels que H_2S, CO, SO_2, NO, CH_4 est aujourd'hui possible dans le laboratoire. La première thèse que j'ai encadrée était axée sur le rôle de ces gaz sur l'évolution d'un site de stockage de CO_2. Plus de 120 expériences ont été réalisées sur différents gaz et avec différents mélanges sur des roches et des minéraux d'intérêt. Si les données acquises sont pour la plupart exploitées, il reste encore un travail important de traitement, d'analyse et de modélisation pour tirer le meilleur parti de ces expériences. De plus, d'autres conditions de pression, température et d'autres temps de réaction doivent être testés afin d'aboutir à une meilleure maîtrise de ces systèmes eau/roche/gaz complexes.

La modélisation chimie/transport des systèmes investigués est d'une grande importance si on souhaite estimer l'évolution d'un stockage de CO_2 à court, moyen et long terme. Pour les laboratoires nancéens qui disposent d'une longue expérience de modélisation 3D, il est un challenge de pouvoir s'imposer et se créer une expertise dans le monde de la modélisation géochimique. Avec mes collègues géochimistes et géo-modélisateurs, j'aimerais participer à la mise en place d'une plate-forme numérique couplant l'ensemble des aspects de modélisation des systèmes naturels afin de pouvoir répondre globalement à la problématique de la séquestration du CO_2, de l'expérience à la prédiction de l'évolution du stockage. Il apparaît évident que la thématique de l'injection de gaz doit apparaître comme un objet d'étude et que les expériences acquises dans ce domaine sont transposables facilement dans les domaines des ressources pour ne citer que ce sujet hautement stratégique actuellement.

Mon investissement dans ces thématiques passe également par la participation à la rédaction en 2011 de deux projets nationaux (ZHIMPA et SIGARR) suite à l'appel d'offres ANR SEED sur les énergies décarbonées. Je porte la responsabilité scientifique pour l'Université de Lorraine du projet SIGARR qui traite principalement de l'acquisition de données thermodynamiques sur gaz annexes en conditions de stockage.

Enfin, j'aimerais continuer à mettre à profit mon expérience de l'altération des verres sur des sujets couplant sciences expérimentales et sciences sociales à travers notamment l'étude de nouvelles découvertes archéologiques. Je participe à ce titre à une recherche archéologique sur des verres de vaisselles et de tesselles issus d'un monastère proche de Gaza dont l'activité a duré du IV$^{\text{ème}}$ au VIII$^{\text{ème}}$ siècle. Outre l'aspect historique concernant par exemple le savoir-faire des verriers ou la provenance des matériaux utilisés pour la fabrication des verres, ces échantillons offrent la possibilité d'améliorer la documentation de l'altération de verres riches en métaux lourds, en plomb notamment, sur des périodes de temps de 1700 ans. Ce sujet, couplant des aspects sociaux-culturels à des aspects de recherche fondamentale (compréhension des mécanismes d'altération) et de recherche appliquée (taux de relâchement de polluants dans des matrices vitreuses), représente un bel exemple de recherche transverse entre sciences humaines et sciences dures.